THE UNIVERSITY
of EDINBURGH

DNA replication and repair in microcephalic dwarfism

Žygimantė Tarnauskaitė

PhD by Research

University of Edinburgh

2018

Declaration

This thesis has been composed entirely by me. Apart from where stated, the experiments were carried out solely by me. The work in this thesis has not been submitted for any other degree or professional qualification.

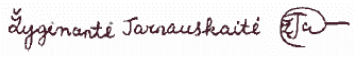

Žygimantė Tarnauskaitė,

November 2018

Abstract

Human height varies greatly between and within populations, and some individuals fall at the extreme ends of this wide spectrum. At the lower end of this distribution, individuals demonstrating extreme prenatal-onset reduction in body size and brain growth are classified as having microcephalic primordial dwarfism (MPD), which encompasses a group of rare single-gene disorders, usually inherited in an autosomal recessive manner. The human brain is particularly susceptible to perturbation during embryonic development, and the inability of neural progenitor cells to complete timely proliferation is thought to be an important contributor to the observed reduction in cerebral cortical size.

Studying genes whose disruption leads to severe reduction in human growth can facilitate our understanding of the molecular pathways underlying cell proliferation and organism development. Mutations in many identified MPD genes result in the extended length of the cell cycle and impaired cell division by affecting essential cellular processes, such as DNA replication, DNA damage response (DDR) signalling, centriole biogenesis and mRNA splicing. The ability of cells to efficiently copy DNA and maintain the stability of their genome by promoting error-free repair of various types of DNA damage caused by endogenous and exogenous sources is particularly important for the timely cell cycle completion and cell survival. Therefore, it is not surprising that many MPD genes play a role in DNA replication, DDR and DNA repair.

In this thesis, three DNA replication and DDR genes, mutated in MPD, are investigated. *DNA2*, encoding an ATP-dependent helicase/nuclease, was found to be mutated in four MPD patients. Experiments to confirm pathogenicity of the identified mutations indicated that they are likely to cause disease by affecting DNA2 transcript splicing and its enzymatic activities. My work described here also analyses the cellular role of TRAIP, an E3 ubiquitin ligase, which was linked to MPD by our laboratory (Harley *et al.*, 2016). Cell experiments using TRAIP knockout cell lines, generated with CRISPR/Cas9 genome editing technology, demonstrated the requirement for TRAIP and its E3 ligase activity in DDR and repair of camptothecin (CPT)-induced DNA damage. Additionally, TRAIP was important for cell survival after mitomycin C (MMC)-induced DNA damage, but no epistasis with the Fanconi Anaemia (FA) interstrand crosslink (ICL) repair pathway was demonstrated, indicating an additive effect of TRAIP and FA-ICL pathways to repair these DNA lesions.

Finally, generation of a mouse model of MPD caused by mutations in *DONSON*, a novel replication fork protection factor (Reynolds *et al.*, 2017), is described in this thesis. DONSON MPD mice, harbouring the mouse equivalent of one of the human MPD missense mutations, showed embryonic lethality, with homozygous mutant embryos significantly smaller than their littermates and exhibiting limb abnormalities. Increased levels of spontaneous DNA damage were observed in mouse embryonic fibroblasts established from these embryos, mimicking the cellular phenotype of human DONSON deficiency.

In summary, this thesis advances our knowledge of the cellular and developmental roles of MPD genes *TRAIP*, *DNA2*, and *DONSON*, that encode proteins maintaining genome stability.

Lay summary

Variation in size is one of the most striking features in mammals, ranging from a tiny bumblebee bat to a large blue whale, with a 75 million-fold weight difference. Human population also exhibits noticeable differences in size and height, influenced both by environment and genetics. However, in rare cases, some individuals can be extremely small for their age, showing proportional reduction in both body growth and brain size, which starts before birth and continues into adulthood. These conditions are classified as microcephalic primordial dwarfism (MPD), which encompasses a number of disorders caused by inactivation of a single gene. Studying these syndromes and their genetic causes can give us insight into what underlies human growth at the level of an individual cell.

One of the most important biological processes taking place in cells is DNA replication, which is the copying of all the genetic information and has to be completed without any errors. This allows cells to divide creating two new copies of a cell and is crucial for an organism to grow. Various alterations to DNA structure, collectively called DNA damage, can prevent the timely DNA replication and cell division. Perhaps not surprisingly, previous research by our and other laboratories demonstrated that mutations in multiple proteins that participate in DNA replication and repair of the DNA damage can cause MPD.

The work described in this thesis aims to investigate the cellular roles of three distinct DNA replication and repair genes, mutated in MPD. In our laboratory, several MPD patients were found to have mutations in the DNA replication and repair gene *DNA2*. The approaches taken to demonstrate the harmful effect of these mutations indicated that disruption of the DNA2 enzymatic activities may underlie the human disease. Another MPD gene, *TRAIP*, which encodes a protein needed to signal DNA damage in cells, is shown to be required for efficient cell response to various types of DNA damage. A third gene, *DONSON*, encodes a recently established DNA replication factor. A mouse model of MPD was made with mutations in this gene to understand its role during embryonic development.

Taken together, the work presented in this thesis provides new insights into the roles of three MPD genes, involved in DNA replication, DNA damage signalling and repair, at the level of an individual cell and in development.

Acknowledgements

There are many people who I would like to thank for helping me during the last four years.

I am extremely grateful to my excellent supervisory team, Andrew, Martin and Olga, for their guidance, encouragement, patience and valuable discussions during the planning and development of this research work. I could not imagine having more supportive supervisors and would sincerely wish every PhD student to have the PhD experience I had.

I would also like to express my gratitude to current and previous members of the Andrew Jackson laboratory, particularly to Patty, Carol-Anne, Adeline, Jennie, Andrea, Dave, Clare, Maggie, Louise, Kaalak and Paula, for their useful suggestions regarding experimental work, willingness to share their expertise and advice, and technical support, as well as for all the fun and positive work environment.

I am also grateful to the amazing technical staff at IGMM, including but not limited to Ann, Matt, Harris, Laura, Lizzie, Stephen, Jeff, Stewart, Sean, Joan, Pam, Pat and Alan.

Additionally, I would like to take this opportunity to thank Alex Von Kriegsheim for mass spectrometry; Joe Marsh for mutation modelling; Lin Deng and the Brigham & Women's Hospital CytoGenomics Core Facility (Boston, MA) for karyotyping analysis; my thesis committee members Ian Adams, Ian Jackson and Maria Christophorou for their useful advice regarding my work progress; and my thesis examiners Anne Donaldson and Kathryn Ball for their insightful comments and suggestions.

I also want to thank the patients, their families and their clinicians for the contribution to advancing the research on microcephalic dwarfism.

I thank the Medical Research Council (MRC) for funding my postgraduate studies.

I would like to thank my parents Egidija and Arūnas, sister Ringailė and grandmother Laimutė for their continuous love and encouragement.

I am also immensely grateful to my husband Daniel for the best bus ride, for his guidance and support, for being my soulmate, and for all great things we did together.

Finally, I would like to thank my baby for the entertainment. I am looking forward to meeting you soon.

Table of Contents

List of figures

List of tables

Abbreviations

*	Translation stop codon
53BP1	p53-Binding Protein 1
A	Alanine (Ala); absorbance
aa	Amino acid
ADP	Adenosine diphosphate
ATCC	American Type Culture Collection
ATM	Ataxia Telangiectasia Mutated
ATP	Adenosine triphosphate
ATR	Ataxia Telangiectasia mutated and Rad3 related
bp	Base pair
BRCA1/2	BReast CAncer susceptibility gene 1/2
BrdU	5-bromo-2'-deoxyuridine
BSA	Bovine Serum Albumin
C	Cysteine (Cys)
c.	Coding
CADD	Combined Annotation Dependent Depletion
CDC	Cell Division Cycle
CDKs	Cyclin-Dependent Kinases
cDNA	Complementary DNA
CHK1/2	CHeckpoint Kinase 1/2
CPT	Camptothecin
CRISPR	Clustered Regularly Interspaced Short Palindromic Repeats
CtIP	CtBP Interacting Protein
Δ, del	Deletion
DAPI	4',6-diamidino-2-phenylindole
DDR	DNA damage response
dH_2O	Distilled water
DMEM	Dulbecco's Modified Eagle Medium
DMSO	Dimethyl sulfoxide
DNA	Deoxyribonucleic acid
DNA-PK	DNA-dependent protein kinase
DNA-PKcs	DNA-PK catalytic subunit

DNase	Deoxyribonuclease
dNTP	Deoxyribonucleotide triphosphate
DSB	Double-strand break
dsDNA	Double-stranded DNA
DTT	Dithiothreitol
E	Embryonic day
ECACC	European Collection of Authenticated Cell Cultures
EDTA	Ethylene diamine tetra-acetic acid
EdU	5-ethynyl-2´-deoxyuridine
EGFP	Enhanced Green Fluorescent Protein
EtOH	Ethanol
Ex	Exon
EXO1	Exonuclease 1
FA	Fanconi Anaemia
FACS	Fluorescence-activated cell sorting
FANCD2	Fanconi ANemia Complementation group D type 2
FBS	Fetal Bovine Serum
FITC	Fluorescein isothiocyanate
g	Grams
GFP	Green Fluorescent Protein
gRNA	Guide RNA
GST	Glutathione S-transferase
γH2AX	H2AX phosphorylated on serine 139
h	Hour(s)
H2AX	H2A histone family, member X
HA	Hemagglutinin
HCl	Hydrochloric acid
HDR	Homology-directed repair
HEPES	4-(2-hydroxyethyl)-1-piperazineethanesulfonic acid
HR	Homologous recombination
hTERT	Human telomerase reverse transcriptase
HU	Hydroxyurea
ICL	Interstrand crosslink
ins	Insertion

int	Intron
IPTG	Isopropyl β-D-1-thiogalactopyranoside
IR	Ionizing radiation
K	Lysine (Lys)
kb	Kilobase
kDa	Kilodaltons
KO	Knockout
LB	Luria-Bertani
M	Molar
MCM	Mini-Chromosome Maintenance
MEF(s)	Mouse embryonic fibroblast(s)
MGS	Meier-Gorlin Syndrome
min	Minute(s)
MMC	Mitomycin C
MMS	Microcephaly-micromelia syndrome
MPD	Microcephalic primordial dwarfism
MRN	MRE11-RAD50-NBS1
mRNA	Messenger RNA
MS	Mass spectrometry
N-	N-terminal
N/A	Not available; not applicable
Neo	Neomycin
NER	Nucleotide excision repair
NHEJ	Non-homologous end-joining
NMD	Nonsense-mediated decay
nt	Nucleotide
NTP	Nucleoside triphosphate
OD	Optical density
ORC	Origin Recognition Complex
P	Patient
p	Phospho-, phosphorylated
p.	Amino acid position
PAM	Protospacer adjacent motif
PBS	Phosphate buffered saline

PCNA	Proliferating Cell Nuclear Antigen
PCR	Polymerase chain reaction
PI3K	Phosphotidyl-Inosine-3 Kinase
PIKK	PI3K-related serine-threonine protein Kinase
PIPES	Piperazine-N,N′-bis(2-ethanesulfonic acid)
PMSF	Phenylmethylsulfonyl fluoride
Pre-IC	Pre-initiation complex
Pre-RC	Pre-replication complex
R	Arginine (Arg)
RNA	Ribonucleic acid
RNAi	RNA interference
RNase	Ribonuclease
RPA	Replication Protein A
rpm	Revolutions per minute
RT	Reverse transcriptase
S	Serine (Ser)
SCE	Sister Chromatid Exchange
SD	Standard deviation
SDS	Sodium dodecyl sulphate
sec	Second(s)
SEM	Standard error of the mean
siRNA	Short/small interfering RNA
sgRNA	Single guide RNA
SNP	Single nucleotide polymorphisms
SSB	Single-strand break
ssDNA	Single-stranded DNA
ssODN	Single-stranded oligodeoxynucleotide
T	Threonine (Thr)
TBE	Tris/Borate/EDTA
TBS/T	Tris-Buffered Saline with Tween 20
TLS	TransLesion Synthesis
T_m	Melting temperature
TOP1	DNA topoisomerase I
Top1cc	TOP1 covalent complex

Tris	Tris(hydroxymethyl)aminomethane
TxRed	Texas Red (sulforhodamine 101 acid chloride)
U	Units
Ub	Ubiquitin
UTR	Untranslated region
UV	Ultraviolet light
UV-C	Short-wave ultraviolet light (100–280 nm)
V	Volt
v/v	Volume of solution in the total volume of solution
w/v	Weight of solution in the total volume of solution
W	Tryptophan (Trp)
WES	Whole exome sequencing
WT	Wild-type
X	Times
x g	Relative centrifugal force

Chapter 1

Introduction

1. Introduction

1.1. Disorders of brain size and body growth

1.1.1. Microcephaly and primordial dwarfism

Human height is a classical quantitative trait with a polygenic additive mode of inheritance (Visscher, 2008). However, mutations in certain genes can cause extreme alterations in stature and brain size, ranging from primary microcephaly to microcephalic primordial dwarfism. Primary autosomal recessive microcephaly is a congenital condition, defined by the reduction of the occipito-frontal circumference (OFC) of the head by at least 4 standard deviations (SD) below the age- and sex-matched average, with overall height normally unaffected (Faheem *et al.*, 2015; Jackson *et al.*, 2002; Roberts *et al.*, 2002). It is associated with impaired fetal brain growth, mild or moderate cognitive impairment, simplification of the cerebral cortical gyral pattern, and the absence of additional neurological deficits (Ross and Frias, 1977; Woods *et al.*, 2005). Primary microcephaly occasionally occurs alongside primordial dwarfism or other congenital abnormalities (Woods and Parker, 2013). Microcephalic primordial dwarfism (MPD) is defined as a group of single-gene disorders, where both brain and body size get severely affected very early during fetal development and continue to be impaired after birth (Klingseisen and Jackson, 2011). Adult height of individuals affected by such an extreme global growth failure may be as little as 1 metre, and growth hormone supplementation does not increase the height of these patients (Hall *et al.*, 2004).

MPD is an umbrella term for several distinct, usually autosomal recessive, growth failure syndromes, characterised by marked growth retardation throughout the body, with the head size as affected or more affected than the overall body growth (Woods and Parker, 2013). In microcephalic osteodysplastic primordial dwarfism type 2 (MOPD II), the affected individuals are proportionally small, with severe prenatal and postnatal retardation in height, weight and OFC, with OFC ranging from −5 SD to −15 SD (Rauch, 2011; Woods and Parker, 2013). Although their intellectual abilities are largely unaffected, individuals with MOPD II tend to have mild skeletal and facial abnormalities and suffer from juvenile mortality due to neurovascular and cardiac problems, as well as insulin resistance (Bober *et al.*, 2010; Rauch, 2011; Woods and Parker, 2013). In contrast, microcephalic osteodysplastic primordial dwarfism type 1 (MOPD I) patients frequently have cortical malformations, incompletely developed corpus callosum,

seizures, skin and hair problems, and skeletal abnormalities (Khetarpal *et al.*, 2016). Disproportionate growth retardation, which affects head circumference to a larger extent than the body size, represents another type of MPD, known as Seckel syndrome. Individuals with Seckel syndrome are very small at birth and usually show severe reduction in head size, prominent bird-like facial features and mental retardation (Majewski *et al.*, 1982). Lastly, Meier-Gorlin syndrome (MGS), also called ear-patella-short stature syndrome (EPS), is characterised not only by the impairment of intrauterine and postnatal growth and microcephaly, but also by absent or underdeveloped patellae and small ears, and despite the presence of microcephaly, intellectual abilities of patients are largely unaffected (Bongers *et al.*, 2001; Bicknell, Walker, *et al.*, 2011).

During the recent Zika virus outbreak in Brazil in 2015, Zika virus infection during pregnancy was strongly associated with congenital brain abnormalities and microcephaly (de Araújo *et al.*, 2017). Although it remains difficult to estimate the number of affected newborn children, Brazilian Ministry of Health reported an apparent 20-fold increase in microcephaly incidence, compared to historical statistics (Koppolu and Raju, 2018). Although causes and phenotypic characteristics of Zika virus-associated microcephaly and primary autosomal recessive microcephaly are distinct (Aragao *et al.*, 2016; Merfeld *et al.*, 2017), this epidemic has brought microcephaly to people's attention worldwide.

1.1.2. The genetics of microcephalic primordial dwarfism

To date, mutations in at least 40 genes have been associated with microcephaly and MPD (***Table 1.1***), and many of them are thought to cause disease by prolonging the cell cycle and affecting cell proliferation, particularly of neural progenitor cells, subsequently resulting in the reduction of total cell numbers throughout the body and brain (Klingseisen and Jackson, 2011). The proteins encoded by these genes are frequently found to participate in several essential cellular processes, including DNA damage response (DDR) signalling, DNA replication, cell division and mRNA splicing (***Table 1.1***). The first gene identified to cause Seckel syndrome was *ATR*, encoding the Phosphotidyl-Inosine-3 Kinase (PI3K)-like Ataxia-Telangiectasia and Rad3-related kinase (O'Driscoll *et al.*, 2003). ATR is a key DDR kinase that is activated in response to replication fork stalling by sensing single-stranded DNA (ssDNA) coated with Replication Protein A complex (RPA) (Cimprich and Cortez, 2008). A synonymous homozygous mutation in *ATR* that affected its splicing was identified as a disease-causing variant, resulting

in highly reduced levels of functional ATR protein and consequent defective H2AX phosphorylation following UV irradiation, which marks ATR-dependent DDR activation (O'Driscoll *et al.*, 2003). Compound heterozygous mutations in *ATRIP*, encoding ATR-Interacting Protein required for ATR stability and recruitment to DNA damage sites (Cortez *et al.*, 2001), were also demonstrated as a cause of MPD via reduced ATRIP and ATR protein levels (Ogi *et al.*, 2012). Furthermore, the first gene identified to cause primary microcephaly, microcephalin (*MCPH1*), was also shown to function in the ATR signalling pathway (Alderton *et al.*, 2006). In recent years, several other DDR and DNA repair factors were also associated with MPD. Biallelic mutations in *RBBP8*, encoding CtBP-Interacting Protein (CtIP), were found to cause Seckel syndrome through impaired DNA end resection and ATR activation in response to DNA damage (Qvist *et al.*, 2011). Additionally, mutations affecting XRCC4 and LIG4, components of the Non-Homologous End Joining (NHEJ) DNA double-strand break (DSB) repair pathway, were also demonstrated to cause MPD (Murray *et al.*, 2015, 2014). More recently, homozygous missense and nonsense mutations in *TRAIP*, encoding an E3 ubiquitin ligase, were found to cause Seckel-like syndrome (Harley *et al.*, 2016). Moreover, a large cohort of MPD patients with homozygous splicing or missense mutations in *DONSON*, which encodes a replication fork protection factor, were identified (Reynolds *et al.*, 2017). These studies provide a strong link between defective DNA repair and severe reduction in human growth, and it is likely that other MPD-causing variants in DDR signalling factors will be identified in the future.

Table 1.1. Primary microcephaly and microcephalic primordial dwarfism genes.
Summary of primary microcephaly and microcephalic primordial dwarfism (MPD) genes, identified so far and given Mendelian Inheritance in Man (MIM) disorder code in Online Mendelian Inheritance in Man (OMIM) database of genetic disorders and traits.

Condition	Phenotype MIM number	Gene(s)	Gene function	Biallelic mutation type	Reference(s)
Primary autosomal recessive microcephaly	616171	*PLK4*	Centriole biogenesis	Truncating	Martin *et al.* (2014)
	251270	*TUBGCP6*	Centriole biogenesis	Truncating/ missense	Puffenberger *et al.* (2012); Martin *et al.* (2014)
	251200	*MCPH1*	Chromosomal condensation, DNA damage response signalling	Truncating	Jackson *et al.* (1998); Jackson *et al.* (2002)
	608716	*ASPM*	Mitotic spindle function, component of centrosome	Truncating	Bond *et al.* (2002)

Condition	Phenotype MIM number	Gene(s)	Gene function	Biallelic mutation type	Reference(s)
	604804	*CDK5RAP2*	Mitotic spindle function, component of centrosome	Truncating/ splicing	Moynihan *et al.*, (2000); Bond *et al.* (2005)
	612703	*STIL*	Centriole duplication	Truncating/ splicing/ missense	Kumar *et al.* (2008)
	604317	*WDR62*	Spindle pole protein, component of centrosome	Truncating/ missense	Bilgüvar *et al.* (2010)
	604321	*KNL1 (CASC5)*	Spindle assembly checkpoint signalling, component of centrosome	Truncating/ missense	Genin *et al.* (2012)
	614673	*CEP135*	Centriole and basal body assembly	Truncating/ splicing	Hussain *et al.* (2012)
	616080	*CDK6*	Cell cycle control, microtubule organisation	Missense	Hussain *et al.* (2013)
	617983	*NCAPD2, NCAPD3, NCAPH*	Mitotic chromosome assembly and segregation	Truncating/ splicing/ missense	Martin *et al.* (2016)
	615414	*PHC1*	Cell cycle regulation, chromatin remodelling	Missense	Awad *et al.* (2013)
	615095	*ZNF335*	Neuronal gene expression and cell fate regulation	Splicing/ missense	Yang *et al.* (2012)
Primary autosomal recessive microcephaly; Seckel syndrome	608393; 613676	*CPAP (CENPJ)*	Centriole biogenesis	Splicing	Leal *et al.* (2003); Bond *et al.* (2005)
	614852; 613823	*CEP152*	Centriole biogenesis, genome stability	Splicing/ missense	Guernsey *et al.* (2010); Kalay *et al.* (2011)
Seckel syndrome	614728	*CEP63*	Microtubule organisation, component of centrosome	Truncating	Sir *et al.* (2011)
	614851	*NIN*	Asymmetric cell division, component of centrosome	Missense	Dauber *et al.* (2012)
	210600	*ATR*	DNA damage response signalling	Splicing	O'Driscoll *et al.* (2003)
	210600	*ATRIP*	DNA damage response signalling	Truncating	Ogi *et al.* (2012)
	606744	*RBBP8*	DNA repair	Splicing/ missense	Qvist *et al.* (2011)
	615807	*DNA2*	DNA replication and repair	Splicing	Shaheen *et al.* (2014)
	616777	*TRAIP*	DNA damage response signalling	Truncating/ missense	Harley *et al.* (2016)

Condition	Phenotype MIM number	Gene(s)	Gene function	Biallelic mutation type	Reference(s)
	617253	*NSMCE2*	DNA repair	Truncating	Payne *et al.* (2014)
Meier-Gorlin syndrome	224690	*ORC1/4/6, CDT1, CDC6*	DNA replication licensing (pre-initiation complex subunits)	Truncating/ missense	Bicknell, Bongers, *et al.* (2011); Bicknell, Walker, *et al.* (2011); Guernsey *et al.* (2011)
	617564	*MCM5*	DNA replication (pre-initiation complex subunit)	Truncating/ missense	Vetro *et al.* (2017)
	617063	*CDC45*	DNA replication (pre-initiation complex subunit)	Truncating/ missense/ splicing	Fenwick *et al.* (2016)
	616835	*GMNN*	Regulation of DNA replication	Truncating/ missense	Burrage *et al.* (2015)
Microcephaly and short stature with other characteristics	616541	*XRCC4*	DNA repair (Non-Homologous End Joining)	Truncating/ missense	Shaheen *et al.* (2014); Murray *et al.* (2015)
	606593	*LIG4*	DNA repair (Non-Homologous End Joining)	Truncating	Murray *et al.* (2014)
	614833	*RTTN*	Ciliary structure maintenance	Truncating/ missense	Kheradmand Kia *et al.* (2012)
	615789	*CRIPT*	Cytoskeletal-membrane interactions	Truncating	Shaheen *et al.* (2014)
Microcephaly and short stature with other characteristics; microcephaly-micromelia syndrome	617604; 251230	*DONSON*	Replication fork stability, checkpoint activation	Truncating/ missense/ splicing	Reynolds *et al.* (2017); Evrony *et al.* (2017)
MOPD II	210720	*PCNT*	Component of centrosome, DNA damage response signalling	Truncating	Griffith *et al.* (2008); Rauch *et al.* (2008)
MOPD I	210710	*RNU4ATAC*	mRNA splicing	Missense	Edery *et al.*, (2011); He *et al.* (2011)

Genes encoding subunits of the pre-Replication Complex (pre-RC), *ORC1/4/6*, *CDC6*, and *CDT1*, were identified as another functionally distinct group of MPD genes, causing Meier-Gorlin syndrome (MGS) (Bicknell *et al.*, 2011a, 2011b; Guernsey *et al.*, 2011). This protein complex licenses DNA replication as it assembles on genomic DNA at origins of replication during late M and early G1 phase of the cell cycle, subsequently facilitating recruitment of the Mini-Chromosome Maintenance (MCM2-7) complex, which is a part of the replicative CMG (CDC45-MCM-GINS) helicase (Bochman and Schwacha, 2009). The MPD-associated partial loss-of-function mutations in the ORC complex subunits are likely to lead to inefficient MCM loading, which then results in fewer replication origins being licensed. Indeed, patient-derived ORC1-deficient cells showed a subtle delay in G1/S transition and S phase progression, most likely because a certain number of fully licensed origins must be reached before a cell can enter S phase (Bicknell *et al.*, 2011b). Efficient licensing of replication origins might become crucial during very rapid cell proliferation with shortened G1 phase, which occurs during mammalian development (Takahashi *et al.*, 1995). Defective function of the replication licensing complex may then become a limiting factor, slowing cellular proliferation and consequently resulting in reduced cell number and a smaller individual. Further strengthening the link between defective DNA replication initiation and MGS, mutations in *MCM5* (Vetro *et al.*, 2017) and *CDC45* (Fenwick *et al.*, 2016), which encode subunits of the replicative CMG helicase, were also recently associated with this syndrome. Furthermore, MGS was also shown to be caused by dominant gain-of-function mutations in *GMNN* (Burrage *et al.*, 2015), encoding CDT1 inhibitor geminin, which prevents the incorporation of the MCM complex into the pre-RC (McGarry and Kirschner, 1998; Wohlschlegel *et al.*, 2000). The *de novo GMNN* mutations were shown to result in proteins lacking the destruction box, consequently leading to increased protein stability and impaired replication licensing (Burrage *et al.*, 2015). Thus, DNA replication initiation is one of the cellular processes impaired in MPD, and other associated genes are likely to be identified as causative in the future.

Dysfunctional centriole function and mitotic spindle defects represent another pathway leading to pathogenesis observed in microcephaly and MPD syndromes. Biallelic mutations associated with impaired cell division are more likely to disproportionately affect the brain size, resulting in prominent primary microcephaly (***Table 1.1***). In contrast, biallelic truncating mutations in *PCNT* cause equal reduction of both body and head size (Griffith *et al.*, 2008; Rauch *et al.*, 2008). Mutations in this gene, which encodes the centrosomal protein pericentrin that facilitates formation of the mitotic spindle, resulted in failure to produce functional PCNT protein, thus impairing mitosis (Griffith *et al.*, 2008; Rauch *et al.*, 2008).

Additionally, MPD patients with mutations in *PCNT* had defects in ATR-dependent checkpoint signalling, linking this centrosomal protein to DDR (Griffith *et al.*, 2008). Several genes playing key roles in centriole biogenesis were also associated with primary microcephaly and MPD, notably *PLK4* (Martin *et al.*, 2014), *CENPJ* (Bond *et al.*, 2005; Leal *et al.*, 2003) and *CEP152* (Guernsey *et al.*, 2011; Kalay *et al.*, 2011), strengthening the idea that slower cell cycle progression and inefficient mitosis could explain the reduced cell number and thus overall growth failure in MPD patients.

Finally, another type of MPD, MOPD I, a condition with severe growth retardation and body malformations, was shown to be caused by loss-of-function mutations in *RNU4ATAC*, encoding a minor spliceosome component, the U4atac small nuclear RNA (snRNA) (Edery *et al.*, 2011; He *et al.*, 2011). U4atac is essential for splicing of atypical U12-type introns, which can be found in about 700 human genes that are involved in DNA replication and repair, transcription, mRNA processing, and translation (Sheth *et al.*, 2006; Will and Lührmann, 2005). It is possible that defective splicing of certain U12 intron-containing transcripts could explain the phenotype of MOPD I patients. More recently, mutations in *RNU4ATAC* were also demonstrated to cause Roifman Syndrome through a characteristic compound heterozygosity pattern, with one variant always affecting U4atac elements already implicated in MOPD I (Merico *et al.*, 2015). Although Roifman Syndrome is also characterised by poor pre- and postnatal growth, it is phenotypically distinct from MOPD I and is additionally associated with antibody deficiency, bone dysplasia and retinal dystrophy (Roifman, 1999).

Recent improvements in next-generation sequencing technology greatly facilitated the discovery of new disease-associated genes, and it is likely that many novel primary microcephaly and MPD genes will be identified in the near future. Moreover, novel cellular processes may be implicated in MPD pathogenesis, and their identification will provide a more complete picture of the molecular mechanisms underlying these human growth disorders and growth regulation.

1.2. DNA replication

1.2.1. Replication initiation, replisome assembly and replication elongation

As one of the fundamental processes of life, DNA replication has been a major focus of molecular biology studies from the very beginning of its discovery, although many aspects of it still remain to be defined. During each cell cycle, all genetic material of a cell has to be accurately copied once, and only once, for cell division to take place. DNA replication is a highly regulated and coordinated process that the cell has to perform flawlessly to ensure the survival of its genetic content. To accomplish the error-free copying of billions of base pairs, multiple specialised proteins are needed, some of which will be discussed in this section.

DNA replication is initiated in a multi-step process at replication origins, which provide a platform for assembly of a large group of proteins known as the pre-Replication Complex (pre-RC) (Parker *et al.*, 2017) (***Figure 1.1***). During final stages of mitosis or G1 phase, the heterohexameric Origin Recognition Complex (ORC) binds the origin DNA in eukaryotic cells and, once joined by the helicase loader CDC6 and the chaperone CDT1, aids the head-to-head loading of inactive double heterohexamers of the Mini-Chromosome Maintenance 2-7 (MCM2-7) replicative helicase complex (Riera *et al.*, 2014). The presence of the core MCM complex renders chromatin 'licensed' for replication and the origin ready to be activated. As the binding of the human ORC complex is not restricted to specific DNA sequences, epigenetic mechanisms, such as nucleosome positioning and chromatin structure, have been suggested to play an important role in regulating replication initiation (Schaarschmidt *et al.*, 2004; Vashee *et al.*, 2003). More recently, ORC was indeed demonstrated to bind open chromatin regions with active chromatin marks, such as acetylated histone H3 and methylated H3 lysine 4 (Dellino *et al.*, 2013; Miotto *et al.*, 2016). Additionally, histone acetylase HBO1 (Feng *et al.*, 2015; Miotto and Struhl, 2010), ATP-dependent chromatin remodeler SNF2H (Sugimoto *et al.*, 2011; Zhou *et al.*, 2005) and histone chaperone GRWD1 (Sugimoto *et al.*, 2015) were also implicated in rearranging chromatin at replication origins and thus promoting MCM2-7 loading, replication licensing and initiation. Furthermore, RAP1-Interacting Factor 1 (RIF1)-directed protein phosphatase 1 (PP1) was shown to promote origin licencing by inhibiting premature phosphorylation and degradation of ORC1, as well as limit DNA replication by dephosphorylating the MCM complex subunits (Hiraga *et al.*, 2017, 2014). However, it remains unclear how the loaded MCM complexes are selected for activation, as many of them are rendered functionally inactive in each cell cycle once they are passed by a replisome originated

at another locus (Santocanale *et al.*, 1999). In each cell cycle, the selection of active MCM complexes is likely to be governed by a rather stochastic mechanism, where the MCM activation at some replication origins simply takes place earlier than at the others (Kelly, 2017).

Once cells enter S phase, the downregulation, suppression or relocalisation of the pre-RC complex components prevents DNA re-replication (Calzada *et al.*, 2000; Labib *et al.*, 1999; Nguyen *et al.*, 2001, 2000). To initiate DNA replication, many replication fork proteins assemble on the pre-RC-bound replication origins to form the pre-initiation complex (pre-IC) (***Figure 1.1***). Two kinases, DDK (Dbf4-Dependent CDC7 Kinase) and S-CDK (S phase Cyclin-Dependent Kinase), phosphorylate MCMs and other replication fork proteins and promote recruitment of CDC45 (Cell Division Cycle 45) and the four-subunit complex GINS (Go-Ichi-Ni-San), which are essential for the conversion of the MCM2-7 complex into the fully active CMG (CDC45-MCM-GINS) helicase capable of translocating on ssDNA (Heller *et al.*, 2011; Yeeles *et al.*, 2015). In addition to the protein kinases, the correct assembly and activity of the CMG helicase relies upon several other proteins, including RECQL4, Treslin and TOPBP1, which were shown to interact with DNA Polymerase epsilon (Pol ε) once it associates with the helicase (Araki *et al.*, 1995; Kamimura *et al.*, 2001, 1998; Tanaka and Araki, 2013). The initial DNA unwinding and initiation of the replication bubble at an origin is driven by one additional protein, MCM10, which was demonstrated to bind MCM2, alter structural conformation of CMG and subsequently stabilise CDC45 and GINS association with the MCM complex, as well as facilitate replication elongation later on (Kanke *et al.*, 2012; Lõoke *et al.*, 2017; van Deursen *et al.*, 2012; Watase *et al.*, 2012). Once DNA is unzipped, ssDNA-binding Replication Protein A (RPA) is needed to protect the exposed ssDNA regions from winding back on itself and restrict formation of aberrant secondary structures (Chen *et al.*, 2013). As the CMG helicase unzips the double helix, topological alterations due to the rotational motion of the enzyme generate supercoiled DNA ahead of the helicase, and specialised enzymes, called topoisomerases, are necessary to release the tension (Wang, 2002).

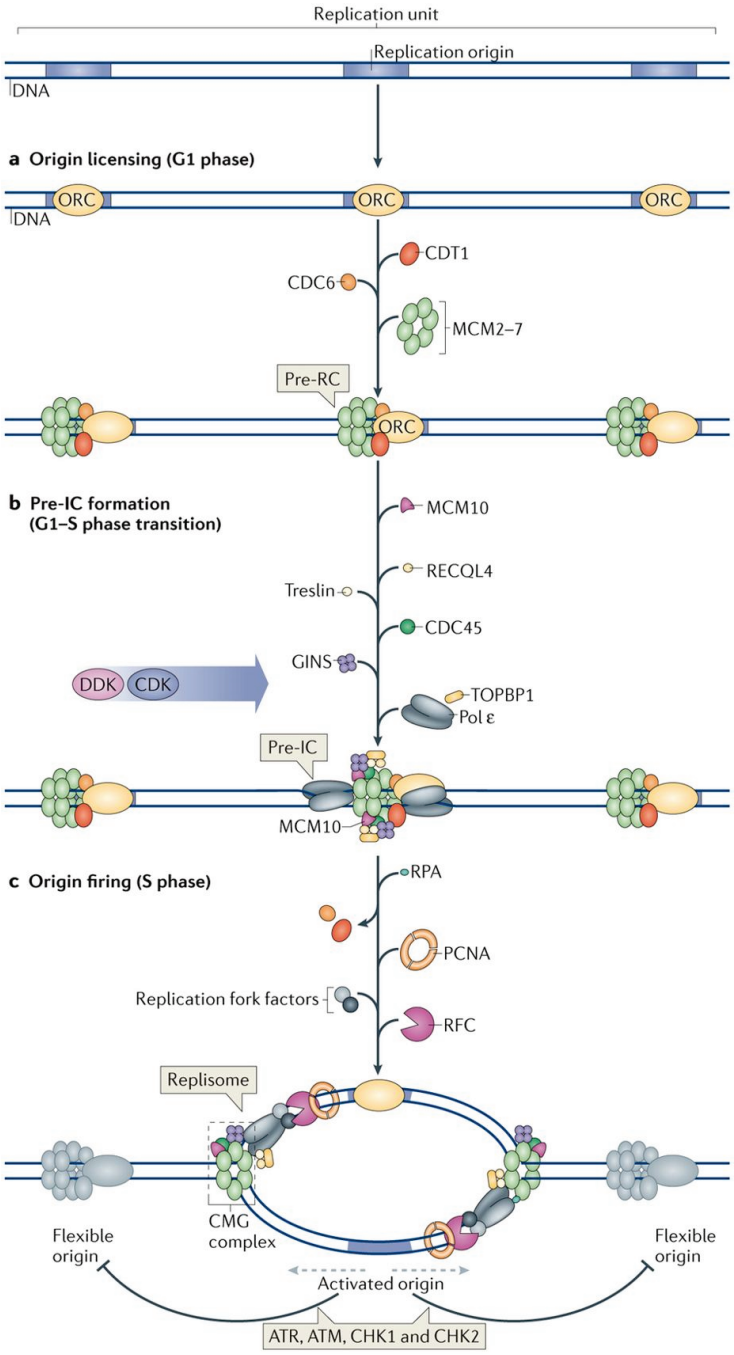

Figure 1.1. A model for the key events preceding eukaryotic replication initiation.
During late mitosis and G1 phase of cell cycle, the inactive MCM2-7 helicase complex is recruited to origin DNA by the ORC proteins, CDC6 and CDT1 to form the pre-Replication Complex (pre-RC) (a). Origin activation in late G1/S phase involves the formation of pre-Initiation Complex (pre-IC) and conversion of the MCM2-7 complex into the fully active CMG (CDC45-MCM-GINS) helicase (b, c). Assembly of pre-IC is facilitated by DDK- and S-CDK-dependent phosphorylation of several replication factors, promoting their loading on replication origins. Activation of replicative helicase promotes recruitment of RFC, PCNA and RPA, which convert the pre-IC into two functional replisome-containing replication forks. Some licenced origins remain inactive, with their inhibition controlled by the DDR kinases ATR and ATM, as well as their substrates CHK1 and CHK2. Figure reproduced from Fragkos *et al.* (2015).

The activated ring-shaped CMG helicase is capable of acting as a motor for DNA synthesis by processively unwinding and separating strands of the parental DNA double helix to form a replication bubble. However, its activation is not enough, and multiple other proteins are recruited to generate a complete replisome at a replication fork, necessary for replication elongation. The recent pioneering work to reconstitute replication of naked DNA and chromatin *in vitro* facilitated identification of the factors that are strictly required for eukaryotic DNA replication to take place (Devbhandari *et al.*, 2017; Kurat *et al.*, 2017; Yeeles *et al.*, 2017). Three DNA polymerases, Pol α, δ and Ɛ, play distinct essential roles during initiation and efficient continuation of DNA replication (Garg and Burgers, 2005; Johnson and O'Donnell, 2005). Due to the antiparallel nature of the DNA duplex strands, one of the strands, called the lagging strand, has to be synthesised discontinuously and multiple short Okazaki fragments ligated to produce a continuous strand. DNA Pol α-primase primes DNA synthesis *de novo* by generating a short tract of RNA complement to the template strand, which can subsequently be extended by the other two DNA polymerases (Arezi and Kuchta, 2000; Kunkel and Burgers, 2008). Before DNA ligase I can stitch the Okazaki fragments together to complete lagging strand synthesis, RNA primers need to be removed, which is thought to occur via strand displacement by the lagging-strand DNA Pol δ and subsequent nucleolytic cleavage of the 5' flaps by nucleases FEN1 (for short flap processing) and DNA2 (for long flap processing) (Balakrishnan and Bambara, 2013).

The other strand of the original DNA, called the leading strand, can be replicated continuously. It was shown in *in vitro* reconstitution experiments that fast replication of the leading strand at a rate comparable to the one required *in vivo* can only be achieved by DNA polymerase epsilon (Pol ε) and the processivity factor Proliferating Cell Nuclear Antigen (PCNA) (Devbhandari *et al.*, 2017; Yeeles *et al.*, 2017). While the CMG-associated Pol ε is responsible for the speedy replication of the leading strand, the sliding DNA clamp PCNA, which is deposited onto DNA by the five-subunit ATPase Replication Factor C (RFC), is needed to enhance processivity of the lagging-strand DNA Pol δ (Langston and O'Donnell, 2008). Moreover, PCNA provides a platform for recruitment of various replisome-associated proteins (Moldovan *et al.*, 2007) and allows the switch between the Pol α-primase to a replicative polymerase during replication initiation (Garg and Burgers, 2005). After Okazaki fragment ligation is completed, PCNA is unloaded from chromatin by the ATPase ATAD5 and recycled (Kubota *et al.*, 2015, 2013; Lee *et al.*, 2013; Shiomi and Nishitani, 2013).

Pol δ was shown to be significantly slower in the reconstitution studies than Pol ε, although able to replace defective DNA Pol ε for the leading strand synthesis if required (Yeeles *et al.*, 2017). Nevertheless, the speed of DNA Pol δ is sufficient for the completion of the lagging strand synthesis, and its strand displacement synthesis role is essential to successfully join nascent Okazaki fragments (Devbhandari *et al.*, 2017). Reconstitution studies also suggested that replisome-associated factors Claspin and Timeless/Tipin contribute to the processivity and translocation rate of the CMG helicase, thus enhancing the speed of DNA replication (Yeeles *et al.*, 2017). It was also demonstrated that the dimeric histone chaperone FACT is necessary for replication to take place, potentially due to its role in removing nucleosomes ahead of the replication fork (Kurat *et al.*, 2017). Other chromatin factors, such as chaperone NHP6, chromatin remodelers INO80 and ISW1A, and histone acetyltransferases pNUA4 and pSAGA, also emerged as important players in proper and speedy replication fork movement (Kurat *et al.*, 2017). Overall, the recent *in vitro* replication reconstitution studies (Devbhandari *et al.*, 2017; Kurat *et al.*, 2017; Yeeles *et al.*, 2017) shed light on the essential factors of the replication machinery, and provided a good starting point for future investigations into how the interplay and coordination between the multitude of proteins at the replisome is achieved.

1.2.2. Replication termination and replisome disassembly

When two convergent replication forks meet, DNA synthesis has to be completed, the replisome dismantled and the two DNA molecules separated. Eukaryotic replication termination is thought to happen in a few distinct steps (Dewar and Walter, 2017) (***Figure 1.2***). At first, the two replication forks moving towards each other converge, and DNA synthesis is then completed locally through gap filling and maturation of the last remaining Okazaki fragment. The replisomes are dismantled and the CMG helicase is extracted from chromatin by specialised proteins in a timely manner. Once the replicative helicase is disassembled, gaps in nascent DNA strands are promptly filled in by enzymes that carry out Okazaki fragment maturation, such as Pol δ, FEN1 and DNA2. Lastly, the introduced topological stress is resolved by topoisomerases before chromosome segregation can take place.

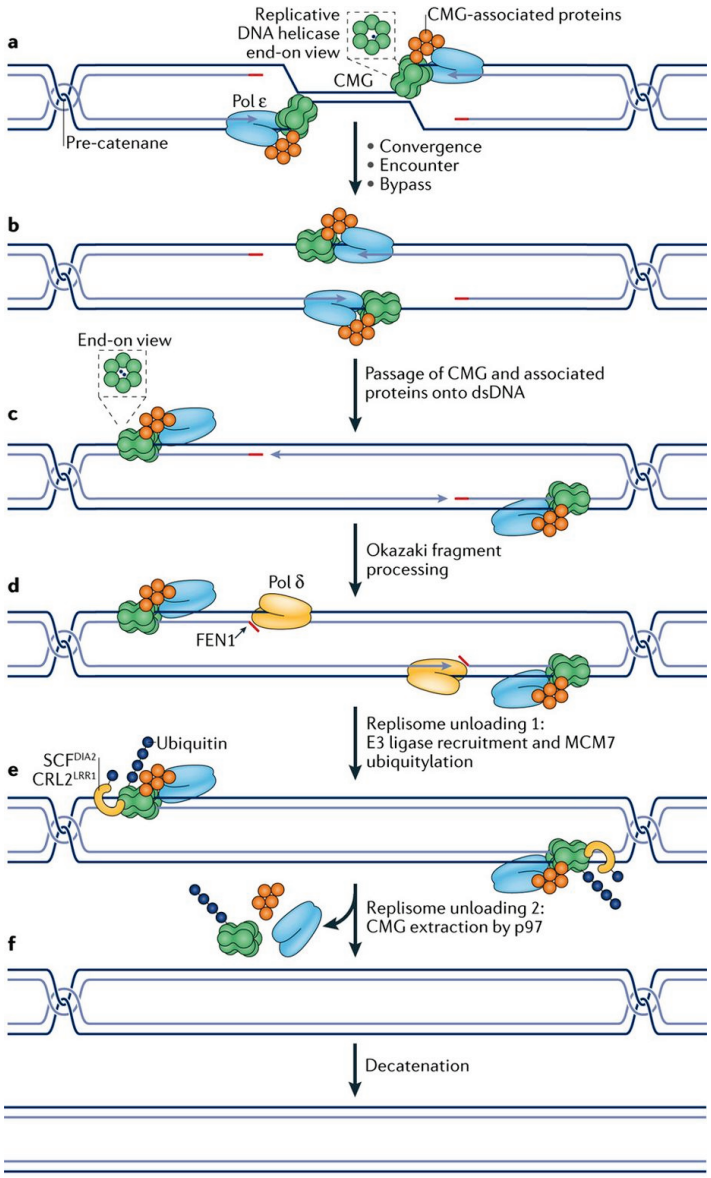

Figure 1.2. A model for the key events of eukaryotic replication termination.
The model shown is based on experiments using *X. laevis* egg extracts. The convergence of two replisomes, where each CMG complex encircles ssDNA, introduces topological stress, which is relieved by the formation of pre-catenanes (a). Without detectable fork stalling, the converging CMG complexes bypass each other (b) and translocate onto dsDNA, allowing leading strands to be joined to the downstream Okazaki fragments (c). The processing of the final Okazaki fragment likely requires DNA Pol δ and flap endonuclease 1 (FEN1) (d). The dsDNA-encircling CMG is poly-ubiquitinated on its MCM7 subunit by specialised E3 ubiquitin ligases, SCF^{DIA2} (Skp, Cullin, F-box-containing complex associated with DIA2) in *S. cerevisiae* or $CRL2^{LRR1}$ (Cullin RING ligase 2 associated with LRR1) in *C. elegans* and *X. laevis*, followed by p97/CDC48-mediated CMG extraction from chromatin (e). Finally, catenanes are removed and chromosomes are separated (f). Figure reproduced from Dewar and Walter (2017).

In *Saccharomyces cerevisiae*, the termination sites were shown to be largely influenced by replication initiation patterns, rather than specific genomic sequences (McGuffee *et al.*, 2013). During artificially synchronised locus-specific termination events in clawed frog (*Xenopus laevis*) egg extracts, replication fork convergence takes place without a noticeable change in replication fork speed (Dewar *et al.*, 2015), suggesting that topological stress gets resolved very efficiently during this termination step. When the two replisomes encounter each other in *X. laevis* egg extracts, the converging CMG helicases bypass each other without any hindrance and pass onto double-stranded DNA (dsDNA), followed by the ligation of leading strands to downstream lagging strands (Dewar *et al.*, 2015). The removal of the CMG helicase from chromatin is considered to be one of the key events in eukaryotic replication termination, and one of the requirements for it to take place appears to be poly-ubiquitination of the CMG helicase component MCM7 (Fullbright *et al.*, 2016; Long *et al.*, 2014; Semlow *et al.*, 2016). Several E3 ubiquitin ligases were recently demonstrated to play an important role in the CMG unloading during replication termination. The E3 ubiquitin ligase SCF^{DIA2} (Skp, Cullin, F-box-containing complex associated with DIA2) was shown to promote both MCM7 poly-ubiquitination and CMG extraction from chromatin in *S. cerevisiae* (Maric *et al.*, 2014), whereas $CRL2^{LRR1}$ (Cullin RING ligase 2 associated with LRR1) was implicated in the same process in *Caenorhabditis elegans* and *X. laevis* (Dewar *et al.*, 2017; Sonneville *et al.*, 2017). Ubiquitinated CMG acts as a substrate for the ATPase and protein remodeler p97/CDC48, which extracts the CMG helicase from DNA (Maric *et al.*, 2014; Moreno *et al.*, 2014). In *X. laevis* egg extracts, the proteasome does not play any significant role in the turnover of ubiquitinated MCM7, suggesting degradation-independent MCM7 deubiquitination and recycling (Fullbright *et al.*, 2016). The lack of $CRL2^{LRR1}$ in *C. elegans* causes CMG to remain on chromatin until prophase, when it gets removed by an alternative pathway orchestrated by p97 and UBXN3 (UBX domain-containing 3), the *C. elegans* orthologue of human FAF1 (FAS-Associated Factor 1) (Sonneville *et al.*, 2017). Combined absence of LRR1 and UBXN3 obliterates both replisome unloading pathways, leaves CMG bound to chromatin until metaphase and is synthetic lethal, showing that replisome disassembly and removal from chromatin is essential for cell viability (Sonneville *et al.*, 2017). It is yet to be determined whether a mitotic CMG unloading pathway is present in vertebrates, which E3 ubiquitin ligase is responsible for CMG unloading in mammalian cells, and whether dysfunctional replisome unloading is linked with any human disease.

The importance of the timely replisome disassembly is exemplified by the synthetic lethality due to inhibition of both replisome unloading pathways (Sonneville *et al.*, 2017). Additionally, premature helicase removal, which could lead to replication fork stalling and collapse, should also be avoided. The main physical trigger for the CMG unloading has not been firmly established yet. One of the proposed hypotheses suggests that the terminating CMG helicase senses dsDNA within its central channel when encountering a downstream Okazaki fragment, which induces structural changes in the CMG complex and facilitates the recruitment or activation of the E3 ubiquitin ligase that ubiquitinates MCM7 (Dewar and Walter, 2017). This model would provide an explanation for the cell adaptation to allow CMG unloading only once dsDNA is encircled, thus preventing the early removal of CMG from active replication forks, where the helicase translocates on ssDNA (Fu *et al.*, 2011). If this hypothesis is confirmed, cells should additionally be able to distinguish between the terminating CMG complexes and newly licensed MCM2-7 helicases in the G1 phase, which also encircle dsDNA. This could be achieved by preventing the CMG unloading when CDC45 and/or GINS bound to MCM2-7 are detected, or when MCM2-7 complexes are dimerised, as during replication licencing (Dewar and Walter, 2017). Moreover, the CMG complex should be prevented from translocating along dsDNA for extended distances before gap filling takes place, as encountering a downstream Okazaki fragment with a 5' flap may initiate genome re-replication (Dewar and Walter, 2017). Indeed, the *C. elegans* E3 ubiquitin ligase $CRL2^{LRR1}$ was shown to be necessary to supress re-replication (Merlet *et al.*, 2010), reiterating the importance of the E3 ubiquitin ligases in eukaryotic replication termination and maintenance of genome stability. In the future, it will be important to determine whether re-replication of parts of the genome in the absence of efficient CMG unloading could contribute to chromosomal instability and human disease.

1.2.2.1. Replisome disassembly during interstrand crosslink repair

Active disassembly of replisome also takes place when replication forks stall at DNA roadblocks, such as DNA Interstrand Crosslinks (ICLs) (Fu *et al.*, 2011; Long *et al.*, 2014). ICLs are defined as covalent links between the two strands of the double helix, creating a physical obstacle for cellular processes that require DNA strand separation, notably DNA replication and transcription (see Section 1.3.5). To repair the highly toxic ICLs, CMG needs to be unloaded from chromatin, and its unloading mechanism at ICLs differs from the conventional CMG

unloading during replication termination (Dewar and Walter, 2017). Although the requirement for MCM7 poly-ubiquitination and p97-mediated CMG extraction is conserved, the replisome disassembly mechanism at ICLs acts on CMG complexes that encircle ssDNA on both sides of a lesion (Fullbright *et al.*, 2016). Moreover, in contrast to termination-promoting CMG unloading, the heterodimeric complex comprising BRCA1, the tumour suppressor protein and homologous recombination (HR) factor, and BARD1 (BRCA1-Associated RING Domain protein 1) is also necessary for stalled CMG unloading to initiate cisplatin-induced ICL repair in *X. laevis* egg extracts (Fullbright *et al.*, 2016; Long *et al.*, 2014). Ubiquitin signalling is required to recruit BRCA1 to the cisplatin-ICL sites and promote removal of the replicative helicase, allowing the extension of leading strands towards the DNA damage site, as well as subsequent FANCI- and FANCD2-dependent endonucleolytic cleavage at the crosslink, lesion bypass, and DSB repair (Long *et al.*, 2014). Although no direct proof for BRCA1-BARD1-dependent CMG ubiquitination was provided by Long *et al.* (2014), their observation supports the previously proposed early HR-independent role of BRCA1 at ICLs before DSB formation (Bunting *et al.*, 2012). Although $CRL2^{LRR1}$ was identified as the E3 ligase that promotes replication termination in vertebrates (Dewar *et al.*, 2017), the E3 ligase that initiates CMG removal from chromatin in response to ICLs is currently unknown.

1.3. Replication stress, DNA damage response and DNA repair

1.3.1. Replication stress and the ATR-CHK1 signalling cascade

To combat threats posed by DNA damage, cells have evolved mechanisms – collectively termed the DNA damage response (DDR) – to detect DNA lesions, signal their presence and promote their repair, thus ensuring genomic stability. Replication stress describes the events that take place in cells exposed to a wide variety of endogenous and exogenous stresses, resulting in the slowing or stalling of replication fork progression and DNA synthesis (Branzei and Foiani, 2010; Osborn *et al.*, 2002). Sources of replication stress include but are not limited to unrepaired DNA lesions, nicks and gaps, repetitive sequences, misincorporated ribonucleotides, secondary DNA structures, DNA–RNA hybrids, dormant replication origins, collisions between replication and transcription complexes, chromatin inaccessibility, fragile sites, and overexpression or constitutive activation of oncogenes (Mazouzi *et al.*, 2014; Zeman and Cimprich, 2014). The replisome is not only extremely efficient at carrying out fast and accurate genome replication, but is also well adapted to overcome various replication barriers along the way, which can result in replication stress (Leman and Noguchi, 2013). Nevertheless, chronic stress or disruption of the major cell signalling pathways that respond to replication stress can lead to the emergence of genomic instability, one of the main hallmarks of cancer (Gaillard *et al.*, 2015). To resolve problematic DNA structures or lesions obstructing the replication machinery, a complex network of signalling pathways is required, leading either to the repair of the lesion, followed by normal cell cycle progression, or to programmed cell death (apoptosis) (Mazouzi *et al.*, 2014).

One of the key proteins that mediate the cellular response to replication stress is PI3K-related serine-threonine protein Kinase (PIKK) Ataxia Telangiectasia and Rad3-related (ATR). Replication stress can result in replication fork stalling, which involves pausing of an ongoing replication fork due to inhibition of either the replicative helicase or polymerase (Labib and Hodgson, 2007). Replication stress-induced fork stalling often leads to the generation of extensive regions of ssDNA, as the replicative helicase continues to unwind the parental DNA after the polymerase has stalled (Pacek and Walter, 2004). ATR is the major kinase that initiates a phosphorylation-based signalling cascade to mediate the cellular response to such ssDNA stretches (López-Contreras and Fernandez-Capetillo, 2010). The ATR signalling pathway is initiated when ATR is activated at sites of RPA-coated ssDNA in a multi-step process (Saldivar *et al.*, 2017) (***Figure 1.3***). Firstly, RPA recruits ATR binding partner and substrate ATR-

Interacting Protein (ATRIP) (Cortez *et al.*, 2001); secondly, RPA promotes accumulation of the ATR–ATRIP complex at sites of DNA damage and stalled replication forks (Ball *et al.*, 2005). Thirdly, RPA recruits RAD17–RFC2–5 (replication factor C subunits 2–5) clamp loader, which is necessary to position the heterotrimeric RAD9–RAD1–HUS1 (9-1-1) complex on chromatin in response to genotoxic damage (Parrilla-Castellar *et al.*, 2004; Zou *et al.*, 2003). The 9-1-1 complex is essential for recruitment and positioning of TOPBP1 (DNA Topoisomerase II Binding Protein) (Bermudez *et al.*, 2003), which activates the ATR–ATRIP complex (Kumagai *et al.*, 2006). Additionally, TOPBP1 recruitment to chromatin is influenced by RHINO (RAD9–RAD1–HUS1-Interacting Nuclear Orphan) (Cotta-Ramusino *et al.*, 2011; Lindsey-Boltz *et al.*, 2015) and the MRE11–RAD50–NBS1 (MRN) complex (Duursma *et al.*, 2013; Lee and Dunphy, 2013). More recently, Ewing Tumor-Associated Antigen 1 (ETAA1) was established as a novel ATR activator, in addition to and independent of TOPBP1 (Bass *et al.*, 2016; Haahr *et al.*, 2016; Lee *et al.*, 2016; Feng *et al.*, 2016). The subsequent ATR activation was shown to be dependent on a single auto-phosphorylation event at threonine 1989 (T1989) (Liu *et al.*, 2011).

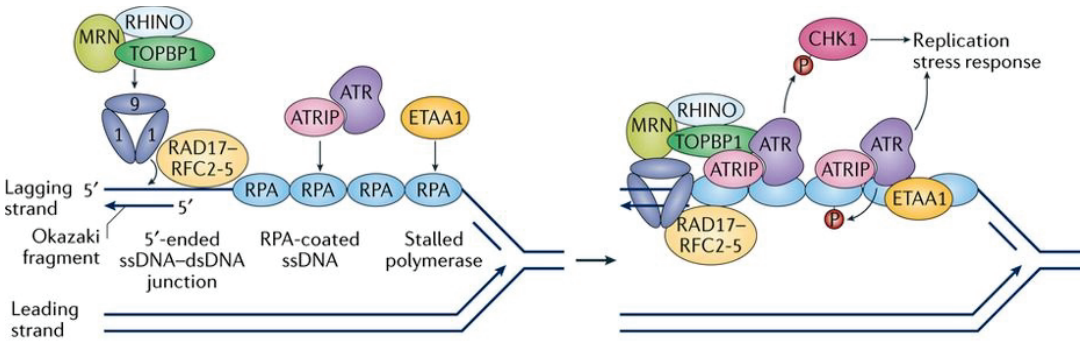

Figure 1.3. Main components of the ATR activation pathway.
Replication fork stalling on the lagging strand results in a stretch of RPA-bound ssDNA, generating a platform for ATR activation. The RAD9–RAD1–HUS1 (9-1-1) clamp complex is loaded at the 5'-ended ssDNA–dsDNA junctions by the RAD17–RFC2–5 clamp loader. The 9-1-1 complex, acting together with RHINO and the MRE11–RAD50–NBS1 (MRN) complex, recruits the ATR activator TOPBP1, allowing activation of ATR and phosphorylation of its downstream effectors, including CHK1 kinase. ETAA1 bound to RPA activates ATR in a parallel TOPBP1-independent pathway. Figure reproduced from Saldivar, Cortez and Cimprich (2017).

Globally, ATR signalling provides cells experiencing replication stress with additional time for DNA repair and ensures the continuation of DNA synthesis in the presence of stalled replication forks; locally, it stabilises and promotes restart of stalled forks and supresses recombination (Cimprich and Cortez, 2008; Zeman and Cimprich, 2014) (***Figure 1.4a***). The key

event in the ATR signalling cascade is ATR-dependent phosphorylation of CHeckpoint Kinase 1 (CHK1) at serine 345 (S345) and its consequent activation (Q. Liu *et al.*, 2000; Patil, Pabla and Dong, 2013). Thus, elevated levels of ATR-dependent pCHK1-S345 signal, as well as direct detection of ssDNA through native BrdU immunofluorescence, are considered to be good readouts of replication stress (Maréchal and Zou, 2013; Nam and Cortez, 2013). Although phosphorylation of the histone variant H2AX at serine 139 (γH2AX) can also be used as a replication stress marker (Ward *et al.*, 2004; Ward and Chen, 2001), H2AX is also phosphorylated by several other kinases in response to DSBs (Wang *et al.*, 2005), making it a less specific readout of replication stress.

One of the main consequences of CHK1 activation is the inhibition of cell cycle progression, allowing sufficient time for DNA repair before replication or mitosis resumes. It is achieved through CHK1-regulated inhibitory phosphorylation of Cyclin-Dependent Kinases (CDKs) (López-Contreras and Fernandez-Capetillo, 2010), which play a major role in cell cycle control. Moreover, CHK1-mediated phosphorylation of the CDC25 phosphatases, CDC25A, CDC25B and CDC25C, which control the G1/S and G2/M transitions through dephosphorylation and activation of CDKs (Blomberg and Hoffmann, 1999; Hoffmann *et al.*, 1994; Mailand *et al.*, 2002), leads to their proteasome-mediated degradation and cell cycle arrest (Jin *et al.*, 2003; Xiao *et al.*, 2003).

ATR-CHK1 signalling also suppresses late origin firing to limit the total number of active replication forks and ensure sufficient supply of DNA precursors and replication factors, necessary for fork progression (Katsuno *et al.*, 2009). Replication initiation in response to replication stress can be inhibited by preventing CDC45 recruitment to the MCM complex via CHK1-mediated phosphorylation of Treslin (Guo *et al.*, 2015). Moreover, ATR-CHK1 pathway activation prevents CDC45 loading and replicative helicase activation by downregulating the kinase activities of S-CDK and DDK via CHK1-dependent phosphorylation of CDC25A, triggering its rapid degradation and CDK inhibition (Mailand *et al.*, 2000; Zhao *et al.*, 2002). Additionally, ATR-mediated activation of CHK1 allows it to inhibit new origin firing (Toledo *et al.*, 2013). This suppression of new origins in the presence of replication stress prevents exhaustion of nuclear RPA by limiting the number of stalled forks that need to be coated by RPA (Toledo *et al.*, 2013). When ATR signalling is disrupted, dormant origins fire, the arising ssDNA rapidly depletes nuclear RPA and results in stretches of unprotected ssDNA, which subsequently cause DSB formation, resulting in pan-nuclear ‘replication catastrophe’ (Toledo *et al.*, 2013).

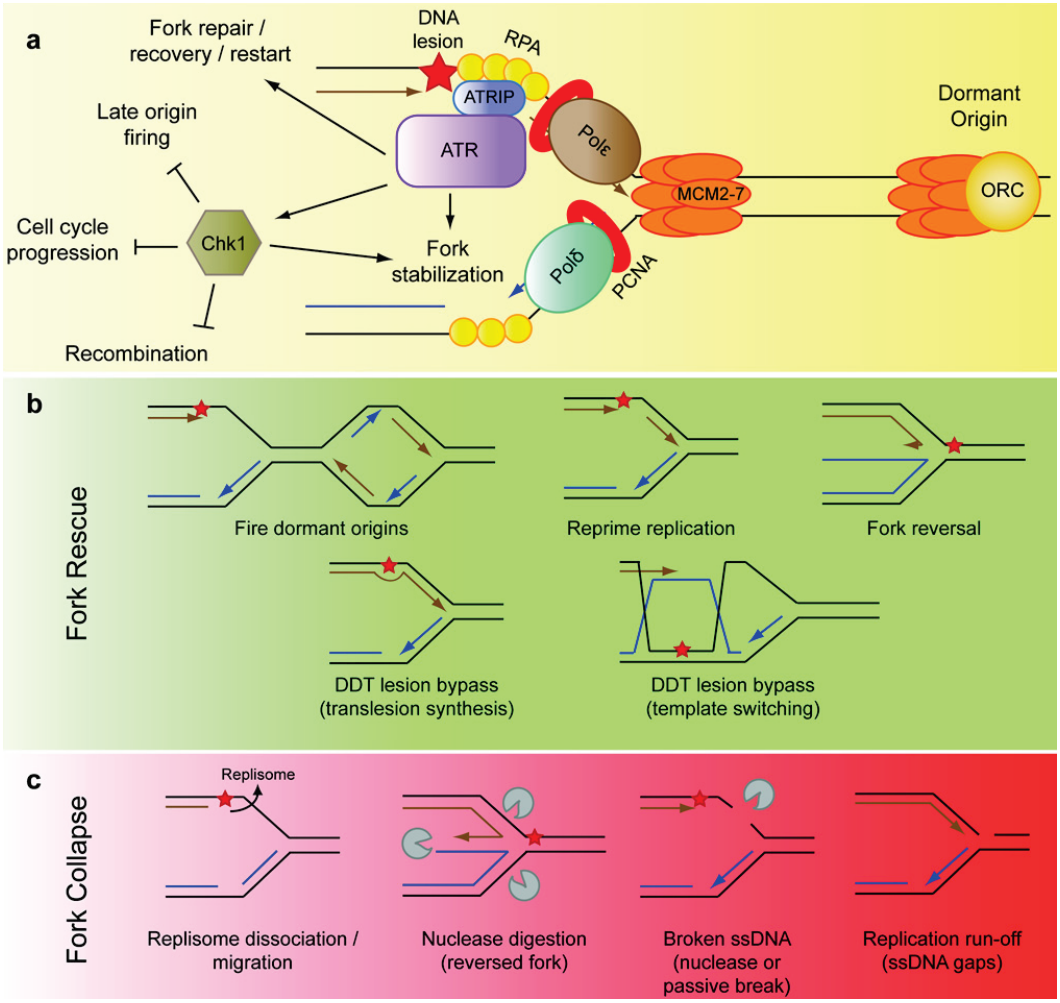

Figure 1.4. The ATR-mediated replication stress response, fork rescue, and fork collapse.
a) ATR and its binding partner ATRIP are activated at the stalled replication fork, where ATR promotes a signalling cascade via phosphorylation and activation of its effector kinase CHK1. The ATR-CHK1 signalling axis facilitates stabilisation and restart of stalled forks, inhibits cell cycle progression and supresses late origin firing and recombination until replication stress is resolved.
b) ATR-dependent stabilisation of stalled replication forks can promote their restart via several mechanisms, including dormant origin firing, replication re-priming, fork reversal, or activation of the DNA damage tolerance (DDT) pathways. Red star indicates a DNA lesion.
c) The lack of stabilisation of stalled replication forks will result in their collapse, preventing replication restart. The possible mechanisms of replication fork collapse include dissociation of replisome components, aberrant nuclease digestion of a reversed or stalled fork or replication run-off.
Figure reproduced from Zeman and Cimprich (2014).

Replication fork reversal occurs when a typical three-arm replication fork is converted into a four-way junction ('chicken-foot' structure) by the annealing of the two newly synthesized strands to form a 'regressed' arm (Neelsen and Lopes, 2015). One of the ATR functions is to prevent nuclease-mediated cleavage of stalled replication forks by regulating

fork reversal. For example, ATR-dependent phosphorylation of the DNA translocase SMARCAL1 was shown to inhibit its ability to reverse forks *in vitro*, thus preventing excessive fork remodelling and suppressing fork collapse in cells (Couch *et al.*, 2013). In ATR-deficient cells, structure-specific SLX4-dependent endonucleases SLX1, XPF, MUS81-EME1 and GEN1 were proposed to process the reversed replication forks, leading to the formation of DSBs (Couch *et al.*, 2013; Ragland *et al.*, 2013). This may occur due to premature CDK-dependent upregulation of these endonuclease complexes, which normally act in the G2/M phase to resolve under-replicated loci and Holliday junctions, the four-way DNA intermediates formed during HR (Wyatt *et al.*, 2013). CHK1 itself is also involved in stabilising stalled replication forks, as its inhibition results in fork collapse dependent on the endonuclease MUS81 (Forment *et al.*, 2011; Murfuni *et al.*, 2013; Técher *et al.*, 2016). Finally, upon replication fork stalling, the ATR-CHK1 pathway was shown to activate the CDC7–ASK kinase complex, promoting efficient lesion bypass repair and preventing fork collapse (Yamada *et al.*, 2013). Overall, the ATR-CHK1 signalling axis stabilises stalled replication forks, prevents their collapse and facilitates their restart, ensuring genome stability.

1.3.2. Collapsed replication forks and the ATM-CHK2 signalling cascade

Once replication stress is resolved, replication forks stabilised by the ATR-CHK1 pathway can be restarted (Petermann and Helleday, 2010) (***Figure 1.4*b**). Additional time for the removal of DNA lesions can be gained by the reversal of stalled replication forks, generating a 'chicken foot' structure (Ray Chaudhuri *et al.*, 2012) (***Figure 1.4*b**). However, some restart mechanisms are active even when the stress cannot be resolved to prevent prolonged replication fork stalling and collapse. Collectively known as DNA damage tolerance (DDT), these processes result in the bypass of the unrepaired DNA lesion using either specialised TransLesion Synthesis (TLS) DNA polymerases or the sister chromatid as a template (template switching) (Gao *et al.*, 2017) (***Figure 1.4*b**). However, collapse of some stalled forks may occur in the presence of ongoing replication stress (Petermann *et al.*, 2010), when they can no longer be efficiently stabilised by the ATR-CHK1 pathway components (Carr *et al.*, 2011; Segurado and Diffley, 2008).

Fork collapse is defined as a lost capacity of a replication fork to perform DNA synthesis, often resulting from the failure to stabilise stalled replication forks, leading to replisome dissociation and formation of DSBs (Cortez, 2015; Zeman and Cimprich, 2014)

(***Figure 1.4*c**). Fork collapse poses a danger to cell viability, as a DSB at the replication fork can be formed either via aberrant structure-specific nuclease-mediated cleavage of reversed forks or failed HR-mediated replication restart (Hanada *et al.*, 2007; Petermann *et al.*, 2010; Segurado and Diffley, 2008) (***Figure 1.4*c**). Moreover, persisting stretches of unprotected ssDNA, resulting from prolonged replication fork stalling, may also be cleaved by endonucleases or undergo spontaneous breakage, leading to the generation of a DSB (Lopes *et al.*, 2006, 2001; Sogo *et al.*, 2002) (***Figure 1.4*c**). The presence of DSBs, which can also be induced by exogenous DNA damaging agents, such as ionising radiation (IR), leads to the activation of two other DDR kinases of the PIKK family: Ataxia Telangiectasia Mutated (ATM) and DNA-dependent Protein Kinase (DNA-PK) (Ciccia and Elledge, 2010).

ATM is the main signal transducer at DSBs, and ATM-mediated phosphorylation of its substrates promotes DNA repair, cell cycle arrest or apoptosis (Lavin, 2008; Shiloh, 2003) (***Figure 1.5***). Like ATR, ATM activation is a multi-step process. The heterotrimeric MRN complex and the MDC1 (Mediator of DNA Damage Checkpoint 1) adaptor protein are initial sensors of DSBs (Coster and Goldberg, 2010; van den Bosch *et al.*, 2003), and their accumulation facilitates recruitment of ATM, which binds MDC1 (Lou *et al.*, 2006) and NBS1 (Cerosaletti *et al.*, 2006; You *et al.*, 2005). ATM is activated by dissociation of the inactive ATM homodimer and trans-autophosphorylation at five residues (S367, T1885, S1893, S1981, and S2996) (Bakkenist and Kastan, 2003; Kozlov *et al.*, 2011), as well as acetylation of lysine 3016 (K3016) by the histone acetyltransferase TIP60 (Sun *et al.*, 2007). Histone variant H2AX (Burma *et al.*, 2001) and MDC1 (Luo *et al.*, 2011; Matsuoka *et al.*, 2007) are phosphorylated in an ATM-dependent manner, and form a scaffold to ensure the retention of DNA damage repair proteins on chromatin. MDC1 also recruits the ubiquitin ligase RNF8 (RING-finger protein 8), which ubiquitinates H2AX to promote recruitment of BRCA1 (breast cancer susceptibility protein 1) and 53BP1 (p53 Binding Protein 1) at the DSB (Huen *et al.*, 2007; Kolas *et al.*, 2007; Mailand *et al.*, 2007), both of which are also phosphorylated by ATM (Gatei *et al.*, 2000; Rappold *et al.*, 2001). One of the key substrates of the ATM kinase activity is CHeckpoint Kinase 2 (CHK2) (Bartek *et al.*, 2001; McGowan, 2002). Both ATM and CHK2 phosphorylate tumour suppressor p53, disrupting its interaction with the ubiquitin ligase MDM2 (Mouse Double Minute 2), the inhibitor of p53 (Chen *et al.*, 2005). Thus, the ATM-CHK2 signalling axis facilitates activation and stabilisation of p53, promoting G1/S checkpoint activation (Senturk and Manfredi, 2013). Additionally, ATM- and CHK2-dependent phosphorylation of the CDC25A phosphatase inhibits its activity, preventing the dephosphorylation of CDK2 and leading to a transient arrest of DNA replication (Falck *et al.*, 2001). Finally, ATM signalling also directly influences DSB repair

pathway choice via phosphorylation of two breast cancer susceptibility proteins, BRCA1 (Lee *et al.*, 2000) and BRCA2 (Bahassi *et al.*, 2008), promoting homologous recombination (HR) over Non-Homologous End Joining (NHEJ) (see Section 1.3.3).

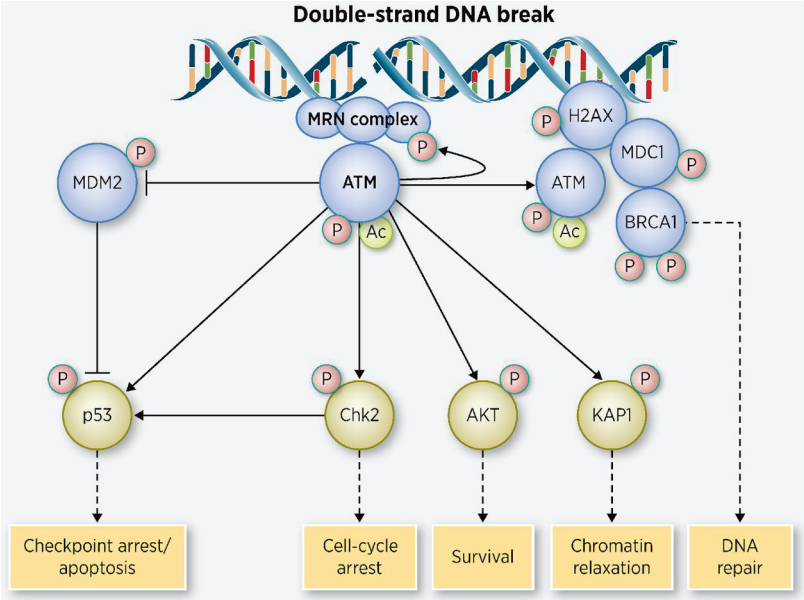

Figure 1.5. ATM signalling in response to DNA double-strand breaks.
DNA DSBs are sensed by the MRN complex, followed by recruitment and activation of ATM. ATM also interacts with and phosphorylates other sensor proteins, MDC1 and histone variant H2AX, which create a platform for rapid accumulation of other DNA repair factors at the DSB sites. One of the main effectors of ATM is the kinase CHK2, phosphorylated in an ATM-dependent manner at threonine 68 (T68), which in turn phosphorylates its own substrates, resulting in cell cycle arrest. ATM and CHK2 also activate and stabilise tumour suppressor p53 via negative regulation of its inhibitor MDM2. Other effectors of ATM include KRAB-associated protein 1 (KAP1), which promotes chromatin relaxation to facilitate recruitment of DNA repair factors, and AKT kinase, which promotes cell survival. ATM pathway also facilitates BRCA1-mediated HR at DSBs. Figure reproduced from Choi, Kipps and Kurzrock (2016).

1.3.3. DNA double-strand break repair and pathway choice

Accurate repair of DSBs is essential for the maintenance of genomic integrity, as the aberrant joining of DNA ends can lead to gross chromosomal rearrangements and genomic instability (Brandsma and Gent, 2012). The two major pathways eliminating these DNA lesions are NHEJ and HR (***Figure 1.6***). The intrinsically mutagenic NHEJ pathway, which is active throughout the cell cycle and predominantly used in the G1 phase, relies on co-joining and ligating the broken DNA ends (Chiruvella *et al.*, 2013). In contrast, the error-free HR pathway

is restricted to S and G2 phase, where the sister chromatid is available to act as a template (Thompson and Schild, 2001). The molecular mechanism of DSB repair pathway choice has been extensively studied, and it has become clear that DNA end resection at a break is a major factor favouring HR repair (Chapman *et al.*, 2012; Symington and Gautier, 2011). Several distinct nucleases were demonstrated to process DNA ends at DSBs: the DSB repair protein MRE11, a component of the MRN complex, initiates short-range resection together with CtIP, whereas the 5'-3' exonuclease EXO1 and the ATP-dependent helicase/nuclease DNA2, acting together with BLM helicase, perform long-range resection (Daley and Sung, 2014; Mimitou and Symington, 2011; Niu *et al.*, 2009). The exposed 3' DNA overhangs are immediately coated by RPA to inhibit formation of DNA hairpins (Chen *et al.*, 2013) (***Figure 1.6***). The major facilitator of HR is the RAD51 recombinase, which displaces ssDNA-bound RPA to form RAD51-ssDNA nucleoprotein filaments (***Figure 1.6***). The main function of the RAD51 nucleofilament is to search for and pair with a homologous sequence elsewhere in the genome to form a heteroduplex displacement DNA (D-loop), where DNA synthesis takes place to repair a DSB (Brandsma and Gent, 2012; Krejci *et al.*, 2012; Sung and Robberson, 1995). Accommodation of both the invading and donor ssDNA strands within the filament leads to the formation of RAD51-dsDNA filament, and once RAD51 is released from dsDNA, it exposes the 3'-hydroxyl as a primer for DNA synthesis (Krejci *et al.*, 2012). The D-loop is finally resolved either via the synthesis-dependent strand annealing (SDSA) pathway or via migrating double Holliday junction intermediates, which are either dissolved by the BLM–RMI–TOP3α complex or processed by resolvases (Panier and Boulton, 2014).

Meanwhile, classical NHEJ is initiated by the rapid binding of the Ku70/80 heterodimer to the non-resected DNA ends (Fell and Schild-Poulter, 2015) and the recruitment of DNA-dependent protein kinase catalytic subunit (DNA-PKcs) (Davis *et al.*, 2014), which belongs to the PIKK family (***Figure 1.6***). DNA-PKcs maintains the broken DNA ends in close proximity and recruits end-processing factors, such as Artemis, PolyNucleotide Kinase/Phosphatase (PNKP), AP Endonuclease 1 (APE1) and Tyrosyl–DNA Phosphodiesterase 1 (TDP1), necessary to generate DNA ends that can be ligated by the protein complex containing XRCC4 (X-ray Repair Cross-Complementing protein 4), XLF (XRCC4-Like Factor), and LIG4 (DNA Ligase 4) (Davis *et al.*, 2014; Lieber, 2010).

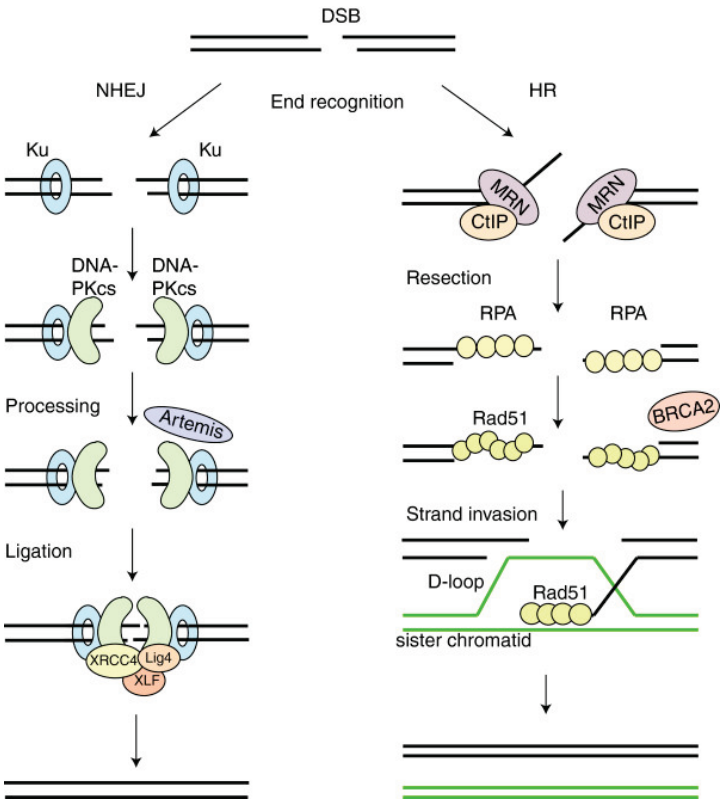

Figure 1.6. Non-homologous end joining and homologous recombination in DNA double-strand break repair.
Repair of DSBs is primarily co-ordinated by 53BP1, which promotes Non-Homologous End Joining (NHEJ), and BRCA1, CtIP and MRN, which facilitate homologous recombination (HR). NHEJ starts with recognition of the DNA ends by the Ku70/80 heterodimer, which recruits DNA-PKcs kinase. Once the DNA ends are processed by nucleases, such as Artemis, the XRCC4–XLF–LIG4 ligation complex can seal the break. In HR, primarily co-ordinated by BRCA1, MRN and CtIP initiate DNA end resection at DSBs to generate ssDNA overhangs and inhibit the NHEJ repair pathway. The ssDNA stretches are first coated by RPA, followed by its subsequent BRCA2-mediated replacement by RAD51 nucleoprotein filaments, which mediate strand invasion on the homologous template. Extension of the heteroduplex DNA (D-loop) and capture of the second end lead to HR repair. Figure reproduced from Brandsma and Gent (2012).

Several proteins were shown to strongly influence the balance between the NHEJ and HR repair pathways. The onset of DNA end resection was proposed to be primarily controlled by two factors that functionally antagonise each other: the ATM kinase substrate 53BP1 and the tumour suppressor BRCA1, implicated in homology-directed repair (Daley and Sung, 2014) (***Figure 1.7***). 53BP1 is known to suppress the nucleolytic processing of DNA termini, thus preventing HR (Hustedt and Durocher, 2017; Panier and Boulton, 2014). The accumulation of 53BP1 at DNA damage foci is dependent on PIKK-induced H2AX phosphorylation (Fernandez-Capetillo *et al.*, 2002; Ward *et al.*, 2003), which in turn stimulates recruitment of the E3

ubiquitin ligases RNF8 and RNF168 (Doil *et al.*, 2009; Huen *et al.*, 2007; Kolas *et al.*, 2007; Mailand *et al.*, 2007; Stewart *et al.*, 2009) to initiate histone ubiquitination at DSBs. The retention of 53BP1 at damaged chromatin is thought to occur via its interaction with constitutive chromatin marks that get exposed upon histone ubiquitination, such as histone H4 di-methylated on lysine 20 (H4K20me2) (Botuyan *et al.*, 2006) (***Figure 1.7***). RIF1 was identified by multiple studies as an effector of 53BP1, shown to be required for NHEJ and removed from DSBs in the S/G2 phase in a BRCA1- and CtIP-dependent manner (Chapman *et al.*, 2013; Di Virgilio *et al.*, 2013; Escribano-Díaz *et al.*, 2013; Zimmermann *et al.*, 2013). 53BP1 also recruits REV7/MAD2L2 to the break sites (Boersma *et al.*, 2015; G. Xu *et al.*, 2015) and interacts with PTIP (Munoz *et al.*, 2007), which recruits nuclease Artemis to prevent DNA end resection and promote NHEJ (Wang *et al.*, 2014) (***Figure 1.7***). More recently, a novel 53BP1 effector complex, shieldin, constituting of SHLD1, SHLD2, SHLD3 and REV7, was reported by multiple laboratories to localise to DSBs in a 53BP1- and RIF1-dependent manner and protect DNA ends from hyper-resection (Dev *et al.*, 2018; Ghezraoui *et al.*, 2018; Gupta *et al.*, 2018; Mirman *et al.*, 2018; Noordermeer *et al.*, 2018).

In S phase, BRCA1 is thought to promote dissociation of NHEJ proteins, such as 53BP1, from DSBs to facilitate DNA end resection and HR (Bunting *et al.*, 2010) (***Figure 1.7***). In cells without BRCA1, DNA end resection in S phase is dysfunctional and aberrant NHEJ takes place at replication-associated DSBs instead, contributing to genomic instability (Bouwman *et al.*, 2010; Bunting *et al.*, 2010; Daley & Sung, 2014). More recently, BRCA1 was also demonstrated to promote 53BP1 dephosphorylation, which subsequently leads to RIF1 release and promotes DNA end resection (Isono *et al.*, 2017). The DNA endonuclease CtIP was shown to be the major mediator of the switch between accumulation of 53BP1 in G1 and BRCA1 in the S/G2 phases of the cell cycle. CtIP physically and functionally interacts with the MRN complex to promote DNA end resection at DSBs, as well as RPA and ATR recruitment to these lesions through stimulation of MRE11 endonuclease activity (Sartori *et al.*, 2007; Shibata *et al.*, 2014). CDK-mediated phosphorylation of CtIP at threonine 847 was demonstrated to be required for the initiation of DNA end resection (Huertas and Jackson, 2009). Histone ubiquitination at DSBs was also implicated in the recruitment of BRCA1 and BARD1. For example, the RNF20-RNF40 heterodimer of RING finger E3 ubiquitin ligases, which mono-ubiquitinate histone H2B (Moyal *et al.*, 2011), promote BRCA1 recruitment by facilitating histone eviction and nuclease-mediated processing of DNA termini (Daley and Sung, 2014). RAP80 (Receptor-Associated Protein 80) and its associated proteins were implicated in targeting the BRCA1-BARD1 complex to ubiquitin marks on chromatin (Sobhian *et al.*, 2007; Wang *et al.*, 2007). Although RNAi-

mediated depletion of RAP80 led to the reduction in BRCA1 foci, it was also found to increase the frequency of HR (Hu *et al.*, 2011), suggesting that RAP80 may be important to inhibit excessive BRCA1-dependent HR.

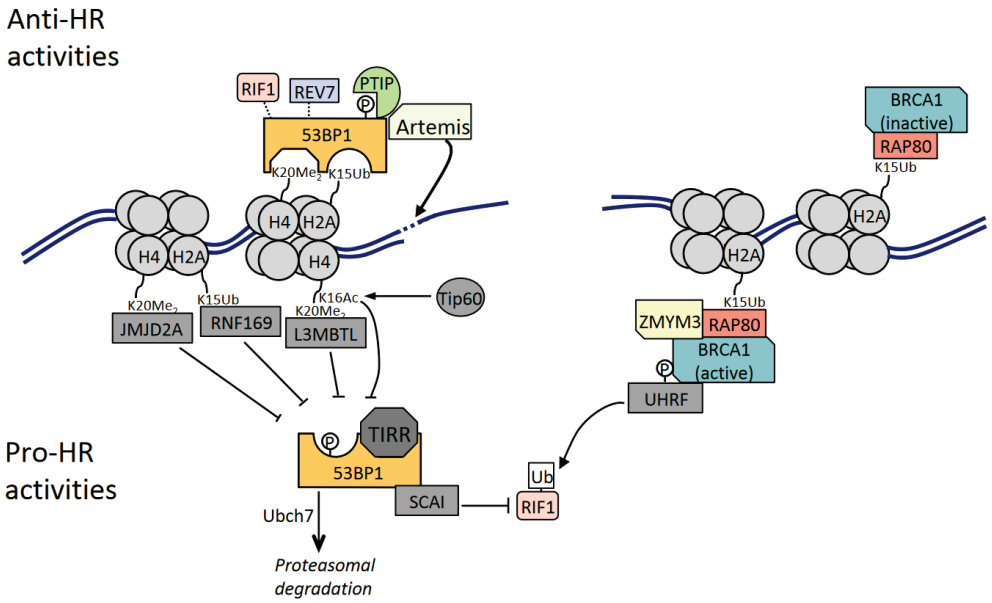

Figure 1.7. The 53BP1–BRCA1 network regulates repair pathway choice at DNA double-strand breaks.
53BP1 acts as the main suppressor of the HR pathway for DSB repair, which is achieved by its recruitment of the downstream regulators RIF1, REV7 and PTIP. These factors inhibit DNA end resection via their recruitment of nuclease Artemis, which processes potentially recombinogenic ssDNA tracts at the lesion site. 53BP1 is antagonised by multiple factors in several different ways: competition for chromatin binding sites (JMJD2A, L3MBTL, RNF169), inhibition of 53BP1 recruitment (TIP60, TIRR), inhibited recruitment of downstream modulators of 53BP1 (SCAI), or degradation of 53BP1 (Ubch7). BRCA1 is recruited to DSBs via RAP80 and activated to promote HR via its interaction with ZMYM3. Additionally, BRCA1 antagonises 53BP1 through recruitment of UHRF, which ubiquitinates RIF1, thus preventing it from being stably retained at the break site. Figure reproduced from Her and Bunting (2018).

1.3.4. TOP1 inhibition and repair of TOP1-mediated DNA damage

Covalent DNA–protein crosslinks (DPCs), also referred to as protein adducts, create bulky obstructions to DNA replication and transcription and are highly toxic to cells, requiring specialised removal pathways (Stingele *et al.*, 2017). Platinum derivatives that are widely used in cancer therapy, such as cisplatin, cause non-enzymatic DPCs by non-specific crosslinking of chromatin-interacting proteins to DNA (Chválová *et al.*, 2007). Meanwhile, certain chemotherapeutic agents, such as camptothecin, etoposide and olaparib, selectively trap

specific enzymes on DNA: DNA topoisomerases I and II and poly(ADP-ribose) polymerase 1 (PARP1), respectively (Murai *et al.*, 2012; Pommier and Marchand, 2012).

Mammalian type IB DNA topoisomerase I (TOP1) is an enzyme that relaxes supercoiled DNA via transient cleaving and re-joining of one strand of the DNA duplex (Wigley, 1995), thus supporting replication fork movement during DNA replication. TOP1 introduces a single-strand break (SSB) via transesterification at a target DNA site, and the resulting phosphodiester and the catalytic tyrosine of TOP1 form a DNA-(3'-phosphotyrosyl)-enzyme intermediate (TOP1 cleavage/covalent complex, or Top1cc) (Pommier, 2013) (***Figure 1.8***). The released DNA strand can freely rotate around the intact strand, thus removing torsional tension generated during DNA replication or transcription. Lastly, re-ligation takes place, where the 5'-hydroxyl of the terminal deoxyribonucleotide attacks the ternary intermediate to expel the catalytic tyrosine, restoring the DNA phosphodiester backbone (Pommier, 2013).

Camptothecin (CPT) is an anti-tumour agent, which was discovered in 1966 in a screening of natural products for anti-cancer drugs and isolated from *Camptotheca acuminata*, a tree growing in China that was well-known for its anti-cancer properties in Traditional Chinese Medicine (Wall *et al.*, 1966). This small-molecule inhibitor and its derivatives topotecan and irinotecan act by stabilising a short-lived covalent DNA-protein reaction intermediate generated between DNA and TOP1 at SSBs and thus interfering with DNA replication and transcription (Hsiang *et al.*, 1985; Pommier *et al.*, 1998; L. F. Liu *et al.*, 2000). This stabilisation prevents re-ligation of two DNA ends, inhibits resolution of the SSB and can lead to the emergence of a replication-associated one-ended DSB once the replication fork collides with the ternary CPT-TOP1-DNA complex. Thus, the dissolution of the stabilised complex is particularly important for continuing DNA replication and cell survival.

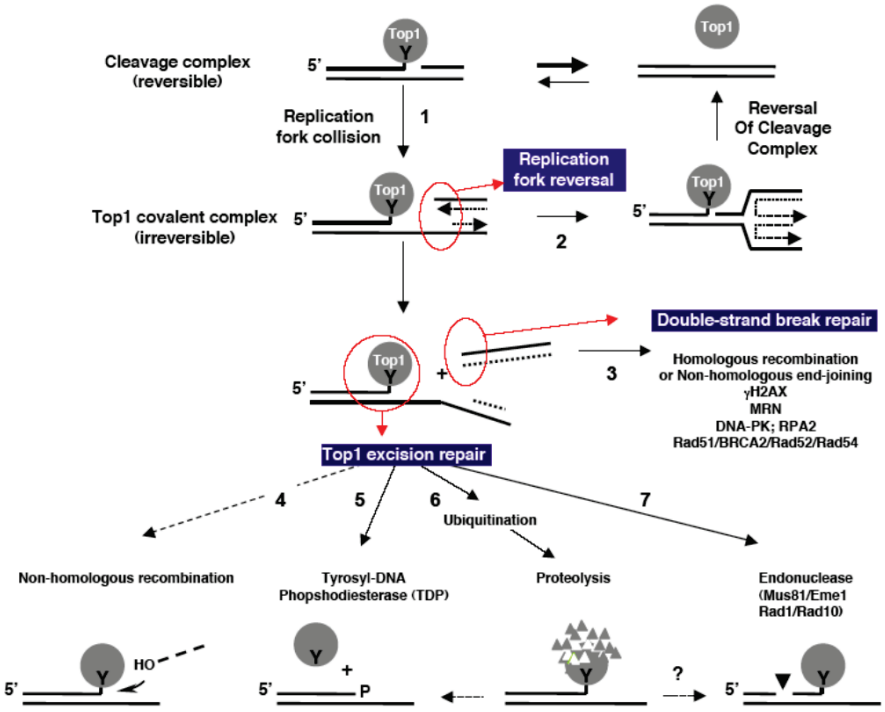

Figure 1.8. Repair of replication-associated TOP1-mediated DNA damage.
Camptothecin (CPT) stabilises TOP1 cleavage complexes, and once the replication fork catches up with the ternary CPT-TOP1-DNA complex, a replication-associated one-ended DSB is generated on the leading strand (1). Replication fork reversal by formation of a 'chicken foot'-like DNA structure can facilitate the dissociation of the newly replicated DNA strand from its template and the consequent spontaneous re-ligation of the broken template (2). In most cases, repair of the replication-associated one-ended DSB will involve either HR or NHEJ (3). Moreover, trapped TOP1 can be eliminated via various TOP1 excision pathways. For example, 5'-hydroxyl-containing DNA strand invasion can release TOP1, resulting in non-homologous recombination (4). One of the main pathways for TOP1 excision involves tyrosyl-DNA phosphodiesterase (TDP1), which hydrolyses the tyrosyl-DNA covalent bond (5). TDP1-mediated repair is greatly facilitated by TOP1 proteolysis (6). Lastly, endonucleases can also mediate excision of the DNA strand covalently bound to TOP1 (7). Figure reproduced from Pommier (2004).

Generally, cells use two distinct pathways to deal with Top1cc. The tyrosyl-DNA phosphodiesterase (TDP1) pathway involves ubiquitination and proteasome-mediated degradation of TOP1 to generate the 3'-phosphate end, which can subsequently be processed by PolyNucleotide Kinase 3'-Phosphatase (PNKP) and turned into a 3'-hydroxyl (El-Khamisy and Caldecott, 2006). Finally, the nick is repaired by canonical SSB repair proteins, such as PARP1, XRCC1 (X-ray Repair Cross-Complementing protein 1) and LIG3 (DNA Ligase 3) (El-Khamisy *et al.*, 2005; Plo *et al.*, 2003) (***Figure 1.9***). The alternative endonuclease pathway for Top1cc repair requires contribution of structure-specific 3'-flap endonucleases, such as ERCC1-XPF (Rad1/Rad10 in budding yeast), MUS81-EME1, and MRE11-RAD50 (Regairaz *et al.*, 2011; Sacho

and Maizels, 2011; Takahata *et al.*, 2015), to cut near the DNA lesion allowing release of the DNA-TOP1 complex (***Figure 1.8***).

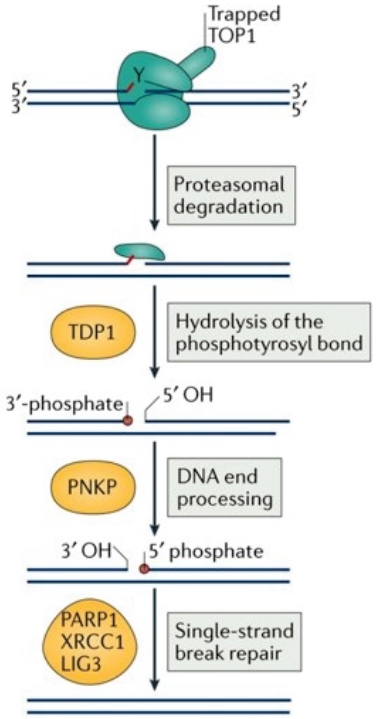

Figure 1.9. Mechanism of TOP1 covalent complex repair by tyrosyl-DNA phosphodiesterase 1.
Repair of covalently-trapped DNA topoisomerase I (TOP1) is initiated by proteasomal degradation of the trapped enzyme, allowing TDP1 to hydrolyse the phosphotyrosyl bond between the protein and the DNA. TDP1-mediated hydrolysis generates a SSB with a 3′-phosphate and 5′-hydroxyl end, which cannot be re-ligated by the SSB repair factors. Subsequent processing of the SSB by PNKP results in dephosphorylation of the 3′ end and phosphorylation of the 5′ DNA end, allowing canonical SSB repair machinery (PARP1, XRCC1 and LIG3) to re-ligate the DNA. Figure reproduced from Stingele, Bellelli and Boulton (2017).

Replication fork collision is the main mechanism of toxicity of TOP1 poisons in dividing cells. If the SSB is not repaired before the start of S phase, it can give rise to a one-ended DSB upon collision with an ongoing replication fork via 'replication run-off' (Pommier, 2006) (***Figure 1.8***). If unrepaired, a single DSB can be lethal to a cell (Pitcher *et al.*, 2005), as it can cause major chromosomal rearrangements and genomic instability. Replication-associated DSBs lead to several molecular responses, such as rapid phosphorylation of the histone variant H2AX (Furuta *et al.*, 2003), as well as subsequent phosphorylation of RPA, ATM, checkpoint kinases CHK1 and CHK2, the Bloom syndrome helicase (BLM) and p53 (Pommier, 2006). The RPA2 subunit of the RPA heterotrimer gets phosphorylated within an hour of CPT treatment and

remains modified on serine 33 (S33) and serine 4 and 8 (S4/S8) while DNA synthesis is inhibited (Shao *et al.*, 1999; Vassin *et al.*, 2009). The kinases thought to be primarily involved in RPA2 and H2AX phosphorylation after CPT treatment are DNA-PK and ATR (Furuta *et al.*, 2003; Shao *et al.*, 1999). CPT-induced replication-associated DSBs were also shown to activate ATM–CHK2 signalling, with its activation defect leading to CPT hypersensitivity (Takemura *et al.*, 2006). Overall, the efficient repair of CPT-TOP1-DNA complexes requires an extensive cellular response with multiple sensors and effectors of the DNA repair network acting together.

In proliferating cells, the repair of replication-associated DSBs is largely dependent on HR (Brandsma and Gent, 2012; Pommier, 2006), which subsequently facilitates the restoration of replication forks to restart DNA replication (***Figure 1.8***). Additionally, it was shown that low doses of TOP1 inhibitor can induce PARP1- and RAD51-mediated replication fork regression (Ray Chaudhuri *et al.*, 2012; Zellweger *et al.*, 2015), resulting in a 'chicken foot' DNA structure (***Figure 1.8***). This repair intermediate is not likely to generate any DSBs, thus avoiding the formation of highly deleterious lesions and potential activation of error-prone NHEJ. The resulting replication fork slowing prevents excessive accumulation of ssDNA and allows time for repair machinery to remove trapped TOP1 (Neelsen and Lopes, 2015; Ray Chaudhuri *et al.*, 2012; Zellweger *et al.*, 2015).

More water-soluble CPT derivatives, such as topotecan and irinotecan, are approved by the Food and Drug Administration (FDA) in the United States of America and widely used in cancer therapy today, as they preferentially affect fast-dividing cancer cells that are highly dependent on efficient DNA replication. CPT itself continues to be used in DNA repair research as an initiator of replication-associated DDR, allowing the identification of novel factors needed for efficient resolution of replication-associated one-ended DSBs.

1.3.5. DNA interstrand crosslink repair and Fanconi Anaemia pathway

DNA interstrand crosslinks (ICLs) are considered to be amongst the most deleterious DNA lesions, obstructing both DNA replication and transcription (Kee and D'Andrea, 2010). A single unrepaired ICL was shown to be sufficient to kill a bacterial or yeast cell (Magana-Schwencke *et al.*, 1982), and approximately 40 unrepaired ICLs can kill a mammalian cell (Lawley and Phillips, 1996). ICLs can be induced by a variety of DNA crosslinking agents, used in cancer therapy, including psoralens, platinum compounds and mitomycins (Deans and West,

2011). Deleterious ICLs can also be generated by endogenous by-products of cellular metabolism, such as acetaldehyde and formaldehyde (Langevin *et al.*, 2011; Pontel *et al.*, 2015). One of the mitomycins commonly used clinically, mitomycin C (MMC), was discovered in 1950s as a fermentation product of the microorganism *Streptomyces caespitosus* (Hata *et al.*, 1956) and was shown to have multiple specific biological effects in mammalian cells, such as suppression of DNA synthesis, mutagenesis, enhanced recombination and genomic instability (Tomasz, 1995). Reductive activation of MMC leads to the formation of mitosene, which alkylates two guanine nucleosides in the sequence 5'-CpG-3' (Tomasz, 1995), thus crosslinking opposite DNA strands. If unrepaired, such a crosslink will block DNA replication and transcription, subsequently inducing genomic instability.

ICL repair through the Fanconi Anaemia (FA) pathway is extensively studied and involves a group of FA proteins whose collective function is to recognise a DNA crosslink and initiate nucleolytic processing of the damaged DNA, followed by lesion bypass, mediated by the TLS pathway, and the repair of the generated DSB by HR (reviewed by Deans and West, 2011) (***Figure 1.10***). The FA protein family includes 19 distinct proteins, and nine of these comprise the FA core complex that activates the FANCI-FANCD2 heterodimer through mono-ubiquitination (Alpi *et al.*, 2008; Garcia-Higuera *et al.*, 2001; Smogorzewska *et al.*, 2007; Wang, 2007). The remaining eight FA factors are required for recombinational and nucleolytic processes to complete ICL repair (Zhang and Walter, 2014). Mutations in most FA genes result in a rare predominantly autosomal recessive chromosomal instability disorder, characterised by various developmental abnormalities affecting the skeleton, kidneys and heart, pre- and postnatal growth retardation, progressive bone marrow failure and cancer predisposition (Joenje and Patel, 2001; Kim and D'Andrea, 2012). FA patient-derived cells exhibit ICL hypersensitivity and accumulation of ICL-induced replication-associated DNA damage, with aberrant repair of ICLs leading to the appearance of highly toxic DNA structures called radial chromosomes, which are considered to be the cellular signature of Fanconi Anaemia (Michl *et al.*, 2016).

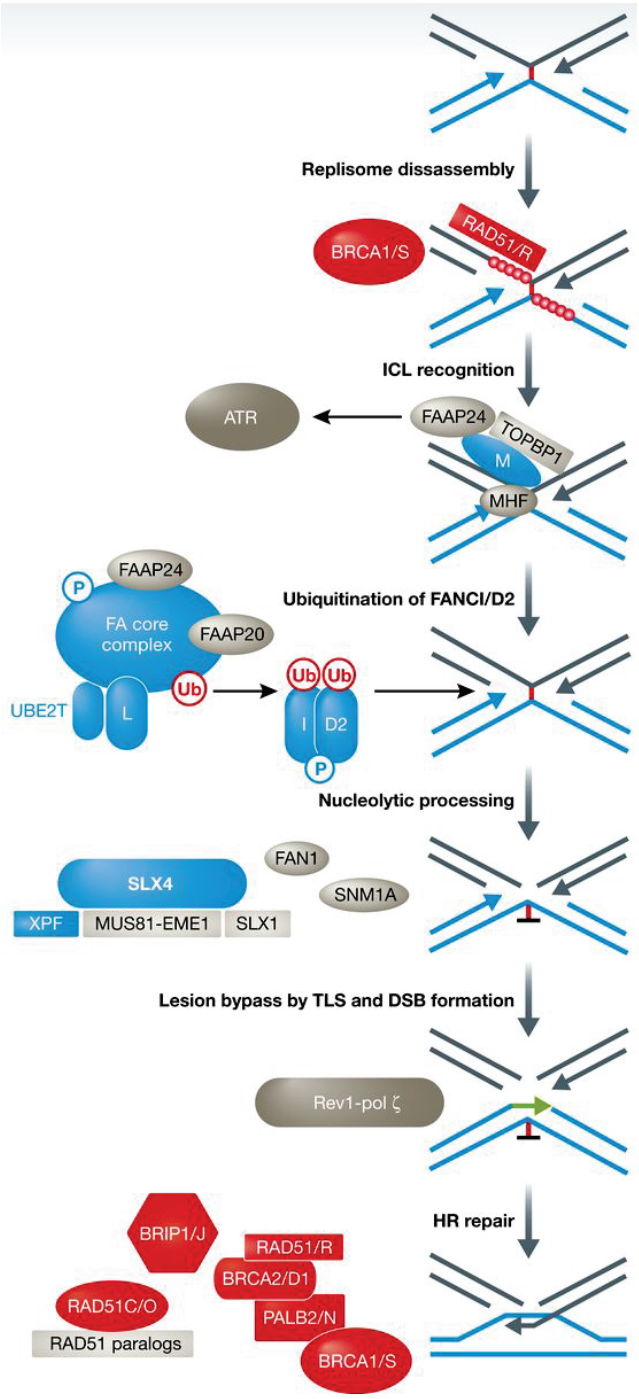

Figure 1.10. The Fanconi Anaemia (FA) pathway of interstrand crosslink (ICL) repair.
Upon replication fork stalling at ICLs, BRCA1-mediated signalling facilitates replisome disassembly, and RAD51 binds ssDNA to protect the fork. The FANCM–FAAP24–MHF1/2 complex is involved in the initial ICL recognition, activation of the ATR signalling cascade and recruitment of the FA core complex. The core complex ubiquitinates the FANCI-FANCD2 heterodimer, which acts as a platform to recruit multiple SLX4-dependent endonucleases involved in ICL processing (ERCC1-XPF, SLX1 and MUS81-EME1). Nucleolytic incisions unhook the ICL and promote lesion bypass via TLS, mediated by REV1 and DNA polymerase zeta (Pol ζ). Finally, the introduced DSB is repaired by HR, mediated by RAD51/FANCR, BRCA1/FANCS, BRCA2/FANCD1, PALB2/FANCN, BRIP1/FANCJ and other HR factors. Figure reproduced from Michl, Zimmer and Tarsounas (2016).

The current model for ICL repair suggests that when two convergent replication forks undergo stalling at an ICL site, the replisome has to be dismantled via extraction of the replicative CMG helicase from chromatin (Amunugama *et al.*, 2018; Fu *et al.*, 2011; Fullbright *et al.*, 2016; Semlow *et al.*, 2016). The unprotected ssDNA is promptly bound by RPA and RAD51 to prevent fork breakage or aberrant nucleolytic degradation, as well as to ensure regulated incisions (Long *et al.*, 2011; Wang *et al.*, 2015). Replisome disassembly allows ICL recognition by FANCM and its binding partners FAAP24 and MHF1/2 (Ciccia *et al.*, 2007; Collis *et al.*, 2008) (***Figure 1.10***). The presence of FANCM at ICLs facilitates recruitment of the core FA complex (de Winter and Joenje, 2009; Kim *et al.*, 2008), as well as ATR-dependent checkpoint activation through chromatin retention of TOPBP1 (Schwab *et al.*, 2010). The central event in the FA-mediated ICL repair is mono-ubiquitination of the FANCI–FANCD2 complex on lysines 523 and 561, respectively, triggered by the FA core complex and performed by the E3 ubiquitin ligase FANCL (Longerich *et al.*, 2014) (***Figure 1.10***). Mono-ubiquitinated FANCI–FANCD2 heterodimer initiates downstream ICL repair processes, including endonucleolytic incision of the DNA lesion, TLS and HR-mediated DSB repair (Garcia-Higuera *et al.*, 2001; Knipscheer *et al.*, 2009) (***Figure 1.10***). Meanwhile, SUMOylation of FANCI–FANCD2 was shown to be required for its removal from sites of DNA damage, suggesting that ubiquitin-SUMO interplay regulates the presence of the FANCI–FANCD2 complex at DNA lesions (Gibbs-Seymour *et al.*, 2015). Several SLX4-dependent endonucleases were implicated in the incision of parental DNA on either side of the ICL ('unhooking'), including MUS81-EME1, SLX1-SLX4, Fanconi-associated nuclease 1 (FAN1), SNM1A and SNM1B (Michl *et al.*, 2016; Zhang and Walter, 2014); however, the key nuclease mediating direct incision that unhooks the crosslink is thought to be XPF-ERCC1 (FANCQ) (Douwel *et al.*, 2014). The ICL excision results in a DNA lesion on one sister chromatid, which is bypassed by REV1- and DNA polymerase zeta (Pol ζ)-mediated TLS (Budzowska *et al.*, 2015), followed by the adduct removal via nucleotide excision repair (NER). Finally, the DSB generated on the second sister chromatid is repaired via HR, completing ICL repair.

1.4. ATP-dependent DNA helicase/nuclease DNA2

1.4.1. Cellular roles of DNA2

The ATP-dependent DNA helicase/nuclease DNA2 is a multi-functional enzyme, which has been extensively studied in the past years and established to have important roles during DNA replication and repair (***Figure 1.11***).

During DNA replication, the lagging strand is copied discontinuously in Okazaki fragments, initiated by an RNA primer (8-10 nt) and extended by 150-200 nt of DNA (Arezi and Kuchta, 2000). The joining of Okazaki fragments requires strand displacement synthesis from one fragment to displace the RNA primer region of the adjacent fragment, generating a flap. The current model is that the majority of flaps are short and primarily removed by FEN1 (Flap Endonuclease 1), whereas the flaps that escape FEN1 activity and are long enough to be coated by RPA (more than 30 nt-long) are processed by DNA2, which displaces RPA and cleaves the flap until it becomes a suitable substrate for FEN1 (Ayyagari *et al.*, 2003; Rossi *et al.*, 2006) (***Figure 1.12***). Indeed, *DNA2* was first characterised in yeast as an essential gene encoding a protein with helicase and endonuclease activities that was involved in long flap Okazaki fragment maturation during DNA lagging strand synthesis (Budd and Campbell, 1997; Kang *et al.*, 2000; Parenteau and Wellinger, 1999). *In vitro* analyses showed that human DNA2 (hDNA2) can also perform this process (Gloor *et al.*, 2012). However, evidence supporting this role for DNA2 in mammalian cells is lacking, as BrdU-alkaline comet assays in U2OS cells failed to detect any significant contribution of DNA2 to Okazaki fragment maturation (Duxin *et al.*, 2012).

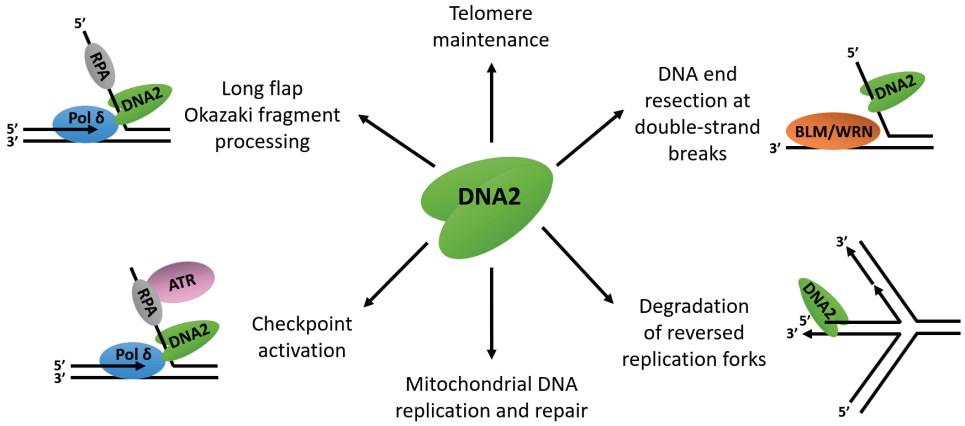

Figure 1.11. DNA2 is a multi-functional enzyme, involved in DNA replication and repair. The outline of the main cellular functions of DNA2 in maintaining genome stability. Figure adapted from Wanrooij and Burgers (2015).

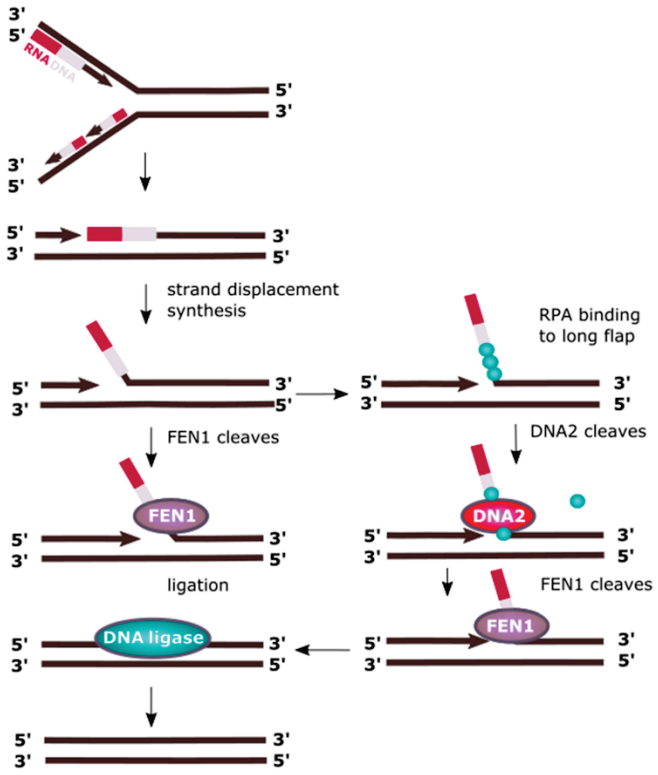

Figure 1.12. The role of DNA2 in Okazaki fragment processing.
DNA2 cooperates with FEN1 in Okazaki fragment maturation during lagging strand synthesis. When DNA Pol δ displaces the preceding Okazaki fragment, a flap structure is formed, which acts as a substrate for FEN1 cleavage. However, long flaps are partly covered by RPA proteins, blocking FEN1 activity. DNA2 trims these long flap structures, thus enabling FEN1 to complete flap processing. Figure reproduced from Pawłowska, Szczepanska and Blasiak (2017).

DNA2 also plays a role in initiating HR-mediated DSB repair through 5'-end DNA resection at DSBs (Cejka *et al.*, 2010; Karanja *et al.*, 2012; Nimonkar *et al.*, 2011; Niu *et al.*, 2010; Sturzenegger *et al.*, 2014). *In vitro* reconstitution of DNA end resection using purified human proteins suggested that RPA- and MRN-dependent cooperation between the nuclease activity of DNA2 and the helicase activity of BLM (Bloom syndrome protein) results in the degradation of 5'-ssDNA, whereas RPA-coated 3'-ssDNA remains intact (Nimonkar *et al.*, 2011). This finding was supported by Sturzenegger *et al.* (2014), demonstrating that BLM and WRN (Werner syndrome ATP-dependent helicase) act epistatically with DNA2 to promote long-range resection of DSB ends in human cells. Additionally, DNA2 was demonstrated to participate in DNA end resection during replication-coupled repair of ICLs, with its depletion leading to defective HR, S phase checkpoint activation, genome instability and sensitivity to replication stress-inducing agents (Karanja *et al.*, 2012). DNA2 was also shown to interact with FANCD2 (Karanja *et al.*, 2012), suggesting that DNA2 may be involved in mediating the

interplay between HR and the FA pathways during ICL repair. However, exonuclease 1 (EXO1) was shown to fully compensate for the absence of DNA2 in DNA end resection, demonstrating functional redundancy between these two nucleases (Karanja *et al.*, 2012; Nimonkar *et al.*, 2011; Zhu *et al.*, 2008). Additionally, DNA2 was suggested to degrade reversed replication forks and promote replication restart after genotoxic stress in human cells, and this depended on the interaction between DNA2 and WRN (Thangavel *et al.*, 2015) (***Figure 1.13***). Unexpectedly, EXO1, MRN and CtIP were shown not to be required for this reversed fork processing pathway, whereas RECQ1 restricted DNA2-WRN activity by preventing extensive nascent strand degradation (Thangavel *et al.*, 2015). Finally, DNA2-depleted U2OS cells showed elevated levels of aneuploidy and internuclear chromatin bridges, indicating that hDNA2 plays an important role in ensuring genome stability in unperturbed cells as well (Duxin *et al.*, 2009). Overall, these studies define the roles of DNA2 in maintaining genome integrity via its nucleolytic activities at DSBs and damaged replication forks.

DNA2 was also implicated as a regulator of replication checkpoint activation (Duxin *et al.*, 2012). Duxin *et al.* (2012) reported cell-cycle dependent association between DNA2 and AND-1 (Acidic Nucleoplasmic DNA-binding protein 1), a replisome protein that anchors the lagging strand DNA Pol α to the CMG replicative helicase complex (Guan *et al.*, 2017). DNA2 depletion in U2OS cells led to S/G2 phase-specific DNA damage, such as increased γH2AX levels, RPA foci and CHK1 activation, suggesting activation of the ATR-mediated S phase checkpoint in unperturbed DNA2-deficient cells (Duxin *et al.*, 2012).

As it was reported to localise to telomeres in G1 and late S/G2 phases, DNA2 is also thought to be involved in telomere maintenance (telomere capping and telomere replication) (Choe *et al.*, 2002). In *in vitro* experiments, both yeast and hDNA2 enzymes were shown to recognise, unwind and cleave the 5’ end of G quadruplexes (G4) in the presence of RPA (Masuda-Sasa *et al.*, 2008). G4 DNA structures are stable guanine-rich DNA sequences that occur at telomeres, and that can cause replication fork stalling, impairing efficient telomere replication and leading to telomere instability (Bochman *et al.*, 2012). As G4 DNA is resistant to most helicases and nucleases that act during DNA replication and repair, DNA2 was suggested to have a crucial role in maintaining telomeres by acting on these structures (Masuda-Sasa *et al.*, 2008). In support of this, a recent study reported that *S. cerevisiae* DNA2 mutants also have telomere length defects (Markiewicz-Potoczny *et al.*, 2018).

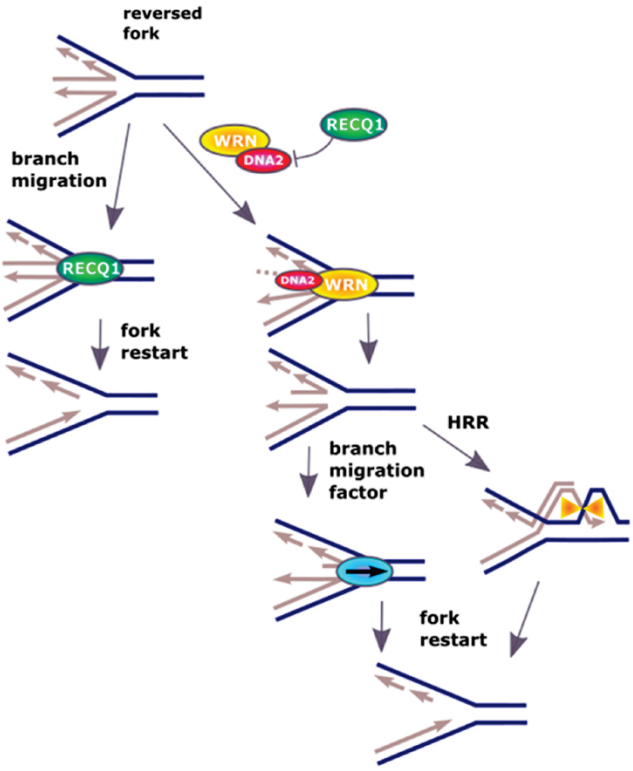

Figure 1.13. The role of DNA2 in restarting reversed replication forks.
Excessive unwinding of the template in DNA replication leads to replication fork regression by pairing of the newly synthesised strands. Resulting 'chicken foot'-like structures are primarily resolved by RECQ1 helicase, but in its absence, DNA2, acting together with WRN, can cleave the 5' DNA end of the regressed fork. Subsequent replication restart is preceded by the action of branch migration factors or homologous recombination repair (HRR) factors. Figure reproduced from Pawłowska, Szczepanska and Blasiak (2017).

Finally, hDNA2 also localises to mitochondria and has been proposed to play a role in mitochondrial DNA (mtDNA) maintenance, as its depletion decreased mtDNA replication intermediates and caused inefficient repair of damaged mtDNA (Duxin *et al.*, 2009). Additionally, Zheng *et al.* (2008) found that mtDNA polymerase gamma (Pol γ) immunoprecipitated with DNA2, and that this interaction enhanced Pol γ activity. The study also showed that DNA2 functions as the flap endonuclease in the mitochondrial long-patch base excision repair (LP-BER) pathway, suggesting the role for hDNA2 in the mitochondrial DNA replication and repair. Supporting the importance of this cellular role, monoallelic mutations in *DNA2* were shown to cause myopathy and mitochondrial disease (Chae *et al.*, 2015; Phowthongkum and Sun, 2017; Ronchi *et al.*, 2013). Taken together, the studies on DNA2 suggest that it is a multifaceted enzyme, whose activity plays important roles in several aspects of DNA replication and repair, contributing to genome stability.

1.4.2. The cryptic helicase activity of DNA2

The DNA2 nuclease activity is essential for its various roles in DNA replication and repair. Although DNA2 also has ATP-dependent helicase activity, in many DNA2-dependent processes this activity is provided by other helicases, such as BLM or WRN during DNA end resection (Nimonkar *et al.*, 2011; Sturzenegger *et al.*, 2014) and WRN during degradation of reversed replication forks (Thangavel *et al.*, 2015). Thus, although the biological importance of DNA2 nuclease activity has been well-established, the functional role of its ATP-dependent helicase activity both in yeast and humans was long poorly understood. In an initial biochemical analysis of DNA2 enzymatic activities, Budd and Campbell (1995) showed the ATP-dependent ability of affinity-purified *S. cerevisiae* DNA2 (scDNA2) to unwind DNA duplex in a 3'-5' direction. Moreover, a mutation in the ATP-binding motif of scDNA2 led to inactivation of both ATPase and helicase activities and caused lethality (Budd *et al.*, 1995), suggesting that yeast DNA2 ATP-dependent helicase activity has an important function *in vivo*. However, initial biochemical analyses of hDNA2 found no evidence for its helicase activity. Human DNA2 was detected to have strong ssDNA-specific endonuclease and ATPase activities *in vitro*, but no helicase activity (Kim *et al.*, 2006). In contrast, another study showed that recombinant hDNA2 was able to perform ATP-dependent unwinding of a forked structure with a non-complementary 18 nt-long 5' tail, even though this activity was weaker than for other helicases, including scDNA2 (Masuda-Sasa *et al.*, 2006). More recent studies showed that both scDNA2 and hDNA2 have processive helicase activity; however, it is inhibited by the nuclease activity cleaving the ssDNA overhangs required for helicase loading (Levikova *et al.*, 2013; Pinto *et al.*, 2016), explaining why the helicase activity appears to be cryptic and hard to detect.

At this stage, the cellular function of this DNA2 motor activity still remained unclear. Mutations in the ATPase motif of the scDNA2 helicase domain had almost no effect on 5' flap processing and DSB resection *in vitro* (Cejka *et al.*, 2010; Niu *et al.*, 2010; Zhu *et al.*, 2008), implying that the helicase activity is not important for the most studied cellular roles of DNA2. However, cell cycle defects observed in DNA2-depleted U2OS cells were rescued upon expression of the wild-type allele, but, like the nuclease-deficient allele, the helicase-deficient allele failed to do so (Duxin *et al.*, 2012). This indicates that both nuclease and helicase activities of DNA2 are essential for maintaining genomic stability in human cells. Unexpectedly, U2OS cells expressing nuclease-deficient DNA2 exhibited cell cycle defects that were more severe than those in DNA2-depleted cells (Duxin *et al.*, 2012). This suggests not only that the

nuclease and helicase activities of hDNA2 are coupled, but also that the helicase activity of hDNA2 can become toxic when nuclease activity is abolished.

Recent biochemical studies offered another explanation for the importance of the ATPase/helicase domain of both yeast and human DNA2, demonstrating that it functions primarily as a translocase along ssDNA, to promote efficient DNA end resection, while the lead helicase function is performed by a cognate RecQ helicase, either BLM or WRN (Levikova *et al.*, 2017; Miller *et al.*, 2017) (***Figure 1.14***). The translocase function of DNA2 is potentiated by its interaction with RPA and contributes to rapid DNA degradation, resulting in longer DNA cleavage products (Levikova *et al.*, 2017). While DNA2 helicase function was masked by its nuclease activity (Levikova *et al.*, 2013; Pinto *et al.*, 2016), the nuclease activity did not prevent translocation on ssDNA (Levikova *et al.*, 2017; Miller *et al.*, 2017). This suggests that ssDNA translocation is the main cellular function of the DNA2 ATPase/helicase domain.

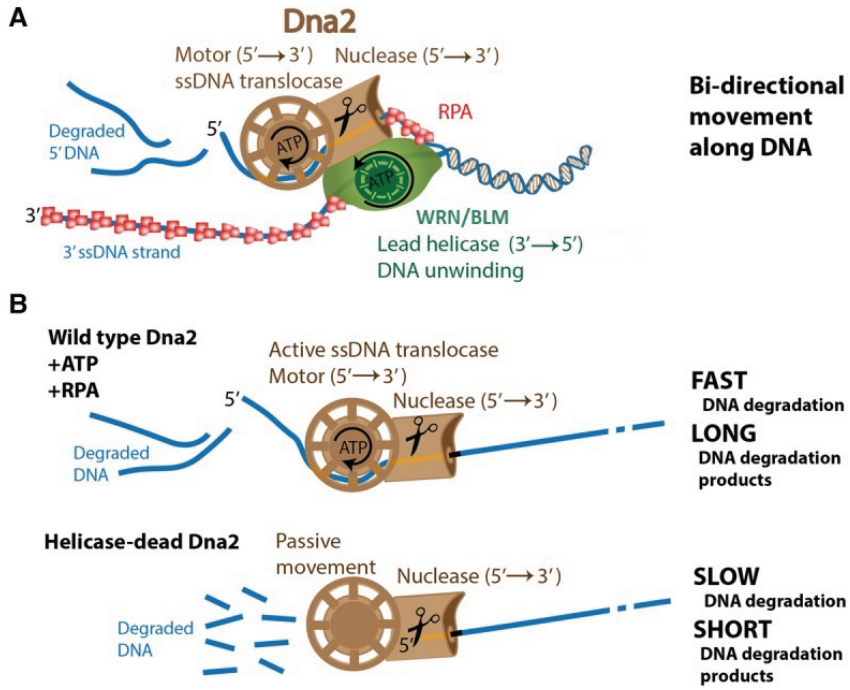

Figure 1.14. Model for the involvement of DNA2 helicase in DNA end resection.
As WRN/BLM helicase functions as the lead helicase translocating in the 3'-5' direction, the motor activity of DNA2 allows translocation on the unwound 5'-terminated DNA strand, which is degraded by its nuclease activity (a). The RPA- and ATP hydrolysis-dependent translocase activity of DNA2 accelerates ssDNA processing, resulting in long DNA degradation fragments (b, top panel). In contrast, for helicase-dead DNA2 without active translocation, DNA2-dependent ssDNA degradation is slow, resulting in short DNA degradation fragments (b, bottom panel). Figure adapted from Levikova, Pinto and Cejka (2017).

1.5. E3 ubiquitin ligase TRAIP

1.5.1. Mutations in *TRAIP* cause microcephalic primordial dwarfism

In the Andrew Jackson laboratory, *TRAIP*, which encodes an E3 ubiquitin ligase, was recently identified as a causative gene of Seckel syndrome, a form of MPD (Harley *et al.*, 2016) (see Section 1.1, ***Table 1.1***) (***Figure 1.15*****a-c**). During whole exome sequencing (WES) of MPD patients, a homozygous nonsense mutation in *TRAIP* (c.553C>T) was identified in one affected individual (P1). This mutation results in a premature stop codon (p.R185*). Sanger sequencing of the *TRAIP* coding exons in a cohort of 262 primary microcephaly and MPD patients identified a second individual (P2) homozygous for the same variant. Finally, WES performed by the Berndt Wollnik laboratory on 28 patients with Seckel syndrome-like characteristics identified a third individual (P3) with a different homozygous variant in *TRAIP*: a missense mutation c.52C>T, resulting in p.R18C substitution. The affected arginine is an evolutionary highly conserved residue within the N-terminal RING finger domain of TRAIP, which was previously demonstrated to exhibit enzymatic E3 ubiquitin ligase activity *in vitro* (Besse *et al.*, 2007) (***Figure 1.15*****a**). All three patients with mutations in *TRAIP* were phenotypically similar: they exhibited microcephaly and global growth failure of prenatal onset (***Figure 1.15*****b**), as well as a reduction in cerebral cortex size, simplified folding of gyri, a narrow elongated face and a small jaw (***Figure 1.15*****c**). Moreover, there was evidence for an increased susceptibility to infections in these patients. As no link between TRAIP and the MPD phenotype had previously been reported at the time, our laboratory carried out experiments to investigate the underlying mechanism of how mutations in *TRAIP* result in reduced growth in MPD patients (Harley *et al.*, 2016).

Firstly, using cell lines derived from all three patients, the deleterious effects of *TRAIP* mutations on transcript and protein levels were established (Harley *et al.*, 2016). The p.R185* mutation was shown to result in nonsense-mediated decay (NMD) of the transcript, leading to a marked reduction in the full-length *TRAIP* transcript, as well as greatly reduced protein levels. However, consistent with the finding that TRAIP is an essential gene for early embryonic development in mice (Park *et al.*, 2007), residual TRAIP protein was present in p.R185* patient-derived cell lines. Additionally, RT-PCR analysis demonstrated the presence of alternatively spliced transcripts allowing production of TRAIP protein products with small internal deletions (Harley *et al.*, 2016). The p.R18C mutation did not affect transcript levels but resulted in

markedly reduced TRAIP protein levels in the patient-derived cell line, likely caused by reduced protein stability arising from the missense mutation.

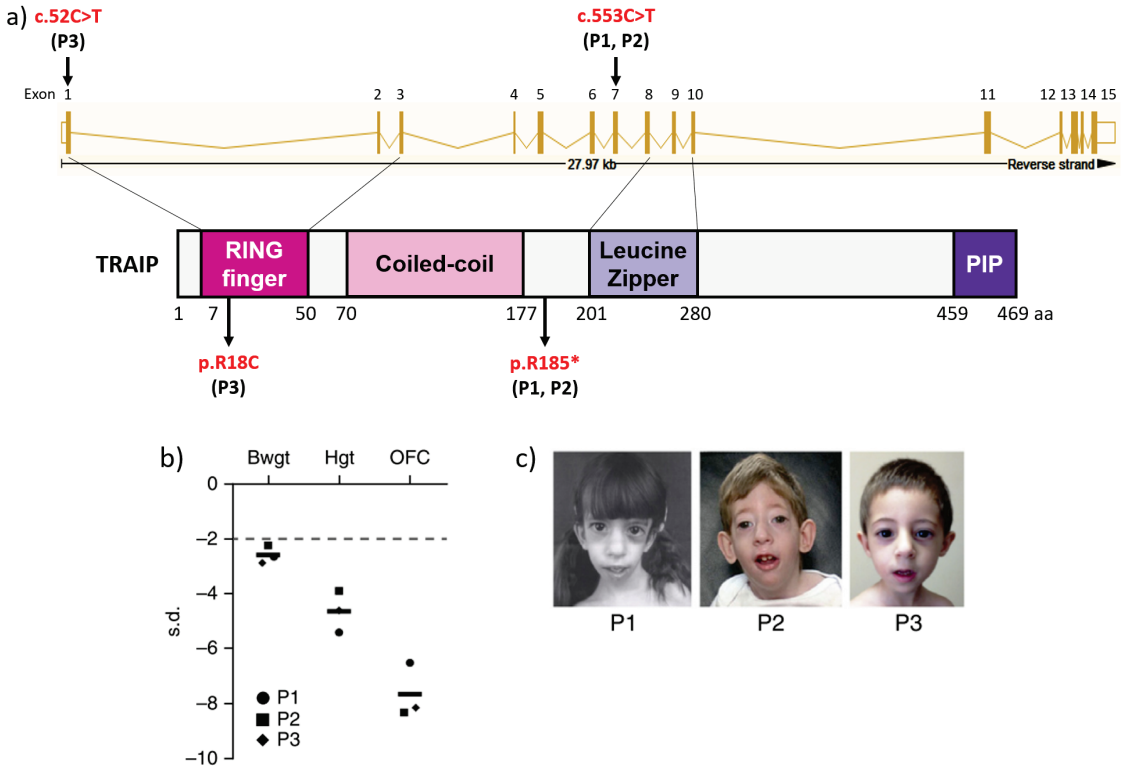

Figure 1.15. *TRAIP* is mutated in microcephalic primordial dwarfism.
a) A schematic structure of the *TRAIP* gene and TRAIP protein, with locations of MPD patient mutations c.52C>T (p.R18C; P3) and c.553C>T (p.R185*; P1 and P2) indicated in red (Harley *et al.*, 2016). The four distinct domains of TRAIP are indicated as well (PIP = PCNA-interacting protein box motif) (Harley *et al.*, 2016; Hoffmann *et al.*, 2016; W. Feng *et al.*, 2016). b) Patients with TRAIP mutations have prenatal onset severe growth failure with disproportionate microcephaly. Birth weight (Bwgt), current height (Hgt) and current head circumference (OFC) are plotted; black bars indicate mean values. 97.5% of the general population will lie above the dashed line at −2 SD. Adapted from Harley *et al.* (2016). c) Photographs of TRAIP patients demonstrating their facial similarities (adapted from Harley *et al.*, 2016).

The protein encoded by *TRAIP* (Tumour Necrosis Factor (TNF) Receptor-Associated Factor (TRAF)-Interacting Partner; TRIP; RNF206) contains an N-terminal RING finger motif, a long coiled-coil domain, a leucine zipper domain, and a PCNA-Interacting Protein (PIP)-box domain (Lee, Lee and Choi, 1997; Hoffmann *et al.*, 2016; W. Feng *et al.*, 2016) (***Figure 1.15*a**). TRAIP was first described as a component of TNFR2 (TNF Receptor 2)- or CD30-containing

signalling complexes, and shown to act as an inhibitor of TRAF2-mediated NF-κB activation, thus preventing TRAF-mediated cell activation and promoting cell death signalling (Lee *et al.*, 1997). TRAIP-mediated inhibition of NF-κB activation was also shown to downregulate production of pro-inflammatory cytokines (E. S. Park *et al.*, 2015), suggesting that TRAIP may have an anti-inflammatory effect. TRAIP was further implicated in downregulation of interferon beta (IFN-β) production and antiviral response through poly-ubiquitination of TBK1 (TANK-Binding Kinase 1), leading to its proteasomal degradation (Zhang *et al.*, 2012). The potential role of TRAIP as an anti-inflammatory factor may explain the increased severity of infections in MPD patients with *TRAIP* mutations.

TRAIP has also been implicated in mitosis, as it was shown to localise to mitotic chromosomes, ensure correct chromosome alignment, and regulate the spindle assembly checkpoint (Chapard *et al.*, 2014). Moreover, TRAIP protein levels were reported to peak in the G2/M phase of the cell cycle (Chapard *et al.*, 2015), and its regulation of mitotic progression required its homodimerisation via the coiled-coil domain (I. S. Park *et al.*, 2015). Finally, TRAIP was also shown to facilitate stable kinetochore-microtubule attachment during meiosis in mouse oocytes, with its knockdown leading to misaligned chromosomes and aneuploidy (Yuan *et al.*, 2016). A role for TRAIP in the spindle assembly checkpoint could also underlie the growth phenotype in TRAIP MPD patients, with increased aneuploidy causing increased cell death. However, no significant aneuploidy was observed in TRAIP patient-derived cells (Harley *et al.*, 2016).

1.5.2. TRAIP in UV-induced DNA damage response signalling

The phenotype of the three MPD patients with *TRAIP* mutations resembled that of Seckel syndrome patients with defective ATR pathway signalling (O'Driscoll *et al.*, 2003). The PI3K-like kinase ATR is one of the key players in sensing DNA damage and signalling it to downstream DDR factors, and is thought to primarily respond to stretches of ssDNA resulting from stalled replication forks (see Section 1.3.1). Additionally, ATR signalling is known to be involved in facilitating the repair of DNA damage induced by ultraviolet (UV) radiation (Zou *et al.*, 2003; Zou and Elledge, 2003). UV radiation induces a variety of mutagenic and cytotoxic DNA lesions, with three major classes representing cyclobutane pyrimidine dimers (CPDs), 6-4 photoproducts (6-4PPs), and 6-4 Dewar dimers (Rastogi *et al.*, 2010). UV-induced DNA lesions are commonly repaired via nucleotide excision repair (NER), base excision repair (BER), and

mismatch repair (MMR) pathways (Rastogi *et al.*, 2010). Additionally, they can undergo post-replication repair, which utilises TransLesion Synthesis (TLS) or template switching (TS) to bypass or avoid DNA lesions and prevent accumulation of ssDNA gaps (Gao *et al.*, 2017). If unrepaired, these bulky DNA lesions obstruct essential processes, such as DNA replication and transcription, and can lead to production of highly deleterious DSBs resulting from collapsed replication forks (Batista *et al.*, 2009; Limoli *et al.*, 2002).

Harley *et al.* (2016) analysed the possible involvement of TRAIP in DDR signalling after UV irradiation and demonstrated that TRAIP promptly relocalises to DNA damage sites after exposure to UV-C (<280 nm). Moreover, patient-derived cells, as well as TRAIP-depleted HeLa cells, showed a significant reduction in UV-C-induced RPA2 phosphorylation on serine residues 4 and 8 (pRPA2-S4/S8) and H2AX phosphorylation on serine 139 (γH2AX). Both were rescued by retroviral complementation of TRAIP-deficient cells with wild-type TRAIP. TRAIP deficiency specifically compromised pRPA2-S4/S8 and γH2AX levels in EdU-positive cells after UV-C-induced DNA damage, suggesting that TRAIP acts during S phase to ensure optimal phosphorylation of these proteins after UV irradiation. TRAIP-deficient cells also had slower doubling times, which were rescued by re-introduction of wild-type TRAIP. Moreover, these cells showed slower progression through S phase compared to control cells, pointing towards a replication-related cell cycle delay. DNA fibre analyses also revealed significantly increased levels of replication fork stalling after UV-C treatment in patient-derived cells, as well as marked fork asymmetry indicative of replication problems caused by bulky UV-associated DNA lesions. Taken together, Harley *et al.* (2016) demonstrated that TRAIP has an S phase-specific role in ensuring replication fork progression past bulky polymerase-stalling UV adducts.

Although a clear reduction in pRPA2-S4/S8 signal was observed in TRAIP-deficient cells, DDR-associated phosphorylation of other key substrates of the PI3K kinases ATR, ATM and DNA-PK was not substantially altered (Harley *et al.*, 2016). Moreover, the G2/M checkpoint was not affected in response to UV-C irradiation in TRAIP-depleted cells (Harley *et al.*, 2016). These results suggested that TRAIP deficiency did not result in global ATR signalling defects but rather specifically compromised phosphorylation of DNA damage markers H2AX and RPA2 after induction of UV damage. Serine 139 (S139) phosphorylation of H2AX, a marker of DSBs, can be mediated by other members of PI3K kinase family, with ATM proposed to be its main modifier (Burma *et al.*, 2001). Additionally, previous cell-free and cell-based studies indicated that RPA2 phosphorylation at S4 and S8 is primarily mediated by DNA-PK in response to DSBs (Anantha *et al.*, 2007; Zernik-Kobak *et al.*, 1997). These studies, combined with results

obtained by Harley *et al.* (2016), suggest that a fraction of ongoing replication forks undergo collapse after UV-C irradiation, generating DSBs and inducing DNA-PK-mediated RPA2 and ATM-mediated γH2AX hyperphosphorylation.

A previous developmental study proposed that overexpression of the *Drosophila melanogaster* orthologue of TRAIP, Nopo, promotes TLS by increased ubiquitination of DNA polymerase eta (Pol η) (Wallace *et al.*, 2014). As TLS is a DNA damage tolerance mechanism that facilitates DNA replication past bulky DNA lesions (Section 1.3.2), it involves temporarily switching replicative DNA polymerases for highly specialised Y family translesion polymerases with larger active sites (Waters *et al.*, 2009). Although the lack of a 3'-to-5' proofreading activity in most translesion polymerases contributes to their low fidelity, Pol η is specifically adapted to mediate error-free bypass of lesions induced by UV treatment, namely CPDs (Waters *et al.*, 2009). However, it is not clear whether the link between TRAIP overexpression and Pol η ubiquitination, observed by Wallace *et al.* (2014), is relevant to the role of TRAIP in responding to UV-induced DNA lesions, reported by Harley *et al.* (2016). Wallace *et al.* (2014) proposed TRAIP-mediated ubiquitination of Pol η based on the data obtained from examining TRAIP overexpression in the absence of exogenous DNA damage. Partial loss-of-function mutations in the Pol η-encoding *POLH* gene cause an autosomal recessive disorder Xeroderma Pigmentosum Variant (XP-V) (Johnson *et al.*, 1999; Masutani *et al.*, 1999), characterised by sunlight sensitivity, photophobia, freckle-like pigmentation and an increased risk of developing skin cancer (Lehmann *et al.*, 2011). However, none of the XP-V clinical features were observed in MPD patients with mutations in *TRAIP*. The substantially different clinical phenotypes due to *POLH* and *TRAIP* mutations therefore suggest different molecular mechanisms. One of the possible roles for TRAIP in UV-induced DDR could be its involvement in template switching (TS), a parallel Pol η-independent HR-mediated pathway to bypass UV-induced replication blocking DNA lesions (X. Xu *et al.*, 2015). RPA2 phosphorylation is known to facilitate RAD51 recruitment and initiate HR at sites of replication fork arrest (Shi *et al.*, 2010). Decreased RPA2 phosphorylation in TRAIP-deficient cells may therefore compromise the TS pathway that normally allows fork progression at bulky UV-induced DNA adducts.

1.5.3. TRAIP in DNA damage response signalling after other types of DNA damage

TRAIP was implicated not only in UV-induced DDR signalling during genome replication (Harley *et al.*, 2016); several studies also linked TRAIP to the cellular response to other types of DNA damage, including hydroxyurea (HU)-induced replication stress, camptothecin (CPT)-induced DNA-TOP1 crosslinks, mitomycin C (MMC)-induced interstrand crosslinks (ICLs), and ionising radiation (IR)-induced DSBs (Hoffmann *et al.*, 2016; Soo Lee *et al.*, 2016; W. Feng *et al.*, 2016) (***Table 1.2***). As some observations in these recent studies seem contradictory, the precise DDR-associated roles of TRAIP remain unclear. For example, Harley *et al.* (2016) observed increased replication fork stalling in TRAIP-deficient cells only following UV-C exposure, but not HU, MMC or aphidicolin treatment, suggesting a specific role for TRAIP in promoting efficient bypass of UV-induced DNA lesions (***Figure 1.16*****a**). In contrast, W. Feng *et al.* (2016) reported compromised replication fork stability, progression and restart in HU-treated TRAIP-depleted cells (***Figure 1.16*****c**). Moreover, Harley *et al.* (2016) reported reduced pRPA2-S4/S8 and γH2AX levels in S phase only after UV-C treatment, whereas Hoffmann *et al.* (2016) observed the same outcome after HU, CPT and MMC treatment as well (***Figure 1.16*****b**). Finally, IR-induced cell survival defect in TRAIP-depleted cells was observed by Soo Lee *et al.* (2016) (***Figure 1.16*****d**), but not by Hoffmann *et al.* (2016).

Table 1.2. Summary of recent studies about the role of TRAIP in DDR.
The cell lines used in each report are indicated, as well as methods of TRAIP depletion, types of DNA damage analysed and outcomes of TRAIP deficiency observed (in unperturbed cells and after DNA damage).

Study	Cell line(s) used	Method of TRAIP depletion	Type of DNA damage	Outcomes of TRAIP deficiency
Harley *et al.*, 2016 (A. Jackson laboratory)	TRAIP patient-derived primary fibroblasts	—	—	• Impaired cell proliferation; • Increase in late S phase and/or G2 cells; • No alteration in replication fork velocity, inter-origin distance and fork stalling
			UV-C	• Reduced pRPA2-S4/S8 and γH2AX levels in S phase; • Increased frequency of replication fork stalling and fork asymmetry; • Reduced levels of ongoing replicating forks
			Aphidicolin	• No effect on replication fork asymmetry
			MMC	• No effect on replication fork asymmetry and stalling
			HU	• No impairment of replication restart
	HeLa	RNAi	—	• Increase in late S phase and/or G2 cells

Study	Cell line(s) used	Method of TRAIP depletion	Type of DNA damage	Outcomes of TRAIP deficiency
			UV-C	• Reduced pRPA2-S4/S8 and γH2AX levels in S phase
Hoffmann *et al.*, 2016 (N. Mailand laboratory)	U2OS	RNAi	—	• Accumulation of G2-phase cells; • Mildly reduced replication fork rates; • Increase in cells with γH2AX–positive micronuclei; • Increase in chromosome alignment and segregation defects in mitosis
			CPT	• Reduced intensity of RPA foci; • Reduced RPA, CHK1 and H2AX phosphorylation in S phase; • Reduced ssDNA generation
			MMC	• Reduced RPA, CHK1 and H2AX phosphorylation in S phase; • Elevated rate of chromosomal aberrations; • Reduced cell survival
			HU	• Reduced RPA, CHK1 and H2AX phosphorylation in S phase; • Reduced replication fork rates
			IR	• No effect on cell survival
W. Feng *et al.*, 2016 (M. S.-Y. Huen laboratory)	HeLa	RNAi	—	• Increase in mitotic aberrations; • No effect on duration of mitosis
			HU	• Increase in mitotic aberrations; • No effect on duration of and cell percentage in mitosis
	U2OS	RNAi	—	• Increase in late S phase and/or G2 cells
			HU	• Increase in the formation of micronuclei, gross chromosomal aberrations and γH2AX–positive cells; • Reduced cell survival; • Compromised fork stability, progression and restart; • Persistence of PCNA and RPA1 accumulation on chromatin
			UV	• Increased chromatin-bound RPA1 levels
			Aphidicolin	• Increased chromatin-bound RPA1 levels
Soo Lee *et al.*, 2016 (H. Kim laboratory)	U2OS	RNAi	—	• Reduced efficiency of HR repair
			Microirradiation	• Impaired accumulation of RAP80 at laser stripes
			IR	• Reduced chromatin localisation of RAP80
	HeLa	RNAi	IR	• Increased numbers of γH2AX foci; • Impaired G2/M checkpoint; • Reduced cell survival
	HEK293T	RNAi	IR	• Reduced BRCA1 recruitment to sites of DNA damage

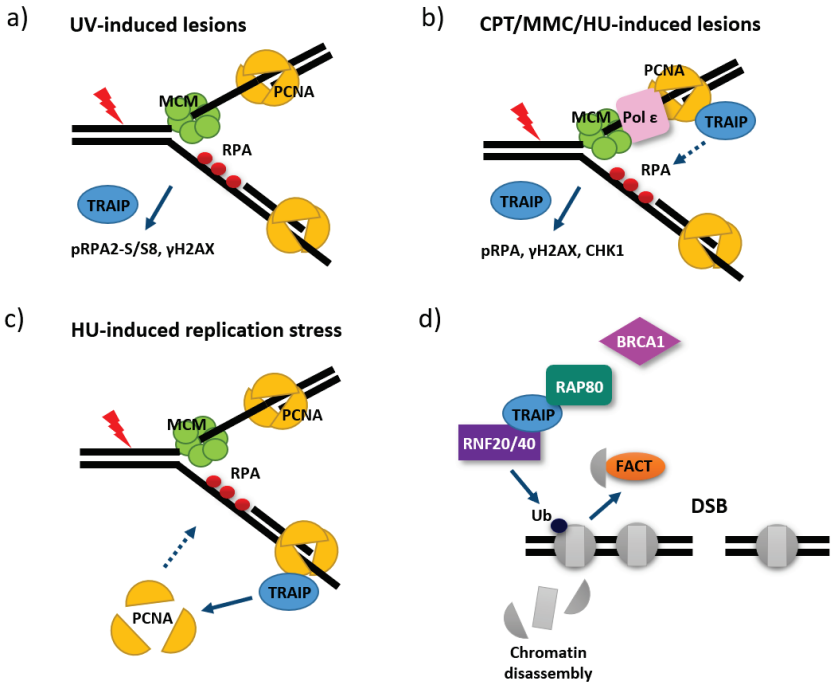

Figure 1.16. Models for the proposed roles of TRAIP in DNA damage response signalling.
a) Harley *et al.* (2016) showed that TRAIP promotes S phase-specific RPA2 and H2AX phosphorylation after DNA damage induction and suggested the role for TRAIP in ensuring replication fork progression past bulky polymerase-stalling DNA lesions induced by UV.
b) Hoffmann *et al.* (2016) showed that TRAIP interacts with PCNA and promotes ssDNA formation at stalled replication forks, as well as phosphorylation of RPA, H2AX and CHK1 and in response to CPT-, MMC- and HU-induced replication stress. The authors suggested that TRAIP may be involved in uncoupling replicative helicase and polymerase after replication stress.
c) W. Feng *et al.* (2016) suggested that TRAIP participates in regulating PCNA unloading from stressed replication forks. According to the authors, TRAIP senses nucleotide shortage after HU treatment and localises to stalled replication forks, where it promotes PCNA unloading via a yet unknown mechanism. TRAIP depletion was suggested to compromise PCNA turnover from chromatin and DNA synthesis. Figure adapted from a working model described by W. Feng *et al.* (2016).
d) Soo Lee *et al.* (2016) proposed that TRAIP is required for recruitment of RAP80 and its functional downstream partners, including BRCA1, to sites of DNA damage. TRAIP itself is suggested to localise to chromatin via direct interaction with RNF20–RNF40 complex, which mono-ubiquitinates histones and facilitates their eviction. Histone chaperone FACT promotes displacement of H2A/H2B at transcription-blocked sites. Figure based on a working model described by Soo Lee *et al.* (2016).

As each of these studies used slightly different approaches (e.g. different cell lines) to arrive at their conclusions, some of the differences in observations may be explained by this. Hoffmann *et al.* (2016) used CHROMASS (chromatin mass spectroscopy) (Räschle *et al.*, 2015) to show that TRAIP localised to psoralen-induced ICL-containing chromatin in *X. laevis* egg extracts, and suggested that TRAIP enrichment at those sites was triggered specifically by the

replication fork encountering such DNA roadblocks. TRAIP was further suggested by this study to play a role in responding to several types of DNA damage-inducing agents: MMC, CPT and HU. Replication fork stalling following cell treatment with MMC led to prominent relocalisation of TRAIP from the nucleolus, where it resides in unperturbed cells, to the nucleoplasm (Hoffmann *et al.*, 2016). After MMC treatment, TRAIP-depleted cells exhibited reduced levels of chromatin-bound pRPA and γH2AX, as well as elevated rates of chromosomal aberrations and reduced cell survival (Hoffmann *et al.*, 2016). In TRAIP-depleted cells treated with CPT, the same reduction in chromatin-bound pRPA and γH2AX was observed, as well as reduced RPA loading in S phase (Hoffmann *et al.*, 2016). Treatment with HU also resulted in pRPA and γH2AX signalling defects in TRAIP-depleted cells, as well as reduced replication fork rates (Hoffmann *et al.*, 2016). However, IR treatment had no effect on cell survival in TRAIP-depleted cells. As similar cellular outcomes were observed after distinct replication stress-inducing agents in TRAIP-depleted cells, but not after IR, Hoffmann *et al.* (2016) proposed a role for TRAIP in reconfiguring stalled replication forks, rather than promoting DNA resection of DSBs (***Figure 1.16*b**).

The importance of TRAIP for replication fork recovery and progression was also noted by W. Feng *et al.* (2016) (***Figure 1.16*c**). This study demonstrated that TRAIP depletion, combined with HU treatment, which slows down DNA synthesis by causing rapid depletion of dNTP pools, leads to reduced cell survival, as well as an increase in micronuclei formation, chromosomal aberrations and γH2AX foci. Consistent with Harley *et al.* (2016) and Hoffmann *et al.* (2016), W. Feng *et al.* (2016) observed the interaction of TRAIP with PCNA, the DNA-encircling processivity factor of DNA polymerases with multiple roles in DNA replication and repair (Moldovan *et al.*, 2007). In agreement with Hoffmann *et al.* (2016), W. Feng *et al.* (2016) also found that TRAIP was recruited to damaged chromatin in response to various sources of replication stress-inducing agents, such as aphidicolin, MMC, UV radiation and cisplatin, but not IR, once again suggesting that TRAIP may have an important role in restructuring and restart of stalled replication forks but may not be required for DSB repair. Moreover, DNA combing analysis of fork progression demonstrated that TRAIP-depleted cells have shorter CldU tracks upon release from HU treatment, strengthening the hypothesis that TRAIP has a role in maintaining fork stability and ensuring restart after replication stress (W. Feng *et al.*, 2016). As TRAIP Q460A/L463A mutant, impaired in PCNA binding, displayed defects in fork progression during cell recovery from HU treatment, W. Feng *et al.* (2016) proposed that the TRAIP-PCNA interaction is important for repair and recovery of HU-stalled forks. Meanwhile,

TRAIP PIP domain deletion (Δ460–469 aa) mutant, used by Hoffmann *et al.* (2016), resulted in impaired HU- and CPT-induced RPA phosphorylation, but did not negatively affect long-term cell survival after MMC treatment. W. Feng *et al.* (2016) also suggested that TRAIP may be directly involved in regulating PCNA levels on chromatin by ensuring PCNA unloading from damaged DNA (***Figure 1.16*c**). Indeed, TRAIP depletion was shown to impair the replication stress-induced reduction of chromatin-bound PCNA, resulting in excessive levels of PCNA, as well as RPA, on chromatin (W. Feng *et al.*, 2016). The authors also noted the hyper-accumulation of chromatin-bound RPA in TRAIP knockdown cells after treatment with various replication stress-inducing drugs, which is in disagreement with Hoffmann *et al.* (2016), who instead observed a reduction in RPA loading in TRAIP-depleted cells after exposure to DNA damaging agents.

In contrast to the studies discussed above, Soo Lee *et al.* (2016) suggested a role for TRAIP in DDR and DNA repair of IR-induced DSBs (***Figure 1.16*d**). The authors observed an increase in IR-induced γH2AX foci at various time points in TRAIP-depleted HeLa cells, which was rescued by introducing siRNA-resistant WT TRAIP, but not a TRAIP mutant unable to interact with RAP80 (Soo Lee *et al.*, 2016). DNA damage response protein RAP80 recognises and binds lysine 63 (K63)-linked poly-ubiquitin chains of chromatin-bound proteins and subsequently recruits BRCA1 and its associated factors to DNA damage loci, particularly IR-induced DSBs (Wu *et al.*, 2012). The result obtained by Soo Lee *et al.* (2016) therefore suggests that the TRAIP–RAP80 interaction aids repair of IR-induced DSBs. Using immunofluorescence experiments, the authors showed that TRAIP depletion results in fewer IR-induced CCDC98/ABRAXAS and MERIT40/NBA1 foci-positive cells, both of which are known to facilitate BRCA1 recruitment to DSBs (L. Feng *et al.*, 2009; Kim *et al.*, 2007). TRAIP knockdown in U2OS cells also led to reduced HR efficiency in the DR-GFP (direct repeat-green fluorescent protein) reporter assay, as well as a reduction in BRCA1 recruitment to IR-induced DNA damage foci in 293T cells, and a defective G2/M checkpoint control after IR in HeLa cells. All these defects were rescued by re-introduction of WT TRAIP but not the RAP80 interaction mutant of TRAIP (Soo Lee *et al.*, 2016). Taken together, these data suggest that TRAIP acts as an upstream regulator of the RAP80-dependent IR-induced BRCA1 recruitment to chromatin (***Figure 1.16*d**).

Overall, the recent studies indicate that TRAIP is mainly required for DDR signalling in response to replication-associated DNA lesions. However, there are some contradictions between studies. Therefore, it is clear that more work is required to elucidate the precise way in which this E3 ubiquitin ligase promotes DDR (see Chapters 4–6 of this thesis).

1.6. Replication fork protection factor DONSON

1.6.1. Mutations in *DONSON* cause microcephalic primordial dwarfism

Mutations in replication fork-associated protein DONSON (DOwnstream Neighbour of SON) were recently linked to pathogenesis of MPD by the Andrew Jackson and Grant Stewart (University of Birmingham) laboratories (Reynolds *et al.*, 2017). Using WES and targeted re-sequencing of MPD patients without a molecular diagnosis, 29 affected individuals were shown to have rare biallelic mutations in the poorly characterised *DONSON* gene (Reynolds *et al.*, 2017). Although various types of mutations were identified, there were no individuals with biallelic nonsense or frameshift mutations in *DONSON* (Reynolds *et al.*, 2017). This suggested that DONSON is an essential protein, and was later supported by the observed lethality of the DONSON knockout mouse (Evrony *et al.*, 2017). Many of the MPD-associated *DONSON* variants resulted in partial loss of DONSON function, with immunoblotting analyses showing a marked decrease of DONSON protein in patient-derived cell lines, but with residual DONSON protein detectable in all cases (Reynolds *et al.*, 2017). Moreover, several of the mutations disrupted the subcellular localisation of GFP-tagged DONSON, leading to a diffuse pan-cellular GFP signal instead of the exclusively nuclear signal seen for wild-type DONSON, suggesting another mechanism by which DONSON protein function is compromised in some of the patients (Reynolds *et al.*, 2017). All MPD patients with *DONSON* mutations had pronounced microcephaly (OFC -7.5±2.4 SD), as well as highly reduced cerebral cortical size and gyri folding. Reduction in height was less marked than reduction in OFC (–3.2±1.4 SD) and less severe than in some other MPD patients. Several individuals with *DONSON* mutations also exhibited subtle skeletal abnormalities, including radial ray defects and underdeveloped patellae, alongside mild intellectual disability.

The Walsh laboratory independently identified DONSON as a cause of human disease through studying microcephaly-micromelia syndrome (MMS) (Evrony *et al.*, 2017). MMS is an extremely rare autosomal recessive condition, so far identified in a single Canadian First Nations population in Saskatchewan; it leads to prenatal growth restriction, severely reduced brain size, craniofacial and limb abnormalities, and neonatal lethality (Evrony *et al.*, 2017). Using linkage analysis of affected pedigrees, Evrony *et al.* (2017) demonstrated that a locus on chromosome 21 was linked to MMS, but no obvious pathogenic protein-coding or splicing variant was identified by DNA sequencing. Eventually, RNA-seq analysis showed significantly increased retention of DONSON intron 6. This was shown to be caused by a non-coding biallelic

variant in the *DONSON* gene present within that locus. Retention of intron 6 is predicted to cause either NMD of the mutant transcript or to result in a severely truncated protein. Taken together, studies by Reynolds *et al.* (2017) and Evrony *et al.* (2017) indicate the importance of functional DONSON protein for normal development and organism growth.

1.6.2. The role of DONSON during genome replication

The DONSON orthologue in *D. melanogaster*, Humpty dumpty (Hd), is expressed during late G1 and S phases and was previously suggested to play a role in genome replication in follicle cells of the ovary and cell proliferation during development, with its depletion causing DNA damage and defective DNA replication (Bandura *et al.*, 2005). This study prompted Reynolds *et al.* (2017) to investigate whether these cellular roles of DONSON are conserved in humans. DONSON depletion in HeLa cells, pulsed with BrdU, led to an increase in BrdU-positive cells observed by FACS, suggesting that DONSON is needed for efficient S phase progression. Moreover, DNA fibre analysis of DONSON-depleted HeLa cells showed higher levels of spontaneous replication fork stalling and increased replication fork asymmetry, and thus fewer ongoing forks. Additionally, unperturbed HeLa cells lacking DONSON, particularly EdU-positive S phase cells, exhibited increased levels of γH2AX and 53BP1 foci. Finally, DONSON-depleted cells also had higher levels of DSBs, as measured by pulsed-field gel electrophoresis. These results indicated that DONSON helps cells to successfully progress through S phase by protecting and stabilising replication forks, as well as preventing spontaneous DNA damage.

A mass spectrometry (MS) screen to identify interaction partners of GFP-DONSON detected various components of the replisome, such as subunits of the MCM complex and PCNA, whose interaction with DONSON was subsequently confirmed by pull-down experiments (Reynolds *et al.*, 2017). These observations were further strengthened by proximity ligation assay (PLA) and fluorescence cross-correlation spectroscopy (FCCS) experiments, demonstrating association of GFP-tagged DONSON with PCNA in replicating HeLa cells (Reynolds *et al.*, 2017). Finally, iPOND (isolation of proteins on nascent DNA) technique (Sirbu *et al.*, 2012, 2011) combined with MS was used to show the enrichment of DONSON at replication forks and nascent DNA, compared to mature chromatin, strongly suggesting that DONSON is a novel component of the replication machinery (Reynolds *et al.*, 2017).

DNA replication defects in DONSON-deficient cells were further exacerbated by exogenous DNA damage (Reynolds *et al.*, 2017). Upon HU and MMC exposure, DONSON-depleted cells showed high levels of fork stalling and failure to prevent new origin firing, compared to wild-type cells, suggesting a defective intra-S phase checkpoint in the absence of DONSON. Additionally, HU- or MMC-treated DONSON-depleted cells exhibited reduced phosphorylation of ATR and its substrates, higher levels of RPA-coated ssDNA, and increased numbers of mitotic cells. Furthermore, elevated levels of micronuclei, chromatid breaks and fragmented metaphase chromosomes were observed in DONSON-depleted cells, particularly upon exogenous replication stress, consistent with defective intra-S phase ATR-dependent checkpoint signalling leading to genome instability. Overall, Reynolds *et al.* (2017) established the importance of DONSON for protection of stalled replication forks, activation of the intra-S phase and G2/M checkpoints and maintenance of genome stability (***Figure 1.17***).

Previous studies suggested that DNA damage in cells with dysfunctional ATR signalling is caused by unscheduled cleavage of stalled replication forks by SLX4-dependent structure-specific nucleases, such as MUS81-EME1, SLX1 or XPF-ERCC1 (Couch *et al.*, 2013; Forment *et al.*, 2011; Hodskinson *et al.*, 2014; Ragland *et al.*, 2013; Svendsen *et al.*, 2009). Indeed, Reynolds *et al.* (2017) showed that DNA damage in DONSON-depleted cells arises via this mechanism as well. When MUS81 or XPF were co-depleted from HeLa cells at the same time as DONSON, cells exhibited partial rescue of replication fork asymmetry, γH2AX hyperphosphorylation, chromatid breaks and chromosome fragmentation (Reynolds *et al.*, 2017). Thus, the lack of DONSON renders stalled replication forks susceptible to nucleolytic processing by structure-specific nucleases MUS81 and XPF, leading to genome instability (***Figure 1.17***).

Retroviral complementation of patient cells with WT DONSON rescued the replication and genome stability-associated defects observed in patient-derived cells, including asymmetric replication forks, more frequent fork stalling and defective intra-S phase checkpoint activation, as well as elevated levels of chromatid gaps and DNA damage during DNA replication (Reynolds *et al.*, 2017). This confirmed the direct causality between these cellular phenotypes and insufficient DONSON activity, resulting from biallelic mutations in the *DONSON* gene (Reynolds *et al.*, 2017).

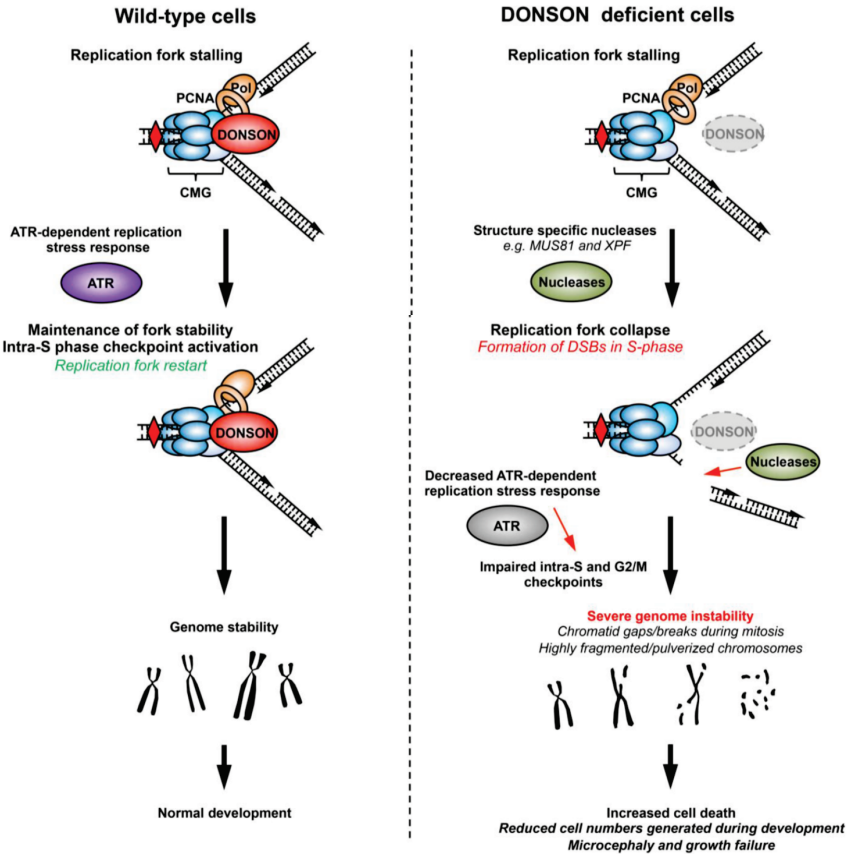

Figure 1.17. Model for the role of DONSON in maintaining genome stability.
Upon replication stress (indicated by red diamond) and replication fork stalling, the presence of functional DONSON and ATR-dependent replication stress response ensures maintenance of replication fork and genome stability. In the absence of functional DONSON, stalled replication forks are cleaved by structure-specific nucleases, such as MUS81 and XPF, leading to the generation of DSBs in S phase. Impaired S phase and G2/M checkpoints eventually lead to elevated mitotic chromosome breaks, increased cell death, and reduced numbers of cells generated during development, resulting in the microcephaly and growth failure. Figure reproduced from Reynolds *et al.* (2017).

1.7. Aims of this thesis

Multiple microcephalic primordial dwarfism (MPD)-associated genes have important functions in DNA replication, DNA damage response signalling and DNA repair (***Table 1.1***). A better understanding of the molecular mechanisms by which mutations in these genes lead to reduced cell proliferation is particularly important for elucidating the link between disrupted genome maintenance and severely affected human growth. The main objective of my thesis work was to advance knowledge of the molecular causes of MPD and gain understanding of how the proteins encoded by MPD genes act in cells and during development.

This thesis focusses on three recently identified MPD genes involved in DNA replication and repair: *DNA2*, *TRAIP* and *DONSON*. The main aims of my work described here were to:

1) Investigate the pathogenicity of biallelic variants at the *DNA2* locus;
2) Establish whether TRAIP-mediated ubiquitination of the protein phosphatase 4 (PP4) complex is the basis for hypophosphorylation of RPA2 and H2AX in TRAIP patient-derived cells;
3) Determine the molecular mechanisms of TRAIP function in DDR and DNA repair in response to different forms of replication-associated DNA damage using TRAIP knockout cell lines;
4) Develop a murine model for MPD caused by *DONSON* mutations.

Chapter 2

Materials and methods

2. Materials and methods

2.1. General reagents

2.1.1. Sources of reagents (chemicals, enzymes, growth reagents, antibodies)

Chemicals were purchased from Sigma Aldrich, BDH Laboratory Supplies (AnalaR, VWR), Fisher Chemicals, and Amersham Biosciences (GE Healthcare). Enzymes were obtained from New England Biolabs, Promega and Roche. Cell culture material was purchased from Gibco (Invitrogen) or Sigma-Aldrich unless otherwise stated.

2.1.2. Preparation of buffer solutions

All commonly used buffers (***Table 2.1***) were made using distilled water (dH_2O). Solutions were sterilised by autoclaving at 121°C for 15 min. Solutions that could not be autoclaved were passed through a 0.22 µm filter (Millipore).

Table 2.1. Commonly used buffers.

Buffer	Chemicals used for preparation
10X TBE	0.89 M Tris base, 0.89 M boric acid, 20 mM EDTA
10X TBS	0.5 M Tris base, 1.5 M NaCl (pH adjusted to 7.5 with HCl)
20X SSC	3 M NaCl, 0.3 M sodium citrate (pH adjusted to 7 with HCl)
1X urea lysis buffer	8 M urea, 50 mM Tris (pH 7.5), 150 mM β-mercaptoethanol, cOmplete mini EDTA-free protease inhibitor cocktail (Roche, catalog number 04693159001)
10X Tris-glycine SDS-PAGE running buffer	250 mM Tris base, 1.92 M glycine, 1% (w/v) SDS
1X immunoblotting transfer buffer	25 mM Tris base, 192 mM glycine, 0.1% (w/v) SDS, 20% (v/v) methanol
4X SDS protein sample loading buffer	0.5 M Tris-HCl (pH 6.8), 50% (v/v) glycerol, 2% (w/v) SDS, 0.1% (w/v) bromophenol blue
1X NETN buffer	20 mM Tris-HCl (pH 8), 100 mM NaCl, 1 mM EDTA, 0.5% NP-40
1X PreScission cleavage buffer	50 mM Tris-HCl (pH 7.5), 150 mM NaCl, 1 mM EDTA, 1 mM DTT
1X Pre-extraction buffer	25 mM HEPES (pH 7.4), 50 mM NaCl, 1 mM EDTA, 3 mM $MgCl_2$, 300 mM sucrose and 0.5% Triton X-100
5X oligo buffer	1 M Tris (pH 8), 1 M KCl
1X TE	10 mM Tris-HCl (pH 8), 1 mM EDTA

2.1.3. Preparation of cell culture drug stock solutions

Drugs were added to tissue culture media immediately prior to use and used at the working concentrations indicated in ***Table 2.2***. Stock solutions were made from powder in tissue culture hoods or purchased already dissolved in dimethyl sulfoxide (DMSO), 4-(2-hydroxyethyl)-1-piperazineethanesulfonic acid (HEPES) or autoclaved dH_2O. After aliquoting, stock solutions were stored at 4˚C, –20˚C or –80˚C.

Table 2.2. Cell culture drug stock solutions.

Drug	Solvent	Stock concentration	Working concentration	Manufacturer	Catalog number	Storage temperature
Colcemid	PBS	10 µg/ml	0.1 µg/ml	Biosera	LM-T1700	4˚C
Puromycin	H_2O	50 mg/ml	20 µg/ml	Sigma-Aldrich	BP2956-100	–20˚C
Neomycin	H_2O	250 mg/ml	500 µg/ml	Sigma-Aldrich	N6386	–20˚C
Blasticidin	HEPES	10 mg/ml	2 µg/ml	InvivoGen	Ant-bl-1	4˚C
Hydrogen peroxide	H_2O	10 M	50–200 mM	Sigma-Aldrich	H1009	4˚C
Hydroxyurea	H_2O	2 M	2 mM	Sigma-Aldrich	H8627	–20˚C
Camptothecin	DMSO	1 mM	2.5 nM–1 µM	Sigma-Aldrich	C9911	–20˚C
Mitomycin C	H_2O	1.2 mM	5–360 nM	Sigma-Aldrich	M4287	–80˚C

2.1.4. Plasmids

Plasmids used throughout this study are listed in ***Table 2.3*** and ***Table 2.4.*** Those that were created for this work (***Table 2.4***) were constructed using standard cloning techniques (Section 2.4) and oligonucleotides described in ***Appendices 1*****a**, ***1*****b**, ***1*****f**, ***1*****g** and ***1*****h**.

Table 2.3. Plasmids used in this study that were purchased commercially or previously generated by other laboratory members.

Plasmid	Description	Source
pSpCas9(BB)-2A-GFP (pX458)	Cas9 from *S. pyogenes* with 2A-EGFP, and multiple cloning site for gRNA	Addgene (plasmid number: 48138) (Ran, Hsu, Wright *et al.*, 2013)
pSpCas9n(BB)-2A-GFP (pX461)	Cas9n (D10A nickase mutant) from *S. pyogenes* with 2A-EGFP, and multiple cloning site for gRNA	Addgene (plasmid number: 48140) (Ran, Hsu, Wright *et al.*, 2013)
pSpCas9n(BB)-2A-Puro (pX462)	Cas9n (D10A nickase mutant) from *S. pyogenes* with 2A-Puro, and multiple cloning site for gRNA	Addgene (plasmid number: 48141) (Ran, Hsu, Wright *et al.*, 2013)

Plasmid	Description	Source
RHCglo	Minigene reporter for identification and analysis of *cis* elements and *trans* factors affecting pre-mRNA splicing	Addgene (plasmid number: 80169) (Singh and Cooper, 2006)
pGEX-6P-1	Bacterial expression vector for purification of glutathione S-transferase (GST)-tagged recombinant proteins with PreScission protease cleavage site	GE Healthcare (product number: 28-9546-48)
pGEX-6P-1-DEST	pGEX-6P-1 bacterial expression vector with a gateway cassette	A. Jackson laboratory, created by A. Robertson
pGEX-6P-1-PP4C	pGEX-6P-1 bacterial expression vector with the GST-tagged protein phosphatase 4 (PP4) catalytic subunit PP4C	A. Jackson laboratory, created by M. Harley
pMSCVpuro	Retroviral Murine Stem Cell Virus (MSCV) vector with puromycin resistance optimized for integration and stable expression of a gene of interest	Clontech (catalog number: 634401)
pMSCVneo	Retroviral Murine Stem Cell Virus (MSCV) vector with neomycin resistance optimized for integration and stable expression of a gene of interest	Clontech (catalog number: 634401)
pMSCVneo-TRAIP-WT	Retroviral Murine Stem Cell Virus (MSCV) vector with neomycin resistance and TRAIP-WT cloned into a gateway cassette	A. Jackson laboratory, created by M. Harley
pMSCVneo-TRAIP-W37A	Retroviral Murine Stem Cell Virus (MSCV) vector with neomycin resistance and TRAIP-W37A cloned into a gateway cassette	A. Jackson laboratory, created by A. Fluteau
pGEX-4T-2	Bacterial expression vector for purification of glutathione S-transferase (GST)-tagged recombinant proteins with thrombin site	GE Healthcare (product number: 28-9545-50)
pGEX-4T-2-TRAIP-N	pGEX-4T-N bacterial expression vector with the GST-tagged N-terminal TRAIP	Gift from R. Geahlen

Table 2.4. Plasmids that were generated for this thesis.

Plasmid generated for this thesis	Description	Plasmid backbone	Figure reference
pX461-DNA2-c.74+4A>C-gRNA1	*DNA2* gRNA1 (CTCTCCGCTCACAGCTCCGC) for CRISPR/Cas9-mediated introduction of c.74+4A>C mutation in a cell line, cloned into pX461	pX461	Figure 3.10a
pX462-DNA2-c.74+4A>C-gRNA9	*DNA2* gRNA9 (GGAGGGTGTGGGAACAAAGC) for CRISPR/Cas9-mediated introduction of c.74+4A>C mutation in a cell line, cloned into pX462	pX462	Figure 3.10a
pX461-DNA2-c.1963A>G-gRNA1	*DNA2* gRNA1 (CTACGATATGTACTCTCGTA) for CRISPR/Cas9-mediated introduction of c.1963A>G mutation in a cell line, cloned into pX461	pX461	Figure 3.10a
pX462-DNA2-c.1963A>G-gRNA9	*DNA2* gRNA9 (GTAGTTGTTTTTCCTGTCCC) for CRISPR/Cas9-mediated introduction of c.1963A>G mutation in a cell line, cloned into pX462	pX462	Figure 3.10a
pX458-DNA2-c.74+4A>C-gRNA1	*DNA2* gRNA1 (CTCTCCGCTCACAGCTCCGC) for CRISPR/Cas9-mediated introduction of c.74+4A>C mutation in a cell line, cloned into pX458	pX458	Figure 3.11a

Plasmid generated for this thesis	Description	Plasmid backbone	Figure reference
pX458-DNA2-c.74+4A>C-gRNA2	*DNA2* gRNA2 (GGAGGAGGCGGAGCTGCCGG) for CRISPR/Cas9-mediated introduction of c.74+4A>C mutation in a cell line, cloned into pX458	pX458	Figure 3.11a
pX458-DNA2-c.74+4A>C-gRNA3	*DNA2* gRNA3 (GCTGCCGGCGGAGCTGTGAG) for CRISPR/Cas9-mediated introduction of c.74+4A>C mutation in a cell line, cloned into pX458	pX458	Figure 3.11a
pX458-TRAIP-gRNA1	*TRAIP* gRNA1 (CTTCGATCACTCCCGCGACG) for CRISPR/Cas9-mediated disruption of *TRAIP* in a cell line, cloned into pX458	pX458	Figure 5.1
pX458-TRAIP-gRNA2	*TRAIP* gRNA2 (ATAGTGCACAGAGCACGGAT) for CRISPR/Cas9-mediated disruption of *TRAIP* in a cell line, cloned into pX458	pX458	Figure 5.1
pX458-mDonson-M440T-gRNA	*Donson* gRNA (TACCTTAAGCATTTGCATTG) for CRISPR/Cas9-mediated introduction of c.1319T>C mutation in mouse, cloned into pX458	pX458	Figure 7.2
RHCglo-DNA2-ex11-13-WT	*DNA2* exons 11 to exon 13 (including intervening intronic/exonic sequence) amplified from control DNA of a healthy individual, cloned into RHCglo	RHCglo	Figure 3.7
RHCglo-DNA2-ex11-13-int11ins53bp	*DNA2* exons 11 to exon 13 (including intervening intronic/exonic sequence) amplified from DNA of a DNA2 patient, cloned into RHCglo	RHCglo	Figure 3.7
RHCglo-DNA2-ex11-13-c.1764-1G>A	Splicing control plasmid generated by site-directed mutagenesis on RHCglo-DNA2-ex11-13-WT	RHCglo	Figure 3.7
RHCglo-DNA2-ex1-2-WT	*DNA2* exon 1 and exon 2 (including intervening intronic sequence) amplified from control DNA of a healthy individual, cloned into RHCglo	RHCglo	Figure 3.8
RHCglo-DNA2-ex1-2-c.74+4A>C	*DNA2* exon 1 and exon 2 (including intervening intronic sequence) amplified from DNA of a DNA2 patient, cloned into RHCglo	RHCglo	Figure 3.8
RHCglo-DNA2-ex1-2-c.74+1G>A	Splicing control plasmid generated by site-directed mutagenesis on RHCglo-DNA2-ex1-2-WT	RHCglo	Figure 3.8
pGEX-6P-1-PP4C-PP4R2-PP4R3α	PP4C, PP4R2 and PP4R3α sequentially cloned into pGEX-6P-1 for bacterial protein expression and purification	pGEX-6P-1	Figure 4.5
pGEX-6P-1-PP4C-PP4R2-PP4R3β	PP4C, PP4R2 and PP4R3β sequentially cloned into pGEX-6P-1 for bacterial protein expression and purification	pGEX-6P-1	Figure 4.5
pGEX-6P-1-PP4C(K26R/K31R/K63R)-PP4R2-PP4R3α	Two rounds of site-directed mutagenesis on pGEX-6P-1-PP4C-PP4R2-PP4R3α to introduce lysine-to-arginine substitutions in PP4C	pGEX-6P-1	Figure 4.7
pGEX-6P-1-PP4C(K26R/K31R/K63R)-PP4R2-PP4R3β	Two rounds of site-directed mutagenesis on pGEX-6P-1-PP4C-PP4R2-PP4R3β to introduce lysine-to-arginine substitutions in PP4C	pGEX-6P-1	Figure 4.7
pGEX-6P-1-PP4C(K183R)-PP4R2-PP4R3β	Site-directed mutagenesis on pGEX-6P-1-PP4C-PP4R2-PP4R3β to introduce K183R substitution in PP4C	pGEX-6P-1	Figure 4.11
pGEX-6P-1-PP4C(K21R/K183R)-PP4R2-PP4R3β	Site-directed mutagenesis on pGEX-6P-1-PP4C(K183R)-PP4R2-PP4R3β to introduce K21R substitution in PP4C	pGEX-6P-1	Figure 4.11
pGEX-4T-2-TRAIP(W37A)-N	Site-directed mutagenesis on pGEX-4T-TRAIP-N bacterial expression vector to introduce W37A substitution in TRAIP-N	pGEX-4T-N	Figure 6.4

2.2. Microbial methods

2.2.1. Growth of bacteria

E. coli strains were grown at 37˚C in/on Luria-Bertani (LB) medium (10 g/l tryptone, 5 g/l yeast extract, 10 g/l NaCl, 1 g/l glucose). To maintain selection for plasmid DNA in transformed cells, the relevant antibiotic(s) (***Table 2.5***) were added to LB at the required concentration.

Table 2.5. Antibiotics used for bacterial selection in this study.

Antibiotic	**Stock concentration**	**Working concentration**	**Solvent**
Ampicillin	50 mg/ml	50 µg/ml	dH_2O
Kanamycin	10 mg/ml	10 µg/ml	dH_2O
Chloramphenicol	34 mg/ml	34 µg/ml	100% EtOH

2.2.2. Transformation of *E. coli*

2.2.2.1. Preparation of chemically-competent bacterial cells for cloning

Preparation of chemically-competent *E. coli* was performed in-house by M. Reijns and A. Fluteau. *E. coli* DH5α cells were grown overnight on LB agar. The next day, a single colony was taken and 5 ml of LB medium with 20 mM $MgSO_4$ was inoculated and grown overnight to stationary phase. Following this, 250 ml of LB with 20 mM $MgSO_4$ was inoculated with 2 ml of the stationary phase culture and incubated at 23˚C in a shaking incubator at a minimum of 200 rpm until OD_{600} reached 0.4–0.6 (usually 8-10 h). The culture was then cooled on ice for about 15 min and cells were kept on ice for all subsequent steps. Cells were sedimented (10 min, 3,000 rpm, 4˚C) and gently resuspended in 80 ml of ice-cold sterilised TB buffer (10 mM PIPES-HCl pH 6.7, 15 mM $CaCl_2$, 0.25 M KCl, 55 mM $MnCl_2$). Cells were left on ice for 10 min, centrifuged for 10 min at 3,000 rpm at 4˚C, and gently resuspended in 20 ml of ice-cold TB buffer. After adding 1.5 ml of DMSO followed by a final 10 min incubation on ice, cells were dispensed into 200 µl aliquots in cold, sterile tubes and snap-frozen in liquid nitrogen. Aliquots were stored at –80˚C until required for transformation.

2.2.2.2. Transformation of chemically competent bacterial cells

For transformation of chemically-competent *E. coli*, approximately 1 ng of plasmid DNA or 1 μl of a ligation reaction was added to 50 μl of competent cells. Cells and DNA were incubated on ice for 30 min before 45 sec heat-shock at 42˚C. Following 2 min recovery on ice, the cells were resuspended in 1 ml of LB medium and incubated at 37˚C for 60 min with shaking. 100 μl of cells was spread onto LB-agar plates containing the appropriate antibiotic(s). The plates were incubated overnight at 37˚C to achieve discrete colonies.

2.3. Cell culture methods

2.3.1. Preparation and growth of cell lines

2.3.1.1. Human cell lines

Cell culture conditions used for the maintenance of the human cell lines in this thesis are summarised in ***Table 2.6***. Cells were trypsinised in trypsin:versene (1:1, v/v) or in 1X TrypLE™ Express Enzyme (Thermo Fisher Scientific, catalog number 12605036) at 37°C for 5 min and passaged at 1:6-1:12, as required.

Table 2.6. Cell culture conditions used for maintaining human cell lines.

Cell line	Cell culture medium	Supplements of cell culture medium	Cell culture conditions	Source
RPE1	DMEM/F-12 Medium (Thermo Fisher Scientific, catalog number 11320033)	10% fetal bovine serum, 100 U/ml penicillin, 100 µg/ml streptomycin	37°C, 5% CO_2, normoxic	ATCC
RPE1 p53-/-Cas9				Gift from D. Durocher (University of Toronto)
U2OS	McCoy's 5a Modified Medium (Thermo Fisher Scientific, catalog number 16600082)			ECACC, catalog no. 92022711)
HCT116				ATCC
HeLa	DMEM Medium (Thermo Fisher Scientific, catalog number 41965039)			Gift from G. Stewart (university of Birmingham); originally from ATCC
HeLa Cas9				Gift from D. Durocher (University of Toronto)
Phoenix E		10% fetal bovine serum, 100 U/ml penicillin, 100 µg/ml streptomycin, 1% glutamine		Gift from G. P. Nolan (Stanford University)

2.3.1.2. Mouse embryonic fibroblast (MEF) cell lines

Mouse embryonic fibroblasts (MEFs) were prepared from embryos collected at 13.5 days post-coitum (E13.5). Each embryo was isolated from the decidua and placed in DMEM culture media. The tails were collected for genotyping and the heads and internal organs removed. Each embryo was minced using a clean scalpel, transferred into a T25 tissue culture flask and maintained in DMEM Medium, supplemented with 10% FBS, 0.1 mM β-mercaptoethanol (BME), 100 U/ml penicillin and 100 µg/ml streptomycin. Fibroblast colonies

were visible following culturing for 48 h at 37° C in 5% CO_2 and 3% O_2. Cells were trypsinised in 1X TrypLE™ Express Enzyme (Thermo Fisher Scientific) at 37°C for 5 min and passaged at 1:3 for up to 4 passages.

2.3.2. Preservation of cell lines

For storage of tissue culture cells, 2–7x10^6 adherent cells were harvested and resuspended in 1 ml of FBS, containing 10% DMSO. The cells were stored in 2 ml cryostat tubes and frozen at –80˚C in Styrofoam containers, and transferred for long-term storage in liquid nitrogen.

2.3.3. Transfection of cultured mammalian cells

2.3.3.1. Short interfering RNA (siRNA) transfections

Short interfering RNA (siRNA) oligonucleotides (***Table 2.7***) were transfected into RPE1 or RPE1 p53-/- Cas9 cells using Lipofectamine™ RNAiMAX transfection reagent (Invitrogen), whereas Oligofectamine transfection reagent (Invitrogen) was used for transfections into HeLa cells. RPE1 or HeLa cells were 30-50% confluent at time of transfection. For each transfection of a 100 mm tissue culture dish, two complexes were prepared. The first contained 40–50 nM siRNA in 500 µl of Opti-MEM Medium (Thermo Fisher Scientific, 31985062) and the second contained 12 µl of transfection reagent in 500 µl Opti-MEM. After 5-10 min incubation, the solutions were combined for 15-20 min and then added to the cells. The cells were incubated in 7 ml Opti-MEM with the transfection mixture for 24 h, after which Opti-MEM was replaced with fresh medium.

Table 2.7. Sequences of siRNA oligonucleotides used in this thesis.

siRNA oligonucleotide	Sequence (5'-3')	Reference
siLUC	CUUACGCUGAGUACUUCGA[dT][dT]	Harley *et al.*, 2016
siTRAIP-524	AGCAGAUGAAGUACUUAGA[dT][dT]	Harley *et al.*, 2016
siTRAIP-2	CCGUGAUGAUAUUGAUCUCAA[dT][dT]	Hoffmann *et al.*, 2016
siTRAIP-B	GAACCAUUAUCAAUAAGCU[dT][dT]	Hoffmann *et al.*, 2016
siFANCD2	CAGAGUUUGCUUCACUCUCUA[dT][dT]	Kratz *et al.*, 2010

2.3.3.2. CRISPR/Cas9 transfections

Plasmids expressing guide RNAs (gRNAs) and Cas9 were introduced into cultured human cells (HCT116, RPE1, RPE1 p53-/- Cas9 and HeLa Cas9) using the Neon® Transfection System (Invitrogen) following the manufacturer's instructions (***Table 2.8***). Alternatively, cultured human cells (U2OS and RPE1) were transfected using Lipofectamine™ 2000 transfection reagent (Invitrogen) according to manufacturer's instructions. Cells expressing GFP were sorted by fluorescence-activated cell sorting (FACS) into 96-well plates 24 h after transfection. Once confluency was reached, clones were replated and collected for rapid preparation of DNA using 40–80 µl DirectPCR Lysis Reagent (Viagen) and 0.4 µg/µl Proteinase K enzyme (Roche). Genomic DNA was isolated from CRISPR clones at 55°C for 16 h, followed by heating to 85°C for 45 min to inactivate Proteinase K. Isolated DNA was used for PCR amplification of the genomic region around the expected nucleotide change. PCR products were sent for Sanger sequencing, and sequencing traces were analysed with Sequencher 4.8 DNA Sequence Analysis Software (Gene Codes Corporation).

Table 2.8. Electroporation conditions used for Neon® transfection of different cell types.

Neon® electroporation parameters									
Cell line	**Pulse voltage (V)**	**Pulse width (ms)**	**Pulse number**	**Neon® tip type**	**Cell culture dish used**	**Cell number**	**Targeted gene**	**Total amount of gRNA(s) used (ng)**	**Amount of repair template used (ng)**
RPE1	1350	20	2	10 µl	12-well plate	$2x10^5$	*TRAIP*	1000	N/A
RPE1 p53-/- Cas9									
HeLa	1005	35							
HCT116	1130	30				$1x10^5$	*DNA2*	250	250

2.3.3.2.1. Guide RNA (gRNA) design and Cas9-expressing plasmid construction

Guide RNAs (gRNAs) for CRISPR/Cas9-based genome editing experiments were designed using the online CRISPR Design Tool created by Feng Zhang laboratory (http://crispr.genome-engineering.org/) and CRISPR gRNA Design Tool DNA2.0 (now ATUM), and ordered from Sigma-Aldrich (***Table 2.9***). The 5' and/or 3' overhangs were added to forward and reverse oligonucleotides to allow cloning into *Bbs*I site of Cas9 vector. The forward oligonucleotide had a 5' overhang CACCG(G)-, whereas the reverse oligonucleotide had a 5' overhang AAAC- and a 3' overhang –(C)C.

The top and bottom strands of oligonucleotides (20 µl of 100 µM oligonucleotide) for each gRNA design were first annealed at 95°C for 5 min in 5X oligo buffer (***Table 2.1***) and allowed to cool down to room temperature. The mixture was then diluted (1:40 in dH_20) and used to set up ligation reactions to insert the guiding sequence into a *Bbs*I-digested Cas9-expressing plasmid (Addgene) plasmid using T4 ligase enzyme, as described by Ran, Hsu, Wright *et al.* (2013). Ligation reactions (10 µl) contained 10X T4 DNA ligase reaction buffer (NEB), 1 µl diluted oligonucleotide duplex, 100 ng Cas9 plasmid, and 0.5 µl T4 DNA ligase (NEB). Ligation was carried out for a minimum of 1.5 h at room temperature. Ligated plasmids were transformed into DH5α competent *E. coli*, purified and sequenced by the Sanger method. CRISPR/Cas9 transfections were carried out as described in Section 2.3.3.2, together with antisense single-stranded oligodeoxynucleotide (ssODN) ultramers (***Table 2.10***), ordered from Integrated DNA Technologies (IDT), or a plasmid generated using Gibson Assembly Cloning Kit (NEB) (Section 2.3.3.2.2).

Table 2.9. List of guide RNAs (gRNAs) used in this thesis.

Targeted gene	Species	Guide RNA (gRNA)	Sequence (5'-3')	Cas9 plasmid used for cloning	Figure reference
DNA2	Human	c.74+4A>C gRNA1	CTCTCCGCTCACAGCTCCGC	pX461, pX458	Figure 3.10a, Figure 3.11a
		c.74+4A>C gRNA2	GGAGGAGGCGGAGCTGCCGG	pX458	Figure 3.11a
		c.74+4A>C gRNA3	GCTGCCGGCGGAGCTGTGAG	pX458	Figure 3.11a
		c.74+4A>C gRNA9	GGAGGGTGTGGGAACAAAGC	pX462	Figure 3.10a
		c.1963A>G gRNA1	CTACGATATGTACTCTCGTA	pX461	Figure 3.10a
		c.1963A>G gRNA9	GTAGTTGTTTTTCCTGTCCC	pX462	Figure 3.10a
TRAIP	Human	TRAIP gRNA1	CTTCGATCACTCCCGCGACG	pX458	Figure 5.1
		TRAIP gRNA2	ATAGTGCACAGAGCACGGAT	pX458	Figure 5.1
Donson	Mouse	c.1319T>C gRNA	TACCTTAAGCATTTGCATTG	pX458	Figure 7.2

Table 2.10. List of single-stranded oligodeoxynucleotides (ssODNs) used in this thesis.

Targeted locus	ssODN	Sequence (5'-3')	Figure reference
DNA2 c.74+4A>C	ODN1a	GGGCCCCGGGCCCGGTCAGTCTGAGGCGGTGCGGACGCAGCCTCTCCCGCTCCTTCTTTCAAATCTACCGCTTTGTTCCCACACCCTCCCCCCTCTCCGCGCACAGCTCCGCCGGCAGCTCCGCCTCCTCCCAAAAACTCTTCTCCATCAGCAGCTCCAGTTCGTTCAGCTGCTCCATCCTGGACGCGGGGATCGCAAAC	Figure 3.10a
	ODN1b	TCCTTCTTTCAAATCTCCCGCTTTGTTCCCACACCCTCCCCCCTCTCCGCGCACAGCTCGGCCGGCAGCTCCGCCTCCTCCCAAAAACTCTTCTCCATCAGCAGCTCCAG	Figure 3.11
	ODN2	CGAACTGGAGCTGCTGATGGAGAAGAGTTTTTGGGAGGAGGCGGAGCTGCCGGCCGAGCTGTGCGCGGAGAGGGGGGAGGGTGTGGGAACAAAGCGGGAGATTTGAAAGAAGGA	Figure 3.11
	ODN3	GCTGCTGATGGAGAAGAGTTTTTGGGAGGAGGCGGAGCTGCCGGCGGAGCTGTGCGCGGAGAGGGGGGAGGGTGTGGGAACAAAGCGGGAGATTTGAAAGAAGGAGCGGG	Figure 3.11
DNA2 c.1963A>G	ODN1	ATATTCAATATTACATCCTCTGAACTGAGGAGAAGCTGATACAAATATTTTGTCTCTAAGCAGAAGAATAATAACCTTACGAGAGTACATATCGTAGTTGCTTTTCCTGTCCCAGGCATACCCACGATGAGTGTGTAGTCTTTTGAAAGAAGTACCTTTTTCATCGCTTGCCTCTGAGGCTTATTCAAACCTACATTTAA	Figure 3.10a
m*Donson* c.1319T>C	ODN1	AAATTGCTGGACTGTATGTAGATGAAGTAAACACTTACCTTAAGCATTTGCGTTGATGCACCTCGGAAGGCTATTGGGGATAAGAGAGTGGGTGGGAGACCTGCCTGT	Figure 7.2

2.3.3.2.2. Generation of CRISPR template plasmid

As an alternative CRISPR repair template to ssODNs, a plasmid containing *DNA2* c.74+4A>C (mutation of interest) and synonymous c.69G>C (PAM site mutation) substitutions was generated using Gibson Assembly Cloning Kit (NEB) according to manufacturer's instructions. RHCglo plasmid (***Table 2.3***), linearised with restriction enzyme *Sal*I (Section 2.4.2.3), was used as a vector. The insert was generated by PCR amplification (Section 2.4.2.5.2) of a 2,018 bp-long *DNA2* fragment from DNA2 patient P4 (see Section 3.1) genomic DNA using primers RHCglo-DNA2-5UTR-F and RHCglo-DNA2-int1-R (***Table 2.11***). Gibson reaction (20 µl) contained: 2X Assembly Master mix; 100 ng vector; 200 ng insert; and dH_2O up to 20 µl. The reaction was incubated at 50°C for 15 min and transformed to chemically-competent *E. coli* (Section 2.2.2.2). Site-directed mutagenesis (Section 2.4.2.8) was used to introduce c.69G>C mutation into the plasmid using primers DNA2-c.69G>C F and DNA2-c.69G>C R (***Table 2.11***). DNA2 c.74+4A>C plasmid was used for CRISPR/Cas9 transfections together with DNA2 c.74+4A>C gRNA1; DNA2 c.74+4A>C/c.69G>C plasmid was used together with DNA2 c.74+4A>C gRNA2 and gRNA3.

Table 2.11. Oligonucleotides used for generating the *DNA2* CRISPR template plasmid.

Oligo nucleotide	Sequence (5'-3')	Description	Figure reference
RHCglo-DNA2-5UTR-F	TGGGAAGCGAAAGGGTTGTCTGCTATTGAAAAAAGG	Forward primer to clone *DNA2* 5' upstream sequences, 5'UTR, exon 1 and 5' of intron 1 into RHCglo plasmid	Figure 3.11b
RHCglo-DNA2-int1-R	CCCAGTTTCTATTGGTGGAAAGTCCTATCATGAGCC	Reverse primer to clone *DNA2* 5' upstream sequences, 5'UTR, exon 1 and 5' of intron 1 into RHCglo plasmid	Figure 3.11b
DNA2-c.69G>C F	GAGCTGCCGGCCGAGCTGTGCGCGG	Forward primer to introduce c.69G>C substitution in *DNA2*	Figure 3.11b
DNA2-c.69G>C R	CCGCGCACAGCTCGGCCGGCAGCTC	Reverse primer to introduce c.69G>C substitution in *DNA2*	Figure 3.11b

2.3.3.2.3. *In vitro* guide RNA (gRNA) testing

Donson c.1319T>C gRNA (***Table 2.9***), cloned into the pX458 plasmid, was amplified by polymerase chain reaction (PCR) (see Section 2.4.2.5.2) using a specific forward primer T7-mDonson-M446T-F (TGTAATACGACTCACTATAGGGTACCTTAAGCATTTGCATTG) and the universal reverse primer (AAAAGCACCGACTCGGTGCC). *In vitro* transcription of gRNA was performed using The HiScribe T7 High Yield RNA Synthesis Kit (New England Biolabs, NEB) according to manufacturer's instructions. The gRNA was treated with 30 U RNase-free DNase I (Qiagen) for 15 min, followed by RNA clean-up using the RNeasy Mini Kit (Qiagen). The *in vitro* cutting reaction, containing Buffer 3 (NEB), bovine serum albumin (BSA, NEB), 60 ng of Donson template (amplified using primers mDonson-F2 and mDonson-R2, ***Appendix 1*e**), 20–40 ng gRNA and 200–680 ng recombinant Cas9 enzyme (Canopy Biosciences) was incubated at 37°C for 3 h. The reaction products were visualised on 2% agarose gels.

2.3.3.3. DNA transfections

DNA was transfected into monolayer cells using Lipofectamine™ 2000 (Invitrogen) according to manufacturer's instructions. HeLa cells were 90% confluent at time of transfection. For each transfection of a well of a 6-well plate two complexes were prepared. The first contained 800 ng – 1 µg of DNA in 500 µl of Opti-MEM reduced serum medium (Invitrogen), and the second contained 1.5 µl Lipofectamine in 500 µl Opti-MEM. After 5 min incubation, the solutions were mixed for 20 min and then added to the cells. The cells were

incubated in 1.5 ml Opti-MEM with the transfection mixture for 4–6 h, after which Opti-MEM was replaced with fresh medium.

2.3.4. Retroviral transduction of cultured mammalian cells

Retroviruses encoding TRAIP-WT and TRAIP-W37A transgenes were generated in amphotropic Phoenix E packaging cell line. Phoenix E cells were plated in 100 mm tissue culture dishes and grown for 24 h, and transfected with 20 µg of pMSCVpuro, pMSCVneo-TRAIP-WT or pMSCVneo-TRAIP-W37A plasmids (***Table 2.3***) using calcium phosphate transfection kit (Sigma-Aldrich, catalog number K278001). 20 µg plasmid DNA was mixed with 37 µl 2 M $CaCl_2$ (provided by manufacturer), and the total volume was made up to 370 µl with dH_2O (provided by manufacturer). The mixture was added dropwise to 370 µl 2X HEPES Buffered Saline (HeBS; provided by manufacturer) while bubbling air through HeBS with another pipette. After 20 min incubation at room temperature, the transfection mix was added to Phoenix E cells. 16 h later medium was replaced. Virus-containing supernatant was collected 48 h post-transfection and filtered through a 0.2 µm Millex-HV sterile filter with PVDF membrane (Millipore). The filtrated viral supernatant was immediately used for infection or aliquoted into 1.5 ml cryovials and stored at –80°C.

2.3.5. Relative surface area of cell culture vessels

The volumes of reagents given for mammalian cell transfections describe either the 6-well plate or 100 mm dish format. Other formats, such as 12-well plates, were also used. The equivalent volumes can be calculated from ***Table 2.12*** below.

Table 2.12. Relative surface area of cell culture vessels.

Culture Vessel	**24-well**	**12-well**	**6-well**	**60 mm**	**100 mm**	**150 mm**	**T25**	**T75**
Surface area (cm^2)	2	4	9	28.2	78.5	176.7	25	75
Ratio to 24-well plate	1	2	4.5	14.1	39.25	88.35	12.5	37.5

2.4. Nucleic acid methods

2.4.1. General methods

2.4.1.1. Spectrophotometric quantification of nucleic acids

The concentration of nucleic acids was determined by measuring the optical density at 260 nm using a NanoDrop 1000 UV-Vis Spectrophotometer (Thermo Fisher Scientific). 1 µl of each sample was used for each measurement. The purity of the nucleic acid sample was determined by measuring the absorbance at 230 nm, 260 nm and 280 nm. The 260/280 ratio of a sample free of protein contamination should be 1.8-2.2 and a 230/260 ratio ≥1.7 indicates a sample free of carbohydrates and lipids.

2.4.1.2. Agarose gel electrophoresis

Nucleic acid samples were analysed by agarose electrophoresis on gels ranging from 0.8% to 2% agarose in TBE (w/v). Gels were prepared by dissolving agarose (Hi-Pure Low EEO agarose, Biogene) in 0.5X TBE buffer by boiling in a microwave oven and adding ethidium bromide (after cooling to ~50°C) to a final concentration of 0.5 µg/ml. DNA samples were mixed with 6X DNA loading buffer (30% (v/v) glycerol, 0.4% (w/v) Orange G), loaded on to the gel, and 5 volts/cm voltage was used to resolve the nucleic acid fragments by size. The nucleic acids were visualised using a UV transilluminator (BioDoc-It System, UVP). For reference, markers containing DNA fragments of known sizes were included (1kb DNA Ladder (Invitrogen) or 100bp DNA Ladder (Promega)).

2.4.2. DNA methods

2.4.2.1. Purification of DNA from *E. coli* cells

2.4.2.1.1. Small scale preparation of plasmid DNA

Plasmid DNA was prepared using the QIAprep Spin Miniprep Kit (Qiagen) following the manufacturer's instructions. DNA was extracted from 5 ml of stationary phase *E. coli* culture

and eluted in 50 µl of elution buffer (10mM Tris-HCl pH 8.5) or DNAse/RNAse-free distilled water (Gibco).

2.4.2.1.2. Large scale preparation of plasmid DNA

For larger scale preparation of plasmid DNA, the ZymoPURE II Plasmid Maxiprep Kit (Zymo Research) was used. DNA was extracted from 100-150 ml of stationary phase *E. coli* following the manufacturer's instructions and eluted in 400 µl of the provided elution buffer.

2.4.2.2. DNA sequencing

Dye terminator sequencing reactions (ABI) were performed and processed by the Institute of Genetics and Molecular Medicine (IGMM) sequencing service on a 3130/3730 genetic analyser (Applied Biosystems). DNA sequencing data was analysed using Sequencher 5.4.6 (Gene Codes Corp.).

2.4.2.2.1. Sanger sequencing of *DNA2* in MPD patients

A typical PCR mixture to screen for *DNA2* mutations contained: 1-50 ng template DNA, ThermoPrime 2X ReddyMix PCR master mix (Thermo Scientific) with 1.5 mM $MgCl_2$, 0.1–0.5 µM forward primer (***Table 2.13***), 0.1–0.5 µM reverse primer (***Table 2.13***), and dH_2O up to a total reaction volume of 10 µl. PCR reactions were performed on a DNA Engine Tetrad 2 thermal cycler (MJ Research) using a touchdown PCR program for increased specificity and sensitivity (Korbie and Mattick, 2008) (see below).

PCR products were separated on a 1.5% 0.5X TBE agarose gel to confirm correct amplification. Successfully amplified exons were sequenced using dye-terminator chemistry and electrophoresed on an ABI 3730 capillary sequencer (Applied Biosystems). Sequences were then analysed using Mutation Surveyor software (Soft Genetics). The frequency of mutations within the normal population was determined using the Exome Aggregation Consortium (ExAC) Browser and the Genome Aggregation Database (gnomAD) (Lek *et al.*, 2016).

Table 2.13. List of *DNA2* primers used for Sanger sequencing of the *DNA2* gene in MPD patients.

Primer	Primer sequence (5' --> 3')
DNA2ex1F	CATTTGGGACATCTGCGG
DNA2ex1R	GCTCCTTCTTTCAAATCTCC
DNA2ex2F	AGAAAACTGGAAGATTGGTTTG
DNA2ex2R	TCACAGAAGCCATTTGATGAG
DNA2ex3F	TTTTGAAGCCTCCCTAATACG
DNA2ex3R	ATTTTATAGGGTTGCTGGGAG
DNA2ex4F	TCTTACCAGTGCATTTTGGC
DNA2ex4R	GCAATTTCAGAAACTCTTCACAG
DNA2ex5F	GCTGACGAACAGTTGGGTTG
DNA2ex5R	TTCAACACACAGAATGGCATC
DNA2ex6F	GCCAAGTGATAATAGTAAGG
DNA2ex6R	GACTACGGTGTTCAATAGAA
DNA2ex7F	GTTGGTTGCAAGACAATGTAAG
DNA2ex7R	TGTATCACTAGAAGCTGAAGTGGG
DNA2ex8F	ACAGGCGTAAGCCATTGTG
DNA2ex8R	TGATGTTATCAATGCCCGTC
DNA2ex9F	ATCTCACTTCGTACCCAGCC
DNA2ex9R	CATAAATTCCAAAGGCCACC
DNA2ex10F	TCCTGGAGTGTTGGGATTAC
DNA2ex10R	AAATACTCAAAGTTGATTGTGGTG
DNA2ex11/12F	GGCCCATTCATTCTTTTAGC
DNA2ex11/12R	CCAAAGAGTCTTGGTCTAAACATTG
DNA2ex13F	AGACTTGGATAGAGACTGCTTTTC
DNA2ex13R	TCTGAACTGAGGAGAAGCTGATAC
DNA2ex14F	AAAATTATCTGGAATTAAAAGTAAGGC
DNA2ex14R	GTTTCTCCCCTCATTCTGGC
DNA2ex15/16F	TATCGAAGGATTCCTGATGC
DNA2ex15/16R	TTTAGTTTTGGTAGATGGAAACAAAC
DNA2ex17F	GCTAGGAGTGGTTTTCATGTTTG
DNA2ex17R	GGCATGTGCTAATGAAAACTG
DNA2ex18F	CAAGTCGGTAGTATAGTCTTTATGGC
DNA2ex18R	CGAGACTTAATGCCAGATTGTAAG
DNA2ex19F	TTTCATCCTGGGAAATATGG
DNA2ex19R	ACAGGGTTTCGCCATGC
DNA2ex20F	ATTTGCACAGGTGTCCATTG
DNA2ex20R	AAAAGGGTTATAGGCTGGGG
DNA2ex21F	AAATAACTCCTGTTGCTTAAAGGC
DNA2ex21R	TTCACAGTTTTCGGTACACCTG

Touchdown PCR program:

	Denaturation	94˚C	5 min
3x	Denaturation	94˚C	30 sec
	Annealing	68˚C	30 sec
	Extension	72˚C	45 sec per kb
3x	Denaturation	94˚C	30 sec
	Annealing	65˚C	30 sec
	Extension	72˚C	45 sec per kb
3x	Denaturation	94˚C	30 sec
	Annealing	62˚C	30 sec
	Extension	72˚C	45 sec per kb
35x	Denaturation	94˚C	30 sec
	Annealing	59˚C	30 sec
	Extension	72˚C	45 sec per kb
	Extension	72˚C	10 min

2.4.2.3. Restriction digests

Plasmid DNA was digested with the appropriate restriction endonuclease in the buffer supplied by the manufacturer (NEB or Roche). To ensure complete restriction digestion before subsequent cloning steps, the digest was performed in a 100 μl of buffer with 2–5 μg of DNA and 20 U of the appropriate enzyme(s) overnight at the appropriate temperature, generally 37°C. For double digests, the optimal buffer conditions were selected for both enzymes using the manufacturer's guidelines.

2.4.2.4. Purification of restriction digested DNA

DNA fragments produced by restriction digestion were resolved by agarose gel electrophoresis. The desired DNA fragment was excised from the gel using a scalpel and purified using the QIAquick Gel Extraction kit (Qiagen) according to the manufacturer's instructions. DNA was eluted in 30 μl elution buffer and stored indefinitely at –20˚C.

2.4.2.5. Amplification of DNA by polymerase chain reaction (PCR)

2.4.2.5.1. Primer design to amplify DNA for cloning

Primers to amplify DNA were designed using the primer design program Primer3 (available online at http://primer3.sourceforge.net/). The primers selected usually had a melting temperature (T_m) of around 55˚C (45–65˚C) which did not differ by more than 4°C between the forward and reverse primers in a pair. The nearest neighbour formula was used to predict the T_m (˚C) of primers (SantaLucia, 1998).

2.4.2.5.2. Polymerase chain reaction (PCR)

Specific regions of DNA were amplified using the polymerase chain reaction (PCR). The designed oligonucleotide primers (see ***Appendix 1*****c-e**) were annealed to denatured template DNA and extended by a thermostable DNA polymerase. Different DNA polymerase-containing PCR master mixes were utilised: ThermoPrime 2X ReddyMix PCR Master Mix with 1.5 mM $MgCl_2$ (Thermo Fisher Scientific, catalog number AB0575DCLDB) for standard PCR, FastStart PCR Master Mix (Roche, catalog number 04710436001) for colony PCR, and Phusion Flash High-Fidelity PCR Master Mix (Thermo Fisher Scientific, catalog number F548S) for when a high level of polymerase accuracy was required.

A typical PCR mixture using ThermoPrime 2X ReddyMix PCR Master Mix contained: 1–100 ng template DNA (plasmid or genomic), 1X ReddyMix PCR Master Mix (provided by manufacturer), 0.1–0.5 µM forward primer, 0.1–0.5 µM reverse primer, and dH_2O up to a total reaction volume of 10–25 µl.

A typical PCR using ReddyMix PCR Master Mix was performed on a DNA Engine Tetrad 2 thermal cycler (MJ Research) as follows:

	Denaturation	95˚C	1 min	
25-35 x	Denaturation		95˚C	30 sec
	Annealing		55-65˚C[1]	30 sec
	Extension		72˚C	60 sec per kb
	Extension	72˚C	5 min	

[1] Annealing temperature is based on the melting temperature of the primer set used in each PCR.

A typical colony PCR mixture using FastStart PCR Master Mix contained: plasmid template DNA (a single bacterial colony picked with a sterile pipette tip), 1X FastStart PCR Master Mix (provided by manufacturer), 0.1–0.5 µM forward primer, 0.1–0.5 µM reverse primer, and dH_2O up to a total reaction volume of 10 µl.

A typical PCR using FastStart PCR Master Mix was performed on a DNA Engine Tetrad 2 thermal cycler (MJ Research) as follows:

	Denaturation		96˚C	10 min
30-35 x	Denaturation		95˚C	30 sec
	Annealing		58˚C	30 sec
	Extension		72˚C	60 sec per kb
	Extension		72˚C	2 min

A typical PCR mixture using Phusion Flash High-Fidelity PCR Master Mix contained: 1–100 ng template DNA (plasmid or genomic), 1X Phusion Flash PCR Master Mix (provided by manufacturer), 0.1–0.5 µM forward primer, 0.1–0.5 µM reverse primer, and dH_2O up to a total reaction volume of 10–20 µl.

A typical PCR using Phusion Flash PCR Master Mix was performed on a DNA Engine Tetrad 2 thermal cycler (MJ Research) as follows:

	Denaturation		98˚C	10 s
30-35 x	Denaturation		98˚C	1 sec
	Annealing		55-65˚C[2]	5 sec
	Extension		72˚C	15 sec per kb
	Extension		72˚C	1 min

2.4.2.6. Purification of PCR products

To purify PCR products, the QIAquick PCR Purification kit (Qiagen) was used according to the manufacturer's instructions. DNA was eluted in 30 µl of elution buffer and stored indefinitely at –20˚C.

[2] For primers >20 nt, annealing was done for 5 sec at a melting temperature (T_m) +3°C of the lower T_m primer. For primers ≤20 nt, annealing temperature equal to the T_m of the lower T_m primer was used.

2.4.2.7. Genotyping of mice and mouse embryos

To genotype mice or mouse embryos for mutations in *Donson*, a PCR was performed using DNA isolated from mouse ear clips or embryonic tails, respectively. Each ear clip was lysed in 50 µl of 25 mM NaOH and 0.2 mM EDTA by boiling at 95°C for 30 min. After boiling, the mixture was cooled to room temperature for 5 min and then 50 µl of 40 mM Tris-HCl pH 7.5 was added to neutralise the base. Each embryonic tail was placed into DirectPCR Lysis Reagent (Viagen) with added Proteinase K enzyme, and incubated at 55˚C for 16 h, followed by heating at 85˚C for 45 min.

The PCR consisted of 0.5 µl of template, ThermoPrime 2X ReddyMix PCR Master Mix (Thermo Scientific) and 0.5–1 µM of each oligonucleotide (***Appendix 1*e**) in a 10 µl final volume. Thermal cycling conditions were as follows:

	Denaturation	95˚C	1 min	
35x	Denaturation		95˚C	30 sec
	Annealing		60˚C	30 sec
	Extension		72˚C	35 sec
	Extension	72˚C	5 min	

2.4.2.8. Site-directed mutagenesis

2.4.2.8.1. Primers for site-directed mutagenesis

Primers for use in site-directed mutagenesis were designed using the QuikChange Primer Design Program (available online at http://www.genomics.agilent.com). The design algorithm adhered to a number of rules. The primers were between 25 and 55 bases in length, with a melting temperature (T_m) of ≥78˚C (see below), and the desired mutation was located near the middle of the primer with a minimum of ~10–15 bases of correct sequence on either side. The T_m of primers was calculated using the following formula:

$$T_m = 81.5 + 0.41(\%GC) – 675/N – \%mismatch$$

in which N = the primer length in bases,

percentage GC = (#G bases + #C bases)/oligonucleotide length, and

percentage mismatch = #mismatches/oligonucleotide length.

2.4.2.8.2. Site-directed mutagenesis

Point mutations were introduced into plasmid vectors using the PCR based QuikChange method (Stratagene). Primers containing the desired mutation(s) (***Appendices 1*f**, ***1*g**, and ***1*h**) were designed to anneal to the same sequence on opposite strands of the plasmid and were extended by PCR, generating a mutated plasmid. The PCR contained: 50 ng plasmid, 0.25 mM dNTPs, 0.2 µM mutagenic primers (forward and reverse), 1X DNA polymerase buffer with $MgCl_2$ (Stratagene) and 1.25 U of *Pfu*Turbo DNA polymerase (Stratagene). Cycling parameters for site-directed mutagenesis were as follows:

Denaturation		95˚C	1 min	
18x	Denaturation		95˚C	30 sec
	Annealing		55˚C	1 min
	Extension		68˚C	1 min per kb
Extension		68˚C	10 min	

The PCR product was treated with 10 U of *Dpn*I (NEB) at 37˚C overnight to digest the methylated parental vector DNA and thereby select for the mutation-containing synthesised DNA. Following incubation, 0.5–1 µl of the *Dpn*I treated DNA was used for transformation into DH5α *E. coli* (Section 2.2.2.2). Resulting colonies were mini-prepped and screened by Sanger sequencing (see Section 2.4.2.2).

2.4.2.9. Ligation of DNA molecules

Ligation reactions contained: 100–200 ng of vector DNA, 2–3X this molar amount of insert DNA, 1 U T4 DNA Ligase (Roche) and 1X Ligation Buffer (Roche). Following incubation for 4–5 h at room temperature, 1 µl ligation mixture was used to transform *E. coli* (Section 2.2.2.2).

2.4.3. RNA methods

2.4.3.1. Purification of RNA from human cells

RNA was prepared from approximately $1.2x10^6$ cells using the RNeasy Mini Kit (Qiagen) following the manufacturer's instructions. Cells were homogenised using a QIAshredder

column (Qiagen) by centrifugation at 16,000 x g for 2 min. To eliminate genomic DNA contamination, an on-column treatment with 30 U RNase-free DNase I (Qiagen) for 15 min was also included. RNA was eluted into 50 µl RNase-free water and stored indefinitely at –80°C.

2.4.3.2. Reverse transcription of RNA

cDNA (DNA complementary to first strand RNA) was generated using reverse transcriptase and random oligomer primers. A typical reaction mixture contained 1 µg of each RNA sample, 125 ng random primers (Promega) and 1 µl dNTPs (10 mM each), made up to 13.5 µl with RNase-free dH_2O. To melt RNA secondary structures, the reaction was incubated at 65°C for 5 min, immediately followed by 5 min on ice. The 6.5 µl reverse transcription mix (Invitrogen) was then added (4 µl 5X First Strand Buffer, 1 µl 0.1 M DTT, 0.5 µl RNaseOUT Recombinant Ribonuclease Inhibitor and SuperScript III Reverse Transcriptase). The reaction was incubated at 25°C for 5 min, followed by 50°C for 60 min, after which the enzyme was deactivated at 70°C for 15 min. cDNA was stored at –20°C until required.

2.4.3.3. Reverse transcription PCR (RT-PCR)

RT-PCR amplification was performed on cDNA generated as described in Section 2.4.3.2. A typical RT-PCR mixture contained: 0.2–0.5 µl cDNA, ThermoPrime 2X ReddyMix PCR master mix with 1.5 mM $MgCl_2$, 0.1 µM forward primer (***Appendices 1*i** and ***1*j**), 0.1 µM reverse primer (***Appendices 1*i** and ***1*j**), and dH_2O up to a total reaction volume of 10 µl. PCRs were performed on a DNA Engine Tetrad 2 thermal cycler (MJ Research) using the PCR program described below:

	Denaturation	95˚C	5 min
35x	Denaturation	94˚C	30 sec
	Annealing	62˚C	30 sec
	Extension	72˚C	45 sec
	Extension	72˚C	5 min

2.5. Protein methods

2.5.1. Protein preparation from cultured mammalian cells

2.5.1.1. Whole cell protein preparations

For whole cell extract preparation, cultured mammalian cells were harvested and lysed by resuspending in appropriate volume (50–80 µl per 10^6 cells) of urea lysis buffer (***Table 2.1***), followed by 2 cycles of sonication for 30 sec (with a 30 sec gap in between) at 4˚C using the Diagenode Bioruptor 300 Sonicator device. The volume of urea lysis buffer was adjusted according to the type and number of cells harvested. The extract was clarified by centrifugation at 17,000 x g for 30 min at 4˚C. The supernatant was removed and stored at –80°C until required.

2.5.1.2. Chromatin-enriched protein lysate preparation

To isolate the Triton-insoluble (chromatin-enriched) fraction, adherent cells in their culture dish were rinsed twice in cold PBS, washed once with pre-extraction buffer (***Table 2.1***), and incubated for 5 min on ice with gentle shaking in pre-extraction buffer, supplemented with 1 mM phenylmethylsulfonyl fluoride (PMSF; Sigma) and protease inhibitors (Roche, catalog number 04693159001). After removal of buffer and rinsing in PBS, adhering cellular material (Triton-insoluble fraction) was harvested by scraping the cells into an appropriate volume (50–80 µl) of urea lysis buffer (***Table 2.1***). The chromatin-enriched fraction was then denatured by heating at 95˚C for 5 min, sonicated, and, after addition of sample loading buffer (***Table 2.1***), analysed by immunoblotting (see Section 2.5.8).

2.5.2. Protein quantification

Total protein concentrations in cell extracts or purified recombinant protein eluates were determined using Quick Start Bradford Protein Assay (Bio-Rad). Initially, a standard curve was drawn using a BSA concentration range of 0.2, 0.4, 0.6, 0.8 and 1.0 mg/ml, provided by manufacturer. 10 µl of each solution was mixed with 190 µl of 1X Bradford dye reagent and the absorbance at 595 nm (A_{595}) was measured after 5 min. Absorbance readings were plotted against protein concentration, and a line of best fit was used. To measure unknown protein

concentrations, 1 µl of protein sample was mixed with 9 µl dH_2O and 190 µl of 1X Bradford dye reagent, and A_{595} was measured after 5 min. The absorbance reading was compared to the BSA standard curve to calculate protein concentration.

2.5.3. Design and purification of recombinant polycistronic protein complexes

Polycistronic PP4 construct was designed to express all the subunits of the complex simultaneously, as previously performed for other protein complexes (Reijns *et al.*, 2011). Subunits of human PP4 complex (PP4C, PP4R2, and PP43Rα/β) were sequentially cloned into pGEX-6P-1 vector (Addgene) (see ***Figure 4.4***). The first subunit cloned, PP4C, was tagged with GST. The plasmid was Sanger-sequenced after each round of cloning to confirm that no unexpected mutations had been introduced.

2.5.4. Recombinant protein purification after expression in Rosetta-2 cells

For recombinant protein expression, plasmids were introduced into Rosetta-2 *E. coli* cells. Bacterial cells were grown in 400 ml LB medium until OD_{595} 0.7 was reached, and protein expression was induced by adding 0.1 mM IPTG, followed by incubation at 18˚C overnight. Bacterial cultures were harvested by centrifugation at 4,400 x g for 4 min at 4°C and resuspended in 10 ml NETN buffer (***Table 2.1***) with 1 mM PMSF (Sigma). Bacterial cells were lysed by sonication (3 cycles of 15 sec at 24 µ), and the soluble and insoluble fractions were separated by centrifugation at 24,000 x g for 15 min at 4°C.

For recombinant PP4 complexes, the soluble fraction was incubated with 250 µl 50% Amersham Glutathione bead slurry on a roller for 4 h at 4˚C. The beads were centrifuged at 500 x g for 2 min at 4°C, followed by washes in ice-cold NETN buffer (1X 10 ml, 2X 5 ml, 1X 1 ml). The beads were washed once with 1 ml PreScission Cleavage Buffer (GE Healthcare) (***Table 2.1***), and incubated in 500 µl PreScission Cleavage Buffer with 5 µl PreScission Protease (GE Healthcare) on a rotator at 4˚C overnight. The following day, beads were centrifuged at 500 x g for 1 min. Resulting supernatant, containing purified protein(s) ('eluate', E1), was removed, aliquoted and stored at –80˚C. The beads were washed with 250 µl PreScission Cleavage Buffer to obtain the second eluate ('wash', E2).

For recombinant N-terminal TRAIP, the soluble fraction was incubated with 25 µl 50% Amersham Glutathione bead slurry on a roller for 4 h at 4˚C. The beads were centrifuged at

500 x g for 2 min at 4°C, followed by washes in ice-cold NETN buffer (2X 5 ml, 1X 1 ml). The beads were washed once with 100 µl Thrombin 1X Cleavage Buffer (Novagen) and incubated in 50 µl Thrombin 1X Cleavage Buffer with 1 µl Biotinylated Human Thrombin (Novagen) on a rotator at 4˚C overnight according to manufacturer's instructions. The following day, beads were centrifuged at 500 x g for 1 min. 25 µl pre-washed streptavidin beads were added to the resulting supernatant, followed by 30 min of incubation on a rotator at room temperature. The beads were centrifuged at 500 x g for 5 min at 4˚C, and the supernatant, containing purified cleaved protein ('eluate'), was removed, aliquoted and stored at -80˚C.

To assess the efficiency of purification, eluates were mixed with 2X SDS protein sample loading buffer and separated by SDS-PAGE (10% acrylamide) (Section 2.5.6).

2.5.5. *In vitro* protein ubiquitination assay

In vitro ubiquitination assays were used to assess the ability of TRAIP E3 ligase to ubiquitinate substrate proteins. In the 20 µl reactions, putative substrates (1 µg monomeric PP4C or 2 µg recombinant PP4 complexes) were incubated with the E3 ligase (0.4 µg N-terminal TRAIP) in the presence of 5 µg ubiquitin (Enzo), 10X ATP regeneration buffer (Enzo), 0.2 µg E1 ubiquitin-activating enzyme (UBE1-His, Enzo), 0.5 µg E2 ubiquitin-conjugating enzyme (UbcH5b-His, Enzo), and ubiquitination buffer (1 M Tris pH 7.5, 1 M $MgCl_2$, 1 M DTT) for 3 h at 37˚C. Reactions were stopped by the addition of 4X SDS loading buffer. Proteins were resolved by SDS-PAGE (Section 2.5.6) and transferred to nitrocellulose membrane. Immunoblots were performed using the appropriate antibodies, and proteins visualized using the Amersham ECL Prime Western Blotting Reagent (GE Healthcare LifeSciences) (Section 2.5.8).

2.5.6. Sodium dodecyl sulphate-polyacrylamide gel electrophoresis (SDS-PAGE)

Protein samples were separated according to their molecular weight by SDS-PAGE (sodium dodecyl sulphate-polyacrylamide gel electrophoresis) using either the 10% or 4–12% Bis-Tris NuPAGE® Novex (Invitrogen) gel system or home-made Tris-glycine gels.

For Tris-glycine gels, the resolving gel was composed of 375 mM Tris (pH 8.8), 0.1% (w/v) SDS and 0.1% (w/v) ammonium persulphate. For different resolving concentrations, the amount of 30% acrylamide/bis-acrylamide (Sigma-Aldrich) and TEMED (N'N'N'N'-tetramethylethylenediamine) was adjusted accordingly (0.08 µl/ml TEMED in 6% acrylamide,

0.06 µl/ml TEMED in 8% acrylamide or 0.04 µl/ml TEMED in 10-15% acrylamide). The stacking gel contained 125 mM Tris (pH 6.8), 0.1% SDS, 0.1% ammonium persulphate, 4.2% acrylamide/bisacrylamide and 1 µl/ml TEMED. Protein samples were electrophoresed alongside Precision Plus Protein All Blue Prestained Protein Standards (Bio-Rad).

Protein samples were denatured by heating at 95°C for 5 min in 1X SDS protein sample loading buffer (***Table 2.1***) and loaded onto the gel. The gels were electrophoresed in different types of running buffer depending on the gel composition: 1X Tris-glycine running buffer (***Table 2.1***) for Tris-glycine gels or NuPAGE MOPS SDS running buffer (Thermo Fisher Scientific, NP0001) for Bis-Tris NuPAGE® gels. A constant voltage of 150–200 volts was applied until the desired separation was achieved.

2.5.7. Coomassie Blue staining of protein gels

To allow visualisation of abundant protein bands following SDS-PAGE, Coomassie stain (0.1% Coomassie Brilliant Blue R-250 dye, 50% methanol, 10% acetic acid) was used. After electrophoresis, the gel was washed three times for 5 min in 100 ml of dH_2O and then stained in 100 ml of the Coomassie staining solution for 1 h, followed by destaining for 1–3 h in destain solution (10% acetic acid, 10% methanol).

2.5.8. Immunoblotting

Proteins resolved by SDS-PAGE were transferred to nitrocellulose membrane (Amersham) using a Mini-Trans-Blot Cell system (Bio-Rad). Electrophoretic blotting was performed in 1X immunoblotting transfer buffer (***Table 2.1***) at 100 V for 1–1.5 h.

After electrophoretic transfer, the nitrocellulose membrane was blocked. To block, the membrane was incubated with either 5% milk solution (prepared using Marvel milk powder, Premier Foods) or 5% bovine serum albumin fraction V (BSA) (Roche) in TBS/T (1X TBS with 0.2% Tween-20) for 1 h at room temperature with constant agitation. Primary antibodies were added to the blocking solution at the appropriate dilution (***Appendix 2*****a**) and incubated overnight at 4°C. The membrane was washed 3 times for 15 min in TBS/T and then the appropriate horseradish peroxidase (HRP)-labelled secondary antibody (***Appendix 2*****b**), diluted in appropriate blocking solution, was added to the membrane for 1 h at room temperature.

To detect HRP immobilised on the membrane, Amersham ECL Prime Western Blotting Reagent (GE Healthcare LifeSciences) was used according to the manufacturer's instructions. For a 20 cm^2 nitrocellulose membrane, 2 ml of ECL solution (1:1 mixture of solutions A and B) was added to the protein side of the nitrocellulose membrane and incubated for 5 min at room temperature. The membrane was blotted to remove any excess liquid, placed between two acetate sheets and exposed to photographic film (Kodak Biomax XAR Film), which was developed using a Konika SRX-101A Developer. Alternatively, chemiluminescence signal on the immunoblot was visualised using ImageQuant LAS 4000 camera system.

2.5.9. Antibodies

TRAIP antibody was previously generated by A. Robertson (A. Jackson laboratory) from recombinant N-terminal fragment of TRAIP protein (aa1–275) using pGEX-4T-2-TRAIP-N (gift from Robert Geahlen, Purdue University, USA). The construct was expressed in bacteria as GST-fusion protein and used as antigen for the immunisation of rabbits (Eurogentec). TRAIP antibody was affinity purified using the fusion protein immobilized on glutathione-agarose and its specificity established using patient cell lysates and RNAi.

All antibodies (***Appendix 2*a-b**) were diluted in 5% milk (Marvel milk powder, Premier Foods) or 5% BSA (Roche).

2.5.10. Immunoblotting image analysis

Quantification of relative band intensities on unsaturated immunoblots, obtained using ImageQuant LAS 4000 camera system, was performed using Fiji/ImageJ software (US National Institutes of Health) (Abràmoff *et al.*, 2004; Schneider *et al.*, 2012). An area encompassing a protein band was defined manually and kept constant for each measurement within the same immunoblot. The mean pixel intensity was calculated for each area. Signal intensity for the band of interest was normalised to a loading control on the same immunoblot.

2.5.11. Protein ubiquitination site mapping by mass spectrometry (MS)

2.5.11.1. Sample preparation

The *in vitro* ubiquitination reactions with and without TRAIP were set up as described in Section 2.5.5, with wild-type PP4 complexes PP4C-PP4R2-PP4R3β and PP4C-PP4R2-PP4R3α as substrates. The reactions were incubated for 3 h at 37°C and stopped by freezing on dry ice for subsequent liquid chromatography (LC)-tandem MS (MS/MS) (performed by Alex Von Kriegsheim, IGMM Mass Spectrometry facility) (Section 2.5.11.2).

2.5.11.2. Sample processing and analysis

To prepare samples for MS analysis, an 8 M urea buffer with 100 mM Tris (pH 8.5) was added to ubiquitination reactions to a final concentration of 2 M urea, followed by addition of a 1 M DTT to a final concentration of 10 mM. Reactions were incubated at 50°C for 30 min. Iodoacetamide was added to the samples to a final concentration of 10 mg/ml (55 mM), followed by incubation for 30 min in the dark. MS grade trypsin (Promega) was added to the samples at 1/100 ratio (trypsin/substrate concentration), and the digestion was carried out at 37°C overnight.

Next day, samples were treated with 1 µl trifluoroacetic acid (TFA) to stop the digestion and desalted in C18 stagetips. The tips were prepared as described by Rappsilber, Ishihama & Mann (2003), placing a small Empore™ disc (3M™) in an ordinary pipette tip for each sample. Tips were activated with 50 µl of 50% acetonitrile and 0.1% TFA-containing buffer and washed with 50 µl of 0.1% TFA. 100 µl of sample was added to the column and washed twice with 50 µl 0.1% TFA solution. Liquid was passed through the pipette tip manually with the aid of a syringe or with a light centrifugation step. Peptides were then eluted with the help of a syringe using 25 µl of 50% acetonitrile and 0.1% TFA-containing buffer twice. Samples were evaporated in a SpeedVac Concentrator™ (Thermo Scientific), resuspended in 12 µl 0.1% TFA buffer and analysed by MS.

The tryptic peptides were analysed on a mass spectrometer connected to an Ultimate Ultra3000 chromatography system (Thermo Scientific) incorporating an autosampler. For each sample, 5 µl of the tryptic peptides were loaded on a homemade column (100 mm length, 75 µm inside diameter) packed with 1.9 µm ReprosilAQ C_{18} (Dr. Maisch HPLC) and separated by an increasing acetonitrile gradient (3%–32%) at a flow rate of 250 nl/min. The mass

spectrometer was operated in positive ion mode with a capillary temperature of 220°C, with 2,000 V applied to the column. Data were acquired with the mass spectrometer operating in automatic data-dependent switching mode, selecting the 12 most intense ions prior to tandem MS (MS/MS) analysis. Mass spectra were analysed and label-free quantitation performed using the MaxQuant Software package (Tyanova *et al.*, 2016). All the samples were analysed as two technical replicates.

2.6. Microscopy methods

2.6.1. Fixation of cells

Adherent human cells or MEFs were plated onto untreated coverslips (VWR) at appropriate density. After any required treatment, the cells were pre-extracted in pre-extraction buffer (***Table 2.1***) for 5–10 min on ice, followed by fixation in 4% formaldehyde (w/v) in PBS for 12–15 min. Cells were then washed in PBS three times for 5 min and stored at 4°C until required.

2.6.2. Immunostaining

Fixed cells were blocked in 3% fetal bovine serum (FBS) in PBS for at least 30 min. Primary antibodies were diluted in blocking solution (3% FBS in PBS) and incubations were performed for 1.5 h at room temperature in a humidified chamber. The cells were then washed three times in wash buffer (0.2% Triton-X100 in PBS) for 5 min before incubation with appropriate Alexa Fluor–488, and –568 conjugated secondary antibodies (1:1,000) (***Appendix 2b***). The cells were then again washed three times in wash buffer for 5 min. Coverslips were mounted with Vectashield® medium containing DAPI (4',6-diamidino-2-phenylindole) (Vector Laboratories, catalog number H-1200-10) and sealed. Samples were analysed by microscopy within a week of their preparation (see Section 2.6.3.1).

2.6.3. Microscopy

2.6.3.1. Immunofluorescence microscopy

Imaging was performed using a Zeiss Axioplan 2 wide-field fluorescence microscope (Zeiss) with iVision image capture software (BioVision Technologies) or Micro-Manager Open Source Microscopy Software at the IGMM Advanced Imaging Facility. Single images or Z-series were captured with a CoolSnap camera (Roper Scientific) using 40X or 63X Plan-APOCHROMAT (1.4 NA) oil-immersion objective. Exposure time, binning, microscope settings and light source intensity were kept constant for all samples within an experiment.

2.6.3.2. Macroscopy

Imaging of Donson embryos was performed using a Nikon brightfield macroscope with Micro-Manager Open Source Microscopy Software at the IGMM Advanced Imaging Facility. Single images were captured with a CoolSnap camera (Roper Scientific) using 0.5X-2X objectives.

2.6.4. Image analysis

Acquired images were analysed using ImageJ/Fiji software (US National Institutes of Health) (Abràmoff *et al.*, 2004; Schneider *et al.*, 2012). Nuclei were segmented on the basis of DAPI staining and then mean pRPA2-S4/S8 signal intensity or γH2AX/53BP1/native BrdU foci were quantified for each nuclear region using defined protocols (scripts) (Sections 2.6.5 and 2.6.6). 50–100 cells were analysed per experiment per condition, as indicated in figure legends for individual experiments.

2.6.5. Quantitative pRPA2, γH2AX and 53BP1 immunofluorescence

Cells were seeded on coverslips and 16-24 h later treated with the drug (e.g. 1 μM CPT). To label cells undergoing DNA replication, 10 μM EdU (5-ethynyl-2´-deoxyuridine) was added for 20 min; if a drug treatment was used, EdU was added for the last 20 min of the drug treatment. To remove soluble proteins prior to immunofluorescence, cells were pre-extracted for 10 min on ice with ice-cold pre-extraction buffer (***Table 2.1***) and then fixed with 4% formaldehyde for 15 min. EdU immunolabeling was performed using the Click-iT EdU Imaging Kit (Invitrogen, C10337) according to the manufacturer's protocol. Cells were washed with PBS, blocked in 3% FBS in PBS for 30 min at room temperature, and stained for pRPA2-S4/S8 (Bethyl Laboratories, A300-245A; 1:2,000), γH2AX (Cell Signaling Technology, 20E3, #9718; 1:2,000) or 53BP1 (Novus Biologicals, NB100-904; 1:2,000), the secondary Alexa Fluor-linked antibody (***Appendix 2*b**) and DAPI (Vector Laboratories, catalog number H-1200-10). Images were captured as described in Section 2.6.3.1. For quantification of mean signal intensities, nuclei were defined on the basis of DAPI staining and mean intensity of pRPA2-S4/S8 signal was detected using 'Analyze particles' function of ImageJ/Fiji software within each nuclear region. For quantification of γH2AX or 53BP1 foci, nuclei were defined on the basis of DAPI staining and foci were counted using 'Find maxima' function of ImageJ/Fiji software within each nuclear

region. During image analysis, the settings in ‘Analyze particles’ or ‘Find maxima’ functions were kept constant for all samples within an experiment.

2.6.6. Quantification of native BrdU foci

For quantification of native BrdU foci, cells were incubated in medium containing 10 µM BrdU (5-bromo-2'-deoxyuridine) for 24 h prior to harvesting. 90 min prior to harvesting, 1 µM CPT was added to the media. To visualise ssDNA foci, cells were pre-extracted for 10 min on ice with ice-cold pre-extraction buffer (***Table 2.1***) and then fixed with 4% formaldehyde for 15 min at room temperature. After fixation, cells were washed with PBS and blocked in 3% FBS in PBS for 30 min at room temperature. ssDNA was visualised using a BrdU antibody (Abcam, ab6326; 1:500). To detect BrdU in dsDNA, DNA was denatured by incubation in 2 M HCl in PBS for 30 min prior to addition of BrdU antibody. Images were acquired with fluorescence microscope and quantified using Fiji/ImageJ software. Nuclei were defined on the basis of DAPI staining and native BrdU foci were detected using ‘Find maxima’ function of ImageJ/Fiji software within each nuclear region. During image analysis, the settings in ‘Find maxima’ function were kept constant for all samples within an experiment. More than 100 cells were analysed per condition.

2.7. Generation and maintenance of transgenic mouse models

2.7.1. Animal husbandry

Transgenic mice were housed at the Central Bioresearch Services (CBS) Transgenic Core Facility (University of Edinburgh). All procedures were carried out under personal and project home office licences by the qualified facility staff.

Mice of mixed background (C57BL/6, CBA and CD-1) and up to 1 year of age were used for the experimental work described in this thesis.

2.7.2. Cytoplasmic injection of CRISPR reagents

Cytoplasmic injections of CRISPR reagents into fertilised eggs were performed to generate transgenic Donson mice. The CRISPR injection mix (20 µl) to target m*Donson* contained: Cas9 mRNA (50 ng/µl), guide RNA (gRNA) (25 ng/µl) (***Table 2.9***) and repair template DNA (150 ng/µl) (***Table 2.10***) in nuclease-free water. The prepared mix was spun down at 17,000 x g for 30 min at 4°C, 18 µl of it was transferred to a new tube and stored at –20°C until injection.

Injections were performed by the staff of CBS Transgenic Core Facility (University of Edinburgh). Fertilised eggs were obtained from super-ovulated female donor mice that were mated with fertile (stud) males. The CRISPR reagents were then microinjected into the cytoplasm of each egg. Injected eggs and un-injected controls were cultured overnight to the two-cell stage and then transferred to the oviducts of pseudo-pregnant ‘recipient’ females (recipients were generated by mating females with vasectomised males so the females do not produce any fertilized embryos of their own).

2.8. Cell-based assays

2.8.1. Chromosome metaphase spreads

Chromosomal aberrations were scored in DAPI-stained metaphase spreads. 60 nM mitomycin C (Sigma Aldrich) was added to cells for 24 h. Three hours prior to harvesting, 100 ng/ml colcemid (Biosera) was added to cells. Growth medium was removed and stored in a 15 ml tube. Cells were gently washed with 1 ml TrypLE™ Express Enzyme (1X) (Thermo Fisher Scientific, catalog number 12605036) (the trypsin wash was combined with the original medium), trypsinised, resuspended in the original conditioned medium (with a trypsin wash) and centrifuged (250 x g, 5 min, 4°C). Cells were then washed with PBS, spun down, resuspended in pre-warmed 75 mM potassium chloride (KCl) and incubated for 30 min at 37°C. Cells were centrifuged again, the supernatant was removed and cells were fixed by drop-wise addition of 1 ml fixative (ice-cold methanol:acetic acid, 3:1) while gently vortexing. An additional 10 ml of fixative was then added and cells were fixed at 4°C for at least 16 h. Once fixed, metaphases were dropped on glass slides humidified with methanol:acetic acid (3:1), rinsed with fixative, air-dried, mounted using Vectashield® medium containing DAPI (Vector Laboratories, catalog number H-1200-10), and imaged at 63X objective on fluorescence microscope.

2.8.2. Sister chromatid exchange assay

Homologous recombination (HR) proficiency of cells was determined by scoring sister chromatid exchanges (SCEs). 10 µM BrdU was added to RPE1 p53-/- Cas9 cells for 2 cycles of replication (47–48 h). For the first cycle, 5 nM CPT or 20 mM MMC was added to cells as well. After 24 h, the drug was washed off with PBS, BrdU-containing medium was refreshed, and cells were grown for another 24 h (second round of DNA synthesis). Three hours prior to harvesting, 100 ng/ml colcemid (Biosera) was added to cells.

Growth medium was removed and stored in a 15 ml tube. Cells were gently washed with 1 ml TrypLE™ Express Enzyme (1X) (Thermo Fisher Scientific, catalog number 12605036) (the trypsin wash was combined with the original medium), trypsinised, resuspended in the original conditioned medium (with a trypsin wash) and centrifuged (250 x g, 5 min, 4°C). Cells were then washed with PBS, spun down, resuspended in pre-warmed 75 mM potassium chloride (KCl) and incubated for 30 min at 37°C. Cells were centrifuged again, the supernatant

was removed and cells were fixed by drop-wise addition of 1 ml fixative (ice-cold methanol:acetic acid, 3:1) while gently vortexing. An additional 10 ml of fixative was then added and cells were fixed at 4°C for at least 16 h. Once fixed, metaphases were dropped on glass slides humidified with methanol:acetic acid (3:1), rinsed with fixative and air-dried overnight (protected from light).

To visualize SCEs, slides were rehydrated in PBS for 5 min and stained with 2 µg/ml Hoechst 33342 (Molecular Probes/Thermo Fisher Scientific) in 2X SSC (300 mM NaCl, 30 mM sodium citrate, pH 7.0) (***Table 2.1***) for 15 min. Stained slides were placed in a plastic tray, covered with a thin layer of 2X SSC and irradiated with 254 nM UV light (~5400 J/m^2). Slides were subsequently dehydrated in a 70%, 95% and 100% ethanol series (5 min each), air-dried and mounted using Vectashield® medium containing DAPI (Vector Laboratories, catalog number H-1200-10). Images were captured as described in Section 2.6.3.1.

2.8.3. Clonogenic cell survival assay

For colony formation assays, cells were plated at low densities (125–4,000 cells per 100 mm tissue culture dish) and treated with the indicated doses of CPT or MMC for 24 h. Cells were then washed extensively, culture medium was replaced, and cells were allowed to form colonies for 8–9 days, at which point they were fixed and stained with 2% methylene blue solution (2% methylene blue solution in 50% EtOH). Colonies were counted manually by visual inspection. The surviving fraction at each dose was calculated after normalisation to the colony number detected for untreated samples. When siRNA transfection (Section 2.3.3.1) was required before plating cells for clonogenic survival assay, cells were treated with drug 48 h post-transfection.

2.8.4. Minigene splicing assay

The splicing minigene reporter RHCglo, generated by the Thomas Cooper laboratory (Singh and Cooper, 2006), was used for all minigene experiments in this thesis. Exons and introns of interest were amplified from control and patient genomic DNA using primers with restriction enzyme sites (***Appendix 1*a**). The PCR products and RHCglo vector were digested with the appropriate restriction enzymes (New England Biolabs, NEB) at 37°C overnight. Digested RHCglo plasmid was treated with Antarctic Phosphatase enzyme (NEB) for 1 h at 37°C to prevent self-ligation. Ligation reactions between RHCglo plasmids and inserts were

performed (Section 2.4.2.9), and the ligated plasmids were transformed into competent DH5α *E. coli* strain (Section 2.2.2.2). A positive control for splicing was generated by introducing a point mutation into the splice donor or acceptor site using site-directed mutagenesis (Section 2.4.2.8) and primers indicated in ***Appendix 1*****f**.

HeLa cells, used for minigene transfections, were plated in 6-well plates and transfected with 800 ng of minigene plasmids, as described in Section 2.3.3.3. Cells were harvested 24 h after transfection, followed by the total cellular RNA extraction (Section 2.4.3.1) and cDNA generation (Section 2.4.3.2). RT-PCR amplification with RHCglo or gene-specific primer mix (***Appendix 1*****i**) was then performed on cDNA (Section 2.4.3.3). Wild-type and mutant cDNA amplicons were resolved on a 2% agarose gel to visualise splicing differences (Section 2.4.1.2). PCR products were cloned into pGEM-T Easy Vector (Promega), and the plasmids were transformed into competent DH5α *E. coli* strain (Section 2.2.2.2). Colony PCR on colonies was performed (Section 2.4.2.5.2), followed by Sanger sequencing of the PCR products (Section 2.4.2.2).

Chapter 3

DNA2 mutations in microcephalic primordial dwarfism

3. *DNA2* mutations in microcephalic primordial dwarfism

DNA2 is an ATP-dependent helicase/nuclease, which has been demonstrated in recent years to play multiple important roles during DNA replication and repair. Most of the well-studied cellular functions of DNA2 have been attributed to its nuclease activity, whereas the helicase activity of DNA2 long remained unclear. However, more recently it was shown to act as an ATP-dependent translocase to promote rapid ssDNA degradation during DNA end resection (Levikova *et al.*, 2017; Miller *et al.*, 2017) (see Section 1.4 for details).

In 2014, *DNA2* was proposed as a candidate Seckel syndrome gene based on the identification of a homozygous intronic mutation in two related individuals (Shaheen *et al.*, 2014) (***Figure 3.1***). This study suggested the mutation to alter splicing of *DNA2* transcripts, resulting in reduced protein levels and DNA damage. However, the report would have greatly benefited from the analysis of more cases, as it was based on a single identified mutation. Identification of multiple individuals exhibiting a specific phenotype with mutations in the same gene can significantly strengthen the association of that gene with a disease. Additionally, analysis of unrelated affected individuals allows better separation of mutation-specific effects and background genetic noise, as well as providing confirmation of the disease-causing nature of a gene. Although some analysis of patient-derived cell lines was provided by Shaheen *et al.* (2014), the mechanism by which mutations in *DNA2* would cause MPD remained to be established. Additionally, monoallelic mutations in *DNA2* were reported to result in muscle deficiency and mitochondrial disease (Chae *et al.*, 2015; Phowthongkum and Sun, 2017; Ronchi *et al.*, 2013), and it is yet to be explained why heterozygous and homozygous mutations in this gene are associated with different phenotypes (see Section 3.6 for discussion).

In the Andrew Jackson laboratory, extensive whole exome sequencing (WES) was performed on a group of MPD patients with unknown molecular cause of disease. This study helped to identify several novel candidate MPD genes, including *DNA2*. In this chapter, the identification and phenotypic characterisation of the individuals with *DNA2* mutations is described, as well as various attempts to address the consequences of the identified variants on *DNA2* transcript splicing and protein levels.

3.1. Identification and phenotypic characterisation of MPD patients with *DNA2* mutations

The novel link established between *DNA2* and MPD by Shaheen *et al.* (2014) was based on the identification of a single variant. Significantly, four patients with biallelic mutations in the *DNA2* gene were identified in the WES study performed in our laboratory on a cohort of 332 individuals, 192 of which were severely affected MPD patients with no known genetic cause for their disease (***Figure 3.1***; ***Table 3.1***; ***Table 3.2***; performed by Louise Bicknell). In total, we identified two intronic variants and one missense mutation in four individuals that are not known to be related to each other. These *DNA2* variants have not been reported in the general population (genome Aggregation Database (gnomAD)), consistent with them being disease-causing. The affected individuals were Sanger-sequenced to confirm the variants identified during WES (***Figure 3.2***). The parents of the affected individuals were shown to be heterozygous for these variants, demonstrating the necessity for biallelic mutations to cause the phenotype and supporting the autosomal recessive mode of inheritance of MPD.

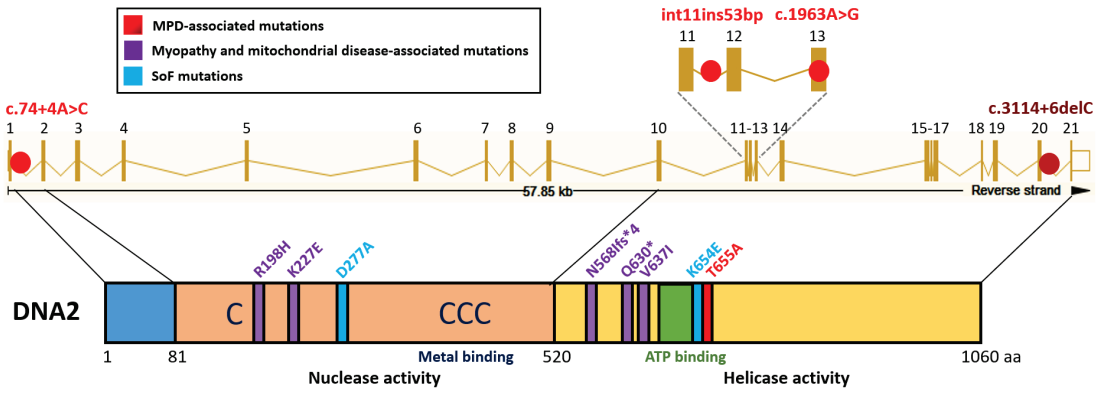

Figure 3.1. Disease-associated variants within the *DNA2* gene.
DNA2 mutations identified in MPD patients are shown in red on a schematic model of *DNA2* gene and protein structure. Variants c.74+4A>C, c.1763+26_1763+27ins53bp (also referred to as int11ins53bp) and c.1963A>G (p.T655A) were identified in four affected individuals by our laboratory, whereas c.3114+6delC mutation (shown in dark red) was described by Shaheen *et al.* (2014). Several monoallelic *DNA2* mutations (shown in purple) were linked to muscle deficiency and mitochondrial disorders (Chae *et al.*, 2015; Phowthongkum and Sun, 2017; Ronchi *et al.*, 2013). Single amino acid substitutions D227A and K654E (shown in light blue) have been employed by multiple studies as separation of function (SoF) mutations to unlink nuclease and helicase activities, with the D277A mutation obliterating the nuclease activity and unmasking the helicase/translocase function, and the K654E mutation abolishing the ATPase activity (Duxin *et al.*, 2012; Fortini *et al.*, 2011; Masuda-Sasa *et al.*, 2006; Nimonkar *et al.*, 2011).

Table 3.1. List of novel mutations in *DNA2* in four MPD-affected individuals.
The table indicates biallelic variants in *DNA2* that were found during WES analysis in four MPD patients (P1–P4), as well as the predicted consequences at protein level that these variants would cause.

Pt	Nucleotide mutations		Amino acid alterations	Sex	Country of origin
	Allele 1	Allele 2			
P1	c.1763+26_1763+27ins53bp	c.1763+26_1763+27ins53bp	?	F	Italy
P2	c.1763+26_1763+27ins53bp	c.1763+26_1763+27ins53bp	?	F	USA
P3	c.1963A>G	c.74+4A>C	p.T655A / ?	F	USA
P4	c.74+4A>C	c.74+4A>C	?	M	Sri Lanka

Table 3.2. Phenotypic characteristics of individuals with *DNA2* mutations.
The table provides a summary of the phenotypic measurements of P1, P3 and P4, as provided by their clinicians. Information that was not available (N/A) is indicated; y = years; m = months.

Pt	Birth					Postnatal				
	Gest (weeks)	Weight (kg)	SD	OFC (cm)	SD	Age at exam	OFC (cm)	SD	Height (cm)	SD
P1	36	1.68	-2.5	N/A	N/A	5y 8m	43	-7.5	88	-5.3
P3	34	0.9	-4.1	N/A	N/A	15y 9m	42.1	-9.6	95.5	-11.1
P4	40	1	-5.9	29	-4.9	10y 7m	45.5	-5.7	112	-4.6

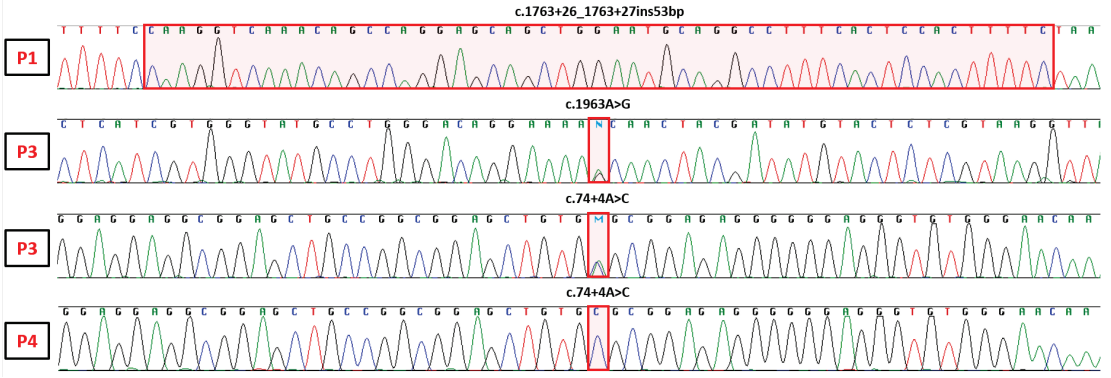

Figure 3.2. Electrophoretic DNA sequencing traces of *DNA2* mutations in MPD patients.
The *DNA2* regions shown by WES analysis to contain rare variants were PCR-amplified and Sanger-sequenced to confirm the presence of biallelic *DNA2* mutations (marked in red).

All four patients exhibited severe microcephaly at the time of their postnatal exam, with the OFC ranging from −5.6 SD to −9.6 SD, as well as markedly reduced height, ranging from −4.6 SD to −11.1 SD (***Table 3.2***; ***Figure 3.3*****a**). No obvious unifying physical appearance

was found to distinguish the individuals with *DNA2* mutations from other MPD patients, although three out of four patients with *DNA2* mutations seem to have minor facial similarities, such as small mouths or large teeth (***Figure 3.3*b**). Patient 1 (P1) was reported to have a prominent nose, mild hypertelorism (increased distance between the eyes), delayed dental age, and ichthyotic (fish scale-resembling) skin over her legs. Not much information was available for P2, as the patient was lost to follow-up, although she was noted to have large front teeth. P3 was reported to have severe kyphoscoliosis, a very small jaw, big teeth, and to experience recurrent chest infections. Finally, P4 was described to have very long arms (relative to body size) and arachnodactyly (abnormally long and slender fingers and toes), large ears, a small mouth, hyperextensible joints, winging of the scapulae and lumbar lordosis, a short broad neck, and sparse hair. No intellectual disability was noted in any of the patients, and all four underwent normal childhood development, with two of them having reached adolescence.

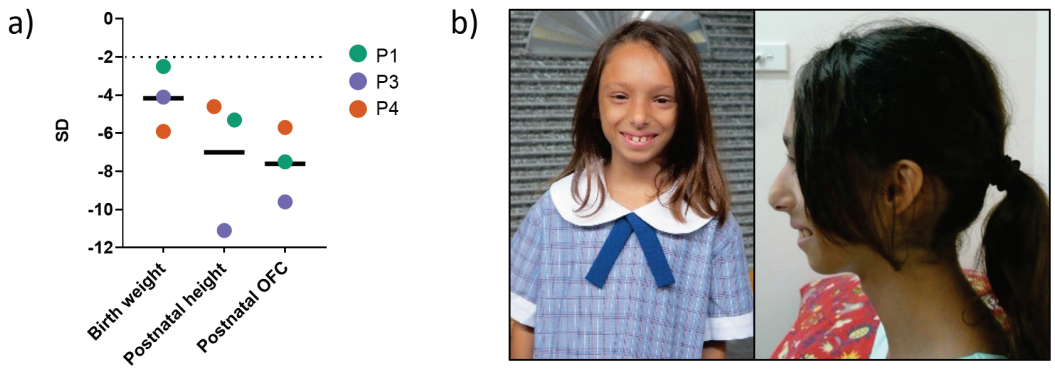

Figure 3.3. Phenotypic characteristics of DNA2 patients.
a) Affected individuals show extremely reduced birth weight, postnatal height and OFC measurements (the black bar represents the mean), indicating global growth failure of prenatal onset and extreme microcephaly (plotted based on ***Table 3.2***). b) DNA2 patients share some craniofacial similarities, including small mouths and prominent teeth, as seen in the photos of patient 1 (P1). Informed consent to publish photographs was obtained from the family.

Two of the MPD patients with *DNA2* mutations (P1 and P2) are homozygous for the same variant, a 53 bp-long insertion in the middle of the small 78 bp-long intron 11 of *DNA2*. These two individuals are not known to be related, but the presence of the same rare mutation in both might suggest at least distant relatedness. The identified insertion results in an intron that is almost double the size of the original one and was detected by WES due to the small

size of intron 11. Using the CADDv1.4-GRCh38 (Combined Annotation Dependent Depletion version 1.4 for Genome Reference Consortium human build 38) tool, the CADD score, which predicts the deleteriousness of variants in the human genome (Kircher *et al.*, 2014), was estimated to be 6.013 for this insertion, indicating a benign variant. In contrast, preliminary bioinformatic analysis, which compared the predictions of five different splicing prediction tools, suggested that this variant might affect splicing of *DNA2* transcript, introducing either a new donor or acceptor splice site (***Figure 3.4***). Although the cause of the 53 bp insertion is unknown, it is noteworthy that the first 37 bp of the insertion can be mapped to a non-coding region on chromosome 3, whereas the following 16 bp of the insertion appear to be a small duplication of part of *DNA2* intron 11 just upstream of the insertion.

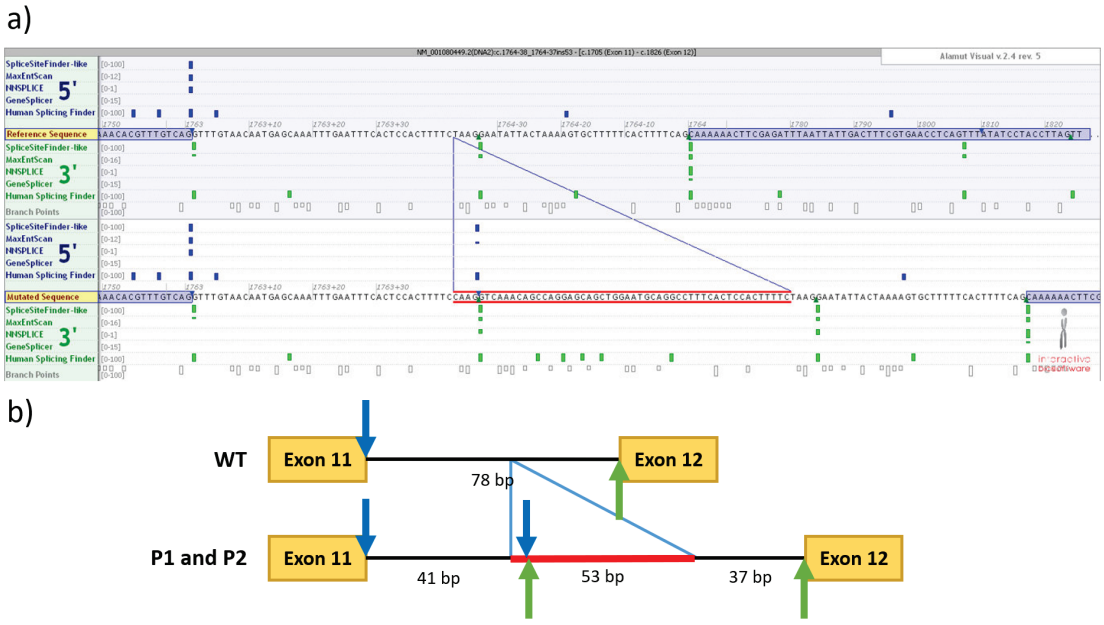

Figure 3.4. *DNA2* int11ins53bp variant is predicted to introduce novel splice sites in intron 11.
The visualisation using Alamut Visual Interactive Biosoftware (a) and the cartoon model (b) of the insertion c.1763+26_1763+27ins53bp (marked in red), which is present in homozygous state in P1 and P2. This variant is predicted to alter *DNA2* transcript splicing by creating a new intronic donor splice site (blue arrow in the cartoon model) and/or a new acceptor splice site (green arrow in the cartoon model).

One of the other patients (P4) is homozygous for a putative splice site mutation in intron 1 (c.74+4A>C). The CADD score for this mutation is 16.43, indicating a potentially deleterious variant, with similar score commonly found for missense and canonical splice site variants (Kircher *et al.*, 2014). This mutation is predicted to diminish the usage of the splice

donor site and may therefore be expected to result in aberrant splicing of the *DNA2* transcript, either through retention of intron 1 or activation of cryptic splice sites within intron 1, both of which would result in a frameshift and premature stop codon (p.L25fs*) (***Figure 3.5***). Lastly, patient P3 was found to be compound heterozygous for two *DNA2* variants predicted to be pathogenic: the already mentioned c.74+4A>C mutation and a missense mutation in exon 13 (c.1963A>G, p.T655A). The latter affects the evolutionarily highly conserved ATP-binding motif of the DNA2 helicase domain and may therefore be expected to impact on the helicase/translocase function of DNA2 (***Figure 3.6***). Moreover, it has the CADD score of 28.2, associated with deleterious variants (Kircher *et al.*, 2014). It is also worth mentioning that P3 has the most severe reduction in height and the smallest head circumference out of the four patients with *DNA2* mutations (***Table 3.2***).

The identification of four MPD patients with biallelic *DNA2* variants that are not present in the general population provides a strong case for *DNA2* as a novel MPD-associated gene. The mutations identified were predicted to cause partial loss of DNA2 function, and experiments testing these predictions are described in Sections 3.3 and 3.4.

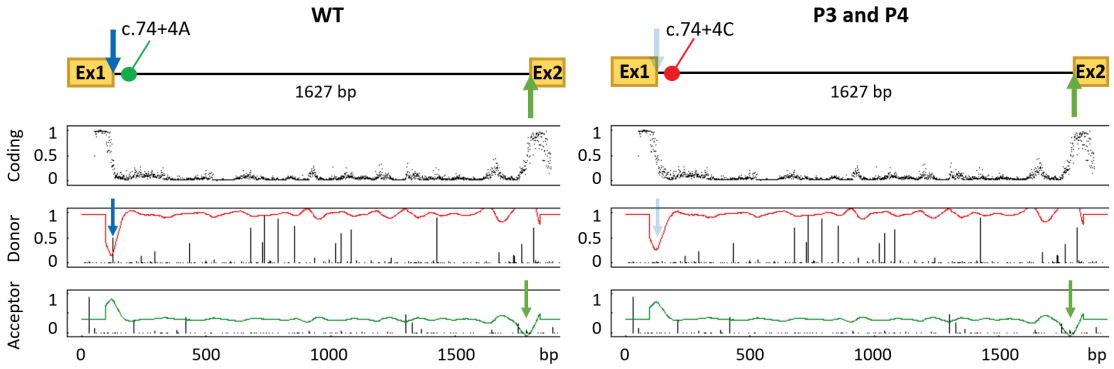

Figure 3.5. *DNA2* c.74+4A>C variant is predicted to weaken the splice donor site of intron 1. P4 is homozygous and P3 is heterozygous for the intronic *DNA2* variant c.74+4A>C, which is predicted to alter *DNA2* transcript splicing by reducing the probability of splicing donor site being used. Above: cartoon model representing the splicing change. Below: visualisation of the splicing prediction in NetGene2 v2.4 neural network splicing prediction tool, available at http://www.cbs.dtu.dk/services/NetGene2. The panel 'Coding' represents prediction of coding regions (values close to 0.0 indicate introns; values close to 1.0 indicate exons). In the 'Donor' and 'Acceptor' panels, splice donor/acceptor site predictions are shown as impulses, with the height of the line representing the strength of the site (values close to 1.0 indicate strong splice donor/acceptor sites). Blue arrows indicate the disappearance of the line representing the splice donor site of intron 1 in the presence of the c.74+4A>C variant. Green arrows indicate the predicted splice acceptor site.

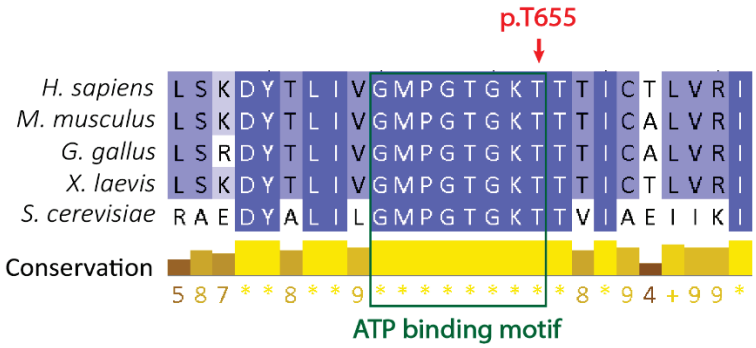

Figure 3.6. *DNA2* threonine 655, mutated in MPD patient P3, is highly conserved through evolution.

c.1963A>G (p.Thr655Ala, p.T655A; shown in red) in exon 13 of *DNA2* affects a highly conserved last residue of the 8 amino acid-long ATP binding motif (shown in dark green) within the helicase/translocase domain. Conservation score of each residue is provided; a yellow star indicates complete conservation of a residue in human, mouse, chicken, African clawed frog and budding yeast. Alignment was generated using Jalview multiple sequence alignment software (Waterhouse *et al.*, 2009).

3.2. Sanger sequencing-based screening of the MPD patient cohort to identify additional variants in *DNA2*

With the aim of identifying additional *DNA2* disease mutations, Sanger sequencing was performed on a group of 76 MPD patients with unknown molecular diagnosis that were not included in the original WES study. The aim was to identify any additional potentially harmful coding and splicing variants in *DNA2*. The primers used for the screen were designed to cover all 21 exons of the gene as well as all the intron-exon junctions (see Section 2.4.2.2.1 for details). Intronic base substitutions, intronic microdeletions and silent exonic variants were detected within this cohort. However, none of these variants is likely to be pathogenic. All of the synonymous exonic variants identified in our cohort occur in the homozygous state in unaffected individuals, with an allele frequency of 0.05% or greater (***Table 3.3***). Therefore, it is highly unlikely that these variants are the cause of the extreme reduction in brain size and growth. Most non-coding variants identified are also commonly found in the healthy population in homozygous state (***Table 3.4***). Small intronic deletions of *DNA2* in the MPD patients were mostly found to occur within long poly(A/T) tracts that frequently flank *DNA2* exons. The majority of identified intronic variants are located far from intron-exon junctions, reducing the likelihood of any influence on splice donor or acceptor sites. However, there remains a possibility that these intronic variants subtly affect *DNA2* transcript splicing by altering important *cis*-acting DNA sequence elements, such as intronic splicing enhancers.

Table 3.3. Synonymous coding variants in *DNA2* identified in our cohort of MPD patients with unknown genetic cause of disease.
The table shows how many of the sequenced MPD patients from our cohort were found to be homozygous and heterozygous for each variant and provides the calculated minor allele frequency (MAF). The proportion of the general population homozygous for the variant and MAF data were obtained from gnomAD Browser Database.

Variant	Amino acid alteration	Our PD cohort			gnomAD Browser data	
		Hom	Het	MAF	Hom	MAF
10:70227964 C / T (rs10998205)	p.L205L	1/75	14/75	10.67%	3261/274866	13.10%
10:70225504 G / T (rs3758626)	p.A255A	2/72	26/72	20.83%	11943/272136	28.20%
10:70191703 C / T (rs116704917)	p.A719A	0/76	2/76	1.32%	11/276736	0.28%
10:70191631 C / T (rs61855090)	p.T743T	0/76	2/76	1.32%	418/275884	4.42%
10:70178815 A / G (rs538200699)	p.F1067F	0/72	1/72	0.69%	1/266294	0.05%

Table 3.4. Non-coding variants in *DNA2* identified in our cohort of MPD patients with unknown genetic cause of disease.

The table shows how many of the sequenced MPD patients from our cohort were found to be homozygous and heterozygous for each variant and provides the calculated minor allele frequency (MAF). The proportion of the general population homozygous for the variant and MAF data were obtained from gnomAD Browser Database. A star (*) indicates a variant that was not reported in gnomAD Browser Database but was indicated as a common single-nucleotide polymorphism (SNP) in Single Nucleotide Polymorphism database (dbSNP 150; NCBI), which reports SNPs found in ≥1% population.

Intronic or UTR variant	Position relative to exon	Our PD cohort			gnomAD Browser (*or dbSNP 150) data	
		Hom	Het	MAF	Hom	MAF
10:70231701 A / G (rs1535539)	c.-79T>C	2/75	16/75	53.33%	6434/276410	19.73%
10:70231513 G / T (rs192015602)	c.75+35C>A	0/75	2/75	1.33%	17/212750	1.10%
10:70206033 TA / T (rs770415045)	c.1057+18delT	1/64	1/64	2.34%	1654/102086	13.47%
10:70204845 GA / G (rs747930650)	c.1058-6delT	0/73	1/73	0.68%	26/239414	0.85%
10:70197115 G / A (rs12775711)	c.1416-117C>T	0/72	2/72	1.39%	672/5008*	13.42%
10:70190155 A / G (rs12221039)	c.2208+38T>C	1/75	13/75	10.00%	2377/187032	13.89%
10:70182697 GT / G (rs141172562)	c.2209-51delA	0/71	2/71	1.41%	417/184322	2.44%
10:70181968 AT / A (rs746777672)	c.2697+13delA	0/74	7/74	4.73%	747/29402	8.78%
10:70179713 C / G (rs7912227)	c.2698-64G>C	2/75	12/75	10.67%	1312/30926	25.29%
10:70179006 T / C (rs41305002)	c.2788-36A>G	0/72	3/72	2.08%	10/119050	1.16%
10:70174885 A / G (rs17460571)	c.3015-21T>C	1/73	14/73	10.96%	2588/189470	14.38%

A few coding and non-coding variants identified, such as exonic rs538200699 or intronic rs1535539, are moderately over-represented in the MPD cohort compared to the healthy population (***Table 3.3*** and ***Table 3.4***). However, this apparent over-representation is likely caused by the low number of patients sequenced in our study and would be matched to the healthy population when more patients are screened. I decided to not pursue any of these variants further, since high allele frequency in general population and existence of multiple unaffected individuals homozygous for a specific variant markedly reduces the probability of the variant being pathogenic and disease-causing.

3.3. Assessing transcript splicing changes caused by *DNA2* mutations

3.3.1. *DNA2* patient mutation int11ins53bp affects the presence of exon 12 in *DNA2* transcripts

To establish the pathogenicity of a variant, it is important to demonstrate that it alters transcript splicing and protein levels. Due to the lack of available patient-derived cell lines to study the effects of *DNA2* mutations on transcript and protein levels, I chose to make use of a minigene-based splicing assay. The minigene splicing assay is a method that can be used to assess the impact of a specific mutation on transcript splicing in a cell line of choice. Transient expression of minigenes in cells has been employed as a valuable tool in various recent studies to address transcript splicing, as well as study *cis*-acting elements that may modulate inclusion or exclusion of exons (Aparisi *et al.*, 2013; Cooper, 2005; De Crescenzo *et al.*, 2015; Steffensen *et al.*, 2014).

The bioinformatics-based modelling of the int11ins53bp mutation suggested that this variant is likely to create a new intronic splicing donor and/or acceptor site (***Figure 3.4***). Experimental demonstration that the 53 bp intronic insertion in the intron 11 of *DNA2* leads to alternative splicing of *DNA2* transcript was required to support our hypothesis of this variant being a pathogenic MPD-causing mutation. Control and DNA2 patient genomic regions surrounding *DNA2* intron 11 were cloned into the splicing minigene reporter RHCglo (Singh and Cooper, 2006) (***Figure 3.7*a**). A splicing control was generated by introducing a nucleotide substitution (c.1764-1G>A) into the acceptor splice site of intron 11 within the wild-type DNA2 minigene (***Figure 3.7*a**). Gel electrophoresis analysis of RT-PCR products generated using minigene backbone primers showed that the most abundant transcript in DNA2 int11ins53bp minigene has higher electrophoretic mobility than the product of the wild-type DNA2 minigene (***Figure 3.7*b**). The control with a disrupted splice site, c.1764-1G>A, demonstrated complete abrogation of correct splicing (***Figure 3.7*b**). In contrast, DNA2 int11ins53bp mutant had some residual amount of normally spliced transcript. Given that DNA2 is an essential gene during mammalian development (Lin *et al.*, 2013), low residual level of wild-type *DNA2* transcript may explain why *DNA2* int11ins53bp mutation is deleterious but does not result in embryonic lethality.

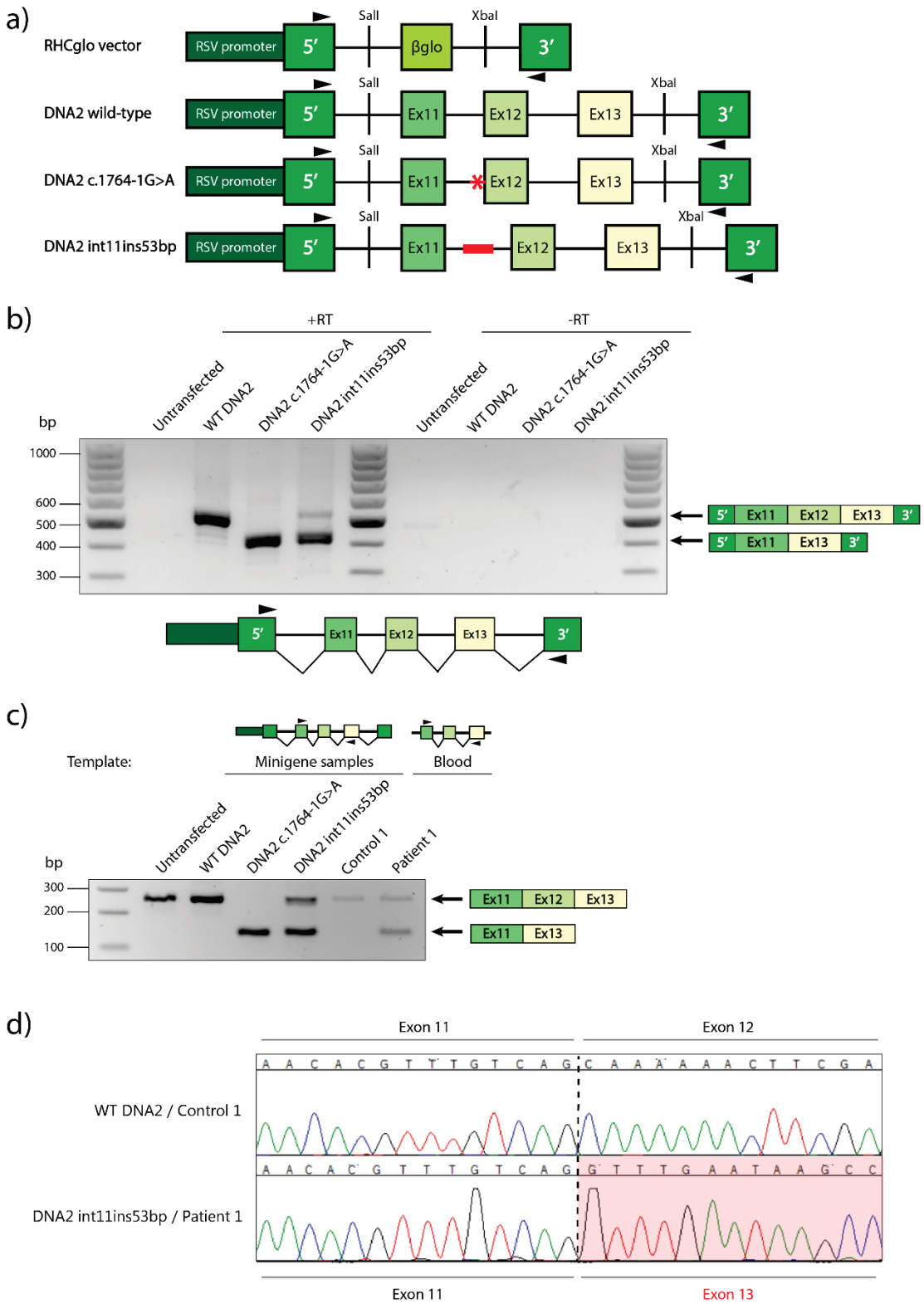

Figure 3.7. *DNA2* int11ins53bp mutation alters correct splicing of *DNA2* transcript.
a) A cartoon model of RHCglo-based constructs used in the minigene splicing assay to assess the effect of int11ins53bp mutation in cells. Minigene plasmids were generated by PCR amplification of intron 11 and the nearby exons from control DNA and patient DNA, and subsequent cloning into the RHCglo minigene plasmid. A positive control for splicing was

generated by introducing a point mutation (c.1764-1G>A) into the acceptor splice site of *DNA2* intron 11. Black arrowheads indicate the locations of primers used for PCR analysis.
b) *DNA2* int11ins53bp mutation affects splicing of *DNA2* transcript. HeLa cells were transfected with minigene constructs, followed by RNA extraction, cDNA generation and RT-PCR analysis to assess *DNA2* transcript splicing patterns caused by the int11ins53bp mutation (see Section 2.8.4). RT-PCR products amplified from the HeLa cDNA of the minigene assay samples using RSV5U and RTRHC primers (indicated by short black arrows) were run on an agarose gel and subsequently cloned for sequencing. Samples where no reverse transcriptase was added during cDNA generation are labelled as '-RT'. Sanger sequencing analysis of the products revealed that the PCR product with higher electrophoretic mobility represents the mutant isoform lacking exon 12, and the lower mobility product the correctly spliced transcript.
c) The splicing defect caused by *DNA2* int11ins53bp can be confirmed by RT-PCR using a blood sample obtained from P1. PCR products were amplified from HeLa cDNA of the minigene assay samples and from peripheral blood leukocyte cDNA from Patient 1 using primers located in exon 11 and exon 13 of *DNA2* (indicated by short black arrows), run on an agarose gel and subsequently cloned for sequencing. Sanger sequencing analysis of the products recapitulated the previous findings.
d) Sanger electropherograms of RT-PCR products demonstrate that the *DNA2* int11ins53bp mutation results in the skipping of exon 12 in *DNA2* transcript.

To understand the splicing alterations that the obtained RT-PCR products represented, the PCR amplicons of each sample were cloned for Sanger sequencing. Sequencing analysis showed that the PCR band of the WT DNA2 minigene represented the correctly spliced mRNA, which included all the exons cloned into RHCglo vector (exons 11-13) (***Figure 3.7*****b**,**d**). In contrast, a fraction of *DNA2* int11ins53bp transcript was spliced abnormally, containing full-length exons 11 and 13 but lacking exon 12 (***Figure 3.7*****b**,**d**). This finding was confirmed using a set of internal primers designed to amplify a cloned region of the minigene and screen specifically for the presence of exon 12 (***Figure 3.7*****c-d**).

Although *DNA2* int11ins53bp variant was predicted to create either a new donor or acceptor splice site (***Figure 3.4***), the data obtained using the minigene splicing assay suggest that this mutation affects the presence of exon 12 in *DNA2* transcript. Given that the absence of DNA2 exon 12 results in a frameshift and a premature termination codon in exon 13 (p.S588Rfs*4), *DNA2* int11ins53bp mutation is likely to cause reduced levels of functional cellular DNA2. Further validation for the disruption of splicing was obtained by *DNA2* transcript splicing analysis of a blood sample donated by P1, demonstrating the same result as the one obtained using the minigene splicing assay (***Figure 3.7*****c-d**). The concordance between these results not only confirms the likely pathogenicity of the *DNA2* int11ins53bp mutation, but also demonstrates the usefulness of the minigene splicing assay for predicting deleterious intronic variants.

3.3.2. *DNA2* patient mutation c.74+4A>C alters splicing of *DNA2* transcript

To analyse the consequences on transcript level of the intronic *DNA2* patient variant c.74+4A>C (***Figure 3.5***), I again employed the minigene assay. Control and DNA2 patient genomic regions surrounding *DNA2* c.74+4 were cloned into the RHCglo reporter and transfected into HeLa cells, alongside the splicing control, c.74+1G>A, where the splice donor site of intron 1 was mutated (***Figure 3.8*****a**).

RT-PCR products were amplified using minigene backbone primers, and gel electrophoresis analysis showed the disruption of splicing in the presence of c.74+4A>C variant, indicated by the appearance of a higher electrophoretic mobility band, which was also present in the control sample with disrupted splice site (***Figure 3.8*****b**). Interestingly, as seen for *DNA2* int11ins53bp, the c.74+4A>C mutant had some residual amount of correctly spliced transcript, indicating that this variant is not likely to cause complete loss of normal DNA2 splicing and suggesting that reduced levels of wild-type DNA2 protein may account for severe growth restriction.

Sequencing analysis of the cloned PCR products showed that the WT DNA2 minigene product represented the correctly spliced mRNA, which included both exon 1 and 2 that had been cloned into the RHCglo vector (***Figure 3.8*****b**). In contrast, a large proportion of the *DNA2* c.74+4A>C transcript was spliced unconventionally, containing exon 2 alone and lacking exon 1 (***Figure 3.8*****b**). The same type of abnormal splicing was also seen for the splicing control c.74+1G>A, where almost no normal splicing could be detected (***Figure 3.8*****b**).

The data obtained using the minigene splicing assay suggest that the *DNA2* c.74+4A>C mutation affects the presence of exon 1 in *DNA2* transcript. However, as we are looking at the first exon of the transcript, this assay may not be entirely representative of what happens in this situation *in vivo*. In patient cells, such aberrant splicing might substantially disrupt production of wild-type *DNA2* transcript and functional protein, either through retention of intron 1 or activation of cryptic splice sites within intron 1. Alternatively, skipping exon 1 may turn exon 2 into the first exon in the case of this abnormal splicing event, or a portion of the non-coding region upstream of the gene may get included into the mutant transcript to 'replace' the missing exon 1. The most biologically relevant way the consequences of the c.74+4A>C mutation on transcript splicing could be elucidated is the analysis of RNA obtained from a blood sample of P4. However, this could not be done, as the patient was not prepared to participate in additional investigations when re-contacted.

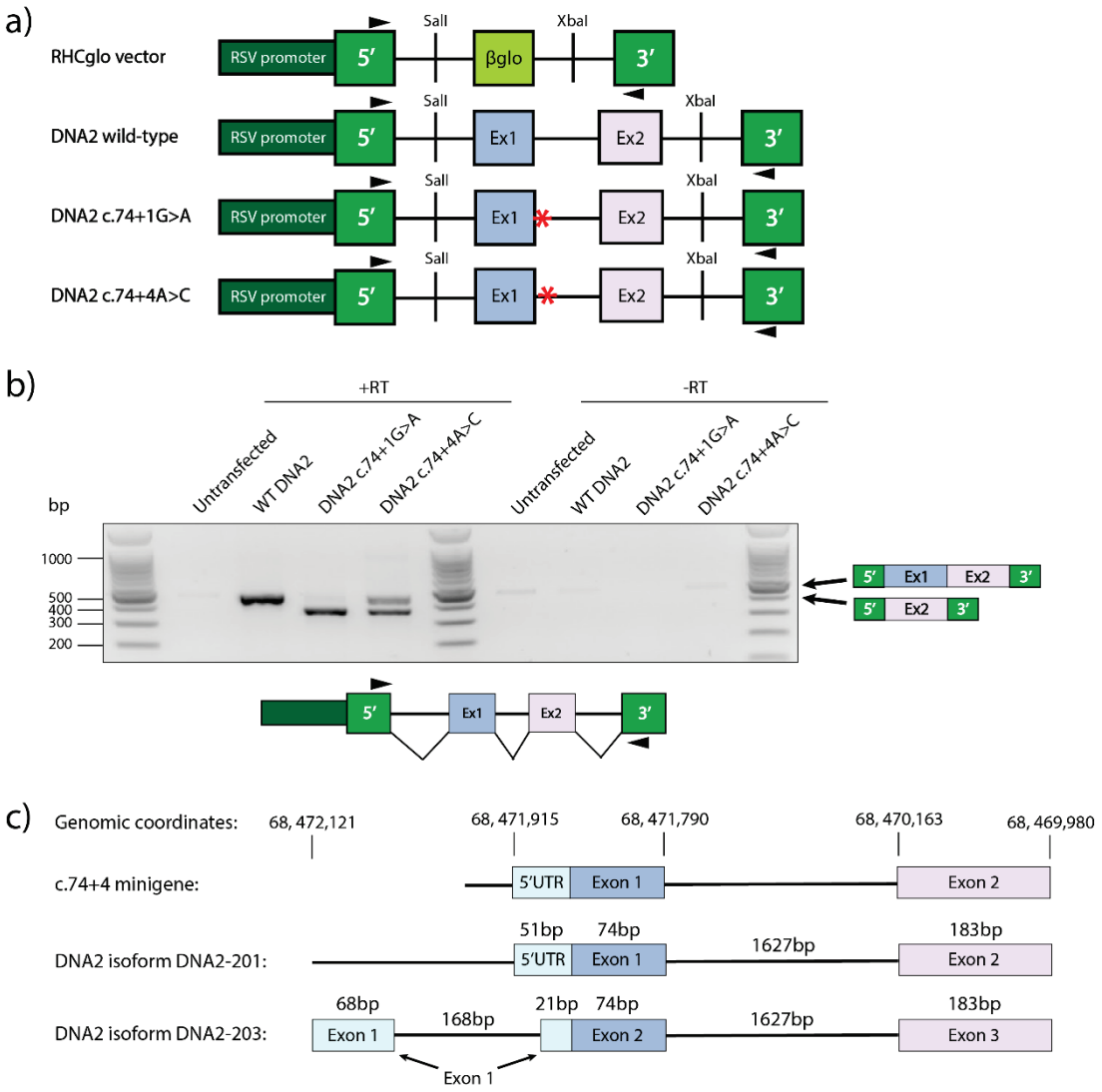

Figure 3.8. *DNA2* c.74+4A>C variant disrupts correct splicing of *DNA2* transcript.
a) A cartoon model of RHCglo-based constructs used in the minigene assay to assess the effect of *DNA2* c.74+4A>C mutation in cells. Minigene plasmids were generated by PCR amplification of the *DNA2* 5' UTR, exon 1, intron 1 and exon 2 (based on the full-length isoform DNA2-201 (Ensembl genome browser)) from control DNA and patient DNA, and subsequent cloning into the RHCglo minigene plasmid. A positive control for splicing was generated by introducing a point mutation (c.74+1G>A) into the splice donor site of intron 1. Black arrowheads indicate the locations of primers used for PCR analysis.
b) *DNA2* c.74+4A>C variant affects splicing of *DNA2* transcript. PCR products amplified from the HeLa cDNA of the minigene assay samples using RSV5U and RTRHC primers (indicated by black arrowheads) were run on an agarose gel and subsequently cloned for sequencing. Samples where no reverse transcriptase was added during cDNA generation are labelled as '-RT'. Sanger sequencing analysis of the products revealed that the PCR product with higher electrophoretic mobility represents the mutant isoform lacking exon 1 and the lower mobility product the correctly spliced transcript.
c) Aside from affecting the canonical splicing isoform DNA2-201, the c.74+4A>C mutation may also disrupt splicing of the isoform DNA2-203, leading to the exclusion of its exon 2. This can be experimentally tested in the future by cloning longer 5' sequences upstream of *DNA2* into the RHCglo vector. Genomic coordinates (GRCh38/hg38 assembly, UCSC Genome Browser) are indicated in the figure.

A possible alternative approach to pinpoint the extent of c.74+4A>C pathogenicity could be the cloning of longer DNA sequences upstream of the 5' UTR (untranslated region) of *DNA2* into the RHCglo reporter, together with exon 1, intron 1 and exon 2. In the experiment described above, the cloned DNA fragment included all 51 bp of 5' UTR and additional 84 bp upstream of it, as indicated by Ensembl genome browser for the full-length DNA2 splicing isoform DNA2-201 (1060 amino acids). However, a shorter protein-coding splicing isoform DNA2-203 (687 amino acids), which lacks the canonical C-terminus (exons 15-21), contains a different first exon than DNA2-201 (***Figure 3.8*c**). It is therefore possible that the c.74+4A>C mutation is additionally deleterious to the shorter DNA2 splicing isoform by reducing the presence of exon 2 (canonical exon 1) in this transcript. At the same time, the presence of the c.74+4A>C mutation may lead to the increased usage of the alternative start site and exon 1 in the full-length DNA2 splicing isoform DNA2-201 as well, to replace the spliced-out canonical exon 1 (***Figure 3.8*b**).

3.4. *DNA2* patient mutation c.1963A>G (p.T655A) is predicted to affect ATP/ADP binding

The only exonic *DNA2* patient mutation we identified, c.1963A>G, affects threonine 655 of DNA2 and changes it to an alanine. The affected amino acid represents the last residue of an evolutionarily highly conserved ATP-binding motif within the helicase/translocase domain (***Figure 3.6***). Two recent studies demonstrated that both yeast (*S. cerevisiae*) and human DNA2 function together with a cognate RecQ family helicase and use their ATP hydrolysis-dependent motor activity to translocate in a 5'-3' direction on the unwound 5'-terminated DNA strand, which is rapidly digested by the nuclease activity (Levikova *et al.*, 2017; Miller *et al.*, 2017) (***Figure 1.14***). Moreover, both studies showed that the ATP motif mutant of DNA2 (K1080E in scDNA2 or K654E in hDNA2) displays reduced resection speed at DSBs *in vitro*, leading to slower DNA degradation and shorter digestion products.

ATP-binding pockets of nucleotide-binding enzymes interact with the substrate ATP and hydrolyse it to the products ADP and a phosphate. The mutation K1080E in scDNA2 (and later its equivalent K654E in hDNA2) was chosen to study helicase activity due to the position of this lysine within the major nucleotide-binding loop of DNA2 (Gly-Lys-Thr, GKT) and its invariability within the so-called consensus *Kinase-1a* NTP-binding motif of various enzymes, where the lysine is essential for binding the phosphates of the ligand (Budd *et al.*, 1995; Traut, 1994). The DNA2 K654E mutant was demonstrated to have no ATPase activity *in vitro* (Budd *et al.*, 1995; Masuda-Sasa *et al.*, 2006). It is therefore plausible that the substitution of T655, directly adjacent to K654, will affect the binding or hydrolysis of ATP as well, thus reducing the rate of translocation of DNA2 along DNA and diminishing efficient DNA2 nuclease-dependent degradation of long stretches of ssDNA. This could occur either due to structural domain changes caused by mutations in the ATP motif or more direct impact on ATP binding and processing.

To test the hypothesis that the mutation p.T655A is deleterious to either protein domain structure or ATP/ADP binding *in silico*, the mutation was modelled based on the crystal structure of mouse DNA2 bound to ADP moiety published by Zhou, Pourmal and Pavletich (2015) (Protein Data Bank (PDB) accession number 5EAW; modelling performed by Joseph Marsh, IGMM) (***Figure 3.9a***). Due to extensive evolutionary conservation of the amino acid sequence of the ATP motif (***Figure 3.6***), the crystal structure of mouse DNA2 provides a good estimation of the effect the mutation has on DNA2 structure. Modelling the effects of the

p.T655A mutation on protein stability using the program FoldX (Guerois *et al.*, 2002) showed that it does not alter any important residue-residue interactions and therefore would result in almost negligible changes on the overall structure of the protein (ΔΔG = -0.24 kcal/mol). Importantly, the affected residue makes extensive contacts with the ADP molecule, burying 25.1 $Å^2$ of solvent-accessible surface area, suggesting that modulation of this interaction could explain pathogenicity of the mutation. The effect of the p.T655A mutation on ADP binding was thus modelled using the program mCSM-lig (Pires *et al.*, 2016). Surprisingly, this approach predicted that the mutation would in fact strengthen the interaction (ΔΔG = -0.81 kcal/mol). This observation was also visualised in PyMOL Molecular Graphics System (Schrödinger, Inc.), demonstrating how the substitution of T655 to A655 reduces the distance between the residue and ADP (***Figure 3.9*b**). The interaction with ATP itself could not be modelled with much confidence, as it is likely that ATP hydrolysis induces conformational changes.

The *in silico* data obtained support the possibility that human DNA2-T655A mutation affects ADP binding by increasing the affinity of DNA2 to this moiety and likely the time the mutant isoform spends in a nucleotide-bound conformation. The slower release of the hydrolysis products ADP and a phosphate will have an impact on the subsequent ATP binding and processing event, thus disrupting normal ATP hydrolysis rate and resulting in reduced processivity of DNA2 motor, as well as reduced speed at which DNA2 nuclease can cleave DNA. Further work to test the consequences of p.T655A on the enzymatic activities of DNA2 *in vitro* would be necessary to strengthen the obtained data. Testing this model in patient-derived or engineered cell lines with the p.T655A mutation would also be beneficial in providing further evidence for the deleterious nature of this missense mutation.

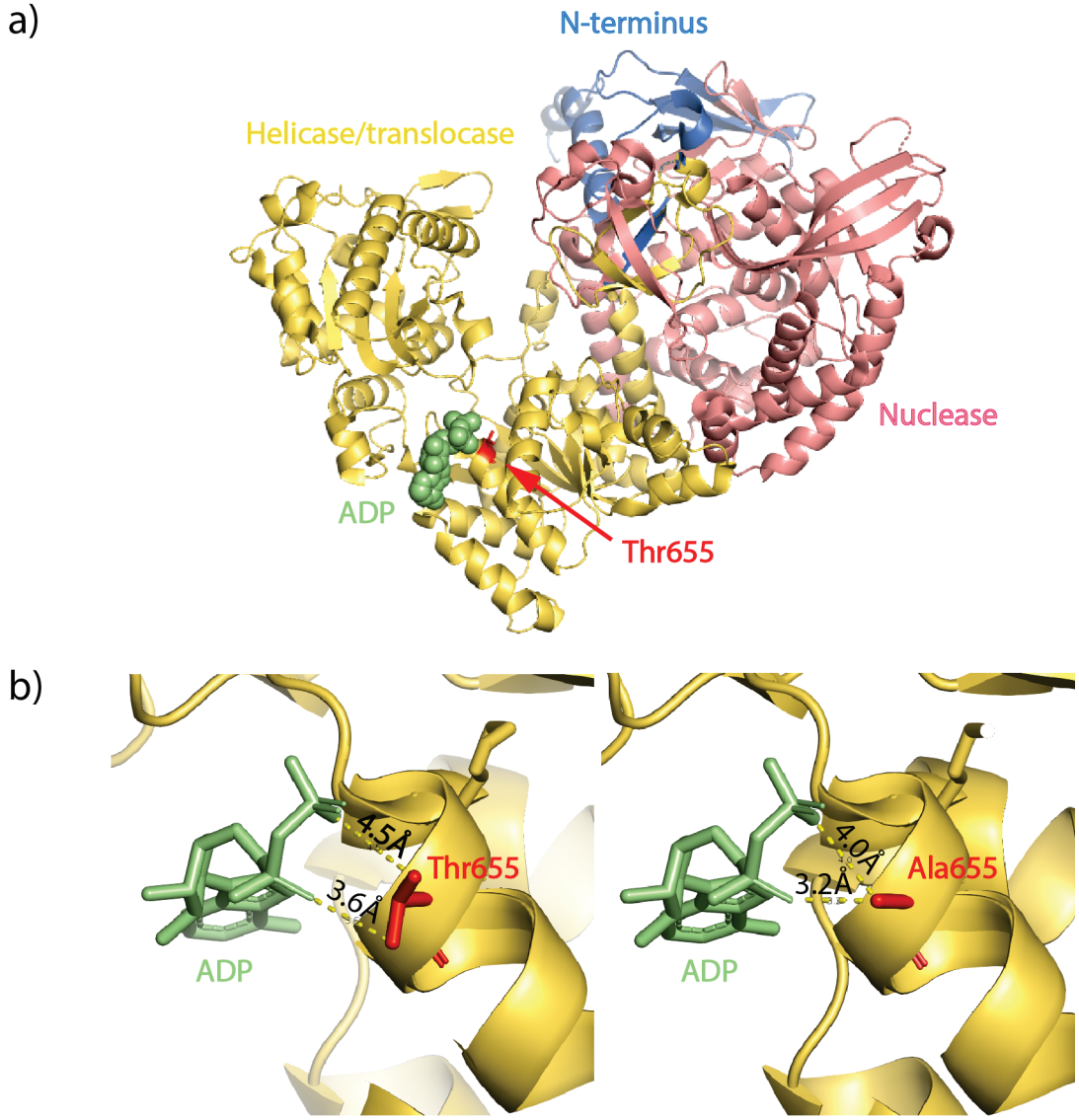

Figure 3.9. *In silico* modelling predicts that DNA2 p.T655A affects ATP/ADP binding.
The DNA2 mutation p.T655A was modelled based on the published crystal structure of mouse DNA2 bound to ADP moiety (Zhou, Pourmal and Pavletich, 2015) (PDB ID 5EAW) in PyMOL Molecular Graphics System (Schrödinger, Inc.).
a) DNA2 protein domains (N-terminal domain, nuclease and helicase/translocase) are represented in different colours. ADP moiety is shown in light green spheres; threonine 655 (Thr655) residue is shown in red.
b) Thr655, mutated in MPD, makes extensive contacts (represented by dashes) with the ADP moiety (left), and its substitution to Ala655 further reduces the distance between the residue and ADP (right), as indicated by modelling in PyMOL Molecular Graphics System (Schrödinger, Inc.).

3.5. Using CRISPR/Cas9 genome editing to generate cell lines with *DNA2* patient mutations

The recent emergence of CRISPR/Cas9-mediated genome editing has greatly facilitated the study of cellular phenotypes caused by disruption of any particular gene. This genome editing technology was developed independently by several research groups in 2012–2013 (Cong *et al.*, 2013; Jinek *et al.*, 2012; Mali *et al.*, 2013). It relies on bacterial Clustered Regularly Interspaced Short Palindromic Repeats (CRISPR) and CRISPR-associated (Cas) genes, which jointly act as an adaptive immune system enabling bacterial cells to protect themselves against foreign genetic material (Barrangou *et al.*, 2007). In the most widely studied Type II CRISPR system, foreign DNA is fragmented and inserted into a CRISPR locus, flanked by 20 bp-long repeats. The subsequent transcription of these loci generates small non-coding RNAs called CRISPR RNAs (crRNAs), which achieve their maturation through interactions with trans-activating crRNAs (tracrRNAs) and can bind Cas9, guiding this endonuclease to the complementary target sequences (Jinek *et al.*, 2012). Cas9 cleavage generates a DSB at sites complementary to the 20 nt target sequence within crRNA (Jinek *et al.*, 2012; Nishimasu *et al.*, 2014), but only when a short 3 nt site (NGG or NAG), called the protospacer-associated motif (PAM), is present 3' of the crRNA-complementary sequence, as it was shown to be essential for Cas9 endonucleolytic activity (Sternberg *et al.*, 2014).

In 2012, the Doudna and Charpentier laboratories were the first ones to demonstrate the potential of adapting the Type II CRISPR/Cas9 system for genome editing (Jinek *et al.*, 2012). A synthetic single guide RNA (sgRNA) was generated to combine functions of both tracrRNA and crRNA, and was shown to be equally efficient at directing Cas9 to the target loci (Jinek *et al.*, 2012). Wild-type Cas9 nuclease generates DSBs, which are most commonly repaired by NHEJ and can lead to insertions or deletions (indels) that disrupt the target locus. In the presence of a donor template, homology-directed repair (HDR) mechanism can be used to generate precise genetic modifications, including nucleotide substitutions (Ran, Hsu, Lin *et al.*, 2013). A Cas9 mutant Cas9-D10A, developed by Cong *et al.* (2013), cleaves only one DNA strand, with this nickase activity facilitating HDR when a donor template is present (Bothmer *et al.*, 2017). Using two paired offset guide RNAs (gRNAs) with Cas9 nickase (Cas9n) to introduce DNA nicks on opposing strands surrounding the target locus also provides increased target specificity, reducing the rate of off-target effects (Ran, Hsu, Lin *et al.*, 2013). More recently, it was shown that in the presence of synthetic single-stranded

oligodeoxyribonucleotides (ssODNs), Cas9-induced single-stranded template repair (SSTR) requires the FA pathway, implicated in ICL repair (Richardson *et al.*, 2018).

Given the lack of the availability of *DNA2* patient-derived cells and no prospect of obtaining them, I decided to use CRISPR/Cas9-based genome editing to engineer cell lines with *DNA2* patient mutations. Studying the effects of the identified mutations in other species (e.g. developing a mouse model) was not applicable in this situation due to the intronic nature of the homozygous patient mutations, combined with the lack of sequence conservation at these sites between species. Meanwhile, isogenic human cell lines carrying *DNA2* patient mutations would allow me to assess changes in DNA2 protein levels caused by those mutations and provide a useful tool for studying the effects of patient mutations on cellular functions of DNA2. Moreover, an isogenic cell system with *DNA2* mutations would make it easier to attribute any observed cellular effects to the introduced mutations in the *DNA2* gene and not to other background genetic differences that are present in primary patient fibroblasts. In the initial CRISPR/Cas9 experiment, I attempted to engineer the *DNA2* point mutations c.74+4A>C (affecting the splice donor of intron 1) and c.1963A>G (resulting in a missense mutation in exon 13) into a human cell line.

The human osteosarcoma U2OS cell line was chosen for CRISPR/Cas9-mediated targeting due to its good characterisation and suitability for a broad panel of DNA repair assays. To introduce specific point mutations in *DNA2*, I used the Cas9n to generate two ssDNA breaks based on co-expression of two gRNA target sequences and a repair template carrying the desired point mutations. The designed pairs of offset gRNAs complementary to opposite strands of the target site for each of the two mutations are shown in ***Figure 3.10*****a**. Two suitable gRNAs with 3 bp offset were identified for the c.74+4A>C mutation; however, the only suitable pair of gRNAs to introduce the c.1963A>G mutation had a small overlap of 4 bp. This is not an ideal setup for Cas9n-mediated targeting, given that such overlaps may cause steric hindrance between two adjacent Cas9–gRNA complexes and thus affect cooperative nicking (Ran, Hsu, Lin *et al.*, 2013). However, due to constraints introduced by the locus specification, this gRNA pair was the highest-scoring one based on CRISPR Design Tool created by Feng Zhang laboratory (http://crispr.mit.edu/). For each of the targets, a 200 nt-long antisense ssODN with the desired mutation in the middle of the sequence was designed to serve as a repair template. Introduction of a repair template with a silent mutation within the PAM site is known to help prevent further Cas9-mediated activity at the target site after correct editing. However, given that three out of four PAM sites are located in protein-coding regions or close to the exon-

intron junction, I could only introduce such a silent mutation at one of the four PAM sites (***Figure 3.10***a).

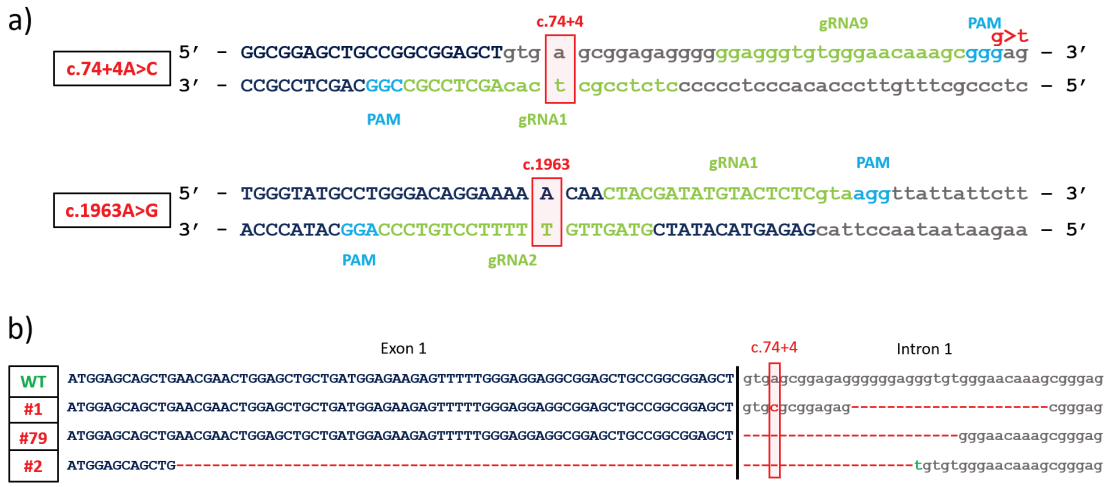

Figure 3.10. Using CRISPR/Cas9 genome editing to generate U2OS cell lines with *DNA2* patient mutations.

a) A representation of gRNA design to introduce *DNA2* mutations c.74+4A>C and c.1963A>G into a cell line. Coding (exonic) sequences are shown in uppercase; non-coding (intronic) are shown in lowercase. The 20 nt-long genomic sequences targeted by gRNAs are highlighted in green; 3 nt-long PAM sites are shown in blue. The target nucleotides c.74+4 and c.1963 are marked in red. The nucleotide changed to alter PAM site in the repair template (g>t) is shown in red.

b) The genotypes of U2OS clones targeted for *DNA2* c.74+4A>C. The genotypes of the clonal cell lines #1, #79 and #2 represent the outcomes observed after targeting *DNA2* c.74+4 locus in the U2OS cell line. The target nucleotide c.74+4 is marked in red; red dotted lines indicate deletions; green nucleotides indicate insertions.

After inserting guiding sequences into GFP-Cas9n-expressing plasmids, U2OS cells were co-transfected with the relevant plasmids and ssODNs. 85 GFP-FACS-sorted U2OS cells targeted for c.74+4A>C mutation and 123 cells targeted for c.1963A>G mutation survived and formed clones. All clones were screened for the presence of the expected mutations by amplifying ~200 bp-long genomic region surrounding the targeted locus and sending amplicons for Sanger sequencing. Out of 85 DNA2 c.74+4A>C U2OS CRISPR clones, DNA sequences of the screened locus remained unchanged in 65 clones, staying identical to the parental wild-type sequence of *DNA2*. The remaining 20 clones were targeted by the CRISPR/Cas9 system. The targeting outcomes observed could be classified into a few distinct categories: 1) monoallelic targeting introducing the mutation of interest (c.74+4A>C), as well as an additional intronic indel (e.g. clone #1); 2) monoallelic targeting introducing intronic

indels (e.g. clone #79); 3) monoallelic targeting introducing exonic/intronic indels (e.g. clone #2) (***Figure 3.10*b**). Therefore, even when the targeting of c.74+4A>C was successful and resulted in the desired substitution, it happened on one allele only, and other undesired genetic alterations were introduced at the same time.

Overall, this experiment suggests that targeting of the c.74+4A>C locus was inefficient, with only 24% of clones being targeted by CRISPR/Cas9 machinery on one allele. Whenever targeting took place, cells appear to have used either NHEJ pathway exclusively or both NHEJ and HDR pathways to repair the lesion instead of relying solely on the supplied repair template for 'clean' HDR repair. The clonal cell lines produced during this experiment could therefore not be used for studying the cellular consequences of the patient mutation c.74+4A>C. For example, if the cell line #1 was used for transcript splicing or protein level analysis, any effect observed could not be clearly attributed to the presence of the variant c.74+4A>C and could be argued to have been caused by the larger intronic deletion downstream. Nevertheless, some of these cell lines could potentially be hypomorphic with lower levels of DNA2 protein (e.g. clone #2) and be useful for broader studies of cellular roles of DNA2.

In the attempt to introduce *DNA2* c.1963A>G mutation, the Sanger sequencing analysis of only 2 out of 123 analysed clones demonstrated any targeting. Instead of containing the c.1963A>G substitution, both mutant clones had monoalellic indels at the target locus in exon 13. The mutations in these clones are predicted to lead to premature stop codons and subsequent degradation of the mutant transcript though nonsense-mediated decay (NMD), a eukaryotic surveillance pathway to eliminate erroneous mRNA transcripts (Hug *et al.*, 2016). Therefore, these cell lines are not suitable for the analysis of the consequences of a precise nucleotide substitution.

I made further attempts to use CRISPR/Cas9 genome editing to introduce the *DNA2* c.74+4A>C mutation. Multiple permutations of the protocol were performed, such as using the wild-type Cas9 nuclease to improve cutting efficiency and testing two additional gRNAs (gRNA2 and gRNA3) (***Figure 3.11*a**). The U2OS cell line I used for targeting is known to be hypertriploid, which may have contributed to the experienced difficulties targeting all alleles. To rule out the cell line-specific challenges in successful *DNA2* targeting, human hTERT-immortalised retinal pigmented epithelium cell line, RPE1, and colorectal carcinoma cell line HCT116, both near-diploid, were selected for further experiments. Lastly, a plasmid generated using Gibson Assembly Cloning Kit (NEB) with c.74+4A>C substitution was used as an alternative repair template, and a more efficient transfection system, Neon® (Invitrogen), was adopted, allowing

to achieve higher levels of transfected GFP-positive cells upon GFP-FACS single cell sorting. All the variations of the CRISPR protocol and their outcomes are summarised in ***Figure 3.11*b**.

a)

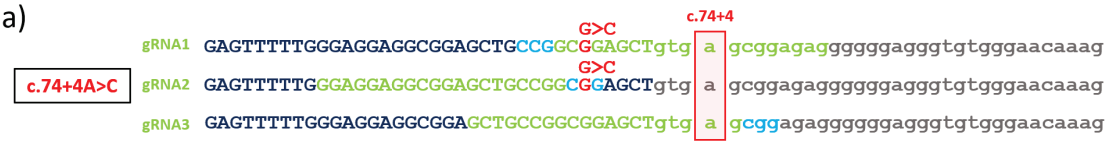

b)

Mutation	sgRNA(s)	Cas9	Repair template	Cell line	Transfection method	Number of clones analysed	Number of clones with indels
c.74+4A>C	gRNA1+gRNA9	Cas9n(D10A)	ssODN (200nt)	U2OS	Lipofectamine 2000	85	20
	gRNA1	Cas9wt	ssODN (110nt)	RPE1	Lipofectamine 2000	71	0
	gRNA2	Cas9wt	ssODN (114nt)	RPE1	Lipofectamine 2000	46	3
	gRNA3	Cas9wt	ssODN (110nt)	RPE1	Lipofectamine 2000	47	0
	gRNA1	Cas9wt	Plasmid with c.74+4A>C	HCT116	Neon	10	1
	gRNA2	Cas9wt	Plasmid with c.74+4A>C	HCT116	Neon	17	0
	gRNA3	Cas9wt	Plasmid with c.74+4A>C	HCT116	Neon	2	0
c.1963A>G	gRNA1+gRNA2	Cas9n(D10A)	ssODN (200nt)	U2OS	Lipofectamine 2000	123	2

Figure 3.11. Summary of variations of the CRISPR protocol used for editing and their observed outcomes.
a) Design of additional gRNAs for *DNA2* c.74+4A>C targeting. Two additional gRNAs (gRNA2 and gRNA3) were designed using CRISPR Design Tool (F. Zhang laboratory) and CRISPR gRNA Design Tool DNA2.0 (now ATUM). All three gRNAs shown were cloned into a plasmid encoding WT Cas9 nuclease (pX458). The 20 nt-long genomic sequences targeted by gRNAs are highlighted in green; 3 nt-long PAM sites are shown in blue. The target nucleotide c.74+4 is marked in red. The nucleotides changed in the repair templates to alter PAM sites or introduce synonymous substitutions in other loci (G>C) are shown in red. Coding (exonic) sequences are shown in uppercase; non-coding (intronic) are shown in lowercase.
b) Table summarising variations of the CRISPR/Cas9 genome editing protocol at two *DNA2* loci and their outcomes.

Furthermore, I designed a screening method to facilitate the initial screening for the desired point mutation c.74+4A>C without the need to Sanger-sequence all the clones. The c.74+4A>C mutation introduces a *Hha*I restriction enzyme site (GCGC), which is not present in exon 1 of *DNA2* (***Figure 3.12*a**). The screening method involved crude genomic DNA isolation from clones, PCR amplification of the locus of interest, subsequent restriction digestion with *Hha*I restriction nuclease, and analysis of products on an agarose gel. However, none of the multiple targeting perturbations (***Figure 3.11*b**) gave the expected results, only very occasionally resulting in any targeting events at all (***Figure 3.12*b**).

Despite the extensive efforts to generate a cell line harbouring the c.74+4A>C mutation in *DNA2*, the targeting was not successful. Targeting of a specific locus for HDR puts restrictions on available gRNAs, making it more difficult to optimise the targeting strategy. Due to variability of targeting efficiency between different genomic loci, disrupting a gene is much

easier than introducing a specific mutation, since one can select the most optimal gRNA for the experiment. Taking all the alterations to the protocol together (***Figure 3.11*b**), the most efficient cutting was achieved using Cas9 nickase and a combination of gRNA1 and gRNA9 in the U2OS cell line. However, in the event of cutting by Cas9n, the targeting exclusively resulted in indels disrupting one allele of *DNA2*. It is also plausible that successfully introduced biallelic c.74+4A>C mutation would have caused reduced cell fitness, thus decreasing the probability of recovering a clone with this mutation. Overall, no cell lines with c.74+4A>C or c.1963A>G mutations were generated using CRISPR/Cas9-mediated targeting. It was therefore not possible to address the consequences of these patient mutations on DNA2 protein levels using CRISPR/Cas9 genome editing.

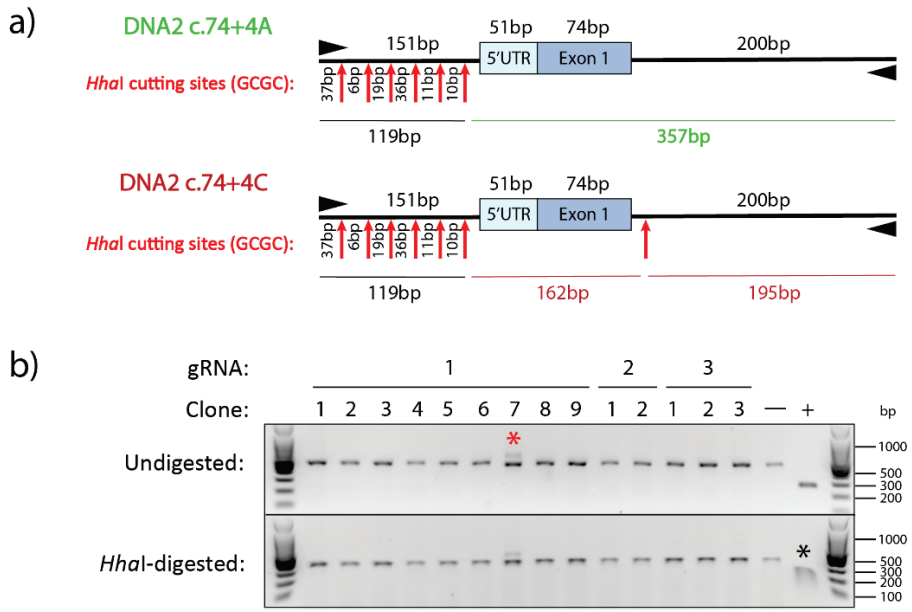

Figure 3.12. The *Hha*I restriction digestion-based screening for correctly targeted *DNA2* c.74+4A>C clones.

a) The design of a screening method for the desired point mutation c.74+4A>C without the need to Sanger-sequence the clones. Black arrowheads indicate the locations of primers used for PCR amplification of a 476 bp product, including 5' upstream DNA sequences of *DNA2*, 5' UTR, exon 1 and a part of intron 1 of *DNA2*. Six *Hha*I cutting sites in the 5' region upstream of *DNA2* would produce very short digestion products in the presence of *Hha*I, likely too small to visualise on an agarose gel, leaving only the 357 bp product large enough to be detected. In the presence of c.74+4A>C substitution, a new *Hha*I cutting site would be created, leading to the generation of two shorter digestion products instead (162 bp and 195 bp).

b) Undigested and *Hha*I-digested PCR amplicons of c.74+4A>C locus were run in parallel for accurate identification of clones containing the desired c.74+4A>C mutation. In this gel, negative control (—) indicates the wild-type exon 1-intron 1 PCR product, amplified from the RPE1 parental cell line. A fragment of exon 18 containing *Hha*I restriction site (GCGC) was used as a positive control (+). Red star indicates a targeting event (insertion); black star indicates restriction digestion products of the positive control, 154 bp and 101 bp.

3.6. Summary and discussion: *DNA2* mutations in human disease

DNA2 is an ATP-dependent helicase/nuclease, extensively studied due to its important roles in DNA end resection and Okazaki fragment maturation, as well as telomere and mtDNA maintenance (see Section 1.4 for details). In this chapter, the identification of four MPD-affected individuals with biallelic *DNA2* mutations was described, as well as various experiments to address the consequences of the identified variants for DNA2 transcript splicing and enzymatic activities.

The results described in this chapter, combined with previous reports by Shaheen *et al.* (2014), Ronchi *et al.* (2013), Chae *et al.* (2015) and Phowthongkum and Sun (2017), link mutations in *DNA2* with two distinct clinical phenotypes: muscle disorders associated with mitochondrial genome instability and MPD showing severe reduction in growth. The first link between *DNA2* and human disease was established in 2013, when monoallelic missense mutations in DNA2 (R198H, K227E and V637I) were demonstrated to cause adult-onset autosomal dominant progressive external ophthalmoplegia with mitochondrial DNA deletions type 6 (PEOA6) (Ronchi *et al.*, 2013) (***Figure 3.1***). Moreover, a nonsense mutation in DNA2 (Q630*) was reported in a single case of metabolic myopathy (Chae *et al.*, 2015), and a recent case study reported on a 17 month-old girl with congenital-onset myopathy and ptosis, who had a novel monoallelic DNA2 frameshift mutation (N568Ifs*4) (Phowthongkum and Sun, 2017) (***Figure 3.1***). Phowthongkum and Sun (2017) postulated that DNA2 protein haploinsufficiency due to truncating mutations may be causing the observed mitochondrial genome instability and clinical symptoms of early-onset myopathy. Comparison of the mutations identified in individuals with *DNA2*-associated mitochondrial disease and growth restriction point towards zygosity underlying the observed phenotypic differences, as all studied individuals with muscle deficiency were heterozygous for coding mutations in *DNA2*. Ronchi *et al.* (2013) tested the effect of the three mutations they identified on enzymatic DNA2 activities *in vitro*, revealing diminished nuclease activity and dysregulated helicase activity. Thus, the disrupted allele in PEOA6 patients alters DNA2 enzymatic activities, but its detrimental effect is likely ameliorated by the fully functional allele. It is not clear yet why mitochondrial functions of DNA2 are particularly susceptible to this partial loss of function. DNA2 was shown to play a critical role in mitochondrial long-patch base-excision repair (LP-BER), a pathway employed by cells to repair DNA damage caused by oxidative stress, alkylating agents and spontaneous hydrolysis (Robertson *et al.*, 2009; Zheng *et al.*, 2008). Ronchi *et al.*

(2013) proposed that disruption of this role of DNA2 may underlie the observed clinical phenotype due to a significant threat of oxidative DNA damage encountered by mitochondria.

In contrast, the six individuals with biallelic mutations in *DNA2,* identified by our laboratory and Shaheen *et al.* (2014), exhibit distinct clinical characteristics, indicative of Seckel syndrome or MPD. Surprisingly, not even a mild mitochondrial phenotype was observed in any of the MPD patients, even though a few previously identified mitochondrial disease-causing *DNA2* mutations affect the helicase domain, where the majority of MPD-associated mutations are found.

In my study, the lack of patient-derived cells and failure to generate CRISPR/Cas9 engineered cell lines with patient mutations in *DNA2* hampered the analysis of the impact of the biallelic non-coding variants. My unsuccessful attempts to generate a suitable CRISPR/Cas9 cell line for this study emphasise the continued importance of patient-derived cell lines for functional analyses. The minigene-based splicing assay proved an important tool, allowing me to determine the effects of these mutations on transcript splicing. The non-coding variants found in MPD patients, c.74+4A>C and int11ins53bp, were demonstrated using this assay to result in the disruption of normal *DNA2* transcript splicing. It is clear from this assay that in both cases the normal transcript splicing is not abolished completely, and that a fraction of normally spliced DNA2 is retained (***Figure 3.7*** and ***Figure 3.8***). Collectively, my data and the findings by Shaheen *et al.* (2014) strongly suggest that the MPD-associated non-coding *DNA2* mutations result in reduced levels of canonical *DNA2* transcript, ultimately leading to a global reduction in DNA2 protein levels and all enzymatic functions. Moreover, *in silico* modelling showed that the missense mutation within the highly conserved ATP-binding motif of DNA2, c.1963A>G (p.T655A), is likely to increase the affinity of DNA2 to the ATP hydrolysis product ADP (***Figure 3.9***). Speculatively, this substitution might result in altered dynamics and processivity of DNA2 motor activity, impacting on efficient processive cleavage by the nuclease. Nevertheless, p.T655A is unlikely to completely disrupt translocation along DNA, strongly supporting the unifying hypomorphic nature of all biallelic mutations identified.

It was previously reported that homozygous DNA2 knockout is embryonic lethal in mice, indicating the importance of DNA2 during mammalian embryonic development (Lin *et al.*, 2013). It is therefore not surprising that both DNA2-associated syndromes result from variable degree insufficiency of its enzymatic activities. It appears that while DNA2 haploinsufficiency results in myopathy phenotype, severe DNA2 deficiency arising from biallelic mutations impairs nuclear genome replication and DNA repair, causing MPD. In

summary, both non-coding and coding *DNA2* mutations identified in MPD patients are likely to cause disease via reduction of both nuclease and motor activities of DNA2. The non-coding mutations are predicted to equally diminish both enzymatic activities via reduced DNA2 protein levels, whereas the coding mutation p.T655A may affect the motor activity directly and the nuclease activity indirectly, likely through a reduction in processivity. The data obtained in this chapter further supports the necessity of adequate DNA2 protein levels during embryonic development, where cell cycle is short and tightly regulated, and the disruption of timely DNA processing may eventually lead to generation of fewer cells and a smaller individual.

Chapter 4

Regulation of the PP4 complex by TRAIP-dependent ubiquitination

4. Regulation of the PP4 complex by TRAIP-dependent ubiquitination

TRAIP was previously reported to undergo auto-ubiquitination *in vitro*, mediated by the E3 ubiquitin ligase activity within its RING finger domain (Besse *et al.*, 2007). Moreover, TRAIP was shown to promote lysine 48 (K48)-linked ubiquitination and proteasomal degradation of TANK-binding kinase 1 (TBK1), leading to negative regulation of type I interferon β (IFN-β) production and the cellular antiviral response in HEK293 cells (Zhang *et al.*, 2012). Recently, the Andrew Jackson laboratory reported that TRAIP facilitates efficient DDR signalling in response to UV-C irradiation in immortalised fibroblast and HeLa cells (Harley *et al.*, 2016). In close succession, several other studies linking TRAIP to the cellular response to DNA damage were published (Hoffmann *et al.*, 2016; Soo Lee *et al.*, 2016; W. Feng *et al.*, 2016). However, it remains unknown what protein substrate(s) TRAIP ubiquitinates to promote DDR at DNA lesions, and establishing their identity is critical for advancing the knowledge of the DDR-related functions of TRAIP.

Two recent studies proposed that the E3 ligase activity of TRAIP may be required for ubiquitinating PCNA at stalled replication forks (Hoffmann *et al.*, 2016; W. Feng *et al.*, 2016). *In vitro* immunoprecipitation experiments and structural data obtained by Hoffmann *et al.* (2016) demonstrated that TRAIP binds PCNA through its C-terminal PIP-box motif. MS analysis and pulldown experiments performed by W. Feng *et al.* (2016) confirmed TRAIP-PCNA interaction. As upon HU-induced replication fork stalling PCNA is rapidly lost from chromatin in both yeast and human cells (Sirbu *et al.*, 2011; Yu *et al.*, 2014; Dungrawala *et al.*, 2015; Hoffmann *et al.*, 2016; W. Feng *et al.*, 2016), both Hoffmann *et al.* (2016) and W. Feng *et al.* (2016) suggested that TRAIP-mediated PCNA ubiquitination could promote its unloading from chromatin upon replication stress. However, neither study provided *in vitro* or *in vivo* evidence supporting this hypothesis. Using the PIP-box mutant of TRAIP, Hoffmann *et al.* (2016) showed that TRAIP interaction with PCNA is less important than its E3 ligase activity in facilitating CPT- and HU-induced RPA2 phosphorylation, as well as promoting cell survival in response to MMC treatment. Additionally, W. Feng *et al.* (2016) demonstrated by immunoblotting that TRAIP depletion in U2OS cells did not significantly affect the level of ubiquitinated PCNA in response to HU- and UV- induced replicative stress. Moreover, this study showed that transient proteasome inhibition did not exacerbate replication stress-induced fork defects (W. Feng *et*

al., 2016), leading to the conclusion that TRAIP may promote PCNA unloading by non-catalytic means.

Another DNA replication and repair factor, the TLS polymerase eta (Pol ŋ), was also suggested as a putative protein substrate of the TRAIP E3 ligase (Wallace *et al.*, 2014). Human TRAIP and its *D. melanogaster* orthologue, Nopo, were shown to co-immunoprecipitate with Pol ŋ, and the overexpression of TRAIP in HeLa cells enhanced Pol ŋ ubiquitination in a cellular ubiquitination assay (Wallace *et al.*, 2014). The authors of the study proposed that TRAIP-dependent ubiquitination of Pol ŋ promotes its recruitment to nuclear foci in human cells, facilitating DNA damage tolerance. However, it is not clear whether these observations are functionally relevant due to several reasons. Firstly, the data supporting TRAIP-mediated ubiquitination of Pol ŋ were obtained from examining the gain-of-function situation, which may not be representative of the ubiquitination events *in vivo*. Moreover, the experiments were conducted in the absence of exogenous DNA damage. The clinical phenotypes of xeroderma pigmentosum variant (XP-V) (Lehmann *et al.*, 2011), caused by mutations in Pol ŋ (Johnson *et al.*, 1999; Masutani *et al.*, 1999), and TRAIP patients are also different, with XP-V not reported to cause growth failure or microcephaly. Hoffmann *et al.* (2016) also investigated Pol ŋ as a potential DDR-related substrate of TRAIP and concluded that Pol ŋ ubiquitination is unlikely to explain the role of TRAIP in maintaining genome stability after replication stress. TRAIP knockdown in U2OS cells did not decrease the formation of DNA damage-induced Pol ŋ foci and Pol ŋ poly-ubiquitination levels (Hoffmann *et al.*, 2016). Additionally, the RING and PIP domain mutants of TRAIP were as efficient at Pol ŋ poly-ubiquitination in U2OS cells as wild-type TRAIP (Hoffmann *et al.*, 2016). Lastly, the authors showed that overexpression of Pol ŋ did not rescue MMC sensitivity, observed in TRAIP-depleted U2OS cells. Therefore, more work is required to identify DDR-relevant substrates of TRAIP and to understand the role of TRAIP in responding to replication stress.

In this chapter, the experimental work investigating another potential substrate of TRAIP, the protein phosphatase 4 (PP4) complex, is described. I postulated that after UV-C irradiation PP4 may be negatively regulated by TRAIP-dependent ubiquitination of its subunits and performed *in vitro* experiments to address this hypothesis. Finally, the relevance of these findings for the role of TRAIP in DDR is discussed.

4.1. Protein phosphatase 4 (PP4) complex: a potential substrate of TRAIP

Although our laboratory demonstrated that TRAIP is required for RPA2 and H2AX phosphorylation following UV-C-induced DNA damage (Harley *et al.*, 2016), the molecular mechanisms underlying this regulation remained unknown. One of the possible explanations is TRAIP-mediated positive regulation of a DDR protein kinase of PIKK family, such as ATR, ATM or DNA-PK, which are known to phosphorylate RPA2 (S. Liu *et al.*, 2012) and H2AX (reviewed by Podhorecka, Skladanowski and Bozko (2010)) in response to replication stress. Alternatively, TRAIP-mediated inhibition of PP2A or PP4 protein phosphatase complexes that dephosphorylate pRPA2-S4/S8 and γH2AX (Chowdhury *et al.*, 2008, 2005; J. Feng *et al.*, 2009; Lee *et al.*, 2010; Nakada *et al.*, 2008) could take place in response to UV-C-induced DNA damage.

To identify potential ubiquitination targets and binding partners of TRAIP, MS analysis of proteins co-immunoprecipitated with GFP-TRAIP was performed in the Andrew Jackson laboratory. Regulatory subunits of the protein phosphatase 4 (PP4) complex, PP4R3α (SMEK1) and PP4R3β (SMEK2), emerged as the most enriched proteins identified in this screen, with 1,000-fold enrichment in the GFP-TRAIP sample, relative to the control GFP sample (M. Harley, unpublished) (***Figure 4.1*****a**). These interactions were confirmed by reciprocal immunoprecipitations of endogenous PP4R3α and PP4R3β by GFP-tagged TRAIP and endogenous TRAIP by HA-tagged PP4R3α and PP4R3β (M. Harley, unpublished) (***Figure 4.1*****b-c**).

Protein phosphatase 4 (PP4) is a ubiquitous serine/threonine phosphatase known to play multiple distinct roles in different cellular processes, including DDR (J. Liu *et al.*, 2012), cell cycle regulation (Zhuang *et al.*, 2014), embryo development (Helps *et al.*, 1998), tumor necrosis factor α (TNF-α) signalling pathway (Mihindukulasuriya *et al.*, 2004; Zhou *et al.*, 2002) and glucose metabolism (Yoon *et al.*, 2010). A combined tandem affinity purification (TAP) tagging and MS approach was previously used to delineate distinct multi-molecular complexes containing the catalytic subunit of PP4 phosphatase, PP4C, in mammalian cells (Gingras *et al.*, 2005). Overall, the data suggested that PP4C forms four distinct complexes: a complex containing regulatory subunits PP4R2 and PP4R3β, a complex containing regulatory subunits PP4R2 and PP4R3α, a binary complex with a regulatory subunit PP4R1, and a complex involving α4 and the chaperone TriC/CCT. These data were later confirmed by Chowdhury *et al.* (2008); however, no interaction between PP4C and α4 was observed. Although human PP4R3β and

PP4R3α share 67% sequence identity and 77% homology at the amino acid level (Gingras *et al.*, 2005), only PP4R3β-containing PP4 complex was implicated in DNA repair. It was previously shown that deletion of the yeast orthologue of PP4R3β, Psy2, renders cells hypersensitive to the DNA crosslinking agent cisplatin (Wu *et al.*, 2004). Gingras *et al.* (2005) demonstrated that deletion of other components of this PP4 complex, PP4C-PP4R2-PP4R3β, also induced cisplatin hypersensitivity in yeast, giving this complex a new name PP4cs (protein phosphatase 4, cisplatin-sensitive) and suggesting its importance for DDR. Moreover, the knockdown of PP4cs components PP4C and PP4R3β was reported to induce replication-associated DNA damage, as well as to impair HR at DSBs in HeLa cells (Chowdhury *et al.*, 2008). Significantly, the PP4C-PP4R2-PP4R3β complex was demonstrated to be required for efficient dephosphorylation of γH2AX, both induced by exogenous and endogenous DNA damage in human cells (Chowdhury *et al.*, 2008; Nakada *et al.*, 2008). Additionally, the PP4C-PP4R2 heterodimer was shown to be involved in efficient dephosphorylation of pRPA2 both *in vitro* and in U2OS cells, as well as required for HR-mediated DSB repair (Lee *et al.*, 2010).

Ubiquitination is critical for the post-translational regulation of cellular protein functions, as well as cell signalling cascades (Udeshi *et al.*, 2013). The observations that the PP4R3β-containing ternary PP4 complex is implicated in DDR signalling and DNA repair led to my hypothesis that TRAIP might act as a negative regulator of PP4 complex activity by ubiquitination (***Figure 4.2***). According to this working model, TRAIP-deficient patient cells would show constitutively increased PP4 phosphatase activity, which would subsequently reduce cellular levels of phosphorylated H2AX and RPA2. However, protein levels of PP4C and the regulatory subunits PP4R3α and PP4R3β were not increased in TRAIP patient-derived cells, compared to wild-type control cells (M. Harley, unpublished). This suggested that rather than leading to a global proteasome-mediated reduction in PP4 protein levels, TRAIP-mediated ubiquitination of PP4 would more likely result in reduced activity or local degradation of PP4 complex (***Figure 4.2***). Only low levels of TRAIP-mediated ubiquitination of one of the regulatory PP4 subunits identified by MS, PP4R3α, were detected in the *in vitro* ubiquitination assays (J. Ding and O. Murina, unpublished). Instead, purified recombinant catalytic subunit PP4C was found to be strongly ubiquitinated by TRAIP (O. Murina, unpublished) (***Figure 4.3*****a**). These *in vitro* data were also supported by the cellular ubiquitination assays (M. Harley, unpublished) (***Figure 4.3*****b**). This suggests that while the regulatory subunit PP4R3β might mediate interaction between TRAIP and the PP4 complex, the substrate of TRAIP is more likely to be the catalytic subunit PP4C. In the following sections of this chapter, approaches taken to

extend these data and provide additional insights into the interplay between TRAIP and the PP4cs complex (PP4C-PP4R2-PP4R3β) are described.

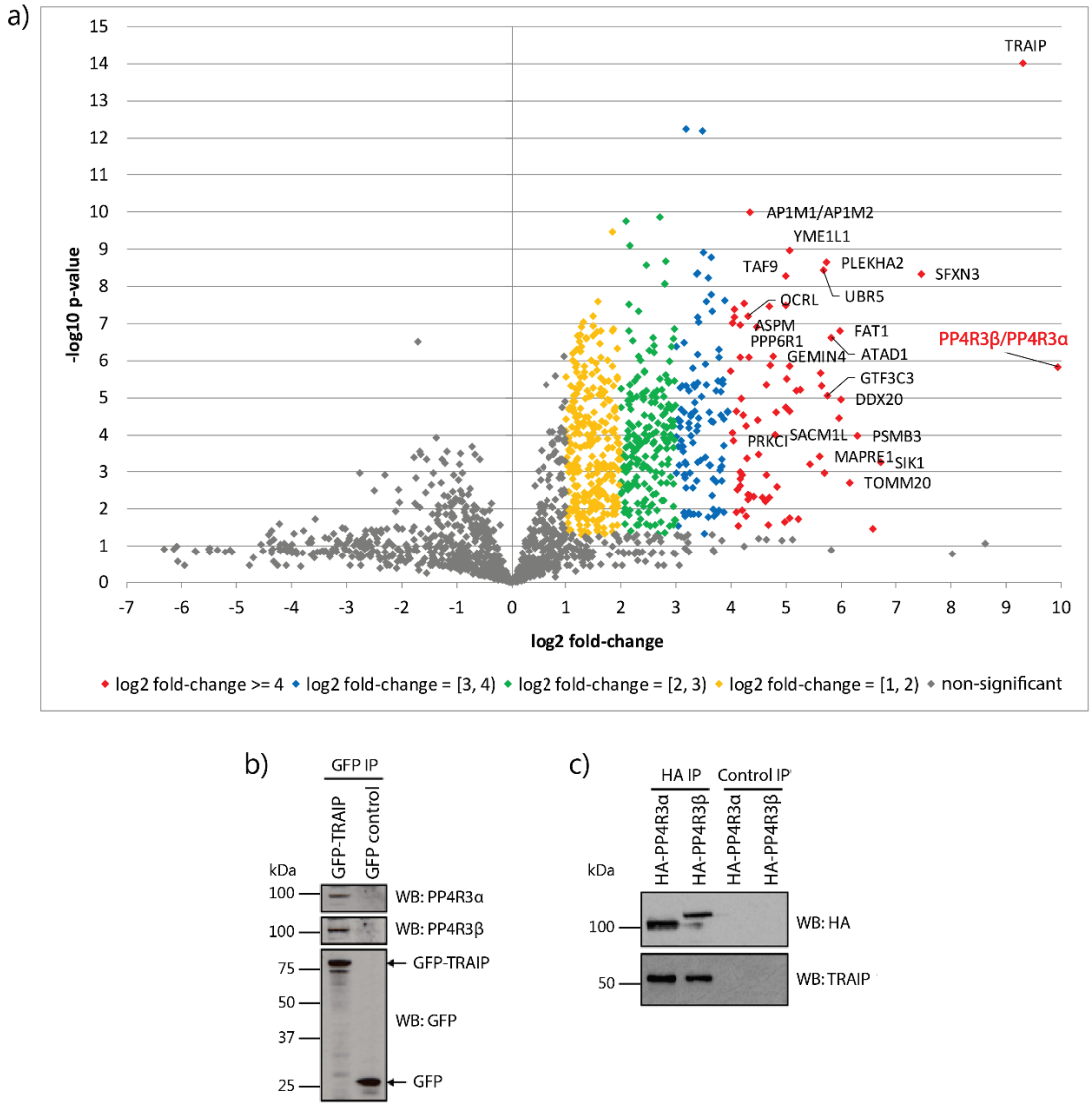

Figure 4.1. TRAIP interacts with PP4R3α and PP4R3β, the regulatory subunits of the PP4 complex.

a) A volcano plot representing the MS analysis of proteins co-immunoprecipitated with GFP-tagged TRAIP, which was expressed at near endogenous levels, enriched versus GFP control (empty) construct that can be used for N-terminal tagging of proteins with GFP (experiment and analysis of the results performed by M. Harley and M. Halachev, respectively). P-value (-log10), indicating significance of the hit, is plotted against fold enrichment (log2) of the protein in a sample, representing results of n=6 replicates from 3 independent experiments. Several of the most enriched proteins (shown as red dots) are indicated in the graph.

b, c) Reciprocal immunoprecipitation (IP) experiments show that endogenous PP4R3α and PP4R3β co-immunoprecipitate with GFP-tagged TRAIP (b), and that endogenous TRAIP is immunoprecipitated by HA-tagged PP4R3α or PP4R3β (c) (experiments performed by M. Harley). GFP control (empty) construct (b) and control IP (agarose without HA antibody) (c) were used to demonstrate the specificity of the interaction between TRAIP and PP4R3α/PP4R3β.

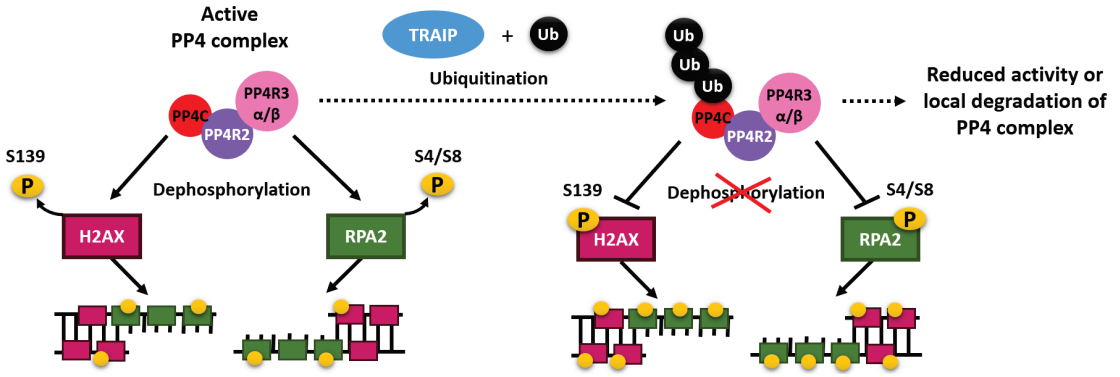

Figure 4.2. A model for the TRAIP-mediated regulation of PP4 complex.
a) Unpublished data from the Andrew Jackson laboratory suggest that TRAIP may regulate PP4 complex by ubiquitination to promote DNA repair. I propose that upon DNA damage, TRAIP may interact with and ubiquitinate one or more of the PP4 complex subunits, which would reduce PP4 activity by yet unknown mechanism or result in local degradation of PP4 complex. In turn, this would preserve H2AX and RPA2 phosphorylation during the initial stages of DNA repair, as well as stimulate the recruitment of DNA repair factors to damaged DNA. In the absence of TRAIP or upon its degradation in a proteasome-dependent manner after the onset of UV-C-induced DDR (Harley *et al.*, 2016), PP4 protein levels or activity would increase, enabling dephosphorylation of H2AX and RPA2 and completion of DNA repair.

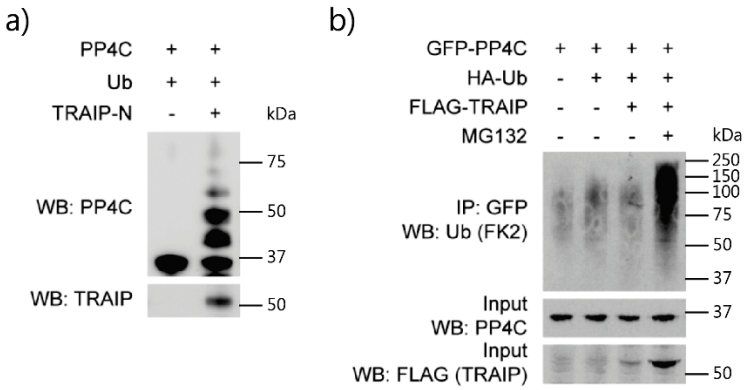

Figure 4.3. TRAIP ubiquitinates PP4C, the catalytic subunit of PP4 complex.
a) Immunoblot showing that PP4C protein is ubiquitinated by the RING domain of TRAIP *in vitro* (experiment performed by O. Murina). Purified recombinant PP4C and ubiquitin (Ub) were incubated in the presence or absence of the recombinant N-terminal part of TRAIP (TRAIP-N), containing the RING domain and E3 ligase activity. Anti-TRAIP and anti-PP4C antibodies were used for immunoblotting.
b) Immunoblot showing that PP4C protein is likely to be poly-ubiquitinated by TRAIP in HeLa cells (experiment performed by M. Harley). HeLa cells were transfected with GFP-tagged PP4C, HA-tagged ubiquitin and FLAG-tagged TRAIP. 24 h post-transfection, proteasome inhibitor MG132 (20 µM) was added for 6 h to prevent degradation of ubiquitinated proteins. Cell lysates were used for GFP immunoprecipitation (IP), and the IP and input samples were analysed by immunoblotting with anti-Ub (FK2), anti-PP4C and anti-FLAG antibodies.

4.2. Design, construction and purification of recombinant heterotrimeric PP4 complexes

Given that TRAIP can ubiquitinate PP4C, but likely interacts with the regulatory subunit PP4R3β, the presence of the ternary PP4cs complex may potentiate the PP4C ubiquitination by TRAIP. Therefore, to further investigate whether PP4 is a ubiquitination substrate of TRAIP, I decided to construct a recombinant PP4cs complex expressed from a polycistronic plasmid and use it in the *in vitro* ubiquitination assays together with TRAIP. The polycistronic expression construct is expected to result in complex formation upon expression in bacteria, instead of *in vitro* reconstitution of individually expressed and purified subunits. *In vitro* reconstitution can be time-consuming, and the yield may be quite low (Selleck and Tan, 2008). In contrast, complex formation in bacterial cells is faster and more efficient, requiring a single round of expression and purification. Moreover, it may improve solubility of the recombinant proteins. This is particularly relevant to this experiment as the regulatory subunit PP4R3β was found to be insoluble and could not be purified separately (J. Ding, unpublished). Additionally, folding and complex assembly takes place in a cellular environment with native folding enzymes, contributing to the stability of a complex and preventing aggregation of nascent unfolded peptides (Ellis and Hartl, 1999; Jaenicke, 1998; Tan, 2001). Thus, a better stoichiometry and solubility of the complex of interest may be achieved through complex formation in bacterial cells.

For co-expression of a protein complex in bacteria, I decided to clone the three subunits of human PP4cs – PP4C, PP4R2, and PP4R3β – into the pGEX-6P-1 bacterial expression vector in the order listed, with the glutathione S-transferase (GST) affinity tag placed at the N-terminus of the catalytic subunit PP4C (***Figure 4.4*a-b**). Additionally, the trimeric PP4 complex containing PP4C, PP4R2, and PP4R3α was constructed to act as a control for further studies, as this complex was not shown to be involved in DDR and DNA repair (***Figure 4.4*a-b**). It was demonstrated that the order of expression of the co-expressed genes from a polycistronic plasmid does not have a major impact on the differential expression levels of the subunits (Tan *et al.*, 2005). Nevertheless, I decided to proceed with the aforementioned order due to previously reported requirement of pre-assembly of the PP4C-PP4R2 binary complex for the subsequent interaction with PP4R3β and formation of the trimeric complex (Gingras *et al.*, 2005). Regarding the position of the affinity tag, its potential interference with the complex formation needs to be carefully considered. Moreover, Selleck and Tan (2008) advise to restrict tagging to a single subunit, since additional tags would increase the chances of inadvertent

destabilisation of the complex. As no data showing the impact of either N- or C-terminal tagging of PP4C on its folding or PP4cs complex formation were available, I decided to tag the N-terminus of PP4C, based on the previous successful expression and purification of the GST-PP4C monomer in our laboratory (O. Murina, unpublished).

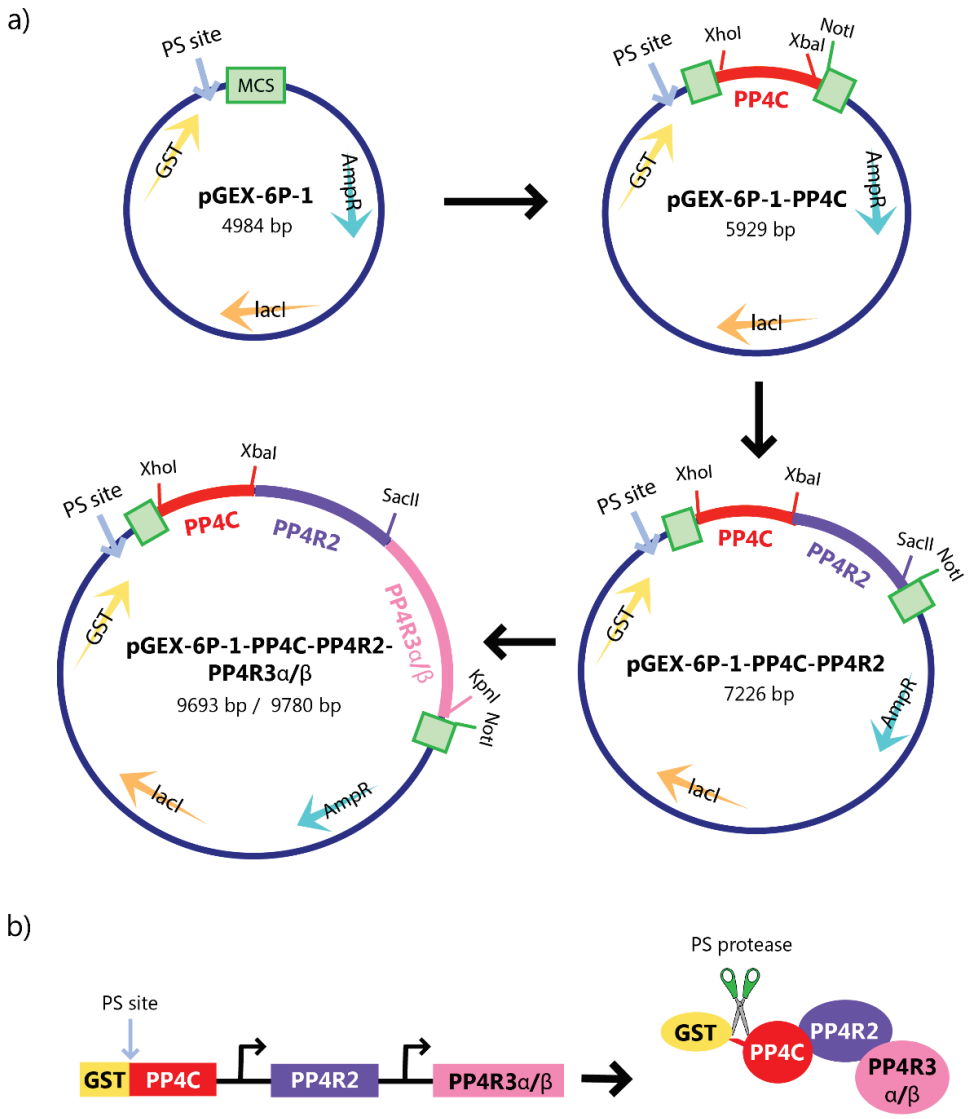

Figure 4.4. Construction of the pGEX-6P-1-based PP4C-PP4R2-PP4R3α/β co-expression vector.
a) Step-by-step cloning of PP4 complex subunits into pGEX-6P-1 bacterial vector for expressing GST fusion proteins with a PreScission (PS) protease site. Restriction endonuclease sites used for cloning are indicated in the plasmid maps. MCS = multiple cloning site; AmpR = ampicillin resistance gene; lacI = the *lac* repressor.
b) The representation of co-expression and *in vivo* reconstitution of the ternary PP4 complex. The GST tag can be removed by PS protease-mediated cleavage.

The two generated pGEX-6P-1 co-expression plasmids, PP4C-PP4R2-PP4R3β and PP4C-PP4R2-PP4R3α, were transformed into bacterial Rosetta-2 cells, expressed and purified as described in Section 2.5.4. The eluate fractions in the Coomassie-stained gels of both co-expression constructs (PP4C-PP4R2-PP4R3β and PP4C-PP4R2-PP4R3α) contained two visible bands, whose sizes corresponded to PP4C (~35 kDa) and PP4R2 (~66 kDa) (***Figure 4.5*****a-b**). Additionally, a very faint lower mobility band, likely corresponding to PP4R3α (~105 kDa), could be observed in the PP4C-PP4R2-PP4R3α gel. To confirm that the eluates contained PP4R3β and PP4R3α regulatory subunits, immunoblotting was performed. PP4R3β and PP4R3α were indeed present in the recombinant complexes (***Figure 4.5*****c-d**), indicating that the whole trimeric PP4 complex was successfully purified using GST-tagged PP4C and confirming that PP4C-PP4R2-PP4R3β and PP4C-PP4R2-PP4R3α complexes were reconstituted in bacteria.

However, the analysis of Coomassie-stained protein gels strongly suggests that the PP4 subunits are not present at 1:1:1 stoichiometry within the recombinant complexes. The two visible bands of PP4C and PP4R2 indicate that the large proportion of the purified complex is composed of the PP4C-PP4R2 dimer, with only a small fraction representing the ternary complex with the regulatory subunit PP4R3β or PP4R3α. Overall, the stoichiometry achieved by expression and purification of heterotrimeric PP4 complex is not optimal. However, I postulated that using the ternary complex may nevertheless allow me to determine ubiquitination of all three subunits in the PP4 complexes in a single experiment. Moreover, if the regulatory subunits strongly impact on PP4C ubiquitination, the effect may be detectable despite low levels of PP4R3β/α. Thus, I decided to use the eluates containing PP4C-PP4R2-PP4R3β and PP4C-PP4R2-PP4R3α in *in vitro* ubiquitination assay to assess whether and which of the PP4 subunits are ubiquitinated by TRAIP (see Section 4.3).

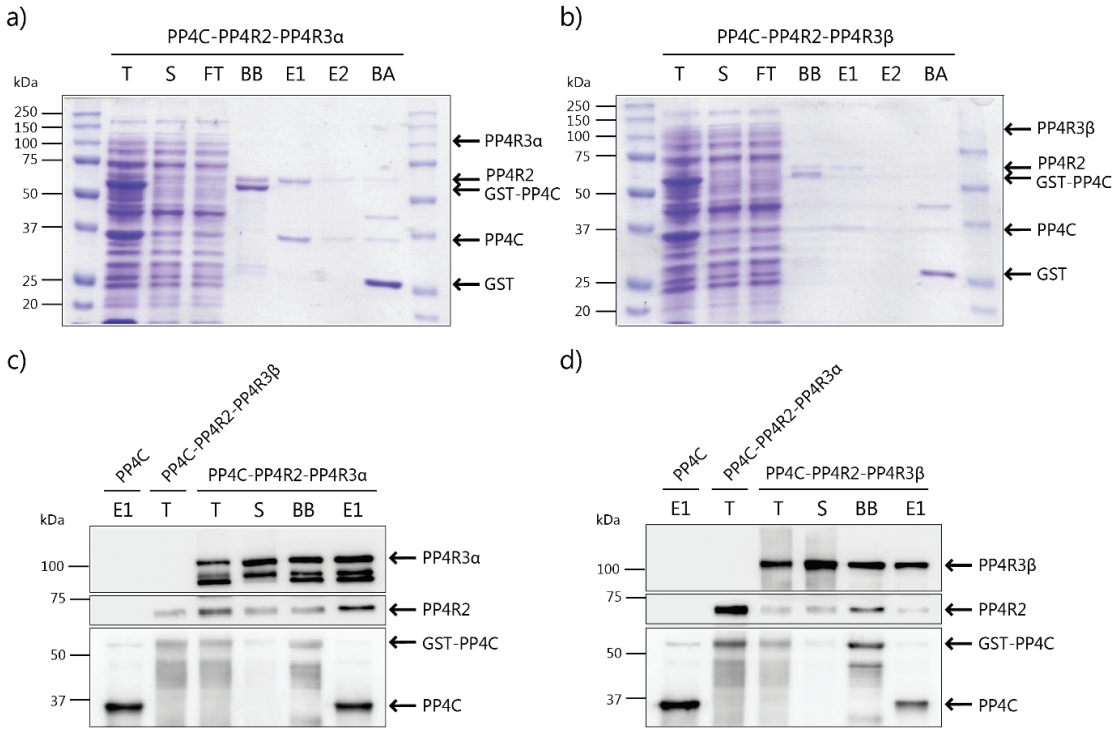

Figure 4.5. Purification of recombinant ternary PP4C-PP4R2-PP4R3α and PP4C-PP4R2-PP4R3β complexes.

a, b) Coomassie Blue-stained protein gels of PP4C-PP4R2-PP4R3α (a) and PP4C-PP4R2-PP4R3β (b), representing several steps of protein purification: T = total protein, S = soluble fraction, FT = flow-through, BB = beads before PS cleavage, E1 = eluate, E2 = second eluate / wash, BA = beads after PS cleavage. Eluate fractions were collected and used as substrates in the *in vitro* ubiquitination reactions. Bands corresponding to the known sizes of GST, PP4C, GST-PP4C, PP4R2, PP4R3α and PP4R3β are indicated.

c, d) Immunoblots showing the presence of all three PP4 subunits within the recombinant complexes PP4C-PP4R2-PP4R3α (c) and PP4C-PP4R2-PP4R3β (d). Samples representing key stages of protein purification were analysed. To control for antibody specificity, samples without the regulatory subunits (eluate of the recombinant PP4C monomer and the total protein fraction of the other ternary complex) were analysed at the same time in each case.

4.3. TRAIP-dependent *in vitro* ubiquitination of PP4C and the regulatory subunits of PP4 complex

To test whether the heterotrimeric PP4 complexes are better substrates for TRAIP-mediated ubiquitination than PP4C subunit alone, *in vitro* ubiquitination reactions using recombinant PP4 complexes were set up. As recombinant full-length TRAIP was found to be insoluble (M. Harley, unpublished data), catalytically active N-terminal part of TRAIP was used in *in vitro* ubiquitination assay instead. Thus, each reaction contained the N-terminal TRAIP and other components required for reconstitution of ubiquitination *in vitro* (see Section 2.5.5). In the absence of TRAIP, 5–7% of total PP4C was ubiquitinated *in vitro*, indicating the background level of non-specific ubiquitination (***Figure 4.6*a-b**). As expected, addition of TRAIP to the reaction enhanced PP4C ubiquitination *in vitro*, compared to the conditions without TRAIP or ubiquitin (***Figure 4.6*a-b**), confirming the previous finding that TRAIP can ubiquitinate PP4C *in vitro*. However, no strong improvement in PP4C ubiquitination was observed in the presence of the whole ternary PP4 complex, compared to PP4C alone, with 25–30% total PP4C ubiquitinated by TRAIP in each case (***Figure 4.6*b**). This result may imply that the regulatory subunits of PP4 complex either do not participate or play a very minor role in facilitating TRAIP-dependent ubiquitination of PP4C *in vitro*. Alternatively, even a small increase in PP4C ubiquitination contributed by the presence of the regulatory subunits PP4R3α and PP4R3β may be meaningful, as PP4R3α/β-containing heterotrimeric complex constitutes only a small fraction of each eluate, used as a substrate. Strong background signal, including PP4C and PP4R3α mono-ubiquitination, was observed in the absence of TRAIP (***Figure 4.6*a**), suggesting that a co-purified contaminant might mono-ubiquitinate these subunits *in vitro*. Moreover, using excessive amount of the E2 enzyme could also have resulted in the strong background seen in the immunoblot. In addition to that, the low specificity of the PP4C antibody may have contributed to the background signal observed in the PP4C immunoblot.

In the previous experiments conducted in the Andrew Jackson laboratory, weak TRAIP-dependent *in vitro* ubiquitination of PP4R3α was observed when it was tested individually in the absence of the ternary complex (J. Ding and O. Murina, unpublished). I was able to confirm this finding by demonstrating TRAIP-dependent ubiquitination of PP4R3α in my assay (***Figure 4.6*a**). TRAIP-dependent PP4R2 ubiquitination was not detected when the PP4C-PP4R2-PP4R3α complex was used as a substrate (***Figure 4.6*a**). Meanwhile, the weak chemiluminescence signal detected for PP4R2 and PP4R3β when using the PP4C-PP4R2-PP4R3β complex was

difficult to interpret. The loss of signal may potentially indicate a shift due to ubiquitination, but no clear lower mobility bands were observed (***Figure 4.6***a).

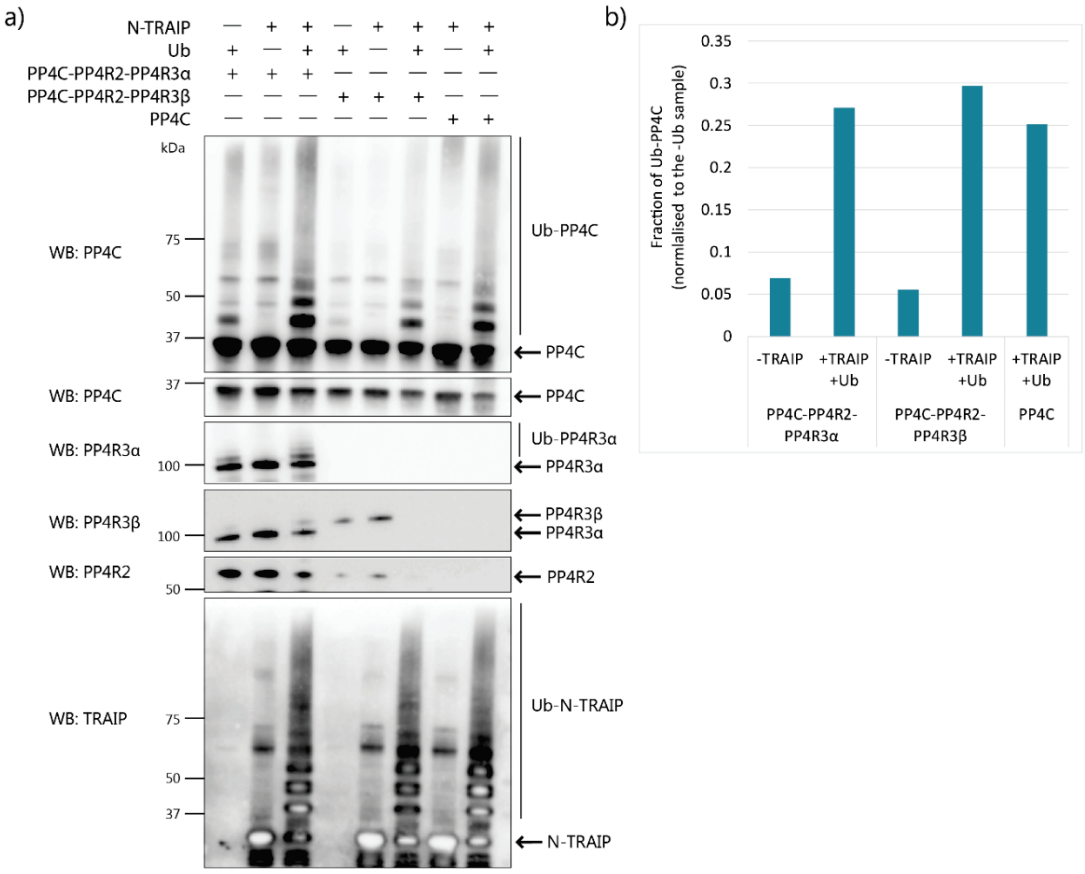

Figure 4.6. TRAIP-dependent *in vitro* ubiquitination of the wild-type ternary PP4 complexes.
a) Immunoblot showing that PP4C protein is poly-ubiquitinated by the RING domain of TRAIP *in vitro*. Ubiquitin (Ub) and the purified recombinant ternary PP4 complexes (PP4C-PP4R2-PP4R3α and PP4C-PP4R2-PP4R3β) or PP4C monomer were incubated in the presence of the recombinant N-terminal portion of TRAIP (N-TRAIP), containing the RING domain and E3 ligase activity. All ubiquitination reactions were supplemented with ATP, as well as E1 and E2 enzymes, and incubated for 3 h at 37˚C. Reactions were stopped by adding sample loading buffer and analysed by immunoblotting with anti-TRAIP, anti-PP4C, anti-PP4R2, anti-PP4R3α and anti-PP4R3β antibodies. Anti-PP4R3α blot was re-probed for anti-PP4R3β.
b) Image analysis to compare PP4C ubiquitination of ternary PP4 complexes and PP4C alone was performed using Fiji/ImageJ software. For ubiquitination analysis, the background signal intensity, defined as signal detected in the lanes without ubiquitin (–Ub), was subtracted from the lanes that contained ubiquitin (+Ub) after the ratio of Ub-PP4C/total PP4C was calculated. '-TRAIP' samples represent control conditions lacking TRAIP but containing all other constituents needed for ubiquitination *in vitro*, including ubiquitin.

The protein-protein interactions between the catalytic and regulatory subunits within the PP4 complex may influence TRAIP-mediated PP4C ubiquitination. However, further

experimental work will be necessary to validate this hypothesis. Firstly, it will be important to generate the ternary PP4 complexes with 1:1:1 stoichiometry, as this would allow better assessment of the role played by PP4R3α/β on the PP4C ubiquitination. Moreover, the N-terminal part of TRAIP was used in our *in vitro* analyses, and the capacity of TRAIP to ubiquitinate PP4C may be altered by the presence of its C-terminus. Therefore, the ability of full-length TRAIP to ubiquitinate PP4C and the regulatory subunits will need to be determined in cellular ubiquitination assays.

4.4. Identifying the residues of PP4 complex subunits that are ubiquitinated by TRAIP *in vitro*

My working model was that TRAIP acts as a negative regulator of PP4 complex that contains the regulatory subunit PP4R3β (***Figure 4.2***). Therefore, I hypothesised that if TRAIP-dependent ubiquitination of the PP4 complex is implicated in the DDR during S phase, then expression of non-ubiquitinatable PP4 mutant would be expected to phenotypically mimic the DDR signalling defects observed in TRAIP-deficient cells. As PP4 complex was shown to have several distinct cellular roles (Cohen *et al.*, 2005), its depletion from cells would likely affect all cellular functions, making interpretion of results difficult. Therefore, to study the potential DDR function of PP4, regulated by TRAIP, I first focussed on identifying the lysine residues of PP4C and the regulatory subunits that are ubiquitinated by TRAIP. Using site-directed mutagenesis, I expected to identify the residues of the PP4 complex that are essential for TRAIP-mediated ubiquitination *in vitro*, followed by assessing their functional significance in cell-based assays.

To get an insight which residues of PP4C could be ubiquitinated by TRAIP *in vitro*, I searched the PhosphoSitePlus protein post-translational modification database (Hornbeck *et al.*, 2015) for the lysine residues of the PP4 subunits that were previously observed to be post-translationally modified by ubiquitination. At the time of my inquiry, three lysine residues of PP4C were reported to be ubiquitinated by high throughput proteomic discovery-mode MS studies: K26 (reported by 31 studies), K31 (reported by 22 studies) and K63 (reported by 2 studies). I substituted these three lysines to the arginines (K>R) within the co-expression vector, as this is predicted to make the residues non-ubiquitinatable by the E3 ligase, while retaining their positive charge and thus diminishing chances of destabilisation and incorrect folding of PP4C. Once the mutations in these residues within PP4C were introduced, the mutant PP4 complexes were purified and their ability to act as substrates for TRAIP-mediated ubiquitination *in vitro* was tested.

As seen previously for wild-type complexes, the purified triple mutant complexes PP4C(K26R/K31R/K63R)-PP4R2-PP4R3β and PP4C(K26R/K31R/K63R)-PP4R2-PP4R3α were mostly composed of the binary PP4C-PP4R2 complex, with the band corresponding to PP4R3β or PP4R3α almost invisible on a Coomassie-stained protein gel (***Figure 4.7*****a-b**). Moreover, it became clear that the four complexes purified so far (the WT and mutant complexes with either PP4R3β or PP4R3α) differed in the amounts of each subunit. Thus, an immunoblotting

experiment was performed to compare the levels of PP4C, PP4R2 and PP4R3β/PP4R3α in these complexes and estimate how much of each eluate to use as an input for the *in vitro* ubiquitination assay to equilibrate the subunit levels (***Figure 4.7*c-d**). The volume of each eluate representative of approximately equivalent input for a fair comparison between the complexes was chosen based on these immunoblots.

However, the *in vitro* ubiquitination assay comparing WT and mutant PP4 complexes showed no substantial decrease in TRAIP-mediated ubiquitination of the mutant complexes, compared to WT complexes (***Figure 4.7*e-h**), suggesting that the mutated lysine residues do not have a strong influence on TRAIP-dependent ubiquitination of PP4C. As before, TRAIP-dependent ubiquitination of PP4R3α was observed; additionally, PP4R3β was also ubiquitinated in a TRAIP-dependent manner (***Figure 4.7*e-f**). Although PP4C, PP4R3α and PP4R3β showed mono-ubiquitination pattern in the absence of TRAIP in the *in vitro* ubiquitination assay, the more extensive multi-mono-ubiquitination or poly-ubiquitination of these subunits required TRAIP (***Figure 4.7*e-h**). In the future, to distinguish between multi-mono-ubiquitination and poly-ubiquitination, which look similar in immunoblots but may lead to distinct fates of the substrate protein, a ubiquitin mutant unable to form chains (where all seven lysines have been mutated to arginines) can be used instead of wild-type ubiquitin. Overall, these experimental data demonstrate that TRAIP promotes ubiquitination of PP4C, PP4R3β and PP4R3α, and that lysines 26, 31 and 63 of PP4C are not the key substrate residues of TRAIP-mediated ubiquitination *in vitro*.

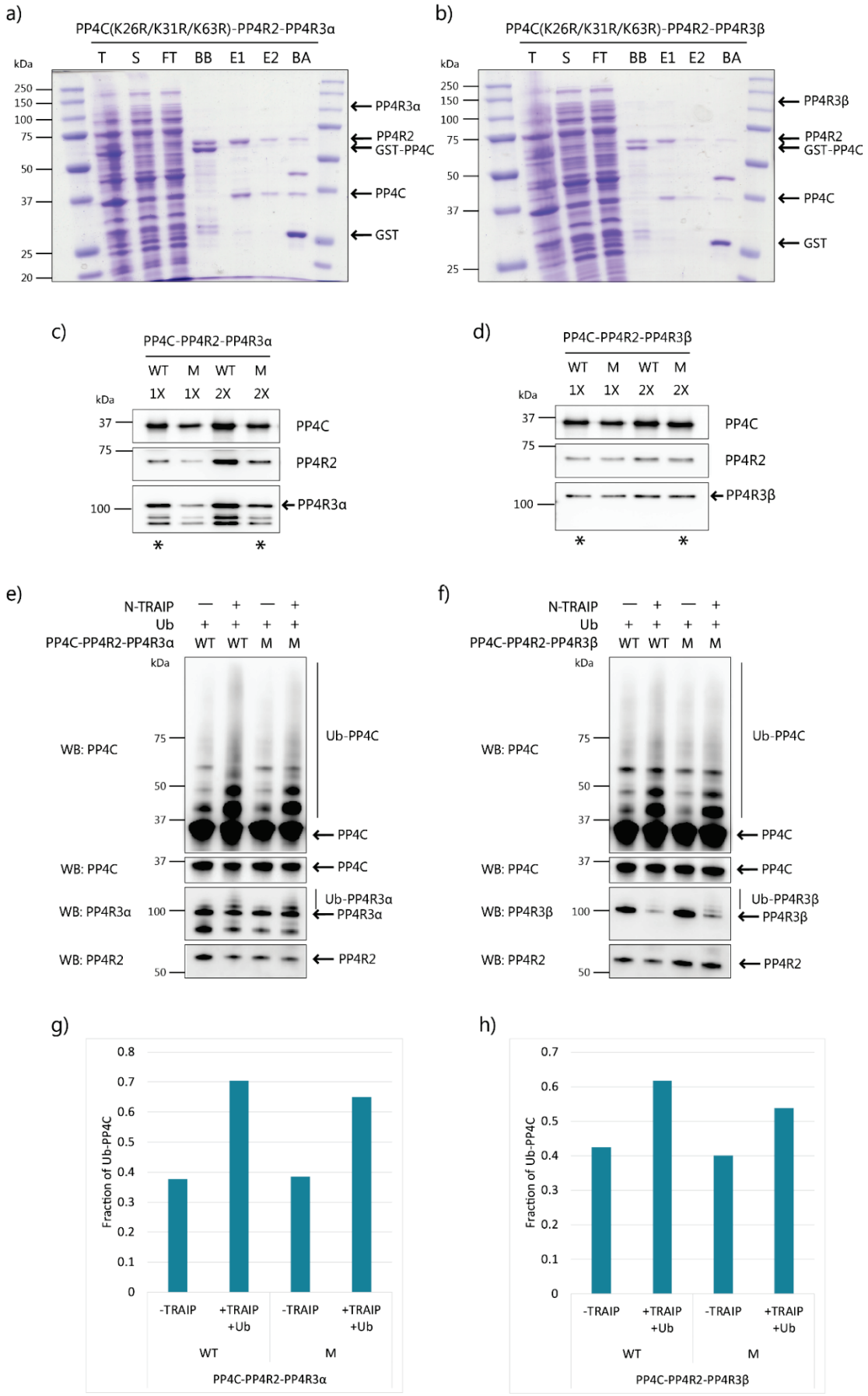
a)
PP4C(K26R/K31R/K63R)-PP4R2-PP4R3α
T S FT BB E1 E2 BA
kDa
250
150
100
75
50
37
25
20
PP4R3α
PP4R2
GST-PP4C
PP4C
GST
b)
PP4C(K26R/K31R/K63R)-PP4R2-PP4R3β
T S FT BB E1 E2 BA
kDa
250
150
100
75
50
37
25
PP4R3β
PP4R2
GST-PP4C
PP4C
GST
c)
PP4C-PP4R2-PP4R3α
WT M WT M
1X 1X 2X 2X
kDa
37
75
100
PP4C
PP4R2
PP4R3α
*
*
d)
PP4C-PP4R2-PP4R3β
WT M WT M
1X 1X 2X 2X
kDa
37
75
100
PP4C
PP4R2
PP4R3β
*
*
e)
N-TRAIP — + — +
Ub + + + +
PP4C-PP4R2-PP4R3α WT WT M M
kDa
WB: PP4C
75
50
37
Ub-PP4C
PP4C
WB: PP4C
37
PP4C
WB: PP4R3α
100
Ub-PP4R3α
PP4R3α
WB: PP4R2
50
PP4R2
f)
N-TRAIP — + — +
Ub + + + +
PP4C-PP4R2-PP4R3β WT WT M M
kDa
WB: PP4C
75
50
37
Ub-PP4C
PP4C
WB: PP4C
37
PP4C
WB: PP4R3β
100
Ub-PP4R3β
PP4R3β
WB: PP4R2
50
PP4R2
g)
Fraction of Ub-PP4C
0.8
0.7
0.6
0.5
0.4
0.3
0.2
0.1
0
-TRAIP
+TRAIP +Ub
-TRAIP
+TRAIP +Ub
WT
M
PP4C-PP4R2-PP4R3α
h)
Fraction of Ub-PP4C
0.7
0.6
0.5
0.4
0.3
0.2
0.1
0
-TRAIP
+TRAIP +Ub
-TRAIP
+TRAIP +Ub
WT
M
PP4C-PP4R2-PP4R3β

Figure 4.7. Triple mutants of PP4C (K26R/K31R/K63R) do not abolish TRAIP-dependent *in vitro* ubiquitination of the ternary PP4 complexes.

a, b) Coomassie-stained protein gels showing purification of the recombinant ternary PP4C(K26R/K31R/K63R)-PP4R2-PP4R3α (a) and PP4C(K26R/K31R/K63R)-PP4R2-PP4R3β (b) complexes. Key steps of protein purification are shown: T = total protein, S = soluble fraction, FT = flow-through, BB = beads before PS cleavage, E1 = eluate, E2 = second eluate / wash, BA = beads after PS cleavage. Eluate fractions were collected and used as substrates in *in vitro* ubiquitination reactions. Bands corresponding to the known sizes of GST, PP4C, GST-PP4C, PP4R2, PP4R3α and PP4R3β are indicated.

c, d) Immunoblots showing the presence of all three PP4 subunits within the recombinant complexes PP4C(K26R/K31R/K63R)-PP4R2-PP4R3α (c) and PP4C(K26R/K31R/K63R)-PP4R2-PP4R3β (d). Eluate fractions of wild-type (WT) and triple mutant PP4C(K26R/K31R/K63R)-containing (M) recombinant PP4 complexes were analysed by immunoblotting with anti-PP4C, anti-PP4R2, anti-PP4R3α and anti-PP4R3β antibodies. Stars below indicate the amounts of each WT and mutant complex (1X or 2X) that were used for the *in vitro* ubiquitination assay shown below.

e, f) Immunoblots showing that both wild-type (WT) and triple mutant K26R/K31R/K63R (M) PP4C proteins within the recombinant PP4R3α (e) and PP4R3β (f) containing complexes are ubiquitinated by the RING domain of TRAIP *in vitro*. Ubiquitin (Ub) and the purified recombinant ternary PP4 complexes (PP4C-PP4R2-PP4R3α and PP4C-PP4R2-PP4R3β) with or without PP4C(K26R/K31R/K63R) mutations were incubated in the presence of the recombinant N-terminal part of TRAIP (N-TRAIP), containing the RING domain required for its E3 ligase activity. All ubiquitination reactions were supplemented with ATP, as well as E1 and E2 enzymes, and incubated for 3 h at 37˚C. Reactions were stopped by adding sample loading buffer and analysed by immunoblotting with anti-PP4C, anti-PP4R2, anti-PP4R3α and anti-PP4R3β antibodies.

g, h) Image analysis to compare ubiquitination (the ratio of Ub-PP4C versus total PP4C) of wild-type (WT) and triple mutant K26R/K31R/K63R (M) PP4C proteins within the recombinant PP4R3α (g) and PP4R3β (h) containing complexes was performed using Fiji/ImageJ software. '-TRAIP' samples represent control conditions lacking TRAIP but containing all other constituents needed for ubiquitination *in vitro*, including ubiquitin.

4.5. Mass spectrometry reveals lysine residues of PP4C, PP4R3β and PP4R3α that are ubiquitinated by TRAIP *in vitro*

Previous results suggested that other lysine residues of PP4 complex subunits are targeted by TRAIP ubiquitination. Given that hypothesis-driven approach did not reveal the key ubiquitination sites *in vitro*, I employed mass spectrometry (MS) to find these residues (performed in collaboration with Alex Von Kriegsheim, IGMM Mass Spectrometry facility (***Figure 4.8*****a**). A semi-quantitative interaction proteomic approach was used to analyse *in vitro* ubiquitination reactions with and without TRAIP, containing wild-type PP4 complexes PP4C-PP4R2-PP4R3β and PP4C-PP4R2-PP4R3α as substrates. Immunoblotting was performed to confirm PP4C ubiquitination (***Figure 4.8*****b**), and the samples were subjected to in-solution trypsin digestion and label-free quantification by liquid chromatography (LC)-tandem MS (MS/MS).

Although signal intensity is proportional to the quantity of analyte, it does not provide a precise quantification due to potential differences in peptide ionisation (Jarnuczak *et al.*, 2016). Nevertheless, the MS experiment allowed semi-quantitative evaluation of the lysine residues ubiquitinated by N-terminal TRAIP *in vitro*. The analysis of MS data revealed five lysine residues of PP4C (lysines 21, 26, 31, 133, and 183) whose ubiquitination *in vitro* was increased in the reactions containing TRAIP, compared to the ones without TRAIP (***Figure 4.8*****c**). Notably, the three lysine residues of PP4C that were previously not reported in the PhosphoSitePlus protein post-translational modification database (K21, K133 and K183) are now in the list of PP4C residues that were found to be ubiquitinated. Moreover, one residue of PP4R3β, lysine 36 (K36), and one residue of PP4R3α, lysine 733 (K733), were identified by the MS analysis as ubiquitinated in a TRAIP-dependent manner *in vitro* (***Figure 4.8*****c**). In contrast, the ubiquitination of these two residues is not reported by the PhosphoSitePlus database.

The results obtained by MS indicate that PP4 complex is ubiquitinated by TRAIP *in vitro*, with several lysine residues of PP4 complex as its main targets. However, various limitations of these data have to be considered. *In vitro* experiments may provide an indication of the events *in vivo*; however, the relatively high protein concentration and the absence of substrate competition or regulation have to be taken into consideration. Additionally, only N-terminal part of TRAIP was used in *in vitro* ubiquitination experiments and MS analysis, and it is plausible that more specific or efficient TRAIP-mediated ubiquitination of PP4 complex would be achieved in the presence of full-length TRAIP. Finally, other or additional factors,

such as a different E2 ubiquitin-conjugating enzyme, may be necessary to enhance TRAIP-dependent PP4 complex ubiquitination in cells.

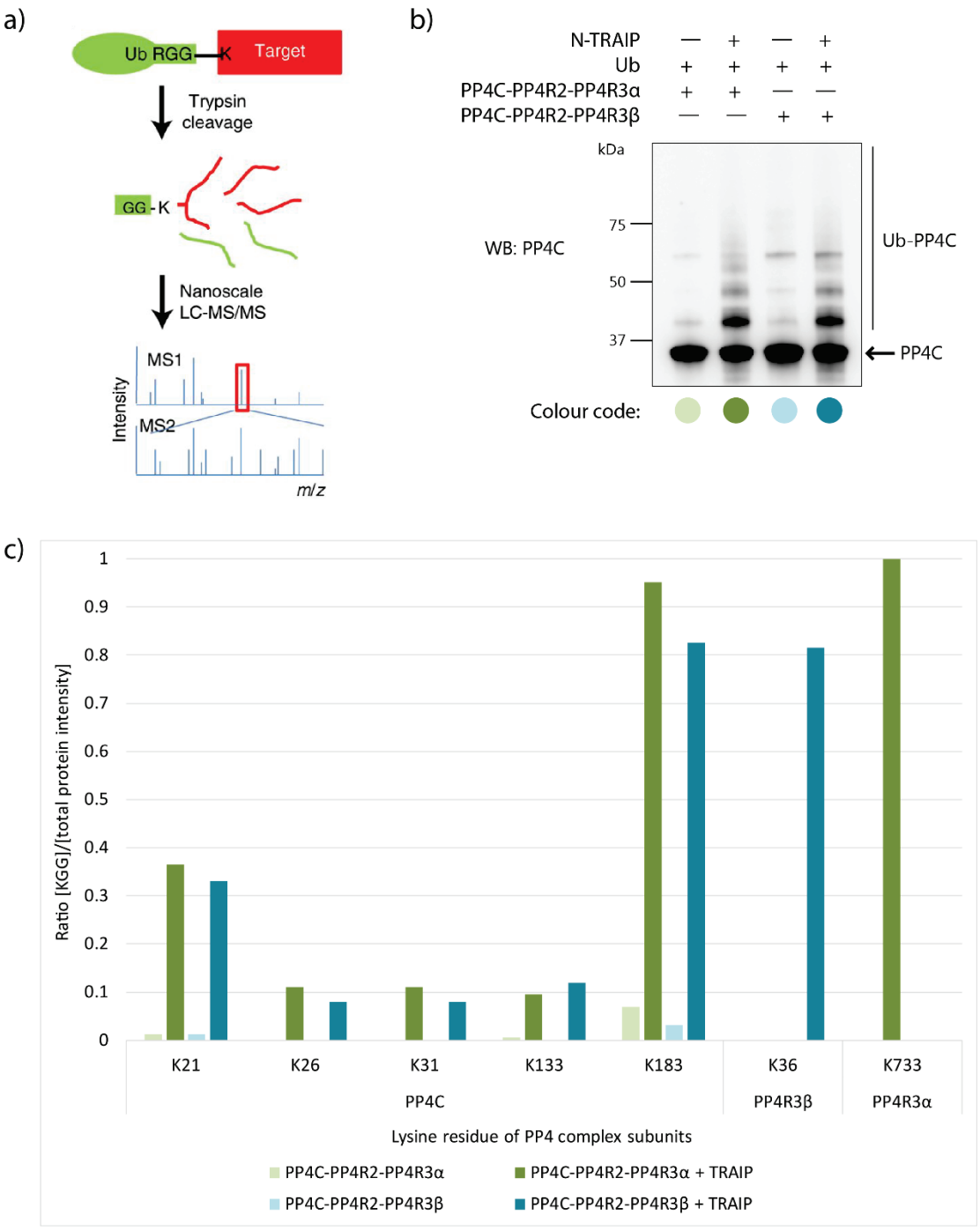

Figure 4.8. MS analysis of TRAIP-dependent *in vitro* ubiquitination of PP4 detects lysine residues targeted by TRAIP.

a) Schematic depiction of the MS strategy to identify ubiquitination sites. Proteins post-translationally modified by ubiquitin moieties are digested with trypsin, leaving a di-glycine remnant attached to the ε-amine of the lysine where ubiquitin was attached (Lys-ε-Gly-Gly, or

K-ε-GG). Thus, K-ε-GG is indicative of proteins containing ubiquitinated lysine side chains. This is followed by the identification of ubiquitinated lysine residues by liquid chromatography (LC)-tandem MS (MS/MS). The obtained raw data contain intensities of K-ε-GG signals for all ubiquitinated lysine residues that were present in the analysed reactions. Image adapted from Lumpkin *et al.* (2017).
b) Immunoblot showing TRAIP-dependent PP4C ubiquitination in the *in vitro* ubiquitination reactions, subsequently analysed by MS. Ubiquitin (Ub) and the purified recombinant ternary PP4 complexes (PP4C-PP4R2-PP4R3α and PP4C-PP4R2-PP4R3β) were incubated in the presence or absence of the recombinant N-terminal part of TRAIP (N-TRAIP). All ubiquitination reactions were supplemented with ATP, as well as E1 and E2 enzymes, and incubated for 3 h at 37˚C. Reactions were stopped by adding sample loading buffer and analysed by immunoblotting with anti-PP4C antibody.
c) Plot representing all lysine (K) residues of PP4 complex subunits PP4C, PP4R2, PP4R3β and PP4R3α that were identified as ubiquitinated by MS analysis in the *in vitro* ubiquitination reactions containing N-TRAIP as an E3 ligase and PP4 complex as a substrate. Ubiquitination reactions were stopped by freezing on dry ice, and samples were subjected to in-solution trypsin digestion to enrich for the di-glycine remnant (K-ε-GG), followed by LC-tandem MS (performed by Alex Von Kriegsheim, IGMM Mass Spectrometry facility). Signal normalisation was performed by dividing raw signal intensity of a ubiquitinated lysine residue ([KGG]) by the total signal intensity of the protein to which the lysine residue belongs ([total protein intensity]). The [KGG]/[total protein intensity] ratios were further normalised within the graph to the highest ratio observed.

The lysine residues of TRAIP that were auto-ubiquitinated by its E3 ligase activity *in vitro* were plotted as well. The MS analysis revealed that TRAIP auto-ubiquitinates at multiple lysines, with three of them preferentially used *in vitro*: K150, K235, and K251 (***Figure 4.9***). According to the PhosphoSitePlus protein post-translational modification database, several discovery-mode MS studies observed ubiquitination of K150 and K235 of TRAIP. In contrast, K251 was not previously reported to be post-translationally modified, although the modification of this residue is highly enriched in our analysis *in vitro*.

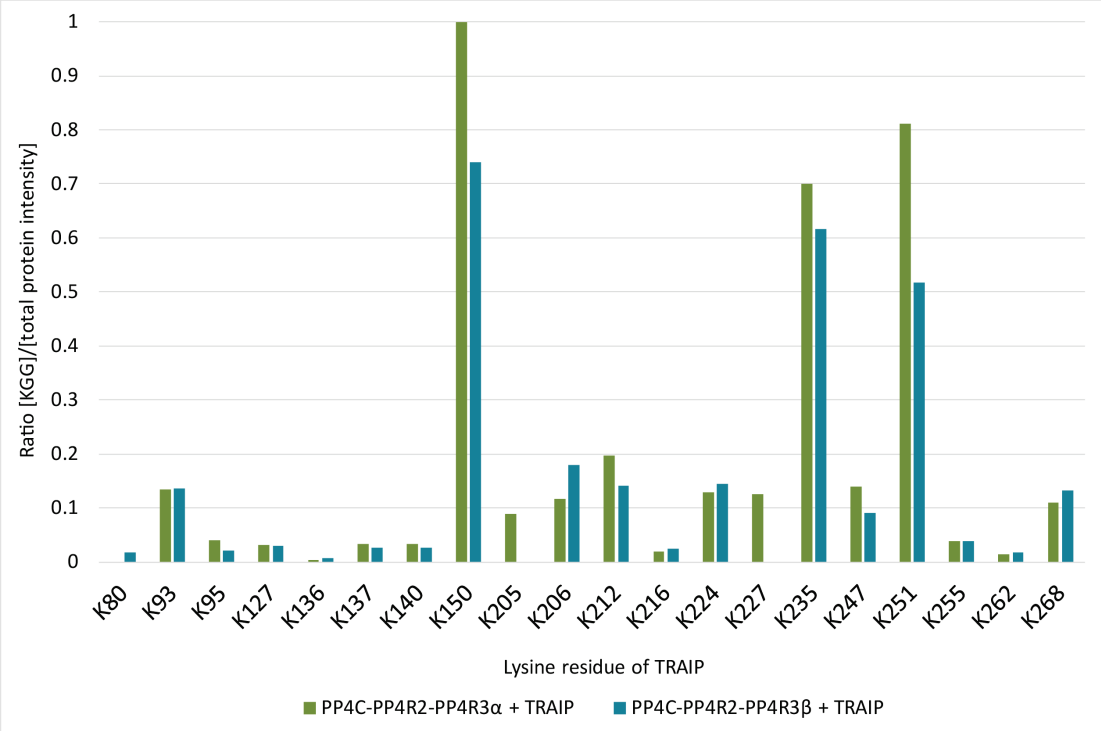

Figure 4.9. MS analysis of TRAIP auto-ubiquitination *in vitro*.
Plot representing all lysines (K) residues of TRAIP that were identified by MS analysis in the *in vitro* ubiquitination reactions containing E3 ligase N-TRAIP and PP4 complex. These sites therefore represent auto-ubiquitinated TRAIP residues. Samples were subjected to in-solution trypsin digestion to enrich for the di-glycine remnant (K-ε-GG), followed by LC-tandem MS (performed by Alex Von Kriegsheim, IGMM Mass Spectrometry facility). Signal normalisation was performed by dividing raw signal intensity of a ubiquitinated lysine residue ([KGG]) by the total signal intensity of the protein to which the lysine residue belongs ([total protein intensity]). The [KGG]/[total protein intensity] ratios were further normalised within the graph to the highest ratio observed.

Ubiquitination is an abundant post-translational modification that involves the generation of an isopeptide linkage between the C-terminus of the ubiquitin moiety and the ε-amino group of a lysine residue on the substrate protein (mono-ubiquitination). Multi-mono-ubiquitination occurs when a single ubiquitin moiety is attached to multiple lysine residues on the same substrate (Akutsu *et al.*, 2016). Moreover, ubiquitin itself has seven lysine residues (lysines 6, 11, 27, 29, 33, 48 and 63), all of which can be further ubiquitinated to generate poly-ubiquitin chains with ubiquitin molecules attached end-to-end to one lysine residue on a substrate protein (Akutsu *et al.*, 2016). The potential of ubiquitin to form a multitude of differently structured chains makes ubiquitin signalling a particularly versatile cellular system capable of regulating and influencing a variety of cellular processes. Alongside other data obtained from the TRAIP-PP4 MS screen of the *in vitro* ubiquitination reactions, I analysed ubiquitin chain linkage distribution by quantifying ubiquitinated ubiquitin peptides. Three

types of ubiquitin chains were strongly enriched in the ubiquitination reactions containing both TRAIP and PP4 complex: K11, K48, and K63 (***Figure 4.10***). The lack of these ubiquitin chain linkages in the reactions without TRAIP suggest that these data are specific to either TRAIP-dependent ubiquitination of PP4 or TRAIP auto-ubiquitination. However, it is difficult to distinguish between these scenarios without additional data. Furthermore, poly-ubiquitin chains can be not only homotypic (single linkage type) but also heterotypic (mixed linkage types; either branched on non-branched), further complicating the analysis. Nevertheless, the most abundant ubiquitin chain linkages can give us some insight into the potential cellular fate of ubiquitinated TRAIP and PP4 complex. To distinguish between TRAIP-dependent ubiquitination of PP4 or TRAIP auto-ubiquitination, further MS analyses with TRAIP as the only substrate of the *in vitro* ubiquitination reaction need to be performed.

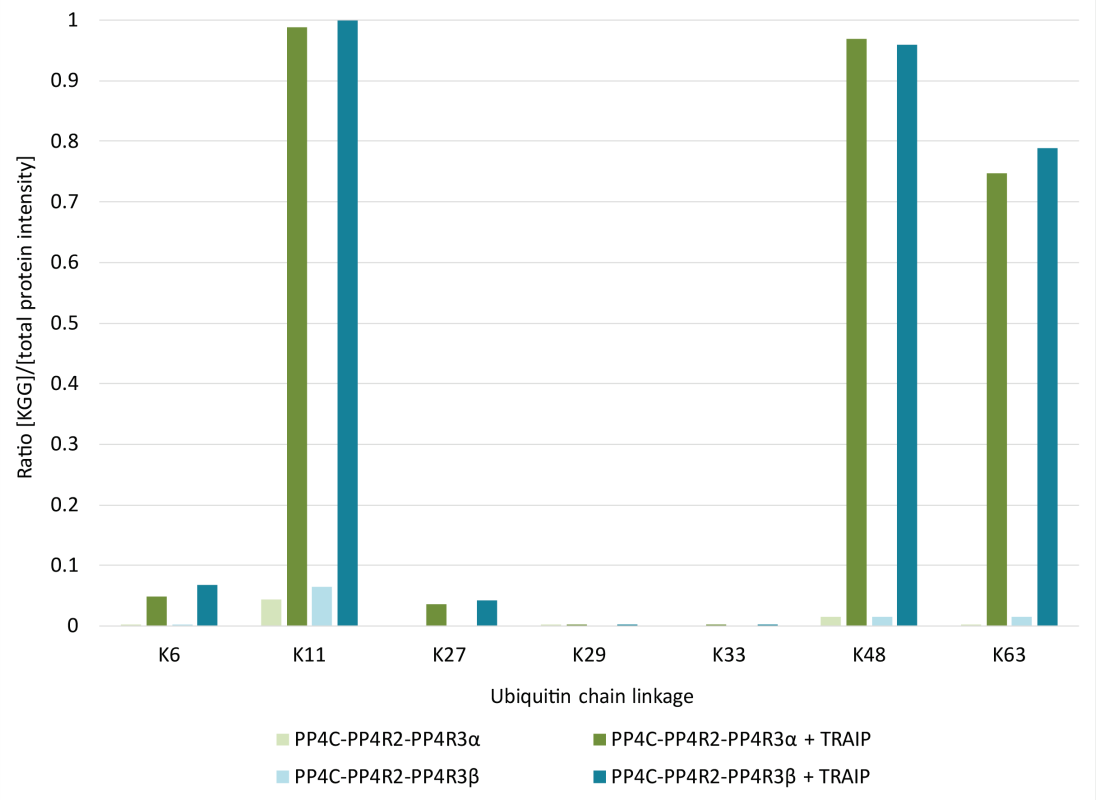

Figure 4.10. MS analysis of TRAIP-dependent *in vitro* ubiquitin chain linkage.
Plot representing the types of ubiquitin chain linkage that were identified by MS analysis in the *in vitro* ubiquitination reactions containing E3 ligase N-TRAIP and PP4 complex. Samples were subjected to in-solution trypsin digestion to enrich for the di-glycine remnant (K-ε-GG), followed by LC-tandem MS (performed by Alex Von Kriegsheim, IGMM Mass Spectrometry facility). Signal normalisation was performed by dividing raw signal intensity of a ubiquitinated lysine residue ([KGG]) by the total signal intensity of the protein to which the lysine residue belongs ([total protein intensity]). The [KGG]/[total protein intensity] ratios were further normalised within the graph to the highest ratio observed.

The differences in ubiquitin chain composition are thought to encode distinct signals, and structurally different chains participate in distinct cellular processes and signalling pathways (Akutsu *et al.*, 2016). The best-studied types of poly-ubiquitin chains are K48- and K63-linked chains, both of which were abundant in the *in vitro* ubiquitination reactions (***Figure 4.10***). K48-linked poly-ubiquitin chains have long been understood to be a canonical signal promoting proteasomal degradation, whereas K63-linked poly-ubiquitin chains are often associated with non-proteolytic roles, instead mediating signal transduction, intracellular trafficking and chromatin localisation of DNA damage factors (Lee *et al.*, 2017; Li and Ye, 2008). Meanwhile, K11 poly-ubiquitin chains have been proposed to be involved in regulating cell cycle and proteasomal degradation (Akutsu *et al.*, 2016). As mentioned before, it is not immediately obvious which types of identified linkages indicate poly-ubiquitination of PP4 subunits and TRAIP. However, TRAIP was previously observed to be degraded via the proteasome in response to UV damage (Harley *et al.*, 2016). Moreover, the addition of proteasome inhibitor MG132 in the cellular ubiquitination assay increased the stability of TRAIP (***Figure 4.3***). It is therefore likely that TRAIP auto-ubiquitination *in vitro* is mainly represented by K48 ubiquitin linkages, suggesting that PP4 subunits may be ubiquitinated by TRAIP via K63-linked and/or K11-linked ubiquitin chains. If this is confirmed by other experiments, such as *in vitro* ubiquitination reactions using only K63-linked ubiquitin moieties or immunoblotting with the anti-K63-specific ubiquitin antibody in cells, it would suggest that TRAIP is involved in non-proteolytic regulation of PP4 activity, such as its re-localisation or recruitment to sites of DNA damage.

Overall, the MS analysis of *in vitro* ubiquitination reactions allowed identification of seven lysine residues of PP4 complex subunits PP4C (K21, K26, K31, K133, and K183), PP4R3β (K36) and PP4R3α (K733), ubiquitinated *in vitro* in a TRAIP-dependent manner. Moreover, ubiquitinated residues of TRAIP itself were detected, indicating positions of three lysine side chains (K150, K235, and K251) that are particularly enriched in this post-translational modification. Finally, certain ubiquitin chain linkages (K11, K48, and K63) were found to be prevalent in the *in vitro* ubiquitination reactions studied. These data constitute important initial observations, which will need to be tested using cell-based experiments in the future (see Section 4.7 for discussion).

4.6. PP4C K183R has reduced levels of TRAIP-dependent ubiquitination *in vitro*

The analysis of TRAIP-dependent ubiquitination sites of PP4 complex by MS revealed high signal intensity of the ubiquitinated PP4C lysine residue 183 (K183) in both wild-type PP4 complexes, PP4C-PP4R2-PP4R3β and PP4C-PP4R2-PP4R3α. Thus, I tested whether a substitution of this lysine to another positively-charged but non-ubiquitinatable residue, an arginine, would diminish the levels of TRAIP-mediated ubiquitination of PP4C *in vitro*. Site-directed mutagenesis was performed on the wild-type PP4 co-expression construct to generate the PP4C(K183R)-PP4R2-PP4R3β plasmid. Once the K183R substitution was confirmed by Sanger sequencing, an additional round of site-directed mutagenesis introduced the second mutation, K21R, into PP4C. As the K21 residue of PP4C was also shown to be extensively ubiquitinated in the MS analysis (see ***Figure 4.8*****c**), I expected to observe further reduction in TRAIP-mediated ubiquitination of PP4C(K21R/K183R)-PP4R2-PP4R3β *in vitro*, compared to PP4C(K183R)-PP4R2-PP4R3β.

Like wild-type PP4 complexes, the purified mutant PP4C(K183R)-PP4R2-PP4R3β and PP4C(K21R/K183R)-PP4R2-PP4R3β complexes contained large amounts of the binary PP4C-PP4R2 complex, with only a small proportion of the eluate corresponding to PP4R3β on a Coomassie-stained protein gel (***Figure 4.11*****a-b**). Therefore, as before, immunoblotting analysis was conducted to compare the levels of PP4C, PP4R2 and PP4R3β subunits in the mutant and wild-type complexes and to decide how much of each eluate to use as a substrate for the *in vitro* ubiquitination assay (***Figure 4.11*****c**). The *in vitro* ubiquitination assay comparing wild-type, single mutant (PP4C(K183R)) and double mutant (PP4C(K21R/K183R)) PP4R3β-containing PP4 complexes was performed. The PP4C(K183R)-PP4R2-PP4R3β complex showed a 2-fold reduction in TRAIP-dependent ubiquitination of PP4C, compared to the wild-type complex (***Figure 4.11*****d-e**), demonstrating that the K183 mutation has a major effect on the fraction of PP4C ubiquitinated by TRAIP *in vitro*. However, PP4C ubiquitination was not abolished completely, suggesting that ubiquitination of other lysine residues of PP4C also contributes to the overall ubiquitination signal. Surprisingly, the double mutant PP4C(K21R/K183R)-PP4R2-PP4R3β did not exacerbate the observed ubiquitination defect (***Figure 4.11*****d-e**). While this observation could suggest that instead of potentiating the effect of K183R, the K21R substitution ameliorates it, the reduction is not significantly different from the single mutant PP4C(K183R) (***Figure 4.11*****e**).

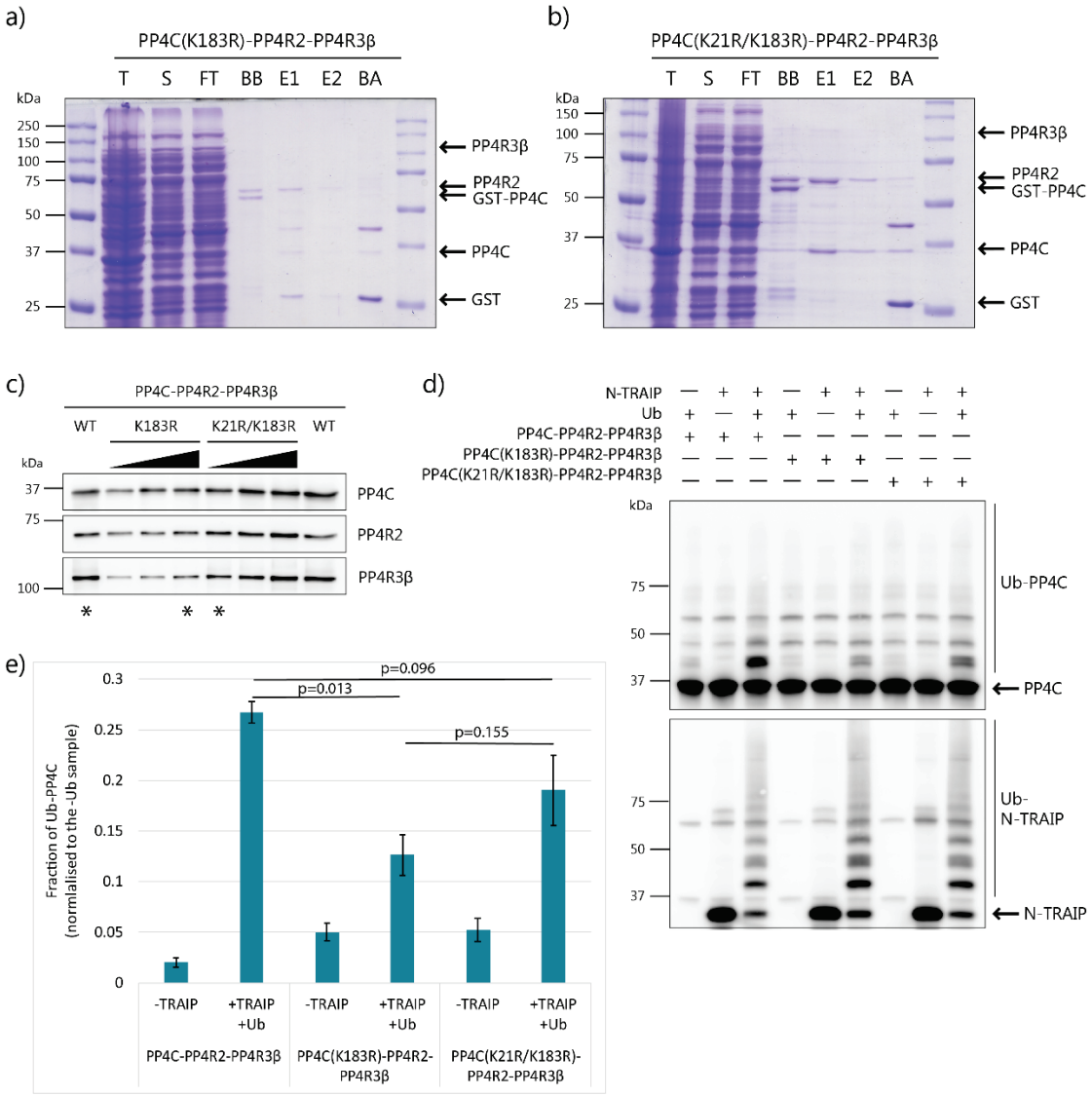

Figure 4.11. TRAIP-dependent *in vitro* ubiquitination of the ternary PP4C-PP4R2-PP4R3β complex with wild-type, K183 and K21R/K183R PP4C identifies K183 as a TRAIP target.

a, b) Coomassie-stained protein gels showing purification of the recombinant ternary PP4C(K183R)-PP4R2-PP4R3β (a) and PP4C(K21R/K183R)-PP4R2-PP4R3β (b) complexes. Key steps of protein purification are shown: T = total protein, S = soluble fraction, FT = flow-through, BB = beads before PS cleavage, E1 = eluate, E2 = second eluate / wash, BA = beads after PS cleavage. Eluate fractions were collected and used as substrates in the *in vitro* ubiquitination reactions. Bands corresponding to the known sizes of GST, PP4C, GST-PP4C, PP4R2 and PP4R3β are indicated.

c) Immunoblot showing the presence of all three PP4 subunits within the eluate fractions of the recombinant PP4C(K183R)-PP4R2-PP4R3β and PP4C(K21R/K183R)-PP4R2-PP4R3β complexes. Immunoblotting analysis was conducted using anti-PP4C, anti-PP4R2 and anti-PP4R3β antibodies. Stars below indicate the amounts of each WT and mutant complex that were used for *in vitro* ubiquitination assays.

d) Representative immunoblot (n=2 independent experiments) showing reduced TRAIP-mediated *in vitro* ubiquitination of PP4C(K183R)-PP4R2-PP4R3β compared to the WT PP4C-PP4R2-PP4R3β complex. Ubiquitin (Ub) and the recombinant ternary wild-type or mutant PP4 complexes (PP4C-PP4R2-PP4R3β, PP4C(K183R)-PP4R2-PP4R3β and PP4C(K21R/K183R)-PP4R2-PP4R3β) were incubated in the presence of the recombinant N-terminal part of TRAIP (N-

TRAIP). All ubiquitination reactions were supplemented with ATP, as well as E1 and E2 enzymes, and incubated for 3 h at 37˚C. Reactions were stopped by adding sample loading buffer and analysed by immunoblotting with anti-PP4C and anti-TRAIP antibodies.
e) Image analysis to compare PP4C ubiquitination of wild-type and mutant PP4 complexes was performed using Fiji/ImageJ software. For ubiquitination analysis, the background signal intensity, defined as signal detected in the lanes without ubiquitin (–Ub), was subtracted from the lanes that contained ubiquitin (+Ub) after the ratio of Ub-PP4C/total PP4C was calculated. '-TRAIP' samples represent control conditions lacking TRAIP but containing all other components of the *in vitro* ubiquitination reaction, including ubiquitin. Results (mean ± SD) from n=2 independent experiments are shown; statistics: unpaired two-tailed t-test.

One of the possible explanations for this result is that differential levels of PP4R3β, which was predicted by MS to mediate TRAIP-PP4 interaction (***Figure 4.1***), may impact on PP4C ubiquitination. As the PP4 complexes used in the *in vitro* ubiquitination reactions did not have 1:1:1 stoichiometry, optimisation of PP4C levels between the wild-type and mutant complexes required compromising on the levels of regulatory subunits. Thus, different amounts of PP4R3β were present in ubiquitination reactions analysed in this section (see ***Figure 4.11*****c**), with the lowest PP4R3β levels in the PP4C(K183R)-PP4R2-PP4R3β complex, for which the weakest TRAIP-dependent ubiquitination was observed. Alternatively, it is plausible that the structural changes within PP4C due to the introduced K21R mutation may cause conformational changes and promote surface exposure of buried lysine residues, which would not be ubiquitinated due to their position in the wild-type PP4C. In other words, the double K21R/K183R mutation within PP4C may destabilise the protein, resulting in the unveiling of additional ubiquitinatable lysine residues.

Overall, these data suggest that lysine residue 183 (K183) of PP4C is a major TRAIP target *in vitro*. The role of K21 residue was not determined with certainty, as the PP4C(K21R/K183R) mutant was ubiquitinated by TRAIP more efficiently, but not significantly so, than the single K183R mutant. In the future, the importance of K21 residue can be assessed by testing wild-type, PP4C(K183) and PP4C(K21R/K183R) monomers for TRAIP-dependent ubiquitination *in vitro*, in the absence of the regulatory PP4 subunits. Furthermore, to confirm these *in vitro* findings, the K183 and K21 residues of PP4C will need to be to be tested in cellular ubiquitination assays and *in vivo* experiments.

4.7. Summary and discussion: PP4 as a substrate of TRAIP

In this chapter, *in vitro* analysis of the E3 ligase activity of TRAIP on protein phosphatase 4 (PP4) complexes was described. The conducted experiments demonstrated the TRAIP-mediated *in vitro* ubiquitination of the catalytic PP4 subunit, PP4C, as well as the regulatory PP4 subunits PP4R3β and PP4R3α. Additionally, the MS analysis of ubiquitination sites of PP4 complex subunits identified seven lysine residues of PP4C, PP4R3β and PP4R3α, whose ubiquitination was highly enriched in the presence of TRAIP *in vitro*. Finally, subsequent *in vitro* experiments indicated the importance of lysine 183 (K183) of PP4C for TRAIP-mediated ubiquitination *in vitro*.

Overall, the experimental work described in this chapter shows the interaction between TRAIP and PP4 complex, as well as its TRAIP-mediated ubiquitination, a relationship that could be relevant to a regulatory role *in vivo*. My initial hypothesis was that TRAIP ubiquitinates PP4 complex in a time-dependent manner in response to DNA damage, leading to the negative regulation of PP4 to maintain phosphorylation of the DNA damage markers RPA2 and H2AX. Upon degradation of TRAIP, the DDR-mediating accumulation of pRPA2 and γH2AX would be dissipated, contributing to the resolution of the DNA damage. Although the TRAIP-dependent ubiquitination of several PP4 subunits was observed *in vitro*, the ubiquitination analyses described in this chapter have technical limitations that make it difficult to confirm this model.

Firstly, only a small increase in TRAIP-mediated PP4C ubiquitination was observed in the presence of the regulatory subunits PP4R3β and PP4R3α, compared to the monomeric PP4C (***Figure 4.6***). However, considering that TRAIP-PP4 interaction is mediated by PP4R3α/β, as suggested by MS, and that only a small amount of heterotrimeric PP4R3α/β-containing PP4 complex is present in the eluates analysed, this result may still be meaningful. Further *in vitro* ubiquitination analyses using ternary PP4 complexes with the optimal 1:1:1 stoichiometry will need to be performed to establish the role of PP4R3β and PP4R3α in promoting TRAIP-mediated PP4C ubiquitination. To overcome solubility issues posed by purification of individual PP4 complex subunits, particularly PP4R3β, C-terminal tagging of PP4R3β and PP4R3α in the co-expression vector may be employed in addition to the N-terminal tagging of PP4C to increase the ratio of the heterotrimeric complex. To achieve a defined stoichiometry of subunits, Frey and Görlich (2014) suggest using orthogonal affinity tags and protease cleavage

sites, followed by successive rounds of affinity capture and proteolytic release, thus ensuring the presence of each tagged subunit individually.

Secondly, *in vitro* ubiquitination reaction conditions may need to be adjusted to better delineate the role of the regulatory subunits PP4R3β and PP4R3α, as well as of the lysine residues of PP4 complex identified by MS (Section 4.5), for the TRAIP-PP4 interaction. RING domain E3 ligases, such as TRAIP, do not form a covalent ligase-ubiquitin intermediate but rather facilitate the direct transfer of ubiquitin from the E2 to the target protein (Deshaies and Joazeiro, 2009) and are not strictly required for non-specific ubiquitination to occur (David *et al*., 2011). Thus, the excessive amount of the E1 and E2 enzymes in the *in vitro* ubiquitination reactions may have resulted in the strong background signal observed in the immunoblots even in the absence of TRAIP or ubiquitin. This could have also led to the non-specific multi-mono-ubiquitination instead of specific and physiologically relevant poly-ubiquitination. Therefore, precise quantification of functional E1 and E2 concentrations and additional controls in the *in vitro* ubiquitination reactions, such as reactions set up in the absence of E2 and ATP, could facilitate detection of specific TRAIP-mediated PP4 ubiquitination (Ronchi and Haas, 2012). Finally, the incubation time of the ubiquitination reaction may need to be optimised by measuring the rate of pyrophosphate production to reduce the risk of reaction saturation and ensure sensitivity of the assay (Berndsen and Wolberger, 2011).

Using the full-length TRAIP, rather than the N-terminal TRAIP, in the *in vitro* ubiquitination reactions may have provided a better insight into the ability of TRAIP to mediate ubiquitination of PP4 complex. As recombinant full-length TRAIP was found to be insoluble in bacterial cells (M. Harley, unpublished data), other methods to generate it could be employed, such as baculovirus–insect cell expression system, routinely used for recombinant protein production (Kost *et al.*, 2005; Kost and Condreay, 1999).

As the UbcH5 class of E2 ubiquitin-conjugating enzymes was shown to be required for TRAIP auto-ubiquitination *in vitro* (Besse *et al.*, 2007), I used the E2 enzyme UbcH5b/UBE2D2 in my *in vitro* ubiquitination reactions. As humans have 38 distinct E2 enzymes (Deshaies and Joazeiro, 2009), and the identity of the E2 enzyme is important for determining the type of ubiquitination produced by RING E3 ligases (Christensen *et al.*, 2007; Windheim *et al.*, 2008), it is plausible that different E2 enzymes are necessary to potentiate TRAIP-dependent ubiquitination of PP4 complex. Moreover, additional cellular factors that were not present in the *in vitro* ubiquitination reactions may be needed to assist TRAIP-dependent ubiquitination

of PP4 complex. For example, RING domain activity of BRCA1 was shown to increase dramatically upon binding the RING domain of BARD1 (Hashizume *et al.*, 2001).

My *in vitro* experiments did not model the presence of DNA damage either, providing limited indication whether the observed interaction between TRAIP and PP4 is enhanced in the presence of a DNA damaging agent. Protein phosphorylation-driven DDR signalling, mediated by PIKK kinases ATR, ATM and DNA-PK (Blackford and Jackson, 2017), may be required to facilitate TRAIP-PP4 interaction *in vivo*, making other *in vitro* systems, such as *Xenopus laevis* cell-free egg extracts, more suitable for modelling TRAIP-mediated PP4 ubiquitination in the context of DDR and the cell cycle (Garner and Costanzo, 2009).

In my *in vitro* experiments, no significant differences between TRAIP-dependent ubiquitination of PP4R3α- and PP4R3β-containing PP4 complexes was observed. As only the PP4R3β-containing PP4 complex was implicated in DDR signalling (Chowdhury *et al.*, 2008; Lee *et al.*, 2010; Nakada *et al.*, 2008), it suggests that the interaction between TRAIP and PP4 and TRAIP-mediated PP4 ubiquitination may not be relevant to the DDR function of TRAIP. Due to their artificial nature, the *in vitro* studies can only give indication of the events *in vivo*, and cell-based analyses are required to establish the importance of the obtained results. Thus, cellular ubiquitination assays using a tagged full-length TRAIP will be necessary to confirm the impact of the lysine mutations on the TRAIP-dependent ubiquitination of PP4 complex subunits, as well as to test the significance of TRAIP-PP4 interaction for DNA repair.

Meanwhile, I decided to prioritise experimental work aimed at generating a TRAIP knockout cell line (Chapter 5). Instead of focusing on a single candidate-based investigation, this allowed me to address the more general questions regarding the TRAIP role in DDR, as well as the possibility of TRAIP promoting DDR signalling via a different mechanism (Chapter 6).

Chapter 5

Generation and characterisation of a TRAIP-KO cell line

5. Generation and characterisation of a TRAIP-KO cell line

When the laboratory of Andrew Jackson demonstrated that biallelic mutations in *TRAIP* cause microcephalic primordial dwarfism (MPD) (Harley *et al.*, 2016), not much was known about the cellular functions of TRAIP, aside from its role in regulating TRAF2-mediated NF-κB activation (Lee *et al.*, 1997), its ability to auto-ubiquitinate through its RING-dependent E3 ubiquitin ligase activity (Besse *et al.*, 2007) and its involvement in TBK1 ubiquitination to mediate antiviral responses (Zhang *et al.*, 2012). Using TRAIP patient-derived cell lines and TRAIP-depleted HeLa cells, Harley *et al.* (2016) established that TRAIP is required for efficient DDR signalling in response to UV-C irradiation. Consistent with these findings, three other studies demonstrated the involvement of TRAIP in the cellular response to other types of DNA damage (Hoffmann *et al.*, 2016; Soo Lee *et al.*, 2016; W. Feng *et al.*, 2016). However, the molecular mechanisms underlying the role of TRAIP as a novel DDR signalling factor and its causative link to human disease still remained elusive.

All of the recent studies addressing the role of TRAIP in DDR and DNA repair used either hypomorphic patient-derived cell lines (Harley *et al.*, 2016) or siRNA-mediated depletion of TRAIP in a cancer cell line (Harley *et al.*, 2016; Hoffmann *et al.*, 2016; Soo Lee *et al.*, 2016; W. Feng *et al.*, 2016). However, it is plausible that residual TRAIP present in all these cell systems has an impact on the observed phenotypes, i.e. complete absence of TRAIP may show more severe and/or different phenotypes, relevant to its biological functions. Therefore, one of the aims of my PhD project was to study the consequences of complete TRAIP ablation on cellular phenotypes, particularly on maintenance of genome stability, both in unperturbed conditions and in response to DNA damage. Additionally, my aim was to address whether TRAIP is essential for cell viability.

In this chapter, the generation of TRAIP knockout (KO) cell lines using CRISPR/Cas9-mediated genome editing is described. Moreover, detailed characterisation of the TRAIP-KO cell lines is reported, using genotyping, analysis of TRAIP protein expression by immunoblotting and karyotyping. Finally, I present and discuss the analysis of DNA damage signalling in TRAIP-KO cells upon exposure to genotoxic agents. Overall, this chapter provides comprehensive analysis and characterisation of the cellular system that was used for further experimental work described in Chapter 6.

5.1. CRISPR/Cas9-mediated targeting of *TRAIP* in human cell lines

To elucidate the cellular functions of TRAIP in DDR, I designed a CRISPR/Cas9-mediated editing strategy to generate a TRAIP knockout (KO) cell line. Such a TRAIP-KO cell line would be a valuable tool for investigating the roles of TRAIP both in unperturbed conditions and in response to DNA damage, for the following reasons. Firstly, a TRAIP-KO cell line generated in parallel with a WT cell line that was not targeted but underwent clonal expansion would constitute an isogenic system, allowing me to study phenotypes specific to TRAIP loss. Secondly, well-characterised fast proliferating human cell lines, such as RPE1 or HeLa, are more suitable for cell biology experiments than the slow-dividing TRAIP patient fibroblast cell lines. Lastly, a TRAIP-KO cell line would enable us to perform CRISPR/Cas9 genome-wide screens. A dropout viability screen with TRAIP-KO could elucidate cellular pathways, loss of which is synthetic lethal with TRAIP deficiency, whereas suppressor screen could potentially identify genetic interactors and substrates of TRAIP.

Three human cell lines were used for the editing experiment: a near-diploid hTERT-immortalised retinal pigmented epithelium cell line RPE1; hTERT-immortalised RPE1 p53-/-; and the HeLa cervical carcinoma cell line, all well-characterised and frequently used for DDR studies. RPE1 p53-/- and HeLa cell lines stably expressed FLAG-Cas9 to facilitate gene targeting. Also, stable Cas9 expression would be beneficial for use of resulting TRAIP-KO cells in genome-wide CRISPR/Cas9 screens. Two guide RNAs (gRNAs) were designed to target exon 1 of *TRAIP*, which encodes a large part of the RING domain (***Figure 5.1***). I chose to target this domain as it is essential for catalytic activity, and abolishing E3 ligase activity of TRAIP should render it unable to perform its cellular functions. In addition, disruption of the first exon is more likely to disrupt protein expression altogether. It is likely to result in a premature stop codon, followed by degradation of the mutant transcript through NMD pathway (Hug *et al.*, 2016). The gRNAs were selected based on their evaluations by CRISPR Design Tool (Feng Zhang lab; http://crispr.mit.edu/) and the CRISPR gRNA Design Tool DNA2.0 (now ATUM) and cloned into the pX458 vector, encoding wild-type GFP-tagged Cas9. For *TRAIP* targeting, two gRNAs were simultaneously introduced into each of the cell lines to enhance the probability of the Cas9-mediated cutting and the introduction of indels. GFP-positive cells were subsequently sorted into individual wells of a 96-well plate and grown for 1-2 weeks until they formed colonies that were subsequently screened for targeting.

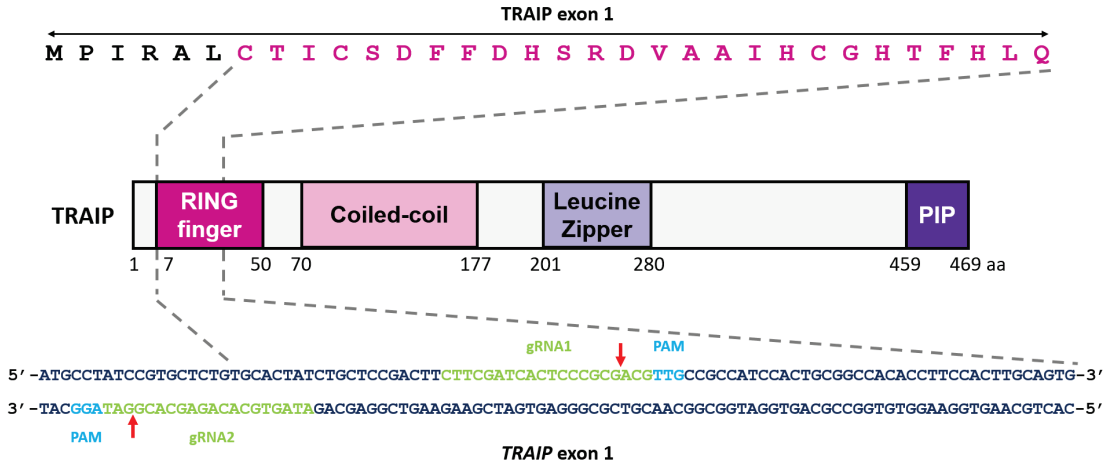

Figure 5.1. Targeting *TRAIP* exon 1, encoding the N-terminal portion of the RING domain, by CRISPR/Cas9 genome editing.

A schematic structure of TRAIP protein with a focus on its exon 1 (amino acid (above) and genomic (below) sequences). The four distinct domains of TRAIP are indicated (PIP = PCNA-interacting protein box motif). The 20 nt-long genomic sequences targeted by gRNAs in exon 1 of *TRAIP* are highlighted in green; 3 nt-long PAM sites are shown in blue. Red arrows point to the predicted incision sites of Cas9.

5.2. Genotypes and TRAIP protein levels of CRISPR clones

CRISPR/Cas9 targeting efficiency in all three cell lines was evaluated at several stages. Firstly, transfection efficiency was estimated during the GFP-FACS single cell sorting procedure. Secondly, some of the GFP-positive cells (200-400 cells) were sorted into individual wells for clonal outgrowth; the rest of the GFP-positive cell pool was used for crude genomic DNA extraction and PCR analysis to determine the presence of indels, as an indicator of successful targeting. Finally, established CRISPR clones were analysed using the same protocol to quantify targeting efficiency and to identify a set of candidate TRAIP-KO and WT clones. Several were selected for each cell line and subsequently analysed by Sanger sequencing and/or immunoblotting to determine which genomic alterations were present and their consequences on TRAIP protein levels.

Good CRISPR/Cas9 transfection efficiency was achieved in RPE1 and RPE1 p53-/- cell lines, where 65% and 70% of cells, respectively, were GFP-positive, indicating successful introduction of gRNAs into cells. The PCR analysis of GFP-positive cells revealed that both RPE1 and RPE1 p53-/- cell lines were targeted, leading to introduction of indels of various sizes in exon 1 of *TRAIP* (***Figure 5.2*****a**). However, only 2 out of 288 (0.7%) GFP-FACS-sorted single *TRAIP* CRISPR RPE1 cells survived and formed clones, both of which turned out to be wild-type upon Sanger sequencing of the targeted locus (***Table 5.1***). Meanwhile, 125 out of 384 (33%) single-sorted RPE1 p53-/- cells formed colonies. 55 of these clones were screened for editing at the targeted *TRAIP* locus by PCR. The majority of analysed clones displayed PCR products of different sizes compared to the parental cell line, and Sanger sequencing analysis confirmed editing at the *TRAIP* locus (***Figure 5.2*****b, *Table 5.1***). Eight successfully edited RPE1 p53-/- clonal cell lines were selected for further analysis. Firstly, their genotypes were determined by sub-cloning of the PCR products, followed by Sanger sequencing. This revealed that a single large deletion frequently occurred at the targeted locus, which in all cases analysed was predicted to lead to a premature stop codon in the 5' end of *TRAIP* exon 2 and protein truncation (***Table 5.2***). Immunoblotting analysis was subsequently performed to evaluate the effect of the indels on TRAIP protein levels. Clonal cell lines selected for immunoblotting showed a strong reduction in TRAIP protein levels with almost undetectable TRAIP levels in the majority of the cell lines tested (***Figure 5.2*****c**). In summary, TRAIP was successfully knocked-out in RPE1 p53-/- cells, producing multiple clonal cell lines lacking TRAIP that can be used for studying its cellular roles. My results targeting *TRAIP* in RPE1 and RPE1 p53-/- cells suggest that TRAIP-KO cells may only viable, or able to form colonies and proliferate, on a *TP53*-deficient background.

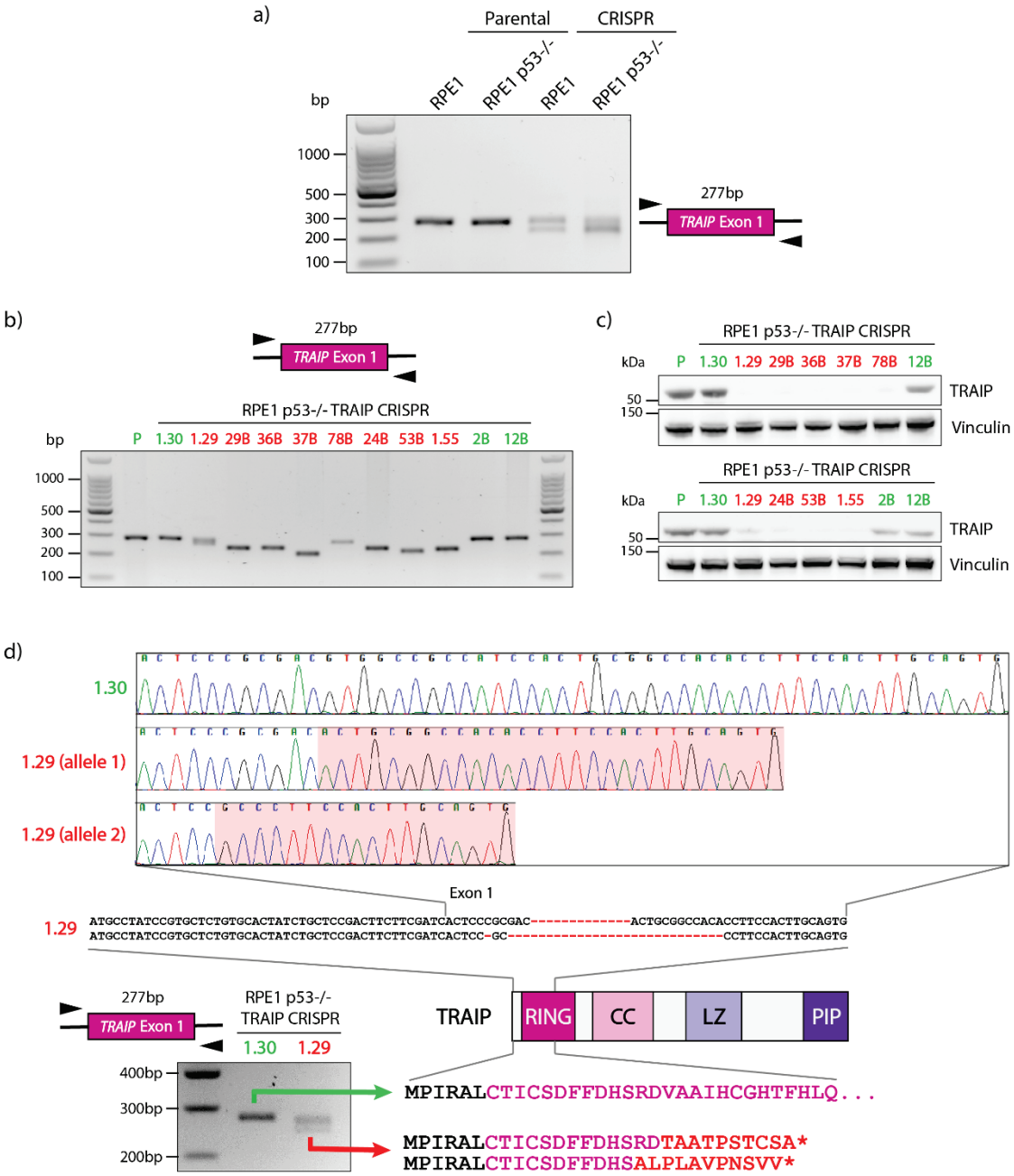

Figure 5.2. Targeting of *TRAIP* exon 1 in RPE1 and RPE1 p53-/- cells by CRISPR/Cas9 genome editing.

a) PCR analysis of CRISPR/Cas9-targeted GFP-positive RPE1 and RPE1 p53-/- cells indicates the presence of indels in *TRAIP* exon 1. Genomic DNA was isolated from untransfected (Parental) and FACS-sorted CRISPR/Cas9-targeted GFP-positive (CRISPR) RPE1 and RPE1 p53-/- cells. PCR amplification of the 277 bp product encompassing exon 1 of *TRAIP* and exon-intron junctions was carried out to screen for CRISPR/Cas9-mediated targeting of *TRAIP* (black arrowheads indicate the positions of primers used for screening). The presence of targeted alleles was visualised on 2% agarose gel.

b) PCR analysis of CRISPR/Cas9 edited RPE1 p53-/- clonal cell lines indicates the presence of indels in *TRAIP* exon 1. Agarose gel represents PCR screening of the targeted *TRAIP* locus (277 bp product encompassing exon 1 of *TRAIP* and exon-intron junctions) in a few of the analysed clonal cell lines. Genomic DNA was extracted from untransfected (Parental, P) and clonal (indicated by numbers and letters) RPE1 p53-/- cells. Primers used for PCR amplification are

indicated by black arrowheads. Clones with biallelic targeting of *TRAIP* confirmed by Sanger sequencing are shown in red; clones confirmed to be wild-type for *TRAIP* are shown in green.
c) Immunoblotting of RPE1 p53-/- TRAIP CRISPR clonal cell lines showing several targeted clones with strongly reduced TRAIP protein levels. The expanded clones (targeted clones shown in red; wild-type clones shown in green) were harvested for immunoblotting with affinity-purified rabbit anti-TRAIP antibody raised against recombinant TRAIP protein (Harley *et al.*, 2016). Vinculin served as a loading control.
d) Both alleles of *TRAIP* are disrupted in the RPE1 p53-/- TRAIP CRISPR clone 1.29. PCR amplification, agarose gel analysis and Sanger sequencing of the clone 1.29 demonstrate biallelic editing, in contrast to the wild-type clonal cell line 1.30. Clone 1.29 is compound heterozygous for two deletions within *TRAIP* exon 1 (c.58_70del (Allele 1) and c.52del+c.55_82del (Allele 2)), resulting in a biallelic genomic disruption of the catalytic RING domain as determined by Sanger sequencing. Both mutant alleles are predicted to lead to a frameshift and an introduction of a premature stop codon, likely resulting in the NMD of the mutant transcript.

Table 5.1. Efficiency of targeting *TRAIP* exon 1 by CRISPR/Cas9 genome editing in different cell lines.
N/A = non-applicable (HeLa cells were not sorted by FACS).

Cell line	Transfection efficiency estimated by FACS (%)	Successful pool targeting (+/-)	Clone survival after FACS (%)	Targeted clones (%)	Null clones confirmed
RPE1	65	+	0.7% (2/288)	0% (0/2) (Sanger sequencing)	0/0
RPE1 p53-/-	70	+	32.6% (125/384)	72.7% (40/55) (Sanger sequencing)	8/8
HeLa	N/A	+	N/A	24.5% (13/53) (PCR analysis)	0/4

Table 5.2. The genotypes of RPE1 p53-/- TRAIP CRISPR clones and predicted consequences on TRAIP protein.
A star (*) indicates a premature stop codon; hom = homozygous; aa = amino acids; NMD = nonsense-mediated decay.

Clone #	Mutation(s)	Predicted TRAIP protein	Predicted TRAIP status
2B	None	469 aa	WT
12B	None	469 aa	WT
1.30	None	469 aa	WT
24B	c.10_55del (46 bp deletion) (Hom)	18 aa (MPITWPPSTAATPSTCSA*)	NMD
29B	c.10_55del (46 bp deletion) (Hom)	18 aa (MPITWPPSTAATPSTCSA*)	NMD
36B	c.12_55del (44 bp deletion) (Hom)	23 aa (MPIRRGRHPLRPHLPLAVPNSVV*)	NMD
37B	c.5_75del (71 bp deletion) (Hom)	14 aa (MRPHLPLAVPNSVV*)	NMD

Clone #	Mutation(s)	Predicted TRAIP protein	Predicted TRAIP status
53B	c.10_14del (5 bp deletion) + c.33_58del (26 bp deletion) + c.61_91del (31 bp deletion) (Hom)	17 aa (MPISVHYLLCAVPNSVV*)	NMD
78B	c.27_40del (14 bp deletion) (Hom)	33 aa (MPIRALCTIRSLPRRGRHPLRPHLPLAVPNSVV*)	NMD
1.29	c.58_70del (13 bp deletion) (Allele 1); c.52del (1 bp deletion) + c.55_82del (28 bp deletion) (Allele 2)	29 aa (MPIRALCTICSDFFDHSRDTAATPSTCSA*); 28 aa (MPIRALCTICSDFFDHSALPLAVPNSVV*)	NMD
1.55	insA (1bp insertion after c.50) + c.51_86 (36 bp deletion) (Hom)	26 aa (MPIRALCTICSDFFDHSPLAVPNSVV*)	NMD

The *TRAIP* gene was also targeted in HeLa cells in a separate CRISPR/Cas9 experiment to generate a complementary TRAIP-KO cell line that could be used together with RPE1 p53-/- to rule out cell line-specific differences. I noted that FACS-sorting of HeLa cells into individual wells of a 96-well plate negatively affected formation of clonal cell lines, as only approximately 2% of non-transfected or CRISPR/Cas9-transfected FACS-sorted HeLa cells survived. Therefore, CRISPR/Cas9-transfected HeLa cells were plated at low density, grown for two weeks, and replated into individual wells of a 96-well plate by scraping. Successful *TRAIP* targeting in HeLa cells was confirmed by PCR analysis of transfected cell pool (***Figure 5.3*****a**). PCR analysis of 53 clonal cell lines showed that 40 were apparently not targeted (single band of the same size as detected in the parental cell line), while the other 13 displayed multiple bands of different sizes (in most cases, three bands could be resolved using >2% agarose gels) (***Figure 5.3*****b**, ***Table 5.1***). As HeLa cells are hypertriploid (Landry *et al.*, 2013), it is not surprising that three alleles of *TRAIP* could be seen by PCR analysis. Eight clonal cell lines (4 apparently wild-type and 4 targeted) were selected for further analysis by Sanger sequencing and immunoblotting. The HeLa clones that displayed a single band in PCR analysis were confirmed to be wild-type. In the targeted HeLa clonal cell lines analysed by Sanger sequencing, double or triple electropherograms were observed, showing that one or two out of three alleles of *TRAIP* had indels at the targeted *TRAIP* locus, while at least one allele remained wild-type. Subcloning and Sanger sequencing of separate alleles of the four clonal cell lines confirmed this observation (***Table 5.3***). Immunoblotting analysis revealed reduced TRAIP protein levels for the targeted clonal cell lines #10 and #23 (***Figure 5.3*****c**). However, cell line #15, which has the same genotype as cell line #23, displayed only a modest reduction in TRAIP protein levels, suggesting that the

two cell lines have different levels of expression of the same alleles. In summary, disruption of two out of three alleles of *TRAIP* in HeLa cells has an effect on TRAIP protein levels, but it seems to be influenced by non-genetic factors as well (***Figure 5.3c***). *TRAIP* targeting in HeLa cells was efficient but yielded only hypomorphic cell lines, which cannot be used for studying the effects of complete loss of TRAIP.

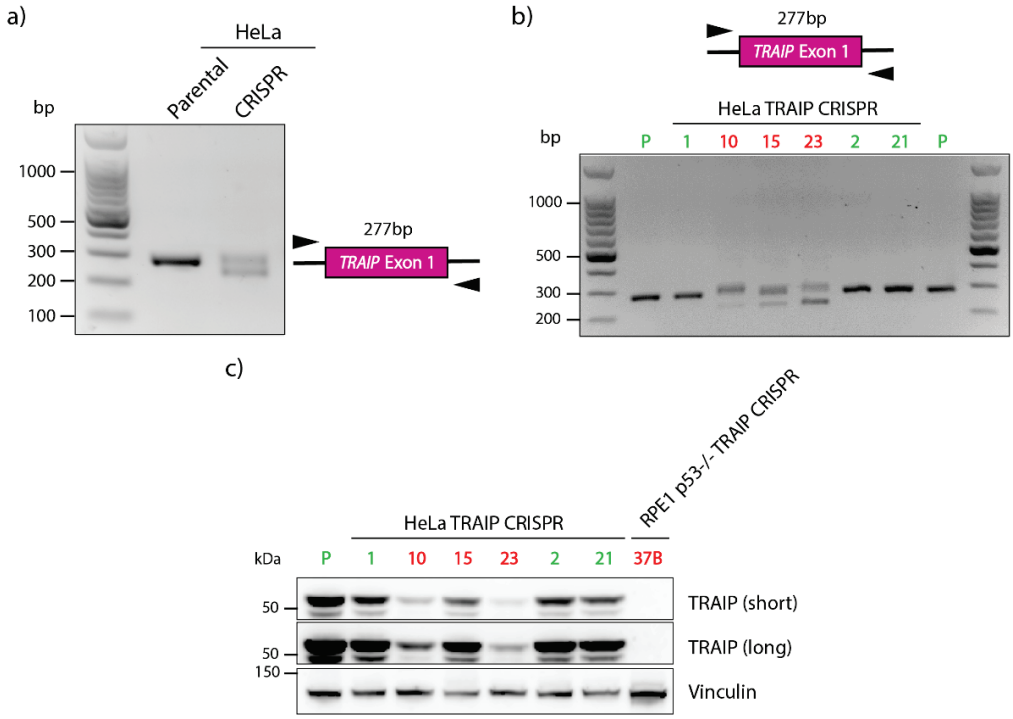

Figure 5.3. Targeting of *TRAIP* exon 1 in HeLa cells by CRISPR/Cas9 genome editing.
a) PCR analysis of CRISPR/Cas9 transfected HeLa cells indicates the presence of indels in *TRAIP* exon 1. Genomic DNA was isolated from untransfected (Parental) and CRISPR/Cas9-targeted (CRISPR) HeLa cells. PCR amplification of the 277 bp product encompassing exon 1 of *TRAIP* and exon-intron junctions was carried out to screen for CRISPR/Cas9-mediated targeting of *TRAIP* (black arrowheads indicate the positions of primers used for screening). The presence of targeted alleles was visualised on a 2% agarose gel.
b) PCR analysis of CRISPR/Cas9 edited HeLa clonal cell lines indicates the presence of indels in *TRAIP* exon 1. Agarose gel represents PCR screening of the targeted *TRAIP* locus (277 bp product encompassing exon 1 of *TRAIP* and exon-intron junctions) from selected clonal cell lines analysed. Genomic DNA was extracted from untransfected (Parental, P) and clonal (indicated by numbers) HeLa cells. Primers used for PCR amplification are indicated by black arrowheads. Clones with targeting of *TRAIP* confirmed by Sanger sequencing are shown in red; clones confirmed to be wild-type for *TRAIP* are shown in green.
c) Immunoblotting of HeLa TRAIP CRISPR clonal cell lines showing several targeted clones with reduced TRAIP protein levels. The expanded clones (targeted clones shown in red; wild-type clones shown in green) were harvested for immunoblotting with affinity-purified rabbit anti-TRAIP antibody raised against recombinant TRAIP protein (Harley *et al.*, 2016). Vinculin served as a loading control. An RPE1 p53-/- TRAIP CRISPR cell line (37B) was used as a knockout (KO) control to demonstrate that TRAIP protein levels in the hypomorphic HeLa CRISPR cell lines are higher than in the RPE1 p53-/- TRAIP-KO cells.

Table 5.3. The genotypes of HeLa TRAIP CRISPR clones and predicted consequences on TRAIP protein.
A star (*) indicates a premature stop codon; aa = amino acids.

Clone #	Mutation(s)	Predicted TRAIP protein
1	None	469 aa
2	None	469 aa
21	None	469 aa
22	None	469 aa
10	Allele 1: none Allele 2: c.56_73del (18 bp deletion) + c.12_40dup (29 bp insertion of duplicated sequence) Allele 3: c.10_55del (46 bp deletion)	Allele 1: 469 aa Allele 2: 37 aa (MPIRALCTICSDFFDHSRVLCALSAPTSAATPSTCSA*) Allele 3: 18 aa (MPITWPPSTAATPSTCSA*)
13	Allele 1: none Allele 2: c.11_55del (45 bp deletion)	Allele 1: 469 aa Allele 2: 454 aa (16 aa deletion (R4-D19) and 1 aa insertion (H4))
15	Allele 1: none Allele 2: c.11_55del (45 bp deletion) Allele 3: c.10_55del (46 bp deletion)	Allele 1: 469 aa Allele 2: 454 aa (16 aa deletion (R4-D19) and 1 aa insertion (H4)) Allele 3: 18 aa (MPITWPPSTAATPSTCSA*)
23	Allele 1: none Allele 2: c.11_55del (45 bp deletion) Allele 3: c.10_55del (46 bp deletion)	Allele 1: 469 aa Allele 2: 454 aa (16 aa deletion (R4-D19) and 1 aa insertion (H4)) Allele 3: 18 aa (MPITWPPSTAATPSTCSA*)

The data obtained during these CRISPR/Cas9 targeting experiments suggest a correlation between the p53 status of a cell line and the efficiency with which a TRAIP-KO can be generated in that background. Given the genome instability observed in TRAIP-deficient cells (see Section 5.3), it is plausible that p53-proficient cells undergo a p53-mediated cell cycle arrest and apoptosis following TRAIP knockout. Indeed, hTERT-immortalised RPE1 cell line has two fully proficient copies of the *TP53* gene, which may have prevented the cells with biallelically disrupted *TRAIP* from surviving and proliferating. At the same time, the lack of RPE1 clones heterozygous for indels in *TRAIP* could be explained by the high editing efficiency in targeted cells, as none of such clones were found on the RPE1 p53-/- background either. Similar to RPE1 cells, no TRAIP-KO clones were established in HeLa cells, but several TRAIP hypomorphic clones were generated. It was previously reported that p53 protein levels in HeLa cells are low, as E6 protein expressed by an endogenous human papilloma virus (HPV) ubiquitinates p53, targeting it for proteasomal degradation (Scheffner *et al.*, 1990). Moreover, apoptosis in HeLa is also attenuated by HPV E7 oncoprotein that binds to retinoblastoma tumour suppressor protein and limits its ability to control cell division (Darnell *et al.*, 2007; Goodwin and DiMaio, 2000). However, even low levels of p53 may be sufficient to prevent

proliferation in HeLa cells following TRAIP disruption, which could explain why only hypomorphic cells survived. In summary, a complete KO of *TRAIP* was achieved solely in RPE1 p53-/- cells that are genetically null for *TP53*. These results therefore imply that TRAIP is essential for cell viability unless *TP53* is disrupted, and that the lack of proliferation of TRAIP-KO cells is mediated by p53. In the future, an attempt to generate a KO of *TRAIP* in another pair of isogenic cell lines that differ in p53 status only could provide further validation for this hypothesis.

To study the cellular consequences of TRAIP absence, an isogenic pair of TRAIP-KO and WT CRISPR clones in the RPE1 p53-/- background were selected for further analysis. RPE1 p53-/- TRAIP clone 1.29 with biallelic deletions resulting in a premature stop codon in each allele, which is predicted to lead to transcript degradation through NMD (***Figure 5.2*****d**), was chosen as the TRAIP-KO cell line. RPE1 p53-/- clone 1.30, confirmed to be wild-type for *TRAIP* by Sanger sequencing, was selected as a control cell line that underwent single cell sorting and clonal expansion in parallel to the TRAIP-KO clone (***Figure 5.2*****d**).

5.3. Genomic instability in TRAIP-KO cell lines

Various proteins associated with replication fork and involved in DDR signalling contribute to protection of cells from DNA damage and genomic instability by recruiting DNA repair factors to sites of damage, activating cell cycle checkpoints, or, if damage is unrepaired, by triggering apoptosis (see Section 1.3). Genomic instability is a hallmark of cancer, where inactivating mutations in DDR factors are frequently associated with tumour initiation and progression (Broustas and Lieberman, 2014). It has been demonstrated that the absence of functional DDR factors, such as BLM and FA proteins, that occurs in cancer-predisposing syndromes leads to increased levels of genomic instability and loss of heterozygosity, which may facilitate tumour formation (Moldovan and D'Andrea, 2009; Traverso *et al.*, 2003).

TRAIP was previously identified by several research groups, including our laboratory, as a protein associated with stalled replication forks and required for efficient DDR signalling after cell exposure to various exogenous DNA damaging agents, such as UV-C, CPT, MMC and HU (Harley *et al.*, 2016; Hoffmann *et al.*, 2016; Soo Lee *et al.*, 2016; W. Feng *et al.*, 2016). I therefore postulated that cells lacking TRAIP protein may exhibit higher levels of chromosomal rearrangements and abnormal karyotypes, since they lose their ability to promote signalling in response to DNA damage. Indeed, U2OS cells depleted for TRAIP were reported to have increased levels of chromosomal aberrations such as chromatid breaks and radial chromosomes in unperturbed cells and upon exposure to MMC (Hoffmann *et al.*, 2016), as well as following HU treatment (W. Feng *et al.*, 2016). Moreover, both unperturbed and HU-treated TRAIP-depleted cells were more likely to display aberrant mitotic structures, such as misaligned and lagging chromosomes (W. Feng *et al.*, 2016). To examine whether TRAIP is necessary for maintaining genome stability in unperturbed TRAIP-KO cells, karyotype analysis on RPE1 p53-/- TRAIP-KO (clone 1.29) and RPE1 p53-/- parental cells was performed. The cell lines were re-genotyped to confirm their TRAIP status and sent for cytogenetic analysis of their karyotypes at 4-5 passages (approximately 12-15 cell divisions) after their generation. The karyotyping data were obtained by Dr Lin Deng through the Brigham & Women's Hospital CytoGenomics Core Facility (Boston, MA).

In the parental RPE1 p53-/- cell line, chromosome counts in all 20 cells analysed were normal (46 chromosomes), with XX sex chromosomes, which is consistent with a female origin of the original hTERT RPE1 cell line (Potapova *et al.*, 2015). All cells karyotyped (6 of the 20) had the typical derivative X chromosome with additional chromosomal material at the terminal

end of the q-arm, a feature previously reported for these hTERT RPE1 cells (Potapova *et al.*, 2015) (***Table 5.4***, ***Figure 5.4***). Interestingly, no other clonal structural or numerical abnormalities were observed, suggesting that the KO of p53 did not induce gross chromosomal instability in RPE1 cells.

Table 5.4. Cytogenetic analysis of RPE1 p53-/- TRAIP CRISPR clonal cell lines.
Chr = chromosome; p = short arm of a chromosome; q = long arm of a chromosome. Clonal chromosomal abnormalities indicate recurrent karyotypic alterations observed in multiple karyotyped cells, whereas non-clonal rearrangements indicate karyotypic alterations observed in a single karyotyped cell.

Cell line	Karyotype (% of 20 metaphase spreads)			Number of cells karyotyped	Derivative X chromosome of RPE1 cell line	Clonal chromosomal abnormalities	Non-clonal rearrangements
	Diploid	Hypo/hyper-diploid	Hypo-tetraploid				
Parental	100%	0%	0%	6	+	—	—
1.29	10%	55%	35%	14	+	+ (loss of chr18)	+
1.29 + TRAIP-WT	55%		45%	8	+	+ (loss of chr18)	—
24B	80%		20%	8	+	+ (deletions in chr5q)	+
36B	0%	80%	20%	9	+	+ (additional material in chr21p)	+
37B	40%		60%	8	+	+ (additional material in chr21p)	+
78B	0%	40%	60%	7	+	+ (additional material in chr15p)	+

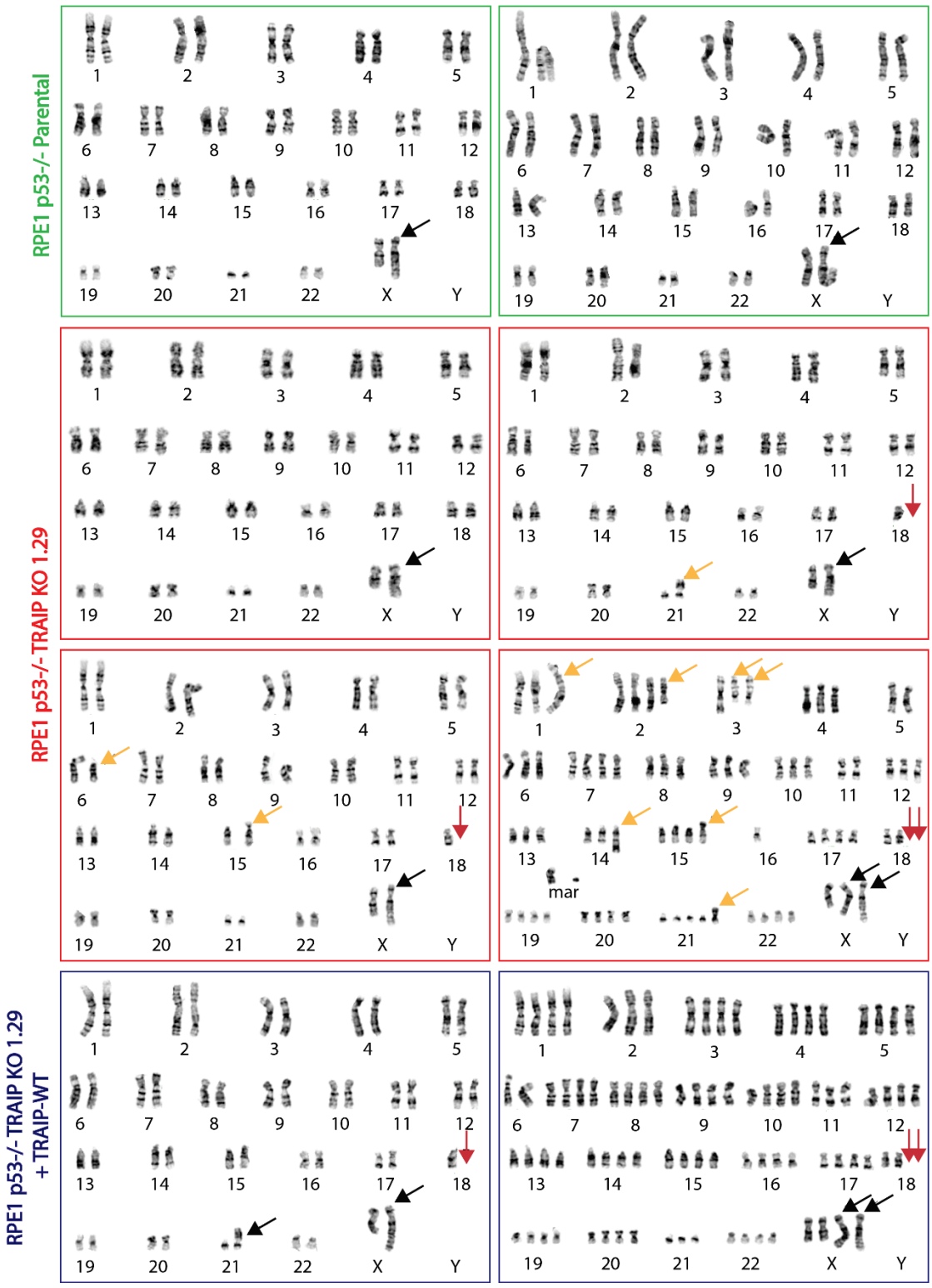

Figure 5.4. Absence of TRAIP in RPE1 p53-/- cell line 1.29 is associated with the increased frequency of gross chromosomal abnormalities in unperturbed cells.
Representative karyotypes of the parental RPE1 p53-/- cells, TRAIP-KO cell line 1.29 and TRAIP-KO cell line 1.29 retrovirally complemented with pMSCV-TRAIP-WT plasmid. Black arrows indicate clonal abnormalities, including the typical derivative X chromosome, observed in hTERT RPE1 cells. Yellow arrows indicate non-clonal abnormalities, and down-facing red arrows indicate clonal loss of chromosome(s) (non-clonal losses are likely to be due to technical

factors). The number of bands observed for all chromosomes in this analysis was 400 or greater. Marker chromosomes (mar) seen in TRAIP-KO cells signify chromosomal fragments that cannot be identified with certainty due to their small size.

In the RPE1 p53-/- TRAIP-KO cell line analysed (1.29), chromosome counts were 46 in 10% (2/20) metaphase spreads, 44-45 in 50% (10/20), 51 in 5% (1/20), 76 in 5% (1/20), and 82-86 in 30% (6/20) spreads (***Table 5.4***). It is unclear whether hypotetraploid TRAIP-KO cells with 76 and 82-86 chromosomes represent actual chromosome losses or random losses due to technical artefacts. Fourteen of the 20 cells were karyotyped, and the cells with 46 chromosomes turned out to be karyotypically normal, containing the typical derivative X chromosome but no additional chromosomal rearrangements. All the other karyotyped cells had one or two copies of the typical derivative X chromosome of the parental RPE1 cell line, as well as additional structural and/or numerical abnormalities (***Figure 5.4***). A clonal loss of chromosome 18 was observed: all karyotyped cells with counts of 44-45 were missing one copy of it, and all karyotyped hypotetraploid cells were missing two copies, consistent with being derived from a doubling of the hypodiploid clone lacking chromosome 18. Additional clonal chromosome losses may have been present in the hypotetraploid sub-clone, however, the quality of the metaphases did not permit complete identification of all chromosome aberrations at this level of analysis. Four of the 10 hypodiploid cells contained one or two structural changes, including deletions, additions of unknown material and a balanced translocation, which were apparently non-clonal in this analysis. The hypotetraploid cells contained 3-9 structural rearrangements, all apparently non-clonal in this analysis as well. These results demonstrate spontaneous chromosomal instability in the RPE1 p53-/- TRAIP-KO 1.29 cell line, suggesting that the loss of TRAIP may be associated with inability of cells to resolve endogenous DNA damage, eventually leading to the proliferation of damaged cells with unstable karyotypes.

Retroviral complementation of TRAIP-KO cells with TRAIP was performed, with the TRAIP-KO cell line 1.29 transduced with a wild-type TRAIP-containing vector, followed by drug selection to kill non-transduced cells (for extended characterisation of the complemented cell line, see Chapter 6). Chromosome counts in complemented cells were 44-46 in 55% (11/20) spreads, 67 in 5% (1/20), 79 in 5% (1/20), and 83-90 in 35% (7/20) spreads (***Figure 5.4***, ***Table 5.4***). Eight of the 20 cells were karyotyped; all had one or two copies of the typical derivative X chromosome of the parental RPE1 cell line, as well as additional structural and/or numerical abnormalities. As in the TRAIP-KO cell line 1.29, a clonal loss of chromosome 18 was observed.

The two karyotyped hypotetraploid cells contained no obvious structural rearrangements, in contrast to the TRAIP-KO cell line 1.29 (***Figure 5.4***). These results indicate chromosome instability in this cell line, but to a lesser extent than that observed in the TRAIP-KO cell line 1.29, indicating that the addback of wild-type TRAIP either reduces the elevated levels of gross structural abnormalities observed in TRAIP-KO cells or prevents further rearrangements from taking place.

Four additional RPE1 p53-/- TRAIP-KO clonal cell lines with distinct deletions in *TRAIP* (24B, 36B, 37B and 78B) (***Table 5.2***) were analysed to confirm genomic instability of TRAIP-KO cells and exclude a possibility of it being a spurious observation in the clone 1.29. All four cell lines had a variety of non-clonal and clonal structural abnormalities, such as deletions or additional material on several chromosomes (***Figure 5.5***, ***Table 5.4***).

The karyotyping data obtained in five distinct TRAIP-KO cell lines strongly suggest that the absence of TRAIP is associated with the increased frequency of tetraploidy and both clonal and non-clonal chromosomal abnormalities in unperturbed cells. The data also show that the genomic instability observed is not due to the absence of p53 per se, as the parental RPE1 p53-/- cell line was karyotypically normal. The complementation of TRAIP-KO cells with wild-type TRAIP reduced the number of non-clonal structural rearrangements observed in metaphase spreads, although clonal abnormalities of the clone 1.29 persisted in this cell line. In summary, although TRAIP-KO cells are viable, they accumulate chromosomal instability and can proliferate only in a p53-deficient background. This observation suggests an important role of TRAIP in maintaining genome stability in unperturbed cells, and further work will be required to investigate the molecular mechanism causing such genomic instability in TRAIP-KO cells.

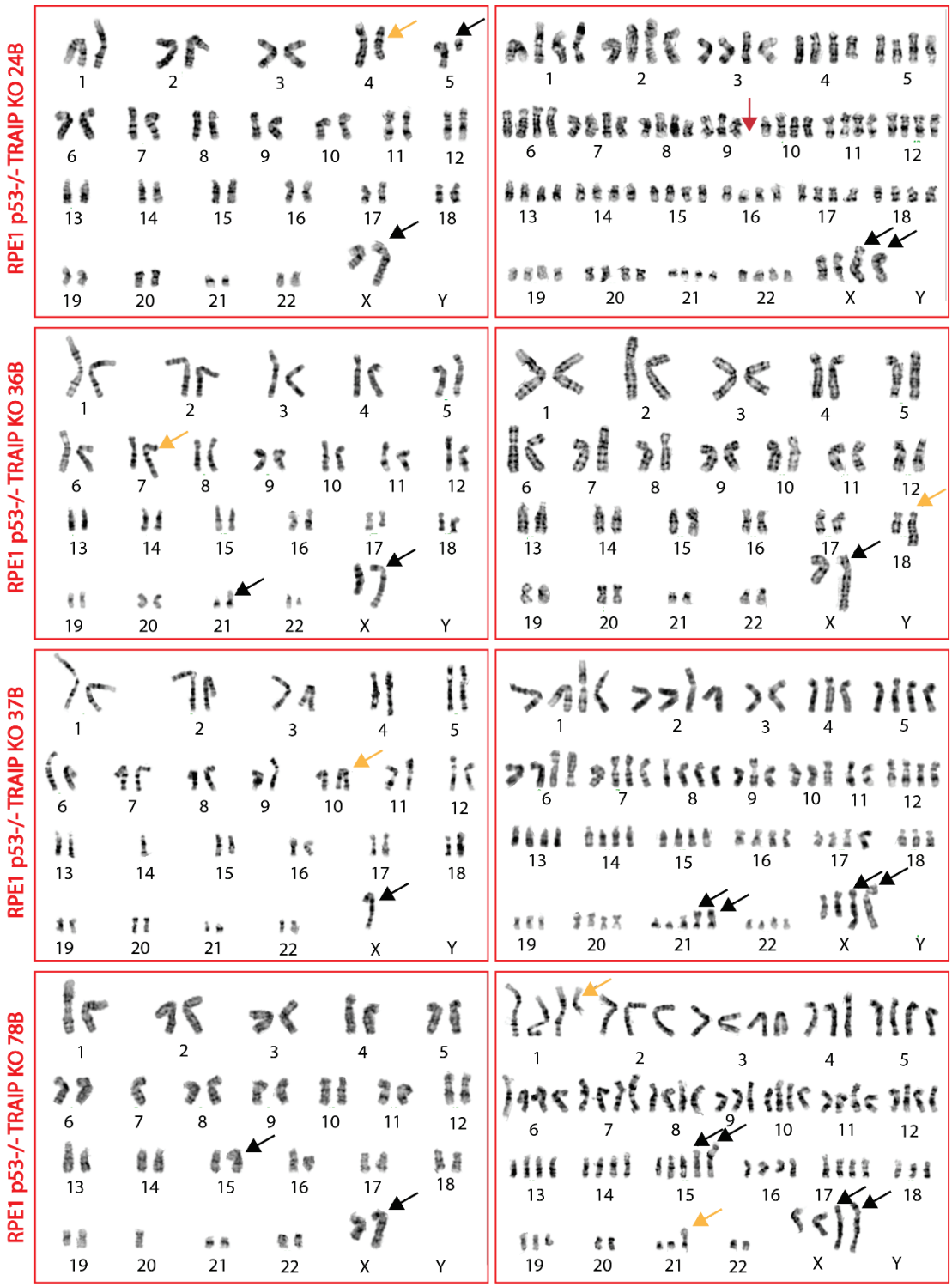

Figure 5.5. RPE1 p53-/- TRAIP-KO cell lines 24B, 36B, 37B and 78B show increased levels of genomic instability in the absence of DNA damage.

Representative karyotypes of the TRAIP-KO cell lines 24B, 36B, 37B and 78B. Black arrows indicate clonal abnormalities, including the typical derivative X chromosome, observed in hTERT RPE1 cells. Yellow arrows indicate non-clonal abnormalities, and down-facing red arrows indicate clonal loss of chromosome(s) (non-clonal losses are likely to be due to technical factors). The number of bands observed for all chromosomes in this analysis was 400 or greater.

5.4. Characterisation of DDR signalling in TRAIP-KO cells

DNA damage response (DDR) signalling collectively describes cellular responses required for maintaining genetic information intact by detecting DNA lesions, signalling their presence and facilitating their repair. Previous studies reported a role for TRAIP in protecting genome integrity and demonstrated that TRAIP-depleted cells exhibit changes in DDR signalling, particularly deregulated phosphorylation of DNA damage markers RPA2 and H2AX (Harley *et al.*, 2016; Hoffmann *et al.*, 2016; Soo Lee *et al.*, 2016; W. Feng *et al.*, 2016) (see ***Table 1.2***). However, some of the findings were contradictory. Our laboratory (Harley *et al.*, 2016) and Hoffmann *et al.* (2016) observed impaired phosphorylation of H2AX (γH2AX) in response to replication-blocking DNA lesions in TRAIP-compromised cells, whereas other studies reported an increase in γH2AX signalling in response to HU (W. Feng *et al.*, 2016) and IR (Soo Lee *et al.*, 2016). Moreover, the studies did not agree on the types of DNA lesions that require TRAIP for efficient repair. Soo Lee *et al.* (2016) reported the involvement of TRAIP in mediating HR repair at IR-induced DNA lesions. In contrast, Hoffmann *et al.* (2016) described the requirement of TRAIP for repair of ICLs and HU- and CPT-induced DNA lesions, W. Feng *et al.* (2016) reported the role of TRAIP after HU treatment, and Harley *et al.* (2016) detected impaired DDR signalling in cells with partial loss of TRAIP only in response to UV-C irradiation (***Table 1.2***). The experiments described below were aimed at delineating whether cells with the complete absence of TRAIP have the DDR signalling defects previously described by our laboratory (Harley *et al.*, 2016) in TRAIP patient cells after UV-C irradiation. Additionally, DDR signalling after other types of DNA damage was examined in TRAIP-KO cells.

To confirm the impact of TRAIP depletion on DDR signalling in RPE1 p53-/- cells, I tested whether the phenotype previously observed in TRAIP patient-derived and HeLa siTRAIP cells after UV-C irradiation (Harley *et al.*, 2016) could be recapitulated in this cell line. siRNA-mediated TRAIP depletion in the RPE1 p53-/- parental cell line, used for CRISPR/Cas9-mediated *TRAIP* targeting, was performed. TRAIP-depleted cells were treated with UV-C and collected 8 hours post-treatment, when pRPA2-S4/S8 and γH2AX signalling was previously detected by immunoblotting in TRAIP patient fibroblasts and TRAIP-depleted HeLa cells (Harley *et al.*, 2016). Immunoblotting on TRAIP-depleted RPE1 p53-/- cells showed a reduction in pRPA2-S4/S8 and γH2AX signalling after UV-C irradiation (***Figure 5.6***). This result demonstrates reproducibility of the DDR signalling defect after UV-C irradiation in TRAIP-deficient HeLa and RPE1 p53-/- cells.

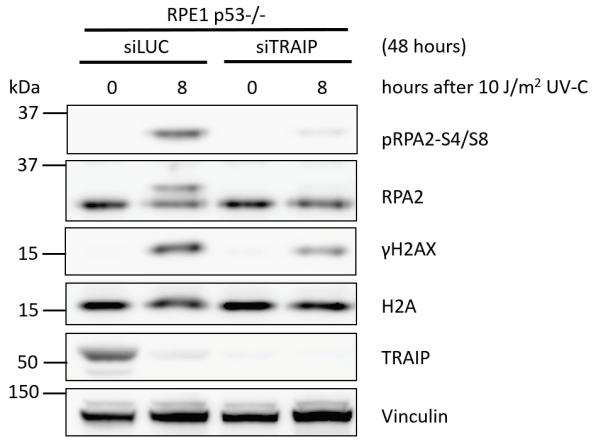

Figure 5.6. pRPA2-S4/S8 and γH2AX levels are reduced in TRAIP-depleted RPE1 p53-/- cells after UV-C irradiation.
RPE1 p53-/- cells were treated with siLUC or siTRAIP and exposed to UV-C 48 h post-transfection. Cells were collected for immunoblotting 8 h after UV-C irradiation and compared to the untreated samples (0 h after 10 J/m^2 UV-C) for phosphorylation of DNA damage markers pRPA2-S4/S8 and γH2AX. UV-C-induced pRPA2-S4/S8 signalling was reduced by 81% and γH2AX signalling by 54% in TRAIP-depleted cells, compared to siLUC-treated cells (quantified using Fiji/ImageJ software). Affinity-purified rabbit anti-TRAIP antibody raised against recombinant TRAIP protein (Harley *et al.*, 2016) was used for immunoblotting, demonstrating a 93% reduction of TRAIP protein levels upon UV-C treatment (quantified using Fiji/ImageJ software). Vinculin served as a loading control.

To test whether partial and complete loss of TRAIP lead to the same DDR signalling defects after UV-C irradiation, I conducted a UV-C time-course experiment in TRAIP-KO cells, followed by immunoblotting analysis. Unexpectedly, no significant changes in phosphorylation of RPA2 and H2AX were observed in TRAIP-KO cell line compared to the WT cell line (***Figure 5.7***). In contrast, it was previously demonstrated by Harley *et al.* (2016) that both TRAIP patient-derived fibroblasts and TRAIP-depleted HeLa cells exhibit reduced pRPA2-S4/S8 and γH2AX signalling after UV-C irradiation at all three time points analysed. The discrepancy between these results could be explained by the differences in TRAIP status in the two experiments. This would suggest that reduction in TRAIP protein levels and complete loss of TRAIP lead to distinct cellular outcomes. Certain adaptations in DNA damage signalling pathways may have arisen in TRAIP-KO cells allowing them to cope with the intrinsic genomic instability (see Section 5.3). Cells without TRAIP may have upregulated DDR signalling cascades to facilitate the repair of spontaneous and exogenous DNA damage, and the higher levels of pRPA2-S4/S8 and γH2AX could be reflective of it. Indeed, pRPA2-S4/S8 and γH2AX signal was found to be significantly increased in unperturbed TRAIP-KO cells, compared to WT cells, as measured by immunofluorescence analysis (***Figure 5.8***).

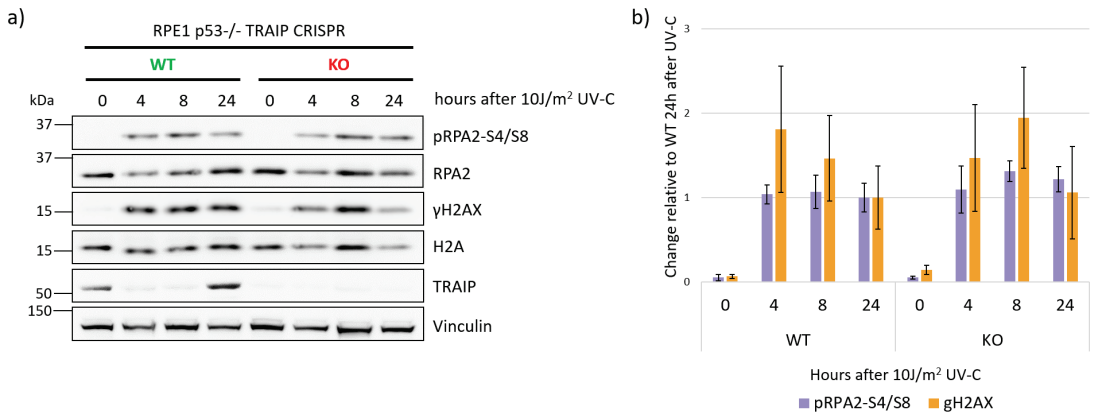

Figure 5.7. pRPA2-S4/S8 and γH2AX levels are not reduced in RPE1 p53-/- TRAIP-KO cell line after UV-C irradiation.

a) Representative immunoblot (n=3 experiments) demonstrating UV-C-induced pRPA2-S4/S8 and γH2AX levels in WT (1.30) and RPE1 p53-/- TRAIP-KO (1.29) cell lines, as well as temporary TRAIP protein degradation upon UV-C treatment in WT cells. Vinculin served as a loading control. Cells were exposed to UV-C irradiation, harvested for immunoblotting 4, 8 or 24 h post-treatment, and untreated (0 h after 10 J/m^2 UV-C) and UV-C-treated samples were compared for phosphorylation of DNA damage markers pRPA2-S4/S8 and γH2AX.

b) Quantification of pRPA2-S4/S8 and γH2AX levels demonstrates no significant changes in UV-C-induced pRPA2-S4/S8 and γH2AX levels between WT and TRAIP-KO cell lines at each time point analysed. Image analysis was performed using Fiji/ImageJ software; pRPA2-S4/S8 and γH2AX levels were normalised to vinculin. Results (mean ± SEM) from three independent experiments are shown.

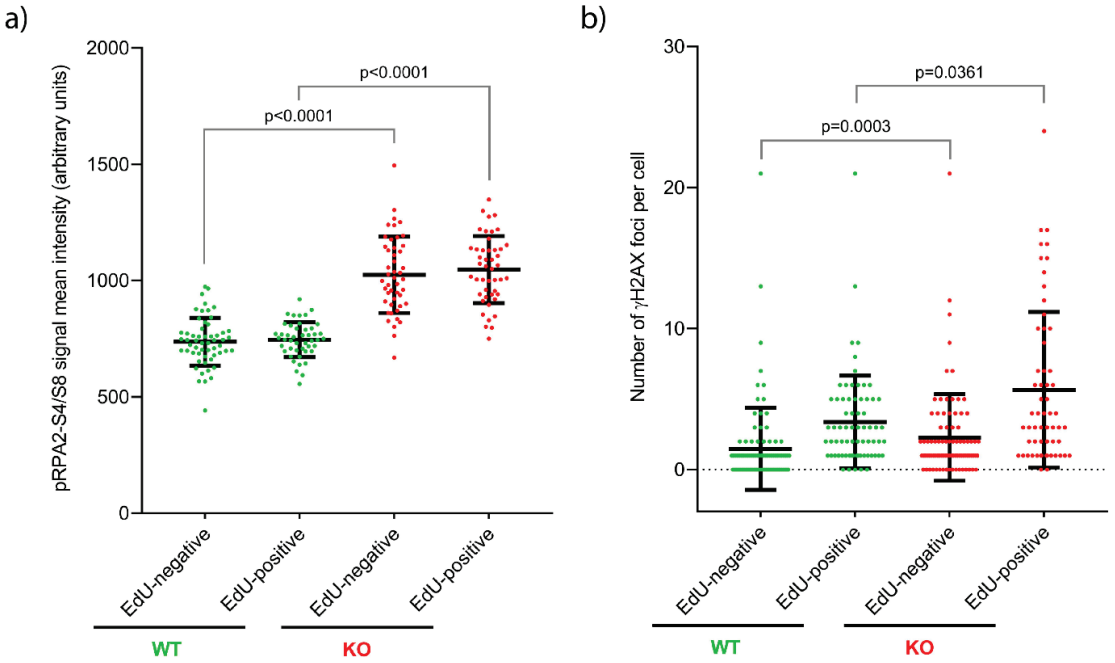

Figure 5.8. pRPA2-S4/S8 signal intensity and the number of γH2AX foci are increased in unperturbed RPE1 p53-/- TRAIP-KO cells.

Immunofluorescence quantification to detect pRPA2-S4/S8 signal (a) and γH2AX foci (b) in EdU-negative and EdU-positive cell populations. RPE1 p53-/- TRAIP-KO (1.29) and WT (1.30)

cells were exposed to 10 μM EdU for 20 min to label cells undergoing DNA replication. Detergent pre-extraction of non-chromatin-bound proteins was performed before cell fixation with formaldehyde. Cells were immunostained for EdU and pRPA2-S4/S8 or γH2AX and visualised using fluorescence microscopy. Image analysis was performed using Fiji/ImageJ software. Black bars indicate the mean, and each dot in the graph represents one cell (more than 45 cells analysed per condition). Statistics: Mann-Whitney test.

Given that partial depletion and complete absence of TRAIP have different consequences for DDR signalling in response to UV-C, I decided to test whether RPE1 p53-/- TRAIP-KO cells are sensitive to other sources of DNA damage, as identifying such DNA damage-inducing agents would be beneficial for studying the role of TRAIP in DDR. Furthermore, at the time this experimental work was performed, sensitivity of TRAIP-depleted cells to replication stress-inducing agents, such as CPT, MMC and HU, was reported by two other groups (Hoffmann *et al.*, 2016; W. Feng *et al.*, 2016). First, I compared the effect of the DNA damaging agents UV-C, CPT and HU on TRAIP-KO cells. Doses and times of treatment were adapted from previous reports investigating pRPA2 and γH2AX signalling (Harley *et al.*, 2016; Hoffmann *et al.*, 2016; Jeong *et al.*, 2013). The immunoblot and its quantification confirmed that no changes in pRPA2-S4/S8 and γH2AX signalling occurred in TRAIP-KO cells after UV-C irradiation (***Figure 5.9***). HU treatment did not affect pRPA2-S4/S8 and γH2AX signalling in TRAIP-KO cells either. In contrast, CPT treatment caused detectable reduction in both pRPA2-S4/S8 and γH2AX signalling in TRAIP-KO cells (***Figure 5.9***), suggesting that TRAIP may be required for DDR signalling induced upon DNA-TOP1 adduct formation (see Chapter 6 for further experimental work).

During embryonic development, oxidative damage (Cooke *et al.*, 2003) and aldehydes (Langevin *et al.*, 2011) can induce endogenous DNA lesions. Due to the requirement for TRAIP for body and brain growth *in utero* (Harley *et al.*, 2016), I tested whether TRAIP is involved in DDR signalling in response to oxidative stress, induced by hydrogen peroxide (H_2O_2) treatment. While the low dose (10 μM) of H_2O_2 did not result in RPA2 phosphorylation, the higher dose (100 μM) caused an increase in pRPA-S4/S8 signal in WT cells, which was less pronounced in TRAIP-KO cells (***Figure 5.10***), suggesting that TRAIP may also play a role in responding to oxidative DNA damage.

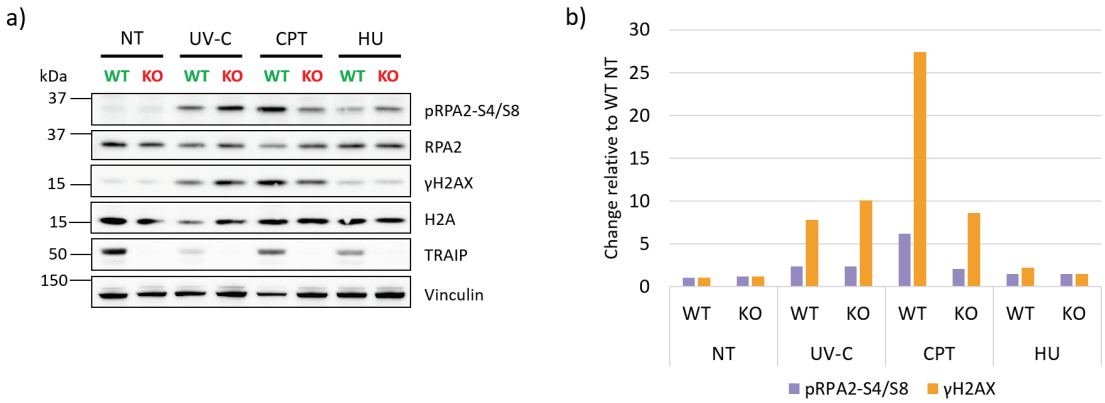

Figure 5.9. pRPA2-S4/S8 and γH2AX levels are reduced in RPE1 p53-/- TRAIP-KO cells after CPT but not UV-C and HU treatment.

a) Immunoblot demonstrating DNA damage-induced pRPA2-S4/S8 and γH2AX levels in untreated (NT) and drug-treated WT (1.30) and RPE1 p53-/- TRAIP-KO (1.29) cells, which were exposed to UV-C (10 J/m^2), CPT (1 µM) and HU (2 mM) treatment and harvested for immunoblotting 4, 1 or 8 hours post-treatment, respectively. Vinculin served as a loading control. In WT cells, TRAIP protein depletion upon UV-C treatment and to the lesser extent upon CPT and HU treatment can be observed.

b) Quantification of pRPA2-S4/S8 and γH2AX levels demonstrates no alterations in UV-C- and HU-induced pRPA2-S4/S8 and γH2AX levels between WT and TRAIP-KO cell lines. In contrast, a strong reduction in pRPA2-S4/S8 and γH2AX levels can be observed upon exposure to CPT. Image analysis was performed using Fiji/ImageJ software; pRPA2-S4/S8 and γH2AX levels were normalised to vinculin. Results from one experiment are shown.

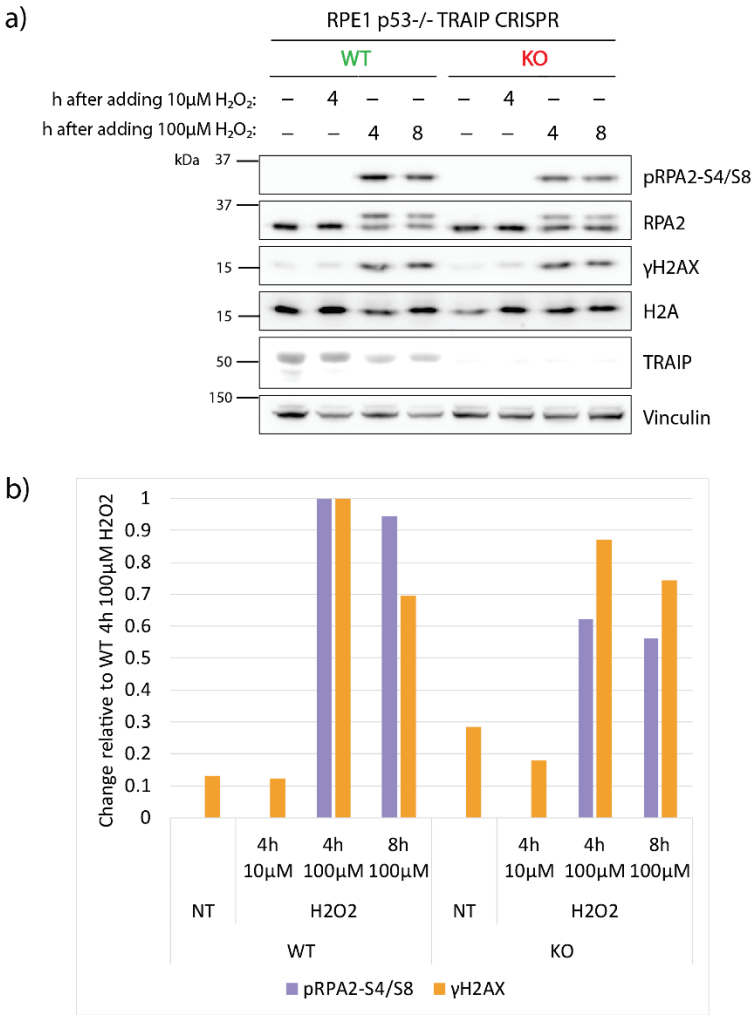

Figure 5.10. pRPA2-S4/S8 levels are reduced in RPE1 p53-/- TRAIP-KO cells after H_2O_2 treatment.

a) Immunoblot demonstrating H_2O_2-induced pRPA2-S4/S8 and γH2AX levels in RPE1 p53-/- WT (1.30) and TRAIP-KO (1.29) cells, which were exposed to H_2O_2 treatment (10 μM or 100 μM) and harvested for immunoblotting 4 or 8 h after addition of H_2O_2. Untreated (—) and H_2O_2-treated samples of both cell lines were compared for phosphorylation of DNA damage markers pRPA2-S4/S8 and γH2AX by immunoblotting. Vinculin served as a loading control.

b) Quantification of pRPA2-S4/S8 and γH2AX levels demonstrates a reduction in pRPA2-S4/S8 signal in TRAIP-KO cells, compared to WT cells, upon exposure to 100 μM H_2O_2. Image analysis was performed using Fiji/ImageJ software; pRPA2-S4/S8 and γH2AX levels were normalised to RPA2 and H2A, respectively. Results from one experiment are shown.

5.5. Summary and discussion: characterisation of TRAIP-KO cells

TRAIP encodes an E3 ubiquitin ligase and was established by our laboratory to be mutated in MPD (Harley *et al.*, 2016). Furthermore, in recent years, TRAIP was demonstrated by several studies to be involved in DDR signalling in response to various types of DNA damage (Hoffmann *et al.*, 2016; Soo Lee *et al.*, 2016; W. Feng *et al.*, 2016). In this chapter, the generation and characterisation of TRAIP-KO cells was described, including analyses of their genotypes, karyotypes, TRAIP protein expression levels and cellular response to DNA damaging agents.

The CRISPR/Cas9 editing strategy employed to generate a TRAIP-KO cell line suggested the importance of p53 status for a successful KO. As discussed in Section 5.2, clonal TRAIP-KO cell lines were generated only in the RPE1 p53-/- background, whereas RPE1 and HeLa cells did not produce any KO clones. The *D. melanogaster* homologue of TRAIP, Nopo, was proposed to be required for the maintenance of genomic integrity during early embryogenesis, and mutations in this gene were shown to lead to maternal effect lethality (Merkle *et al.*, 2009). Moreover, TRAIP-KO mice die early in embryonic development (E6.5–7.5), as dysregulation of cell proliferation and increased levels of apoptosis result in loss of primitive embryonic tissues (Park *et al.*, 2007). Similarly, loss of an important mammalian genome surveillance enzyme, RNase H2, activity also resulted in p53-mediated arrest of cell growth, leading to embryonic lethality of RNaseH2-null mice (Reijns *et al.*, 2012). Taken together, recent studies on TRAIP implicate it as an evolutionarily conserved factor, which maintains genome stability and is essential during early embryonic development. It is therefore not surprising that no MPD patients with complete loss of TRAIP were identified (Harley *et al.*, 2016) and that only inactivation of the major apoptosis regulator p53 (Burns and el Deiry, 1999) allows survival of TRAIP-KO cells.

The experiments I conducted show a clear difference in DDR signalling in TRAIP-depleted RPE1 cells (knock-down) and in cells lacking TRAIP (knock-out). RNA interference (RNAi), used by previous studies on TRAIP, reduces gene function but does not entirely abrogate it. To our knowledge, the TRAIP-KO cell line generated and characterised in this chapter is the first true genetic null cell line where both copies of *TRAIP* gene are disrupted, leading to the complete loss of the protein (***Figure 5.2***). Unexpectedly, TRAIP-KO cells did not have the DDR signalling defect observed in TRAIP-depleted cells in response to UV-C irradiation by Harley *et al.* (2016). Phenotypic differences between knockouts and knockdowns in human

cell lines are well documented (Evers *et al.*, 2016; Karakas *et al.*, 2007; Morgens *et al.*, 2016), and genetic compensation (upregulation of related genes) in response to gene loss was proposed as one of the major reasons for these discrepancies (El-Brolosy and Stainier, 2017). Therefore, complete loss of TRAIP may result in cellular adaptations to increased genomic instability arising from unrepaired endogenous DNA lesions (as shown in ***Figure 5.4-5.5***), at the same time impacting DDR signalling after UV irradiation.

In this chapter, I also demonstrated that TRAIP-KO cells have impaired phosphorylation of DNA damage markers RPA2 and H2AX after CPT treatment (***Figure 5.9***), and experiments further investigating the role of TRAIP in DDR after CPT-induced DNA damage are described in Chapter 6. Moreover, H_2O_2-induced RPA2 phosphorylation was also decreased in TRAIP-KO cells, compared to WT cells (***Figure 5.10***). Meanwhile, TRAIP absence did not have any effect on the DDR signalling after HU treatment (***Figure 5.9***), in contrast with the study by W. Feng *et al.* (2016), which reported increased numbers of γH2AX-positive cells in HU-treated TRAIP-depleted cells. This again suggests that distinct cellular phenotypes may be observed in TRAIP knock-down and knock-out cells after the same type of DNA damage. Moreover, additional discrepancies between the reported data may be caused by different cell lines used, as all the previous studies on the TRAIP role in DDR used transformed cancer cell lines (Hoffmann *et al.*, 2016; Soo Lee *et al.*, 2016; W. Feng *et al.*, 2016). Additionally, the dose and length of treatments may influence the results; for example, I used 2 mM HU for 8 h for my immunoblotting analysis, whereas W. Feng *et al.* (2016) used 5 mM HU for 4 h for their immunofluorescence experiment. Thus, further experimental work will be required to elucidate the actual roles of TRAIP in DDR and to explain the phenotypic differences seen in distinct cellular systems and conditions.

Thus far, the generated RPE1 p53-/- TRAIP-KO cell line has only been used to address the role of TRAIP in DDR signalling (Chapter 6). However, additional studies using these cells may elucidate other pathways and/or cellular processes TRAIP is required for. The loss of TRAIP in mice (Park *et al.*, 2007) and *D. melanogaster* (Merkle *et al.*, 2009) is known to be embryonic lethal primarily due to aberrant proliferation and mitosis. As impaired cell proliferation and an increase in late S and/or G2 phase cells was observed in unperturbed TRAIP patient-derived fibroblasts and TRAIP-depleted HeLa cells (Harley *et al.*, 2016), prolonged cell cycle and inefficient mitosis are also likely to contribute to the reduced growth phenotype of TRAIP MPD patients. Thus, the role of TRAIP in regulating cell cycle and mitosis, previously proposed by several studies (Chapard *et al.*, 2015, 2014), could be investigated further. Notably, TRAIP was

demonstrated to localise to mitotic chromosomes and regulate the spindle assembly checkpoint (SAC), and its depletion in HeLa cells was shown to lead to the faster progression through early phases of mitosis, as well as mitotic defects (Chapard *et al.*, 2014). Moreover, TRAIP protein expression was reported to peak in G2/M phase of the cell cycle (Chapard *et al.*, 2015). Thus, it remains to be elucidated whether the loss of TRAIP results in prolonged or accelerated cell cycle, and what its precise role in mitosis is. In the future, TRAIP-KO cells may be a valuable tool to address these questions.

Chapter 6

Molecular mechanisms of TRAIP function in DDR and DNA repair

6. Molecular mechanisms of TRAIP function in DDR and DNA repair

TRAIP encodes a RING finger domain E3 ubiquitin ligase (Besse *et al.*, 2007). Mutations in *TRAIP* were demonstrated by our laboratory to be linked to microcephalic primordial dwarfism (MPD), a reduction of brain and body size (Harley *et al.*, 2016). Biallelic *TRAIP* mutations were shown to result in severely reduced TRAIP protein levels, as well as impaired cell cycle progression and cell proliferation (Harley *et al.*, 2016). Moreover, disrupted DDR signalling in response to UV-C irradiation was observed in cells lacking functional TRAIP protein (Harley *et al.*, 2016). UV-C-irradiated patient-derived cells, as well as TRAIP-depleted HeLa cells, exhibited reduced RPA2 and H2AX phosphorylation in S phase, suggesting that DNA repair defect may underlie TRAIP-associated MPD phenotype. However, it remained unknown whether TRAIP solely promotes the repair of UV-C-induced replication-blocking lesions or contributes to the cellular response to other types of DNA lesions as well. TRAIP-KO cells were generated to address these questions (see Chapter 5), as they provide a good tool to investigate DDR defects and underlying mechanisms. Preliminary data suggested that TRAIP-KO cells may have defective DDR signalling in response to camptothecin (CPT)-induced DNA damage (***Figure 5.9***), and this observation is further investigated in Section 6.1.

To understand the role of TRAIP as a DNA repair protein in DDR signalling, the impact of another replication-associated DNA damaging agent, mitomycin C (MMC), is investigated to determine whether TRAIP acts in the repair of MMC-induced DNA interstand crosslinks (ICLs) (Section 6.2). Overall, the objective of the work described in this chapter is to use TRAIP-KO cells as a tool to gain a better understanding of the TRAIP function in the cellular response to replication-associated DNA damage.

6.1. TRAIP is required for efficient cell response to CPT-induced replication blocking DNA lesions

6.1.1. Camptothecin, TOP1-DNA complexes and their repair

The initial observation that TRAIP-KO cells have reduced pRPA2-S4/S8 and γH2AX signal in response to camptothecin (CPT) treatment (see Section 5.4., ***Figure 5.9***) was intriguing, and I decided to investigate it further. The anti-tumour agent CPT disrupts DNA replication and transcription by trapping DNA topoisomerase I (TOP1) at single-stranded breaks (SSBs), thus stabilising TOP1 covalent complex (Top1cc), preventing re-ligation of the broken DNA ends and resolution of a SSB (Pommier, 2006) (***Figure 6.1***) (see Section 1.3.4). The toxic DNA-protein adduct needs to be swiftly removed via one of the two main TOP1 excision pathways, mediated by either tyrosyl-DNA phosphodiesterase (TDP1) (El-Khamisy and Caldecott, 2006) or structure-specific 3'-flap endonucleases, such as XPF/ERCC1, MUS81/EME1, and MRE11-RAD50 (Regairaz *et al.*, 2011; Sacho and Maizels, 2011; Takahata *et al.*, 2015). In the presence of a low dose of TOP1 inhibitor, SSBs can also be resolved by PARP1- and RAD51-mediated replication fork regression (Ray Chaudhuri *et al.*, 2012; Zellweger *et al.*, 2015), resulting in a 'chicken foot'-like DNA structure (***Figure 6.1***). Fork reversal slows down replication fork progression, preventing excessive accumulation of ssDNA and allows time for repair machinery to remove trapped TOP1 (Neelsen and Lopes, 2015; Ray Chaudhuri *et al.*, 2012; Zellweger *et al.*, 2015).

An unrepaired SSB can give rise to a one-ended double-strand break (DSB) upon collision with an ongoing replication fork in S phase (Pommier, 2006) (***Figure 6.1***). CPT-induced replication-associated DSBs lead to DDR signalling, such as phosphorylation of H2AX (Furuta *et al.*, 2003), RPA (Huang *et al.*, 2010; Shao *et al.*, 1999; Vassin *et al.*, 2009) and checkpoint kinases CHK1 and CHK2 (Huang *et al.*, 2010; Pommier, 2006). In proliferating cells, the repair of replication-associated DSBs is largely dependent on homologous recombination (HR) (Pommier, 2006), leading to the replication fork restoration and the restart of DNA replication.

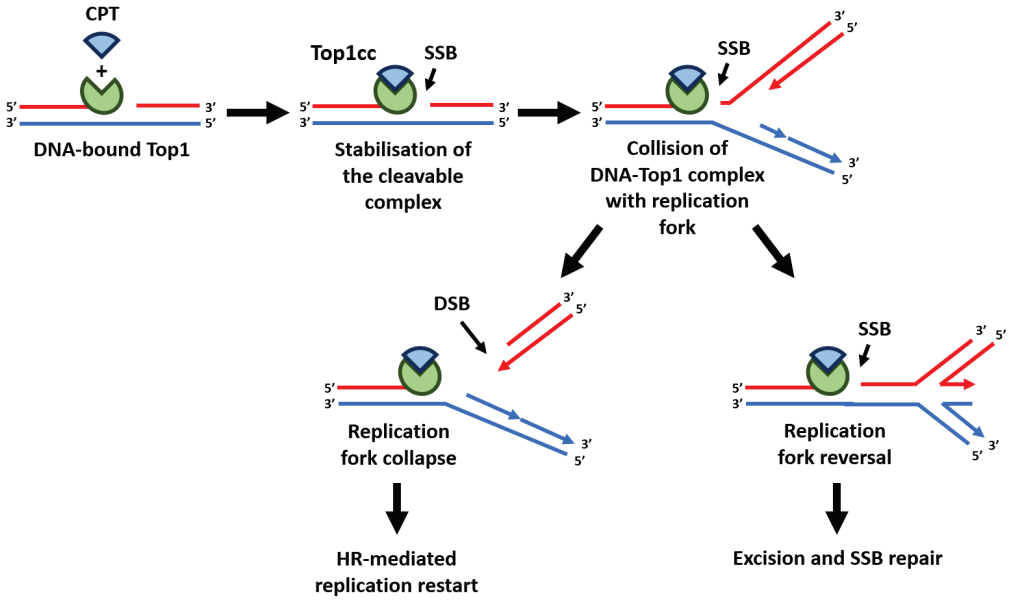

Figure 6.1. Generation and repair of the TOP1-DNA covalent complex (Top1cc).
Camptothecin (CPT) is an anti-tumour agent that stabilises and inhibits DNA topoisomerase I (TOP1) bound to DNA (Top1cc) and prevents resealing of the broken strand. Upon collision with the replication fork, the SSB can be turned into a DSB, which subsequently triggers DDR signalling and needs to be rapidly repaired via HR. Alternatively, replication fork reversal can take place forming a 'chicken foot' DNA structure and facilitating repair of the SSB.

6.1.2. The TRAIP E3 ligase promotes DDR signalling in response to CPT lesions

Studying the effect of several DNA damaging agents on TRAIP-KO cells suggested that phosphorylation of RPA2 and H2AX is impaired in TRAIP-KO cells upon CPT treatment (see Section 5.4., ***Figure 5.9***). To confirm this observation and investigate the defective response to CPT in TRAIP-KO cells further, RPE1 p53-/- WT (1.30) and TRAIP-KO (1.29) cells were treated with 1 µM CPT. At the time points sampled, pRPA2-S4/S8 levels were significantly reduced in TRAIP-KO cell line after CPT treatment (23±5.5% of the WT signal 90 min into treatment) (***Figure 6.2*a-b**), confirming the previous observation. CPT-induced γH2AX and pCHK1-S345 signal was also found to be diminished in TRAIP-KO cells, although to a lesser extent (64±11.0% and 48±13.3% of the WT signal 90 min into treatment, respectively) (***Figure 6.2*a-b**). Altogether, this result demonstrates the diminished ability of TRAIP-KO cells to efficiently promote CPT-induced DNA damage signalling.

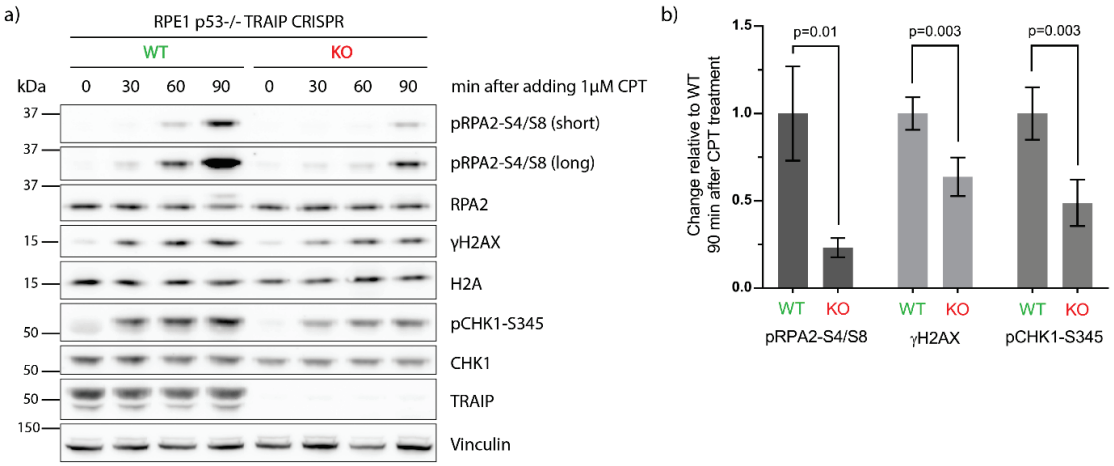

Figure 6.2. CPT-induced DDR signalling is reduced in RPE1 p53-/- TRAIP-KO cells.
a) Representative immunoblot (n=3 independent experiments) showing reduced CPT-induced pRPA2-S4/S8, γH2AX and pCHK1-S345 levels in RPE1 p53-/- TRAIP-KO (clone 1.29) cells, compared to WT (clone 1.30) cells. Cells were exposed to CPT treatment (1 µM) and harvested for immunoblotting 30, 60 or 90 min after addition of CPT. Untreated (0 min after adding 1 µM CPT) and CPT-treated samples of both cell lines were compared for phosphorylation of DNA damage markers pRPA2-S4/S8, γH2AX and pCHK1-S345 by immunoblotting. Vinculin served as a loading control.
b) Quantification of pRPA2-S4/S8, γH2AX and pCHK1-S345 levels 90 min post-CPT addition demonstrates significant reduction of CPT-induced DDR signalling in TRAIP-KO cell lines. Image analysis was performed using Fiji/ImageJ software. pRPA2-S4/S8 and pCHK1-S345 levels were normalised to vinculin; γH2AX levels were normalised to H2A. Results (mean ± SD) from three independent experiments are shown; statistics: unpaired two-tailed t-test.

CRISPR/Cas9-mediated targeting has emerged as a valuable tool to investigate the cellular function of a gene allowing the generation and study of knockout cell lines. However, the cell lines that I compare (WT and TRAIP-KO) required clonal expansion after CRISPR/Cas9-mediated gene targeting. It could therefore be argued that in the resulting clones, mutations at other sites due to off-target effects of the gRNAs used may account for observed phenotypes, rather than TRAIP loss. To demonstrate that the DDR signalling defect seen in TRAIP-KO cells is caused specifically by the absence of TRAIP, the TRAIP-KO cell line 1.29 was complemented by retroviral infection. KO cells were transduced with either empty or wild-type TRAIP-containing retroviral vector, followed by drug selection to kill non-transduced cells and generate pools of complemented cells. TRAIP protein levels, assessed by immunoblotting, revealed that TRAIP is overexpressed in the TRAIP-WT complemented cells, compared to WT and parental RPE1 p53-/- cells (***Figure 6.3*****a**). DDR signalling in response to CPT, including phosphorylation of RPA2, was rescued by the complementation of TRAIP-KO cells with TRAIP-WT, but not with the empty vector (***Figure 6.3*****b**). This experiment therefore demonstrates that reduction in pRPA2-S4/S8, γH2AX and pCHK1-S345 signal seen in RPE1 p53-/- TRAIP-KO cell line after CPT treatment is specific to TRAIP loss and not due to off-target effects of CRISPR/Cas9 genome editing.

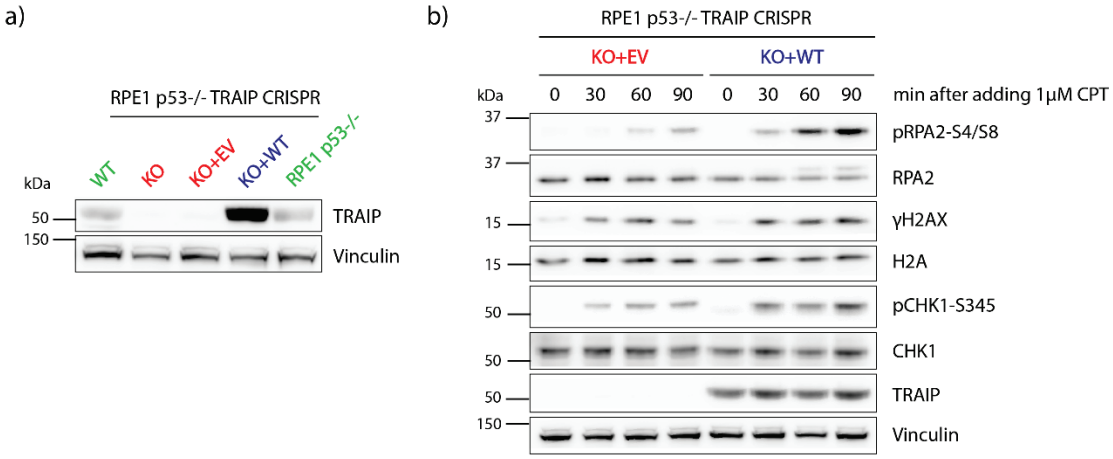

Figure 6.3. Reduction in CPT-induced DDR signalling in RPE1 p53-/- TRAIP-KO cells is specific to TRAIP loss.
a) Complementation of TRAIP-KO cells with TRAIP-WT (KO+WT) leads to overexpression of TRAIP, compared to TRAIP levels observed in WT cells. Cell lines used: RPE1 p53-/- parental (RPE1 p53-/-), WT (clone 1.30), TRAIP-KO (KO; clone 1.29), TRAIP-KO complemented with empty vector (KO+EV), and TRAIP-KO complemented with TRAIP-WT (KO+WT). Vinculin served as a loading control.

b) Reduction in pRPA2-S4/S8, γH2AX and pCHK1-S345 levels post-CPT treatment is rescued by the complementation of TRAIP-KO cells with TRAIP-WT (KO+WT), but not with empty vector (KO+EV). RPE1 p53-/- TRAIP-KO cells (clone 1.29) complemented with either empty vector (KO+EV) or TRAIP-WT (KO+WT) were exposed to CPT treatment (1 μM) and harvested for immunoblotting 30, 60 or 90 min after addition of CPT. Untreated (0 min) and CPT-treated samples of both cell lines were compared for phosphorylation of DNA damage markers pRPA2-S4/S8, γH2AX and pCHK1-S345 by immunoblotting. Vinculin served as a loading control.

As TRAIP is a RING finger E3 ligase, an important question is whether this ubiquitin ligase activity is essential for its role in DNA replication and repair. TRAIP contains an N-terminal RING finger motif, a long coiled-coil domain, a leucine zipper domain, and a PIP-box domain (Lee, Lee and Choi, 1997; Hoffmann *et al.*, 2016; W. Feng *et al.*, 2016). The coiled-coil domain of TRAIP was shown to be required for its homodimerisation (I. S. Park *et al.*, 2015), whereas the RING domain was speculated to have NF-κB-unrelated regulatory roles (Lee *et al.*, 1997). Many RING finger proteins function as E3 ubiquitin ligases, which transfer ubiquitin moiety from E2 ubiquitin-conjugating enzyme to the substrate protein, targeting it for degradation, affecting its cellular localisation or modulating its activity (Brown and Jackson, 2015). It is therefore important to understand whether and how the E3 ligase activity aids TRAIP-mediated DDR at stalled replication forks.

A recent study by Hoffmann *et al.* (2016) tested the importance of TRAIP E3 ligase activity in facilitating DNA repair. The group generated a stable cell line expressing a siRNA-resistant TRAIP mutant lacking the RING domain (ΔRING, Δaa7–50), and showed that it did not rescue HU- and CPT-induced RPA phosphorylation defect, observed in siTRAIP-treated U2OS cells (Hoffmann *et al.*, 2016). The ΔRING allele also failed to rescue cell survival defect of siTRAIP-treated U2OS cells exposed to MMC (Hoffmann *et al.*, 2016). However, the ΔRING allele used in this study appeared to be toxic to cells, further reducing RPA phosphorylation and exacerbating MMC hypersensitivity in the absence of endogenous TRAIP (Hoffmann *et al.*, 2016). It is therefore not clear whether the cellular defects observed in the presence of the ΔRING mutant are indeed due to its dominant-negative effect or due to the altered protein structure. The deletion of the entire protein domain can negatively affect protein folding-structure-function relationship, resulting in protein misfolding, mislocalisation or altered protein-protein interactions, which would not occur in the context of the full-length protein (Doyle *et al*., 1986; W. Feng *et al*., 2016; Filippello *et al*., 2013; Izumi *et al*., 2000). I therefore postulated that introduction of point mutations disrupting TRAIP E3 ligase would circumvent

these caveats and provide a better indication of the importance of this activity for DDR and DNA repair.

To address this, a cell line complemented with a TRAIP RING domain mutant C7A/C10A was previously generated in our laboratory (performed by M. Harley and O. Murina). In this E3 ligase mutant, two structurally essential cysteine residues in the catalytic site (C7 and C10) were substituted by alanines. DNA fibre experiments showed replication fork asymmetry after UV damage in C7A/C10A-complemented cells, suggesting that the role of TRAIP in DNA replication is dependent on its E3 ubiquitin ligase activity. However, highly reduced stability of the mutant protein was detected by immunoblotting (M. Harley and O. Murina, data not shown). TRAIP-C7A/C10A protein expression levels were higher than TRAIP expression in the patient-derived cell line, but lower compared to TRAIP expression in wild-type control fibroblasts, which was likely caused by reduced protein stability and its degradation. Therefore, it was not possible to conclude whether E3 ligase activity of TRAIP is required for its function in DNA replication and DNA damage signalling.

To establish the importance of E3 ubiquitin ligase activity of TRAIP for its role in DDR signalling, I utilised a different TRAIP mutant deficient in E3 ligase activity, TRAIP-W37A (based on personal communication with Prof Helen Walden, University of Glasgow). The tryptophan residue is evolutionarily conserved within the RING domain, and its substitution to alanine has been used by several studies to inactivate the ligase activity of other RING domain E3 ubiquitin ligases (Brzovic *et al.*, 2001; Dodd *et al.*, 2004; Joazeiro *et al.*, 1999; Katoh *et al.*, 2003). The tryptophan-to-alanine substitution of this residue was predicted and demonstrated to disrupt the interaction between the E3 ligase and the E2 ubiquitin-conjugating enzyme, which is necessary for efficient substrate ubiquitination (Dodd *et al.*, 2004; Joazeiro *et al.*, 1999; Katoh *et al.*, 2003). Although the TRAIP-W37A mutant was not predicted to completely obliterate E3 ligase activity, it was expected to compromise it while retaining structural domain stability and allowing mutant protein to reach levels similar to the wild-type protein. TRAIP-KO cells were complemented by retroviral transduction with TRAIP-W37A (KO+W37A) and phosphorylation of DNA damage markers compared to TRAIP-WT complemented cells (KO+WT) by immunoblotting. The reduced pRPA2-S4/S8, γH2AX and pCHK1-S345 signal in TRAIP-KO cells was not rescued by the complementation with TRAIP-W37A (***Figure 6.4*****a**), suggesting that the E3 ligase activity of TRAIP is essential for its role in promoting DDR upon CPT treatment. TRAIP protein levels in KO+WT and KO+W37A cells lines were comparable, with no significant differences in protein levels, although average TRAIP-W37A mutant levels were slightly lower

(83±8.3% TRAIP protein relative to TRAIP-WT complementation) (***Figure 6.4b***). However, the TRAIP protein expression levels of the E3 ligase mutant were 5.5-fold higher than those of the WT cell line.

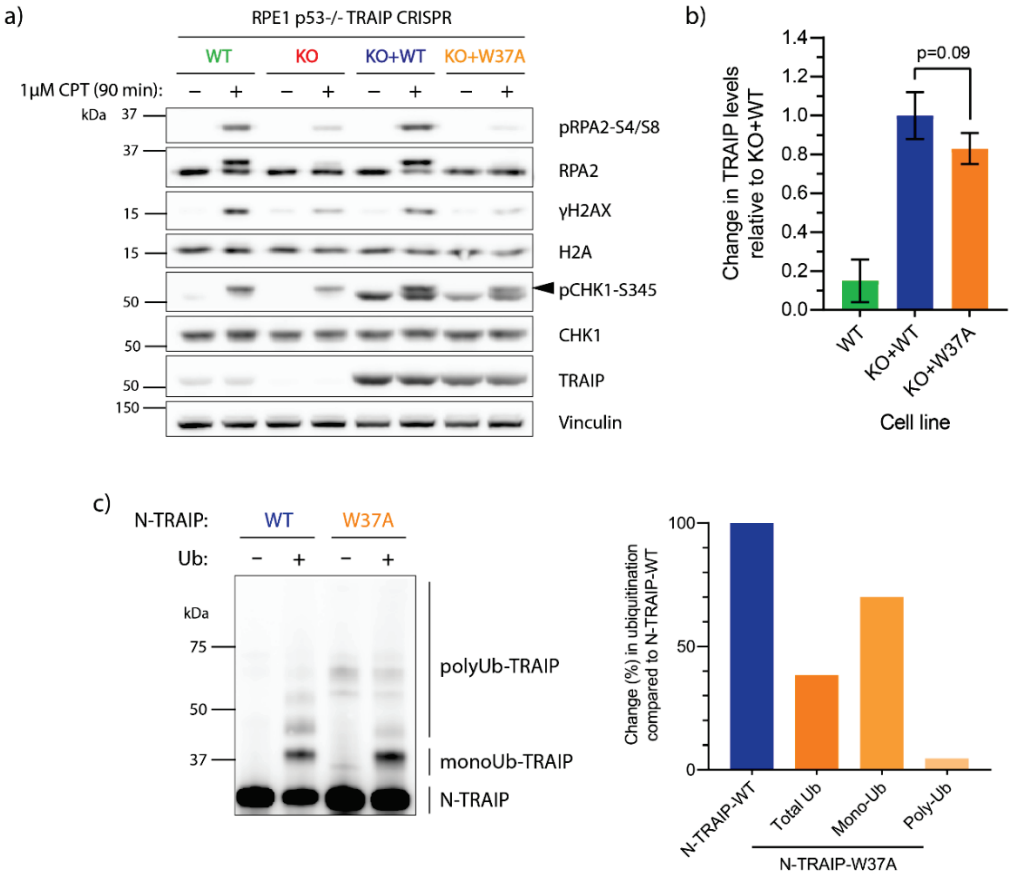

Figure 6.4. Reduction in CPT-induced DDR signalling in RPE1 p53-/- TRAIP-KO cells is dependent on TRAIP E3 ligase.

a) Representative immunoblot (n=2 independent experiments) demonstrating that reduction in pRPA2-S4/S8, γH2AX and pCHK1-S345 levels post-CPT treatment is rescued by the complementation of TRAIP-KO cells with TRAIP-WT (KO+WT), but not with the E3 ligase-deficient mutant TRAIP-W37A (KO+W37A). RPE1 p53-/- WT, TRAIP-KO (KO; clone 1.29), TRAIP-KO complemented with TRAIP-WT (KO+WT) and TRAIP-KO complemented with TRAIP-W37A (KO+W37A) cells were exposed to CPT treatment (1 μM) for 90 min and harvested for immunoblotting. Vinculin served as a loading control. Black arrowhead indicates the pCHK1-S345 band, as pCHK1-S345 signal was detected by re-probing the membrane fraction used for TRAIP detection (lower band).

b) TRAIP protein levels in KO+WT and KO+W37A cells lines are comparable. The TRAIP-W37A mutant complemented cells expressed 83±8.3% TRAIP protein relative to TRAIP-WT complemented cells (a non-significant difference). TRAIP protein expression levels of both TRAIP-WT and TRAIP-W37A are much higher than those of the WT cell line 1.30 (14.8+11.3% TRAIP protein relative to TRAIP-WT complementation). Image analysis was performed using Fiji/ImageJ software. TRAIP levels were normalised to vinculin. Results (mean ± SD) from four independent immunoblots are shown; statistics: unpaired two-tailed t-test.

c) Immunoblotting (left) and quantification (right) of *in vitro* ubiquitination reactions shows that total auto-ubiquitination of TRAIP-W37A is lower than of TRAIP-WT, with strongly reduced poly-ubiquitination but relatively normal mono-ubiquitination. Recombinant N-terminal part of WT TRAIP (TRAIP-WT) or of W37A mutant (TRAIP-W37A) was used both as an E3 ligase and a substrate in *in vitro* ubiquitination reaction in the absence or presence of ubiquitin (Ub). All ubiquitination reactions were supplemented with ATP, as well as E1 and E2 enzymes, and incubated for 3 h at 37˚C. Reactions were stopped by adding sample loading buffer and analysed by immunoblotting with anti-TRAIP antibody (Harley *et al.*, 2016). Image analysis to compare TRAIP-WT and TRAIP-W37A auto-ubiquitination was performed using Fiji/ImageJ software. For auto-ubiquitination analysis, the signal intensity of the lanes without ubiquitin (–Ub) was subtracted from the lanes that contained ubiquitin (+Ub).

TRAIP was previously shown to auto-ubiquitinate through its N-terminal RING-dependent E3 ubiquitin ligase activity (Besse *et al.*, 2007). To determine the E3 ligase activity of the TRAIP-W37A protein, N-terminal TRAIP-WT and TRAIP-W37A proteins were expressed in bacterial cells, purified and tested *in vitro* for their ability to auto-ubiquitinate. TRAIP-W37A retained 38% of its auto-ubiquitination activity, compared with TRAIP-WT, showing efficient mono-ubiquitination (70% compared to TRAIP-WT) but reduced poly-ubiquitination (4.5% compared to TRAIP-WT) (***Figure 6.4*****c**). Although TRAIP-W37A must retain some interaction with the E2 enzymes as it can still auto-ubiquitinate, at least *in vitro*, its ability to poly-ubiquitinate itself is strongly affected. Most significantly, in cells, full-length TRAIP-W37A has the same defect in CPT-induced DDR signalling as TRAIP-KO cells (***Figure 6.4*****a**). This suggests that TRAIP-W37A is not functional *in vivo*, despite much higher TRAIP protein levels in KO+W37A cells than in WT cells, consistent with the lack of rescue in DDR signalling being due to its defective E3 ligase activity.

Next, I assessed whether the observed RPA2 phosphorylation defect was specific to S phase. To avoid synchronisation-based experiments, which could potentially induce even more DNA damage into cells, the pRPA2-S4/S8 signal was analysed in individual cells by immunofluorescence microscopy, using EdU added for the last 20 min of the CPT treatment to label cells undergoing DNA replication. There was no significant difference in pRPA2-S4/S8 mean signal intensity between EdU-negative WT and TRAIP-KO cells, although it was slightly decreased in EdU-negative KO+WT cells and increased in KO+W37A cells, relative to WT cells (***Figure 6.5*****b**). In WT and KO+WT cells undergoing DNA replication (EdU-positive), a significant increase in pRPA2-S4/S8 mean signal intensity was observed, compared to EdU-negative cells (***Figure 6.5*****a-b**). However, no significant increase was observed in KO and KO+W37A cells, where pRPA2-S4/S8 signal intensity was similar in EdU-negative and EdU-positive cells (***Figure***

***6.5*a-b**). This result suggests that after CPT treatment, the E3 ligase activity of TRAIP is required for efficient RPA2 phosphorylation during S phase.

Overall, I conclude that reduction in CPT-induced DDR signalling observed in RPE1 p53-/- TRAIP-KO cells is caused by disruption of E3 ligase activity of TRAIP, and that TRAIP is required for RPA2 phosphorylation at CPT lesions during S phase. In the following sections, further experiments to delineate the mechanism of this defect are described.

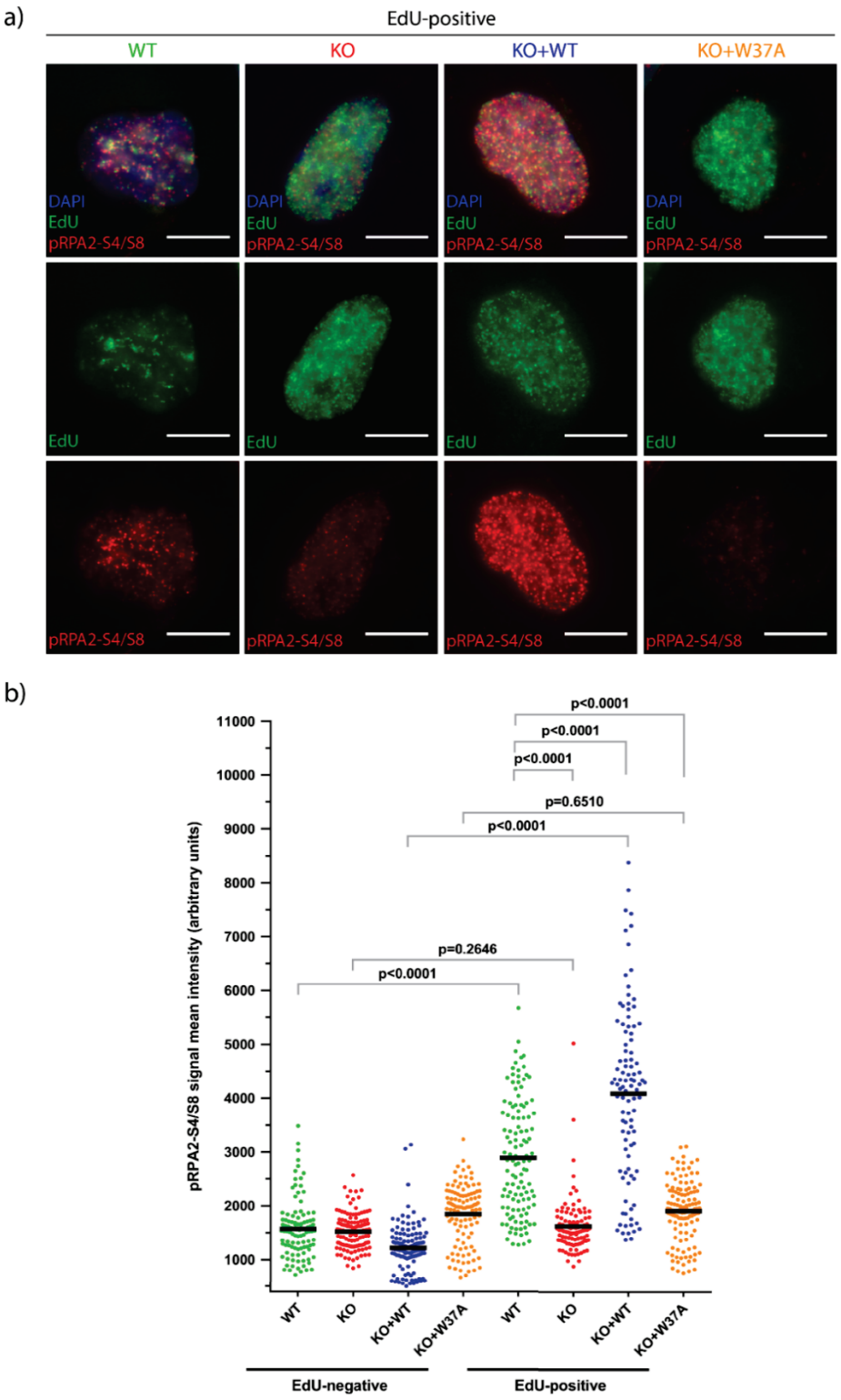

Figure 6.5. Reduction in CPT-induced pRPA2-S4/S8 signal intensity in EdU-positive TRAIP-KO cells is rescued by complementation with TRAIP-WT but not E3 ligase-deficient mutant TRAIP-W37A.

a) Representative images of EdU-positive CPT-treated WT, KO, KO+WT and KO+W37A cells, stained for pRPA2-S4/S8 and visualised using fluorescence microscopy. DAPI signal is shown in blue; EdU in green; pRPA2-S4/S8 in red. Scale bars: 10 µm.

b) Immunofluorescence quantification to detect pRPA2-S4/S8 in EdU-negative and EdU-positive cell populations. RPE1 p53-/- WT (clone 1.30), TRAIP-KO (KO; clone 1.29), TRAIP-KO complemented with TRAIP-WT (KO+WT) and TRAIP-KO complemented with TRAIP-W37A (KO+W37A) cells were treated with 1 µM CPT for 1 h, and 10 µM EdU was added for the last 20 min of the CPT treatment to label cells undergoing DNA replication. Detergent pre-extraction of non-chromatin-bound proteins was performed before cell fixation with formaldehyde. Cells were immunostained for EdU and pRPA2-S4/S8 and visualised using fluorescence microscopy. Image analysis was performed using Fiji/ImageJ software. Black bars indicate the mean, and each dot in the graph represents one cell (>100 cells analysed per condition). Statistics: Mann-Whitney test.

6.1.2.1. TRAIP is not depleted after CPT treatment

One notable observation based on the experiments described in Chapter 5 and Section 6.1 was different regulation of TRAIP protein levels following the treatment with distinct DNA damaging agents. To investigate this further, I tested whether TRAIP protein levels change following the recovery from CPT treatment for 4 and 8 hours, as they were not observed to decrease after short (30–90 min) CPT treatment (see ***Figure 6.2***). Immediately after the 30 min CPT treatment, as well as several hours after CPT release, TRAIP levels in WT cells were not substantially different, compared to untreated cells (***Figure 6.6***), indicating that the removal of the DNA damaging agent did not result in TRAIP depletion. Additionally, I previously observed that TRAIP protein levels were only slightly reduced after CPT, HU and H_2O_2 treatment (***Figure 5.9***-***5.10***). This is in contrast to UV-C irradiation, after which TRAIP protein levels dramatically decrease, as seen in ***Figures 5.6***, ***5.7*** and ***5.9*** and shown by Harley *et al.* (2016). This reduction was shown by our laboratory to be caused by proteasome-mediated degradation of TRAIP (Harley *et al.*, 2016), suggesting that TRAIP levels are regulated in response to UV-C. These results therefore suggest that TRAIP may promote DNA repair via distinct mechanisms in response to different types of replication-associated DNA lesions.

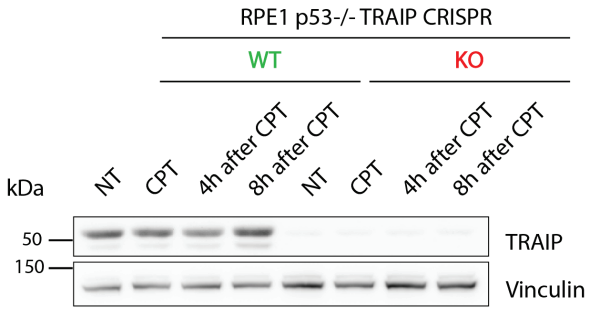

Figure 6.6. TRAIP is not depleted after CPT treatment or several hours after its removal. Immunoblotting of TRAIP protein levels after CPT treatment in WT and TRAIP-KO cells. RPE1 p53-/- WT (clone 1.30) and TRAIP-KO (clone 1.29) cells were exposed to CPT treatment (1 μM) for 30 min and either harvested for immunoblotting immediately following the treatment (CPT) or collected 4 or 8 hours after the drug was removed by extensive PBS washing. Untreated (NT) and CPT-treated samples of both cell lines were compared for TRAIP protein levels by immunoblotting. Vinculin served as a loading control.

6.1.3. Cell survival, HR efficiency and DNA end resection after CPT treatment are reduced in TRAIP-KO cells

Efficient cellular DDR signalling in response to damage is crucial for error-free DNA repair, maintenance of genomic stability and long-term cell survival. I therefore postulated that the observed defect of TRAIP-KO cells in CPT-induced DDR signalling would lead to adverse downstream effects on timely DNA repair and cell survival.

Firstly, the ability of cells lacking TRAIP to survive and form colonies after CPT treatment was assessed in the clonogenic cell survival assays. TRAIP-KO cells were observed to be much more sensitive to CPT treatment than WT cells, as they formed fewer colonies at all doses of CPT used in the experiment (***Figure 6.7***). Complementation of KO cells with TRAIP-WT (KO+WT) rescued the observed CPT-induced hypersensitivity and colony formation defect of TRAIP-KO cells (***Figure 6.7***). Unexpectedly, complementation with TRAIP-W37A (KO+W37A) resulted in an intermediate level of sensitivity to CPT, suggesting a partial rescue by the E3 ligase-deficient mutant (***Figure 6.7***). One possible explanation for this observation is the residual levels of E3 ligase activity in the TRAIP-W37A mutant, as it was shown to retain some E3 ligase activity in the *in vitro* ubiquitination assay (***Figure 6.4c***). In addition, it could be that overexpression of the ligase-deficient mutant partially restores the reduced interaction with the E2 ubiquitin-conjugating enzyme. Together, this may allow sufficient activity to partially rescue the cell survival defect. However, this would not explain the complete failure of TRAIP-W37A to rescue the CPT-induced DDR signalling defect. Therefore, the partial survival rescue

could be due to a non-catalytic role of TRAIP that contributes to cell survival after CPT treatment but is not required for CPT-induced DDR signalling.

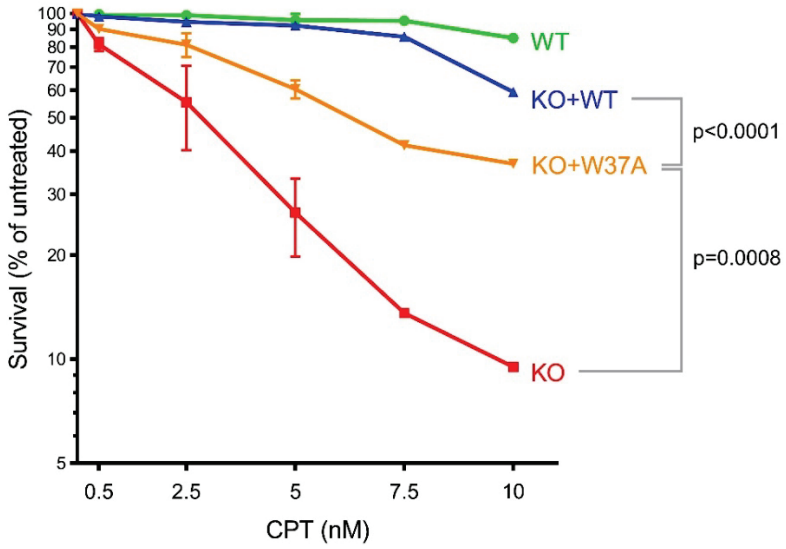

Figure 6.7. Reduced colony formation ability and survival of CPT-treated TRAIP-KO cells is rescued by complementation with TRAIP-WT, whereas complementation with E3 ligase-deficient mutant TRAIP-W37A provides a partial rescue.
RPE1 p53-/- WT, TRAIP-KO (KO; clone 1.29), TRAIP-KO complemented with TRAIP-WT (KO+WT) and TRAIP-KO complemented with TRAIP-W37A (KO+W37A) cells were plated at very low density and treated with CPT (0.5 nM – 10 nM) for 24 hours. The drug was removed by PBS washing, and cells were grown for 8 days until colonies were formed, followed by fixation, staining and colony counting. For CPT doses 0.5 nM – 5 nM, mean ± SD of n=2 independent experiments is shown (for 7.5 and 10 nM, n=1 experiment). Statistics: two-way ANOVA for 0.5, 2.5, and 5 nM CPT.

The rapid repair of one-ended DSBs breaks in S phase is required to facilitate restoration of replication forks and to restart DNA replication, and is largely dependent on HR repair (Arnaudeau *et al.*, 2001). On the other hand, NHEJ of one-ended DSBs can lead to gross chromosomal rearrangements and formation of radial chromosomes, eventually leading to genomic instability and cell death. Having previously shown that TRAIP is important for DDR signalling and survival after CPT-induced DNA damage, I next tested whether TRAIP E3 ligase activity is necessary for HR in response to CPT.

To evaluate HR proficiency, sister chromatid exchange (SCE) assays were performed. Sister chromatids can physically exchange reciprocal regions of the parental strands during unperturbed DNA replication, but in response to DNA damage, the number of SCEs observed dramatically increases and is reflective of ongoing HR-mediated DNA repair (Sonoda *et al.*,

1999). Thus, assessing these exchanges provides an estimate of HR efficiency in cells. For this assay, cells are grown for two rounds of DNA replication in the presence of BrdU, followed by preparation of metaphase spreads, treatment with the UV-sensitive dye Hoechst, long-wave UV light exposure and DAPI staining. All of the exchanges of genetic material that happen can subsequently be visualised by fluorescence microscopy. After the second round of DNA replication, the two sister chromatids will have different amounts of BrdU incorporated, making one look darker than the other (Wilson and Thompson, 2007). When no exchange occurs during either round of DNA replication, one sister chromatid appears uniformly dark and the other uniformly light (***Figure 6.8*a**). Meanwhile, an exchange results in an abrupt switching of light and dark staining regions of a chromatid (***Figure 6.8*a**) (Stults *et al.*, 2014).

When unperturbed, all four cell lines (WT, KO, KO+WT and KO+W37A) exhibited similarly low levels of sister chromatid exchanges (on average 0.16–0.19 SCEs per chromosome per metaphase) (***Figure 6.8*b-d**). CPT treatment resulted in a 13-fold increase in the number of SCEs observed in WT cells (2.3±0.5 SCEs per chromosome per metaphase) (***Figure 6.8*c-d**). In contrast, a much more modest 5-fold increase was detected in TRAIP-KO cells (1.0±0.2 SCEs per chromosome per metaphase), demonstrating an HR defect caused by the absence of TRAIP (***Figure 6.8*c-d**). This CPT-mediated recombination deficiency was rescued by the complementation of KO cells with TRAIP-WT (KO+WT) but not with the E3 ligase-deficient TRAIP-W37A (KO+W37A) (***Figure 6.8*c-d**), indicating that the E3 ligase activity of TRAIP is necessary for promoting HR in response to CPT-induced DNA damage.

Once DNA lesions are sensed by sensor proteins, an important repair step leading to efficient HR is DNA end resection at a lesion to generate a 3' overhang, which can be coated by RPA and is needed for homology searching (Huertas, 2010; Longhese *et al.*, 2010; Mimitou and Symington, 2011). The observed reduction in CPT-induced pRPA2-S4/S8 signal during S phase in TRAIP-KO cells could indicate either a direct defect of phosphorylation of these RPA2 residues or a defect of RPA loading due to impaired DNA end resection reducing available ssDNA, which would also lead to reduced levels of RPA2 phosphorylation. I therefore tested for defective DNA end resection in TRAIP-KO cells.

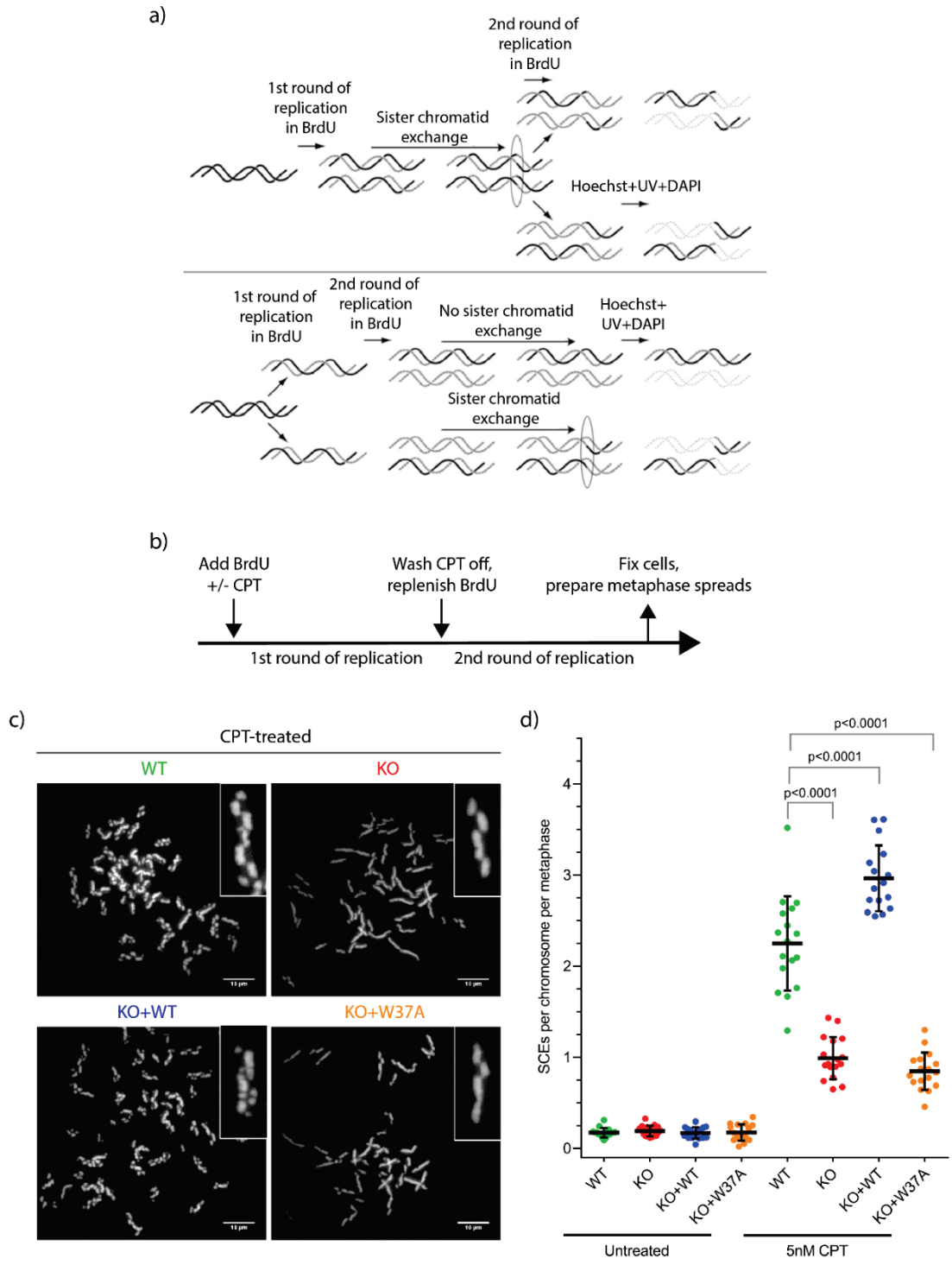

Figure 6.8. Impaired HR in CPT-treated TRAIP-KO and TRAIP E3 ligase-deficient cells.
a) Schematic representation of sister chromatid staining using two rounds of BrdU incorporation during DNA replication, followed by Hoechst staining, exposure to UV light, and staining with DAPI. A SCE event can occur following first round (top panel) or second round (bottom panel) of DNA synthesis in the presence of BrdU, resulting in abrupt switching of light and dark staining regions of a chromatid. Figure adapted from Stults, Killen and Pierce (2014).
b) Schematic of the SCE experiment.
c) Representative images of CPT-treated WT, KO, KO+WT and KO+W37A metaphase spreads, stained with DAPI and visualised using fluorescence microscopy. Scale bars: 10 µm.

d) Quantification of sister chromatid exchange (SCE) experiment to evaluate HR efficiency in the presence or absence of CPT-induced DNA damage. RPE1 p53-/- WT, TRAIP-KO (KO; clone 1.29), TRAIP-KO complemented with TRAIP-WT (KO+WT) and TRAIP-KO complemented with TRAIP-W37A (KO+W37A) cells were grown for two rounds of DNA replication (47-48 hours) in BrdU-containing medium; for the DNA damage samples, 5 nM CPT was added during the first round as well. Cells were fixed, and the prepared metaphase spreads were treated with the UV-sensitive dye Hoechst, long-wave UV light exposure and stained with DAPI. Metaphase spreads were visualised using fluorescence microscopy, and image analysis was performed using Fiji/ImageJ software. Results (mean ± SD) from one experiment are shown, and each dot in the graph represents one metaphase spread (16-17 spreads analysed per condition). Statistics: unpaired two-tailed t-test.

To test whether TRAIP and its E3 ligase activity are required for efficient CPT-induced DNA end resection, I quantified native BrdU foci as a proxy for ssDNA formation, as under native conditions, BrdU antibody will only detect patches of ssDNA, indicating DNA end resection. In unperturbed conditions, all four cell lines analysed (WT, KO, KO+WT and KO+W37A) had similarly low levels of native BrdU foci, with the average number of foci per cell ranging from 0.8 in KO+WT cells to 2 in KO cells (***Figure 6.9*****b**). There was a rise in the number of native BrdU foci in CPT-treated WT cells, averaging 6.5 foci per cell (***Figure 6.9*****a-b**). However, no such increase was observed in CPT-treated TRAIP-KO cells, where the average of only 1.5 foci per cell was detected (***Figure 6.9*****a-b**). The complementation of TRAIP-KO cells with TRAIP-WT (KO+WT), but not TRAIP-W37A (KO+W37A), rescued the formation of native BrdU foci in response to CPT (***Figure 6.9*****a-b**), suggesting the importance of E3 ligase activity of TRAIP in promoting DNA end resection at CPT-induced breaks. To ensure that the reduction in native BrdU foci is not primarily caused by reduced BrdU incorporation in TRAIP-KO cells, e.g. due to reduced proliferation, all cell lines were treated with 2 M HCl to denature DNA prior to addition of the BrdU antibody. This control condition did not reveal any substantial differences of BrdU incorporation in the four cell lines (***Figure 6.9*****c**), indicating that the differences in cell cycle progression were unlikely to have a major influence on the results obtained. Consistent with this result, Hoffmann *et al.* (2016) showed that TRAIP-depleted U2OS cells generate less ssDNA in response to CPT treatment, compared to wild-type cells. Overall, the observed DNA end resection defect provides an explanation for the reduced pRPA2-S4/S8 signalling in TRAIP-KO cells as less ssDNA is available for RPA binding, resulting in diminished RPA2 phosphorylation. As this result suggests that the reduced pRPA2 signal in TRAIP-deficient cells may be caused indirectly, it provides an alternative explanation to the dysregulated PP4-mediated dephosphorylation of RPA2 in TRAIP-KO cells (see Chapter 4).

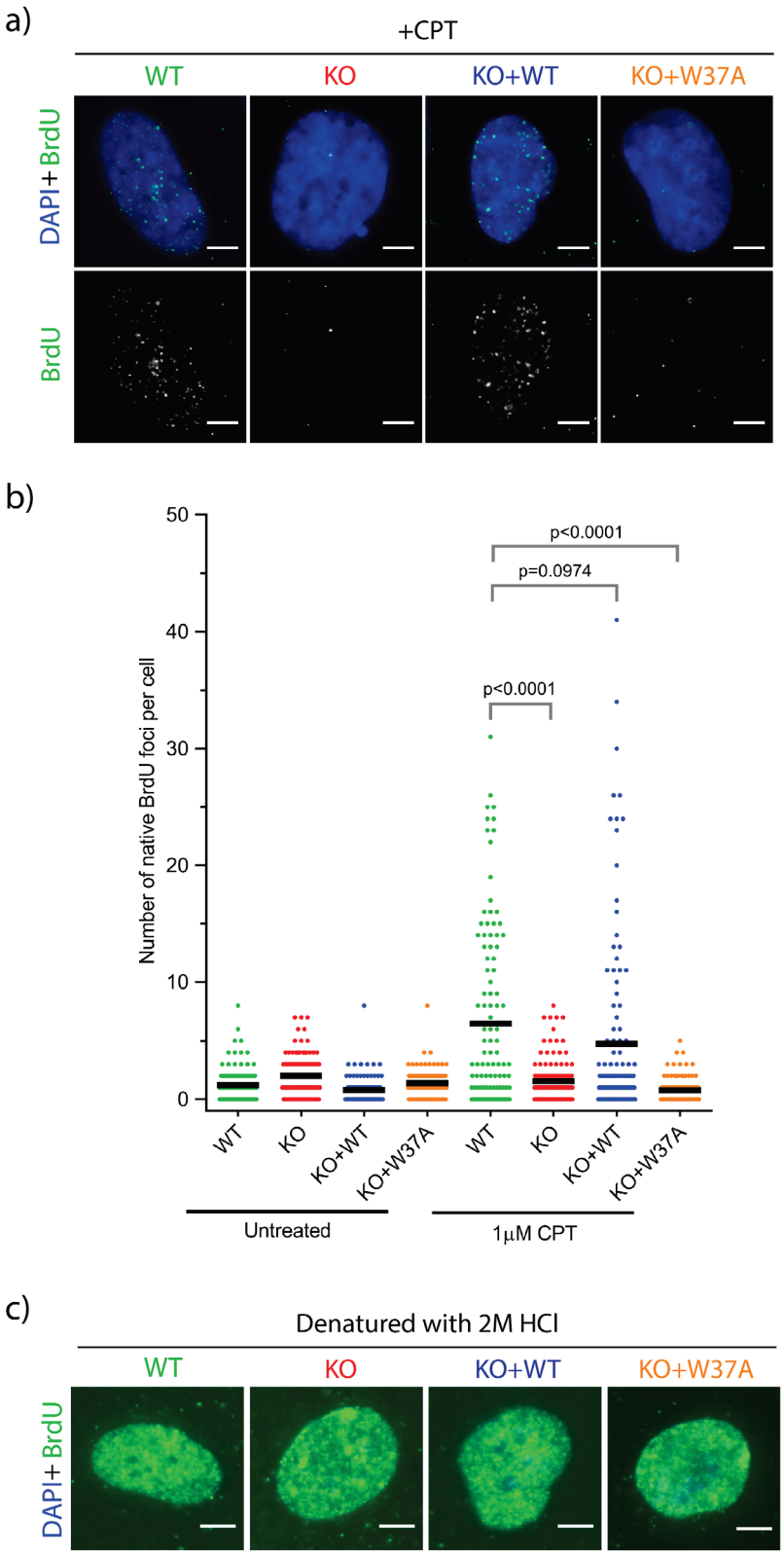

Figure 6.9. CPT-induced ssDNA formation is reduced in TRAIP-KO and E3 ligase-deficient cells.
a) Representative images of CPT-treated (+CPT) WT, KO, KO+WT and KO+W37A cells, stained for BrdU (FITC; green channel) under native conditions. Scale bars: 5 μm.
b) Quantification of native BrdU foci formation to assess ssDNA generation in the presence and in the absence of CPT treatment. RPE1 p53-/- WT, TRAIP-KO (KO; clone 1.29), TRAIP-KO complemented with TRAIP-WT (KO+WT) and TRAIP-KO complemented with TRAIP-W37A

(KO+W37A) cells were grown in the presence of 10 µM BrdU for 24h, and 1 µM CPT was added for the last 90 min before cell fixation. Detergent pre-extraction of non-chromatin-bound proteins was performed before cell fixation with formaldehyde. Cells were immunostained for BrdU and visualised using fluorescence microscopy. Image analysis was performed using Fiji/ImageJ software. Results from one experiment are shown; black bars indicate the mean, and each dot in the graph represents one cell (more than 100 cells analysed per condition). Statistics: unpaired two-tailed t-test.
c) Representative images of CPT-treated (+CPT) WT, KO, KO+WT and KO+W37A cells, stained for BrdU (FITC; green channel) under denatured conditions (treatment with 2 M HCl prior to addition of BrdU antibody). Scale bars: 5 µm.

6.1.4. Chromatin recruitment of BRCA1 and 53BP1 is not affected in TRAIP-KO cells

The results described in the previous section suggest that TRAIP may be involved in promoting DNA end resection after CPT treatment and therefore may act as a regulator of DSB repair pathway choice, potentiating HR and suppressing NHEJ. The possible ways to achieve this could be either a) TRAIP-dependent ubiquitination of a DNA end resection protagonist (a component of HR machinery) to activate it or promote its translocation or recruitment to chromatin, or b) TRAIP-dependent ubiquitination of a DNA end resection antagonist (a component of NHEJ machinery) to promote its proteasomal degradation, inactivation or relocalisation.

To investigate what proteins are affected by TRAIP in response to CPT-induced DNA damage, I conducted immunoblotting analysis in CPT-treated TRAIP-KO cells to detect chromatin recruitment of replication fork-associated proteins that are known components of DNA end resection machinery or DNA end protection. Using a candidate approach, I looked at chromatin enrichment of two key players in DSB repair pathway choice: BRCA1, which promotes DNA end resection and HR repair in response to replication stress, and 53BP1, which facilitates DNA end protection and NHEJ (Daley and Sung, 2014) (see Section 1.3.3). If TRAIP was involved in regulating one of these factors in response to CPT-induced DNA damage, one may expect to see changes in the recruitment of these proteins to chromatin. Notably, siTRAIP-treated cells were previously reported to show reduced BRCA1 recruitment to sites of IR-induced DNA damage (Soo Lee *et al.*, 2016); however, it is not known if this occurs at CPT-induced DNA lesions as well.

No major changes in the recruitment of BRCA1 and 53BP1 to chromatin took place in KO and KO+W37A cells, compared to WT and KO+WT cells (***Figure 6.10***). In both total protein and chromatin-enriched fractions, a shift for BRCA1 and 53BP1 protein bands was observed

after CPT-induced DNA damage, likely indicating DNA damage-dependent phosphorylation of these proteins. Although slightly reduced total BRCA1 levels in KO and KO+W37A cells were observed, the CPT-induced recruitment of this factor to chromatin was unaffected (***Figure 6.10***). As BRCA1 protein expression is regulated in a cell cycle-dependent manner (Vaughn *et al.*, 1996), this result could potentially reflect cell cycle differences between the cell lines analysed, as TRAIP-KO cells were observed to divide at a slower rate than WT cells in cell culture.

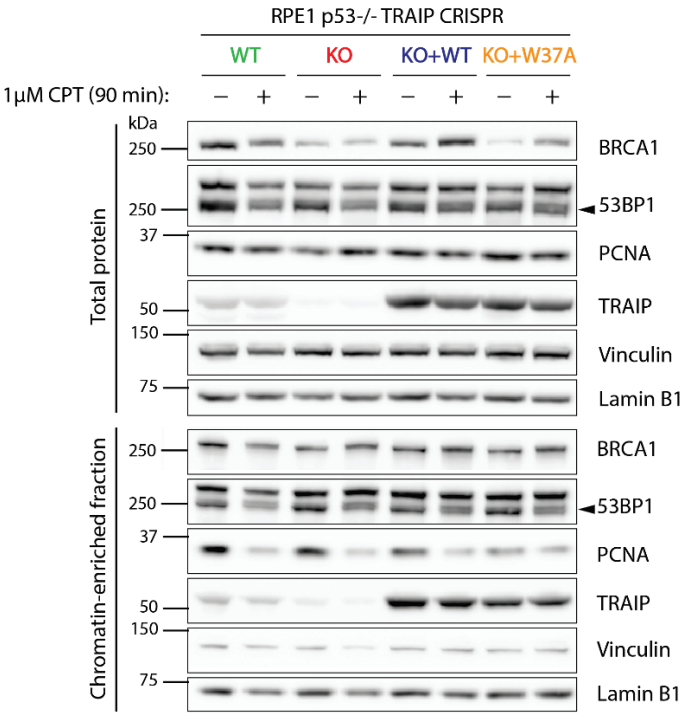

Figure 6.10. CPT-induced BRCA1 and 53BP1 recruitment to chromatin is unaffected in RPE1 p53-/- TRAIP-KO and E3 ligase-deficient cells.
Immunoblotting demonstrates CPT-induced chromatin recruitment of BRCA1, 53BP1 and PCNA. RPE1 p53-/- WT, TRAIP-KO (KO; clone 1.29), TRAIP-KO complemented with TRAIP-WT (KO+WT) and TRAIP-KO complemented with TRAIP-W37A (KO+W37A) cells were exposed to CPT treatment (1 μM) for 90 min and harvested for immunoblotting without (total protein) or with pre-extraction step (chromatin-enriched fraction). Untreated (–) and CPT-treated (+) samples of the four cell lines were compared for protein levels of BRCA1, 53BP1 and PCNA by immunoblotting. Vinculin served as a loading control. Black arrowhead indicates the expected 53BP1 protein band.

As previously observed by multiple studies (Görisch *et al.*, 2008; Sirbu *et al.*, 2011; W. Feng *et al.*, 2016), PCNA was unloaded from chromatin in response to replication-associated DNA damage in this analysis, while total PCNA levels remained constant (***Figure 6.10***), demonstrating successful enrichment of chromatin-bound proteins in the chromatin-enriched

fraction. W. Feng *et al.* (2016) suggested that TRAIP depletion disrupts efficient PCNA unloading, however, this was not observed in this experiment.

In summary, alterations in BRCA1 and 53BP1 chromatin recruitment were not detected by immunoblotting in CPT-treated TRAIP-KO and E3 ligase-deficient cells. Although defective DNA end resection at CPT-induced one-stranded DSBs was observed in TRAIP-KO cells, BRCA1 recruitment to chromatin was not impaired, suggesting that TRAIP mediates CPT-induced DNA end resection in a more complex manner, possibly independent of BRCA1 and 53BP1.

6.1.5. Summary: TRAIP and CPT-induced DNA damage

In this section, it was shown that TRAIP-KO cells do not properly respond to CPT treatment, demonstrating reduced DNA end resection, lower levels of phosphorylation of DNA damage markers, defective HR, and reduced cell survival. Furthermore, using cells deficient in E3 ligase activity (TRAIP-KO cells complemented with TRAIP-W37A mutant), proper E3 ubiquitin ligase activity of TRAIP was shown to be required for all the above functions of TRAIP. However, cell survival was not fully dependent on the E3 ligase activity of TRAIP, suggesting that either residual levels of E3 ligase activity due to overexpression of the TRAIP-W37A mutant or a potential non-catalytic role of TRAIP in mediating CPT resistance contribute to maintaining cell viability.

The most pronounced DDR signalling defect observed in TRAIP-KO cells, impaired pRPA2-S4/S8 signal, is likely due to TRAIP promoting DNA end resection at one-ended DSBs, which allows RPA loading onto ssDNA. Upon CPT treatment, the absence of TRAIP may lead to an increase in collapsed and unrepaired replication forks, eventually resulting in the cell survival defect. TRAIP-KO cells also exhibited reduced levels of γH2AX and pCHK1-S345 in response to CPT treatment. The effect of the absence of TRAIP on these DNA damage markers may be indirectly mediated through reduced RPA2 loading and phosphorylation, as RPA-coated ssDNA is a well-established signal for ATR activation and subsequent phosphorylation of its downstream effectors (Zeman and Cimprich, 2014) (***Figure 6.11*b**). An alternative explanation is that TRAIP instead promotes efficient CPT-induced phosphorylation of H2AX and CHK1, which subsequently allows timely DNA end resection, RPA loading and RPA2 phosphorylation (***Figure 6.11*a**). Distinguishing between these possibilities and defining the mechanism by which TRAIP works at CPT-induced DNA lesions will require further

experiments, and establishing the targets of TRAIP-mediated ubiquitination will be of particular importance. Moreover, given the reduced numbers of sister chromatid exchanges in CPT-treated TRAIP-KO cells, TRAIP may also be considered a novel HR-promoting factor, which indirectly facilitates it by allowing efficient DNA end resection to take place.

Overall, consistent with findings by Hoffmann *et al.* (2016), my current data indicate that TRAIP supports ATR-dependent checkpoint signalling in response to CPT-induced DNA damage, likely by facilitating processes at replication fork that result in the formation of RPA-coated ssDNA regions.

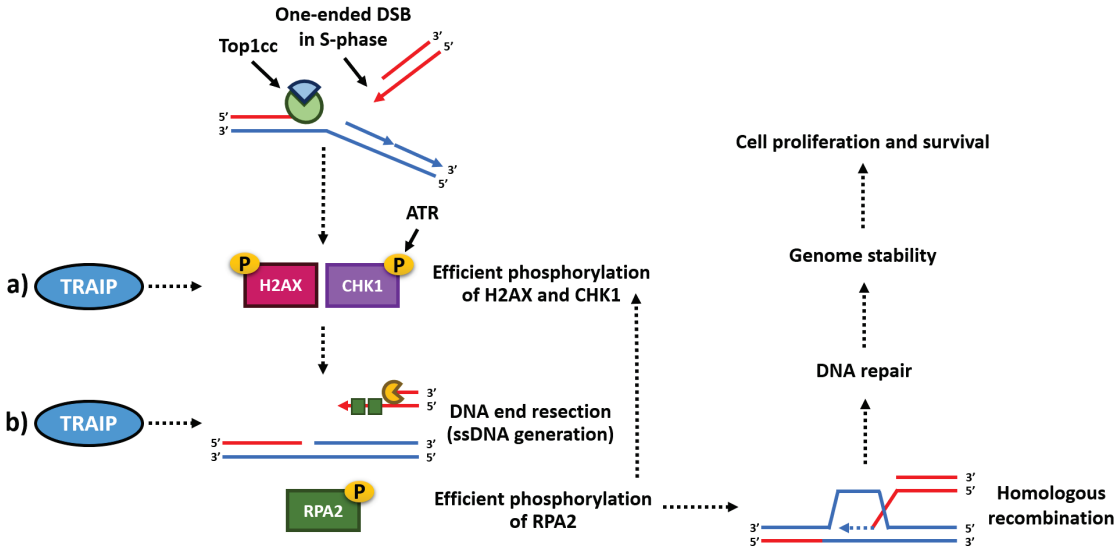

Figure 6.11. A model for the role of TRAIP in responding to CPT-induced DNA damage.
In this section of my thesis, TRAIP-KO cells were shown to fail at responding to CPT-induced DNA damage, demonstrating reduced DNA end resection, lower levels of phosphorylation of DNA damage markers, defective HR, and reduced cell survival. CPT treatment causes stabilisation of the TOP1 covalent complex (Top1cc) and a SSB, which is turned into a one-ended DSB upon collision with the replication fork. I postulate that TRAIP may promote the repair of CPT-induced DNA damage by acting on DDR signalling (a), e.g. ensuring efficient phosphorylation of DNA damage markers H2AX and CHK1, which subsequently allows efficient DNA end resection and RPA2 phosphorylation. Alternatively, TRAIP may be involved in directly promoting DNA end resection (b), which then allows efficient RPA2 phosphorylation and stimulates H2AX and CHK1 phosphorylation.

6.2. The role of TRAIP in MMC-ICL repair

6.2.1. Does TRAIP mediate CMG unloading and replisome disassembly, required for ICL repair?

Having established the importance of TRAIP for DNA repair of CPT-induced DNA lesions, I decided to investigate whether TRAIP has a role at other types of DNA lesions that induce replication fork stalling. In particular, I focussed on the DNA interstrand crosslinking (ICL) agent mitomycin C (MMC), as TRAIP was shown to be involved in ICL repair in egg extracts of African clawed frog (*Xenopus laevis*) (personal communication with Prof Johannes Walter and Prof David Pellman; Wu, Semlow *et al.*, unpublished).

ICLs are one of the most toxic types of DNA lesions, blocking both DNA replication and transcription (Kee and D'Andrea, 2010). Endogenous ICLs emerge following accumulation of reactive aldehydes, the by-products of several metabolic processes (Langevin *et al.*, 2011; Pontel *et al.*, 2015), whereas various chemotherapeutic agents, such as psoralens, platinum compounds and mitomycins, are exogenous sources of ICLs (reviewed by Deans and West, 2011). Canonical ICL repair involves the Fanconi Anaemia (FA) pathway to recognise and unhook the DNA lesion, followed by TLS-mediated lesion bypass and HR to repair the generated DSB (see Section 1.3.5 and ***Figure 1.10***). Recently, an alternative ICL repair pathway was discovered in *X. laevis* (Semlow *et al.*, 2016). This pathway was shown to be dependent on the NEIL3 glycosylase and mainly involved in processing psoralen- and abasic (apurinic/apyrimidinic) site ICLs (AP-ICLs) (***Figure 6.12***). The NEIL3 pathway does not require introduction of a DSB or involvement of FA proteins; instead, NEIL3 unhooks an ICL by *N*-glycosylation, allowing TLS to take place (Semlow *et al.*, 2016). Semlow *et al.* (2016) also observed that in the absence of NEIL3, psoralen- and AP-ICLs can be repaired by the FA pathway, which is preferred for repairing MMC- and cisplatin-ICLs (***Figure 6.12***). Overall, the FA pathway is the main choice of cells for repairing MMC- and cisplatin-ICLs, whereas psoralen- and AP-ICLs are preferentially repaired by the NEIL3 pathway, which avoids the introduction of a DSB and thus a threat to cell viability.

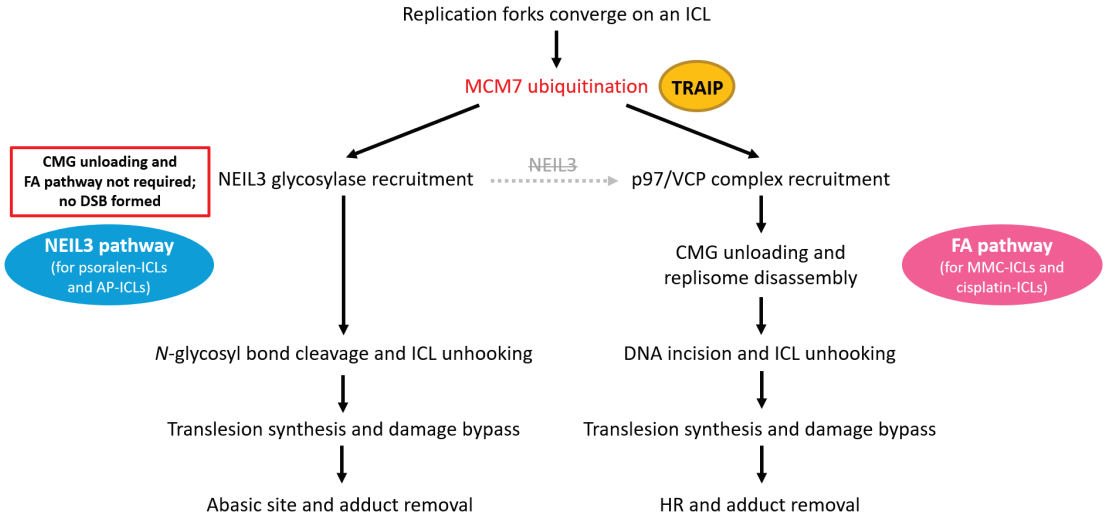

Figure 6.12. A model for the role of TRAIP in ICL repair.
Unpublished data by Wu, Semlow *et al.* (Prof Johannes Walter and Prof David Pellman laboratories) suggest that TRAIP is involved in both FA- and NEIL3-mediated ICL repair pathways by promoting replisome disassembly and NEIL3 recruitment, respectively. According to their recent findings using *X. laevis* egg extracts, TRAIP-mediated addition of longer ubiquitin chains on the CMG component MCM7 facilitates its unloading from stalled replication forks, subsequently destabilising the replisome and promoting its extraction from chromatin (FA pathway). Alternatively, TRAIP-mediated addition of shorter ubiquitin chains on MCM7 is required for the recruitment of NEIL3 glycosylase (NEIL3 pathway), suggesting that TRAIP dictates ICL repair pathway choice. Figure modified and adapted from Semlow *et al.* (2016).

One of the first events leading to efficient FA-mediated ICL repair is the unloading of CMG helicase complex, which includes MCM2-7, CDC45, and GINS, from DNA and dissolution of the replisome at the site of stalled replication (Fullbright *et al.*, 2016; Semlow *et al.*, 2016). In a cell-free system, CMG removal is necessary for replication fork reversal and subsequent generation of a DNA structure that allows cisplatin-ICL incision, unhooking and repair (Amunugama *et al.*, 2018). It was reported that E3 ligase-dependent ubiquitination of the CMG subunit MCM7 is the key requirement for efficient unloading of the CMG helicase, its extraction from chromatin by the ATPase p97/VCP and subsequent recycling (Fullbright *et al.*, 2016; Long *et al.*, 2014; Semlow *et al.*, 2016). Significantly, TRAIP was recently shown to be required for MCM7 ubiquitination at cisplatin- and AP-ICLs, leading to CMG unloading (FA pathway) and NEIL3 recruitment (NEIL3 pathway), respectively, in *X. laevis* egg extracts (Wu, Semlow *et al.*, unpublished) (***Figure 6.12*****).** These observations suggest that TRAIP is a key mediator of ICL repair pathway choice in a cell-free system. TRAIP-mediated deposition of longer ubiquitin chains on the CMG component MCM7 was shown to promote its unloading from stalled replication forks, resulting in replisome destabilisation and its extraction from

chromatin in the ATPase p97/VCP-dependent manner, which initiated FA pathway (Wu, Semlow *et al.*, unpublished). Meanwhile, TRAIP-mediated deposition of short ubiquitin chains on MCM7 was required for NEIL3 recruitment and ICL repair via NEIL3 pathway (Wu, Semlow *et al.*, unpublished). Overall, TRAIP-dependent ubiquitination of MCM7 was observed to be essential for both ICL repair pathways in *X. laevis*, but the relevance of these findings in mammalian cells remained unclear.

In the following sections of this chapter, the experiments conducted to establish the role of TRAIP in ICL repair in a mammalian cell system are described. If TRAIP is involved in MCM7 ubiquitination in mammalian cells as well, epistatic relationship between TRAIP and FA pathway, as well as between TRAIP and NEIL3 pathway, would be expected. In the following section (Section 6.2.2), experiments delineating effects of MMC treatment on TRAIP-KO cells are described, providing a set of readouts to study whether TRAIP is epistatic with FANCD2, a key component of the FA pathway (Section 6.2.3).

6.2.2. Phenotypic characterisation of TRAIP-KO cells in response to MMC

Firstly, the RPE1 p53-/- TRAIP-KO cell line was used to establish the phenotype of the cells lacking TRAIP in response to the ICL-inducing drug MMC. The sensitivity of TRAIP-depleted U2OS cells to MMC was previously demonstrated by Hoffmann *et al.* (2016), and so I tested whether this finding could be replicated in RPE1 p53-/- TRAIP-KO cells. In clonogenic cell survival assay, TRAIP-KO cells formed fewer clones than WT cells at all doses tested, with only 1.1% of the plated single cells surviving and forming clones at the highest MMC dose tested (60 nM), compared to 54.7% of the WT cells (***Figure 6.13***). This result confirmed that TRAIP-KO cells are hypersensitive to MMC treatment, consistent with findings by Hoffmann *et al.* (2016).

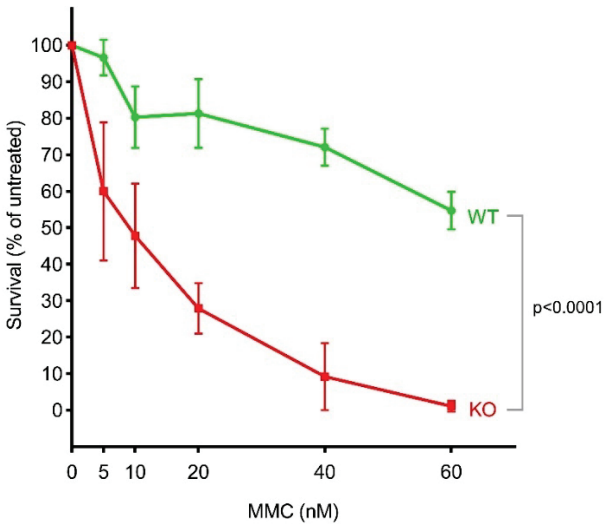

Figure 6.13. TRAIP-KO cells are hypersensitive to MMC.
RPE1 p53-/- WT and TRAIP-KO (KO; clone 1.29) cells were plated at very low density and treated with MMC (5 nM – 60 nM) for 24 hours. The drug was removed by extensive PBS washing, and cells were grown for 8 days until colonies were formed, followed by fixation, staining and colony counting. Results (mean ± SD) from 2-4 independent experiments where those doses were examined are shown (5 nM and 60 nM MMC: 2 independent experiments; 20 nM and 40 nM MMC: 3 independent experiments; 10 nM MMC: 4 independent experiments). Two-way ANOVA was used for statistical analysis.

To understand whether the same DDR signalling defect underlies MMC and CPT hypersensitivity of TRAIP-KO cells, immunoblotting analysis of pRPA2-S4/S8, γH2AX and pCHK1-S345 in RPE1 p53-/- TRAIP-KO cells exposed to MMC treatment was performed. Surprisingly, the effect opposite to the one seen after CPT treatment was observed. At each of the three time points tested (16 h, 24 h and 32 h post-addition of MMC), pRPA2-S4/S8 phosphorylation was elevated in TRAIP-KO cells, compared to WT cells (***Figure 6.14*a-b**). The complementation of TRAIP-KO cells with TRAIP-WT (KO+WT) rescued the pRPA2-S4/S8 increase (***Figure 6.14*c**), showing it to be specific to TRAIP loss. Although MMC-induced pRPA2-S4/S8 levels were significantly elevated in TRAIP-KO cells (4±1.8 times increase 24 h post-MMC), no consistent changes in H2AX and CHK1 phosphorylation were observed (***Figure 6.14*b**). These observations suggest that disruption of distinct mechanisms underlies the sensitivity of TRAIP-KO cells to MMC and to CPT (described in Section 6.1), as upon CPT treatment, TRAIP-KO cells have lower levels of replication-associated ssDNA generation, reduced pRPA2-S4/S8 signal and HR efficiency, while showing hypersensitivity to this drug. However, differences in the time points analysed need to be considered as well, as MMC-induced RPA2 phosphorylation is detected much later (16–32 h post-treatment) than the CPT-induced RPA2 signal (30–90 min post-treatment).

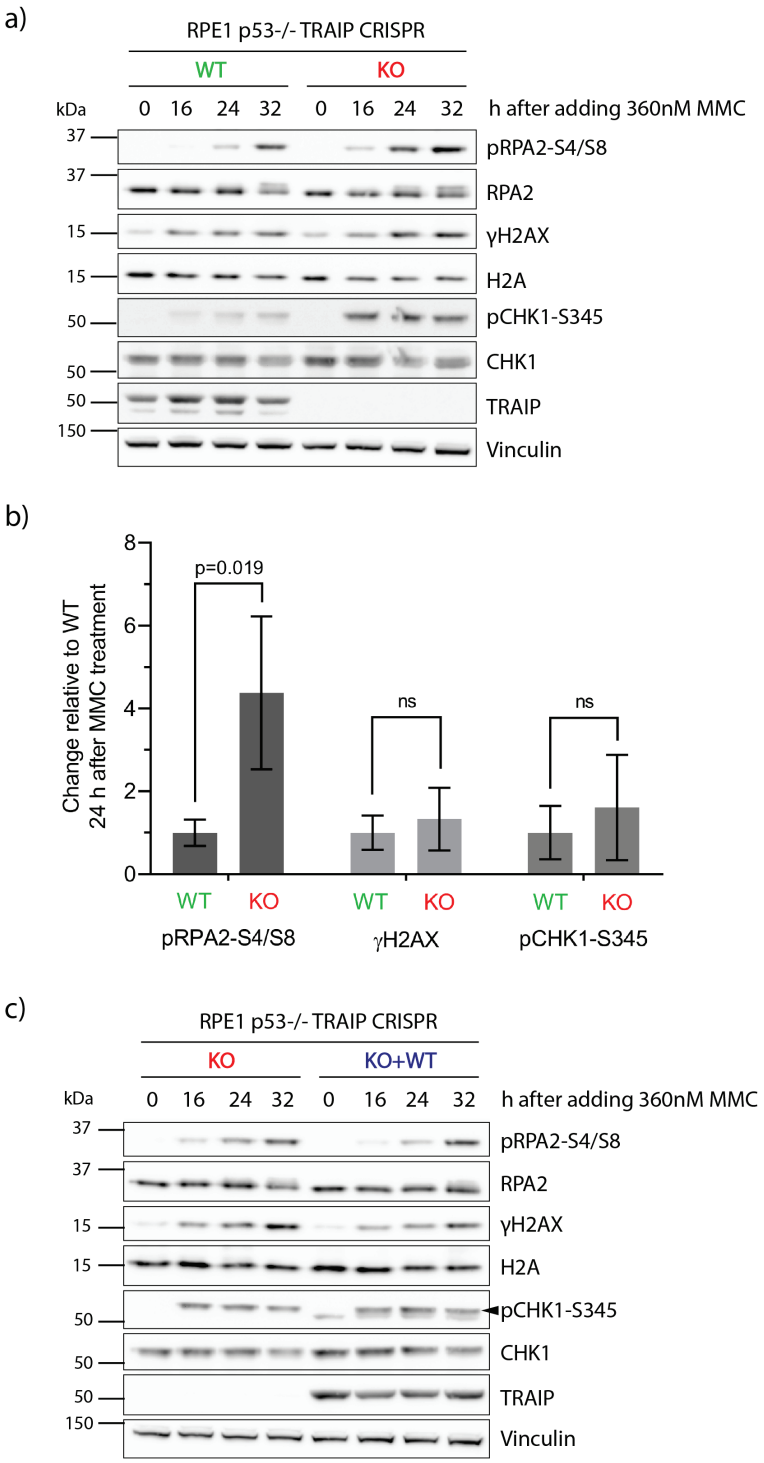

Figure 6.14. MMC-induced RPA2 phosphorylation is increased in RPE1 p53-/- TRAIP-KO cells.
a) Representative immunoblot (n=3 independent experiments) demonstrating MMC-induced pRPA2-S4/S8, γH2AX and pCHK1-S345 levels in RPE1 p53-/- WT (clone 1.30) and TRAIP-KO (clone 1.29) cell lines. Untreated (0 h) cells and cells exposed to MMC treatment (360 nM) for 16, 24 or 32 h were harvested and analysed by immunoblotting. Vinculin served as a loading control.
b) Quantification of pRPA2-S4/S8, γH2AX and pCHK1-S345 levels 24 hours post-MMC addition demonstrates significant increase in MMC-induced pRPA2-S4/S8 in TRAIP-KO cell lines. Image analysis was performed using Fiji/ImageJ software. pRPA2-S4/S8, γH2AX and pCHK1-S345

levels were normalised to RPA2, H2A and CHK1, respectively. Results (mean ± SD) from n=3 independent experiments are shown; statistics: unpaired two-tailed t-test.
c) Immunoblotting experiment demonstrating that the increase in pRPA2-S4/S8 levels post-MMC treatment is rescued by the complementation of TRAIP-KO cells with TRAIP-WT (KO+WT). Black arrowhead indicates the pCHK1-S345 band, as pCHK1-S345 signal was detected by re-probing the membrane used for TRAIP detection (lower band).

To establish more details on the mechanism underlying the MMC sensitivity of TRAIP-KO cells, I decided to use sister chromatid exchange assay to assess HR, which was observed to be defective in CPT-treated TRAIP-KO cells (***Figure 6.8***). Strikingly, the SCE assay indicated no significant change in HR efficiency in MMC-treated TRAIP-KO cells, compared to WT cells (***Figure 6.15***). This result suggested that TRAIP does not promote HR in response to MMC-induced DNA damage, in agreement with different mechanisms behind the role of TRAIP in response to CPT and MMC.

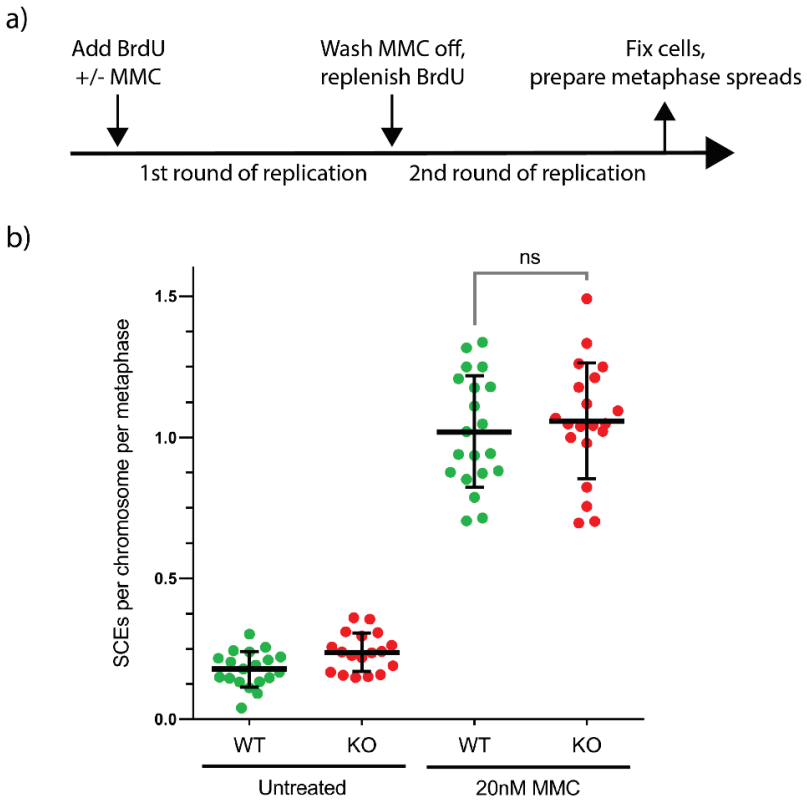

Figure 6.15. HR efficiency is not affected in TRAIP-KO cells exposed to MMC.
a) Schematic of the SCE experiment.
b) Quantification of sister chromatid exchange (SCE) experiment to evaluate HR efficiency in the presence or absence of MMC-induced DNA damage. RPE1 p53-/- WT and TRAIP-KO (KO; clone 1.29) cells were grown for two rounds of DNA replication (47-48 hours) in BrdU-containing medium; for the DNA damage samples, 20 nM MMC was added during the first

round as well. Cells were fixed, and the prepared metaphase spreads were treated with the UV-sensitive dye Hoechst, long-wave UV light exposure and stained with DAPI. Metaphase spreads were visualised using fluorescence microscopy, and image analysis was performed using Fiji/ImageJ software. Results (mean ± SD) from one experiment are shown, and each dot in the graph represents one metaphase spread. Statistics: unpaired two-tailed t-test.

Cells deficient of FA factors are known to exhibit increased levels of genomic instability (rewieved by Palovcak *et al.*, 2017). TRAIP-depleted U2OS cells were also observed to have elevated levels of chromatid breaks and radial chromosomes in response to MMC treatment (Hoffmann *et al.*, 2016). Additionally, multiple chromosomal aberrations in karyotypes of unperturbed TRAIP-KO cells were previously observed (see Section 5.3). To establish if elevated levels of genomic instability were present in MMC-treated TRAIP-deficient cells, RPE1 p53-/- WT, TRAIP-KO and KO+WT cells were treated with MMC for 24 h, followed by preparation and analysis of metaphase spreads. As expected, the loss of TRAIP contributed to the increase in genomic instability in cells exposed to MMC, represented by elevated numbers of chromatid breaks, compared to MMC-treated WT cells (***Figure 6.16*****a-b**). Additionally, a few metaphases with radial chromosomes were observed in MMC-treated TRAIP-KO cells (***Figure 6.16*****c**). Even in unperturbed conditions, TRAIP-KO cells exhibited higher levels of genomic instability (***Figure 6.16*****b-c**), consistent with the karyotyping analyses performed in Section 5.3. The chromosomal aberrations in unperturbed and MMC-treated TRAIP-KO cells were shown to be TRAIP-specific, as complementation of KO cells with TRAIP-WT rescued the phenotype (***Figure 6.16*****b-c**).

In summary, the experiments described in this section showed that after MMC treatment TRAIP is needed for optimal cell survival, as well as for proper RPA2-S4/S8 phosphorylation and maintenance of genomic stability.

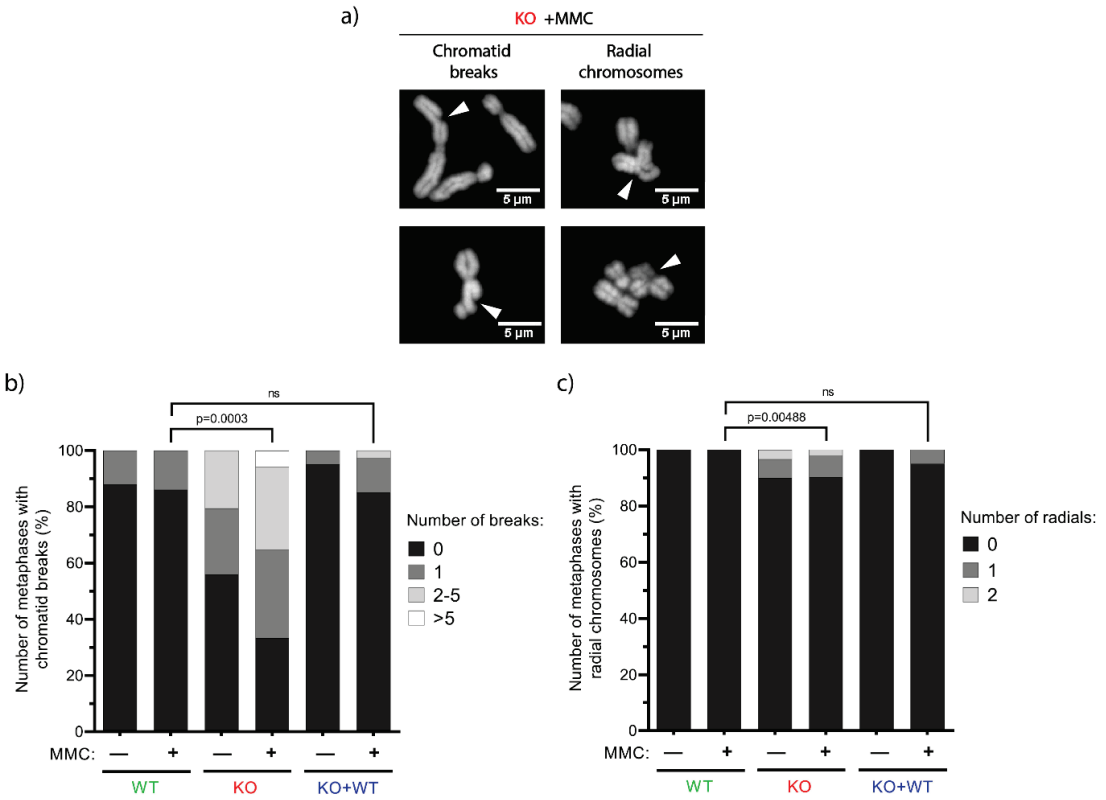

Figure 6.16. Genomic instability is increased in TRAIP-KO cells after MMC treatment.
a) Representative images of chromosomal aberrations in MMC-treated TRAIP-KO metaphase spreads, stained with DAPI and visualised using immunofluorescence microscopy. Scale bars: 5 µm.
b, c) Quantification of chromatid breaks (b) and radial chromosomes (c) in RPE1 p53-/- WT, TRAIP-KO and TRAIP-KO complemented with TRAIP-WT (KO+WT) cells with and without MMC treatment demonstrates significant increase in genomic instability in MMC-treated TRAIP-KO cell lines, which is rescued by complementation with TRAIP-WT. To visualise chromosomal abnormalities, cells were grown in the presence or absence of 60 nM MMC for 24 h, followed by cell fixation and preparation of metaphase spreads, which were stained with DAPI. Image analysis was performed using Fiji/ImageJ software. Approximately 40 metaphase spreads were evaluated per condition. Results from one experiment are shown. Statistics: unpaired two-tailed t-test between the average number of chromosomal aberrations per metaphase spread.

6.2.3. TRAIP is not epistatic with the FA pathway in MMC-ICL repair

In *X. laevis* egg extracts, TRAIP is required for MCM7 ubiquitination for ICL repair through both the FA and NEIL3 pathways (Wu, Semlow *et al.*, unpublished). To elucidate the role of TRAIP in MMC-ICL repair in mammalian somatic cells, I analysed the epistatic relationship between TRAIP and the FA pathway in the context of MMC-induced ICLs. Epistasis between them would mean that, after MMC treatment, the lack of TRAIP and the depletion of a FA pathway factor would result in the same cellular outcome, and that the absence of both

proteins would not cause a more severe phenotype than loss of each one individually. For these epistasis experiments, I chose to deplete FANCD2, a central component of the FA pathway. Mono-ubiquitination of FANCD2 in response to DNA damage is the key regulatory step in MMC-ICL repair, triggering its re-localisation to ICLs. Mono-ubiquitinated FANCD2 then coordinates downstream repair events, including HR (Garner and Smogorzewska, 2011) (see Section 1.3.5). Therefore, depletion of FANCD2 is expected to abrogate the ability of cells to repair MMC-induced ICLs.

FANCD2 was depleted from WT and TRAIP-KO cells, and the effects of this depletion on DDR signalling, chromosomal abnormalities and cell survival were analysed (***Figure 6.17***). Consistent with my previous results (***Figure 6.14*****b**), immunoblotting analysis revealed a significant increase in pRPA2-S4/S8 signal in siLUC-treated TRAIP-KO cells, compared to siLUC-treated WT cells (***Figure 6.18*****a-b**). Although the lack of TRAIP and of FANCD2 resulted in similar levels of pRPA2-S4/S8 signal, it was not found to be significantly elevated in FANCD2-depleted WT cells, compared to siLUC-treated WT cells, due to large experiment-to-experiment variation (***Figure 6.18*****a-b**).

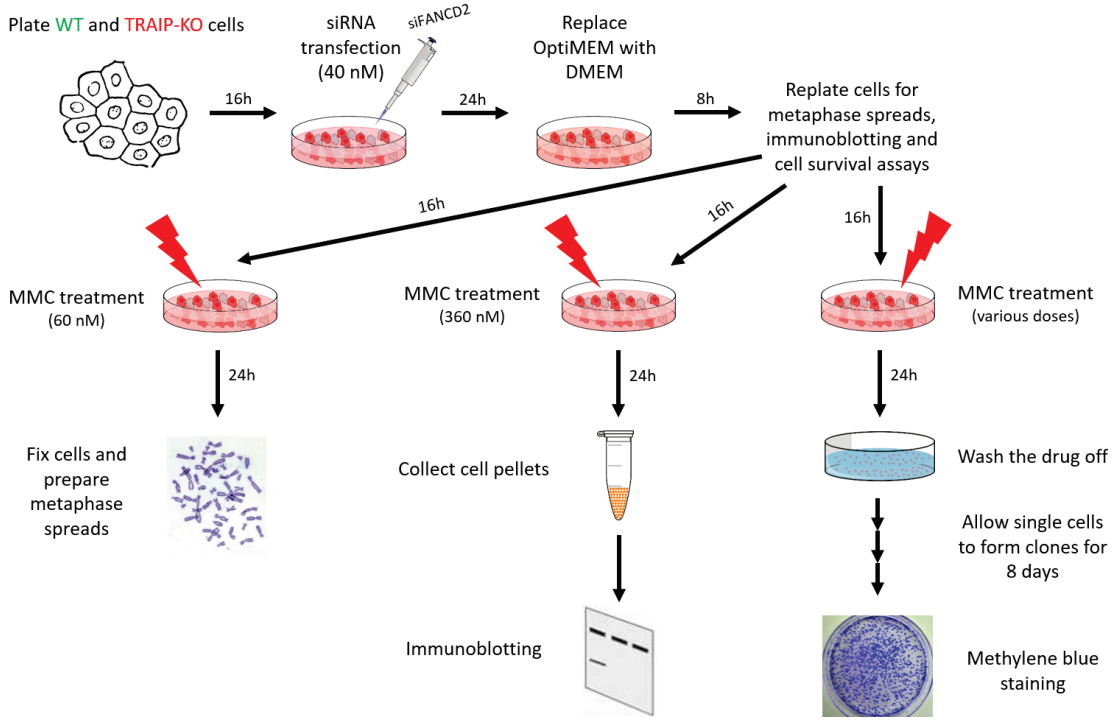

Figure 6.17. Experimental setup of TRAIP and FANCD2 epistasis analysis in mammalian somatic cells.
RPE1 p53-/- WT and TRAIP-KO (clone 1.29) cells were transfected with siFANCD2 and subsequently used for three different analyses: immunoblotting to assess RPA2 phosphorylation, metaphase spreads for detecting chromosomal aberrations, and clonogenic cell survival assays.

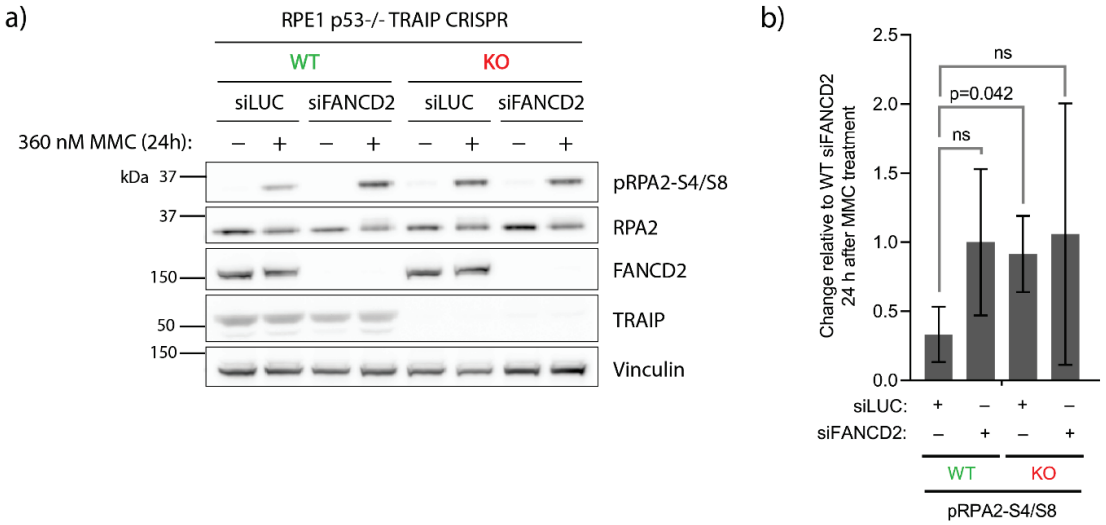

Figure 6.18. pRPA2-S4/S8 levels are similarly increased in TRAIP-KO and siFANCD2-treated WT cells after MMC treatment.

a) Representative immunoblot (n=3 independent experiments) demonstrating MMC-induced pRPA2-S4/S8 levels in RPE1 p53-/- WT (clone 1.30) and TRAIP-KO (clone 1.29) cells, which were transfected with siLUC or siFANCD2 for 48 hours, exposed to MMC treatment (360 nM) and harvested for immunoblotting 24 h after the treatment was started. Untreated (–) and MMC-treated (+) samples were compared for phosphorylation of pRPA2-S4/S8; vinculin served as a loading control.

b) Quantification of pRPA2-S4/S8 levels 24 h post-MMC addition in the four conditions. Image analysis was performed using Fiji/ImageJ software. pRPA2-S4/S8 levels were normalised to vinculin. Results (mean ± SD) from n=3 independent experiments are shown; statistics: unpaired two-tailed t-test.

Although consistent with epistasis between TRAIP and FANCD2 in MMC-ICL repair, the DDR experiments exhibited high experiment-to-experiment variation, preventing me from making this conclusion. Thus, in addition to the DDR signalling, I decided to assess the epistasis between these factors at maintaining genome stability. Metaphase spreads were prepared using FANCD2-depleted WT and TRAIP-KO cells, with or without MMC treatment, and analysed for chromatid breaks and radial chromosomes. In unperturbed cells, the lack of TRAIP, but not FANCD2 depletion, resulted in the significantly increased numbers of chromatid breaks per metaphase (***Figure 6.19*b**), consistent with a requirement of TRAIP during unperturbed cell cycle progression. This observation recapitulates the overall increase in gross chromosomal abnormalities previously seen in karyotypes of TRAIP-KO cells (see Section 5.3).

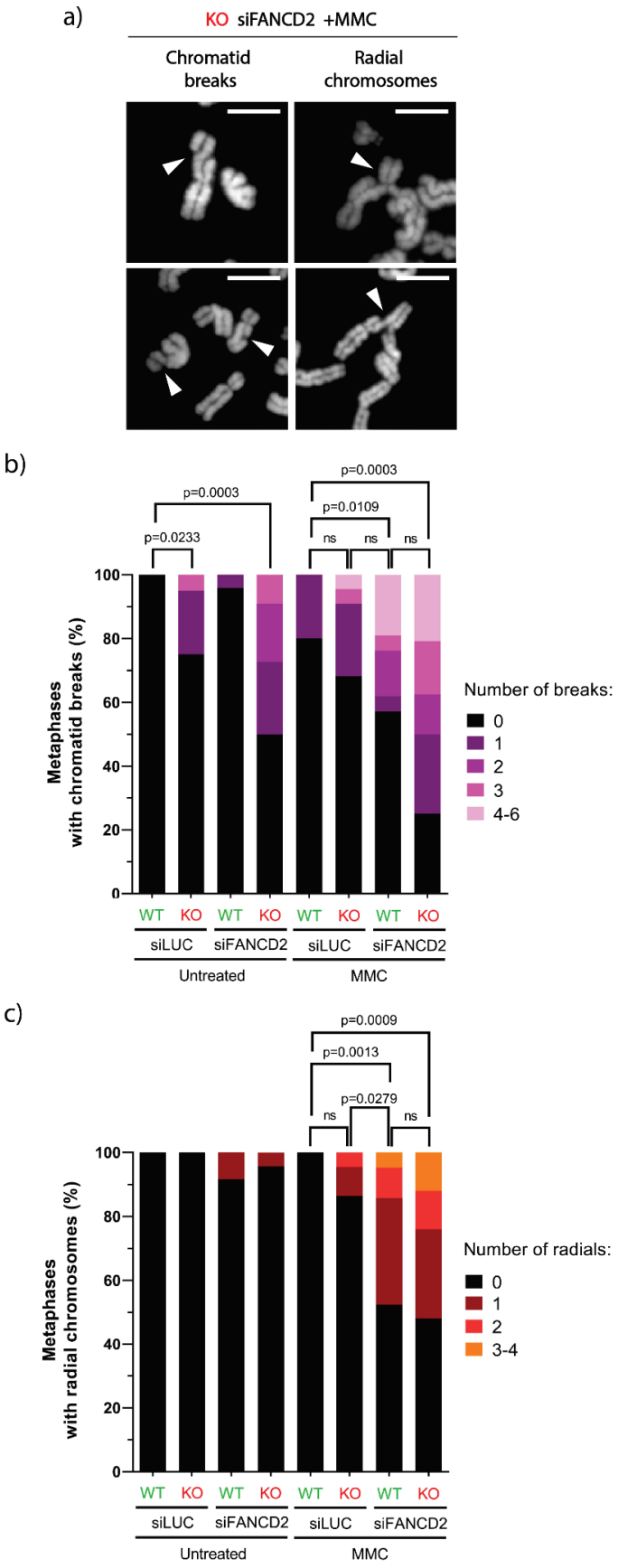

Figure 6.19. TRAIP and FANCD2 are not epistatic in maintaining genomic stability upon MMC treatment.

a) Representative images of chromosomal aberrations in MMC-treated FANCD2-depleted TRAIP-KO metaphase spreads, stained with DAPI and visualised using immunofluorescence microscopy. Scale bars: 5 µm.
b, c) Quantification of chromatid breaks (b) and radial chromosomes (c) in siLUC- or siFANCD2-treated RPE1 p53-/- WT and TRAIP-KO cells with and without MMC treatment is shown. To visualise chromosomal abnormalities, cells were grown in the presence or absence of 60 nM MMC for 24 h, followed by cell fixation and preparation of metaphase spreads, which were stained with DAPI. Image analysis was performed using Fiji/ImageJ software. Approximately 20-25 metaphase spreads were analysed per condition. Results from one experiment are shown. Statistics: unpaired two-tailed t-test between the average number of chromosomal aberrations per metaphase spread.

More MMC-induced chromatid breaks were detected in FANCD2-depleted WT cells than in siLUC-treated WT cells or TRAIP-KO cells (***Figure 6.19*b**). An additive exacerbation of this phenotype was observed in cells lacking both of these factors (***Figure 6.19*a-b**). These data indicate that TRAIP and FANCD2 likely operate in different pathways to maintain genomic stability upon MMC exposure, as the absence of both factors results in a more severe effect on genome stability than the lack of each of them individually.

Inactivation of the FA pathway was previously demonstrated to cause increased appearance of toxic radial chromosomes (Deans and West, 2011; Newell *et al.*, 2004) as a result of NHEJ-mediated repair of DSBs. Indeed, while a few radial chromosomes were observed in TRAIP-KO cells after MMC treatment, FANCD2 depletion had a much stronger effect on radial chromosome frequency (***Figure 6.19*c**). The highest average number of radial chromosomes was observed in MMC-treated cells lacking both factors, again suggesting additive effect (***Figure 6.19*a-c**). Thus, this result is consistent with the lack of epistasis between TRAIP and FANCD2 in maintaining genome stability upon MMC treatment.

Lastly, I used clonogenic cell survival assays to analyse whether TRAIP and FANCD2 are epistatic regarding cell survival after MMC treatment. This revealed an additive effect of the loss of TRAIP and FANCD2 depletion towards cell sensitivity to MMC (***Figure 6.20***). FANCD2-depleted WT cells were substantially more sensitive to MMC treatment than TRAIP-KO cells, and the sensitivity was further exacerbated when both factors were absent.

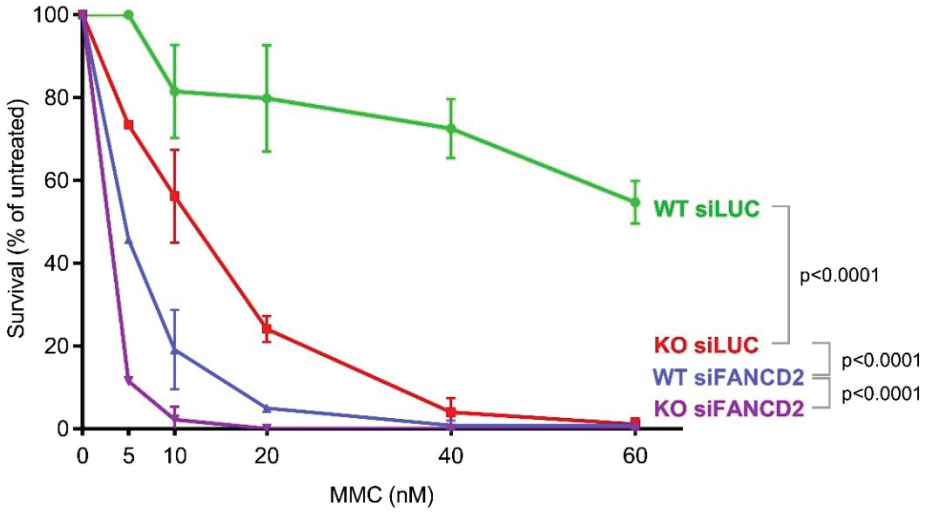

Figure 6.20. TRAIP and FANCD2 are not epistatic in terms of cell sensitivity to MMC. siLUC- or siFANCD2-depleted RPE1 p53-/- WT and TRAIP-KO (KO; clone 1.29) cells were plated at very low density and treated with several doses of MMC (5 nM – 60 nM) for 24 hours. The drug was removed by extensive PBS washing, and cells were incubated for 8 days to form colonies, followed by fixation, staining and colony counting. Results (mean ± SD) from 2 independent experiments are shown. Two-way ANOVA was used for statistical analysis.

As chronic loss of a protein may lead to cellular adaptations, the comparison between the depletion of one protein and the complete absence of another may not be adequate for these experiments, and so it may be more relevant to either deplete both factors by RNAi or generate double knockout cell lines. To rule out the possibility of the experimental design affecting the results obtained, I knocked-down TRAIP and FANCD2 in RPE1 p53-/- cell line and performed the clonogenic cell survival assay. First, three different siTRAIP oligonucleotides were tested, all showing similar effect on TRAIP depletion and cell survival after MMC treatment (***Figure 6.21*a-b**). As TRAIP-depleted cells were less sensitive to MMC treatment than TRAIP-KO cells, higher doses of MMC were used in cell survival assays (***Figure 6.21*b**). The RNAi-mediated depletion of TRAIP and FANCD2 was observed to result in very distinct effects on RPE1 p53-/- cell survival after MMC treatment (***Figure 6.21*c**). siTRAIP-treated cells showed a much milder MMC-induced cell survival defect than FANCD2-depleted cells (***Figure 6.21*c**). These results and the experimental work conducted using RPE1 p53-/- TRAIP-KO cells strongly suggest that TRAIP and FANCD2 are not epistatic during MMC-ICL repair. Consequently, it is possible that TRAIP is instead required for the alternative NEIL3-mediated ICL repair pathway in human cells. Therefore, in the future it will be of interest to experimentally address whether TRAIP acts upstream of NEIL3 during psoralen-ICL repair.

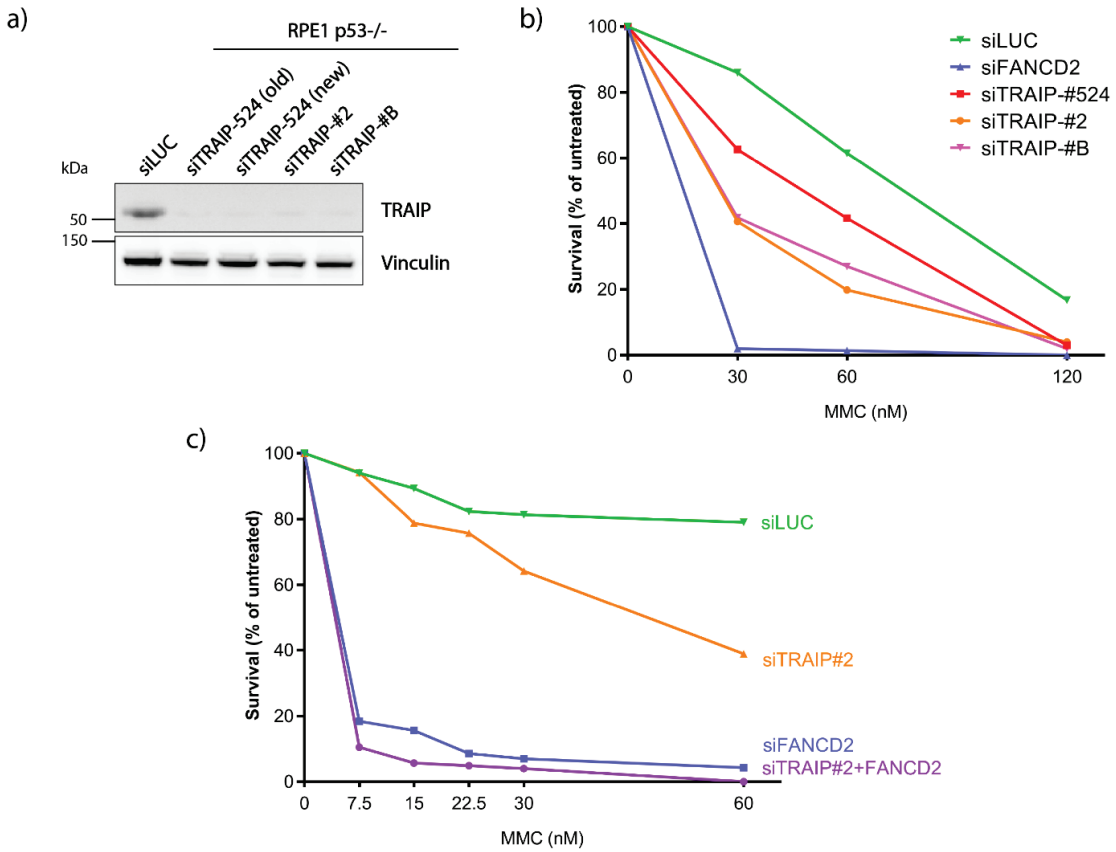

Figure 6.21. Depletion of TRAIP and of FANCD2 are not epistatic in terms of cell survival after MMC treatment.

a) Immunoblot demonstrating that TRAIP depletion using different siRNA oligonucleotides results in similar depletion efficiency. RPE1 p53-/- cells were treated with 50 nM siRNA (siLUC or siTRAIP) and harvested for immunoblotting 48 h after the treatment was started. Old and new stocks of the siTRAIP-524 oligonucleotide were used for the experiment, as indicated in the figure. Vinculin served as a loading control.

b) RPE1 p53-/- cells depleted of TRAIP using various siRNA oligonucleotides were plated at very low density and treated with several doses of MMC (30 nM – 120 nM) for 24 h. The drug was removed by extensive PBS washing, and cells were incubated for 8 days to form colonies, followed by fixation, staining and colony counting. Results from one experiment are shown.

c) Cell survival experiment showing that TRAIP-depleted cells (siTRAIP#2) formed significantly fewer colonies at all doses of MMC tested, compared to siLUC-depleted cells. However, FANCD2 depletion resulted in a much more severe MMC-induced cell survival defect than TRAIP depletion, consistent with a lack of epistasis between TRAIP and FA pathways in response to MMC-induced DNA damage. RPE1 p53-/- cells were treated with siRNA for 48 h prior to start of MMC treatment. Cells treated with siLUC, siTRAIP or both siRNAs were plated at very low density and treated with MMC (7.5 nM – 60 nM) for 24 h. The drug was removed by extensive PBS washing, and cells were incubated for 8 days to form colonies, followed by fixation, staining and colony counting. Results from one experiment are shown.

6.2.4. Summary: TRAIP in MMC-ICL repair

In this section, I demonstrated that TRAIP-KO cells are hypersensitive to MMC treatment and exhibit reduced cell survival. TRAIP was also required for normal RPA2 phosphorylation following MMC treatment, as well as the maintenance of genomic stability. In contrast to CPT treatment, TRAIP-KO cells were not observed to have defective HR in response to MMC. Further experiments were conducted to investigate the potential mechanistic link between TRAIP and the FA pathway, based on the observations that TRAIP is required for efficient ICL repair in *X. laevis* egg extracts (Wu, Semlow *et al.*, unpublished). However, the experiments in TRAIP-KO cells provided no evidence to support the existence of an epistatic relationship between TRAIP and FA pathways in repairing MMC-ICLs in mammalian somatic cells.

There are several possible explanations for the observed lack of experimental support for the epistatic model. Firstly, although widely used to study genome maintenance pathways (Hoogenboom *et al.*, 2017), *X. laevis* egg extract is a cell-free *in vitro* system, which provides an indication of the events *in vivo* but has a limited power to mimic circumstances of a living cell. Moreover, our cell line choice for these experiments may have influenced the results, as gene expression patterns, physiological properties and the tissue of origin differ between cultured human cell lines (Ross *et al.*, 2000). Single cells in genetically homogeneous populations of cultured mammalian cells were also noted to spontaneously develop phenotypic heterogeneity (Stockholm *et al.*, 2007). Thus, testing the effects of DNA damage in several TRAIP-KO cell lines with different tissue origins and phenotypic characteristics could be used to exclude cell line-specific findings, whereas clone variability could be addressed by using several RPE1 p53-/- TRAIP-KO clones for the epistasis experiments.

However, if our current findings were replicated in other TRAIP-KO cell lines as well, what could be the alternative mechanism by which TRAIP contributes the resolution of MMC-ICLs? One of the possibilities is that in mammalian somatic cells, the FA pathway-dependent repair of MMC-ICLs does not rely on the upstream event of CMG unloading, which is mediated by TRAIP in *X. laevis* (***Figure 6.22a***). This hypothesis would suggest that both TRAIP and FA pathways contribute to efficient MMC-ICL resolution but are not dependent on each other. However, such a model is not supported by experimental data obtained in *X. laevis* egg extracts and is only a speculation based on my findings in TRAIP-KO cells. As TRAIP-mediated ubiquitination of MCM7 is yet to be demonstrated in mammalian cells, another possibility is

that CMG unloading during MMC-ICL repair is mediated not by TRAIP, but by a different E3 ligase, whereas TRAIP works in a distinct pathway to contribute to genome stability and cell survival after MMC treatment (***Figure 6.22*b**). In summary, none of these alternative possibilities is currently supported by experimental data, and extensive further work will be needed to delineate the role of TRAIP in mammalian ICL repair. However, such analyses may be challenging due to the lack of available reagents and assays to assess CMG unloading in mammalian systems, as well as the cellular abundance of MCM complex subunits and their replication-independent roles (Das *et al.*, 2014).

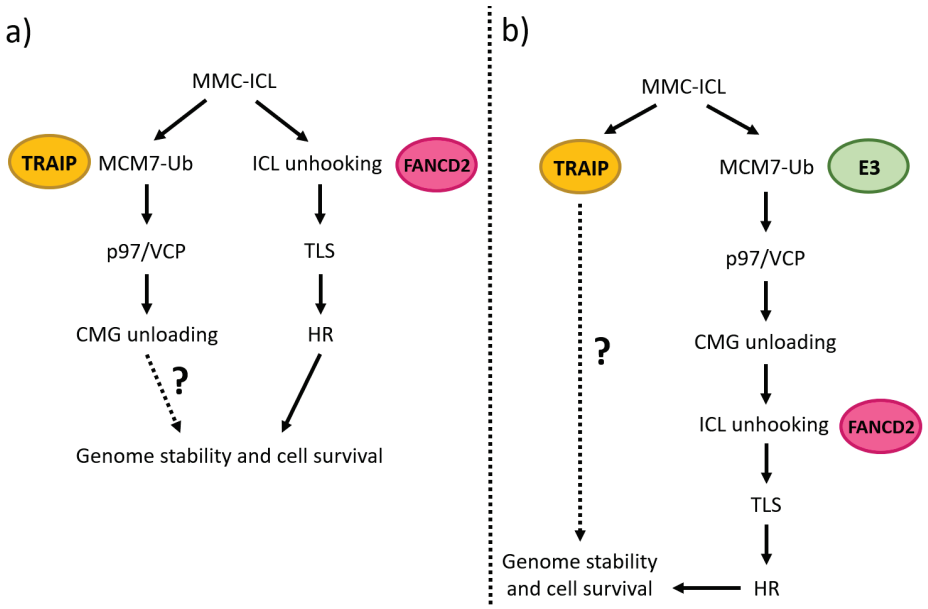

Figure 6.22. Cartoon models representing hypothetical roles of TRAIP in MCM-ICL repair.
a) The model suggesting that the FA pathway-dependent repair of MMC-ICLs acts in parallel to TRAIP to promote genome stability and cell survival, implying that the TRAIP-mediated CMG unloading is not required for efficient MMC-ICL repair in mammalian cells.
b) The model suggesting that CMG unloading during MMC-ICL repair is mediated not by TRAIP, but by a different E3 ligase. Meanwhile, TRAIP works in a distinct pathway to contribute to genome stability and cell survival after MMC treatment.

6.3. Discussion: the role of TRAIP in DDR and DNA repair

In this chapter, extensive analysis on the role of TRAIP in promoting the repair of replication-associated DNA damage was described. Firstly, I experimentally tested whether TRAIP facilitates resolution of CPT-induced DNA damage. Using TRAIP-KO cells, complemented with either wild-type TRAIP or its E3 ligase-deficient variant, TRAIP E3 ligase activity was demonstrated to mediate CPT-induced DNA end resection, DDR signalling and efficient HR (***Figure 6.11***). Overall, these results indicate the importance of the proper E3 ligase activity of TRAIP in resolving CPT-induced DNA damage. Nevertheless, E3 ligase-deficient TRAIP-W37A mutant provided partial rescue in cell survival assays. I demonstrated that TRAIP-W37A retains partial auto-ubiquitination proficiency (***Figure 6.4*****c**), suggesting that the W37A mutation may not fully abolish the interaction between E2 and E3, but rather confers partial loss of E3 ligase activity. Indeed, a recent nuclear magnetic resonance-based report investigating the effects of the tryptophan-to-alanine (W>A) subsitution within the RING domain of E3 ligases demonstrated only minor structural differences between W>A mutant and WT RING (Birkou *et al.*, 2017). Alanine was also shown to have a substantial intrinsic α-helix-stabilising tendency (Rohl *et al*., 1999; Spek *et al*., 1999), and the W37A substitution may have conferred structural rigidity and the lack of flexibility to the whole RING domain and other domains of TRAIP, subsequently negatively affecting its cellular function. It is likely that TRAIP domain structure would have been better preserved by substituting the tryptophan residue with a more structurally similar residue, such as another aromatic amino acid. Additionally, Birkou *et al.* (2017) demonstrated that tryptophan-to-arginine (W>R) mutant induces structural changes within the RING domain that completely obliterate the interaction with E2. Thus, complementing TRAIP-KO cells with a more suitable TRAIP RING domain point mutant, such as TRAIP-W37R, may give us a clearer insight into the cellular roles of the E3 ligase activity of TRAIP. However, the structural changes introduced by W37R mutation could also lead to the complete destabilisation of the RING domain and significant reduction of TRAIP protein levels, as previously seen with C7A/C10A mutant (see Section 6.1.2). It is therefore possible that deleting the entire RING domain rather than using point mutants would allow the best preservation of native TRAIP folding, stability and function required for investigating the role of its E3 ligase activity in DNA replication and repair.

Previous report by Hoffmann *et al.* (2016) demonstrated that siTRAIP-treated U2OS cells do not properly respond to replication-associated DNA damage, including CPT treatment, as indicated by reduction in RPA foci intensity, ssDNA generation, and S phase phosphorylation

of RPA, CHK1 and H2AX (see ***Figure 1.16*****b**). Overall, my experiments, together with the data obtained by Hoffmann *et al.* (2016), strongly implicate TRAIP E3 ligase in contributing to the resolution of CPT-induced DNA damage, likely by facilitating ATR-dependent checkpoint signalling. However, it remains unclear which step of CPT-induced DNA repair TRAIP directly contributes to. Extensive CHK1 and RPA2 phosphorylation indicates activation of the replication checkpoint, and is known to persist until DNA damage is resolved and DNA synthesis restored (Pommier, 2006; Shao *et al.*, 1999). Such phosphorylation, particularly of RPA2, is reduced in TRAIP-KO cells, and it remains to be established whether the observed defect is due to a reduced rate (delay) or failure of phosphorylation.

W. Feng *et al.* (2016) suggested that TRAIP promotes PCNA unloading from chromatin after HU treatment (see ***Figure 1.16*****c**), having observed that TRAIP depletion impaired the HU-induced reduction of chromatin-bound PCNA. Although I did not perform extensive analysis of how TRAIP-KO cells respond to HU treatment, CPT-induced PCNA unloading from chromatin was not disrupted in TRAIP-KO cells (***Figure 6.10***). This suggests that TRAIP may be involved in unloading PCNA specifically upon HU-induced replication stress. The recent study by Soo Lee *et al.* (2016) proposed that TRAIP mediates recruitment of BRCA1 to IR-induced DSBs (see ***Figure 1.16*****d**). Although I did not test the role of TRAIP in responding to IR-induced DNA lesions, BRCA1 recruitment to chromatin following CPT treatment in TRAIP-KO or E3 ligase-deficient cells was unaffected (***Figure 6.10***). This may indicate that distinct TRAIP-dependent DDR signalling cascades facilitate the repair of replication-associated one-ended DSBs and IR-induced two-ended DSBs (Chapman *et al.*, 2012), where TRAIP-mediated BRCA1 recruitment to chromatin is required. Alternatively, the distinct experimental setup used by me, W. Feng *et al.* (2016) and Soo Lee *et al.* (2016), such as different cell lines and TRAIP depletion methods, may have contributed to the conflicting results obtained.

The identity of the DDR-relevant TRAIP ubiquitination substrates at stalled replication forks also remains elusive. Two recent studies on TRAIP proposed PCNA as a potential substrate of the E3 ligase activity of TRAIP (Hoffmann *et al.*, 2016; W. Feng *et al.*, 2016) but no substantive *in vitro* or *in vivo* evidence for the TRAIP-mediated ubiquitination of PCNA was provided by either study. Notably, W. Feng *et al.* (2016) showed that the inactivation of TRAIP did not significantly affect the levels of ubiquitinated PCNA in response to replicative stress, and that inhibition of the proteasome did not impair fork recovery, leading to their conclusion that TRAIP may promote PCNA unloading by non-catalytic means. The TLS polymerase eta (Pol ŋ) was proposed as another putative substrate of TRAIP based on the finding that

overexpression of the *D. melanogaster* orthologue of TRAIP (Nopo) promotes Pol ŋ polyubiquitination (Wallace *et al.*, 2014). However, follow-up experimental work by Hoffmann *et al.* (2016) suggested that TRAIP-mediated ubiquitination of Pol ŋ was unlikely to underlie the role of TRAIP in maintaining genome stability after replication stress. The authors demonstrated that TRAIP depletion did not affect formation of Pol ŋ foci upon DNA damage, and that TRAIP-mediated ubiquitination of Pol ŋ was not dependent on its RING or PIP domain. Furthermore, the sensitivity of TRAIP-depleted cells to replication stress-inducing agents could not be rescued by overexpression of Pol ŋ (Hoffmann *et al.*, 2016). Overall, these data implied that Pol ŋ is not a substrate of TRAIP that is relevant to its role in maintaining genome stability after replication stress. In Chapter 4, the analysis of interaction between TRAIP and protein phosphatase 4 (PP4) complex, as well as the possibility of TRAIP-mediated PP4 ubiquitination, is described and discussed. However, the experiments in this chapter indicated that reduced CPT-induced DDR signalling in TRAIP-deficient cells, particularly RPA2 phosphorylation, is more likely to be caused indirectly through defective RPA loading on ssDNA after CPT treatment (see ***Figure 6.9***). This alternative explanation minimises the potential role of TRAIP-dependent PP4 ubiquitination at CPT-induced DNA lesions. However, it remains possible that TRAIP-mediated PP4 regulation occurs in response to other types of DNA lesions, such as the ones induced by UV irradiation. Overall, the identity of DDR-relevant substrates of TRAIP remains an open question, and their identification will be necessary to fully elucidate what role TRAIP has in responding to replication stress.

In the future, several methods could be employed to facilitate the identification of TRAIP interaction partners and substrates. Given that TRAIP adds K48-linked ubiquitin chains on its substrates (Zhang *et al.*, 2012), TRAIP-dependent ubiquitination of its DDR substrates may well occur and lead to their degradation in a proteasome-dependent manner, detectable by mass spectrometry (MS) analysis. Additionally, indirect effects of the TRAIP loss on the proteome could be detected as well, providing insight into cellular pathways that are upregulated or downregulated in unperturbed or damaged cells when TRAIP is absent. For direct detection of CPT-induced proteomic changes at replication forks, isolation of protein on nascent DNA (iPOND) method could be applied to purify replication fork-associated proteins, followed by their analysis by MS (Leung *et al.*, 2013). Moreover, MS identification of transient TRAIP interactions with other proteins in living cells could be achieved using proximity-dependent biotin identification (BioID) method (Roux *et al.*, 2012). Finally, MS for targeted detection of ubiquitination sites may be a valuable direct approach for elucidating the substrates of the E3 ligase activity of TRAIP.

In agreement with the results obtained by Hoffmann *et al.* (2016), I observed the elevated rates of chromosomal aberrations and reduced cell survival in response to MMC in TRAIP-deficient cells (Section 6.2.2). However, pRPA2-S4/S8 signal in MMC-treated RPE1 p53-/- TRAIP-KO cells was increased, in contrast to the reduction seen by Hoffmann *et al.* (2016) in TRAIP-depleted U2OS cells. The experiments described in Section 6.2.3 did not provide support for epistatic relationship between TRAIP and FA-mediated ICL repair pathway in mammalian cells, as the loss of TRAIP led to less severe MMC-induced chromosomal instability and cell survival defects than the ones observed in FANCD2-depleted cells. While the possibility of the involvement of TRAIP in CMG unloading is exciting, the lack of experimental evidence for epistasis between TRAIP and FA pathways at MMC-ICLs in mammalian cells prompts consideration of alternative models for the role of TRAIP at ICLs, which will need to be explored in the future. Instead of acting upstream of FANCD2 to promote CMG unloading needed for MMC-ICL repair, TRAIP may mediate an alternative pathway that promotes genome stability and cell survival after MMC-induced DNA lesions. For example, replication-independent ICL repair (RIR), which recognises ICL lesions via sensing DNA helix distortion or ICL collision with a transcribing polymerase, does not rely on the FA pathway (Williams *et al.*, 2013). Moreover, ICL incision and TLS steps in RIR, which often operates outside of S phase, involve different set of enzymes than the ones acting in FA-dependent ICL repair and include NER proteins (Enoiu *et al.*, 2012; Williams *et al.*, 2013). As the absence of TRAIP resulted in milder defects in genome stability and cell survival than FANCD2 depletion, TRAIP may be a component of a pathway that normally plays a less prominent role in repairing ICLs but is indispensable in the absence of the functional FA pathway. Alternatively, TRAIP may contribute to MMC-ICL repair by regulating ATR signalling or DNA end resection, and further work is required to address these possibilities.

The experiments described in this chapter and Chapter 5 also indicate that TRAIP promotes DNA repair via distinct mechanisms in response to different types of DNA lesions. My results, together with the data presented by Harley *et al.* (2016), strongly support the proteasome-dependent degradation of TRAIP following UV-C irradiation. In contrast to this, CPT and MMC treatment did not induce TRAIP depletion in wild-type cells, as shown by immunoblotting analyses, pointing towards different roles and cellular fates of TRAIP in response to different DNA lesions. UV-induced photoproducts, such as covalent adducts between adjacent pyrimidines on the same DNA strand (cyclobutane pyrimidine dimers), cause problems primarily by distorting the structure of DNA (Rastogi *et al.*, 2010), whereas CPT or MMC treatment creates a direct blockage to DNA replication, either by generating a bulky

DNA-protein adduct (CPT) or by sealing the two DNA strands together (MMC-ICL). Although in each case collision of the DNA lesion with the replication fork could lead to the emergence of DSBs, these can be structurally distinct and require different proteins for their repair (Michl *et al*., 2016; Pommier, 2004; Rastogi *et al*., 2010). My data suggest that TRAIP facilitates repair of replication-associated one-ended DSBs arising upon CPT treatment (see Section 6.1.5) and is required for ensuring genome stability and cell survival upon MMC treatment (see Section 6.2.2), consistent with its adaptation to influence efficient repair of several structurally distinct types of DNA damage.

Having investigated the effects of two replication-associated DNA damaging agents, CPT and MMC, in TRAIP-KO cells, it will be of particular importance to explore the involvement of TRAIP in facilitating the repair of endogenously induced DNA lesions. During embryonic development, DNA lesions arising from oxidative damage (Cooke *et al.*, 2003) and aldehydes (Langevin *et al.*, 2011) are likely to be encountered by cells. Such endogenous DNA damage may be deleterious in TRAIP-deficient cells during rapid cell proliferation, eventually leading to the loss of cells and restriction of normal body growth. My initial data suggest that hydrogen peroxide treatment, which induces oxidative stress, causes a slight reduction in pRPA2-S4/S8 signal (see ***Figure 5.10***) and cell survival in TRAIP-KO cells, compared to WT cells. In the future, further investigation of the role of TRAIP in sensing oxidative stress and repairing aldehyde-induced DNA damage will be necessary for clarifying the functional link between the phenotype of TRAIP-KO cells and primordial dwarfism.

Chapter 7

A mouse model of MPD caused by DONSON deficiency

7. A mouse model of MPD caused by DONSON deficiency

Multiple DNA damage response (DDR) factors are essential for cell viability due to their key role in signalling the presence of DNA lesions and promoting their repair, thus ensuring genomic stability. Until recently, little was known about the cellular function of the human protein encoded by the *DONSON* gene. Its orthologue in *D. melonogaster*, known as Humpty dumpty (*Hd*), was previously demonstrated to be essential for DNA amplification in follicle cells of the ovary and required for cell proliferation during development (Bandura *et al.*, 2005). Recently, a link between *DONSON* and human disease was established, as the Andrew Jackson and the Grant Stewart (University of Birmingham) laboratories reported that biallelic mutations in this gene cause microcephalic primordial dwarfism (MPD) (Reynolds *et al.*, 2017). *DONSON* was demonstrated to encode a replication fork-associated protein, which protects and stabilises replication forks and prevents spontaneous DNA damage, thus promoting efficient S phase progression (Reynolds *et al.*, 2017). More recently, a biallelic intronic variant in *DONSON* was also implicated as a cause of the rare microcephaly-micromelia syndrome (MMS), characterised by severe prenatal growth restriction, microcephaly, craniofacial anomalies, skeletal dysplasia and neonatal lethality (Evrony *et al.*, 2017).

As *DONSON* emerged as a new disease-associated gene, we decided that a DONSON mouse model would provide a valuable tool for studying the biological function of this protein. In particular, a DONSON patient mutation knock-in mouse could provide us with a better understanding of the impact *DONSON* mutations have on mammalian organism growth and development. Moreover, it would provide an isogenic system allowing verification of the cellular defects previously observed in patient-derived cell lines. Lastly, characterising the development of the mouse model of MPD caused by mutations in *DONSON* might enable discovery of additional phenotypes associated with biallelic *DONSON* mutations.

No viable mouse disease model of MPD caused by *DONSON* mutations was available; therefore, in this chapter, a CRISPR/Cas9 genome targeting strategy to introduce a DONSON patient mutation in mouse is described. Its consequences on embryonic development are assessed alongside cellular characterisation of DONSON MPD mouse-derived embryonic fibroblasts.

7.1. CRISPR/Cas9-mediated targeting of murine Donson to introduce the MPD mutation

To establish phenotypes associated with a DONSON knock-in mouse at a cellular and organism level, I chose to model the DONSON mutation M446T. This mutation, substitution of a highly conserved methionine residue to threonine at amino acid position 466 (p.M466T), is caused by the homozygous transition c.1337T>C in exon 8 of the human *DONSON* gene. This was identified by WES as a cause of MPD in one consanguineous family of Palestinian descent (Reynolds *et al.*, 2017). The three affected individuals were previously reported to have a Fanconi Anaemia (FA)-like disorder, with patients exhibiting microcephaly, short stature and forearm and thumb dysplasia, although there was no evidence for bone marrow failure (Milner *et al.*, 1993). The cells derived from the three affected individuals showed reduced levels of DONSON protein, and exogenous expression of p.M446T mutant protein was consistent with reduced stability due to this missense mutation (Reynolds *et al.*, 2017). As this mutation is the only homozygous exonic mutation identified in the MPD cohort, it was an attractive choice for CRISPR/Cas9-mediated genome editing in mouse. Human DONSON (hDONSON) and mouse Donson (mDonson) proteins are 76% identical and share 83% similarity at amino acid level, and the DNA sequences surrounding p.M446 (corresponding to p.M440 in mouse) are highly conserved at the protein level (***Figure 7.1***).

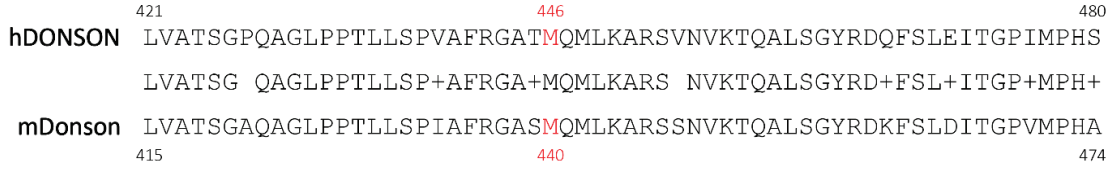

Figure 7.1. Amino acid sequence alignment of human and mouse DONSON proteins.
Comparison between amino acid sequences of human and mouse DONSON orthologues, performed using NCBI Basic Local Alignment Search Tool (BLAST), indicates a high degree of evolutionary conservation of this protein between the two species. Methionine 446 (M446) in human DONSON (hDONSON) and its equivalent methionine 440 (M440) in mouse Donson (mDonson) are shown in red. The middle lane indicates amino acid conservation between the two organisms: amino acids that are identical between human and mouse DONSON are named; the plus sign (+) indicates substitutions that preserve the physico-chemical properties of the original residue, leading to similarity at amino acid level. Gaps (spaces) in the alignment indicate non-equivalent amino acids in one sequence relative to the other.

To introduce p.M440T in mouse *Donson* (m*Donson*), a gRNA that scored highly based on both the CRISPR Design Tool (Feng Zhang lab; http://crispr.mit.edu/) and the CRISPR gRNA Design Tool DNA2.0 (now ATUM) was selected for targeting (***Figure 7.2***). A 108 bp-long ssODN repair template was designed to introduce the desired nucleotide substitution (c.1319T>C) directly at the predicted Cas9 cutting site, as well as a silent PAM site mutation 5 nt upstream (CTT PAM site changed to CAT) (***Figure 7.2***). The 20 nt-long targeting sequence to allow production of the gRNA was inserted into the pX458 plasmid, encoding wild-type Cas9 nuclease, and tested *in vitro* to evaluate its efficiency at cutting the *Donson* DNA template, encompassing M440 within exon 8 (***Figure 7.3***). This *in vitro* assay showed efficient cutting of the template, and the gRNA was therefore used for cytoplasmic injections in BL6CBAF1 zygotes (50% C57BL6/J, 50% CBA/J).

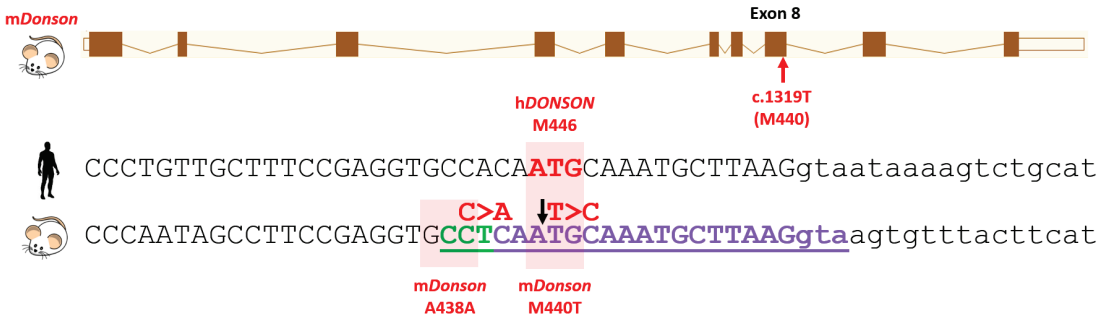

Figure 7.2. Targeting c.1319T (p.M440) in m*Donson* by CRISPR/Cas9 genome editing.
Above: schematic of the mouse *Donson* (m*Donson*) gene with exon 8 and c.1319T (p.M440) indicated. Below: alignment of genomic sequences of exon 8 (uppercase) and intron 8 (lowercase) of human and mouse *DONSON*. The 20 nt-long genomic sequence targeted by the gRNA in exon 8 of m*Donson* is highlighted in purple; 3 nt-long PAM site is shown in green. Black arrow indicates the predicted incision site of WT Cas9. The nucleotides changed to introduce the M440T mutation (T>C) and alter PAM site (C>A, silent A438A mutation) in the repair template are shown in red.

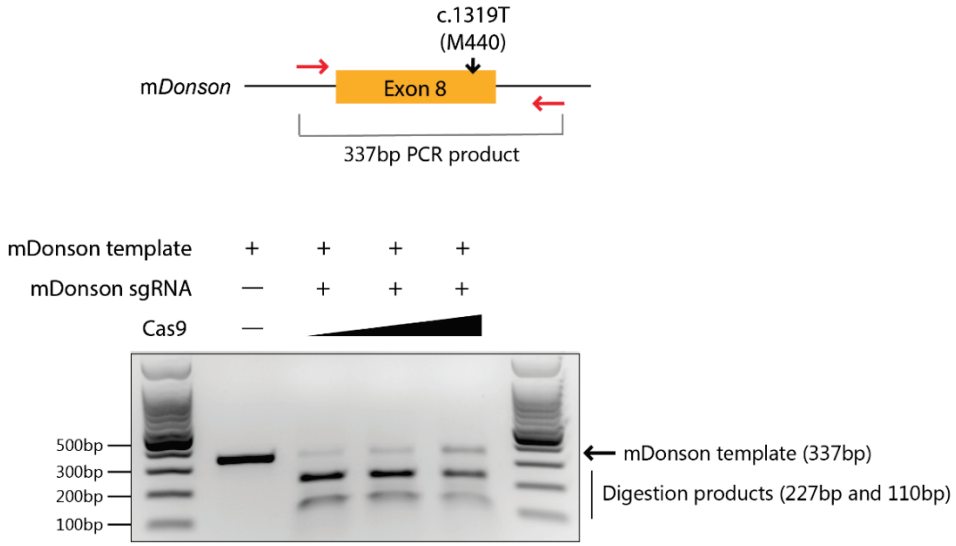

Figure 7.3. SgRNA for CRISPR/Cas9-mediated introduction of c.1319T>C (p.M440T) mutation in mouse cleaves its template *in vitro*.

Analysis of *in vitro* cutting reaction, containing *Donson* DNA template, the *in vitro* transcribed sgRNA, and recombinant wild-type Cas9 enzyme (200—680 ng). *Donson* template (337 bp PCR product), encompassing exon 8 of m*Donson* and exon-intron junctions, was amplified by PCR using primers indicated by red arrows. The presence of *in vitro* digestion products (227 bp and 110 bp) was visualised on a 2% agarose gel.

7.2. Screening founder mice for mutations in m*Donson*

To generate transgenic mice, the CRISPR/Cas9 reagents were microinjected into the cytoplasm of a fertilised eggs, which were cultured overnight to the 2-cell stage and then transferred to the oviducts of pseudo-pregnant 'recipient' females (performed by the staff of CBS Transgenic Core Facility, University of Edinburgh) (see Section 2.7.2). Two cytoplasmic injection sessions and 6 embryo transfers resulted in a total of 5 pregnant mice, 3 of which gave birth. The first injection session yielded only 3 mouse pups, born to 3 pregnant females, whereas the second injection session resulted in 13 pups born to 2 pregnant females (7 and 6 pups, respectively). Tissue biopsies (ear clips) of the 16 infant pups (9 male pups and 7 female pups) were collected and used for genomic DNA extraction and PCR amplification of the genomic locus surrounding the p.M440T substitution, using primers indicated in ***Figure 7.3***. The resulting PCR products were sub-cloned and Sanger-sequenced to determine the genotypes of founder (F0) mice (***Table 7.1***). Four pups were not targeted by CRISPR/Cas9, only showing non-mutated *Donson*. Six pups were heterozygous for the M440T mutation, with the second allele shown to be wild-type (Donson M440T/+) (***Table 7.1***). All these animals except one had the PAM site mutation as well. To avoid unanticipated consequences due to the silent PAM site mutation, the pup that was wild-type for the PAM site sequence and heterozygous for M440T was selected for further breeding to establish the Donson M440T mouse line.

Mutations other than the intended M440T substitution were found in several animals as well (***Table 7.1***). One pup was shown to be heterozygous for M440T, with the second allele harbouring a methionine to isoleucine substitution at amino acid position 440 (M440T/M440I). Additionally, 5 pups were demonstrated to be heterozygous for short insertions or deletions (1-5 bp long), with the genotypes insT/+, delAA/+, and del5bp/+ (***Table 7.1***). In all cases, the indel was predicted to result in a frameshift and lead to the introduction of a premature stop codon in exon 8, likely resulting in the degradation of the mutant transcript through NMD. The female Donson del5bp/+ pup was selected for further breeding to establish a Donson knockout (KO) mouse line.

Table 7.1. Summary of the genotypes of CRISPR/Cas9-targeted founder (F0) mice.
Genotypes of founder (F0) mice at the intended substitution (m*Donson* c.1319T>C) and the PAM site (c.1314C>A) are indicated, together with the number of F0 mice with that particular genotype, the predicted length of Donson protein and the predicted Donson status resulting from the mutations. The ATG codon corresponding to methionine 440 (M440) is underlined; aa = amino acids.

Genotype				Number of pups	Predicted Donson protein	Predicted Donson status
c.1319T>C (M440T)		c.1314C>A (A438A; PAM)				
Mutation	Het/Hom	Mutation	Het/Hom			
WT	Hom	WT	Hom	4	560 aa	+/+
ATG>ACG (M440T)	Het	CCT>CAT (A438A)	Hom	1	560 aa	M440T/+
ATG>ACG (M440T)	Het	CCT>CAT (A438A)	Het	4	560 aa	M440T/+
ATG>ACG (M440T)	Het	WT	Hom	1	560 aa	M440T/+
ATG>ACG (M440T) / ATG>ATA (M440I)	Het (compound)	CCT>CAT (A438A)	Het	1	560 aa	M440T/M440I
ATG>ATTG (insT)	Het	WT	Hom	3	443 aa (premature stop codon in exon 8)	+/-
CAATG>CTG (delAA)	Het	WT	Hom	1	442 aa (premature stop codon in exon 8)	+/-
ATGCAAATG>AATG (delTGCAA; del5bp)	Het	WT	Hom	1	441 aa (premature stop codon in exon 8)	+/-

7.3. Mice homozygous for Donson M440T and Donson del5bp are not viable

The selected founder (F0) pups (Donson M440T/+ and Donson del5bp/+) were crossed to CD-1 mice once they reached maturity at six weeks to establish germline transmission (***Figure 7.4***). F1 pups heterozygous for each of the Donson mutations were born, and germline transmission of the mutations of interest was established. Heterozygous F1 pups on this mixed genetic background (50% CD-1, 50% BL6CBAF1) were inter-crossed with the intention of generating homozygous mutant mice. Although multiple litters were produced for both mouse lines, they contained only wild-type and heterozygote individuals with no homozygous pups born, as determined by Sanger sequencing (***Figure 7.4***). The heterozygous mice with Donson M440T/+ and del5bp/+ genotypes did not visibly differ in size, compared to their wild-type littermates. No gross phenotypic abnormalities were reported for heterozygotes in either of the mouse lines. In contrast, the absence of homozygotes was statistically significant and strongly suggested their failure to survive *in utero* (***Figure 7.4***).

The absence of viable homozygous offspring (del5bp/del5bp) in the Donson-/- line is consistent with the early embryonic lethality of Donson-/- embryos recently observed by Evrony *et al.* (2017). However, it is surprising that no homozygous offspring (M440T/M440T) were born in the Donson knock-in mouse line, as three MPD patients homozygous for the corresponding mutation (M446T) in humans were identified (Reynolds *et al.*, 2017). I next determined at what stage of early embryonic development embryos homozygous for Donson del5bp/+ and Donson M440T/+ can still be detected.

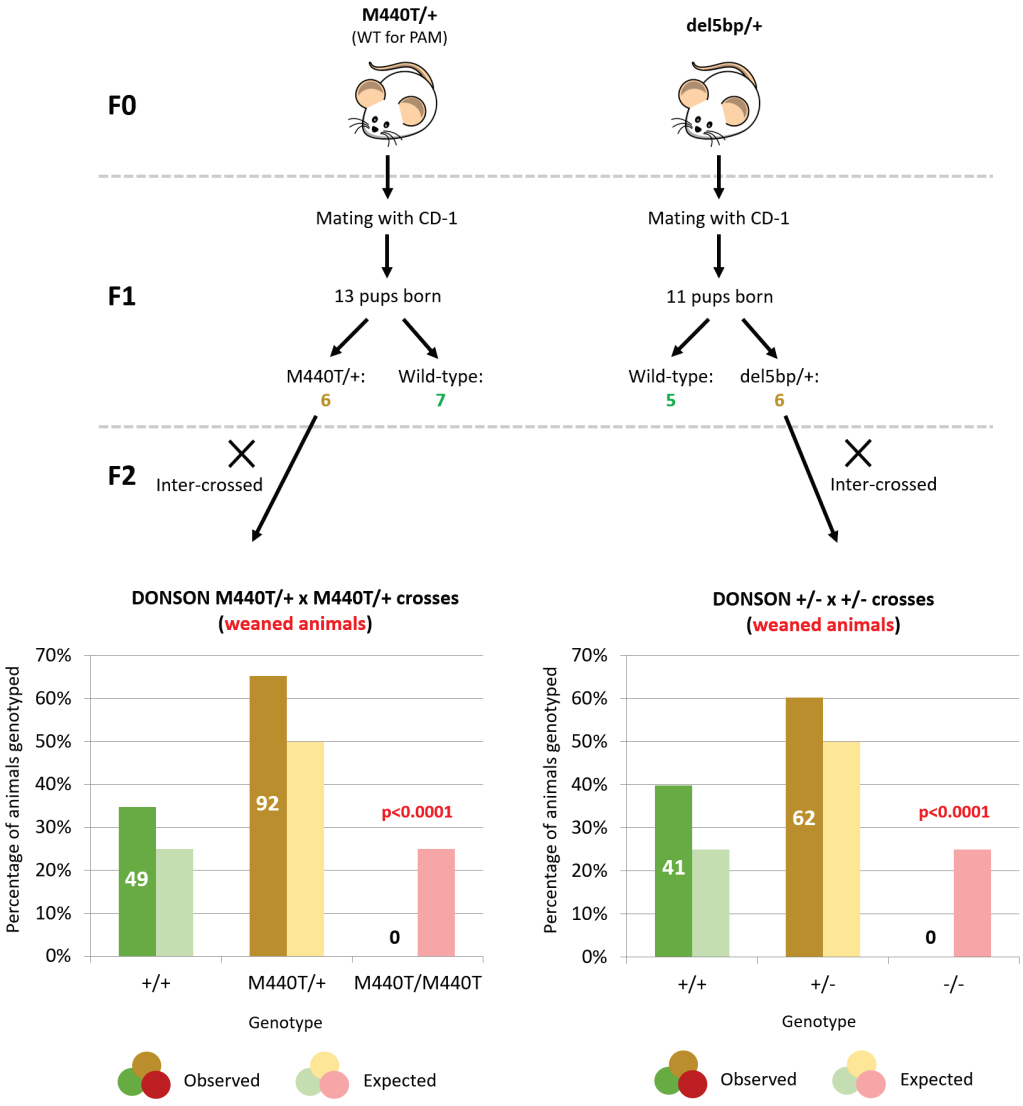

Figure 7.4. Mice homozygous for Donson M440T or del5bp are not viable.
Above: schematic representation of the first crosses initiated using Donson founder (F0) pups. The two selected founders were first crossed with CD-1 mice, and the heterozygous first filial generation (F1) pups were inter-crossed in an attempt to establish homozygous transgenic mouse lines. Below: the graphs demonstrating statistically significant absence of homozygous second filial generation (F2) animals for both knock-in (M440T) (left) and knock-out (right) Donson mouse lines. All weaned animals were wild-type or heterozygous for the Donson mutations. The experimentally observed distribution of genotypes is compared to their expected Mendelian distribution. The number of mice with each genotype is indicated on the columns in the graphs. Statistics: chi-squared test.

7.4. Donson M440T/M440T embryos are present at least up to E16.5

To determine at what stage of embryonic development M440T/M440T are no longer present, dissections of embryonic day 11.5 (E11.5) embryos were performed and the tail clips of the dissected embryos used for genotyping. Homozygous M440T/M440T embryos were present in the dissected litters, although their numbers were lower than expected (***Figure 7.5*****a**,**c**). Additionally, several spontaneous embryo resorptions, where the embryo implanted but was partially or fully resorbed before dissection, were found. A disproportionately large number of embryo resorptions genotyped as homozygotes (5 out of 7; 71%), indicating the phenotypic variability of genetically identical embryos. Moreover, a subtle difference in size was observed in the homozygous mutant embryos, compared to wild-type or heterozygous embryos (***Figure 7.5*****b**). The visually indistinguishable +/+ (n=2) and M440T/+ (n=2) embryos from the same litter measured 4.4±0.2 mm in length, whereas the smaller littermate M440T/M440T embryo (n=1) measured only 3.7 mm.

I next analysed the viability and size differences of Donson M440T embryos at later stages of development. M440T/M440T embryos were present in the dissected litters and, surprisingly, were found at the expected Mendelian ratio at E13.5 (***Figure 7.6*****a**). However, a statistically significant effect on embryo length and head size was observed during image analysis of Donson embryos at this stage of embryonic development (***Figure 7.6*****b-d**). The average length of a Donson M440T/M440T embryo at E13.5 was 5.1±0.2 mm, and the occipito-frontal distance was 2.5±0.2 mm; meanwhile, the average length of a wild-type embryo was 6.5±0.2 mm, with the head size of 3.2±0.1 mm (***Figure 7.6*****c-d**). These data indicate clear reduction in brain and body size in Donson M440T/M440T embryos at E13.5, when compared to wild-type or heterozygous embryos, which are indistinguishable in these parameters. The observed reduction in occipito-frontal distance in Donson M440T/M440T embryos was proportional to the reduction in their overall body length.

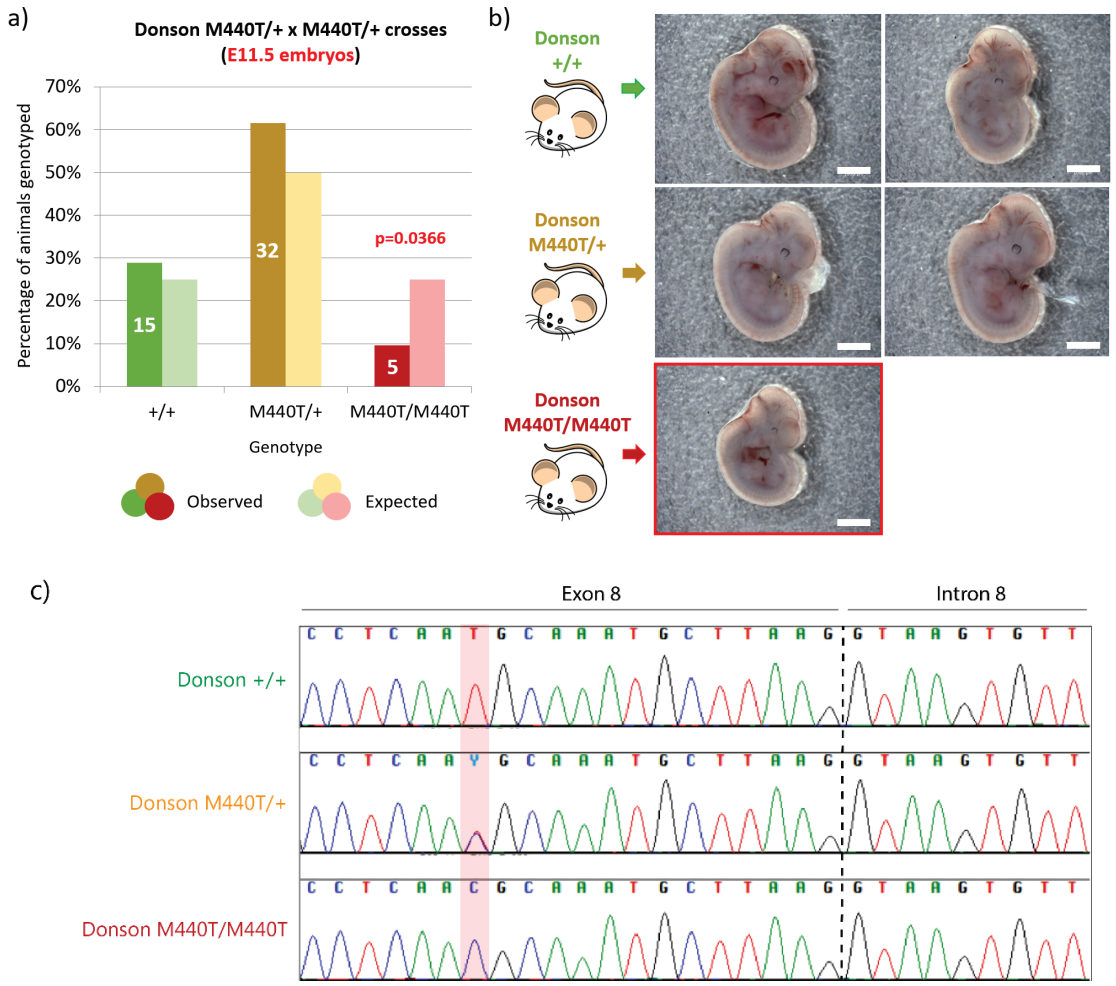

Figure 7.5. Embryos homozygous for Donson M440T are present at embryonic day 11.5 (E11.5) at sub-mendelian frequency.

a) The graph demonstrating the presence of mouse embryos homozygous for M440T mutation at E11.5. The experimentally observed distribution of genotypes is compared to their expected Mendelian distribution. Statistically significant reduction in the number of homozygous mutants is indicated (statistics: chi-squared test). The number of mice with each genotype is indicated on the columns in the graphs.

b) Representative images of E11.5 littermate embryos wild-type (+/+), heterozygous (M440T/+) or homozygous (M440T/M440T) for Donson M440T. Scare bars: 1 mm.

c) Sequencing electropherograms of embryos wild-type (+/+), heterozygous (M440T/+) or homozygous (M440T/M440T) for Donson M440T (indicated in red). Black dotted line indicates an exon-intron junction.

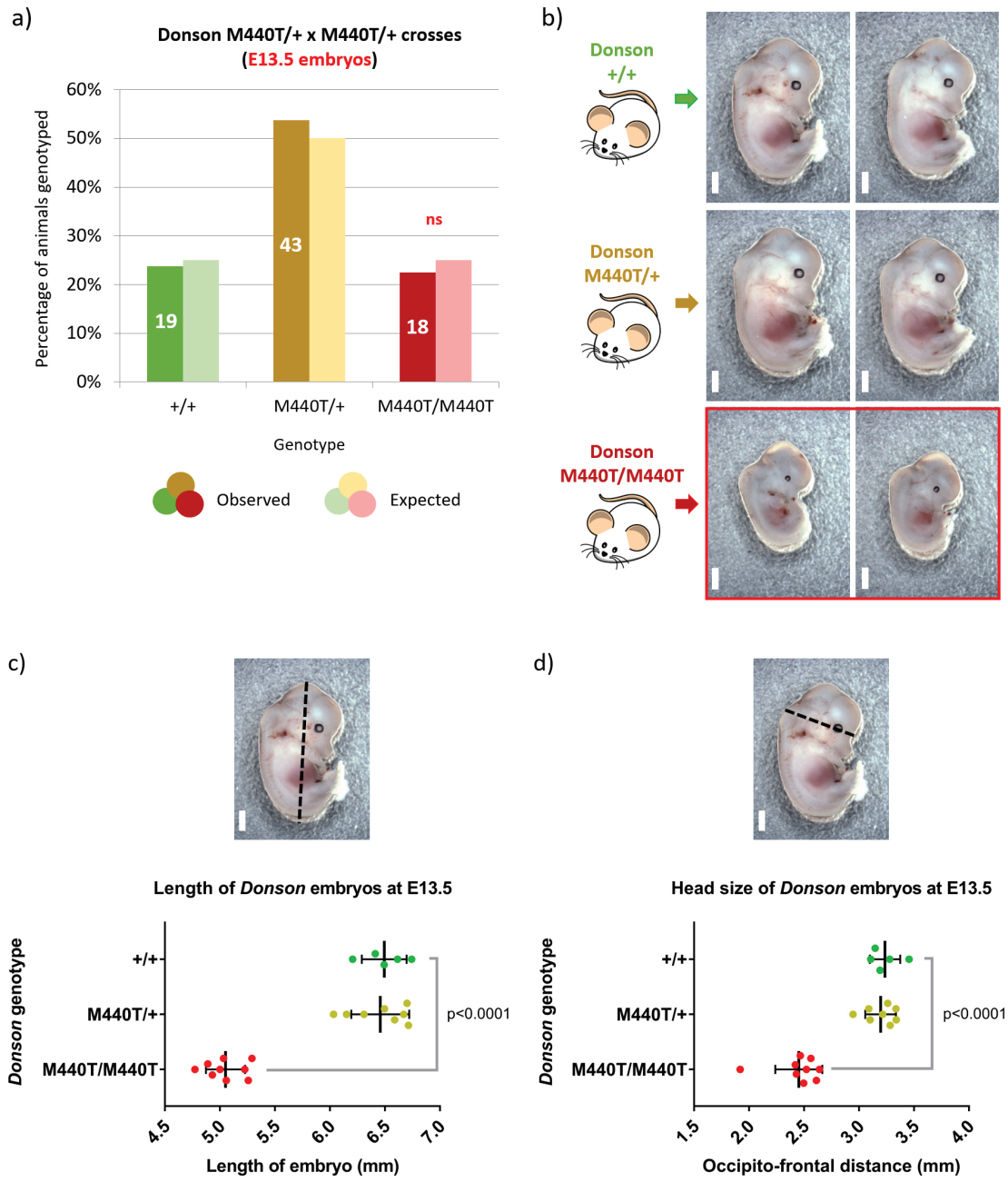

Figure 7.6. Embryos homozygous for Donson M440T are present at embryonic day 13.5 (E13.5) and are significantly smaller than their littermates.

a) Graph demonstrating the presence of mouse embryos homozygous for M440T mutation at E13.5. The experimentally observed distribution of genotypes is compared to their expected Mendelian distribution (statistics: chi-squared test). The number of mice with each genotype is indicated on the columns in the graphs.

b) Representative images of E13.5 littermate embryos wild-type (+/+), heterozygous (M440T/+) or homozygous (M440T/M440T) for Donson M440T. Scare bars: 1 mm.

c, d) E13.5 embryos homozygous for Donson M440T are significantly smaller in length (c) and occipito-frontal distance (d) than wild-type and heterozygous embryos. Each dot represents an embryo that was imaged and measured (as demonstrated by the dotted lines) using ImageJ/Fiji software. Statistics: unpaired t-test; black bars indicate mean ± SD.

The single dissection performed at E16.5 suggested the Mendelian distribution of genotypes, given the presence of two M440T homozygotes out of 11 embryos (***Figure 7.7*****a**). Both embryos were substantially smaller than their littermates, with extreme but proportional reduction in body and head size (***Figure 7.7*****b**-**d**). The average length of a Donson M440T/M440T embryo at E16.5 was 10.9±1.2 mm, and the head size was 5.6±0.3 mm; meanwhile, the average length of a wild-type embryo was 16.8±0.6 mm, with the head size of 9.1±0.5 mm (***Figure 7.7*****c**-**d**). This is in contrast to human DONSON patients, who present with the marked microcephaly (mean occipito-frontal circumference (OFC) –7.5±2.4 SD), whereas their height is reduced to a lesser degree than observed in other MPD-associated disorders (–3.2±1.4 SD).

Moreover, limb abnormalities were observed in the two M440T/M440T embryos at this embryonic stage, with upper and lower limbs disproportionately short and underdeveloped (***Figure 7.8*****a**-**b**). Digits also appeared to be malformed, suggesting an additional effect of the M440T mutation on limb development. Additionally, craniofacial dysmorphism, including reduced snout size and underdeveloped jaw, can be observed in the two Donson M440T/M440T embryos (***Figure 7.8*****a**). Notably, limb abnormalities were displayed by human patients with biallelic *DONSON* mutations as well (Reynolds *et al.*, 2017). These results also suggest that Donson M440T/M440T embryos mimic microcephaly-micromelia syndrome (MMS), characterised by perinatal lethality, severe microcephaly, craniofacial abnormalities and marked limb malformations (Evrony *et al.*, 2017).

No dissections at later stages of embryonic development were performed due to home office licence restrictions. Thus, I concluded that Donson M440T/M440T animals are not viable and exhibit embryonic lethality, but can survive at least until E16.5. Mice homozygous for Donson M440T are lost between E16.5 and weaning, and their growth is markedly stunted from E11.5 through to E16.5. Additionally, my experimental work suggests that the Donson M440T mutation leads to a more severe phenotype in mice than in humans, at least on the genetic background that was used for these experiments.

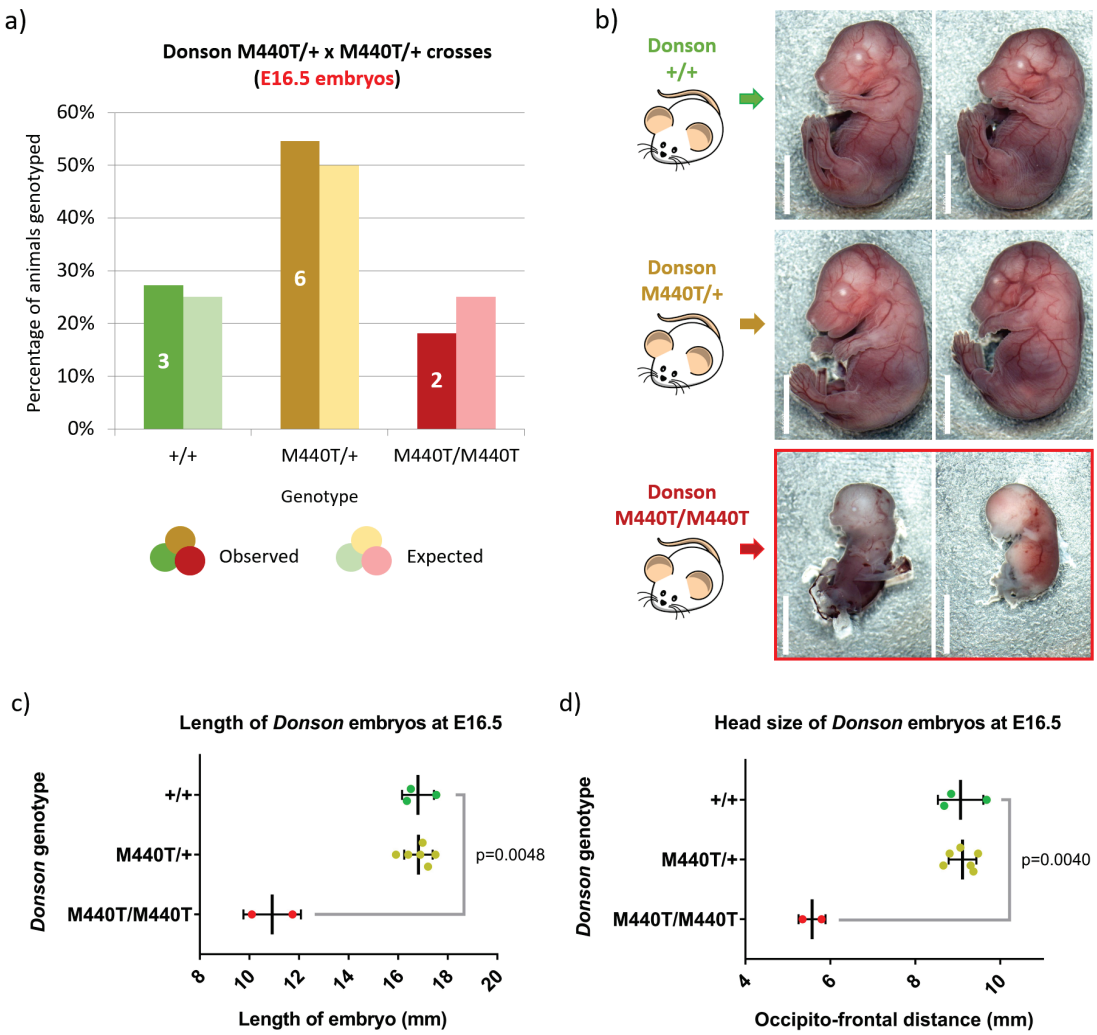

Figure 7.7. Embryos homozygous for Donson M440T are present at embryonic day 16.5 (E16.5) and are substantially smaller than their littermates.

a) The graph demonstrates the presence of mouse embryos homozygous for M440T mutation at E16.5. The experimentally observed distribution of genotypes in a single litter is compared to their expected Mendelian distribution. The number of mice with each genotype is indicated on the columns in the graphs.

b) Representative images of E16.5 littermate embryos wild-type (+/+), heterozygous (M440T/+) or homozygous (M440T/M440T) for Donson M440T. Scare bars: 5 mm.

c, d) E16.5 embryos homozygous for Donson M440T are significantly smaller in length (d) and head size (e) than wild-type and heterozygous embryos. Each dot represents an embryo that was imaged and measured using ImageJ/Fiji software. Statistics: unpaired t-test; black bars indicate mean ± SD.

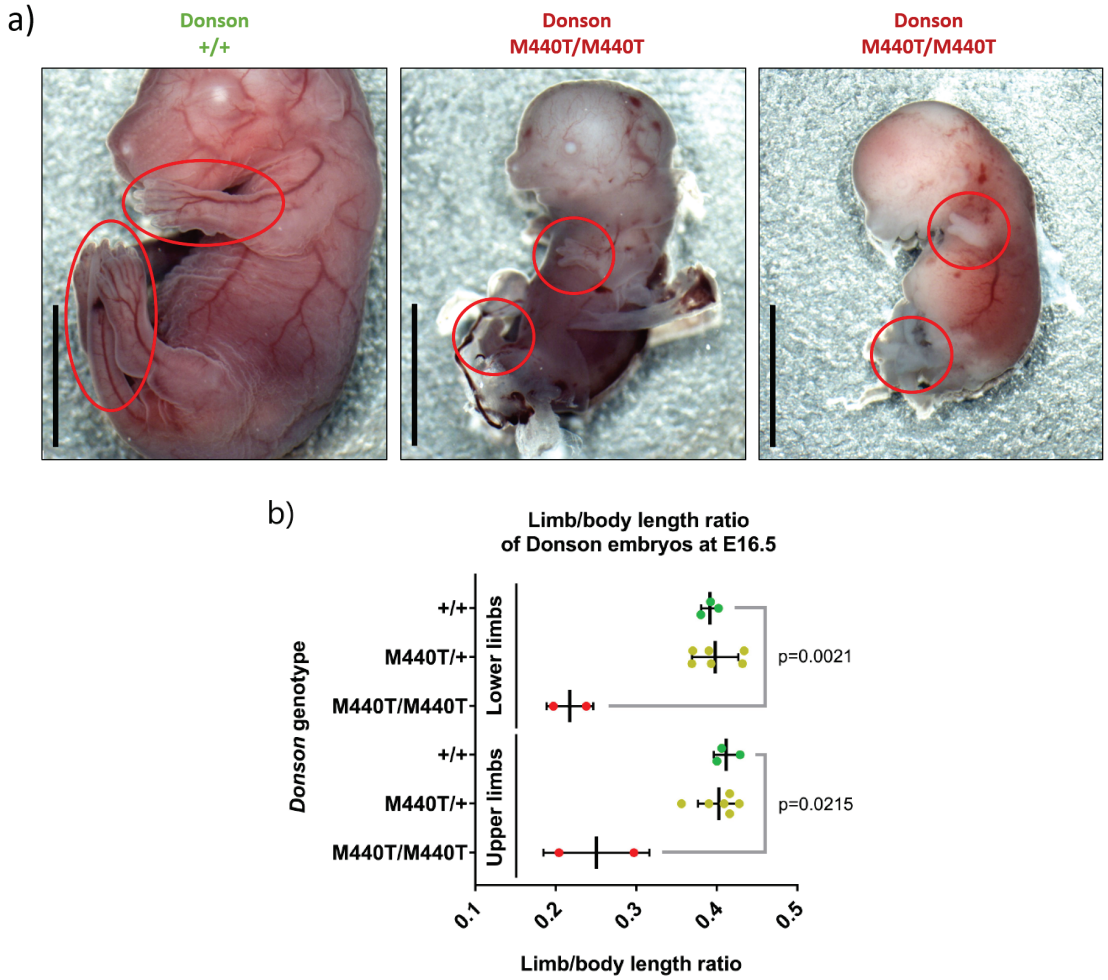

Figure 7.8. Embryos homozygous for Donson M440T present with disproportionately shorter and abnormal limbs.

a) Limbs in a wild-type (+/+) and the two Donson M440T/M440T E16.5 embryos are indicated by red circles. Scare bars: 5 mm.

b) Limb/body length ratio in Donson embryos at E16.5. Each dot represents an embryo that was imaged and measured using ImageJ/Fiji software. Statistics: unpaired t-test; black bars indicate mean ± SD.

7.5. Mice homozygous for Donson del5bp are not present at E10.5 or later

To determine if DONSON is essential for mammalian embryonic development and to establish mouse embryonic fibroblast (MEF) cell lines, embryo dissections of E13.5 Donson del5bp/+ crosses were performed, and the tail clips of the dissected embryos were used for genotyping. No E13.5 embryos homozygous for Donson del5bp were present (***Figure 7.9*****b-c**). Embryos heterozygous for Donson del5bp/+ did not visibly differ in size from their wild-type littermates at this stage of embryonic development. I then performed embryo dissections of Donson del5bp/+ crosses at an earlier developmental stage, E10.5, to assess for the presence of Donson del5bp/del5bp embryos. Again, no homozygous null embryos were detected (***Figure 7.9*****a**), and no gross phenotypic abnormalities or differences in size were found in heterozygotes at this stage of embryonic development.

Overall, the absence of Donson del5bp/del5bp embryos even at early stages of embryonic development that I tested (E10.5 and E13.5) suggests DONSON to be required for early mammalian development. These findings are consistent with work by Evrony *et al.* (2017), showing early embryonic lethality of mice homozygous for a Donson gene-trap KO cassette by demonstrating their absence at embryonic day 9.5 (E9.5) and afterwards.

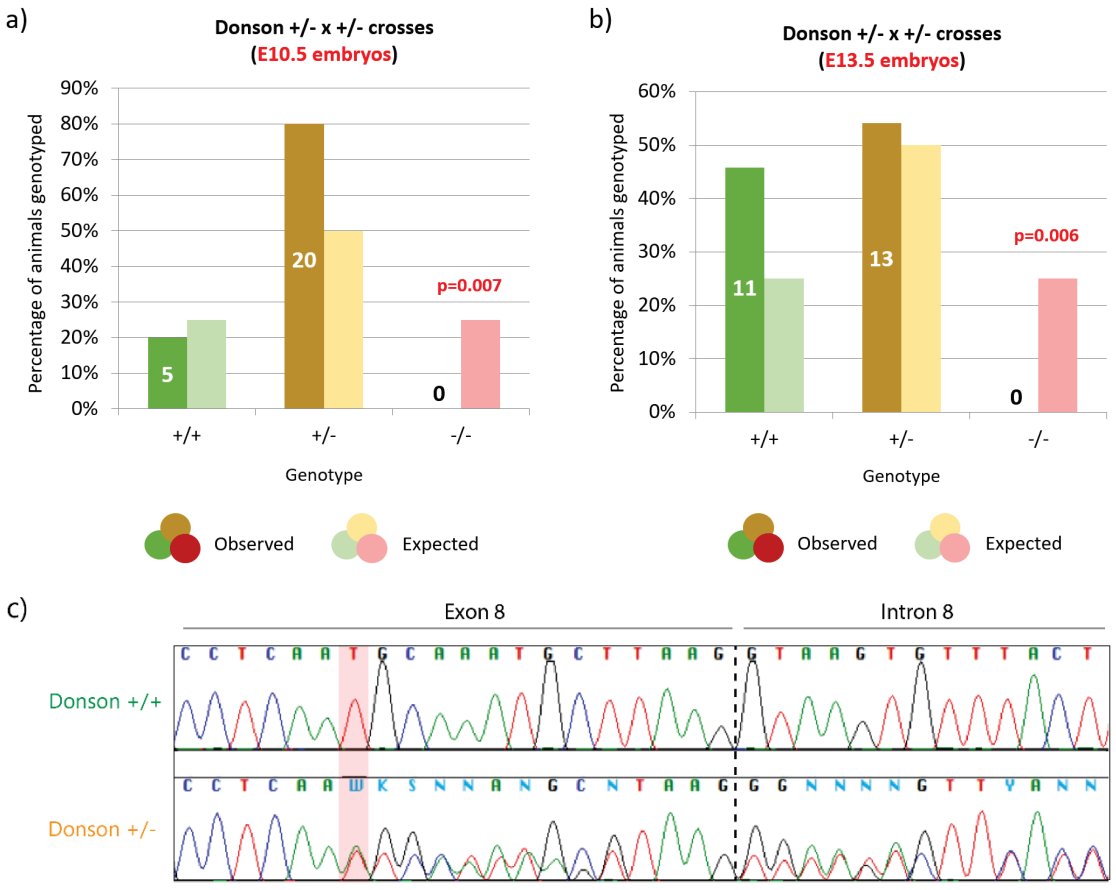

Figure 7.9. Mice homozygous for del5bp (Donson-/-) are not present at embryonic day 10.5 (E10.5) and 13.5 (E13.5).

a, b) Graphs demonstrating absence of homozygous offspring for knockout (del5bp) Donson mouse line at E10.5 (a) and E13.5 (b). All embryos present were wild-type or heterozygous for the del5bp mutation in *Donson*. The experimentally observed distribution of genotypes is compared to their expected Mendelian distribution. The number of mice with each genotype is indicated on the columns in the graphs. Statistics: chi-squared test.

c) Sequencing electropherograms of embryos wild-type (+/+) or heterozygous (+/-) for Donson del5bp. The M440T is indicated in red; black dotted line indicates an exon-intron junction.

7.6. Phenotypic analysis of Donson mouse embryonic fibroblasts

As mice homozygous for the Donson M440T were not viable, as initially expected, I generated Donson E13.5 mouse embryonic fibroblast (MEF) cell lines and used them for functional analysis.

Firstly, I postulated that the absence of viable Donson M440T/M440T mice may be caused by the disrupted splicing of mDonson mRNA, due to the substitution M440T having unexpected consequences on splicing, such as an altered exonic splicing enhancer (ESE) site. To test this hypothesis, total RNA was isolated from E13.5 MEF cell lines that were wild-type, heterozygous or homozygous for Donson M440T mutation. Complementary DNA (cDNA) was subsequently generated from the purified RNA and used as a template for reverse transcription (RT)-PCR analysis to assess splicing of mDonson exon 8 (***Figure 7.10*****a**). The gel electrophoresis analysis indicated that no alterations in mDonson exon 8 splicing were introduced by the M440T mutation (***Figure 7.10*****b**), and to further confirm this, the RT-PCR products were analysed by Sanger sequencing, establishing that splicing of mDonson exon 8 is not affected by the M440T mutation (***Figure 7.10*****c**). This result demonstrates that the failure of mice homozygous for Donson M440T to survive during the later stages of embryonic development is not caused by aberrant *Donson* transcript splicing.

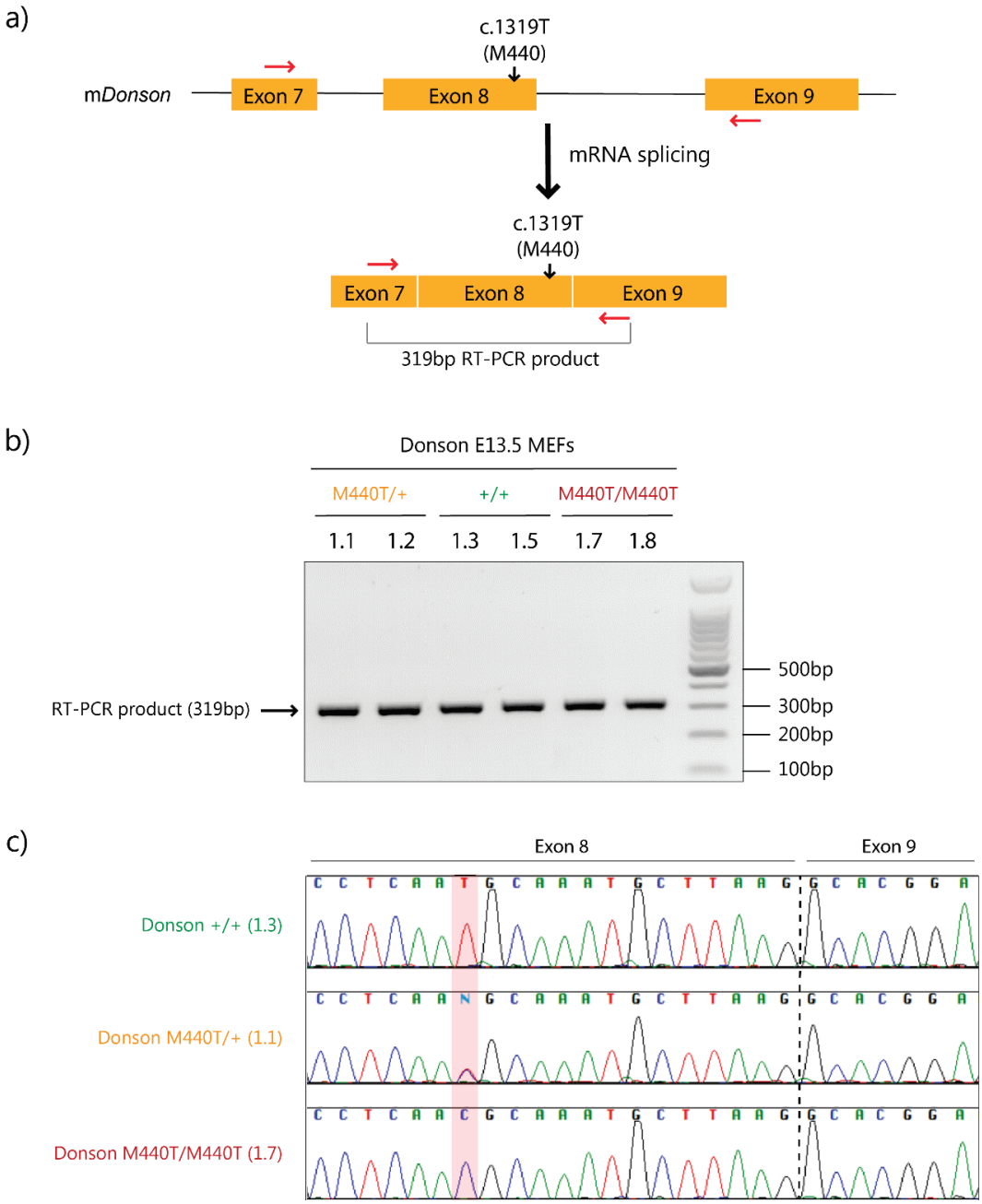

Figure 7.10. Splicing of m*Donson* transcript is unaffected by the M440T mutation.
a) Schematic representation of the RT-PCR analysis to assess splicing of mDonson exon 8, containing methionine 440 (M440). Red arrows indicate the locations of PCR primers used for amplification of exon 7, exon 8 and exon 9 from m*Donson* cDNA, resulting in a 319 bp-long RT-PCR product.
b) RT-PCR analysis of Donson E13.5 mouse embryonic fibroblast (MEF) cell lines demonstrates that no alterations in *Donson* transcript splicing occur in the presence of the M440T substitution. RNA isolated from six E13.5 MEF cell lines with three different genotypes, Donson +/+ (cell lines 1.3 and 1.5), M440T/+ (cell lines 1.1 and 1.2), and M440T/M440T (cell lines 1.7 and 1.8), was reverse transcribed to generate cDNA, which was used as a template for RT-PCR reactions. The RT-PCR products were visualised on a 2% agarose gel and Sanger sequenced.
c) Sequencing electropherograms of RT-PCR products wild-type (+/+; 1.3), heterozygous (M440T/+; 1.1) or homozygous (M440T/M440T; 1.7) for Donson M440T (indicated in red). Black dotted line indicates an exon-exon junction.

Human DONSON was implicated in maintaining genome stability, as DONSON depletion in HeLa cells was shown to result in a high proportion of cells exhibiting spontaneous γH2AX and 53BP1 foci, markers of DNA damage and DSBs (Reynolds *et al.*, 2017). Elevated levels of γH2AX and 53BP1 foci were also observed in unperturbed fibroblasts from patients with hypomorphic *DONSON* mutations (Reynolds *et al.*, 2017). To test whether spontaneous DNA damage also arises in MEFs homozygous for Donson M440T, numbers of 53BP1 and γH2AX foci were assessed in unperturbed MEF lines by immunofluorescence. Image analysis revealed significantly elevated levels of 53BP1 and γH2AX foci in Donson M440T/M440T MEFs, compared to wild-type (+/+) MEFs (***Figure 7.11*a-c**). No significant increase in 53BP1 foci was observed in heterozygous Donson +/- (del5bp/+) and Donson M440T/+ MEF lines (***Figure 7.11*b**), although numbers of γH2AX foci showed a small but significant increase in Donson +/- (del5bp/+) cells (***Figure 7.11*c**). These observations suggest that siRNA-mediated DONSON depletion in human cells and the biallelic Donson M440T mutation in mouse cause similar genome instability defects, as determined by elevated levels of DNA damage foci, marked by 53BP1 and γH2AX, in unperturbed cells. Although Donson M440T/M440T MEF lines 1.7 and 1.8 exhibited different severity of this phenotype (***Figure 7.11*b-c**), potentially due to documented heterogeneity of MEF populations (Singhal *et al.*, 2016) or the mixed genetic background (Montagutelli, 2000; Schauwecker, 2011), my experiments strongly suggested that DNA damage is significantly elevated in the presence of the biallelic M440T mutation in mice.

Unresolved replication-associated damage can impair DNA segregation during mitosis, giving rise to chromatin bridges, lagging chromosomes or chromatin fragments, each of which can subsequently lead to the formation of micronuclei (Terradas *et al.*, 2010). Thus, the number of cells with micronuclei is another indicator of unresolved genome instability. As significantly elevated levels of spontaneously arising micronuclei were previously observed in DONSON-depleted HeLa cells (Reynolds *et al.*, 2017), I determined the proportion of unperturbed MEF cells of different genotypes (wild-type (+/+), Donson +/- (del5bp/+), Donson M440T/+, and Donson M440T/M440T) containing one or more micronuclei. As expected, significantly higher percentage of Donson M440T/M440T MEFs had at least one micronucleus (15.5% for both cell lines 1.7 and 1.8), compared to wild-type cells (3.5% and 6.4% for cell lines 1.3 and 1.5, respectively) (***Figure 7.11*d**). This result, together with elevated levels of 53BP1 and γH2AX foci, strongly indicates that, like the DONSON-depleted HeLa and DONSON patient-derived cells, mouse cells homozygous for Donson M440T undergo spontaneous DNA damage.

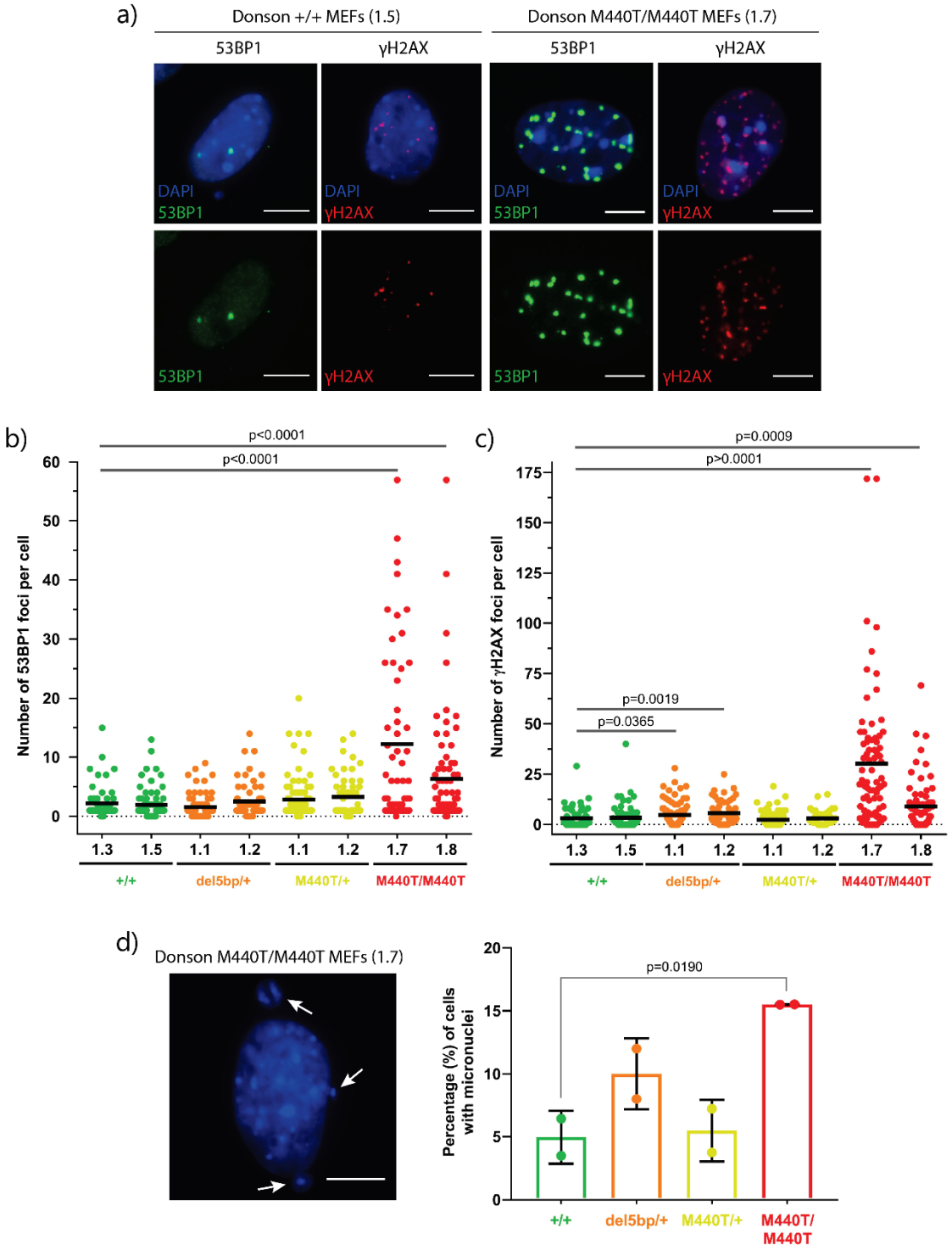

Figure 7.11. Number of 53BP1 and γH2AX foci, as well as proportion of cells with micronuclei, are increased in unperturbed Donson M440T/M440T mouse embryonic fibroblasts.

a) Representative images of unperturbed E13.5 Donson +/+ (cell line 1.5) and M440T/M440T (cell line 1.7) mouse embryonic fibroblasts (MEFs), stained for 53BP1 (FITC; green channel) or γH2AX (TxRed; red channel) and visualised using fluorescence microscopy. DAPI signal is shown in blue. Scale bars: 10 µm.

b, c) Immunofluorescence quantification to assess the numbers of 53BP1 (b) and γH2AX (c) foci in unperturbed E13.5 Donson MEFs. Two MEF cell lines of each genotype (wild-type (+/+), Donson +/- (del5bp/+), Donson M440T/+ and Donson M440T/M440T) were plated on

coverslips. Next day, detergent pre-extraction of non-chromatin-bound proteins was performed before cell fixation with formaldehyde. Cells were immunostained for 53BP1 and γH2AX and visualised using fluorescence microscopy. Image analysis was performed using Fiji/ImageJ software. Black bars indicate the mean, and each dot in the graph represents one cell (more than 50 cells analysed per condition). Statistics: unpaired two-tailed t-test.
d) Left: representative image of an unperturbed E13.5 Donson M440T/M440T (cell line 1.7) mouse embryonic fibroblast (MEF) with micronuclei (indicated by white arrows); scale bar: 10 µm. Right: percentage of unperturbed wild-type (+/+), Donson +/- (del5bp/+), Donson M440T/+ and Donson M440T/M440T MEF cells with micronuclei. Cells were visualised using fluorescence microscopy, and image analysis was performed using Fiji/ImageJ software. To estimate the percentage of cells with micronuclei, more than 100 cells were analysed per condition. The dots in the graph represent values obtained for individual MEF cell lines; results indicate mean ± SD. Statistics: unpaired two-tailed t-test.

7.7. Summary and discussion: DONSON MPD mouse model

In summary, this chapter describes the CRISPR/Cas9-based generation and phenotypic analysis of a mouse model of MPD caused by mutations in *DONSON*. I demonstrated that no mice homozygous for mDonson M440T, equivalent to MPD patient mutation hDONSON M446T, are born, although embryos with this genotype could be found up to embryonic development stage E16.5, exhibiting a significant reduction in body and head size. Additionally, Donson M440T/M440T embryos presented with craniofacial and limb abnormalities at this embryonic development stage, with forelimbs and hindlimbs disproportionately shorter and underdeveloped, compared to the wild-type or heterozygous littermates.

Notably, limb malformations, such as forearm and thumb dysplasia, were displayed by MPD patients homozygous for DONSON M446T as well, whereas several individuals with other *DONSON* mutations had fifth finger clinodactyly, syndactyly, brachydactyly, and bilateral radius and thumb hypoplasia (Reynolds *et al.*, 2017). In the family with the most extreme phenotype, Reynolds *et al.* (2017) observed substantial limb shortening and fetal lethality. Similar phenotypic characteristics were reported in MMS patients as well, where limb malformations in most affected individuals showed bilateral oligodactyly with absent thumbs and absent or poorly developed fifth fingers, as well as short lower limbs with frequent toe syndactyly (Evrony *et al.*, 2017). Furthermore, other diagnostic features for MMS are craniofacial anomalies, such as small mouth and undersized jaw, and neonatal lethality (Evrony *et al.*, 2017), and my Donson M440T/M440T embryos appeared to mimic the phenotypes associated with this syndrome.

Limb abnormalities were previously associated with disruption of other MPD and genome maintenance genes as well. Severe limb abnormality phenotype was observed in the ORC1 mouse model of MPD, generated in our laboratory, with complete loss of forelimbs and shortened hindlimbs with oligodactyly seen in newborn mice (F. Cooper, unpublished). Mutations in *RECQL4*, a DNA replication gene implicated in maintaining genome integrity (Bruck and Kaplan, 2014; Kaiser *et al.*, 2017; Petkovic *et al.*, 2005), were shown to cause RAPADILINO syndrome, characterised by growth retardation, radial defects, limb abnormalities and other malformations (Siitonen *et al.*, 2003). Notably, radial and thumb abnormalities are also commonly associated with Fanconi Anaemia (FA), with up to 35% patients having a thumb abnormality and another 7% displaying absent or hypoplastic radii (Triemstra *et al.*, 2015). Considering that the phenotype of the family with the DONSON M446T

mutation was first associated with FA (Milner *et al.*, 1993) and that DONSON-depleted cells display various cellular defects after MMC treatment (Reynolds *et al.*, 2017), there may be a functional overlap between FA proteins and DONSON, which will need to be addressed in the future.

The statistically significant absence of viable Donson M440T/M440T mice was surprising, as the corresponding mutation in hDONSON, M446T/M446T, does not confer embryonic lethality (Reynolds *et al.*, 2017). The lymphoblastoid cell lines derived from the three MPD patients homozygous for DONSON M446T were shown to have reduced DONSON protein levels (Reynolds *et al.*, 2017), potentially due to compromised stability of the mutant protein. Moreover, the *DONSON* mutations identified in MPD patients were demonstrated to be hypomorphic, with mutant protein retaining some residual function (Reynolds *et al.*, 2017). Unfortunately, the protein levels in my Donson M440T/M440T MEFs could not be assessed by immunoblotting due to the lack of a suitable antibody. One possibility is that the missense mutation M440T may have a bigger impact on the stability of Donson protein in mice than in humans. Additionally, mouse development may be more sensitive to Donson deficiency, thus resulting in an early embryonic lethality.

Alternatively, the absence of Donson M440T/M440T mice may be influenced by the genetic background of mice used in my experiments. The genetic background of a mouse strain is known to affect the observed phenotype, resulting from a particular mutation, due to differences in modifier genes, which act together with the causative gene (Montagutelli, 2000). In some cases, the modulation of the phenotype can be considerable, as demonstrated by the mouse model with targeted disruption of the epidermal growth factor receptor gene, where phenotypes ranged from peri-implantation death of embryos on a CF-1 background to survival for up to 3 weeks after birth for animals on a CD-1 background (Threadgill *et al.*, 1995). Moreover, mice deficient for RIF1, which interacts with 53BP1 and is involved in DSB repair (Silverman *et al.*, 2004), were viable only on the CD-1 background, whereas the same mutation in 129/Ola and MF-1 mouse strains resulted in embryonic lethality (Chapman *et al.*, 2013). Thus, it may be expected that genetic differences between mouse strains result in varying degrees of genome instability in the presence of mutations that disrupt DNA replication and repair genes.

For the breeding of Donson transgenic mice, a mixed background, CD-1 crossed with BL6CBAF1, was used. It is worth noting that in the dissections performed on Donson M440T E11.5–E16.5 embryos, 14 out of 17 (82%) spontaneous embryo resorptions, for which yolk sac

was genotyped, were homozygous for Donson M440T. This observation clearly indicates size variability of genetically identical E11.5–E16.5 M440T/M440T embryos, ranging from a spontaneous resorption to a small embryo, which may result from the mixed genetic background. In the future, it would be interesting to test whether viable mutant homozygotes could be obtained by transferring the Donson M440T mutation onto different genetic backgrounds, such as the CD-1 strain.

Rescue experiments could be performed to gain insight into genetic factors that result in increased genomic instability in Donson-deficient mice. Reynolds *et al.* (2017) demonstrated that the severe genome instability observed in DONSON-depleted HeLa cells was due to unscheduled nucleolytic processing of damaged replication forks by structure-specific nucleases, such as MUS81. Moreover, co-depletion of DONSON and MUS81 was shown to partially rescue the spontaneous replication fork asymmetry and increased γH2AX phosphorylation of DONSON-depleted cells (Reynolds *et al.*, 2017). MUS81 KO mice were previously demonstrated to be viable and develop normally, with cultured MUS81-deficient MEFs showing elevated levels of DNA damage, chromosomal aberrations and hypersensitivity to DNA crosslinking agents (Dendouga *et al.*, 2005). Therefore, crossing Donson M440T mouse line with MUS81 KO mice might potentially rescue embryonic lethality of Donson M440T/M440T mice, at the same time confirming the mechanism of pathogenicity caused by Donson M440T mutation.

Additionally, the co-deletion of p53 led to the rescue of microcephaly-associated phenotypes in several MPD mouse models, such as ASPM (Williams *et al.*, 2015) and CEP63 (Marjanović *et al.*, 2015) mice, indicating the importance of p53 in mediating pathogenesis of MPD syndromes. Mouse embryonic lethality caused by the inactivation of DNA repair genes, such as XRCC4, was also rescued by p53 deficiency due to attenuated cell cycle checkpoint control, apoptosis and senescence allowing cells with genomic instability to survive (Bogue *et al.*, 1996; Gao *et al.*, 2000; Lim *et al.*, 2000). Thus, the cross between Donson M440T and p53 KO mouse lines may be another way to rescue lethality of biallelic Donson M440T mutation in mice.

As proposed by Reynolds *et al.* (2017), DONSON may reduce the number of cells generated during development via a failure to maintain replication fork stability in the presence of endogenous replication stress, thus explaining the decreased organism size observed. The importance of the replication stress response in mammalian development was highlighted by the mouse model of Seckel syndrome resulting from ATR deficiency (Murga *et*

al., 2009). ATR-Seckel mice underwent high levels of replication stress during embryonic development, demonstrating that ATR signalling is required for efficient resolution of endogenous DNA damage *in utero* (Murga *et al.*, 2009). Moreover, ATR-Seckel-derived MEFs showed an increase in γH2AX and 53BP1 foci, indicating an activation of the replication stress-associated DDR (Murga *et al.*, 2009). Similar to observations by Murga *et al.* (2009), I showed that unperturbed fibroblast cell lines derived from Donson M440T/M440T embryos presented with significant increase in the numbers of 53BP1 and γH2AX foci, and a larger proportion of them had micronuclei, indicating spontaneously arising genome instability in murine Donson M440T/M440T cells, recapitulating the human cellular phenotype associated with DONSON deficiency (Reynolds *et al.*, 2017). The Donson M440T mouse line could therefore be further used to study the involvement of Donson in stimulating the ATR signalling axis, as well as to establish the embryonic development stage and brain areas that are particularly susceptible to prenatal replication stress.

At the moment, it is still not clear at which stage of mammalian embryonic development DONSON plays an essential role. Taken together, our data and results obtained by Evrony *et al.* (2017) demonstrate early embryonic lethality of Donson-/- mice, indicating their absence at embryonic development stage E9.5 and after. These observations suggest that Donson is essential for the initial stages of embryonic development in mice, but further analyses are needed to pinpoint the mammalian embryonic development stage that is particularly vulnerable to the complete absence of DONSON.

Chapter 8

Discussion

8. Discussion

8.1. Summary of the main findings in this thesis

Variation in size is one of the most striking features in mammals, ranging from a tiny bumblebee bat to a large blue whale and representing a weight difference of 75 million fold (Oldham *et al.*, 2000). Human height is a classical quantitative trait, highly variable between and within populations and affected by multiple genes with small effect sizes (Stulp and Barrett, 2016; Visscher, 2008). During development, organ size in humans is tightly controlled to ensure the symmetry and maintenance of relative proportions (Wolpert, 2010). It is evident that regulation of cell proliferation during embryogenesis plays a major role in determining body and organ size, but many aspects of it are still poorly understood. The identification and characterisation of genes that, when mutated, cause the most extreme human growth phenotypes may provide valuable insights into the molecular mechanisms of cell growth and proliferation, as well as physiological regulation of organism growth. In this thesis, functional analysis and characterisation of three genes that promote genome stability and are associated with microcephalic primordial dwarfism (MPD) is described.

In our laboratory, novel biallelic mutations in *DNA2*, encoding an ATP-dependent helicase/nuclease with multiple roles in DNA replication and repair (Pawłowska *et al.*, 2017; Wanrooij and Burgers, 2015) were identified in four MPD patients. In this thesis, the experiments to confirm the deleteriousness of these variants were conducted (Chapter 3). Using the minigene splicing assay, I showed that *DNA2* transcript splicing is altered in the presence of the non-coding mutations identified in MPD patients. Additionally, *in silico* analyses predicted that the identified coding mutation within the ATP binding motif of DNA2 would strengthen the interaction between DNA2 and the ADP moiety, potentially increasing the time the mutant isoform spends in a nucleotide-bound conformation. Collectively, these data suggest that mutations in *DNA2* lead to diminished DNA2 protein levels and enzymatic function, contributing to MPD pathogenesis.

TRAIP, encoding an E3 ubiquitin ligase (Besse *et al.*, 2007), was previously established as an MPD gene by our laboratory and implicated in responding to genotoxic lesions during genome replication (Harley *et al.*, 2016). My work was to further investigate and elucidate the molecular mechanisms by which TRAIP promotes genome stability in unperturbed and damaged cells. A putative role for TRAIP in regulating the activity of protein phosphatase 4

(PP4) complex by ubiquitination was analysed (Chapter 4). Biochemical experiments, coupled with mass spectrometry analysis of TRAIP-dependent PP4 ubiquitination sites, identified lysine 183 (K183) of PP4 catalytic subunit PP4C as an important residue for TRAIP-mediated ubiquitination *in vitro*. However, my experimental work did not provide evidence that TRAIP-mediated PP4C ubiquitination is relevant to its DNA damage response (DDR) function. Therefore, RPE1 p53-/- TRAIP-KO cell line was generated using CRISPR/Cas9 genome editing technology to facilitate the investigation of the DDR function of TRAIP (Chapter 5). Subsequent characterisation of these cells demonstrated the disruption of both *TRAIP* alleles, and the absence of TRAIP protein was associated with the increased frequency of tetraploidy and both clonal and non-clonal chromosomal abnormalities in unperturbed cells. DDR signalling analysis also revealed the failure of TRAIP-KO cells to properly respond to camptothecin (CPT)-induced DNA damage, prompting further investigation of the molecular mechanisms underlying this defect (Chapter 6). My experimental work showed that diminished response to CPT-induced DNA lesions in TRAIP-KO cells, including reduced RPA2 phosphorylation and ssDNA generation, defective HR, and reduced cell survival, was dependent on the proper E3 ubiquitin ligase activity of TRAIP. Finally, TRAIP-KO cells were used in epistasis experiments to address the potential interplay between TRAIP and Fanconi Anaemia (FA) pathways in interstrand crosslink (ICL) repair, based on other groups' work in *Xenopus laevis* (personal communication with Prof Johannes Walter and Prof David Pellman; Wu, Semlow *et al.*, unpublished). Unexpectedly, my data indicated an additive effect of the loss of TRAIP and FANCD2 depletion towards cell sensitivity to ICL-inducing agent mitomycin C (MMC), suggesting that TRAIP acts in alternative FA pathway-independent processes that contribute to ICL tolerance in mammalian cells.

Finally, I established a murine model of MPD caused by DONSON deficiency (Chapter 7), which contained a missense mutation corresponding to a human MPD mutation in this replication fork protection factor (Reynolds *et al.*, 2017). Homozygous mice showed embryonic lethality after embryonic day 16.5 (E16.5), with mutant embryos being substantially smaller than control littermates at all embryonic stages sampled. Additionally, limb abnormalities in these embryos were prominent at E16.5, phenocopying human MPD patients with the equivalent mutation (Reynolds *et al.*, 2017) and microcephaly-micromelia syndrome (MMS), also caused by biallelic mutations in *DONSON* (Evrony *et al.*, 2017). Furthermore, mouse embryonic fibroblasts established from these embryos demonstrated increased levels of spontaneous DNA damage, recapitulating the phenotype observed in siRNA-depleted and DONSON patient-derived cell lines. This further supports the pathogenicity of the biallelic mutations in the *DONSON* gene. Lastly, the early embryonic lethality of DONSON-null mouse

was observed, occurring before E10.5 and, together with the data obtained by Evrony *et al.* (2017), supporting the essential role for DONSON during early mammalian embryonic development.

Collectively, the experiments described in this thesis strengthen previously observed links between *DNA2*, *TRAIP* and *DONSON* and human disease, at the same time providing additional insights into cellular and/or developmental roles of these MPD genes in DNA replication and repair.

8.2. How do mutations in *DNA2*, *TRAIP* and *DONSON* result in MPD?

8.2.1. Similarities in molecular mechanisms by which DNA2, TRAIP and DONSON maintain genome stability

Genes associated with microcephaly and MPD encode proteins that participate in several key cellular processes, such as DDR (Harley *et al.*, 2016; O'Driscoll *et al.*, 2003; Reynolds *et al.*, 2017), DNA replication (Bicknell *et al.*, 2011a, 2011b; Burrage *et al.*, 2015; Fenwick *et al.*, 2016; Guernsey *et al.*, 2011; Vetro *et al.*, 2017), DNA repair (Murray *et al.*, 2015, 2014; Qvist *et al.*, 2011; Shaheen *et al.*, 2014), centriole biogenesis (Bond *et al.*, 2005; Guernsey *et al.*, 2010; Kalay *et al.*, 2011; Leal *et al.*, 2003; Martin *et al.*, 2014), cell division (Bond *et al.*, 2002; Jackson *et al.*, 2002, 1998; Martin *et al.*, 2016; Moynihan *et al.*, 2000) and mRNA processing (Edery *et al.*, 2011; He *et al.*, 2011) (Section 1.1.2). Although their cellular functions are distinct, mutations in these genes are thought to cause disease via convergent mechanisms, particularly through prolonged cell cycle and impaired cell division, which ultimately affect cell numbers throughout the body and brain (Klingseisen and Jackson, 2011). Collectively, the three MPD genes investigated in this thesis, *DNA2*, *TRAIP* and *DONSON*, have important roles during DNA replication and ATR-dependent S phase checkpoint signalling, thus facilitating maintenance of genome stability.

8.2.1.1. Roles of DNA2, TRAIP and DONSON in DNA replication

It is possible that similar mechanisms underlie reduced cell proliferation, caused by biallelic mutations in *DNA2*, *TRAIP* and *DONSON*, as all three factors were shown to be physically associated with ongoing and/or stalled replication forks. A direct interaction between DNA2 and replisome protein AND-1 was observed in replicating HeLa cells, suggesting that DNA2 is a component of the replisome (Duxin *et al.*, 2012). Moreover, the crystal structure of mouse DNA2 demonstrated its association with ssDNA and RPA (Zhou *et al.*, 2015), while it was shown to interact with PCNA in human breast epithelial cells (Peng *et al.*, 2012). Likewise, TRAIP was also found to associate with the replisome through its interaction with PCNA, particularly upon genotoxic stress (Hoffmann *et al.*, 2016; W. Feng *et al.*, 2016). Additionally, using nascent chromatin capture (NCC) (Alabert *et al.*, 2014) analysis in HeLa cells, Hoffmann *et al.* (2016) showed that TRAIP is present at nascent, but not

mature, chromatin, implicating it as a component of the replication machinery. Finally, DONSON was demonstrated to interact with multiple components of the replisome, including the MCM complex and PCNA, as well as shown to be enriched at replication forks and nascent DNA, compared to mature chromatin (Reynolds *et al.*, 2017). Thus, although no direct interaction between DNA2, TRAIP and DONSON has been observed so far, all were shown to physically associate with PCNA and replication machinery. The close interaction of DNA2, TRAIP and DONSON with the replisome could be expected to facilitate their rapid response to endogenously arising DNA damage during embryogenesis, thus ensuring efficient cell cycle progression.

8.2.1.2. DNA2, TRAIP and DONSON in ATR-dependent S phase checkpoint signalling and DNA repair

Unresolved endogenous DNA damage is likely to be the major threat to cell viability during embryonic development. My work, alongside published studies, established that DNA2, TRAIP and DONSON are required for ATR-dependent S phase checkpoint activation in response to endogenous and exogenous replication-associated DNA damage, initiating DDR and DNA repair.

In support to this, the deficiency of all three genes, *DNA2*, *TRAIP* and *DONSON*, was observed to result in dysregulated cell cycle. DNA2-depleted U2OS cells (Duxin *et al.*, 2012, 2009) and patient-derived cell lines with mutations in *TRAIP* (Harley *et al.*, 2016) and *DONSON* (Reynolds *et al.*, 2017) have prolonged cell cycle and accumulate in S and/or G2 phase, demonstrating the importance of all three proteins for DNA replication and timely cell cycle progression. It is likely that the cell cycle defects seen upon DNA2, TRAIP and DONSON depletion are linked to the absence of these proteins at stalled replication forks, where they are needed to maintain genome stability by responding to spontaneous DNA damage.

The nucleolytic activity of DNA2 was shown to facilitate HR by resecting DNA ends at DSBs (Cejka *et al.*, 2010; Karanja *et al.*, 2012; Nimonkar *et al.*, 2011; Niu *et al.*, 2010; Sturzenegger *et al.*, 2014) and promote replication fork restart by degrading reversed replication forks (Thangavel *et al.*, 2015). While the involvement of DNA2 in regulating replication checkpoint activation in unperturbed cells was demonstrated to be dependent on both its nuclease and helicase enzymatic activities (Duxin *et al.*, 2012), Karanja *et al.*

(2012) and Thangavel *et al.* (2015) showed that DNA end resection activity of DNA2 is specifically involved in ATR-dependent checkpoint activation under conditions of replication stress. DNA2 and exonuclease 1 (EXO1) were demonstrated to play redundant roles in DNA end resection at CPT-induced replication-associated DSBs, as indicated by diminished levels of CPT-induced pRPA2-S4/S8 signal, RPA foci and pCHK1-S345 levels upon the depletion of both factors in U2OS cells (Karanja *et al.*, 2012). Additionally, DNA2 was required for RPA2 phosphorylation after exposure to DNA crosslinking agent cisplatin, implicating DNA2 in ICL repair (Karanja *et al.*, 2012). DNA2-depleted U2OS cells also accumulated unrepaired CPT- and cisplatin-induced DSBs, as indicated by increased frequency of chromatid breaks in metaphase chromosome spreads (Karanja *et al.*, 2012). Finally, DNA2 was shown to physically interact with and function downstream of FANCD2, as well as participate in HDR *in vivo* (Karanja *et al.*, 2012).

Requirement for TRAIP to promote DDR signalling at damaged replication forks was noted by multiple studies (Harley *et al.*, 2016; Hoffmann *et al.*, 2016; W. Feng *et al.*, 2016). Additionally, karyotypes of unperturbed TRAIP-KO cells demonstrated accumulation of high levels of chromosomal instability (Section 5.3), indicating the importance of TRAIP in responding to endogenous replication stress as well. Like DNA2, TRAIP may have a role in DNA end resection, as indicated by my experimental work (Chapter 6) showing that the loss of TRAIP and its E3 ligase activity result in reduced pRPA2-S4/S8 signal upon CPT treatment, as well as defective ssDNA production (also demonstrated by Hoffmann *et al.*, 2016). In constrast to DNA2, TRAIP most likely affects DNA end resection indirectly through facilitating processes at replication fork that result in the formation of RPA-coated ssDNA regions, such as ubiquitination of replication fork-associated proteins and/or DNA repair factors. Nevertheless, these findings implicate ligase activity of TRAIP in facilitating ATR-dependent checkpoint signalling by promoting DNA end resection in response to CPT-induced replication-associated DNA damage. TRAIP was also shown to be necessary for efficient DDR signalling, genome stability and cell survival after HU- (W. Feng *et al.*, 2016) and MMC-induced DNA damage (Chapter 6; Hoffmann *et al.*, 2016). Although no evidence implicating TRAIP and FANCD2 in the same ICL repair pathway was found in human cells (Section 6.2.3), the importance of TRAIP after MMC-induced DNA damage (Section 6.2.2; Hoffmann *et al.*, 2016) points to its potential involvement in facilitating ICL repair via mechanism that is yet to be established, potentially by promoting ATR-dependent S phase checkpoint signalling, DNA end resection and/or HR. However, in contrast to the subtle reduction in MMC-induced pCHK1-S345 and γH2AX signal observed by Hoffmann *et al.* (2016), my data suggested that

MMC treatment-induced CHK1 and H2AX phosphorylation is not significantly altered in TRAIP-KO cells (Section 6.2.2). As my results also showed that MMC-induced HR is not affected in TRAIP-KO cells (Section 6.2.2), it is more likely that TRAIP promotes MMC-ICL repair in a different manner, independent of ATR signalling.

Similar to TRAIP and DNA2, DONSON was shown to promote the ATR-dependent replication stress response and stabilise replication forks both upon spontaneous stalling and after exogenous DNA damage, as demonstrated by inefficient HU- or MMC-induced RPA2 and CHK1 phosphorylation in DONSON-depleted HeLa cells (Reynolds *et al.*, 2017). However, DONSON depletion led to increased levels of RPA-coated ssDNA following replication stress (Reynolds *et al.*, 2017), suggesting that unlike TRAIP or DNA2, DONSON is not required for DNA end resection but rather facilitates downstream steps of the ATR-dependent replication stress response activation. DONSON-deficient HeLa cells also exhibited spontaneous genome instability, further exacerbated by HU and MMC treatment (Reynolds *et al.*, 2017). In support to this, DONSON MPD mouse model showed increased levels of unrepaired endogenous DNA damage, as indicated by elevated levels of 53BP1 and γH2AX foci and micronuclei (Chapter 7). Similarly, spontaneously arising genome instability that was further aggravated by exogenous DNA damaging agents was observed in DNA2-deficient (Duxin *et al.*, 2012, 2009; Karanja *et al.*, 2012) and TRAIP-deficient cells (Chapters 5–6), demonstrating that all three proteins analysed in this thesis have important cellular roles that prevent accumulation of DNA damage and ensure genome stability.

Overall, DNA2, TRAIP and DONSON are required for efficient resolution of replication-associated DNA damage and proper ATR-dependent S phase checkpoint activation, and deficiency of each of these factors results in impaired DDR signalling, genome instability and reduced cell survival. Consistent with these three genes being essential for cell survival, MPD-associated mutations in *DNA2*, *TRAIP* and *DONSON* were shown to cause reduced protein levels (Harley *et al.*, 2016; Reynolds *et al.*, 2017; Shaheen *et al.*, 2014), likely resulting in insufficient levels of functional protein needed for efficient cellular response to endogenous replication stress and DNA damage. It remains to be defined whether these three factors are involved in the same process or pathway to promote genome stability, or whether their roles converge on a certain downstream outcome, such as dissipation of replication stress. Notably, depletion of all three proteins investigated in this thesis also appears to be linked to defective ICL repair and/or signalling of DNA damage induced by DNA crosslinking agents. The FA-like limb anomalies observed in humans and mice with *DONSON*

mutations (Reynolds *et al.*, 2017; Chapter 7) suggest that the clinical phenotype caused by DONSON deficiency could be considered a variation of FA. However, no limb abnormalities or radial ray defects were observed in DNA2 or TRAIP patients (Chapter 3; Shaheen *et al.*, 2014; Harley *et al.*, 2016) and none of the three genes were associated with bone marrow failure, one of the key characteristics of the FA syndrome (Ceccaldi *et al.*, 2012). Additionally, my experiments did not show TRAIP to be epistatic with FANCD2, a key component of the FA pathway, in ICL repair (Section 6.2.3). Nevertheless, results obtained using *X. laevis* egg extracts suggested that TRAIP plays a major role in ICL repair (Wu, Semlow *et al.*, unpublished; Section 6.2.1), and DNA2 was demonstrated to physically interact with FANCD2 in human cells (Karanja *et al.*, 2012). Therefore, in the future, it remains of interest to further elucidate the potential link between mutations in *DNA2*, *TRAIP* and *DONSON* and dysfunctional ICL repair.

8.2.2. Determination of brain size through regulation of mitosis and replication stress-induced cell death

For many years, mice have been used in biomedical research based on their genetic and physiological similarities with humans, providing an invaluable tool to study development of human diseases (Perlman, 2016). Disruption of *DNA2* (Lin *et al.*, 2013), *TRAIP* (Park *et al.*, 2007) and *DONSON* (Chapter 7; Evrony *et al.*, 2017) confers embryonic lethality in mice, reiterating the importance of all three genes for mammalian embryonic development. The prenatal development of the mammalian brain appears to be particularly susceptible to perturbations in cell division, with alterations in neural progenitor cell proliferation, differentiation and apoptosis being important contributors to the final cell number and the emergence of microcephaly (Chenn and Walsh, 2002; Klingseisen and Jackson, 2011; Kuida *et al.*, 1998; Roth *et al.*, 2000). Although the length of G1 phase is modulated throughout murine neuronal cytogenesis by extrinsic and intrinsic mechanisms, the length of S phase or combined G2/M phase remains constant (Takahashi *et al.*, 1995). This could suggest a crucial role for the timely completion of DNA replication and cell division within the specific time frame to ensure unperturbed regulation of cell numbers.

Although many microcephaly and MPD genes are ubiquitously expressed, the developing brain is exceptionally sensitive to mutations in these genes. It was proposed that in most developing tissues, reduced cell proliferation and cell number can be counteracted

by alternative compensatory mechanisms, which are not available in the developing brain due to the strict lineage control pathways (Homem *et al.*, 2015; Malatesta *et al.*, 2000). Additionally, rapid cell proliferation was suggested to cause high levels of DSBs, observed in mammalian embryonic brain (Barazzuol and Jeggo, 2016), and mutations in some MPD genes may hinder the repair of those DNA lesions (Section 1.1.2).

Several pathways are thought to result in slower cell cycle and cell loss during brain development *in utero*, including aberrant mitosis and defective resolution of DNA damage. Mouse models of MPD caused by mutations in centrosomal genes *CENPJ* (McIntyre *et al.*, 2012) and *CEP63* (Marjanović *et al.*, 2015) highlighted the importance of p53-dependent neural progenitor cell death, induced by mitotic errors during embryonic development, for the observed reduction in brain size. Additionally, CDK5RAP2 mice exhibited impaired mitotic progression and abnormal mitotic spindle orientation, as well as increased apoptosis in neuronal progenitor cells (Lizarraga *et al.*, 2010). Furthermore, ASPM deficiency in mouse neural progenitor cells led to alterations in division orientation and cell cycle exit kinetics (Williams *et al.*, 2015). Overall, centrosome defects caused by mutations in centrosomal MPD genes would be expected to affect neurogenesis through mis-positioned spindles, thus influencing the early symmetric divisions required for expansion of neuroepithelial cells before neurogenesis (Homem *et al.*, 2015). Moreover, further strengthening the link between reduction in brain size and disrupted mitosis, hypomorphic NCAPD2 mice displayed increased levels of anaphase chromatin bridges in apical neural progenitor cells during neurogenesis, indicating dysfunctional sister chromatid separation (Martin *et al.*, 2016). As this can lead to chromosome segregation errors and increased aneuploidy in daughter cells, this study implicated aberrant mitosis as a key mechanism for the microcephaly phenotype observed in these mutant mice.

Prevention of replication stress and DNA damage in neural progenitor cells is also important for normal brain development (Alt *et al.*, 2017; Eguren *et al.*, 2013; McKinnon, 2017). One of the main sources of replication stress during embryonic development is unrepaired DNA lesions, resulting from by-products of cellular metabolism (Zeman and Cimprich, 2014). Normal cellular metabolism produces reactive oxygen species (ROS), which can result in various oxidised DNA base lesions, such as 8-oxo-2'-deoxyguanosine, that need to be removed by base excision repair (BER) or nucleotide excision repair (NER) pathways (Cooke *et al.*, 2003). Additionally, naturally produced reactive aldehydes, arising during alcohol metabolism (Brooks and Theruvathu, 2005; Langevin *et al.*, 2011) or histone

demethylation (Shi *et al.*, 2004), may represent the primary endogenous source of replication stress, ICLs and DNA-protein crosslinks (Barker *et al.*, 2005; Cheng *et al.*, 2003; Stein *et al.*, 2006; Wang *et al.*, 2000). It is therefore crucial that cellular pathways required for signalling and repair of such endogenous DNA damage are intact.

The importance of the efficient resolution of endogenous replication stress *in utero* was exemplified by the ATR-Seckel mouse model, which underwent high levels of replication stress during embryogenesis (Murga *et al.*, 2009). As ATR provides a key genome maintenance function in S phase (Brown and Baltimore, 2003) and its complete knockout is embryonic lethal in mice (de Klein *et al.*, 2000), the Seckel syndrome-associated *ATR* mutation (O'Driscoll *et al.*, 2003), resulting in a severely hypomorphic ATR protein, was used to generate a viable mammalian model to study the developmental function of this kinase (Murga *et al.*, 2009). ATR-Seckel mice were born at a sub-mendelian ratio with severe overall dwarfism and microcephaly already evident at birth, as well as Seckel syndrome-associated characteristics such as an undersized jaw (Murga *et al.*, 2009). All Seckel mice died before 40 weeks of age, displaying several phenotypes associated with ageing, including hair graying, osteoporosis, fat accumulation in the bone marrow, decreased density of hair follicles and a thinner epidermis, indicating the development of a progeroid syndrome in Seckel mice (Murga *et al.*, 2009). This is in contrast to human MPD patients with mutations in *ATR*, where a progeroid phenotype is not reported (Goodship *et al.*, 2000). Mouse embryonic fibroblasts derived from the mutant mice showed increased accumulation of cells in G2 phase, as well as elevated numbers of cells with pan-nuclear γH2AX staining, consistent with an activation of the replication stress-associated DDR (Murga *et al.*, 2009). Moreover, the mutant cells also showed an increase in 53BP1 foci and higher frequency of chromosomal breakage, indicating replication fork collapse and accumulation of DSBs (Murga *et al.*, 2009).

Massive cell death of post-mitotic neurons during cortical development, reported in the XRCC4 and LIG4 knockout mice (Gao *et al.*, 1998), may also be explained by a particular sensitivity of the developing brain to unrepaired DSBs. Considering the function of DNA2, TRAIP and DONSON in maintaining genome stability (Chapters 5–7; Duxin *et al.*, 2009, 2012; Karanja *et al.*, 2012; Harley *et al.*, 2016; Hoffmann *et al.*, 2016; W. Feng *et al.*, 2016; Reynolds *et al.*, 2017), it is likely that all of them are essential for cellular response to replication stress and endogenous DNA damage arising during embryogenesis, with their absence resulting in prolonged cell cycle and emergence of DSBs due to unrepaired DNA lesions. Consequently,

this would lead to slow proliferation, reducing total cell number, and elevated numbers of cells eliminated by apoptosis during embryogenesis, resulting in a smaller organism.

The coordination between genome duplication, cell cycle and mitotic progression is particularly important for the maintenance of genome stability, as unresolved replication stress can give rise to under-replicated DNA or problematic DNA structures that may persist into mitosis and delay or hinder chromosome segregation, eventually resulting in the gains or losses of genetic material (Burrell *et al.*, 2013; Chan *et al.*, 2009; Fragkos and Naim, 2017; Naim and Rosselli, 2009; Terradas *et al.*, 2010). Thus, increased replication stress and emergence of mitotic problems may be closely interlinked in terms of MPD development, with both leading to the similar phenotypes at the cellular and organismal level. Collectively, several murine models of congenital human brain size disorders suggest that aberrant mitosis, lost self-renewal capacity, premature differentiation and defective resolution of DNA damage, which lead to p53-mediated apoptosis of neural progenitor cells, are the major causes of reduced brain size in mammals. The co-deletion of p53 often led to the rescue of microcephaly-associated phenotypes (Gao *et al.*, 2000; Marjanović *et al.*, 2015; Williams *et al.*, 2015), indicating the importance of p53 in mediating pathogenesis of MPD syndromes. In contrast to this, a study by Murga *et al.* (2009) described synthetic lethality between ATR and p53, with the loss of both factors greatly exacerbating the microcephaly phenotype, replication stress and cell death. The authors suggested that faster replication kinetics may be achieved in the absence of p53, leading to the increased accumulation of replication stress when ATR signalling is compromised. This exemplifies that distinct molecular mechanisms may well underlie different growth reduction syndromes. Therefore, to further delineate the molecular mechanisms by which mutations in *DNA2*, *TRAIP* and *DONSON* cause severe reduction in growth, crosses between mice deficient in these proteins and p53-null mice would be particularly informative.

8.3. Future work and outstanding questions

Although this thesis contributes to our current understanding of the importance of DNA2, TRAIP and DONSON in DNA replication and repair, there are outstanding questions remaining, particularly regarding the links between the cellular function of these proteins and human disease.

The work described here suggested that MPD-associated mutations in *DNA2* have an effect on its transcript splicing and ATPase activity (Chapter 3). However, I was unable to assess DNA2 protein levels in cells with patient mutations, either engineered using CRISPR/Cas9 technology or obtained from patients, and it will be important to do so in the future. Reduced DNA2 protein levels would suggest that both non-coding and coding mutations identified in MPD patients likely reduce all enzymatic activities of DNA2. Additionally, biochemical analysis of DNA2 protein containing patient mutation p.T655A is necessary to assess whether, as predicted, DNA2 ATP-dependent motor function is dysregulated in the presence of this alteration, and whether its nuclease activity and overall protein stability are affected. Such experiments would provide more support for the interplay between nuclease and ATPase/helicase activities of DNA2, as well as the importance of the ATPase/helicase function for efficient cell proliferation. Although DNA2 nucleolytic function is well-established (Cejka *et al.*, 2010; Karanja *et al.*, 2012; Nimonkar *et al.*, 2011; Niu *et al.*, 2010; Sturzenegger *et al.*, 2014), its ATP-dependent helicase domain was only recently implicated in maintaining genomic stability in human cells (Duxin *et al.*, 2012) and, using *in vitro* experiments, proposed to promote efficient DNA end resection by mediating ssDNA translocation (Levikova *et al.*, 2017; Miller *et al.*, 2017). Collectively, these studies suggest that ssDNA translocation is the main function of the DNA2 ATPase/helicase domain in human cells, required to prevent genomic instability. In the future, cell-based experiments will be required to confirm this hypothesis and elucidate the mechanisms leading to genomic instability in the absence of this DNA2 activity.

Recent studies on the involvement of TRAIP in DDR (Harley *et al.*, 2016; Hoffmann *et al.*, 2016; Soo Lee *et al.*, 2016; W. Feng *et al.*, 2016), as well as the work described in this thesis (Chapter 5–6), established it as a new component of DDR signalling in response to several exogenous DNA damaging agents. However, the identity of TRAIP substrate(s) at stalled replication forks (discussed in Section 6.3) and the exact DNA structures at which TRAIP acts remain to be established. TRAIP appears to predominantly respond to replication-associated DNA damage at stalled replication forks, induced by cell treatments with UV, CPT, MMC and

HU (Chapter 6; Harley *et al.*, 2016; Hoffmann *et al.*, 2016; W. Feng *et al.*, 2016), whereas TRAIP function at ionising radiation (IR)-induced DNA lesions was reported only by a single study (Soo Lee *et al.*, 2016). Failure to stabilise stalled replication forks can lead to their collapse, giving rise to one-ended DSBs, which are structurally distinct from the two-ended DSBs induced by IR (Chapman *et al.*, 2012). Moreover, distinct cellular mechanisms are required to sense and repair these different types of lesions (Pardo *et al.*, 2009). My work demonstrated distinct cellular phenotypes to specific forms of DNA damage (Chapters 5–6), and therefore further investigation will be needed to determine whether TRAIP promotes DDR at distinct DNA lesions via the same mechanism, or whether it is a multi-functional protein that participates in more than one DDR signalling pathway. As biallelic *TRAIP* mutations were linked to severe prenatal-onset reduction in human growth (Harley *et al.*, 2016), the importance of TRAIP at signalling endogenous DNA lesions, encountered by cells during embryogenesis, will also need to be assessed, with both oxidative and aldehyde-mediated lesions being stong candidates (Cooke *et al.*, 2003; Langevin *et al.*, 2011).

More is currently known about the involvement of DNA2 and TRAIP in maintaining genome stability than about the cellular role of DONSON. Mutations in *DONSON* were only recently implicated in the pathogenesis of two distinct human growth retardation syndromes: MPD (Reynolds *et al.*, 2017) and microcephaly-micromelia syndrome (MMS) (Evrony *et al.*, 2017). Human patients described in these studies, together with the DONSON mouse model (Chapter 7), suggest particular sensitivity of mammalian limb development to DONSON deficiency, which is not commonly observed in other MPD-associated disorders. However, limb abnormalities are also associated with other DNA replication disorders, characterised by short stature, such as RAPADILINO syndrome (Siitonen *et al.*, 2003), and ICL repair disorders as Fanconi Anaemia (FA) (Triemstra *et al.*, 2015). It will therefore be important to understand whether the absence of DONSON and other DNA replication and genome stability proteins lead to limb anomalies through similar or distinct molecular mechanisms.

To link mutations in *DONSON* to disrupted human growth, Reynolds *et al.* (2017) proposed that biallelic *DONSON* mutations render cells unable to stabilise replication forks and efficiently deal with endogenous replication stress during key stages of embryonic development, thus leading to cell death and reducing the final number of cells in an organism (***Figure 1.17***). Brain development is particularly sensitive to disruptions in DNA replication, since rapid expansion of neural progenitor cell population has to be achieved within a specific developmental time frame (Takahashi *et al.*, 1995). This observation may explain why the

reduction in head size is much more pronounced in *DONSON* patients than the reduction in height. In the future, additional studies will be necessary to pinpoint the molecular mechanism by which DONSON promotes the stability of replication forks and activation of cell cycle checkpoints. Moreover, clarification of whether DONSON is directly involved in regulating ATR-CHK1 pathway will be needed. As DONSON-depleted cells were proficient at generating RPA-coated ssDNA (Reynolds *et al.*, 2017), their capacity to initiate activation of the ATR pathway seemed unchanged, suggesting that DONSON may be involved in indirectly stimulating the ATR signalling axis. Additionally, investigating whether DONSON-deficient mice, similarly to the ATR-Seckel mice (Murga *et al.*, 2009), exhibit elevated levels of replication stress *in utero* could provide further support for DONSON being a novel factor in the ATR–CHK1 replication stress response.

In summary, my work has confirmed *DNA2* to be a human disease gene conferring microcephalic primordial dwarfism phenotype, extended our knowledge on cellular roles of TRAIP, and established a developmental murine model for DONSON. Given the strong phenotypic links at both organismal and cellular levels between the three genes, future studies will be important for demonstrating whether the proteins encoded by these genes also function together at the molecular level.

Appendices

Appendices

Appendix 1. Oligonucleotides

a) Oligonucleotides used for generating minigene plasmids

Oligo nucleotide	**Sequence (5'-3')**	**Description**
dna2-SalI-int10-F	TTTAATAGCTAGTCGACGGCCCATTCATTCATTCTTTTAGC	Forward primer to clone DNA2 exon 10, intron 11, exon 12, intron 12 and exon 13 into into RHCglo plasmid
dna2-XbaI-int13-R	AGGATGTAATATTTCTAGATCTGAACTGAGGAGAAGCTGATAC	Reverse primer to clone DNA2 exon 10, intron 11, exon 12, intron 12 and exon 13 into into RHCglo plasmid
dna2-SalI-5utr-F	ACGCGTCGACCATTTGGGACATCTGCGGG	Forward primer to clone DNA2 exon 1, intron 1 and exon 2 into RHCglo plasmid
dna2-XbaI-int2-R	CTAGTCTAGACCCTTAAGATTCAAATCGGTG	Reverse primer to clone DNA2 exon 1, intron 1 and exon 2 into RHCglo plasmid

b) Oligonucleotides used for generating polycistronic PP4-expressing plasmids

Oligo nucleotide	**Sequence (5'-3')**	**Description**
BamHI-XhoI-PP4C-F	TCCGGGATCCCTCGAGATGGCGGAGATCAGCGACC	Forward primer for cloning the PP4C into pGEX6P1
NotI-XbaI-PP4C-R	ATAAGAATGCGGCCGCTCTAGATCACAGGAAGTAGTCGGCC	Reverse primer for cloning the PP4C into pGEX6P1
XbaI-PP4R2-F	CTAGTCTAGATTTTGTTTAACTTTAAGAAGGAGATATACATATGGACGTCGAGAGGCTCC	Forward primer for cloning the PP4R2 into pGEX6P1-PP4C
NotI-SacII-PP4R2-R	ATAAGAATGCGGCCGCCCGCGGTTAGTCTTGTTCCATTGGTTCATC	Reverse primer for cloning the PP4R2 into pGEX6P1-PP4C
SacII-PP4R3α-F	TCCCCCGCGGTTTTGTTTAACTTTAAGAAGGAGATATACATATGACCGACACCCGGCGG	Forward primer for cloning the PP4R3α into pGEX6P1-PP4C-PP4R2
NotI-KpnI-PP4R3α-R	ATAAGAATGCGGCCGCGGTACCTTATGAATCAAATTTTGCTTTCTTTG	Reverse primer for cloning the PP4R3α into pGEX6P1-PP4C-PP4R2
SacII-PP4R3β-F	TCCCCCGCGGTTTTGTTTAACTTTAAGAAGGAGATATACATATGTCGGATACGCGGCGG	Forward primer for cloning the PP4R3β into pGEX6P1-PP4C-PP4R2
NotI-KpnI-PP4R3β-R	ATAAGAATGCGGCCGCGGTACCTTATGAGCCAAGACGAGGTCT	Reverse primer for cloning the PP4R3β into pGEX6P1-PP4C-PP4R2

c) Oligonucleotides used for sequencing of minigene plasmids

Oligo nucleotide	**Sequence (5'-3')**	**Description**
RHCglo-F	GCAGTTGGATGCTTTCCCCC	Forward primer to amplify the 5' of the RHCglo insert
RHCglo-R	GATGCGGCCCTGAAGTTGTTC	Forward primer to amplify the 3' of the RHCglo insert
dna2-ex11-F	TTGTCGGTCCTTCCAGAATC	Forward primer to to amplify the DNA2 ex11-int11-ex12-int12-ex13 insert in the RHCglo plasmid
dna2-ex13-R	CATCGCTTGCCTCTGAGGC	Reverse primer to to amplify the DNA2 ex11-int11-ex12-int12-ex13 insert in the RHCglo plasmid
dna2-int1a-R	TGCTCGGCGAGGGAGAGTC	Reverse primer to amplify the first part of the DNA2 ex1-int1-ex2 insert in the RHCglo plasmid
dna2-int1b-F	CCTGCCTCCCAAGGTGTTC	Forward primer to amplify the second part of the DNA2 ex1-int1-ex2 insert in the RHCglo plasmid
dna2-int1c-R	CGCAAGATTGGCTATGATGCC	Reverse primer to amplify the second part of the DNA2 ex1-int1-ex2 insert in the RHCglo plasmid
dna2-int1d-F	GAGGGACTTTTGCGTTTGGGC	Forward primer to amplify the third part of the DNA2 ex1-int1-ex2 insert in the RHCglo plasmid
dna2-int1e-R	CACTGAAAGTCCTATCATGAGCC	Reverse primer to amplify the third part of the DNA2 ex1-int1-ex2 insert in the RHCglo plasmid
dna2-int1f-F	CCGGCATTACTTTAGCAGGTTG	Forward primer to amplify the fourth part of the DNA2 ex1-int1-ex2 insert in the RHCglo plasmid
dna2-int1g-R	GAGCAAAGACACAGAAGAATTCC	Reverse primer to amplify the fourth part of the DNA2 ex1-int1-ex2 insert in the RHCglo plasmid
dna2-int1h-F	GTTTGAAATGGCATTACTTCTGG	Forward primer to amplify the fifth part of the DNA2 ex1-int1-ex2 insert in the RHCglo plasmid

d) Oligonucleotides used for sequencing of polycistronic PP4 plasmids

Oligo nucleotide	Sequence (5'-3')	Description
PP4C 1 F	ATGGCGGAGATCAGCGACC	Forward primer to sequence the first part of PP4C insert in pGEX-6P-1-PP4C
PP4C 1 R	CGAACCTTAAGTGCCAGCAG	Reverse primer to sequence the first part of PP4C insert in pGEX-6P-1-PP4C
PP4C 2 F	GACCGTGGCTTCTATAGCG	Forward primer to sequence the second part of PP4C insert in pGEX-6P-1-PP4C
PP4C 2 R	CGTTGAACTGGGCCACCAC	Reverse primer to sequence the second part of PP4C insert in pGEX-6P-1-PP4C
PP4C 3 F	GGAGCCGGCTACCTATTTG	Forward primer to sequence the third part of PP4C insert in pGEX-6P-1-PP4C
PP4C 3 R	TCACAGGAAGTAGTCGGCC	Reverse primer to sequence the third part of PP4C insert in pGEX-6P-1-PP4C
PP4R2 1 F	ATGGACGTCGAGAGGCTCC	Forward primer to sequence the first part of PP4R2 insert in pGEX-6P-1-PP4C-PP4R2
PP4R2 1 R	GACCTCTTGGCTCAGGAGC	Reverse primer to sequence the first part of PP4R2 insert in pGEX-6P-1-PP4C-PP4R2
PP4R2 2 F	GTCGAATATATTCCCTTTGATG	Forward primer to sequence the second part of PP4R2 insert in pGEX-6P-1-PP4C-PP4R2
PP4R2 2 R	GTCTGTGCTCTCAGGCAAC	Reverse primer to sequence the second part of PP4R2 insert in pGEX-6P-1-PP4C-PP4R2
PP4R2 3 F	GGCCACTTAATCGACCAAAG	Forward primer to sequence the third part of PP4R2 insert in pGEX-6P-1-PP4C-PP4R2
PP4R2 3 R	GTGCTGCCGGGTACAACG	Reverse primer to sequence the third part of PP4R2 insert in pGEX-6P-1-PP4C-PP4R2
PP4R2 4 F	GGTAGGAGAAACAGAAGCATC	Forward primer to sequence the fourth part of PP4R2 insert in pGEX-6P-1-PP4C-PP4R2
PP4R2 4 R	TTAGTCTTGTTCCATTGGTTCAT	Reverse primer to sequence the fourth part of PP4R2 insert in pGEX-6P-1-PP4C-PP4R2
PP4R3α 1 F	ATGACCGACACCCGGCGG	Forward primer to sequence the first part of PP4R3α insert in pGEX-6P-1-PP4C-PP4R2-PP4R3α
PP4R3α 1 R	CACGACGAAGAGGTGAAGG	Reverse primer to sequence the first part of PP4R3α insert in pGEX-6P-1-PP4C-PP4R2-PP4R3α
PP4R3α 2 F	GCTTAGAATTGCCATCTTGTG	Forward primer to sequence the second part of PP4R3α insert in pGEX-6P-1-PP4C-PP4R2-PP4R3α
PP4R3α 2 R	GAGTTGGTAGAACCATATCTTG	Reverse primer to sequence the second part of PP4R3α insert in pGEX-6P-1-PP4C-PP4R2-PP4R3α
PP4R3α 3 F	CATCAGACATACAGAGTTCAG	Forward primer to sequence the third part of PP4R3α insert in pGEX-6P-1-PP4C-PP4R2-PP4R3α
PP4R3α 3 R	GCAGTGGCTAGCATGTTCTC	Reverse primer to sequence the third part of PP4R3α insert in pGEX-6P-1-PP4C-PP4R2-PP4R3α

Oligo nucleotide	Sequence (5'-3')	Description
PP4R3α 4 F	CAGCTTATGGGCCTGCTTC	Forward primer to sequence the fourth part of PP4R3α insert in pGEX-6P-1-PP4C-PP4R2-PP4R3α
PP4R3α 4 R	CATCTCTATTATGGCAGAGTTC	Reverse primer to sequence the fourth part of PP4R3α insert in pGEX-6P-1-PP4C-PP4R2-PP4R3α
PP4R3α 5 F	GAACCAGTAGTGAAAGCATTTC	Forward primer to sequence the fifth part of PP4R3α insert in pGEX-6P-1-PP4C-PP4R2-PP4R3α
PP4R3α 5 R	GTTAGTCTTCGTTCCACTGG	Reverse primer to sequence the fifth part of PP4R3α insert in pGEX-6P-1-PP4C-PP4R2-PP4R3α
PP4R3α 6 F	GCAGAGCCCAAGTTTCAAGC	Forward primer to sequence the sixth part of PP4R3α insert in pGEX-6P-1-PP4C-PP4R2-PP4R3α
PP4R3α 6 R	TTATGAATCAAATTTTGCTTTCTTT	Reverse primer to sequence the sixth part of PP4R3α insert in pGEX-6P-1-PP4C-PP4R2-PP4R3α
PP4R3β 1 F	ATGTCGGATACGCGGCGG	Forward primer to sequence the first part of PP4R3β insert in pGEX-6P-1-PP4C-PP4R2-PP4R3β
PP4R3β 1 R	GCTTGGAACAGCTGCAATAG	Reverse primer to sequence the first part of PP4R3β insert in pGEX-6P-1-PP4C-PP4R2-PP4R3β
PP4R3β 2 F	CTCTCCTCACCTATCCGTAG	Forward primer to sequence the second part of PP4R3β insert in pGEX-6P-1-PP4C-PP4R2-PP4R3β
PP4R3β 2 R	GCCCATTACAATTTCAAGAGC	Reverse primer to sequence the second part of PP4R3β insert in pGEX-6P-1-PP4C-PP4R2-PP4R3β
PP4R3β 3 F	GGAGTTTTGTGCATTTTCTCAG	Forward primer to sequence the third part of PP4R3β insert in pGEX-6P-1-PP4C-PP4R2-PP4R3β
PP4R3β 3 R	CCACACAAAATGTGAGTAACTC	Reverse primer to sequence the third part of PP4R3β insert in pGEX-6P-1-PP4C-PP4R2-PP4R3β
PP4R3β 4 F	CAAACAGCACAGCTACTTGC	Forward primer to sequence the fourth part of PP4R3β insert in pGEX-6P-1-PP4C-PP4R2-PP4R3β
PP4R3β 4 R	CCAGGAGATGTCCTTTTGGG	Reverse primer to sequence the fourth part of PP4R3β insert in pGEX-6P-1-PP4C-PP4R2-PP4R3β
PP4R3β 5 F	CCTAAGCCAGAAGATGATTTTC	Forward primer to sequence the fifth part of PP4R3β insert in pGEX-6P-1-PP4C-PP4R2-PP4R3β
PP4R3β 5 R	TTATGAGCCAAGACGAGGTCT	Reverse primer to sequence the fifth part of PP4R3β insert in pGEX-6P-1-PP4C-PP4R2-PP4R3β

e) Oligonucleotides used for screening of CRISPR/Cas9 cell lines

Oligonucleotide	Sequence (5'-3')	Description
DNA2ex1-F	CATTTGGGACATCTGCGG	Forward primer to amplify DNA2 regions surrounding c.74+4A>C (ex1-int1 junction) (use together with dna2-int1_scr-R primer; product size for WT: 382 bp)
dna2-int1_scr-R	GAACACCTTGGGAGGCAG	Reverse primer to amplify DNA2 regions surrounding c.74+4A>C (ex1-int1 junction) (use together with dna2ex1-F primer; product size for WT: 382 bp)
DNA2ex13-F	AGACTTGGATAGAGACTGCTTTTC	Forward primer to amplify DNA2 regions surrounding c.1963A>G (ex13) (use together with dna2-int13_scr-R primer; product size for WT: 312 bp)
dna2-int13_scr-R	GACACTGAATTAAAATTCAGCCC	Reverse primer to amplify DNA2 regions surrounding c.1963A>G (ex13) (use together with dna2ex13-F primer; product size for WT: 312 bp)
hDNA2-F2	CTGTCTACAGTTTGCGATCC	Forward primer to amplify DNA2 regions surrounding c.74+4A>C (ex1-int1 junction) (use together with hDNA2-R2 primer; product size for WT: 305 bp)
hDNA2-F3	CCCTGCTGCTCAGGTGAG	Forward primer to amplify DNA2 regions surrounding c.74+4A>C (ex1-int1 junction) (use together with hDNA2-R2 primer; product size for WT: 476 bp)
hDNA2-R2	CAGGCTCTGGCTGAATGTG	Reverse primer to amplify DNA2 regions surrounding c.74+4A>C (ex1-int1 junction) (use together with hDNA2-F2 or hDNA2-F3 primer; product size for WT: 305 bp and 476 bp, respectively)
hTRAIP-ex1-F	GTTGTCACTTCCGGCCCG	Forward primer to amplify TRAIP exon 1 (use together with hTRAIP-ex1-R primer; product size for WT: 277 bp)
hTRAIP-ex1-R	GGTACCCGGGCAAACACC	Reverse primer to amplify TRAIP exon 1 (use together with hTRAIP-ex1-F primer; product size for WT: 277 bp)
mDonson-F2	CCTCTGTGAGCTACTTTTGC	Forward primer to genotype mDonson regions surrounding M440T (use together with mDonson-R2 primer; product size for WT: 337 bp)
mDonson-R2	GTAGTCTATGTCCAGGACAG	Reverse primer to genotype mDonson regions surrounding M440T (use together with mDonson-F2 primer; product size for WT: 337 bp)

f) Oligonucleotides used for site-directed mutagenesis of minigene plasmids

Oligonucleotide	Sequence (5'-3')	Description
dna2-c.1764-1A>G F	AGTCAATAATTAAATCTCGAAGTTTTTTGTTGAAAAGTGAAAAAGCACTTTTAGTAATA	Forward primer to introduce c.1764-1A>G mutation in the splice acceptor site of *DNA2* intron 11
dna2-c.1764-1A>G R	TATTACTAAAAGTGCTTTTTCACTTTTCAACAAAAAACTTCGAGATTTAATTATTGACT	Reverse primer to introduce c.1764-1A>G mutation in the splice acceptor site of *DNA2* intron 11
dna2-c.74+1G>A F	CTGCCGGCGGAGCTATGAGCGGAGAGGG	Forward primer to introduce c.74+1G>A mutation in the splice donor site of *DNA2* intron 1
dna2-c.74+1G>A R	CCCTCTCCGCTCATAGCTCCGCCGGCAG	Reverse primer to introduce c.74+1G>A mutation in the splice donor site of *DNA2* intron 1

g) Oligonucleotides used for site-directed mutagenesis of polycistronic PP4 plasmids

Oligonucleotide	Sequence (5'-3')	Description
PP4C-K26R-K31R F	GAAGTCAGGGCCCTGTGCGCTAGGGCCAG	Forward primer to introduce K26R and K31R substitutions in PP4C
PP4C-K26R-K31R R	CTGGCCCTAGCGCACAGGGCCCTGACTTC	Reverse primer to introduce K26R and K31R substitutions in PP4C
PP4C-K63R F	GACAATTCTATGACCTCAGAGAGCTGTTCAGAGTAGG	Forward primer to introduce K63R substitutions in PP4C
PP4C-K63R R	CCTACTCTGAACAGCTCTCTGAGGTCATAGAATTGTC	Reverse primer to introduce K63R substitutions in PP4C
PP4C-K21R F	CTGCGAGCTCATCAGGGAGAGCGAAGTC	Forward primer to introduce K21R substitutions in PP4C
PP4C-K21R R	GACTTCGCTCTCCCTGATGAGCTCGCAG	Reverse primer to introduce K21R substitutions in PP4C
PP4C-K183R F	GACAATCGACCGAAGGCAAGAGGTGCCTC	Forward primer to introduce K183R substitutions in PP4C
PP4C-K183R R	GAGGCACCTCTTGCCTTCGGTCGATTGTC	Reverse primer to introduce K183R substitutions in PP4C

h) Oligonucleotides used for site-directed mutagenesis of TRAIP

Oligonucleotide	Sequence (5'-3')	Description
TRAIP-W37A F	GCAGTGCCTAATTCAGGCGTTTGAGACAGCACCAAG	Forward primer to introduce W37A substitution in TRAIP
TRAIP-W37A R	CTTGGTGCTGTCTCAAACGCCTGAATTAGGCACTGC	Reverse primer to introduce W37A substitution in TRAIP

i) Oligonucleotides used for RT-PCR analysis of minigene plasmids

Oligonucleotide	Sequence (5'-3')	Description
RSV5U	CATTCACCACATTGGTGTGC	Forward primer in the artificial exon of RHCglo to detect splicing alterations of minigenes
RTRHC	GGGCTTTGCAGCAACAGTAAC	Reverse primer in the artificial exon of RHCglo to detect splicing alterations of minigenes
dna2-ex11-F	TTGTCGGTCCTTCCAGAATC	Forward primer to detect splicing alterations in the DNA2 intron 11 minigene
dna2-ex13-R	CATCGCTTGCCTCTGAGGC	Reverse primer to detect splicing alterations in the DNA2 intron 11 minigene

j) Oligonucleotides used for RT-PCR analysis of m*Donson* transcript

Oligonucleotide	Sequence (5'-3')	Description
mDonson-ex7F	GCTGGAAGAGATAGGCGTG	Forward primer in exon 7 of mDonson to detect splicing alterations
mDonson-ex9R	CAAACTAAACTTATCTCTGTATC	Reverse primer in exon 9 of mDonson to detect splicing alterations

Appendix 2. Antibodies

a) Primary antibodies

Antibody	Species	Dilution for WB or IF	Reference
53BP1	Rabbit	1:2,000 (WB, IF)	Novus Biologicals, NB100-904
BRCA1 (C-20)	Mouse	1:200 (WB)	Santa Cruz Biotechnology, sc-642
BrdU (BU1/75 ICR1)	Rat	1:500 (IF)	Abcam, ab6326
CHK1 (G-4)	Mouse	1:250 (WB)	Santa Cruz Biotechnology, sc-8408
phospho-CHK1 (S345)	Rabbit	1:500 (WB)	Cell Signaling, 2341
FANCD2 (FI17)	Mouse	1:500 (WB)	Santa Cruz Biotechnology, sc-20022
phospho-H2AX (S139)	Mouse	1:1,000 (WB)	Millipore, 05-636
phospho-H2AX (S139)	Rabbit	1:2,000 (IF)	Cell Signaling, 9718
H2A	Rabbit	1:5,000 (WB)	Millipore, 07-146
Lamin B1	Rabbit	1:20,000 (WB)	Abcam, ab16048
PCNA (PC10)	Mouse	1:800 (WB)	Santa Cruz Biotechnology, sc-56
PP4C	Rabbit	1:5,000 (WB)	Bethyl Labs, A300-835A
PP4R2	Rabbit	1:2,000 (WB)	Bethyl Labs, A300-838A
PP4R3α / SMEK1	Rabbit	1:1,000 (WB)	Bethyl Labs, A300-840A
PP4R3β / SMEK2	Rabbit	1:1,000 (WB)	Bethyl Labs, A300-842A
phospho-RPA32 (S4/S8)	Rabbit	1:1,000 (WB); 1:2,000 (IF)	Bethyl Labs, A300-245A
RPA32	Rabbit	1:1,000 (WB)	Santa Cruz Biotechnology, sc-28709
TRAIP #89	Rabbit	1:50-1:200 (WB)	Produced by A. Jackson laboratory
Vinculin	Mouse	1:2,000 (WB)	Sigma, V9264

b) Secondary antibodies

Antibody	Species	Dilution for WB or IF	Reference
Anti-rabbit IgG, HRP linked	Goat	1:5000 (WB)	Cell Signaling Technology, 7074
Anti-mouse IgG, HRP linked	Goat	1:5000 (WB)	Dako, P0447
Anti-rabbit IgG, Alexa Fluor 488 linked	Goat	1:1000 (IF)	Invitrogen, A11008
Anti-rabbit IgG, Alexa Fluor 568 linked	Goat	1:1000 (IF)	Invitrogen, A11036
Anti-mouse IgG, Alexa Fluor 488 linked	Goat	1:1000 (IF)	Invitrogen, A11029
Anti-mouse IgG, Alexa Fluor 568 linked	Goat	1:1000 (IF)	Invitrogen, A11031
Anti-rat IgG, Alexa Fluor 488 linked	Goat	1:1000 (IF)	Invitrogen, A11006

References

References

Abràmoff, M.D., Magalhães, P.J., Ram, S.J., 2004. Image processing with imageJ. Biophotonics Int. 11, 36–41.

Akutsu, M., Dikic, I., Bremm, A., 2016. Ubiquitin chain diversity at a glance. J. Cell Sci. 129, 875–880.

Alabert, C., Bukowski-Wills, J.-C., Lee, S.-B., Kustatscher, G., Nakamura, K., Alves, F.D.L., Menard, P., Mejlvang, J., Rappsilber, J., Groth, A., 2014. Chromatin Dynamics During DNA Replication and Uncharacterized Replication Factors determined by Nascent Chromatin Capture (NCC) Proteomics. Nat. Cell Biol. 16, 281–293.

Alderton, G.K., Galbiati, L., Griffith, E., Surinya, K.H., Neitzel, H., Jackson, A.P., Jeggo, P.A., O'Driscoll, M., 2006. Regulation of mitotic entry by microcephalin and its overlap with ATR signalling. Nat. Cell Biol. 8, 725–733.

Alpi, A.F., Pace, P.E., Babu, M.M., Patel, K.J., 2008. Mechanistic Insight into Site-Restricted Monoubiquitination of FANCD2 by Ube2t, FANCL, and FANCI. Mol. Cell 32, 767–777.

Alt, F.W., Wei, P.-C., Schwer, B., 2017. Recurrently Breaking Genes in Neural Progenitors: Potential Roles of DNA Breaks in Neuronal Function, Degeneration and Cancer. In: Jaenisch, R., Zhang, F., Gage, F. (Eds.), Genome Editing in Neurosciences. Springer, Cham, pp. 63–72.

Amunugama, R., Willcox, S., Wu, R.A., Abdullah, U.B., El-Sagheer, A.H., Brown, T., McHugh, P.J., Griffith, J.D., Walter, J.C., 2018. Replication Fork Reversal during DNA Interstrand Crosslink Repair Requires CMG Unloading. Cell Rep. 23, 3419–3428.

Anantha, R.W., Vassin, V.M., Borowiec, J.A., 2007. Sequential and synergistic modification of human RPA stimulates chromosomal DNA repair. J. Biol. Chem. 282, 35910–35923.

Aparisi, M.J., García-García, G., Aller, E., Sequedo, M.D., Martínez-Fernández de la Cámara, C., Rodrigo, R., Armengot, M., Cortijo, J., Milara, J., Díaz-LLopis, M., Jaijo, T., Millán, J.M., 2013. Study of USH1 Splicing Variants through Minigenes and Transcript Analysis from Nasal Epithelial Cells. PLoS One 8, e57506.

Aragao, M.D.F.V., Van Der Linden, V., Brainer-Lima, A.M., Coeli, R.R., Rocha, M.A., Da Silva, P.S., Gomes, M.D.C., De Carvalho, Van Der Linden, A., De Holanda, A.C., Valenca, M.M., 2016. Clinical features and neuroimaging (CT and MRI) findings in presumed Zika virus related congenital infection and microcephaly: Retrospective case series study. BMJ 353, i1901.

Araki, H., Leem, S.H., Phongdara, A., Sugino, A., 1995. Dpb11, which interacts with DNA polymerase II(epsilon) in Saccharomyces cerevisiae, has a dual role in S-phase progression and at a cell cycle checkpoint. PNAS 92, 11791–11795.

Arezi, B., Kuchta, R.D., 2000. Eukaryotic DNA primase. Trends Biochem. Sci. 25, 572–576.

Arnaudeau, C., Lundin, C., Helleday, T., 2001. DNA double-strand breaks associated with replication forks are predominantly repaired by homologous recombination involving an exchange mechanism in mammalian cells. J. Mol. Biol. 307, 1235–1245.

Awad, S., Al-Dosari, M.S., Al-Yacoub, N., Colak, D., Salih, M.A., Alkuraya, F.S., Poizat, C., 2013. Mutation in PHC1 implicates chromatin remodeling in primary microcephaly pathogenesis. Hum. Mol. Genet. 22, 2200–2213.

Ayyagari, R., Gomes, X. V., Gordenin, D.A., Burgers, P.M.J., 2003. Okazaki fragment maturation in yeast: I. Distribution of functions between FEN1 and DNA2. J. Biol. Chem. 278, 1618–1625.

Bahassi, E.M., Ovesen, J.L., Riesenberg, A.L., Bernstein, W.Z., Hasty, P.E., Stambrook, P.J., 2008. The checkpoint kinases Chk1 and Chk2 regulate the functional associations between hBRCA2 and Rad51 in response to DNA damage. Oncogene 27, 3977–3985.

Bakkenist, C.J., Kastan, M.B., 2003. DNA damage activates ATM through intermolecular autophosphorylation and dimer dissociation. Nature 421, 499–506.

Balakrishnan, L., Bambara, R.A., 2013. Okazaki Fragment Metabolism. Cold Spring Harb. Perspect.

Biol. 5, a010173.

Ball, H.L., Myers, J.S., Cortez, D., 2005. ATRIP Binding to Replication Protein A-Single-stranded DNA Promotes ATR–ATRIP Localization but Is Dispensable for Chk1 Phosphorylation. Mol. Biol. Cell 16, 2372–2381.

Bandura, J.L., Beall, E.L., Bell, M., Silver, H.R., Botchan, M.R., Calvi, B.R., 2005. humpty dumpty is required for developmental DNA amplification and cell proliferation in Drosophila. Curr. Biol. 15, 755–759.

Barazzuol, L., Jeggo, P.A., 2016. In vivo sensitivity of the embryonic and adult neural stem cell compartments to low-dose radiation. J. Radiat. Res. 57, i2–i10.

Barker, S., Weinfeld, M., Murray, D., 2005. DNA-protein crosslinks: Their induction, repair, and biological consequences. Mutat. Res. - Rev. Mutat. Res. 589, 111–135.

Barrangou, R., Fremaux, C., Deveau, H., Richards, M., Boyaval, P., Moineau, S., Romero, D.A., Horvath, P., 2007. CRISPR Provides Acquired Resistance Against Viruses in Prokaryotes. Science 315, 1709–1712.

Bartek, J., Falck, J., Lukas, J., 2001. CHK2 kinase - a busy messenger. Nat. Rev. Mol. Cell Biol. 2, 877–886.

Bass, T.E., Luzwick, J.W., Kavanaugh, G., Carroll, C., Dungrawala, H., Glick, G.G., Feldkamp, M.D., Putney, R., Chazin, W.J., Cortez, D., 2016. ETAA1 acts at stalled replication forks to maintain genome integrity. Nat. Cell Biol. 18, 1185–1195.

Batista, L.F.Z., Kaina, B., Meneghini, R., Menck, C.F.M., 2009. How DNA lesions are turned into powerful killing structures: Insights from UV-induced apoptosis. Mutat. Res. - Rev. Mutat. Res. 681, 197–208.

Bermudez, V.P., Lindsey-Boltz, L.A., Cesare, A.J., Maniwa, Y., Griffith, J.D., Hurwitz, J., Sancar, A., 2003. Loading of the human 9-1-1 checkpoint complex onto DNA by the checkpoint clamp loader hRad17-replication factor C complex in vitro. PNAS 100, 1633–1638.

Berndsen, C.E., Wolberger, C., 2011. A spectrophotometric assay for conjugation of ubiquitin and ubiquitin-like proteins. Anal. Biochem. 418, 102–110.

Besse, A., Campos, A.D., Webster, W.K., Darnay, B.G., 2007. TRAF-interacting protein (TRIP) is a RING-dependent ubiquitin ligase. Biochem. Biophys. Res. Commun. 359, 660–664.

Bicknell, L.S., Bongers, E.M.H.F., Leitch, A., Brown, S., Schoots, J., Harley, M.E., Aftimos, S., Al-Aama, J.Y., Bober, M., Brown, P.A.J., Van Bokhoven, H., Dean, J., Edrees, A.Y., Feingold, M., Fryer, A., Hoefsloot, L.H., Kau, N., Knoers, N.V.A.M., MacKenzie, J., Opitz, J.M., Sarda, P., Ross, A., Temple, I.K., Toutain, A., Wise, C.A., Wright, M., Jackson, A.P., 2011a. Mutations in the pre-replication complex cause Meier-Gorlin syndrome. Nat. Genet. 43, 356–360.

Bicknell, L.S., Walker, S., Klingseisen, A., Stiff, T., Leitch, A., Kerzendorfer, C., Martin, C.A., Yeyati, P., Al Sanna, N., Bober, M., Johnson, D., Wise, C., Jackson, A.P., O'Driscoll, M., Jeggo, P.A., 2011b. Mutations in ORC1, encoding the largest subunit of the origin recognition complex, cause microcephalic primordial dwarfism resembling Meier-Gorlin syndrome. Nat. Genet. 43, 350–356.

Bilgüvar, K., Öztürk, A.K., Louvi, A., Kwan, K.Y., Choi, M., Tatli, B., Yalnizoğlu, D., Tüysüz, B., Çağlayan, A.O., Gökben, S., Kaymakçalan, H., Barak, T., Bakircioğlu, M., Yasuno, K., Ho, W., Sanders, S., Zhu, Y., Yilmaz, S., Dinçer, A., Johnson, M.H., Bronen, R.A., Koçer, N., Per, H., Mane, S., Pamir, M.N., Yalçinkaya, C., Kumandaş, S., Topçu, M., Özmen, M., Šestan, N., Lifton, R.P., State, M.W., Günel, M., 2010. Whole exome sequencing identifies recessive WDR62 mutations in severe brain malformations. Nature 467, 207–210.

Birkou, M., Chasapis, C.T., Marousis, K.D., Loutsidou, A.K., Bentrop, D., Lelli, M., Herrmann, T., Carthy, J.M., Episkopou, V., Spyroulias, G.A., 2017. A Residue Specific Insight into the Arkadia E3 Ubiquitin Ligase Activity and Conformational Plasticity. J. Mol. Biol. 429, 2373–2386.

Blackford, A.N., Jackson, S.P., 2017. ATM, ATR, and DNA-PK: The Trinity at the Heart of the DNA Damage Response. Mol. Cell 66, 801–817.

Blomberg, I., Hoffmann, I., 1999. Ectopic expression of Cdc25A accelerates the G(1)/S transition and leads to premature activation of cyclin E- and cyclin A-dependent kinases. Mol. Cell. Biol. 19, 6183–6194.

Bober, M.B., Khan, N., Kaplan, J., Lewis, K., Feinstein, J.A., Scott, C.I., Steinberg, G.K., 2010. Majewski osteodysplastic primordial dwarfism type II (MOPD II): Expanding the vascular phenotype. Am. J. Med. Genet. Part A 152, 960–965.

Bochman, M.L., Paeschke, K., Zakian, V.A., 2012. DNA secondary structures: stability and function of G- quadruplex structures. Nat. Rev. Genet. 13, 770–780.

Bochman, M.L., Schwacha, A., 2009. The Mcm Complex: Unwinding the Mechanism of a Replicative Helicase. Microbiol. Mol. Biol. Rev. 73, 652–683.

Boersma, V., Moatti, N., Segura-Bayona, S., Peuscher, M.H., Van Der Torre, J., Wevers, B.A., Orthwein, A., Durocher, D., Jacobs, J.J.L., 2015. MAD2L2 controls DNA repair at telomeres and DNA breaks by inhibiting 5' end resection. Nature 521, 537–540.

Bogue, M.A., Zhu, C., Aguilar-Cordova, E., Donehower, L.A., Roth, D.A., 1996. p53 is required for both radiation-induced differentiation and rescue of V(D)J rearrangement in scid mouse thymocytes. Genes Dev. 10, 553–565.

Bond, J., Roberts, E., Mochida, G.H., Hampshire, D.J., Scott, S., Askham, J.M., Springell, K., Mahadevan, M., Crow, Y.J., Markham, A.F., Walsh, C.A., Geoffrey Woods, C., 2002. ASPM is a major determinant of cerebral cortical size. Nat. Genet. 32, 316–320.

Bond, J., Roberts, E., Springell, K., Lizarraga, S., Scott, S., Higgins, J., Hampshire, D.J., Morrison, E.E., Leal, G.F., Silva, E.O., Costa, S.M.R., Baralle, D., Raponi, M., Karbani, G., Rashid, Y., Jafri, H., Bennett, C., Corry, P., Walsh, C.A., Woods, C.G., 2005. A centrosomal mechanism involving CDK5RAP2 and CENPJ controls brain size. Nat. Genet. 37, 353–355.

Bothmer, A., Phadke, T., Barrera, L.A., Margulies, C.M., Lee, C.S., Buquicchio, F., Moss, S., Abdulkerim, H.S., Selleck, W., Jayaram, H., Myer, V.E., Cotta-Ramusino, C., 2017. Characterization of the interplay between DNA repair and CRISPR/Cas9-induced DNA lesions at an endogenous locus. Nat. Commun. 8, 13905.

Botuyan, M.V., Lee, J., Ward, I.M., Kin, J.-E., Thompson, J.R., Chen, J., Mer, G., 2006. Structural Basis for the Methylation State-Specific Recognition of Histone H4-K20 by 53BP1 and Crb2 in DNA Repair. Cell 127, 1361–1373.

Bouwman, P., Aly, A., Escandell, J.M., Pieterse, M., Bartkova, J., Van Der Gulden, H., Hiddingh, S., Thanasoula, M., Kulkarni, A., Yang, Q., Haffty, B.G., Tommiska, J., Blomqvist, C., Drapkin, R., Adams, D.J., Nevanlinna, H., Bartek, J., Tarsounas, M., Ganesan, S., Jonkers, J., 2010. 53BP1 loss rescues BRCA1 deficiency and is associated with triple-negative and BRCA-mutated breast cancers. Nat. Struct. Mol. Biol. 17, 688–695.

Brandsma, I., Gent, D.C., 2012. Pathway choice in DNA double strand break repair: Observations of a balancing act. Genome Integr. 3, 9–19.

Branzei, D., Foiani, M., 2010. Maintaining genome stability at the replication fork. Nat. Rev. Mol. Cell Biol. 11, 208–219.

Brooks, P.J., Theruvathu, J.A., 2005. DNA adducts from acetaldehyde: Implications for alcohol-related carcinogenesis. Alcohol 35, 187–193.

Broustas, C.G., Lieberman, H.B., 2014. DNA Damage Response Genes and the Development of Cancer Metastasis. Radiat. Res. 181, 111–130.

Brown, E.J., Baltimore, D., 2003. Essential and dispensable roles of ATR in cell cycle arrest and genome maintenance. Genes Dev. 17, 615–628.

Brown, J.S., Jackson, S.P., 2015. Ubiquitylation, neddylation and the DNA damage response. Open Biol. 5, 150018.

Bruck, I., Kaplan, D.L., 2014. The replication initiation protein Sld2 regulates helicase assembly. J. Biol. Chem. 289, 1948–1959.

Brzovic, P.S., Rajagopal, P., Hoyt, D.W., King, M.-C., Klevit, R.E., 2001. Structure of a BRCA1–BARD1

heterodimeric RING–RING complex. Nat. Struct. Biol. 8, 833–837.

Budd, M.E., Campbell, J.L., 1995. A yeast gene required for DNA replication encodes a protein with homology to DNA helicases. PNAS 92, 7642–7646.

Budd, M.E., Campbell, J.L., 1997. A yeast replicative helicase, Dna2 helicase, interacts with yeast FEN-1 nuclease in carrying out its essential function. Mol. Cell. Biol. 17, 2136–2142.

Budd, M.E., Choe, W.C., Campbell, J.L., 1995. DNA2 encodes a DNA helicase essential for replication of eukaryotic chromosomes. J. Biol. Chem. 270, 26766–26769.

Budzowska, M., Graham, T.G., Sobeck, A., Waga, S., Walter, J.C., 2015. Regulation of the Rev1-pol zeta complex during bypass of a DNA interstrand cross-link. EMBO J. 34, 1971–1985.

Bunting, S., Callen, E., Kozak, M., Kim, J., Wong, N., Lopez-Contreras, A., Ludwig, T., Baer, R., Faryabi, R., Malhowski, A., Chen, H., Fernandez-Capetillo, O., D'Andrea, A., Nussenzweig, A., 2012. BRCA1 functions independently of homologous recombination in DNA interstrand crosslink repair. Mol. Cell 46, 125–135.

Bunting, S.F., Callén, E., Wong, N., Chen, H., Polato, F., Gunn, A., Bothmer, A., Feldhahn, N., Fernandez-capetillo, O., Cao, L., Xu, X., Deng, C., Finkel, T., Nussenzweig, M., Stark, J.M., Nussenzweig, A., 2010. 53BP1 inhibits homologous recombination in Brca1-deficient cells by blocking resection of DNA breaks. Cell 141, 243–254.

Burma, S., Chen, B.P., Murphy, M., Kurimasa, A., Chen, D.J., 2001. ATM Phosphorylates Histone H2AX in Response to DNA Double-strand Breaks. J. Biol. Chem. 276, 42462–42467.

Burns, T.F., el Deiry, W.S., 1999. The p53 pathway and apoptosis. J. Cell. Physiol. 181, 231–239.

Burrage, L.C., Charng, W.L., Eldomery, M.K., Willer, J.R., Davis, E.E., Lugtenberg, D., Zhu, W., Leduc, M.S., Akdemir, Z.C., Azamian, M., Zapata, G., Hernandez, P.P., Schoots, J., De Munnik, S.A., Roepman, R., Pearring, J.N., Jhangiani, S., Katsanis, N., Vissers, L.E.L.M., Brunner, H.G., Beaudet, A.L., Rosenfeld, J.A., Muzny, D.M., Gibbs, R.A., Eng, C.M., Xia, F., Lalani, S.R., Lupski, J.R., Bongers, E.M.H.F., Yang, Y., 2015. De Novo GMNN Mutations Cause Autosomal-Dominant Primordial Dwarfism Associated with Meier-Gorlin Syndrome. Am. J. Hum. Genet. 97, 904–913.

Burrell, R.A., McClelland, S.E., Endesfelder, D., Groth, P., Weller, M.-C., Shaikh, N., Domingo, E., Kanu, N., Dewhurst, S.M., Gronroos, E., Chew, S.K., Rowan, A.J., Schenk, A., Sheffer, M., Howell, M., Kschischo, M., Behrens, A., Helleday, T., Bartek, J., Tomlinson, I.P., Swanton, C., 2013. Replication stress links structural and numerical cancer chromosomal instability. Nature 494, 492–496.

Calzada, A., Sánchez, M., Sánchez, E., Bueno, A., 2000. The stability of the Cdc6 protein is regulated by cyclin-dependent kinase/cyclin B complexes in Saccharomyces cerevisiae. J. Biol. Chem. 275, 9734–9741.

Carr, A.M., Paek, A.L., Weinert, T., 2011. DNA replication: Failures and inverted fusions. Semin. Cell Dev. Biol. 22, 866–874.

Ceccaldi, R., Parmar, K., Mouly, E., Delord, M., Kim, J.M., Regairaz, M., Pla, M., Vasquez, N., Zhang, Q.S., Pondarre, C., Peffault De Latour, R., Gluckman, E., Cavazzana-Calvo, M., Leblanc, T., Larghero, J., Grompe, M., Socié, G., D'Andrea, A.D., Soulier, J., 2012. Bone marrow failure in fanconi anemia is triggered by an exacerbated p53/p21 DNA damage response that impairs hematopoietic stem and progenitor cells. Cell Stem Cell 11, 36–49.

Cejka, P., Cannavo, E., Polaczek, P., Masuda-Sasa, T., Pokharel, S., Campbell, J.L., Kowalczykowski, S.C., 2010. DNA end resection by Dna2-Sgs1-RPA and its stimulation by Top3-Rmi1 and Mre11-Rad50-Xrs2. Nature 467, 112–116.

Cerosaletti, K., Wright, J., Concannon, P., 2006. Active role for Nibrin in the kinetics of Atm activation. Mol. Cell. Biol. 26, 1691–1699.

Chae, J.H., Vasta, V., Cho, A., Lim, B.C., Zhang, Q., Eun, S.H., Hahn, S.H., 2015. Utility of next generation sequencing in genetic diagnosis of early onset neuromuscular disorders. J. Med. Genet. 52, 208–216.

Chan, K.L., Palmai-Pallag, T., Ying, S., Hickson, I.D., 2009. Replication stress induces sister-chromatid bridging at fragile site loci in mitosis. Nat. Cell Biol. 11, 753–760.

Chapard, C., Hohl, D., Huber, M., 2015. The TRAF-interacting protein (TRAIP) is a novel E2F target with peak expression in mitosis. Oncotarget 6, 20933–20945.

Chapard, C., Meraldi, P., Gleich, T., Bachmann, D., Hohl, D., Huber, M., 2014. TRAIP is a regulator of the spindle assembly checkpoint. J. Cell Sci. 127, 5149–5156.

Chapman, J.R., Barral, P., Vannier, J.B., Borel, V., Steger, M., Tomas-Loba, A., Sartori, A.A., Adams, I.R., Batista, F.D., Boulton, S.J., 2013. RIF1 Is Essential for 53BP1-Dependent Nonhomologous End Joining and Suppression of DNA Double-Strand Break Resection. Mol. Cell 49, 858–871.

Chapman, J.R., Taylor, M.R.G., Boulton, S.J., 2012. Playing the End Game: DNA Double-Strand Break Repair Pathway Choice. Mol. Cell 47, 497–510.

Chen, H., Lisby, M., Symington, L.S., 2013. RPA Coordinates DNA End Resection and Prevents Formation of DNA Hairpins. Mol. Cell 50, 589–600.

Chen, L., Gilkes, D.M., Pan, Y., Lane, W.S., Chen, J., 2005. ATM and Chk2-dependent phosphorylation of MDMX contribute to p53 activation after DNA damage. EMBO J. 24, 3411–3422.

Cheng, G., Shi, Y., Sturla, S.J., Jalas, J.R., McIntee, E.J., Villalta, P.W., Wang, M., Hecht, S.S., 2003. Reactions of formaldehyde plus acetaldehyde with deoxyguanosine and DNA: Formation of cyclic deoxyguanosine adducts and formaldehyde cross-links. Chem. Res. Toxicol. 16, 145–152.

Chenn, A., Walsh, C.A., 2002. Neural Precursors Regulation of Cerebral Cortical Size by Control of Cell Cycle Exit in Neural Precursors. Science 297, 365–370.

Chiruvella, K.K., Liang, Z., Wilson, T.E., 2013. Repair of double-strand breaks by end joining. Cold Spring Harb. Perspect. Biol. 5, a012757.

Choe, W., Budd, M., Imamura, O., Hoopes, L., Campbell, J.L., 2002. Dynamic localization of an Okazaki fragment processing protein suggests a novel role in telomere replication. Mol. Cell. Biol. 22, 4202–17.

Choi, M., Kipps, T., Kurzrock, R., 2016. ATM Mutations in Cancer: Therapeutic Implications. Mol. Cancer Ther. 15, 1781–1791.

Chowdhury, D., Keogh, M.C., Ishii, H., Peterson, C.L., Buratowski, S., Lieberman, J., 2005. γ-H2AX dephosphorylation by protein phosphatase 2A facilitates DNA double-strand break repair. Mol. Cell 20, 801–809.

Chowdhury, D., Xu, X., Zhong, X., Ahmed, F., Zhong, J., Liao, J., Dykxhoorn, D.M., Weinstock, D.M., Pfeifer, G.P., Lieberman, J., 2008. A PP4-phosphatase complex dephosphorylates γ-H2AX generated during DNA replication. Mol. Cell 31, 33–46.

Christensen, D.E., Brzovic, P.S., Klevit, R.E., 2007. E2-BRCA1 RING interactions dictate synthesis of mono- or specific polyubiquitin chain linkages. Nat. Struct. Mol. Biol. 14, 941–948.

Chválová, K., Brabec, V., Kašpárková, J., 2007. Mechanism of the formation of DNA-protein cross-links by antitumor cisplatin. Nucleic Acids Res. 35, 1812–1821.

Ciccia, A., Elledge, S.J., 2010. The DNA Damage Response: Making It Safe to Play with Knives. Mol. Cell 40, 179–204.

Ciccia, A., Ling, C., Coulthard, R., Yan, Z., Xue, Y., Meetei, A.R., Laghmani, E.H., Joenje, H., McDonald, N., de Winter, J.P., Wang, W., West, S.C., 2007. Identification of FAAP24, a Fanconi Anemia Core Complex Protein that Interacts with FANCM. Mol. Cell 25, 331–343.

Cimprich, K.A., Cortez, D., 2008. ATR: An Essential Regulator of Genome Integrity. Nat. Rev. Mol. Cell Biol. 9, 616–627.

Cohen, P.T.W., Philp, A., Vázquez-Martin, C., 2005. Protein phosphatase 4 - From obscurity to vital functions. FEBS Lett. 579, 3278–3286.

Collis, S.J., Ciccia, A., Deans, A.J., Hořejší, Z., Martin, J.S., Maslen, S.L., Skehel, J.M., Elledge, S.J., West, S.C., Boulton, S.J., 2008. FANCM and FAAP24 Function in ATR-Mediated Checkpoint Signaling Independently of the Fanconi Anemia Core Complex. Mol. Cell 32, 313–324.

Cong, L., Ran, F.A., Cox, D., Lin, S., Barretto, R., Hsu, P.D., Wu, X., Jiang, W., Marraffini, L.A., Zhang, F., 2013. Multiplex Genome Engineering Using CRISPR/Cas Systems. Science 339, 819–823.

Cooke, M.S., Evans, M.D., Dizdaroglu, M., Lunec, J., 2003. Oxidative DNA damage: mechanisms, mutation, and disease. FASEB J. 17, 1195–1214.

Cooper, T.A., 2005. Use of minigene systems to dissect alternative splicing elements. Methods 37, 331–340.

Cortez, D., 2015. Preventing Replication Fork Collapse to Maintain Genome Integrity. DNA Repair (Amst) 32, 149–157.

Cortez, D., Guntuku, S., Qin, J., Elledge, S.J., 2001. ATR and ATRIP: Partners in checkpoint signaling. Science 294, 1713–1716.

Coster, G., Goldberg, M., 2010. The cellular response to DNA damage: A focus on MDC1 and its interacting proteins. Nucleus 1, 166–178.

Cotta-Ramusino, C., McDonald 3 3rd, E.R., Hurov, K., Sowa, M.E., Harper, J.W., Elledge, S.J., 2011. A DNA Damage Response Screen Identifies RHINO: a 9-1-1 and TopBP1 interacting protein required for ATR signaling. Science 332, 1313–1317.

Couch, F.B., Bansbach, C.E., Driscoll, R., Luzwick, J.W., Glick, G.G., Bétous, R., Carroll, C.M., Jung, S.Y., Qin, J., Cimprich, K.A., Cortez, D., 2013. ATR phosphorylates SMARCAL1 to prevent replication fork collapse. Genes Dev. 27, 1610–1623.

Daley, J.M., Sung, P., 2014. 53BP1, BRCA1, and the Choice between Recombination and End Joining at DNA Double-Strand Breaks. Mol. Cell. Biol. 34, 1380–1388.

Darnell, G.A., Schroder, W.A., Antalis, T.M., Lambley, E., Major, L., Gardner, J., Birrell, G., Cid-Arregui, A., Suhrbier, A., 2007. Human papillomavirus E7 requires the protease calpain to degrade the retinoblastoma protein. J. Biol. Chem. 282, 37492–37500.

Das, M., Singh, S., Pradhan, S., Narayan, G., 2014. MCM Paradox: Abundance of Eukaryotic Replicative Helicases and Genomic Integrity. Mol. Biol. Int. 574850.

Dauber, A., LaFranchi, S.H., Maliga, Z., Lui, J.C., Moon, J.E., McDeed, C., Henke, K., Zonana, J., Kingman, G.A., Pers, T.H., Baron, J., Rosenfeld, R.G., Hirschhorn, J.N., Harris, M.P., Hwa, V., 2012. Novel microcephalic primordial dwarfism disorder associated with variants in the centrosomal protein ninein. J. Clin. Endocrinol. Metab. 97, 2140–2151.

David, Y., Ternette, N., Edelmann, M.J., Ziv, T., Gayer, B., Sertchook, R., Dadon, Y., Kessler, B.M., Navon, A., 2011. E3 ligases determine ubiquitination site and conjugate type by enforcing specificity on E2 enzymes. J. Biol. Chem. 286, 44104–44115.

Davis, A.J., Chen, B.P.C., Chen, D.J., 2014. DNA-PK: A dynamic enzyme in a versatile DSB repair pathway. DNA Repair (Amst) 17, 21–29.

de Araújo, T.V.B., Ximenes, R.A. de A., Miranda-Filho, D. de B., Souza, W.V., Montarroyos, U.R., de Melo, A.P.L., Valongueiro, S., de Albuquerque, M. de F.P.M., Braga, C., Filho, S.P.B., Cordeiro, M.T., Vazquez, E., Cruz, D. di C.S., Henriques, C.M.P., Bezerra, L.C.A., Castanha, P.M. da S., Dhalia, R., Marques-Júnior, E.T.A., Martelli, C.M.T., Rodrigues, L.C., 2017. Association between microcephaly, Zika virus infection, and other risk factors in Brazil: Final report of a case-control study. Lancet Infect. Dis. 18, 328–336.

De Crescenzo, A., Citro, V., Freschi, A., Sparago, A., Palumbo, O., Cubellis, M.V., Carella, M., Castelluccio, P., Cavaliere, M.L., Cerrato, F., Riccio, A., 2015. A splicing mutation of the HMGA2 gene is associated with Silver-Russell syndrome phenotype. J. Hum. Genet. 60, 287–293.

de Klein, A., Muijtjens, M., Van Os, R., Verhoeven, Y., Smit, B., Carr, A.M., Lehmann, A.R., Hoeijmakers, J.H.J., 2000. Targeted disruption of the cell-cycle checkpoint gene ATR leads to early embryonic lethality in mice. Curr. Biol. 10, 479–482.

de Winter, J.P., Joenje, H., 2009. The genetic and molecular basis of Fanconi anemia. Mutat. Res. - Fundam. Mol. Mech. Mutagen. 668, 11–19.

Deans, A.J., West, S.C., 2011. DNA interstrand crosslink repair and cancer. Nat. Rev. Cancer 11, 467–480.

Dellino, G.I., Cittaro, D., Piccioni, R., Luzi, L., Banfi, S., Segalla, S., Cesaroni, M., Mendoza-Maldonado, R., Giacca, M., Pelicci, P.G., 2013. Genome-wide mapping of human DNA-replication origins: Levels of transcription at ORC1 sites regulate origin selection and replication timing. Genome Res. 23, 1–11.

Dendouga, N., Gao, H., Moechars, D., Janicot, M., Vialard, J., McGowan, C.H., 2005. Disruption of Murine Mus81 Increases Genomic Instability and DNA Damage Sensitivity but Does Not Promote Tumorigenesis. Mol. Cell. Biol. 25, 7569–7579.

Deshaies, R.J., Joazeiro, C.A.P., 2009. RING Domain E3 Ubiquitin Ligases. Annu. Rev. Biochem. 78, 399–434.

Dev, H., Chiang, T.W.W., Lescale, C., de Krijger, I., Martin, A.G., Pilger, D., Coates, J., Sczaniecka-Clift, M., Wei, W., Ostermaier, M., Herzog, M., Lam, J., Shea, A., Demir, M., Wu, Q., Yang, F., Fu, B., Lai, Z., Balmus, G., Belotserkovskaya, R., Serra, V., O'Connor, M.J., Bruna, A., Beli, P., Pellegrini, L., Caldas, C., Deriano, L., Jacobs, J.J.L., Galanty, Y., Jackson, S.P., 2018. Shieldin complex promotes DNA end-joining and counters homologous recombination in BRCA1-null cells. Nat. Cell Biol. 20.

Devbhandari, S., Jiang, J., Kumar, C., Whitehouse, I., Remus, D., 2017. Chromatin Constrains the Initiation and Elongation of DNA Replication. Mol. Cell 65, 131–141.

Dewar, J.M., Budzowska, M., Walter, J.C., 2015. The mechanism of DNA replication termination in vertebrates. Nature 525, 345–350.

Dewar, J.M., Low, E., Mann, M., Räschle, M., Walter, J.C., 2017. CRL2Lrr1 promotes unloading of the vertebrate replisome from chromatin during replication termination. Genes Dev. 31, 275–290.

Dewar, J.M., Walter, J.C., 2017. Mechanisms of DNA replication termination. Nat. Rev. Mol. Cell Biol. 18, 507–516.

Di Virgilio, M., Callen, E., Yamane, A., Zhang, W., Jankovic, M., Gitlin, A.D., Feldhahn, N., Resch, W., Oliveira, T.Y., Chait, B.T., Nussenzweig, A., Casellas, R., Robbiani, D.F., Nussenzweig, M.C., 2013. Rif1 Prevents Resection of DNA Breaks and Promotes Immunoglobulin Class Switching. Science 339.

Dodd, R.B., Allen, M.D., Brown, S.E., Sanderson, C.H., Duncan, L.M., Lehner, P.J., Bycroft, M., Read, R.J., 2004. Solution structure of the Kaposi's sarcoma-associated herpesvirus K3 N-terminal domain reveals a novel E2-binding C4HC3-type RING domain. J. Biol. Chem. 279, 53840–53847.

Doil, C., Mailand, N., Bekker-Jensen, S., Menard, P., Larsen, D.H., Pepperkok, R., Ellenberg, J., Panier, S., Durocher, D., Bartek, J., Lukas, J., Lukas, C., 2009. RNF168 Binds and Amplifies Ubiquitin Conjugates on Damaged Chromosomes to Allow Accumulation of Repair Proteins. Cell 136, 435–446.

Douwel, D.K., Boonen, R.A.C.M., Long, D.T., Szypowska, A.A., Räschle, M., Walter, J.C., Knipscheer, P., 2014. XPF-ERCC1 Acts in Unhooking DNA Interstrand Crosslinks in Cooperation with FANCD2 and FANCP/SLX4. Mol. Cell 54, 460–471.

Doyle, C., Sambrook, J., Gething, M.J., 1986. Analysis of progressive deletions of the transmembrane and cytoplasmic domains of influenza hemagglutinin. J. Cell Biol. 103, 1193–1204.

Dungrawala, H., Rose, K.L., Bhat, K.P., Mohni, K.N., Glick, G.G., Couch, F.B., Cortez, D., 2015. The Replication Checkpoint Prevents Two Types of Fork Collapse without Regulating Replisome Stability. Mol. Cell 59, 998–1010.

Duursma, A.M., Driscoll, R., Elias, J.E., Cimprich, K.A., 2013. A role for the MRN complex in ATR activation through TOPBP1 recruitment. Mol. Cell 50, 116–122.

Duxin, J.P., Dao, B., Martinsson, P., Rajala, N., Guittat, L., Campbell, J.L., Spelbrink, J.N., Stewart, S.A., 2009. Human Dna2 Is a Nuclear and Mitochondrial DNA Maintenance Protein. Mol. Cell. Biol. 29, 4274–4282.

Duxin, J.P., Moore, H.R., Sidorova, J., Karanja, K., Honaker, Y., Dao, B., Piwnica-Worms, H., Campbell, J.L., Monnat, R.J., Stewart, S.A., 2012. Okazaki fragment processing-independent role for human Dna2 enzyme during DNA replication. J. Biol. Chem. 287, 21980–21991.

Edery, P., Marcaillou, C., Sahbatou, M., Labalme, A., Chastang, J., Touraine, R., Tubacher, E., Senni, F., Bober, M.B., Nampoothiri, S., Jouk, P.-S., Steichen, E., Berland, S., Toutain, A., Wise, C.A., Sanlaville, D., Rousseau, F., Clerget-Darpoux, F., Leutenegger, A.-L., 2011. Association of TALS Developmental Disorder with Defect in Minor Splicing Component U4atac snRNA. Science 332, 240–244.

Eguren, M., Porlan, E., Manchado, E., García-Higuera, I., Cañamero, M., Fariñas, I., Malumbres, M., 2013. The APC/C cofactor Cdh1 prevents replicative stress and p53-dependent cell death in neural progenitors. Nat. Commun. 4, 2880.

El-Brolosy, M.A., Stainier, D.Y.R., 2017. Genetic compensation: A phenomenon in search of mechanisms. PLoS Genet. 13, e1006780.

El-Khamisy, S.F., Caldecott, K.W., 2006. TDP1-dependent DNA single-strand break repair and neurodegeneration. Mutagenesis 21, 219–224.

El-Khamisy, S.F., Saifi, G.M., Weinfeld, M., Johansson, F., Helleday, T., Lupski, J.R., Caldecott, K.W., 2005. Defective DNA single-strand break repair in spinocerebellar ataxia with axonal neuropathy-1. Nature 434, 108–113.

Ellis, R.J., Hartl, F.U., 1999. Principles of protein folding in the cellular environment. Curr. Opin. Struct. Biol. 9, 102–110.

Enoiu, M., Jiricny, J., Schärer, O.D., 2012. Repair of cisplatin-induced DNA interstrand crosslinks by a replication-independent pathway involving transcription-coupled repair and translesion synthesis. Nucleic Acids Res. 40, 8953–8964.

Escribano-Díaz, C., Orthwein, A., Fradet-Turcotte, A., Xing, M., Young, J.T.F., Tkáč, J., Cook, M.A., Rosebrock, A.P., Munro, M., Canny, M.D., Xu, D., Durocher, D., 2013. A Cell Cycle-Dependent Regulatory Circuit Composed of 53BP1-RIF1 and BRCA1-CtIP Controls DNA Repair Pathway Choice. Mol. Cell 49, 872–883.

Evers, B., Jastrzebski, K., Heijmans, J.P.M., Grernrum, W., Beijersbergen, R.L., Bernards, R., 2016. CRISPR knockout screening outperforms shRNA and CRISPRi in identifying essential genes. Nat. Biotechnol. 34, 631–633.

Evrony, G.D., Cordero, D.R., Shen, J., Partlow, J.N., Yu, T.W., Rodin, R.E., Hill, R.S., Coulter, M.E., Lam, A.T.N., Jayaraman, D., Gerrelli, D., Diaz, D.G., Santos, C., Morrison, V., Galli, A., Tschulena, U., Wiemann, S., Martel, M.J., Spooner, B., Ryu, S.C., Elhosary, P.C., Richardson, J.M., Tierney, D., Robinson, C.A., Chibbar, R., Diudea, D., Folkerth, R., Wiebe, S., Barkovich, A.J., Mochida, G.H., Irvine, J., Lemire, E.G., Blakley, P., Walsh, C.A., 2017. Integrated genome and transcriptome sequencing identifies a noncoding mutation in the genome replication factor DONSON as the cause of microcephaly-micromelia syndrome. Genome Res. 27, 1323–1335.

Faheem, M., Naseer, M.I., Rasool, M., Chaudhary, A.G., Kumosani, T.A., Ilyas, A.M. uhamma., Pushparaj, P., Ahmed, F., Algahtani, H.A., Al-Qahtani, M.H., Saleh Jamal, H., 2015. Molecular genetics of human primary microcephaly: an overview. BMC Med. Genomics 8, S4.

Falck, J., Mailand, N., Syljuåsen, R.G., Bartek, J., Lukas, J., 2001. The ATM-Chk2-Cdc25A checkpoint pathway guards against radioresistant DNA synthesis. Nature 410, 842–847.

Fell, V.L., Schild-Poulter, C., 2015. The Ku heterodimer: Function in DNA repair and beyond. Mutat. Res. - Rev. Mutat. Res. 763, 15–29.

Feng, J., Wakeman, T., Yong, S., Wu, X., Kornbluth, S., Wang, X.-F., 2009. Protein phosphatase 2A-dependent dephosphorylation of replication protein A is required for the repair of DNA breaks induced by replication stress. Mol. Cell. Biol. 29, 5696–709.

Feng, L., Huang, T., Chen, J., 2009. MERIT40 facilitates BRCA1 localization and DNA damage repair. Genes Dev. 23, 719–728.

Feng, S., Zhao, Y., Xu, Y., Ning, S., Huo, W., Hou, M., Gao, G., Ji, J., Guo, R., Xu, D., 2016. Ewing tumor-associated antigen 1 interacts with replication protein A to promote restart of stalled replication forks. J. Biol. Chem. 291, 21956–21962.

Feng, W., Guo, Y., Huang, J., Deng, Y., Zang, J., Huen, M.S.-Y., 2016. TRAIP regulates replication fork

recovery and progression via PCNA. Cell Discov. 2, 16016.

Feng, Y., Vlassis, A., Roques, C., Lalonde, M., González-Aguilera, C., Lambert, J., Lee, S., Zhao, X., Johansen, J. V, Paquet, E., Yang, X., Gingras, A., Côté, J., 2015. BRPF3-HBO1 regulates replication origin activation and histone H3K14 acetylation. EMBO J. 35, 176–192.

Fenwick, A.L., Kliszczak, M., Cooper, F., Murray, J., Sanchez-Pulido, L., Twigg, S.R.F., Goriely, A., McGowan, S.J., Miller, K.A., Taylor, I.B., Logan, C., Bozdogan, S., Danda, S., Dixon, J., Elsayed, S.M., Elsobky, E., Gardham, A., Hoffer, M.J.V., Koopmans, M., McDonald-McGinn, D.M., Santen, G.W.E., Savarirayan, R., de Silva, D., Vanakker, O., Wall, S.A., Wilson, L.C., Yuregir, O.O., Zackai, E.H., Ponting, C.P., Jackson, A.P., Wilkie, A.O.M., Niedzwiedz, W., Bicknell, L.S., 2016. Mutations in CDC45, Encoding an Essential Component of the Pre-initiation Complex, Cause Meier-Gorlin Syndrome and Craniosynostosis. Am. J. Hum. Genet. 99, 125–138.

Fernandez-Capetillo, O., Chen, H.T., Celeste, A., Ward, I., Romanienko, P.J., Morales, J.C., Naka, K., Xia, Z., Camerini-Otero, R.D., Motoyama, N., Carpenter, P.B., Bonner, W.M., Chen, J., Nussenzweig, A., 2002. DNA damage-induced G2-M checkpoint activation by histone H2AX and 53BP1. Nat. Cell Biol. 4, 993–997.

Filippello, A., Lorenzi, P., Bergamo, E., Romanelli, M.G., 2013. Identification of nuclear retention domains in the RBM20 protein. FEBS Lett. 587, 2989–2995.

Forment, J. V., Blasius, M., Guerini, I., Jackson, S.P., 2011. Structure-specific DNA endonuclease Mus81/Eme1 generates DNA damage caused by Chk1 inactivation. PLoS One 6, e23517.

Fortini, B.K., Pokharel, S., Polaczek, P., Balakrishnan, L., Bambara, R.A., Campbell, J.L., 2011. Characterization of the endonuclease and ATP-dependent flap endo/exonuclease of Dna2. J. Biol. Chem. 286, 23763–23770.

Fragkos, M., Ganier, O., Coulombe, P., Méchali, M., 2015. DNA replication origin activation in space and time. Nat. Rev. Mol. Cell Biol. 16, 360–374.

Fragkos, M., Naim, V., 2017. Rescue from replication stress during mitosis. Cell Cycle 16, 613–633.

Frey, S., Görlich, D., 2014. Purification of protein complexes of defined subunit stoichiometry using a set of orthogonal, tag-cleaving proteases. J. Chromatogr. A 1337, 106–115.

Fu, Y. V, Yardimci, H., Long, D.T., Ho, T.V., Guainazzi, A., Bermudez, V.P., Hurwitz, J., Oijen, A. Van, Schärer, O.D., Walter, J.C., 2011. Selective bypass of a lagging strand roadblock by the eukaryotic replicative DNA helicase. Cell 146, 931–941.

Fullbright, G., Rycenga, H.B., Gruber, J.D., Long, D.T., 2016. p97 Promotes a Conserved Mechanism of Helicase Unloading during DNA Cross-Link Repair. Mol. Cell. Biol. 36, 2983–2994.

Furuta, T., Takemura, H., Liao, Z.Y., Aune, G.J., Redon, C., Sedelnikova, O.A., Pilch, D.R., Rogakou, E.P., Celeste, A., Chen, H.T., Nussenzweig, A., Aladjem, M.I., Bonner, W.M., Pommier, Y., 2003. Phosphorylation of histone H2AX and activation of Mre11, Rad50, and Nbs1 in response to replication-dependent DNA double-strand breaks induced by mammalian DNA topoisomerase I cleavage complexes. J. Biol. Chem. 278, 20303–20312.

Gaillard, H., García-Muse, T., Aguilera, A., 2015. Replication stress and cancer. Nat. Rev. Cancer 15, 276–280.

Gao, Y., Ferguson, D.O., Xie, W., Manis, J.P., Sekiguchi, J.A., Frank, K.M., Chaudhuri, J., Horner, J., DePinho, R.A., Alt, F.W., 2000. Interplay of p53 and DNA-repair protein XRCC4 in tumorigenesis, genomic stability and development. Nature 404, 897–900.

Gao, Y., Mutter-Rottmayer, E., Zlatanou, A., Vaziri, C., Yang, Y., 2017. Mechanisms of post-replication DNA repair. Genes (Basel) 8, 64.

Gao, Y., Sun, Y., Frank, K.M., Dikkes, P., Fujiwara, Y., Seidl, K.J., Sekiguchi, J.A.M., Rathbun, G.A., Swat, W., Wang, J., Bronson, R.T., Malynn, B.A., Bryans, M., Zhu, C., Chaudhuri, J., Davidson, L., Ferrini, R., Stamato, T., Orkin, S.H., Greenberg, M.E., Alt, F.W., 1998. A critical role for DNA end-joining proteins in both lymphogenesis and neurogenesis. Cell 95, 891–902.

Garcia-Higuera, I., Taniguchi, T., Ganesan, S., Meyn, M.S., Timmers, C., Hejna, J., Grompe, M., D'Andrea, A.D., 2001. Interaction of the Fanconi anemia proteins and BRCA1 in a common

pathway. Mol. Cell 7, 249–262.

Garg, P., Burgers, P.M.J., 2005. DNA polymerases that propagate the eukaryotic DNA replication fork. Crit. Rev. Biochem. Mol. Biol. 40, 115–128.

Garner, E., Costanzo, V., 2009. Studying the DNA damage response using in vitro model systems. DNA Repair (Amst) 8, 1025–1037.

Garner, E., Smogorzewska, A., 2011. Ubiquitylation and the Fanconi Anemia Pathway Elizabeth. FEBS Lett. 585, 247–253.

Gatei, M., Scott, S.P., Filippovitch, I., Soronika, N., Lavin, M.F., Weber, B., Khanna, K.K., 2000. Role for ATM in DNA damage-induced phosphorylation of BRCA1. Cancer Res. 60, 3299–3304.

Genin, A., Desir, J., Lambert, N., Biervliet, M., Van der Aa, N., Pierquin, G., Killian, A., Tosi, M., Urbina, M., Lefort, A., Libert, F., Pirson, I., Abramowicz, M., 2012. Kinetochore KMN network gene CASC5 mutated in primary microcephaly. Hum. Mol. Genet. 21, 5306–5317.

Ghezraoui, H., Oliveira, C., Becker, J.R., Bilham, K., Moralli, D., Anzilotti, C., Fischer, R., Deobagkar-Lele, M., Sanchiz-Calvo, M., Fueyo-Marcos, E., Bonham, S., Kessler, B.M., Rottenberg, S., Cornall, R.J., Green, C.M., Chapman, J.R., 2018. 53BP1 cooperation with the REV7–shieldin complex underpins DNA structure-specific NHEJ. Nature 560, 122–127.

Gibbs-Seymour, I., Oka, Y., Rajendra, E., Weinert, B.T., Passmore, L.A., Patel, K.J., Olsen, J. V., Choudhary, C., Bekker-Jensen, S., Mailand, N., 2015. Ubiquitin-SUMO circuitry controls activated fanconi anemia ID complex dosage in response to DNA damage. Mol. Cell 57, 150–164.

Gingras, A.-C., Caballero, M., Zarske, M., Sanchez, A., Hazbun, T.R., Fields, S., Sonenberg, N., Hafen, E., Raught, B., Aebersold, R., 2005. A Novel, Evolutionarily Conserved Protein Phosphatase Complex Involved in Cisplatin Sensitivity. Mol. Cell. Proteomics 4, 1725–1740.

Gloor, J.W., Balakrishnan, L., Campbell, J.L., Bambara, R.A., 2012. Biochemical analyses indicate that binding and cleavage specificities define the ordered processing of human Okazaki fragments by Dna2 and FEN1. Nucleic Acids Res. 40, 6774–6786.

Goodship, J., Gill, H., Carter, J., Jackson, A., Splitt, M., Wright, M., 2000. Autozygosity Mapping of a Seckel Syndrome Locus to Chromosome 3q22.1-q24. Am. J. Hum. Genet. 67, 498–503.

Goodwin, E.C., DiMaio, D., 2000. Repression of human papillomavirus oncogenes in HeLa cervical carcinoma cells causes the orderly reactivation of dormant tumor suppressor pathways. PNAS 97, 12513–12518.

Görisch, S.M., Sporbert, A., Stear, J.H., Grunewald, I., Nowak, D., Warbrick, E., Leonhardt, H., Cardoso, M.C., 2008. Uncoupling the replication machinery: Replication fork progression in the absence of processive DNA synthesis. Cell Cycle 7, 1983–1990.

Griffith, E., Walker, S., Martin, C.A., Vagnarelli, P., Stiff, T., Vernay, B., Sanna, N. Al, Saggar, A., Hamel, B., Earnshaw, W.C., Jeggo, P.A., Jackson, A.P., O'Driscoll, M., 2008. Mutations in pericentrin cause Seckel syndrome with defective ATR-dependent DNA damage signaling. Nat. Genet. 40, 232–236.

Guan, C., Li, J., Sun, D., Liu, Y., Liang, H., 2017. The structure and polymerase-recognition mechanism of the crucial adaptor protein AND-1 in the human replisome. J. Biol. Chem. 292, 9627–9636.

Guernsey, D.L., Jiang, H., Hussin, J., Arnold, M., Bouyakdan, K., Perry, S., Babineau-Sturk, T., Beis, J., Dumas, N., Evans, S.C., Ferguson, M., Matsuoka, M., MacGillivray, C., Nightingale, M., Patry, L., Rideout, A.L., Thomas, A., Orr, A., Hoffmann, I., Michaud, J.L., Awadalla, P., Meek, D.C., Ludman, M., Samuels, M.E., 2010. Mutations in centrosomal protein CEP152 in primary microcephaly families linked to MCPH4. Am. J. Hum. Genet. 87, 40–51.

Guernsey, D.L., Matsuoka, M., Jiang, H., Evans, S., MacGillivray, C., Nightingale, M., Perry, S., Ferguson, M., Leblanc, M., Paquette, J., Patry, L., Rideout, A.L., Thomas, A., Orr, A., McMaster, C.R., Michaud, J.L., Deal, C., Langlois, S., Superneau, D.W., Parkash, S., Ludman, M., Skidmore, D.L., Samuels, M.E., 2011. Mutations in origin recognition complex gene ORC4 cause Meier-Gorlin syndrome. Nat. Genet. 43, 360–365.

Guerois, R., Nielsen, J.E., Serrano, L., 2002. Predicting changes in the stability of proteins and protein complexes: A study of more than 1000 mutations. J. Mol. Biol. 320, 369–387.

Guo, C., Kumagai, A., Schlacher, K., Shevchenko, A., Shevchenko, A., Dunphy, W.G., 2015. Interaction of Chk1 with Treslin Negatively Regulates the Initiation of Chromosomal DNA Replication. Mol Cell 57, 492–505.

Gupta, R., Somyajit, K., Narita, T., Maskey, E., Stanlie, A., Kremer, M., Typas, D., Lammers, M., Mailand, N., Nussenzweig, A., Lukas, J., Choudhary, C., 2018. DNA Repair Network Analysis Reveals Shieldin as a Key Regulator of NHEJ and PARP Inhibitor Sensitivity. Cell 173, 972–988.e23.

Haahr, P., Hoffmann, S., Tollenaere, M.A.X., Ho, T., Toledo, L.I., Mann, M., Bekker-Jensen, S., Räschle, M., Mailand, N., 2016. Activation of the ATR kinase by the RPA-binding protein ETAA1. Nat. Cell Biol. 18, 1196–1207.

Hall, J.G., Flora, C., Scott, C.I., Pauli, R.M., Tanaka, K.I., 2004. Majewski osteodysplastic primordial dwarfism type II (MOPD II): Natural history and clinical findings. Am. J. Med. Genet. 130A, 55–72.

Hanada, K., Budzowska, M., Davies, S.L., Van Drunen, E., Onizawa, H., Beverloo, H.B., Maas, A., Essers, J., Hickson, I.D., Kanaar, R., 2007. The structure-specific endonuclease Mus81 contributes to replication restart by generating double-strand DNA breaks. Nat. Struct. Mol. Biol. 14, 1096–1104.

Harley, M.E., Murina, O., Leitch, A., Higgs, M.R., Bicknell, L.S., Yigit, G., Blackford, A.N., Zlatanou, A., Mackenzie, K.J., Reddy, K., Halachev, M., McGlasson, S., Reijns, M.A.M., Fluteau, A., Martin, C.A., Sabbioneda, S., Elcioglu, N.H., Altmüller, J., Thiele, H., Greenhalgh, L., Chessa, L., Maghnie, M., Salim, M., Bober, M.B., Nürnberg, P., Jackson, S.P., Hurles, M.E., Wollnik, B., Stewart, G.S., Jackson, A.P., 2016. TRAIP promotes DNA damage response during genome replication and is mutated in primordial dwarfism. Nat. Genet. 48, 36–43.

Hashizume, R., Fukuda, M., Maeda, I., Nishikawa, H., Oyake, D., Yabuki, Y., Ogata, H., Ohta, T., 2001. The RING Heterodimer BRCA1-BARD1 Is a Ubiquitin Ligase Inactivated by a Breast Cancer-derived Mutation. J. Biol. Chem. 276, 14537–14540.

Hata, T., Hoshi, T., Kanamori, K., Matsumae, A., Sano, Y., Shima, T., Sugawara, R., 1956. Mitomycin, a new antibiotic from Streptomyces. I. J. Antibiot. (Tokyo). 9, 141–146.

He, H., Liyanarachchi, S., Akagi, K., Nagy, R., Li, J., Dietrich, R.C., Li, W., Sebastian, N., Wen, B., Xin, B., Singh, J., Yan, P., Alder, H., Haan, E., Wieczorek, D., Albrecht, B., Puffenberger, E., Wang, H., Westman, J.A., Padgett, R.A., Symer, D.E., De La Chapelle, A., 2011. Mutations in U4atac snRNA, a component of the minor spliceosome, in the developmental disorder MOPD I. Science 332, 238–240.

Heller, R.C., Kang, S., Lam, W.M., Chen, S., Chan, C.S., Bell, S.P., 2011. Eukaryotic origin-dependent DNA replication in vitro reveals sequential action of DDK and S-CDK kinases. Cell 146, 80–91.

Helps, N.R., Brewis, N.D., Lineruth, K., Davis, T., Kaiser, K., Cohen, P.T., 1998. Protein phosphatase 4 is an essential enzyme required for organisation of microtubules at centrosomes in Drosophila embryos. J. Cell Sci. 111, 1331–1340.

Her, J., Bunting, S.F., 2018. How cells ensure correct repair of DNA double-strand breaks. J. Biol. Chem. 293, 10502–10511.

Hiraga, S., Alvino, G.M., Chang, F., Lian, H.Y., Sridhar, A., Kubota, T., Brewer, B.J., Weinreich, M., Raghuraman, M.K., Donaldson, A.D., 2014. Rif1 controls DNA replication by directing Protein Phosphatase 1 to reverse Cdc7-mediated phosphorylation of the MCM complex. Genes Dev. 28, 372–383.

Hiraga, S., Ly, T., Garzón, J., Hořejší, Z., Ohkubo, Y., Endo, A., Obuse, C., Boulton, S.J., Lamond, A.I., Donaldson, A.D., 2017. Human RIF1 and protein phosphatase 1 stimulate DNA replication origin licensing but suppress origin activation. EMBO Rep. 18, 403–419.

Hodskinson, M.R.G., Silhan, J., Crossan, G.P., Garaycoechea, J.I., Mukherjee, S., Johnson, C.M., Schärer, O.D., Patel, K.J., 2014. Mouse SLX4 Is a Tumor Suppressor that Stimulates the Activity

of the Nuclease XPF-ERCC1 in DNA Crosslink Repair. Mol. Cell 54, 472–484.

Hoffmann, I., Draetta, G., Karsenti, E., 1994. Activation of the phosphatase activity of human cdc25A by a cdk2-cyclin E dependent phosphorylation at the G1/S transition. EMBO J. 13, 4302–4310.

Hoffmann, S., Smedegaard, S., Nakamura, K., Mortuza, G.B., Räschle, M., de Opakua, A.I., Oka, Y., Feng, Y., Blanco, F.J., Mann, M., Montoya, G., Groth, A., Bekker-Jensen, S., Mailand, N., 2016. TRAIP is a PCNA-binding ubiquitin ligase that protects genome stability after replication stress. J. Cell Biol. 212, 63–75.

Homem, C.C.F., Repic, M., Knoblich, J.A., 2015. Proliferation control in neural stem and progenitor cells. Nat. Rev. Neurosci. 16, 647–659.

Hoogenboom, W.S., Douwel, D.K., Knipscheer, P., 2017. Xenopus egg extract: A powerful tool to study genome maintenance mechanisms. Dev. Biol. 428, 300–309.

Hornbeck, P. V., Zhang, B., Murray, B., Kornhauser, J.M., Latham, V., Skrzypek, E., 2015. PhosphoSitePlus, 2014: Mutations, PTMs and recalibrations. Nucleic Acids Res. 43, D512–D520.

Hsiang, Y.H., Hertzberg, R., Hecht, S., Liu, L.F., 1985. Camptothecin induces protein-linked DNA breaks via mammalian DNA topoisomerase I. J. Biol. Chem. 260, 14873–14878.

Hu, Y., Scully, R., Sobhian, B., Xie, A., Shestakova, E., Livingston, D.M., 2011. RAP80-directed tuning of BRCA1 homologous recombination function at ionizing radiation-induced nuclear foci. Genes Dev. 25, 685–700.

Huang, T.H., Chen, H.C., Chou, S.M., Yang, Y.C., Fan, J.R., Li, T.K., 2010. Cellular processing determinants for the activation of damage signals in response to topoisomerase I-linked DNA breakage. Cell Res. 20, 1060–1075.

Huen, M.S.Y., Grant, R., Manke, I., Minn, K., Yu, X., Yaffe, M.B., Chen, J., 2007. The E3 ubiquitin ligase RNF8 transduces the DNA damage signal via an ubiquitin-dependent signaling pathway. Cell 131, 901–914.

Huertas, P., 2010. DNA resection in eukaryotes: deciding how to fix the break. Nat. Struct. Mol. Biol. 17, 11–16.

Huertas, P., Jackson, S.P., 2009. Human CtIP Mediates Cell Cycle Control of DNA End Resection and Double Strand Break Repair. J. Biol. Chem. 284, 9558–9565.

Hug, N., Longman, D., Cáceres, J.F., 2016. Mechanism and regulation of the nonsense-mediated decay pathway. Nucleic Acids Res. 44, 1483–1495.

Hussain, M.S., Baig, S.M., Neumann, S., Nürnberg, G., Farooq, M., Ahmad, I., Alef, T., Hennies, H.C., Technau, M., Altmüller, J., Frommolt, P., Thiele, H., Noegel, A.A., Nürnberg, P., 2012. A truncating mutation of CEP135 causes primary microcephaly and disturbed centrosomal function. Am. J. Hum. Genet. 90, 871–878.

Hussain, M.S., Baig, S.M., Neumann, S., Peche, V.S., Szczepanski, S., Nürnberg, G., Tariq, M., Jameel, M., Khan, T.N., Fatima, A., Malik, N.A., Ahmad, I., Altmüller, J., Frommolt, P., Thiele, H., Höhne, W., Yigit, G., Wollnik, B., Neubauer, B.A., Nürnberg, P., Noegel, A.A., 2013. CDK6 associates with the centrosome during mitosis and is mutated in a large pakistani family with primary microcephaly. Hum. Mol. Genet. 22, 5199–5214.

Hustedt, N., Durocher, D., 2017. The control of DNA repair by the cell cycle. Nat. Cell Biol. 19, 1–9.

Isono, M., Niimi, A., Oike, T., Hagiwara, Y., Sato, H., Sekine, R., Yoshida, Y., Isobe, S.Y., Obuse, C., Nishi, R., Petricci, E., Nakada, S., Nakano, T., Shibata, A., 2017. BRCA1 Directs the Repair Pathway to Homologous Recombination by Promoting 53BP1 Dephosphorylation. Cell Rep. 18, 520–532.

Izumi, M., Vaughan, O.A., Hutchison, C.J., Gilbert, D.M., 2000. Head and/or CaaX Domain Deletions of Lamin Proteins Disrupt Preformed Lamin A and C But Not Lamin B Structure in Mammalian Cells. Mol. Biol. Cell 11, 4323–4337.

Jackson, A.P., Eastwood, H., Bell, S.M., Adu, J., Toomes, C., Carr, I.M., Roberts, E., Hampshire, D.J., Crow, Y.J., Mighell, A.J., Karbani, G., Jafri, H., Rashid, Y., Mueller, R.F., Markham, A.F., Woods,

C.G., 2002. Identification of Microcephalin, a Protein Implicated in Determining the Size of the Human Brain. Am. J. Hum. Genet. 71, 136–142.

Jackson, A.P., McHale, D.P., Campbell, D.A., Jafri, H., Rashid, Y., Mannan, J., Karbani, G., Corry, P., Levene, M.I., Mueller, R.F., Markham, A.F., Lench, N.J., Woods, C.G., 1998. Primary autosomal recessive microcephaly (MCPH1) maps to chromosome 8p22-pter. Am. J. Hum. Genet. 63, 541–546.

Jaenicke, R., 1998. Protein self-organization in vitro and in vivo: partitioning between physical biochemistry and cell biology. Biol. Chem. 379, 237–243.

Jarnuczak, A.F., Lee, D.C.H., Lawless, C., Holman, S.W., Eyers, C.E., Hubbard, S.J., 2016. Analysis of Intrinsic Peptide Detectability via Integrated Label-Free and SRM-Based Absolute Quantitative Proteomics. J. Proteome Res. 15, 2945–2959.

Jeong, Y.T., Rossi, M., Cermak, L., Saraf, A., Florens, L., Washburn, M.P., Sung, P., Schildkraut, C., Pagano, M., 2013. FBH1 promotes DNA double-strand breakage and apoptosis in response to DNA replication stress. J. Cell Biol. 200, 141–149.

Jin, J., Shirogane, T., Xu, L., Nalepa, G., Qin, J., Elledge, S.J., Harper, J.W., 2003. SCFβ-TRCP links Chk1 signaling to degradation of the Cdc25A protein phosphatase. Genes Dev. 17, 3062–3074.

Jinek, M., Chylinski, K., Fonfara, I., Hauer, M., Doudna, J.A., Charpentier, E., 2012. A Programmable Dual-RNA–Guided DNA Endonuclease in Adaptive Bacterial Immunity. Science 337, 816–822.

Joazeiro, C.A.P., Wing, S.S., Huang, H.K., Leverson, J.D., Hunter, T., Liu, Y.C., 1999. The tyrosine kinase negative regulator c-Cbl as a RING-type, E2-dependent ubiquitin-protein ligase. Science 286, 309–312.

Joenje, H., Patel, K.J., 2001. The emerging genetic and molecular basis of Fanconi anaemia. Nat. Rev. Genet. 2, 446–457.

Johnson, A., O'Donnell, M., 2005. Cellular DNA Replicases: Components and Dynamics at the Replication Fork. Annu. Rev. Biochem. 74, 283–315.

Johnson, R.E., Kondratick, C.M., Prakash, S., Prakash, L., 1999. hRAD30 mutations in the variant form of xeroderma pigmentosum. Science 285, 263–265.

Kaiser, S., Sauer, F., Kisker, C., 2017. The structural and functional characterization of human RecQ4 reveals insights into its helicase mechanism. Nat. Commun. 8, 15907.

Kalay, E., Yigit, G., Aslan, Y., Brown, K.E., Pohl, E., Bicknell, L.S., Kayserili, H., Li, Y., Tüysüz, B., Nürnberg, G., Kiess, W., Koegl, M., Baessmann, I., Buruk, K., Toraman, B., Kayipmaz, S., Kul, S., Ikbal, M., Turner, D.J., Taylor, M.S., Aerts, J., Scott, C., Milstein, K., Dollfus, H., Wieczorek, D., Brunner, H.G., Hurles, M., Jackson, A.P., Rauch, A., Nürnberg, P., Karagüzel, A., Wollnik, B., 2011. CEP152 is a genome maintenance protein disrupted in Seckel syndrome. Nat. Genet. 43, 23–26.

Kamimura, Y., Masumoto, H., Sugino, A., Araki, H., 1998. Sld2, which interacts with Dpb11 in Saccharomyces cerevisiae, is required for chromosomal DNA replication. Mol. Cell. Biol. 18, 6102–6109.

Kamimura, Y., Tak, Y.S., Sugino, A., Araki, H., 2001. Sld3, which interacts with Cdc45 (Sld4), functions for chromosomal DNA replication in saccharomyces cerevisiae. EMBO J. 20, 2097–2107.

Kang, H.Y., Choi, E., Bae, S.H., Lee, K.H., Gim, B.S., Kim, H.D., Park, C., MacNeill, S.A., Seo, Y.S., 2000. Genetic analyses of Schizosaccharomyces pombe dna2(+) reveal that dna2 plays an essential role in Okazaki fragment metabolism. Genetics 155, 1055–1067.

Kanke, M., Kodama, Y., Takahashi, T.S., Nakagawa, T., Masukata, H., 2012. Mcm10 plays an essential role in origin DNA unwinding after loading of the CMG components. EMBO J. 31, 2182–2194.

Karakas, B., Weeraratna, A.T., Abukhdeir, A.M., Konishi, H., Gustin, J.P., Vitolo, M.I., Bachman, K.E., Ben, H.P., 2007. P21 Gene Knock Down Does Not Identify Genetic Effectors Seen With Gene Knock Out. Cancer Biol. Ther. 6, 1025–1030.

Karanja, K.K., Cox, S.W., Duxin, J.P., Stewart, S.A., Campbell, J.L., 2012. DNA2 and EXO1 in replication-coupled, homology-directed repair and in the interplay between HDR and the

FA/BRCA network. Cell Cycle 11, 3983–3996.

Katoh, S., Hong, C., Tsunoda, Y., Murata, K., Takai, R., Minami, E., Yamazaki, T., Katoh, E., 2003. High precision NMR structure and function of the RING-H2 finger domain of EL5, a rice protein whose expression is increased upon exposure to pathogen-derived oligosaccharides. J. Biol. Chem. 278, 15341–15348.

Katsuno, Y., Suzuki, A., Sugimura, K., Okumura, K., Zineldeen, D.H., Shimada, M., Niida, H., Mizuno, T., Hanaoka, F., Nakanishi, M., 2009. Cyclin A-Cdk1 regulates the origin firing program in mammalian cells. PNAS 106, 3184–3189.

Kee, Y., D'Andrea, A.D., 2010. Expanded roles of the Fanconi anemia pathway in preserving genomic stability. Genes Dev. 24, 1680–1694.

Kelly, T., 2017. Historical Perspective of Eukaryotic DNA Replication. In: Masai, H., Foiani, M. (Eds.), DNA Replication. Advances in Experimental Medicine and Biology. Springer Nature Ltd., Singapore.

Kheradmand Kia, S., Verbeek, E., Engelen, E., Schot, R., Poot, R.A., De coo, I.F.M., Lequin, M.H., Poulton, C.J., Pourfarzad, F., Grosveld, F.G., Brehm, A., De Wit, M.C.Y., Oegema, R., Dobyns, W.B., Verheijen, F.W., Mancini, G.M.S., 2012. RTTN mutations link primary cilia function to organization of the human cerebral cortex. Am. J. Hum. Genet. 91, 533–540.

Khetarpal, P., Das, S., Panigrahi, I., Munshi, A., 2016. Primordial dwarfism: overview of clinical and genetic aspects. Mol. Genet. Genomics 291, 1–15.

Kim, H., D'Andrea, A.D., 2012. Regulation of DNA cross-link repair by the Fanconi anemia / BRCA pathway. Genes Dev. 26, 1393–1408.

Kim, H., Huang, J., Chen, J., 2007. CCDC98 is a BRCA1-BRCT domain–binding protein involved in the DNA damage response. Nat. Struct. Mol. Biol. 14, 710–715.

Kim, J.H., Kim, H.D., Ryu, G.H., Kim, D.H., Hurwitz, J., Seo, Y.S., 2006. Isolation of human Dna2 endonuclease and characterization of its enzymatic properties. Nucleic Acids Res. 34, 1854–1864.

Kim, J.M., Kee, Y., Gurtan, A., Andrea, A.D.D., 2008. Cell cycle–dependent chromatin loading of the Fanconi anemia core complex by FANCM/FAAP24. Blood 111, 5215–5222.

Kircher, M., Witten, D.M., Jain, P., O'Roak, B.J., Cooper, G.M., Shendure, J., 2014. A general framework for estimating the relative pathogenicity of human genetic variants. Nat. Genet. 46, 310–315.

Klingseisen, A., Jackson, A.P., 2011. Mechanisms and pathways of growth failure in primordial dwarfism. Genes Dev. 25, 2011–2024.

Knipscheer, P., Räschle, M., Smogorzewska, A., Enoiu, M., Vinh Ho, T., Schärer, O.D., Elledge, S.J., Walter, J.C., 2009. The Fanconi anemia pathway promotes replication-dependent DNA interstrand cross-link repair. Science 326, 1698–1701.

Kolas, N.K., Chapman, J.R., Nakada, S., Ylanko, J., Chahwan, R., Sweeney, F.D., Panier, S., Mendez, M., Wildenhain, J., Thomson, T.M., Pelletier, L., Jackson, S.P., Durocher, D., 2007. Orchestration of the DNA-damage response by the RNF8 ubiquitin ligase. Science 318, 1637–1640.

Koppolu, V., Raju, T.S., 2018. Zika virus outbreak: a review of neurological complications, diagnosis, and treatment options. J. Neurovirol. 24, 255–272.

Korbie, D.J., Mattick, J.S., 2008. Touchdown PCR for increased specificity and sensitivity in PCR amplification. Nat. Protoc. 3, 1452–1456.

Kost, T.A., Condreay, J.P., 1999. Recombinant baculoviruses as expression vectors for insect and mammalian cells. Curr. Opin. Biotechnol. 10, 428–433.

Kost, T.A., Condreay, J.P., Jarvis, D.L., 2005. Baculovirus as versatile vectors for protein expression in insect and mammalian cells. Nat. Biotechnol. 23, 567–575.

Kozlov, S. V., Graham, M.E., Jakob, B., Tobias, F., Kijas, A.W., Tanuji, M., Chen, P., Robinson, P.J.,

Taucher-Scholz, G., Suzuki, K., So, S., Chen, D., Lavin, M.F., 2011. Autophosphorylation and ATM activation: Additional sites add to the complexity. J. Biol. Chem. 286, 9107–9119.

Kratz, K., Schöpf, B., Kaden, S., Sendoel, A., Eberhard, R., Lademann, C., Cannavó, E., Sartori, A.A., Hengartner, M.O., Jiricny, J., 2010. Deficiency of FANCD2-Associated Nuclease KIAA1018/FAN1 Sensitizes Cells to Interstrand Crosslinking Agents. Cell 142, 77–88.

Krejci, L., Altmannova, V., Spirek, M., Zhao, X., 2012. Homologous recombination and its regulation. Nucleic Acids Res. 40, 5795–5818.

Kubota, T., Katou, Y., Nakato, R., Shirahige, K., Donaldson, A.D., 2015. Replication-Coupled PCNA Unloading by the Elg1 Complex Occurs Genome-wide and Requires Okazaki Fragment Ligation. Cell Rep. 12, 774–787.

Kubota, T., Nishimura, K., Kanemaki, M.T., Donaldson, A.D., 2013. The Elg1 Replication Factor C-like Complex Functions in PCNA Unloading during DNA Replication. Mol. Cell 50, 273–280.

Kuida, K., Haydar, T.F., Kuan, C.Y., Gu, Y., Taya, C., Karasuyama, H., Su, M.S.S., Rakic, P., Flavell, R.A., 1998. Reduced apoptosis and cytochrome C-mediated caspase activation in mice lacking Caspase 9. Cell 94, 325–337.

Kumagai, A., Lee, J., Yoo, H.Y., Dunphy, W.G., 2006. TopBP1 activates the ATR-ATRIP complex. Cell 124, 943–955.

Kumar, A., Girimaji, S.C., Duvvari, M.R., Blanton, S.H., 2008. Mutations in STIL, encoding a pericentriolar and centrosomal protein, cause primary microcephaly. Am. J. Hum. Genet. 84, 286–290.

Kunkel, T.A., Burgers, P.M., 2008. Dividing the workload at a eukaryotic replication fork. Trends Cell Biol. 18, 521–527.

Kurat, C.F., Yeeles, J.T.P., Patel, H., Early, A., Diffley, J.F.X., 2017. Chromatin Controls DNA Replication Origin Selection, Lagging-Strand Synthesis, and Replication Fork Rates. Mol. Cell 65, 117–130.

Labib, K., Diffley, J.F.X., Kearsey, S.E., 1999. G1-phase and B-type cyclins exclude the DNA-replication factor Mcm4 from the nucleus. Nat. Cell Biol. 1, 415–422.

Labib, K., Hodgson, B., 2007. Replication fork barriers: Pausing for a break or stalling for time? EMBO Rep. 8, 346–353.

Landry, J.J.M., Pyl, P.T., Rausch, T., Zichner, T., Tekkedil, M.M., Stütz, A.M., Jauch, A., Aiyar, R.S., Pau, G., Delhomme, N., Gagneur, J., Korbel, J.O., Huber, W., Steinmetz, L.M., 2013. The Genomic and Transcriptomic Landscape of a HeLa Cell Line. G3 3, 1213–1224.

Langevin, F., Crossan, G.P., Rosado, I. V., Arends, M.J., Patel, K.J., 2011. Fancd2 counteracts the toxic effects of naturally produced aldehydes in mice. Nature 475, 53–59.

Langston, L.D., O'Donnell, M., 2008. DNA polymerase δ is highly processive with proliferating cell nuclear antigen and undergoes collision release upon completing DNA. J. Biol. Chem. 283, 29522–29531.

Lavin, M.F., 2008. Ataxia-telangiectasia: From a rare disorder to a paradigm for cell signalling and cancer. Nat. Rev. Mol. Cell Biol. 9, 759–769.

Lawley, P.D., Phillips, D.H., 1996. DNA adducts from chemotherapeutic agents. Mutat. Res. 355, 13–40.

Leal, G.F., Roberts, E., Silva, E.O., Costa, S.M.R., Hampshire, D.J., Woods, C.G., 2003. A novel locus for autosomal recessive primary microcephaly (MCPH6) maps to 13q12.2. J. Med. Genet. 40, 540–542.

Lee, B.L., Singh, A., Mark Glover, J.N., Hendzel, M.J., Spyracopoulos, L., 2017. Molecular Basis for K63-Linked Ubiquitination Processes in Double-Strand DNA Break Repair: A Focus on Kinetics and Dynamics. J. Mol. Biol. 429, 3409–3429.

Lee, D., Pan, Y., Kanner, S., Sung, P., Borowiec, J.A., Chowdhury, D., 2010. A PP4 phosphatase complex dephosphorylates RPA2 to facilitate DNA repair via homologous recombination. Nat. Struct. Mol. Biol. 17, 365–372.

Lee, J., Collins, K.M., Brown, A.L., Lee, C., Chung, J.H., 2000. hCds-mediated phosphorylation of BRCA1 regulates the DNA damage response. Nature 404, 201–204.

Lee, J., Dunphy, W.G., 2013. The Mre11-Rad50-Nbs1 (MRN) complex has a specific role in the activation of Chk1 in response to stalled replication forks. Mol. Biol. Cell 24, 1343–1353.

Lee, K.Y., Fu, H., Aladjem, M.I., Myung, K., 2013. ATAD5 regulates the lifespan of DNA replication factories by modulating PCNA level on the chromatin. J. Cell Biol. 200, 31–44.

Lee, S.Y., Lee, S.Y., Choi, Y., 1997. TRAF-interacting Protein (TRIP): A Novel Component of the Tumor Necrosis Factor Receptor (TNFR)- and CD30-TRAF Signaling Complexes That Inhibits TRAF2-mediated NF-κB Activation. J. Exp. Med. 185, 1275–1286.

Lee, Y.C., Zhou, Q., Chen, J., Yuan, J., 2016. RPA-Binding Protein ETAA1 Is an ATR Activator Involved in DNA Replication Stress Response. Curr. Biol. 26, 3257–3268.

Lehmann, A.R., McGibbon, D., Stefanini, M., 2011. Xeroderma pigmentosum. Orphanet J. Rare Dis. 6, 70.

Lek, M., Karczewski, K.J., Minikel, E. V., Samocha, K.E., Banks, E., Fennell, T., O'Donnell-Luria, A.H., Ware, J.S., Hill, A.J., Cummings, B.B., Tukiainen, T., Birnbaum, D.P., Kosmicki, J.A., Duncan, L.E., Estrada, K., Zhao, F., Zou, J., Pierce-Hoffman, E., Berghout, J., Cooper, D.N., Deflaux, N., DePristo, M., Do, R., Flannick, J., Fromer, M., Gauthier, L., Goldstein, J., Gupta, N., Howrigan, D., Kiezun, A., Kurki, M.I., Moonshine, A.L., Natarajan, P., Orozco, L., Peloso, G.M., Poplin, R., Rivas, M.A., Ruano-Rubio, V., Rose, S.A., Ruderfer, D.M., Shakir, K., Stenson, P.D., Stevens, C., Thomas, B.P., Tiao, G., Tusie-Luna, M.T., Weisburd, B., Won, H.H., Yu, D., Altshuler, D.M., Ardissino, D., Boehnke, M., Danesh, J., Donnelly, S., Elosua, R., Florez, J.C., Gabriel, S.B., Getz, G., Glatt, S.J., Hultman, C.M., Kathiresan, S., Laakso, M., McCarroll, S., McCarthy, M.I., McGovern, D., McPherson, R., Neale, B.M., Palotie, A., Purcell, S.M., Saleheen, D., Scharf, J.M., Sklar, P., Sullivan, P.F., Tuomilehto, J., Tsuang, M.T., Watkins, H.C., Wilson, J.G., Daly, M.J., MacArthur, D.G., 2016. Analysis of protein-coding genetic variation in 60,706 humans. Nature 536, 285–291.

Leman, A.R., Noguchi, E., 2013. The replication fork: Understanding the eukaryotic replication machinery and the challenges to genome duplication. Genes (Basel) 4, 1–32.

Leung, K.H.T., El Hassan, M.A., Bremner, R., 2013. A rapid and efficient method to purify proteins at replication forks under native conditions. Biotechniques 55, 204–206.

Levikova, M., Klaue, D., Seidel, R., Cejka, P., 2013. Nuclease activity of Saccharomyces cerevisiae Dna2 inhibits its potent DNA helicase activity. PNAS E1992–E2001.

Levikova, M., Pinto, C., Cejka, P., 2017. The motor activity of DNA2 functions as an ssDNA translocase to promote DNA end resection. Genes Dev. 31, 493–502.

Li, W., Ye, Y., 2008. Polyubiquitin chains: Functions, structures, and mechanisms. Cell. Mol. Life Sci. 65, 2397–2406.

Lieber, M.R., 2010. The Mechanism of Double-Strand DNA Break Repair by the Nonhomologous DNA End Joining Pathway. Annu. Rev. Biochem. 79, 181–211.

Lim, D.-S., Vogel, H., Willerford, D.M., Sands, A.T., Platt, K.A., Hasty, P., 2000. Analysis of ku80-Mutant Mice and Cells with Deficient Levels of p53. Mol. Cell. Biol. 20, 3772–3780.

Limoli, C.L., Giedzinski, E., Bonner, W.M., Cleaver, J.E., 2002. UV-induced replication arrest in the xeroderma pigmentosum variant leads to DNA double-strand breaks, gH2AX formation, and Mre11 relocalization. PNAS 99, 233–238.

Lin, W., Sampathi, S., Dai, H., Liu, C., Zhou, M., Hu, J., Huang, Q., Campbell, J., Shin-Ya, K., Zheng, L., Chai, W., Shen, B., 2013. Mammalian DNA2 helicase/nuclease cleaves G-quadruplex DNA and is required for telomere integrity. EMBO J. 32, 1425–1439.

Lindsey-Boltz, L.A., Kemp, M.G., Capp, C., Sancar, A., 2015. RHINO forms a stoichiometric complex with the 9-1-1 checkpoint clamp and mediates ATR-Chk1 signaling. Cell Cycle 14, 99–108.

Liu, J., Xu, L., Zhong, J., Liao, J., Li, J., Xu, X., 2012. Protein phosphatase PP4 is involved in NHEJ-mediated repair of DNA double-strand breaks. Cell Cycle 11, 2643–2649.

Liu, L.F., Duann, P., Lin, C.-T., D'Arpa, P., Wu, J., 2000. Mechanism of Action of Camptothecin. Ann. N. Y. Acad. Sci. 922, 1–10.

Liu, Q., Guntuku, S., Cui, X.S., Matsuoka, S., Cortez, D., Tamai, K., Luo, G., Carattini-Rivera, S., DeMayo, F., Bradley, A., Donehower, L.A., Elledge, S.J., 2000. Chk1 is an essential kinase that is regulated by Atr and required for the G2/M DNA damage checkpoint. Genes Dev. 14, 1448–1459.

Liu, S., Opiyo, S.O., Manthey, K., Glanzer, J.G., Ashley, A.K., Amerin, C., Troksa, K., Shrivastav, M., Nickoloff, J.A., Oakley, G.G., 2012. Distinct roles for DNA-PK, ATM and ATR in RPA phosphorylation and checkpoint activation in response to replication stress. Nucleic Acids Res. 40, 10780–10794.

Liu, S., Shiotani, B., Lahiri, M., Maréchal, A., Tse, A., Chung, C., Leung, Y., Glover, J.N.M., Yang, X.H., Zou, L., 2011. ATR autophosphorylation as a molecular switch for checkpoint activation. Mol. Cell 43, 192–202.

Lizarraga, S.B., Margossian, S.P., Harris, M.H., Campagna, D.R., Han, A.P., Blevins, S., Mudbhary, R., Barker, J.E., Walsh, C.A., Fleming, M.D., 2010. Cdk5rap2 regulates centrosome function and chromosome segregation in neuronal progenitors. Development 137, 1907–1917.

Long, D.T., Joukov, V., Budzowska, M., Walter, J.C., 2014. BRCA1 promotes unloading of the CMG Helicase from a stalled DNA replication fork. Mol. Cell 56, 174–185.

Long, D.T., Räschle, M., Joukov, V., Walter, J.C., 2011. Mechanism of RAD51-Dependent DNA Interstrand Cross-Link Repair. Science 333, 84–88.

Longerich, S., Kwon, Y., Tsai, M.S., Hlaing, A.S., Kupfer, G.M., Sung, P., 2014. Regulation of FANCD2 and FANCI monoubiquitination by their interaction and by DNA. Nucleic Acids Res. 42, 5657–5670.

Longhese, M.P., Bonetti, D., Manfrini, N., Clerici, M., 2010. Mechanisms and regulation of DNA end resection. EMBO J. 29, 2864–2874.

Lõoke, M., Maloney, M.F., Bell, S.P., 2017. Mcm10 regulates DNA replication elongation by stimulating the CMG replicative helicase. Genes Dev. 31, 291–305.

Lopes, M., Cotta-Ramusino, C., Pellicioli, A., Liberi, G., Plevani, P., Muzi-Falconi, M., Newlon, C.S., Foiani, M., 2001. The DNA replication checkpoint response stabilizes stalled replication forks. Nature 412, 557–561.

Lopes, M., Foiani, M., Sogo, J.M., 2006. Multiple mechanisms control chromosome integrity after replication fork uncoupling and restart at irreparable UV lesions. Mol. Cell 21, 15–27.

López-Contreras, A.J., Fernandez-Capetillo, O., 2010. The ATR barrier to replication-born DNA damage. DNA Repair (Amst) 9, 1249–1255.

Lou, Z., Minter-Dykhouse, K., Franco, S., Gostissa, M., Rivera, M.A., Celeste, A., Manis, J.P., Van Deursen, J., Nussenzweig, A., Paull, T.T., Alt, F.W., Chen, J., 2006. MDC1 maintains genomic stability by participating in the amplification of ATM-dependent DNA damage signals. Mol. Cell 21, 187–200.

Lumpkin, R.J., Gu, H., Zhu, Y., Leonard, M., Ahmad, A.S., Clauser, K.R., Meyer, J.G., Bennett, E.J., Komives, E.A., 2017. Site-specific identification and quantitation of endogenous SUMO modifications under native conditions. Nat. Commun. 8, 1171.

Luo, K., Yuans, J., Lous, Z., 2011. Oligomerization of MDC1 protein is important for proper DNA damage response. J. Biol. Chem. 286, 28192–28199.

Magana-Schwencke, N., Henriques, J.A., Chanet, R., Moustacchi, E., 1982. The fate of 8-methoxypsoralen photoinduced crosslinks in nuclear and mitochondrial yeast DNA: comparison of wild-type and repair-deficient strains. PNAS 79, 1722–1726.

Mailand, N., Bekker-Jensen, S., Faustrup, H., Melander, F., Bartek, J., Lukas, C., Lukas, J., 2007. RNF8 Ubiquitylates Histones at DNA Double-Strand Breaks and Promotes Assembly of Repair Proteins. Cell 131, 887–900.

Mailand, N., Falck, J., Lukas, C., Syljuåsen, R.G., Welcker, M., Bartek, J., Lukas, J., 2000. Rapid

destruction of human Cdc25A in response to DNA damage. Science 288, 1425–1429.

Mailand, N., Podtelejnikov, A. V., Groth, A., Mann, M., Bartek, J., Lukas, J., 2002. Regulation of G2/M events by Cdc25A through phosphorylation-dependent modulation of its stability. EMBO J. 21, 5911–5920.

Majewski, F., Goecke, T., Opitz, J.M., 1982. Studies of microcephalic primordial dwarfism I: Approach to a delineation of the Seckel syndrome. Am. J. Med. Genet. 12, 7–21.

Malatesta, P., Hartfuss, E., Götz, M., 2000. Isolation of radial glial cells by fluorescent-activated cell sorting reveals a neuronal lineage. Development 127, 5253–5263.

Mali, P., Yang, L., Esvelt, K.M., Aach, J., Guell, M., DiCarlo, J.E., Norville, J.E., Church, G.M., 2013. RNA-Guided Human Genome Engineering via Cas9. Science 339, 823–826.

Maréchal, A., Zou, L., 2013. DNA Damage Sensing by the ATM and ATR Kinases. Cold Spring Harb. Perspect. Biol. 5, a012716.

Maric, M., Maculins, T., De Piccoli, G., Labib, K., 2014. Cdc48 and a ubiquitin ligase drive disassembly of the CMG helicase at the end of DNA replication. Science 346, 1253596.

Marjanović, M., Sánchez-Huertas, C., Terré, B., Gómez, R., Scheel, J.F., Pacheco, S., Knobel, P.A., Martínez-Marchal, A., Aivio, S., Palenzuela, L., Wolfrum, U., McKinnon, P.J., Suja, J.A., Roig, I., Costanzo, V., Lüders, J., Stracker, T.H., 2015. CEP63 deficiency promotes p53-dependent microcephaly and reveals a role for the centrosome in meiotic recombination. Nat. Commun. 6, 7676.

Markiewicz-Potoczny, M., Lisby, M., Lydall, D., 2018. A critical role for Dna2 at unwound telomeres. Genetics 209, 129–141.

Martin, C.A., Ahmad, I., Klingseisen, A., Hussain, M.S., Bicknell, L.S., Leitch, A., Nürnberg, G., Toliat, M.R., Murray, J.E., Hunt, D., Khan, F., Ali, Z., Tinschert, S., Ding, J., Keith, C., Harley, M.E., Heyn, P., Müller, R., Hoffmann, I., Daire, V.C., Dollfus, H., Dupuis, L., Bashamboo, A., McElreavey, K., Kariminejad, A., Mendoza-Londono, R., Moore, A.T., Saggar, A., Schlechter, C., Weleber, R., Thiele, H., Altmüller, J., Höhne, W., Hurles, M.E., Noegel, A.A., Baig, S.M., Nürnberg, P., Jackson, A.P., 2014. Mutations in PLK4, encoding a master regulator of centriole biogenesis, cause microcephaly, growth failure and retinopathy. Nat. Genet. 46, 1283–1292.

Martin, C.A., Murray, J.E., Carroll, P., Leitch, A., Mackenzie, K.J., Halachev, M., Fetit, A.E., Keith, C., Bicknell, L.S., Fluteau, A., Gautier, P., Hall, E.A., Joss, S., Soares, G., Silva, J., Bober, M.B., Duker, A., Wise, C.A., Quigley, A.J., Phadke, S.R., Wood, A.J., Vagnarelli, P., Jackson, A.P., 2016. Mutations in genes encoding condensin complex proteins cause microcephaly through decatenation failure at mitosis. Genes Dev. 30, 2158–2172.

Masuda-Sasa, T., Imamura, O., Campbell, J.L., 2006. Biochemical analysis of human Dna2. Nucleic Acids Res. 34, 1865–1875.

Masuda-Sasa, T., Polaczek, P., Peng, X.P., Chen, L., Campbell, J.L., 2008. Processing of G4 DNA by Dna2 helicase/nuclease and replication protein A (RPA) provides insights into the mechanism of Dna2/RPA substrate recognition. J. Biol. Chem. 283, 24359–24373.

Masutani, C., Kusumoto, R., Yamada, A., Dohmae, N., Yokol, M., Yuasa, M., Araki, M., Iwai, S., Takio, K., Hanaoka, F., 1999. The XPV (xeroderma pigmentosum variant) gene encodes human DNA polymerase η. Nature 399, 700–704.

Matsuoka, S., Ballif, B.A., Smogorzewska, A., Mcdonald Iii, E.R., Hurov, K.E., Luo, J., Bakalarski, C.E., Zhao, Z., Solimini, N., Lerenthal, Y., Shiloh, Y., Gygi, S.P., Elledge, S.J., 2007. Supporting Online Material for ATM and ATR Substrate Analysis Reveals Extensive Protein Network Responsive to DNA Damage. Science 316, 1160–1167.

Mazouzi, A., Velimezi, G., Loizou, J.I., 2014. DNA replication stress: Causes, resolution and disease. Exp. Cell Res. 329, 85–93.

McGarry, T.J., Kirschner, M.W., 1998. Geminin, an inhibitor of DNA replication, is degraded during mitosis. Cell 93, 1043–1053.

McGowan, C.H., 2002. Checking in on Cds1 (Chk2): A checkpoint kinase and tumor suppressor.

BioEssays 24, 502–511.

McGuffee, S.R., Smith, D.J., Whitehouse, I., 2013. Quantitative, genome-wide analysis of eukaryotic replicatio initiation and temrination. Mol. Cell 50, 123–135.

McIntyre, R.E., Lakshminarasimhan Chavali, P., Ismail, O., Carragher, D.M., Sanchez-Andrade, G., Forment, J. V., Fu, B., Del Castillo Velasco-Herrera, M., Edwards, A., van der Weyden, L., Yang, F., Ramirez-Solis, R., Estabel, J., Gallagher, F.A., Logan, D.W., Arends, M.J., Tsang, S.H., Mahajan, V.B., Scudamore, C.L., White, J.K., Jackson, S.P., Gergely, F., Adams, D.J., 2012. Disruption of Mouse Cenpj, a Regulator of Centriole Biogenesis, Phenocopies Seckel Syndrome. PLoS Genet. 8, e1003022.

McKinnon, P.J., 2017. Genome integrity and disease prevention in the nervous system. Genes Dev. 31, 1180–1194.

Merfeld, E., Ben-Avi, L., Kennon, M., Cerveny, K.L., 2017. Potential mechanisms of Zika-linked microcephaly. Wiley Interdiscip. Rev. Dev. Biol. 6, e273.

Merico, D., Roifman, M., Braunschweig, U., Yuen, R.K.C., Alexandrova, R., Bates, A., Reid, B., Nalpathamkalam, T., Wang, Z., Thiruvahindrapuram, B., Gray, P., Kakakios, A., Peake, J., Hogarth, S., Manson, D., Buncic, R., Pereira, S.L., Herbrick, J.A., Blencowe, B.J., Roifman, C.M., Scherer, S.W., 2015. Compound heterozygous mutations in the noncoding RNU4ATAC cause Roifman Syndrome by disrupting minor intron splicing. Nat. Commun. 6, 8718.

Merkle, J.A., Rickmyre, J.L., Garg, A., Loggins, E.B., Jodoin, J.N., Lee, E., Wu, L.P., Lee, L.A., 2009. no poles encodes a predicted E3 ubiquitin ligase required for early embryonic development of Drosophila. Development 136, 449–459.

Merlet, J., Burger, J., Tavernier, N., Richaudeau, B., Gomes, J.-E., Pintard, L., 2010. The CRL2LRR-1 ubiquitin ligase regulates cell cycle progression during C. elegans development. Development 137, 3857–3866.

Michl, J., Zimmer, J., Tarsounas, M., 2016. Interplay between Fanconi anemia and homologous recombination pathways in genome integrity. EMBO J. 35, 909–923.

Mihindukulasuriya, K.A., Zhou, G., Qin, J., Tan, T.H., 2004. Protein phosphatase 4 interacts with and down-regulates insulin receptor substrate 4 following tumor necrosis factor-α stimulation. J. Biol. Chem. 279, 46588–46594.

Miller, A.S., Daley, J.M., Pham, N.T., Niu, H., Xue, X., Ira, G., Sung, P., 2017. A novel role of the Dna2 translocase function in DNA break resection. Genes Dev. 31, 503–510.

Milner, R.D.G., Khallouf, K.A., Gibson, R., Hajianpour, A., Mathew, C.G., 1993. A new autosomal recessive anomaly mimicking Fanconi's anaemia phenotype. Arch. Dis. Child. 68, 101–103.

Mimitou, E.P., Symington, L.S., 2011. DNA end resection - unraveling the tail. DNA Repair (Amst) 10, 344–348.

Miotto, B., Ji, Z., Struhl, K., 2016. Selectivity of ORC binding sites and the relation to replication timing, fragile sites, and deletions in cancers. PNAS 113, E4810–E4819.

Miotto, B., Struhl, K., 2010. HBO1 Histone Acetylase Activity Is Essential for DNA Replication Licensing and Inhibited by Geminin. Mol. Cell 37, 57–66.

Mirman, Z., Lottersberger, F., Takai, H., Kibe, T., Gong, Y., Takai, K., Bianchi, A., Zimmermann, M., Durocher, D., de Lange, T., 2018. 53BP1–RIF1–shieldin counteracts DSB resection through CST- and Polα-dependent fill-in. Nature 560, 112–116.

Moldovan, G.-L., D'Andrea, A.D., 2009. How the Fanconi Anemia Pathway Guards the Genome. Annu. Rev. Genet. 43, 223–249.

Moldovan, G.-L., Pfander, B., Jentsch, S., 2007. PCNA, the Maestro of the Replication Fork. Cell 129, 665–679.

Montagutelli, X., 2000. Effect of the genetic background on the phenotype of mouse mutations. J. Am. Soc. Nephrol. 11, S101–S105.

Moreno, S.P., Bailey, R., Campion, N., Herron, S., Gambus, A., 2014. Polyubiquitylation drives

replisome disassembly at the termination of DNA replication. Science 346, 477–481.

Morgens, D.W., Deans, R.M., Li, A., Bassik, M.C., 2016. Systematic comparison of CRISPR-Cas9 and RNAi screens for Essential Genes. Nat. Biotechnol. 34, 634–636.

Moyal, L., Lerenthal, Y., Mass, G., So, S., Eppink, B., Chung, Y.M., Shalev, G., Shema, E., Shkedy, D., Smorodinsky, N.I., Vliet, N. Van, Kuster, B., Mann, M., Dahm-daphi, J., Kanaar, R., Hu, M.C., Chen, D.J., Oren, M., Shiloh, Y., 2011. Requirement of ATM-Dependent Monoubiquitylation of Histone H2B for Timely Repair of DNA Double-Strand Breaks. Mol. Cell 41, 529–542.

Moynihan, L., Jackson, A.P., Roberts, E., Karbani, G., Lewis, I., Corry, P., Turner, G., Mueller, R.F., Lench, N.J., Woods, C.G., 2000. A Third Novel Locus for Primary Autosomal Recessive Microcephaly Maps to Chromosome 9q34. Am. J. Hum. Genet. 66, 724–727.

Munoz, I.M., Jowsey, P.A., Toth, R., Rouse, J., 2007. Phospho-epitope binding by the BRCT domains of hPTIP controls multiple aspects of the cellular response to DNA damage. Nucleic Acids Res. 35, 5312–5322.

Murai, J., Huang, S.N., Das, B.B., Renaud, A., Zhang, Y., Doroshow, J.H., Ji, J., Takeda, S., Pommier, Y., 2012. Differential trapping of PARP1 and PARP2 by clinical PARP inhibitors. Cancer Res. 72, 5588–5599.

Murfuni, I., Basile, G., Subramanyam, S., Malacaria, E., Bignami, M., Spies, M., Franchitto, A., Pichierri, P., 2013. Survival of the Replication Checkpoint Deficient Cells Requires MUS81-RAD52 Function. PLoS Genet. 9, e1003910.

Murga, M., Bunting, S., Montaña, M.F., Soria, R., Mulero, F., Cañamero, M., Lee, Y., McKinnon, P.J., Nussenzweig, A., Fernandez-Capetillo, O., 2009. A mouse model of the ATR-Seckel Syndrome reveals that replicative stress during embryogenesis limits mammalian lifespan. Nat. Genet. 41, 891–898.

Murray, J.E., Bicknell, L.S., Yigit, G., Duker, A.L., van Kogelenberg, M., Haghayegh, S., Wieczorek, D., Kayserili, H., Albert, M.H., Wise, C.A., Brandon, J., Kleefstra, T., Warris, A., van der Flier, M., Bamforth, J.S., Doonanco, K., Adès, L., Ma, A., Field, M., Johnson, D., Shackley, F., Firth, H., Woods, C.G., Nürnberg, P., Gatti, R.A., Hurles, M., Bober, M.B., Wollnik, B., Jackson, A.P., 2014. Extreme Growth Failure is a Common Presentation of Ligase IV Deficiency. Hum. Mutat. 35, 76–85.

Murray, J.E., Van Der Burg, M., Ijspeert, H., Carroll, P., Wu, Q., Ochi, T., Leitch, A., Miller, E.S., Kysela, B., Jawad, A., Bottani, A., Brancati, F., Cappa, M., Cormier-Daire, V., Deshpande, C., Faqeih, E.A., Graham, G.E., Ranza, E., Blundell, T.L., Jackson, A.P., Stewart, G.S., Bicknell, L.S., 2015. Mutations in the NHEJ component XRCC4 cause primordial dwarfism. Am. J. Hum. Genet. 96, 412–424.

Naim, V., Rosselli, F., 2009. The FANC pathway and BLM collaborate during mitosis to prevent micro-nucleation and chromosome abnormalities. Nat. Cell Biol. 11, 761–768.

Nakada, S., Chen, G.I., Gingras, A.C., Durocher, D., 2008. PP4 is a γH2AX phosphatase required for recovery from the DNA damage checkpoint. EMBO Rep. 9, 1019–1026.

Nam, E. a., Cortez, D., 2013. ATR signaling: more than meeting at the fork Edward. Biochem J 436, 527–536.

Neelsen, K.J., Lopes, M., 2015. Replication fork reversal in eukaryotes: From dead end to dynamic response. Nat. Rev. Mol. Cell Biol. 16, 207–220.

Newell, A.E.H., Akkari, Y.M.N., Torimaru, Y., Rosenthal, A., Reifsteck, C.A., Cox, B., Grompe, M., Olson, S.B., 2004. Interstrand crosslink-induced radials form between non-homologous chromosomes, but are absent in sex chromosomes. DNA Repair (Amst) 3, 535–542.

Nguyen, V.Q., Co, C., Irie, K., Li, J.J., 2000. Clb/Cdc28 kinases promote nuclear export of the replication initiator proteins Mcm2-7. Curr. Biol. 10, 195–205.

Nguyen, V.Q., Co, C., Li, J.J., 2001. Cyclin-dependent kinases prevent DNA re-replication through multiple mechanisms. Nature 411, 1068–1073.

Nimonkar, A. V., Genschel, J., Kinoshita, E., Polaczek, P., Campbell, J.L., Wyman, C., Modrich, P.,

Kowalczykowski, S.C., 2011. BLM-DNA2-RPA-MRN and EXO1-BLM-RPA-MRN constitute two DNA end resection machineries for human DNA break repair. Genes Dev. 25, 350–362.

Nishimasu, H., Ran, F.A., Hsu, P.D., Konermann, S., Shehata, S.I., Dohmae, N., Ishitani, R., Zhang, F., Nureki, O., 2014. Crystal structure of Cas9 in complex with guide RNA and target DNA. Cell 156, 935–949.

Niu, H., Chung, W., Zhu, Z., Kwon, Y., Zhao, W., Chi, P., Prakash, R., Seong, C., Liu, D., Lu, L., Ira, G.G., Sung, P., 2010. Mechanism of the ATP-dependent DNA End Resection Machinery from S. cerevisiae. Nature 467, 108–111.

Niu, H., Raynard, S., Sung, P., 2009. Multiplicity of DNA end resection machineries in chromosome break repair. Genes Dev. 23, 1481–1486.

Noordermeer, S.M., Adam, S., Setiaputra, D., Barazas, M., Pettitt, S.J., Ling, A.K., Olivieri, M., Álvarez-Quilón, A., Moatti, N., Zimmermann, M., Annunziato, S., Krastev, D.B., Song, F., Brandsma, I., Frankum, J., Brough, R., Sherker, A., Landry, S., Szilard, R.K., Munro, M.M., McEwan, A., Goullet de Rugy, T., Lin, Z.-Y., Hart, T., Moffat, J., Gingras, A.-C., Martin, A., van Attikum, H., Jonkers, J., Lord, C.J., Rottenberg, S., Durocher, D., 2018. The shieldin complex mediates 53BP1-dependent DNA repair. Nature 560, 117–121.

O'Driscoll, M., Ruiz-Perez, V.L., Woods, C.G., Jeggo, P.A., Goodship, J.A., 2003. A splicing mutation affecting expression of ataxia-telangiectasia and Rad3-related protein (ATR) results in Seckel syndrome. Nat. Genet. 33, 497–501.

Ogi, T., Walker, S., Stiff, T., Hobson, E., Limsirichaikul, S., Carpenter, G., Prescott, K., Suri, M., Byrd, P.J., Matsuse, M., Mitsutake, N., Nakazawa, Y., Vasudevan, P., Barrow, M., Stewart, G.S., Taylor, A.M.R., O'Driscoll, M., Jeggo, P.A., 2012. Identification of the First ATRIP-Deficient Patient and Novel Mutations in ATR Define a Clinical Spectrum for ATR-ATRIP Seckel Syndrome. PLoS Genet. 8, e1002945.

Oldham, S., Bohni, R., Stocker, H., Brogiolo, W., Hafen, E., 2000. Genetic control of size in Drosophila. Philos. Trans. R. Soc. B Biol. Sci. 355, 945–952.

Osborn, A.J., Elledge, S.J.S.J., Zou, L., 2002. Checking on the fork: the DNA-replication stress-response pathway. Trends Cell Biol. 12, 509–516.

Pacek, M., Walter, J.C., 2004. A requirement for MCM7 and Cdc45 in chromosome unwinding during eukaryotic DNA replication. EMBO J. 23, 3667–3676.

Palovcak, A., Liu, W., Yuan, F., Zhang, Y., 2017. Maintenance of genome stability by Fanconi anemia proteins. Cell Biosci. 7, 8.

Panier, S., Boulton, S.J., 2014. Double-strand break repair: 53BP1 comes into focus. Nat. Rev. Mol. Cell Biol. 15, 7–18.

Pardo, B., Gómez-González, B., Aguilera, A., 2009. DNA double-strand break repair: How to fix a broken relationship. Cell. Mol. Life Sci. 66, 1039–1056.

Parenteau, J., Wellinger, R.J., 1999. Accumulation of single-stranded DNA and destabilization of telomeric repeats in yeast mutant strains carrying a deletion of RAD27. Mol. Cell. Biol. 19, 4143–4152.

Park, E.S., Choi, S., Kim, J.M., Jeong, Y., Choe, J., Park, C.S., Choi, Y., Rho, J., 2007. Early embryonic lethality caused by targeted disruption of the TRAF-interacting protein (TRIP) gene. Biochem. Biophys. Res. Commun. 363, 971–977.

Park, E.S., Choi, S., Shin, B., Yu, J., Yu, J., Hwang, J.M., Yun, H., Chung, Y.H., Choi, J.S., Choi, Y., Rho, J., 2015. Tumor necrosis factor (TNF) receptor-associated factor (TRAF)-interacting protein (TRIP) negatively regulates the TRAF2 ubiquitin-dependent pathway by suppressing the TRAF2-sphingosine 1-phosphate (S1P) interaction. J. Biol. Chem. 290, 9660–9673.

Park, I.S., Jo, K.S., Won, H.S., Kim, H., 2015. Dimerization of TRAF-interacting protein (TRAIP) regulates the mitotic progression. Biochem. Biophys. Res. Commun. 463, 864–869.

Parker, M.W., Botchan, M.R., Berger, J.M., 2017. Mechanisms and regulation of DNA replication initiation in eukaryotes. Crit. Rev. Biochem. Mol. Biol. 52, 107–144.

Parrilla-Castellar, E.R., Arlander, S.J.H., Karnitz, L., 2004. Dial 9-1-1 for DNA damage: The Rad9-Hus1-Rad1 (9-1-1) clamp complex. DNA Repair (Amst) 3, 1009–1014.

Patil, M., Pabla, N., Dong, Z., 2013. Checkpoint kinase 1 in DNA damage response and cell cycle regulation. Cell. Mol. Life Sci. 70, 4009–4021.

Pawłowska, E., Szczepanska, J., Blasiak, J., 2017. DNA2—An important player in DNA damage response or just another DNA maintenance protein? Int. J. Mol. Sci. 18, 1–20.

Payne, F., Colnaghi, R., Rocha, N., Seth, A., Harris, J., Carpenter, G., Bottomley, W.E., Wheeler, E., Wong, S., Saudek, V., Savage, D., O'Rahilly, S., Carel, J.C., Barroso, I., O'Driscoll, M., Semple, R., 2014. Hypomorphism in human NSMCE2 linked to primordial dwarfism and insulin resistance. J. Clin. Invest. 124, 4028–4038.

Peng, G., Dai, H., Zhang, W., Hsieh, H.-J., Pan, M.-R., Park, Y.-Y., Tsai, Y.-L., Bedrosian, I., Lee, J.-S., Ira, G., Lin, S.-Y., 2012. Human Nuclease/helicase DNA2 Alleviates Replication Stress by Promoting DNA End Resection. Cancer Res. 72, 2802–2813.

Perlman, R.L., 2016. Mouse Models of Human Disease: An Evolutionary Perspective. Evol. Med. Public Heal. 170–176.

Petermann, E., Helleday, T., 2010. Pathways of mammalian replication fork restart. Nat. Rev. Mol. Cell Biol. 11, 683–687.

Petermann, E., Orta, M.L., Issaeva, N., Schultz, N., Helleday, T., 2010. Hydroxyurea-Stalled Replication Forks Become Progressively Inactivated and Require Two Different RAD51-Mediated Pathways for Restart and Repair. Mol. Cell 37, 492–502.

Petkovic, M., Dietschy, T., Freire, R., Jiao, R., Stagljar, I., 2005. The human Rothmund-Thomson syndrome gene product, RECQL4, localizes to distinct nuclear foci that coincide with proteins involved in the maintenance of genome stability. J. Cell Sci. 118, 4261–4269.

Phowthongkum, P., Sun, A., 2017. Novel truncating variant in DNA2-related congenital onset myopathy and ptosis suggests genotype–phenotype correlation. Neuromuscul. Disord. 27, 616–618.

Pinto, C., Kasaciunaite, K., Seidel, R., Cejka, P., 2016. Human DNA2 possesses a cryptic DNA unwinding activity that functionally integrates with BLM or WRN helicases. Elife 5, 1–24.

Pires, D.E.V., Blundell, T.L., Ascher, D.B., 2016. MCSM-lig: Quantifying the effects of mutations on protein-small molecule affinity in genetic disease and emergence of drug resistance. Sci. Rep. 6, 29575.

Pitcher, R.S., Wilson, T.E., Doherty, A.J., 2005. New insights into NHEJ repair processes in prokaryotes. Cell Cycle 4, 675–678.

Plo, I., Liao, Z.Y., Barceló, J.M., Kohlhagen, G., Caldecott, K.W., Weinfeld, M., Pommier, Y., 2003. Association of XRCC1 and tyrosyl DNA phosphodiesterase (Tdp1) for the repair of topoisomerase I-mediated DNA lesions. DNA Repair (Amst) 2, 1087–1100.

Podhorecka, M., Skladanowski, A., Bozko, P., 2010. H2AX phosphorylation: Its role in DNA damage response and cancer therapy. J. Nucleic Acids 920161.

Pommier, Y., 2004. Camptothecins and topoisomerase I: a foot in the door. Targeting the genome beyond topoisomerase I with camptothecins and novel anticancer drugs: importance of DNA replication, repair and cell cycle checkpoints. Curr. Med. Chem. Anti-cancer agents 4, 429–434.

Pommier, Y., 2006. Topoisomerase I inhibitors: Camptothecins and beyond. Nat. Rev. Cancer 6, 789–802.

Pommier, Y., 2013. Drugging Topoisomerases: Lessons and Challenges. ACS Chem. Biol. 8, 82–95.

Pommier, Y., Marchand, C., 2012. Interfacial inhibitors: Targeting macromolecular complexes. Nat. Rev. Drug Discov. 11, 25–36.

Pommier, Y., Pourquier, P., Fan, Y., Strumberg, D., 1998. Mechanism of action of eukaryotic topoisomerase I and drugs targeted to the enzyme. Biochim. Biophys. Acta - Gene Struct. Expr. 1400, 83–106.

Pontel, L.B., Rosado, I. V., Burgos-Barragan, G., Garaycoechea, J.I., Yu, R., Arends, M.J., Chandrasekaran, G., Broecker, V., Wei, W., Liu, L., Swenberg, J.A., Crossan, G.P., Patel, K.J., 2015. Endogenous Formaldehyde Is a Hematopoietic Stem Cell Genotoxin and Metabolic Carcinogen. Mol. Cell 60, 177–188.

Potapova, T.A., Unruh, J.R., Box, A.C., Bradford, W.D., Seidel, C.W., Slaughter, B.D., Sivagnanam, S., Wu, Y., Li, R., 2015. Karyotyping human and mouse cells using probes from single-sorted chromosomes and open source software. Biotechniques 59, 335–346.

Puffenberger, E.G., Jinks, R.N., Sougnez, C., Cibulskis, K., Willert, R.A., Achilly, N.P., Cassidy, R.P., Fiorentini, C.J., Heiken, K.F., Lawrence, J.J., Mahoney, M.H., Miller, C.J., Nair, D.T., Politi, K.A., Worcester, K.N., Setton, R.A., DiPiazza, R., Sherman, E.A., Eastman, J.T., Francklyn, C., Robey-Bond, S., Rider, N.L., Gabriel, S., Morton, D.H., Strauss, K.A., 2012. Genetic mapping and exome sequencing identify variants associated with five novel diseases. PLoS One 7, e28936.

Qvist, P., Huertas, P., Jimeno, S., Nyegaard, M., Hassan, M.J., Jackson, S.P., Børglum, A.D., 2011. CtIP mutations cause Seckel and Jawad syndromes. PLoS Genet. 7, e1002310.

Ragland, R.L., Patel, S., Rivard, R.S., Smith, K., Peters, A.A., Bielinsky, A.K., Brown, E.J., 2013. RNF4 and PLK1 are required for replication fork collapse in ATR-deficient cells. Genes Dev. 27, 2259–2273.

Ran, F.A., Hsu, P.D., Lin, C.Y., Gootenberg, J.S., Konermann, S., Trevino, A.E., Scott, D.A., Inoue, A., Matoba, S., Zhang, Y., Zhang, F., 2013. Double nicking by RNA-guided CRISPR Cas9 for enhanced genome editing specificity. Cell 154, 1380–1389.

Ran, F.A., Hsu, P.D., Wright, J., Agarwala, V., Scott, D.A., Zhang, F., 2013. Genome engineering using the CRISPR-Cas9 system. Nat. Protoc. 8, 2281–2308.

Rappold, I., Iwabuchi, K., Date, T., Chen, J., 2001. Tumor Suppressor p53 Binding Protein 1 (53BP1) Is Involved in DNA Damage–signaling Pathways. J. Cell Biol. 153, 613–620.

Rappsilber, J., Ishihama, Y., Mann, M., 2003. Stop And Go Extraction tips for matrix-assisted laser desorption/ionization, nanoelectrospray, and LC/MS sample pretreatment in proteomics. Anal. Chem. 75, 663–670.

Räschle, M., Smeenk, G., Hansen, R.K., Temu, T., Oka, Y., Hein, M.Y., Nagaraj, N., Long, D.T., Walter, J.C., Hofmann, K., Storchova, Z., Cox, J., Bekker-Jensen, S., Mailand, N., Mann, M., 2015. Proteomics reveals dynamic assembly of Repair complexes during bypass of DNA cross-links. Science 348, 1253671.

Rastogi, R.P., Richa, Kumar, A., Tyagi, M.B., Sinha, R.P., 2010. Molecular mechanisms of ultraviolet radiation-induced DNA damage and repair. J. Nucleic Acids 592980.

Rauch, A., 2011. The shortest of the short: Pericentrin mutations and beyond. Best Pract. Res. Clin. Endocrinol. Metab. 25, 125–130.

Rauch, A., Thiel, C.T., Schindler, D., Wick, U., Crow, Y.J., Ekici, A.B., Essen, A.J. Van, Goecke, T.O., Al-gazali, L., Chrzanowska, K.H., 2008. Mutations in the Pericentrin (PCNT) Gene Cause Primordial Dwarfism. Science 319, 816–819.

Ray Chaudhuri, A., Hashimoto, Y., Herrador, R., Neelsen, K.J., Fachinetti, D., Bermejo, R., Cocito, A., Costanzo, V., Lopes, M., 2012. Topoisomerase I poisoning results in PARP-mediated replication fork reversal. Nat. Struct. Mol. Biol. 19, 417–423.

Regairaz, M., Zhang, Y.W., Fu, H., Agama, K.K., Tata, N., Agrawal, S., Aladjem, M.I., Pommier, Y., 2011. Mus81-mediated DNA cleavage resolves replication forks stalled by topoisomerase I-DNA complexes. J. Cell Biol. 195, 739–749.

Reijns, M.A.M., Bubeck, D., Gibson, L.C.D., Graham, S.C., Baillie, G.S., Jones, E.Y., Jackson, A.P., 2011. The structure of the human RNase H2 complex defines key interaction interfaces relevant to enzyme function and human disease. J. Biol. Chem. 286, 10530–10539.

Reijns, M.A.M., Rabe, B., Rigby, R.E., Mill, P., Astell, K.R., Lettice, L.A., Boyle, S., Leitch, A., Keighren, M., Kilanowski, F., Devenney, P.S., Sexton, D., Grimes, G., Holt, I.J., Hill, R.E., Taylor, M.S., Lawson, K.A., Dorin, J.R., Jackson, A.P., 2012. Enzymatic removal of ribonucleotides from DNA

is essential for mammalian genome integrity and development. Cell 149, 1008–1022.

Reynolds, J.J., Bicknell, L.S., Carroll, P., Higgs, M.R., Shaheen, R., Murray, J.E., Papadopoulos, D.K., Leitch, A., Murina, O., Tarnauskaitė, Ž., Wessel, S.R., Zlatanou, A., Vernet, A., Von Kriegsheim, A., Mottram, R.M.A., Logan, C. V., Bye, H., Li, Y., Brean, A., Maddirevula, S., Challis, R.C., Skouloudaki, K., Almoisheer, A., Alsaif, H.S., Amar, A., Prescott, N.J., Bober, M.B., Duker, A., Faqeih, E., Seidahmed, M.Z., Al Tala, S., Alswaid, A., Ahmed, S., Al-Aama, J.Y., Altmüller, J., Al Balwi, M., Brady, A.F., Chessa, L., Cox, H., Fischetto, R., Heller, R., Henderson, B.D., Hobson, E., Nürnberg, P., Percin, E.F., Peron, A., Spaccini, L., Quigley, A.J., Thakur, S., Wise, C.A., Yoon, G., Alnemer, M., Tomancak, P., Yigit, G., Taylor, A.M.R., Reijns, M.A.M., Simpson, M.A., Cortez, D., Alkuraya, F.S., Mathew, C.G., Jackson, A.P., Stewart, G.S., 2017. Mutations in DONSON disrupt replication fork stability and cause microcephalic dwarfism. Nat. Genet. 49, 537–549.

Richardson, C.D., Kazane, K.R., Feng, S.J., Zelin, E., Bray, N.L., Schäfer, A.J., Floor, S.N., Corn, J.E., 2018. CRISPR–Cas9 genome editing in human cells occurs via the Fanconi anemia pathway. Nat. Genet. 50, 1132–1139.

Riera, A., Tognetti, S., Speck, C., 2014. Helicase loading: How to build a MCM2-7 double-hexamer. Semin. Cell Dev. Biol. 30, 104–109.

Roberts, E., Hampshire, D.J., Pattison, L., Springell, K., Jafri, H., Corry, P., Mannon, J., Rasid, Y., Crow, Y., Bond, J., Woods, C.G., 2002. Autosomal recessive primary microcephaly: an analysis of locus heterogeneity and phenotypic variation. J. Med. Genet. 39, 718–721.

Robertson, A.B., Klungland, A., Rognes, T., Leiros, I., 2009. Base excision repair: The long and short of it. Cell. Mol. Life Sci. 66, 981–993.

Rohl, C.A., Fiori, W., Baldwin, R.L., 1999. Alanine is helix-stabilizing in both template-nucleated and standard peptide helices. PNAS 96, 3682–3687.

Roifman, C.M., 1999. Antibody deficiency, growth retardation, spondyloepiphyseal dysplasia and retinal dystrophy: A novel syndrome. Clin. Genet. 55, 103–109.

Ronchi, D., Di Fonzo, A., Lin, W., Bordoni, A., Liu, C., Fassone, E., Pagliarani, S., Rizzuti, M., Zheng, L., Filosto, M., Ferrò, M.T., Ranieri, M., Magri, F., Peverelli, L., Li, H., Yuan, Y.C., Corti, S., Sciacco, M., Moggio, M., Bresolin, N., Shen, B., Comi, G. Pietro, 2013. Mutations in DNA2 link progressive myopathy to mitochondrial DNA instability. Am. J. Hum. Genet. 92, 293–300.

Ronchi, V.P., Haas, A.L., 2012. Measuring Rates of Ubiquitin Chain Formation as a Functional Readout of Ligase Activity. Methods Mol. Biol. 832, 197–218.

Ross, D.T., Scherf, U., Eisen, M.B., Perou, C.M., Rees, C., Spellman, P., Iyer, V., Jeffrey, S.S., Van de Rijn, M., Waltham, M., Pergamenschikov, A., Lee, J.C., Lashkari, D., Shalon, D., Myers, T.G., Weinstein, J.N., Botstein, D., Brown, P.O., 2000. Systematic variation in gene expression patterns in human cancer cell lines. Nat. Genet. 24, 227–35.

Ross, J.J., Frias, J.L., 1977. Microcephaly. In: Congenital Malformations of the Brain and Skull Part 1. Vol. 30: Handbook of Clinical Neurology. pp. 507–524.

Rossi, M.L., Purohit, V., Brandt, P.D., Bambara, R.A., 2006. Lagging strand replication proteins in genome stability and DNA repair. Chem. Rev. 106, 453–473.

Roth, K.A., Kuan, C.-Y., Haydar, T.F., D'Sa-Eipper, C., Shindler, K.S., Zheng, T.S., Kuida, K., Flavell, R.A., Rakic, P., 2000. Epistatic and independent functions of caspase-3 and Bcl-X(L) in developmental programmed cell death. PNAS 97, 466–471.

Roux, K.J., Kim, D.I., Raida, M., Burke, B., 2012. A promiscuous biotin ligase fusion protein identifies proximal and interacting proteins in mammalian cells. J. Cell Biol. 196, 801–810.

Sacho, E.J., Maizels, N., 2011. DNA repair factor MRE11/RAD50 cleaves 3'-phosphotyrosyl bonds and resects DNA to repair damage caused by topoisomerase 1 poisons. J. Biol. Chem. 286, 44945–44951.

Saldivar, J.C., Cortez, D., Cimprich, K.A., 2017. The essential kinase ATR: Ensuring faithful duplication of a challenging genome. Nat. Rev. Mol. Cell Biol. 18, 622–636.

SantaLucia, J., 1998. A unified view of polymer, dumbbell, and oligonucleotide DNA nearest-

neighbor thermodynamics. PNAS 95, 1460–1465.

Santocanale, C., Sharma, K., Diffley, J.F.X., 1999. Activation of dormant origins of DNA replication in budding yeast. Genes Dev. 13, 2360–2364.

Sartori, A.A., Lukas, C., Coates, J., Mistrik, M., Fu, S., Bartek, J., Baer, R., Lukas, J., Jackson, S.P., 2007. Human CtIP promotes DNA end resection. Nature 450, 509–514.

Schaarschmidt, D., Baltin, J., Stehle, I.M., Lipps, H.J., Knippers, R., 2004. An episomal mammalian replicon: Sequence-independent binding of the origin recognition complex. EMBO J. 23, 191–201.

Schauwecker, P.E., 2011. The relevance of individual genetic background and its role in animal models of epilepsy. Epilepsy Res. 97, 1–11.

Scheffner, M., Werness, B.A., Huibregtse, J.M., Levine, A.J., Howley, P.M., 1990. The E6 oncoprotein encoded by human papillomavirus types 16 and 18 promotes the degradation of p53. Cell 63, 1129–1136.

Schneider, C.A., Rasband, W.S., Eliceiri, K.W., 2012. NIH Image to ImageJ: 25 years of image analysis. Nat. Methods 9, 671–675.

Schwab, R.A., Blackford, A.N., Niedzwiedz, W., 2010. ATR activation and replication fork restart are defective in FANCM-deficient cells. EMBO J. 29, 806–818.

Segurado, M., Diffley, J., 2008. Separate roles for the DNA damage checkpoint protein kinases in stabilizing DNA replication forks. Genes Dev. 1816–1827.

Selleck, W., Tan, S., 2008. Recombinant protein complex expression in E. coli. Curr. Protoc. Protein Sci. Chapter 5, ps0521s52.

Semlow, D.R., Zhang, J., Budzowska, M., Drohat, A.C., Walter, J.C., 2016. Replication-Dependent Unhooking of DNA Interstrand Cross-Links by the NEIL3 Glycosylase. Cell 167, 498–511.

Senturk, E., Manfredi, J.J., 2013. p53 and Cell Cycle Effects After DNA Damage. Methods Mol. Biol. 962, 49–61.

Shaheen, R., Faqeih, E., Ansari, S., Abdel-Salam, G., Al-Hassnan, Z.N., Al-Shidi, T., Alomar, R., Sogaty, S., Alkuraya, F.S., 2014. Genomic analysis of primordial dwarfism reveals novel disease genes. Genome Res. 24, 291–299.

Shao, R.G., Cao, C.X., Zhang, H., Kohn, K.W., Wold, M.S., Pommier, Y., 1999. Replication-mediated DNA damage by camptothecin induces phosphorylation of RPA by DNA-dependent protein kinase and dissociates RPA:DNA-PK complexes. EMBO J. 18, 1397–1406.

Sheth, N., Roca, X., Hastings, M.L., Roeder, T., Krainer, A.R., Sachidanandam, R., 2006. Comprehensive splice-site analysis using comparative genomics. Nucleic Acids Res. 34, 3955–3967.

Shi, W., Feng, Z., Zhang, J., Gonzalez-Suarez, I., Vanderwaal, R.P., Wu, X., Powell, S.N., Roti Roti, J.L., Gonzalo, S., Zhang, J., 2010. The role of RPA2 phosphorylation in homologous recombination in response to replication arrest. Carcinogenesis 31, 994–1002.

Shi, Y., Lan, F., Matson, C., Mulligan, P., Whetstine, J.R., Cole, P.A., Casero, R.A., Shi, Y., 2004. Histone demethylation mediated by the nuclear amine oxidase homolog LSD1. Cell 119, 941–953.

Shibata, A., Moiani, D., Arvai, A.S., Perry, J.J.P., Harding, S.M., Genois, M.-M., Maity, R., van Rossum-Fikkert, S., Kertokalio, A., Romoli, F., Ismail, A., Ismalaj, E., Petricci, E., Matthew, J.N., Bristow, R.G., Masson, J., Wyman, C., Jeggo, P., Tainer, J.A., 2014. DNA Double Strand Break Repair Pathway Choice Is Directed by Distinct MRE11 Nuclease Activities. Mol. Cell 53, 7–18.

Shiloh, Y., 2003. ATM and related protein kinases: safeguarding genome integrity. Nat. Rev. Cancer 3, 155–168.

Shiomi, Y., Nishitani, H., 2013. Alternative replication factor C protein, Elg1, maintains chromosome stability by regulating PCNA levels on chromatin. Genes to Cells 18, 946–959.

Siitonen, H.A., Kopra, O., Kääriäinen, H., Haravuori, H., Winter, R.M., Säämänen, A.M., Peltonen, L., Kestilä, M., 2003. Molecular defect of RAPADILINO syndrome expands the phenotype

spectrum of RECQL diseases. Hum. Mol. Genet. 12, 2837–2844.

Silverman, J., Takai, H., Buonomo, S.B.C., Eisenhaber, F., De Lange, T., 2004. Human Rif1, ortholog of a yeast telomeric protein, is regulated by ATM and 53BP1 and functions in the S-phase checkpoint. Genes Dev. 18, 2108–2119.

Singh, G., Cooper, T.A., 2006. Minigene reporter for identification and analysis of cis elements and trans factors affecting pre-mRNA splicing. Biotechniques 41, 177–181.

Singhal, P.K., Sassi, S., Lan, L., Au, P., Halvorsen, S.C., Fukumura, D., Jain, R.K., Seed, B., 2016. Mouse embryonic fibroblasts exhibit extensive developmental and phenotypic diversity. PNAS 113, 122–127.

Sir, J.H., Barr, A.R., Nicholas, A.K., Carvalho, O.P., Khurshid, M., Sossick, A., Reichelt, S., D'Santos, C., Woods, C.G., Gergely, F., 2011. A primary microcephaly protein complex forms a ring around parental centrioles. Nat. Genet. 43, 1147–1153.

Sirbu, B.M., Couch, F.B., Cortez, D., 2012. Monitoring the spatiotemporal dynamics of proteins at replication forks and in assembled chromatin using Isolation of Proteins On Nascent DNA (iPOND). Nat. Protoc. 7, 594–605.

Sirbu, B.M., Couch, F.B., Feigerle, J.T., Bhaskara, S., Hiebert, S.W., 2011. Analysis of protein dynamics at active, stalled, and collapsed replication forks. Genes Dev. 25, 1320–1327.

Smogorzewska, A., Matsuoka, S., Vinciguerra, P., McDonald III, E.R., Hurov, K.E., Luo, J., Ballif, B.A., Gygi, S.P., Hofmann, K., D'Andrea, A.D., Elledge, S.J., 2007. Identification of the Fanconi anemia (FANC) I protein, a monoubiquitinated FANCD2 paralog required for crosslink repair. Cell 129, 289–301.

Sobhian, B., Shao, G., Lilli, D.R., Culhane, A.C., Moreau, L.A., Livingston, D.M., Greenberg, R.A., 2007. RAP80 Targets BRCA1 to Specific Ubiquitin Structures at DNA Damage Sites. Science 316, 1198–1202.

Sogo, J.M., Lopes, M., Foiani, M., 2002. Fork reversal and ssDNA accumulation at stalled replication forks owing to checkpoint defects. Science 297, 599–602.

Sonneville, R., Moreno, S.P., Knebel, A., Johnson, C., Hastie, C.J., Gartner, A., Gambus, A., Labib, K., 2017. CUL-2Lrr-1 and UBXN-3/FAF1 drive replisome disassembly during DNA replication termination and mitosis. Nat. Cell Biol. 19, 468–479.

Sonoda, E., Sasaki, M.S., Morrison, C., Yamaguchi-Iwai, Y., Takata, M., Takeda, S., 1999. Sister chromatid exchanges are mediated by homologous recombination in vertebrate cells. Mol. Cell. Biol. 19, 5166–5169.

Soo Lee, N., Jin Chung, H., Kim, H.J., Yun Lee, S., Ji, J.H., Seo, Y., Hun Han, S., Choi, M., Yun, M., Lee, S.G., Myung, K., Kim, Y., Chul Kang, H., Kim, H., 2016. TRAIP/RNF206 is required for recruitment of RAP80 to sites of DNA damage. Nat. Commun. 7, 10463.

Spek, E.J., Olson, C.A., Shi, Z., Kallenbach, N.R., 1999. Alanine is an intrinsic α-helix stabilizing amino acid. J. Am. Chem. Soc. 121, 5571–5572.

Steffensen, A.Y., Dandanell, M., Jønson, L., Ejlertsen, B., Gerdes, A.M., Nielsen, F.C., Hansen, T. v. O., 2014. Functional characterization of BRCA1 gene variants by mini-gene splicing assay. Eur. J. Hum. Genet. 22, 1362–1368.

Stein, S., Lao, Y., Yang, I.Y., Hecht, S.S., Moriya, M., 2006. Genotoxicity of acetaldehyde- and crotonaldehyde-induced 1,N2-propanodeoxyguanosine DNA adducts in human cells. Mutat. Res. - Genet. Toxicol. Environ. Mutagen. 608, 1–7.

Sternberg, S.H., Redding, S., Jinek, M., Greene, E.C., Doudna, J.A., 2014. DNA interrogation by the CRISPR RNA-guided endonuclease Cas9. Nature 507, 62–67.

Stewart, G.S., Panier, S., Townsend, K., Al-Hakim, A.K., Kolas, N.K., Miller, E.S., Nakada, S., Ylanko, J., Olivarius, S., Mendez, M., Oldreive, C., Wildenhain, J., Tagliaferro, A., Pelletier, L., Taubenheim, N., Durandy, A., Byrd, P.J., Stankovic, T., Taylor, A.M.R., Durocher, D., 2009. The RIDDLE Syndrome Protein Mediates a Ubiquitin-Dependent Signaling Cascade at Sites of DNA Damage. Cell 136, 420–434.

Stingele, J., Bellelli, R., Boulton, S.J., 2017. Mechanisms of DNA-protein crosslink repair. Nat. Rev. Mol. Cell Biol. 18, 563–573.

Stockholm, D., Benchaouir, R., Picot, J., Rameau, P., Neildez, T.M.A., Landini, G., Laplace-Builhé, C., Paldi, A., 2007. The origin of phenotypic heterogeneity in a clonal cell population in vitro. PLoS One 2, e394.

Stulp, G., Barrett, L., 2016. Evolutionary perspectives on human height variation. Biol. Rev. 91, 206–234.

Stults, D.M., Killen, M.W., Pierce, A.J., 2014. The Sister Chromatid Exchange (SCE) Assay. In: Phouthone Keohavong and Stephen G. Grant (eds.) (Ed.), Molecular Toxicology Protocols, Methods in Molecular Biology. Springer Science, New York, pp. 439–455.

Sturzenegger, A., Burdova, K., Kanagaraj, R., Levikova, M., Pinto, C., Cejka, P., Janscak, P., 2014. DNA2 cooperates with the WRN and BLM RecQ helicases to mediate long-range DNA end resection in human cells. J. Biol. Chem. 289, 27314–27326.

Sugimoto, N., Maehara, K., Yoshida, K., Yasukouchi, S., Osano, S., Watanabe, S., Aizawa, M., Yugawa, T., Kiyono, T., Kurumizaka, H., Ohkawa, Y., Fujita, M., 2015. Cdt1-binding protein GRWD1 is a novel histone-binding protein that facilitates MCM loading through its influence on chromatin architecture. Nucleic Acids Res. 43, 5898–5911.

Sugimoto, N., Yugawa, T., Iizuka, M., Kiyono, T., Fujita, M., 2011. Chromatin remodeler sucrose nonfermenting 2 homolog (SNF2H) is recruited onto DNA replication origins through interaction with Cdc10 protein-dependent transcript 1 (Cdt1) and promotes pre-replication complex formation. J. Biol. Chem. 286, 39200–39210.

Sun, Y., Xu, Y., Roy, K., Price, B.D., 2007. DNA Damage-Induced Acetylation of Lysine 3016 of ATM Activates ATM Kinase Activity. Mol. Cell. Biol. 27, 8502–8509.

Sung, P., Robberson, D.L., 1995. DNA strand exchange mediated by a RAD51-ssDNA nucleoprotein filament with polarity opposite to that of RecA. Cell 82, 453–461.

Svendsen, J.M., Smogorzewska, A., Sowa, M.E., O'Connell, B.C., Gygi, S.P., Elledge, S.J., Harper, J.W., 2009. Mammalian BTBD12/SLX4 Assembles A Holliday Junction Resolvase and Is Required for DNA Repair. Cell 138, 63–77.

Symington, L.S., Gautier, J., 2011. Double-Strand Break End Resection and Repair Pathway Choice. Annu. Rev. Genet. 45, 247–271.

Takahashi, T., Nowakowski, R.S., Caviness, V.S., 1995. The cell cycle of the pseudostratified ventricular epithelium of the embryonic murine cerebral wall. J. Neurosci. 15, 6046–6057.

Takahata, C., Masuda, Y., Takedachi, A., Tanaka, K., Iwai, S., Kuraoka, I., 2015. Repair synthesis step involving ERCC1-XPF participates in DNA repair of the Top1-DNA damage complex. Carcinogenesis 36, 841–851.

Takemura, H., Rao, V.A., Sordet, O., Furuta, T., Miao, Z.H., Meng, L.H., Zhang, H., Pommier, Y., 2006. Defective Mre11-dependent activation of Chk2 by Ataxia Telangiectasia Mutated in colorectal carcinoma cells in response to replication-dependent DNA double strand breaks. J. Biol. Chem. 281, 30814–30823.

Tan, S., 2001. A modular polycistronic expression system for overexpressing protein complexes in Escherichia coli. Protein Expr. Purif. 21, 224–234.

Tan, S., Kern, R.C., Selleck, W., 2005. The pST44 polycistronic expression system for producing protein complexes in Escherichia coli. Protein Expr. Purif. 40, 385–395.

Tanaka, S., Araki, H., 2013. Helicase activation and establishment of replication forks at chromosomal origins of replication. Cold Spring Harb. Perspect. Biol. 5, a010371.

Técher, H., Koundrioukoff, S., Carignon, S., Wilhelm, T., Millot, G.A., Lopez, B.S., Brison, O., Debatisse, M., 2016. Signaling from Mus81-Eme2-Dependent DNA Damage Elicited by Chk1 Deficiency Modulates Replication Fork Speed and Origin Usage. Cell Rep. 14, 1114–1127.

Terradas, M., Martín, M., Tusell, L., Genescà, A., 2010. Genetic activities in micronuclei: Is the DNA entrapped in micronuclei lost for the cell? Mutat. Res. - Rev. Mutat. Res. 705, 60–67.

Thangavel, S., Berti, M., Levikova, M., Pinto, C., Gomathinayagam, S., Vujanovic, M., Zellweger, R., Moore, H., Lee, E.H., Hendrickson, E.A., Cejka, P., Stewart, S., Lopes, M., Vindigni, A., 2015. DNA2 drives processing and restart of reversed replication forks in human cells. J. Cell Biol. 208, 545–562.

Thompson, L.H., Schild, D., 2001. Homologous recombinational repair of DNA ensures mammalian chromosome stability. Mutat. Res. - Fundam. Mol. Mech. Mutagen. 477, 131–153.

Threadgill, D.W., Dlugosz, A.A., Hansen, L.A., Tennenbaum, T., Lichti, U., Yee, D., LaMantia, C., Mourton, T., Herrup, K., Harris, R.C., Barnard, J.A., Yuspa, S.H., Coffey, R.J., Magnuson, T., 1995. Targeted disruption of mouse EGF receptor: effect of genetic background on mutant phenotype. Science 269, 230–234.

Toledo, L.I., Altmeyer, M., Rask, M.B., Lukas, C., Larsen, D.H., Povlsen, L.K., Bekker-Jensen, S., Mailand, N., Bartek, J., Lukas, J., 2013. ATR prohibits replication catastrophe by preventing global exhaustion of RPA. Cell 155, 1088–1103.

Tomasz, M., 1995. Mitomycin C: small, fast and deadly (but very selective). Chem. Biol. 2, 575–579.

Traut, T.W., 1994. The functions and consensus motifs of nine types of peptide segments that form different types of nucleotide-binding sites. Eur. J. Biochem. 222, 9–19.

Traverso, G., Bettegowda, C., Kraus, J., Rgen Kraus, J., Speicher, M.R., Kinzler, K.W., Vogelstein, B., Lengauer, C., 2003. Hyper-Recombination and Genetic Instability in BLM-Deficient Epithelial Cells. Cancer Res. 63, 8578–8581.

Triemstra, J., Pham, A., Rhodes, L., Waggoner, D.J., Onel, K., 2015. A Review of Fanconi Anemia for the Practicing Pediatrician. Pediatr. Ann. 44, 444–452.

Tyanova, S., Temu, T., Cox, J., 2016. The MaxQuant computational platform for mass spectrometry-based shotgun proteomics. Nat. Protoc. 11, 2301–2319.

Udeshi, N.D., Mertins, P., Svinkina, T., Carr, S.A., 2013. Large-Scale Identification of Ubiquitination Sites by Mass Spectrometry. Nat. Protoc. 8, 1950–1960.

van den Bosch, M., Bree, R.T., Lowndes, N.F., 2003. The MRN complex: Coordinating and mediating the response to broken chromosomes. EMBO Rep. 4, 844–849.

van Deursen, F., Sengupta, S., De Piccoli, G., Sanchez-Diaz, A., Labib, K., 2012. Mcm10 associates with the loaded DNA helicase at replication origins and defines a novel step in its activation. EMBO J. 31, 2195–2206.

Vashee, S., Cvetic, C., Lu, W., Simancek, P., Kelly, T.J., Walter, J.C., 2003. Sequence-independent DNA binding and replication initiation by the human origin recognition complex. Genes Dev. 17, 1894–1908.

Vassin, V.M., Anantha, R.W., Sokolova, E., Kanner, S., Borowiec, J.A., 2009. Human RPA phosphorylation by ATR stimulates DNA synthesis and prevents ssDNA accumulation during DNA-replication stress. J. Cell Sci. 122, 4070–4080.

Vaughn, J.P., Davis, P.L., Jarboe, M.D., Huper, G., Evans, C.A., Wiseman, R.W., Berchuck, A., Iglehart, J.D., Futreal, P.A., Marks, J.R., 1996. BRCA1 Expression Is Induced before DNA Synthesis in Both Normal and Tumor-derived Breast Cells. Cell Growth Differ. 7, 711–715.

Vetro, A., Savasta, S., Russo Raucci, A., Cerqua, C., Sartori, G., Limongelli, I., Forlino, A., Maruelli, S., Perucca, P., Vergani, D., Mazzini, G., Mattevi, A., Stivala, L.A., Salviati, L., Zuffardi, O., 2017. MCM5: A new actor in the link between DNA replication and Meier-Gorlin syndrome. Eur. J. Hum. Genet. 25, 646–650.

Visscher, P.M., 2008. Sizing up human height variation. Nat. Genet. 40, 489–490.

Wall, M.E., Wani, M.C., Cook, C.E., Palmer, K.H., McPhail, A.T., Sim, G.A., 1966. Plant Antitumor Agents. I. The Isolation and Structure of Camptothecin, a Novel Alkaloidal Leukemia and Tumor Inhibitor from Camptotheca acuminata. J. Am. Chem. Soc. 88, 3888–3890.

Wallace, H.A., Merkle, J.A., Yu, M.C., Berg, T.G., Lee, E., Bosco, G., Lee, L.A., 2014. TRIP/NOPO E3 ubiquitin ligase promotes ubiquitylation of DNA polymerase. Development 141, 1332–1341.

Wang, A.T., Kim, T., Wagner, J.E., Conti, B.A., Lach, F.P., Huang, A.L., Molina, H., Sanborn, E.M., Zierhut, H., Cornes, B.K., Abhyankar, A., Sougnez, C., Gabriel, S.B., Auerbach, A.D., Kowalczykowski, S.C., Smogorzewska, A., 2015. A Dominant Mutation in Human RAD51 Reveals Its Function in DNA Interstrand Crosslink Repair Independent of Homologous Recombination. Mol. Cell 59, 478–490.

Wang, B., Matsuoka, S., Ballif, B.A., Zhang, D., Smogorzewska, A., Giyi, S., Elledge, S.J., Gygi, S.P., Elledge, S.J., 2007. Abraxas and Rap80 form a novel BRCA1 protein complex required for the DNA damage response. Science 316, 1194–1198.

Wang, H., Wang, M., Wang, H., Böcker, W., Iliakis, G., 2005. Complex H2AX phosphorylation patterns by multiple kinases including ATM and DNA-PK in human cells exposed to ionizing radiation and treated with kinase inhibitors. J. Cell. Physiol. 202, 492–502.

Wang, J., Aroumougame, A., Lobrich, M., Li, Y., Chen, D., Chenj, J., Gong, Z., 2014. PTIP associates with Artemis to dictate DNA repair pathway choice. Genes Dev. 28, 2693–2698.

Wang, J.C., 2002. Cellular roles of DNA topoisomerases: a molecular perspective. Nat. Rev. Mol. Cell Biol. 3, 430–441.

Wang, M., McIntee, E.J., Cheng, G., Shi, Y., Villalta, P.W., Hecht, S.S., 2000. Identification of DNA adducts of acetaldehyde. Chem. Res. Toxicol. 13, 1149–1157.

Wang, W., 2007. Emergence of a DNA-damage response network consisting of Fanconi anaemia and BRCA proteins. Nat. Rev. Genet. 8, 735–748.

Wanrooij, P.H., Burgers, P.M., 2015. Yet another job for Dna2: checkpoint activation. DNA Repair (Amst) 32, 17–23.

Ward, I.M., Chen, J., 2001. Histone H2AX Is Phosphorylated in an ATR-dependent Manner in Response to Replicational Stress. J. Biol. Chem. 276, 47759–47762.

Ward, I.M., Minn, K., Chen, J., 2004. UV-induced Ataxia-telangiectasia-mutated and Rad3-related (ATR) Activation Requires Replication Stress. J. Biol. Chem. 279, 9677–9680.

Ward, I.M., Minn, K., Jorda, K.G., Chen, J., 2003. Accumulation of checkpoint protein 53BP1 at DNA breaks involves its binding to phosphorylated histone H2AX. J. Biol. Chem. 278, 19579–19582.

Watase, G., Takisawa, H., Kanemaki, M.T., 2012. Mcm10 plays a role in functioning of the eukaryotic replicative DNA helicase, Cdc45-Mcm-GINS. Curr. Biol. 22, 343–349.

Waterhouse, A.M., Procter, J.B., Martin, D.M.A., Clamp, M., Barton, G.J., 2009. Jalview Version 2-A multiple sequence alignment editor and analysis workbench. Bioinformatics 25, 1189–1191.

Waters, L.S., Minesinger, B.K., Wiltrout, M.E., D'Souza, S., Woodruff, R. V., Walker, G.C., 2009. Eukaryotic Translesion Polymerases and Their Roles and Regulation in DNA Damage Tolerance. Microbiol. Mol. Biol. Rev. 73, 134–154.

Wigley, D.B., 1995. Structure and Mechanism of DNA Topoisomerases. Annu. Rev. Biophys. Biomol. Struct. 24, 185–208.

Will, C.L., Lührmann, R., 2005. Splicing of a rare class of introns by the U12-dependent spliceosome. Biol. Chem. 386, 713–724.

Williams, H.L., Gottesman, M.E., Gautier, J., 2013. The differences between ICL repair during and outside of S-Phase. Trends Biochem. Sci. 38, 386–393.

Williams, S.E., Garcia, I., Crowther, A.J., Li, S., Stewart, A., Liu, H., Lough, K.J., O'Neill, S., Veleta, K., Oyarzabal, E.A., Merrill, J.R., Shih, Y.-Y.I., Gershon, T.R., 2015. Aspm sustains postnatal cerebellar neurogenesis and medulloblastoma growth in mice. Development 142, 3921–3932.

Wilson, D.M., Thompson, L.H., 2007. Molecular mechanisms of sister-chromatid exchange. Mutat. Res. - Fundam. Mol. Mech. Mutagen. 616, 11–23.

Windheim, M., Peggie, M., Cohen, P., 2008. Two different classes of E2 ubiquitin-conjugating enzymes are required for the mono-ubiquitination of proteins and elongation by polyubiquitin chains with a specific topology. Biochem. J. 409, 723–729.

Wohlschlegel, J.A., Dwyer, B.T., Dhar, S.K., Cvetic, C., Walter, J.C., Dutta, A., 2000. Inhibition of

eukaryotic DNA replication by geminin binding to Cdt1. Science 290, 2309–2312.

Wolpert, L., 2010. Arms and the man: The problem of symmetric growth. PLoS Biol. 8, 9–11.

Woods, C.G., Bond, J., Enard, W., 2005. Autosomal Recessive Primary Microcephaly (MCPH): A Review of Clinical, Molecular, and Evolutionary Findings. Am. J. Hum. Genet. 76, 717–728.

Woods, C.G., Parker, A., 2013. Investigating microcephaly. Arch. Dis. Child. 98, 707–713.

Wu, H.I., Brown, J.A., Dorie, M.J., Wu, H.I., Brown, J.A., Dorie, M.J., Lazzeroni, L., Brown, J.M., 2004. Genome-Wide Identification of Genes Conferring Resistance to the Anticancer Agents Cisplatin, Oxaliplatin, and Mitomycin C. Cancer Res. 3940–3948.

Wu, J., Liu, C., Chen, J., Yu, X., 2012. RAP80 protein is important for genomic stability and is required for stabilizing BRCA1-A complex at DNA damage sites in vivo. J. Biol. Chem. 287, 22919–22926.

Wyatt, H.D.M., Sarbajna, S., Matos, J., West, S.C., 2013. Coordinated actions of SLX1-SLX4 and MUS81-EME1 for holliday junction resolution in human cells. Mol. Cell 52, 234–247.

Xiao, Z., Chen, Z., Gunasekera, A.H., Sowin, T.J., Rosenberg, S.H., Fesik, S., Zhang, H., 2003. Chk1 mediates S and G2 arrests through Cdc25A degradation in response to DNA-damaging agents. J. Biol. Chem. 278, 21767–21773.

Xu, G., Chapman, J.R., Brandsma, I., Yuan, J., Mistrik, M., Bartkova, J., Gogola, E., Warmerdam, D., Barazas, M., Jaspers, J.E., Watanabe, K., Pieterse, M., Kersbergen, A., Sol, W., Celie, P.H.N., Schouten, P.C., Van Den Broeck, B., Salman, A., Nieuwland, M., de Rink, I., de Ronde, J., Jalink, K., Boulton, S.J., Chen, J., van Gent, D.C., Bartek, J., Jonkers, J., Borst, P., Rottenberg, S., 2015. REV7 counteracts DNA double-strand break resection and impacts PARP inhibition. Nature 521, 541–544.

Xu, X., Blackwell, S., Lin, A., Li, F., Qin, Z., Xiao, W., 2015. Error-free DNA-damage tolerance in Saccharomyces cerevisiae. Mutat. Res. - Rev. Mutat. Res. 764, 43–50.

Yamada, M., Watanabe, K., Mistrik, M., Vesela, E., Protivankova, I., 2013. ATR–Chk1–APC/C Cdh1 - dependent stabilization of Cdc7 – ASK (Dbf4) kinase is required for DNA lesion bypass under replication stress. Genes Dev. 27, 2459–2472.

Yang, Y.J., Baltus, A.E., Mathew, R.S., Murphy, E.A., Evrony, G.D., Gonzalez, D.M., Wang, E.P., Marshall-Walker, C.A., Barry, B.J., Murn, J., Tatarakis, A., Mahajan, M.A., Samuels, H.H., Shi, Y., Golden, J.A., Mahajnah, M., Shenhav, R., Walsh, C.A., 2012. Microcephaly gene links trithorax and REST/NRSF to control neural stem cell proliferation and differentiation. Cell 151, 1097–1112.

Yeeles, J.T.P., Deegan, T.D., Janska, A., Early, A., Diffley, J.F.X., 2015. Regulated eukaryotic DNA replication origin firing with purified proteins. Nature 519, 431–435.

Yeeles, J.T.P., Janska, A., Early, A., Diffley, J.F.X., 2017. How the Eukaryotic Replisome Achieves Rapid and Efficient DNA Replication. Mol. Cell 65, 105–116.

Yoon, Y.-S., Lee, M.-W., Ryu, D., Kim, J.H., Ma, H., Seo, W.-Y., Kim, Y.-N., Kim, S.S., Lee, C.H., Hunter, T., Choi, C.S., Montminy, M.R., Koo, S.-H., 2010. Suppressor of MEK null (SMEK)/protein phosphatase 4 catalytic subunit (PP4C) is a key regulator of hepatic gluconeogenesis. PNAS 107, 17704–17709.

You, Z., Chahwan, C., Bailis, J., Hunter, T., Russell, P., 2005. ATM Activation and Its Recruitment to Damaged DNA Require Binding to the C Terminus of Nbs1. Mol. Cell. Biol. 25, 5363–5379.

Yu, C., Gan, H., Han, J., Zhou, Z.X., Jia, S., Chabes, A., Farrugia, G., Ordog, T., Zhang, Z., 2014. Strand-Specific Analysis Shows Protein Binding at Replication Forks and PCNA Unloading from Lagging Strands when Forks Stall. Mol. Cell 56, 551–563.

Yuan, Y.F., Ren, Y.X., Yuan, P., Yan, L.Y., Qiao, J., 2016. TRAIP is involved in chromosome alignment and SAC regulation in mouse oocyte meiosis. Sci. Rep. 6, 29735.

Zellweger, R., Dalcher, D., Mutreja, K., Berti, M., Schmid, J.A., Herrador, R., Vindigni, A., Lopes, M., 2015. Rad51-mediated replication fork reversal is a global response to genotoxic treatments in human cells. J. Cell Biol. 208, 563–579.

Zeman, M.K., Cimprich, K.A., 2014. Causes and Consequences of Replication Stress. Nat. Cell Biol. 16, 2–9.

Zernik-Kobak, M., Vasunia, K., Connelly, M., Anderson, C.W., Dixon, K., 1997. Sites of UV-induced phosphorylation of the p34 subunit of replication protein a from HeLa cells. J. Biol. Chem. 272, 23896–23904.

Zhang, J., Walter, J.C., 2014. Mechanism and regulation of incisions during DNA interstrand cross-link repair. DNA Repair (Amst) 19, 135–142.

Zhang, M., Wang, L., Zhao, X., Zhao, K., Meng, H., Zhao, W., Gao, C., 2012. TRAF-interacting protein (TRIP) negatively regulates IFN-β production and antiviral response by promoting proteasomal degradation of TANK-binding kinase 1. J. Exp. Med. 209, 1703–1711.

Zhao, H., Watkins, J.L., Piwnica-Worms, H., 2002. Disruption of the checkpoint kinase 1/cell division cycle 25A pathway abrogates ionizing radiation-induced S and G2 checkpoints. PNAS 99, 14795–14800.

Zheng, L., Zhou, M., Guo, Z., Lu, H., Qian, L., Dai, H., Yakubovskaya, E., Bogenhagen, D.F., Demple, B., Shen, B., 2008. Human DNA2 is a mitochondrial nuclease/helicase for efficient processing of DNA replication and repair intermediates. Mol. Cell 32, 325–336.

Zhou, C., Pourmal, S., Pavletich, N.P., 2015. Dna2 nuclease-helicase structure, mechanism and regulation by Rpa. Elife 4, e09832.

Zhou, G., Mihindukulasuriya, K.A., MacCorkle-Chosnek, R.A., Van Hooser, A., Hu, M.C.-T., Brinkley, B.R., Tan, T.-H., 2002. Protein phosphatase 4 is involved in tumor necrosis factor-alpha-induced activation of c-Jun N-terminal kinase. J. Biol. Chem. 277, 6391–6398.

Zhou, J., Chau, C.M., Deng, Z., Shiekhattar, R., Spindler, M.P., Schepers, A., Lieberman, P.M., 2005. Cell cycle regulation of chromatin at an origin of DNA replication. EMBO J. 24, 1406–1417.

Zhu, Z., Chung, W.-H., Shim, E.Y., Lee, S.E., Ira, G., 2008. Sgs1 helicase and two nucleases Dna2 and Exo1 resect DNA double strand break ends. Cell 134, 981–994.

Zhuang, X., Semenova, E., Maric, D., Craigie, R., 2014. Dephosphorylation of barrier-to-autointegration factor by protein phosphatase 4 and its role in cell mitosis. J. Biol. Chem. 289, 1119–1127.

Zimmermann, M., Lottersberger, F., Buonomo, S.B., Sfeir, A., de Lange, T., 2013. 53BP1 regulates DSB repair using Rif1 to control 5' end resection. Science 339, 700–704.

Zou, L., Elledge, S.J., 2003. Sensing DNA Damage Through ATRIP Recognition of RPA-ssDNA Complexes. Science 300, 1542–1548.

Zou, L., Liu, D., Elledge, S.J., 2003. Replication protein A-mediated recruitment and activation of Rad17 complexes. PNAS 100, 13827–13832.